Title
Elucidating Virus and Host Determinants of Nipah Virus Matrix Protein Trafficking and Budding

Author
Park, Arnold

Publication Date
2014

Peer reviewed|Thesis/dissertation

UNIVERSITY OF CALIFORNIA

Los Angeles

Elucidating Virus and Host Determinants of Nipah Virus Matrix Protein Trafficking and Budding

A dissertation submitted in partial satisfaction of the
requirements for the degree Doctor of Philosophy
in Microbiology, Immunology and Molecular Genetics

by

Arnold Park

2014

ABSTRACT OF THE DISSERTATION

Elucidating Virus and Host Determinants of
Nipah Virus Matrix Protein Trafficking and Budding

by

Arnold Park
Doctor of Philosophy in Microbiology, Immunology and Molecular Genetics
University of California, Los Angeles, 2014
Professor Benhur Lee, Chair

Nipah virus is a founding member of the newly described *Henipavirus* genus within the *Paramyxoviridae* family. The henipaviruses first came to light via spillover from their fruit bat reservoir, causing high mortality and instigating great concern. The cause of this high mortality, unusual among the paramyxoviruses, is unknown. Here, we investigate the molecular mechanisms underlying the functions of the Nipah virus matrix protein (NiV-M), which has the central role in virus assembly and budding, yet remains poorly understood. First, we developed new methods to modify the virus and the host to facilitate functional investigations. For the virus, we established and improved a reverse genetics system for Nipah virus to allow efficient rescue of replication-competent viruses from cDNA, which can be modified with mutations or insertion of useful reporter genes. For the host, we used the CRISPR/Cas gene-editing technology to knock-in a destabilization domain tag on all copies of an essential gene, thus allowing inducible knockdown of the tagged protein upon removal of the stabilizing compound

from cell culture. We then investigated NiV-M function with two complementary approaches: mutagenesis of conserved residues and motifs in NiV-M, some of which mediated interactions with host factors, and comprehensive identification of cellular factors and pathways interacting with NiV-M. In doing so, we identified post-translational modifications, palmitoylation and ubiquitination, that regulate NiV-M function, and specifically found that ubiquitination of a conserved lysine within a nuclear localization sequence regulated nuclear-cytoplasmic trafficking of NiV-M. The conserved interaction of NiV-M and other paramyxovirus matrix proteins with nuclear import/export factors, vesicular trafficking pathways, and factors involved in actin cytoskeletal dynamics confirmed the importance of intracellular trafficking pathways for matrix function. Finally, we extended our study of matrix function beyond matrix itself by describing the Nipah virus C protein-mediated recruitment of the cellular ESCRT complex, which was required for efficient NiV-M-driven budding of Nipah virus.

The dissertation of Arnold Park is approved.

Arnold J. Berk

Jeffery F. Miller

Margot E. Quinlan

Benhur Lee, Committee Chair

University of California, Los Angeles

2014

I would like to dedicate this work to my parents, Jae and Yang Park,

whose boundless support made this possible.

TABLE OF CONTENTS

LIST OF FIGURES

Chapter 1.1

Chapter 1.2

Chapter 2.1

Chapter 2.2

Chapter 2.3

Chapter 2.4

Chapter 2.5

Chapter 3.1

Chapter 3.3

Chapter 4.1

Chapter 5.1

LIST OF TABLES

Chapter 2.2

Chapter 2.5

ACKNOWLEDGMENTS

First and foremost, I'd like to thank Benhur Lee, my mentor. I was truly lucky to have ended up with someone with such a unique combination of scientific acumen, passion for research, passion for mentoring, intense curiosity, and a personal touch that reflected your total investment in this enterprise. Such commitment doesn't come without its costs, which is why I am all the more grateful to have been the recipient of your generosity and teaching over the past 6 years. Working with you was a rare opportunity to spend years working with someone with not only the intrepid curiosity to follow the leads wherever they might lead and to strike in new directions, but also the drive and sheer *energy* to make it happen. I don't think I will ever match your level of energy and enthusiasm, but you have given me a great gift in this time of exploration, which has left me hopeful and determined to continue to follow my own passions and curiosity wherever they might lead. Thank you so very much.

I would like to thank all members of the Lee lab, both past and present, for a great experience both in and out of lab. Our scuffles were minor, our collaboration and camaraderie epic. The past 6 years have left so many memories. All of you are to me extended family… Jen, Mike Wolf, Mike Cerrato, Shirley, Patrick, Maggie, Zeynep, Stephan, Jonathan, Tim, Faye, Eric, Kelechi, Karina, Fred, Nic, Woytek, Olivier, Ruixue, Shannon, Mickey, Taylor, Hector, Yao. I particularly want to thank Yao for not only taking me under her wing when I joined the lab, but also being a great support and sounding board, both in and out of lab, as well as unstintingly always willing to help – you are an amazing person. I also wish to thank Hector, who was and continues to be a great role model for me during a formative period of my life. I believe I would be a much different person today if not for you.

I thank all the people who kept me sane and happy in my time at UCLA. In particular, I thank my roommate and best friend, Chuck, who saw me through the hard times and regardless of whatever time, was uniquely able to draw me away from the obsessions of lab.

Thank you to my committee, Drs. Arnie Berk, Jeff F. Miller, and Margot Quinlan. Your unqualified encouragement for the past several years both boosted my confidence as well as motivated me to redouble my efforts. I truly appreciated the helpful advice from all of you not only on the science, but also in regards to my presentation skills and career. Many thanks for your time invested and sincere mentorship.

Finally, I would like to thank my mom, Yang, and my dad, Jae, for their steadfast support, whatever my choices. In the end, their only concern is for my happiness. I love you and am so glad that my time here has made you proud.

I gratefully acknowledge funding from the Cellular and Molecular Biology Training Grant (NIH GM007185) at UCLA, with thanks to Chris Briganti and Drs. Steven Clarke and Sabeeha Merchant. I also thank the Warsaw family for providing funding for the Warsaw fellowship (awarded by the Department of Microbiology, Immunology and Molecular Genetics), which provided critical support for an additional year of research.

The work described here is the combined work of many people. Beyond the specific author contributions listed below, I'd like to acknowledge the hard work of Stephan Chiu and Jonathan Yang, who as undergraduate researchers really helped advance the work in Chapters 3.1 and 4.1, respectively. Drs. James Wohlschlegel and Ajay Vashisht were responsible for the comprehensive mass spectrometric identifications in Chapters 3.3 and 4.1. Much of chapter 2.3 reflects the work of Shannon Beaty. Further, I would like to thank Drs. Alexander Freiberg and Tatyana Yun, at University of Texas - Galveston, who handled most of the biosafety level 4 experiments described in this work.

The following chapters are reprints of published manuscripts:

Chapter 3.2
Yao E. Wang, Arnold Park, Michael Lake, Mickey Pentecost, Betsabe Torres, Tatyana E. Yun, Mike C. Wolf, Michael R. Holbrook, Alexander N. Freiberg, Benhur Lee. (2010) PLoS Pathogens, 6(11): e1001186. DOI: 10.1371/journal.ppat.1001186

Chapter 4.2
Arnold Park, Sohui T. Won, Mickey Pentecost, Wojciech Bartkowski, Benhur Lee. (2014) PLoS One, 9(4): e95101. DOI: 10.1371/journal.pone.0095101

The following chapters are modified versions of manuscripts in submission, with the following

author contributions:

* indicates equal contribution

Chapter 1.1
Arnold Park, Sheli R. Radoshitzky, Jens H. Kuhn, Benhur Lee.

Chapter 2.2
Arnold Park*, Tatyana Yun*, Terence E. Hill, Olivier Pernet, Shannon M. Beaty, Terry L. Juelich, Jennifer K. Smith, Lihong Zhang, Yao E. Wang, Frederic Vigant, Junling Gao, Ping Wu, Benhur Lee*, Alexander Freiberg*.

Chapter 2.4
Omai B. Garner, Tatyana Yun, Olivier Pernet, Hector C. Aguilar, Arnold Park, Thomas A. Bowden, Alexander N. Freiberg, Benhur Lee*, Linda G. Baum*.

Chapter 2.5
Olivier Pernet, Bradley S. Schneider, Shannon M. Beaty, Matthew LeBreton, Tatyana E. Yun, Arnold Park, Trevor T. Zachariah, Thomas A. Bowden, Peta Hitchens, Christina M.R. Kitchen, Peter Daszak, Jonna Mazet, Alexander N. Freiberg, Nathan D. Wolfe, Benhur Lee.

Chapter 3.3
Mickey Pentecost, Ajay A. Vashisht, Talia Lester, Tim Voros, Shannon M. Beaty, Arnold Park, Yao E. Wang, Tatyana E. Yun, Alexander N. Freiberg, James A. Wohlschlegel, Benhur Lee.

VITA

2005	A.B., Biology Harvard University
2005 – 2008	Research Assistant Harvard School of Public Health
2010, 2012	Teaching Assistant Department of Microbiology, Immunology and Molecular Genetics University of California, Los Angeles

PUBLICATIONS

1. **Park A**, Won ST, Pentecost M, Bartkowski W, Lee B. CRISPR/Cas9 allows efficient and complete knock-in of a destabilization domain-tagged essential protein in a human cell line, allowing rapid knockdown of protein function. PLoS One, 2014. 9(4):e95101.

2. Wang YE, **Park A**, Lake M, Pentecost M, Torres B, Yun TE, Wolf MC, Holbrook MR, Freiberg AN, Lee B. Ubiquitin-regulated nuclear-cytoplasmic trafficking of the Nipah virus matrix protein is important for viral budding. PLoS Pathogens, 2010. 6(11):e1001186.

3. Aliprantis AO, Ueki Y, Sulyanto R, **Park A**, Sigrist KS, Sharma SM, Ostrowski MC, Olsen BR, Glimcher LH. NFATc1 in mice represses osteoprotegerin during osteoclastogenesis and dissociates systemic osteopenia from inflammation in cherubism. J Clin Invest, 2008. 118(11):3775-3789.

4. Rengarajan J, Murphy E, **Park A**, Krone CL, Hett EC, Bloom BR, Glimcher LH, Rubin EJ. Mycobacterium tuberculosis Rv2224c modulates innate immune responses. PNAS, 2008. 105(1):264-269.

ABSTRACT PRESENTATIONS

* indicates equal contribution

1. **Park A***, Yun TE*, Hill TE, Pernet O, Beaty SM, Juelich TL, Smith JK, Zhang L, Wang YE, Vigant F, Gao J, Wu P, Freiberg AN*, Lee B*. 2014. Isogenic comparisons of recombinant chimeric henipaviruses reveal functional differences between Nipah and Hendra virus structural proteins. American Society for Virology 33rd Annual Meeting in Fort Collins, CO.

2. **Park A**, Chiu S, Lee B. 2012. Conserved mutants of Nipah virus matrix protein reveal defects in its budding pathway. Keystone Symposium on the Cell Biology of Virus Entry, Replication and Pathogenesis in Whistler, Canada.

3. **Park A**, Wang Y, Vashisht A, Pentecost M, Wohlschlegel J, Lee B. 2011. Interrogating the intracellular trafficking, assembly, and budding pathway of Nipah virus matrix protein. UCLA Molecular Biology Institute Annual Retreat in Lake Arrowhead, CA.

4. **Park A**, Wang Y, Lee B. 2010. HIV-1 Gag enhances the ESCRT-independent budding of Nipah virus matrix protein. American Society for Virology 29th Annual Meeting in Bozeman, MT.

CHAPTER 1

INTRODUCTION

CHAPTER 1.1

THE HENIPAVIRUSES, EMERGENT AND DEADLY PARAMYXOVIRUSES

INTRODUCTION

Henipaviruses were not discovered until 1994, when a novel virus, later called Hendra virus (HeV), was identified as the etiological agent of fatal viral encephalitis in Hendra, Australia. Another virus closely related to HeV, Nipah virus (NiV), emerged in Malaysia in 1998. Subsequently, the genus *Henipavirus* was established within the family *Paramyxoviridae* as a taxonomic home for both HeV and NiV. HeV and NiV are high-consequence pathogens that are thought to be potential starting materials for biological weapons construction because they cause diseases with high case fatality rates; have the potential for aerosol transmission; are easily grown in cell culture to high titers; and have an unusually wide host range that encompasses humans and livestock, such as pigs and horses. The recent discovery of new henipaviruses of unknown virulence and spillover potential in bats[1-3] emphasizes the need to deepen our understanding of this emergent group of viruses.

As disease agents posing a severe threat to both agricultural livestock and human health, HeV and NiV are considered "overlap" Select Agents regulated by both the US Animal and Plant Health Inspection Service (APHIS) and the US Centers for Disease Control and Prevention (CDC). As is the case for most Select Agents, approved therapeutics for human henipavirus infections currently do not exist. Promisingly, however, there have been rapid advances in developing new therapies and in re-purposing existing US FDA-approved drugs for use in henipavirus infection treatment.

HISTORY AND EMERGENCE OF HENIPAVIRUSES

Hendra Virus

Thoroughbred horse racing has long been one of the great pastimes of Australia. The public imagination was struck in September 1994 when a prominent racehorse trainer, Vic Rail, 13 of his horses, and another horse from a neighboring property died of a sudden illness in Hendra, Australia. Rail's stablehand also became ill, but recovered after an extended convalescence. The

illness in both horses and patients was characterized by respiratory distress with neurological signs, in horses culminating in blood-tinged, frothy nasal discharge.[4,5]

A major outbreak investigation ensued, resulting in the identification of a new "equine morbillivirus" from infected horse and human samples. Experimental inoculation of this virus into naïve horses reproduced the disease.[6] Preliminary phylogenetic analysis resulted in the placement of this new agent in the genus *Morbillivirus* (of which measles virus is the prototype member) in the family *Paramyxoviridae*. As this "equine morbillivirus" had unique molecular and pathogenic features that distinguished it from other morbilliviruses, the agent was renamed Hendra virus (HeV) and finally reclassified in a novel paramyxoviral genus, *Henipavirus*.[7]

A year after the Hendra outbreak, a horse stud owner died of relapsed encephalitis and was retrospectively diagnosed with HeV infection, originating from an encephalitic illness that predated the Hendra outbreak by several weeks. This single infection, which had no known epidemiological link to the Hendra outbreak, occurred 970 km north of Hendra, near Mackay. As in the Hendra outbreak, transmission to the trainer involved horses, two of which died.[8] Since the 2004 outbreaks, HeV infection has emerged only periodically and briefly, in 1999 and 2004, but then yearly from 2006, and then in a truly accelerated fashion from 2011, all in Australia and ranging up and down the east coast (Figure 1-1).[9] All disease outbreaks involved horses with a case fatality in horses of 84%,[10] and of the seven human cases, including the 1994 outbreaks, four died. Considering that retrospective inspection of laboratory records and historical samples did not reveal signs of pre-1994 spillover of HeV to horses,[11] HeV infection truly appears to have emerged from its natural reservoir in or around 1994. The lack of an epidemiological link between the outbreaks[11] suggested potential spillover from another animal reservoir to the horses. However, extensive sampling of domestic animals and wildlife initially revealed no sign of HeV.[11-14] A more targeted investigation based on outbreak characteristics (host should be present in both outbreak locales, be able to move or interchange between the locales, and plausibly have contact with horses) revealed that fruit bats of genus *Pteropus*

(Figure 1-2), otherwise known as “flying foxes”, had anti-HeV antibodies[15] and sometimes were infected with HeV itself.[16]

Nipah Virus

The emergence of NiV has several parallels to that of HeV, but with much more dramatic consequence. NiV is named after Sungai Nipah, Malaysia, the home village of the patient from whom NiV was first isolated. NiV, like HeV, emerged from pteropid fruit bats, but in this case spilled over to domesticated pigs (*Sus scrofa*), which served as highly effective amplifying hosts. The first recorded potential NiV spillover occurred in 1997, with unusual pig deaths at pig farms near Ipoh, Malaysia that were attributed at the time to classical swine fever. However, retrospective analysis of serum samples from several patients presenting with encephalitis in 1997 detected anti-NiV antibodies.[17] Beginning in September 1998, also near Ipoh, pigs and pig farmers became ill in a major outbreak of febrile encephalitis with respiratory symptoms. The mosquito-borne Japanese encephalitis virus (JEV), endemic to Southeast Asia, was immediately suspected, especially since domestic pigs are known to serve as an amplifying host for JEV,[18] and also because 4 of 28 initial human cases tested positive for anti-JEV antibodies.[17] Despite extensive anti-JEV measures, however, including mosquito control and a JEV vaccination campaign,[19] the outbreak continued unabated, spreading into neighboring districts and afflicting increasing numbers of pigs and humans. Worse, the outbreak spread to Singapore via exported infected pigs.[20] Furthermore, the outbreak included widespread disease mainly afflicting adults,[21] whereas Japanese encephalitis is asymptomatic in the vast majority of cases and is more likely to cause disease in children.[18] Also, cerebrospinal fluid from an infected patient gave rise to syncytia (multinucleated cells formed by cell-cell fusion) in Vero cell culture, indicative of a pH-independent fusion mechanism of the infectious agent.[22] Such formation is uncharacteristic of JEV, which has a pH-dependent fusion mechanism. Finally, the US Centers for Disease Control and Prevention determined by cross-reactive immunofluorescence, serology, and sequence analysis that the novel agent was closely related to HeV.[23]

At the end of the 1998-1999 outbreak, at least 294 human infections resulting in clinical encephalitis had been recorded in Malaysia and Singapore, of which 106 were fatal.[17,20] The inclusion of milder non-encephalitic cases (as determined by exposure to infected pigs and seroconversion, and a number of which later developed late onset encephalitis) would increase the total number of cases to more than 360.[24,25] Over a million pigs were culled in an effort to contain the outbreak, resulting in severe economic damage and widespread changes to the pig farming industry.[26,27] Subsequent outbreaks of NiV infection have occurred in Bangladesh and adjacent areas of India on an almost yearly basis (Figure 1-1). In contrast to the Malaysian outbreak, these subsequent spillovers from pteropid bats have mainly occurred without the involvement of a domestic animal intermediate, and generally have had higher case fatality rates, ranging from 40 to 100%.[28] These differences may be the result of differences among disparate NiV strains, the standard of care in Bangladesh/India versus Malaysia, or sociocultural factors unique to Bangladesh/India.[29,30] For example, a major route of spillover during the Bangladesh outbreaks is the consumption of fresh date palm sap, a seasonal delicacy that can become contaminated with fruit bat saliva or excreta during collection (Figure 1-3).[31]

Newly Identified Henipaviruses

After nearly two decades of intensive investigation of HeV and NiV, evidence of novel henipaviruses in bats of diverse species beyond the *Pteropus* genus have been cause for increased public health concern.[2,3,32,33] These new findings extended the potential geographic distribution of henipaviruses from Southeast Asia/Australia to Africa and Central/South America (Figure 1-1). At least one novel henipavirus could be isolated in culture, but was found to be non-pathogenic in small animal models.[32] The discovery of a potential henipavirus spillover to humans in Cameroon, however, emphasizes the need to both increase vigilance and deepen our understanding of this latent pool of henipaviruses.[3] Human sera from Cameroon capable of neutralizing NiV were significantly associated with bat butchering in areas of intensive deforestation.[3] This association highlights the role of environmental changes and

specific human behaviors in determining the risk of zoonotic transmission. Although the pathogenicity and virulence of newly discovered henipaviruses remain to be determined, the repeated misdiagnosis of NiV as Japanese encephalitis in Southeast Asia remains a cautionary tale. Henipavirus-derived illness may often be ascribed to other encephalitic diseases known to occur in the affected area.

EPIZOOTIOLOGY AND EPIDEMIOLOGY OF HENIPAVIRUSES

Pteropid (fruit) bats appear to be the major reservoir host for HeV and NiV, as no appreciable signs of HeV and NiV infections have been found in other wildlife or domestic animals.[11,34] Anti-HeV or anti-NiV antibodies are highly prevalent in pteropid bat populations throughout Southeast Asia and Australia[34,35]; HeV and NiV have been isolated from *Pteropus* fruit bats throughout their geographic range[34]; and all known outbreaks of HeV and NiV infection are linked to exposure of domestic animals or humans to fruit bats or their excretions.[30] Further, experimental infection of *Pteropus* bats belonging to different species with HeV or NiV did not result in clinical signs of infection, despite inconsistent signs of seroconversion, viral replication in tissues, and virion excretion in urine.[36-39] These data support the hypothesis that HeV and NiV are not pathogenic in their natural hosts, and may persist subclinically in *Pteropus* bat populations.

Despite their apparent long co-evolutionary history with bats and likely endemic nature,[34] HeV and NiV emerged to cause human disease suddenly and nearly simultaneously, likely signaling common factors driving their emergence. A retrospective study of environmental factors and man-driven changes in Malaysia identified slash-and-burn agriculture with concomitant loss of forest habitat, a resulting impenetrable smoke haze that led to crop failures, and severe drought as precipitating factors.[40] Fruit bats were driven to populate cultivated fruit orchards, which were often located adjacent to pig farms, thus providing a means of transmission. In one plausible scenario, half-eaten fruits contaminated with NiV-infected bat

saliva are dropped into a pig farm and then eaten by the pigs. Indeed, such half-eaten fruits were found in pig farms near the epicenter of the 1998-1999 NiV encephalitis outbreak.[40] Similar environmental and man-made pressures facing fruit bat populations across Southeast Asia and Australia are likely behind the persistent upsurge in HeV and NiV spillovers in recent years.

Hendra Virus

All seven known human cases of HeV infection resulted from intimate contact with sick horses. HeV is highly virulent in horses, and infection often culminates in copious production of infectious respiratory secretions.[35] Human infections were traced back to efforts to save these horses without the use of personal protective equipment (PPE). A horse trainer, for example, attempted to force-feed a sick mare with abrased bare hands.[5] However, such cases of horse-to-human transmission remain the exception. Many other people who were also highly exposed to contaminated horse bodily fluids, even to fluids from horses that were implicated in HeV transmission to other humans, did not develop signs of HeV infection.[30] With increased public awareness of the risk of HeV transmission and the corresponding increase in proper use of PPE, the risk of spillover to humans has been mitigated.[4] The introduction of a HeV vaccine for horses in 2012, Equivac HeV®, will hopefully further minimize human transmission risk.

It remains to be elucidated how horses become infected in the first place. Equine cases of infection may result from horses grazing on pastures contaminated with bat excreta or remains of half-eaten fruit.[11,34] Infected horses inefficiently transmit the virus, even to other horses, but some horse-to-horse transmission may occur through licking of infectious nasal discharge.[11] Respiratory transmission of HeV has never been demonstrated experimentally or during natural infection.[34] The inefficiency of HeV transmission is buttressed by findings that despite a continuous low prevalence of HeV in *Pteropus* bats in Queensland and New South Wales,[41] people having extensive contact with *Pteropus* bats in these areas, with bat bites and exposures to bat blood in many cases, had no sign of HeV exposure.[42] Direct comparisons of NiV and HeV

infection in golden hamster and mouse animal models suggest that HeV may be less efficient in infecting through the intranasal route.[43,44]

Nipah Virus

Malaysia outbreak, 1998-1999. During the large Malaysia outbreak, pigs served as a highly efficient amplifying reservoir, contracting infection and transmitting NiV so efficiently that the infection rate among pigs at affected farms approached 100%.[27] The risk to humans posed by this spread was exacerbated by the mild illness NiV caused in the pigs, with a lethality of less than 1-5% and often presenting asymptomatically.[27] Unsuspecting farmers thus moved asymptomatic pigs to other farms and slaughterhouses, quickly spreading the virus. A subset of infected pigs developed febrile illness, respiratory signs such as labored breathing and harsh non-productive cough, and often neurological signs such as myocloni and uncoordinated gait.[27] Nearly all human cases during the Malaysia NiV encephalitis outbreak can be attributed to direct contact with or close proximity to infected pigs, and most cases were pig farmers.[30,45,46] One person who denied any recent proximity to pig farms in fact worked repairing pig cages, suggesting that the virion-containing secretions remained infectious on surfaces for extended periods of time.[47] A few human infections may have resulted from secondary transmission through dogs, which were commonly infected during the outbreak.[11,46,48] Evidence of human-to-human transmission is very limited. A large cohort study of 393 health-care workers intimately involved in caring for NiV-infected patients identified only three nurses who seroconverted and had potential illness, despite many reported high risk exposures.[49] Risk may have been minimized by precautions taken by the healthcare workers, because patients clearly shed infectious NiV in respiratory secretions and urine, especially during the early phase of illness.[50] Human-to-human transmission possibly may have played a role in the NiV outbreak, although the epidemiological record does not provide such evidence. Finally, retrospective investigations appear to show that NiV was causing disease in pigs as early as 1996, but that the mild symptoms and rough similarity to other diseases (e.g., classical swine fever) did not raise

suspicion of anything unusual.[11,51] The advent of increasingly inexpensive, high-throughput sequencing may make disease surveillance and agent identification more likely to catch emerging pathogens such as NiV in the future.

Bangladesh and India, 2001-present. In comparison to the Malaysia NiV encephalitis outbreak, subsequent outbreaks in Bangladesh and India are of greater concern because of evidence of clear chains of human-to-human transmission.[30] As in Malaysia, infected patients shed NiV in their bodily fluids including saliva,[52,53] and the intimate care for sick family members, involving physical contact, sharing utensils and food, and sleeping in the same bed to provide them comfort, greatly increased the risk of transmission.[54] The longest documented transmission chain involved five generations, with the third generation involving a religious leader who infected 22 family members and followers.[54,55] A major 2001 outbreak in Siliguri, India was also characterized by hospital-associated transmission: one admitted patient became the source of over 40 subsequent infections within a hospital and nursing homes. As with the outbreak in Malaysia, Japanese encephalitis was initially suspected, and the causative agent was not identified as NiV until samples were retrospectively analyzed several years later.[56]

The outbreaks in Bangladesh and India are also notable for the apparent lack of a domestic animal intermediate between the *Pteropus* bat reservoir and humans. Although a few incidents appear to involve domestic animals such as cows, pigs, or goats,[57-59] the major route of spillover has been the consumption of contaminated fresh date palm sap.[31] Date palm trees are tapped for their sweet sap in the winter, and bats often lick the sap stream. Defecation and urination into or near the collection pots, or even drowned dead bats, have been observed.[31,60] Fortunately, the use of a simple bamboo skirt to cover and protect the sap stream, a method local to northwest Bangladesh that has not been consistently or widely used, appears to be highly effective in preventing contamination (Figure 1-3).[61] More widespread use of this and other interventions to minimize risk would help the affected regions of the Indian subcontinent break out of its cycle of yearly NiV encephalitis outbreaks.

CLINICAL PRESENTATION OF HENIPAVIRUS INFECTIONS

The incubation period of HeV or NiV infection and illness typically ranges from a few days to fourteen days.[62] Although information on HeV infection is limited due to the few human cases, the clinical signs and pathology of HeV and NiV infections are similar.[63] The hallmarks of henipavirus pathogenesis are extensive vasculopathy, respiratory distress, and encephalitic disease with corresponding neurological symptoms. Respiratory and encephalitic symptoms may appear to varying degrees: during the first Malaysia NiV disease outbreak, clinical signs were mainly encephalitic in nature with minor pulmonary involvement, whereas in subsequent outbreaks in Bangladesh, encephalitis was more commonly joined by severe respiratory distress.[29,59] Whether these differences are due to genetic differences among viral variants, the route of transmission, or other factors is an active area of investigation.

Clinical Signs and Symptoms

Neurological signs and symptoms may include fever, headache, confusion, myocloni, seizures, meningism, and motor deficits including areflexia and hypotonia.[5,29,45,56,64,65] Brain stem involvement, a poor prognostic factor, may be evidenced by a reduced level of consciousness, vomiting, abnormal pupillary and doll's eye reflex, hypertension, and tachycardia.[45] Cerebrospinal fluid is characterized by elevated white cell counts and/or protein concentration in a substantial proportion of cases.[45,66]

A minority of survivors (less than 10%) of HeV and NiV infection may experience relapsing encephalitis after apparent recovery or even initial asymptomatic or apparently non-encephalitic infection. Relapse may occur soon after apparent recovery or long after, with an average of eight months and up to 11 years documented.[62] Even without relapsing or progressive disease, a substantial proportion of survivors may experience long-term neurological deficits.[67,68]

Although the Malaysia outbreak of NiV disease was mainly characterized by encephalitic signs, a substantial proportion of patients still developed pulmonary signs such as cough and

abnormal chest radiographs.[20,45,69] More severe pulmonary symptoms, as seen in subsequent NiV disease outbreaks and also some cases of HeV infection (e.g., a horse trainer who developed progressive respiratory failure[5]), may also include atypical pneumonia, difficulty breathing, and acute respiratory distress syndrome.[29,62]

Pathology

Infection of microvascular endothelial cells leads to systemic vasculitis, thrombosis and resultant microinfarction, especially in major organs such as kidneys, heart, lungs, and brain.[62,70] Focal perivascular necrosis or hemorrhage is seen in highly vascular organs such as the spleen.[71] Occasional syncytia (giant multinucleated cell) formation can been seen in the endothelium (Figure 1-4) and among parenchymal cells of major organs. In the brain, discrete plaque-like lesions with varying degrees of necrosis, edema, and inflammation likely correspond to the small hyperintense lesions in both grey and white matter seen by MR (Figure 1-4).[62] The dual pathology of vasculitis with associated microinfarction and direct infection of parenchyma of major organs is a distinguishing feature of henipavirus pathogenesis.[62] Tissue damage in the central nervous system from both microinfarction and direct infection of neuronal cells distinguishes henipavirus infections from other viral encephalitic diseases.[72] Relapse encephalitis appears to result from recrudescent infection, with extensive parenchymal necrosis, edema and inflammation corresponding to confluent lesions seen in MR scans (as opposed to the more discrete foci usually seen during acute encephalitis during early illness). Pathology associated with relapsing encephalitis is only found in the central nervous system, and no sign of vasculopathy is present, even in the brain.[25,73]

MOLECULAR BIOLOGY OF HENIPAVIRUSES

Virus structure

Henipaviruses are negative-sense RNA viruses that produce enveloped virions. Henipaviruses are currently classified as members of the genus *Henipavirus*, family *Paramyxoviridae*, subfamily *Paramyxovirinae*, order *Mononegavirales*.

Virus structure. Like other paramyxoviruses, Hendra and Nipah virions have pleomorphic shapes, usually more spherical although sometimes filamentous as well (Figure 1-5), and range in size from under 200 nm to well over 1,000 nm in diameter.[74,75] The virions contain helical ribonucleocapsids with the herringbone appearance characteristic of, and unique to, the paramyxoviruses (Figure 1-5). A unique feature of Hendra virions is the frequent presence of a double fringe surrounding the particle,[75] which may be due to differing lengths or conformations of the envelope proteins; in contrast, Nipah virions predominantly display a single fringe.

Virus genome. Like all mononegaviruses, henipaviruses have a linear, monopartite, single-stranded RNA genome of negative polarity. The overall structure of henipavirus genomes is similar to those of other paramyxoviruses, with 3' leader and 5' trailer sequences at the termini of the genomes that act as virus-specific promoters, 5' and 3' untranslated regions (UTRs) flanking each gene, and a conserved intergenic signal between each gene.[76] With a few recently described exceptions, henipaviruses have the longest known paramyxoviral genomes (≈18 kb). The especially long 3' UTRs are unique features of henipavirus genomes and account for much of the extra length compared to other paramyxoviruses (≈15 kb).[77] The functional relevance of these long UTRs remains to be determined.

Viral proteins. Henipavirus genomes contain six genes, which encode a nucleocapsid protein (N), phosphoprotein (P), matrix protein (M), fusion protein (F), attachment glycoprotein (G), and large RNA-dependent RNA polymerase (L). N encapsulates the genome, thereby forming the ribonucleoprotein complex. Like the genomes of other paramyxoviruses, henipavirus genomes have nucleotide lengths that are evenly divisible by six, a feature likely due to the periodicity of N protein encapsidation of the genome. P and L together form the polymerase complex, which replicates the viral genome and transcribes viral mRNAs.

M is responsible for assembly and budding of virions and underlies the viral envelope. M transits through the nucleus as well, although the ultimate significance of this transit for henipavirus replication and pathogenesis remains unclear. G binds to the cellular receptor(s), and F catalyzes the membrane-membrane fusion responsible for viral entry. G and F can also catalyze cell-cell fusion, leading to syncytia (giant multinucleated cells) formation, which is a hallmark of henipavirus infection (Figure 1-5). The henipavirus attachment protein is unique among paramyxoviruses in that it does not possess any hemagglutinin activity (although it should be noted that morbilliviruses such as measles virus will only agglutinate red blood cells from certain primate species).[78] The tissue tropism of HeV and NiV is determined by entry receptor use. The receptor tyrosine kinase ephrin-B2 serves as an entry receptor for all known henipaviruses,[32,79,80] but at least HeV and NiV can also use the related ephrin-B3 as an alternative receptor.[81,82] As cellular factors that are critical during embryogenesis, ephrin-B2 and -B3 are highly evolutionarily conserved. This high level of conservation contributes to the unusually wide potential host range of HeV and NiV, which have been shown to infect mammals spanning six orders.[83] Ephrin-B2 and -B3 from a wide range of mammals allow viral entry,[84] chicken embryos are susceptible to NiV infection,[85] and even zebrafish ephrin-B2 can serve as an entry receptor.[70] The tropism of the henipaviruses is also not restricted by the cellular protease required for F protein cleavage, a maturation step required to render it fusion-competent. Unlike some paramyxoviral F proteins that require a protease of limited tissue distribution, the henipavirus F protein uses the ubiquitously expressed endosomal protease cathepsin L,[86,87] thereby further extending tissue and possibly host tropism.

PATHOGENESIS

The pathogenesis of henipavirus encephalitis has been examined predominantly using animal models. The oronasal route of infection is used most often during such experiments as it reflects at least one type of natural transmission and might also simulate exposure during a biological

attack.[88] Similar to results obtained *in vitro*, *in vivo* tropism is predominantly determined by the absence or presence of henipavirus receptors on potential target cells.

Ephrin-B2 is highly expressed on the endothelial and smooth muscle cells that line arterial vessels, lungs, and brain. The human airway epithelium expresses both ephrin-B2 and -B3,[89] and upon infection, the virus likely crosses the epithelium via limited basolateral virion release, while disruption of the epithelium via cell-cell fusion may also facilitate systemic entry. In many animal models of Nipah encephalitis, the alveolar epithelium tests immunopositive for NiV antigens, and the alveolar wall frequently undergoes fibrinoid necrosis.[90] Interestingly, in pigs, an increased number of alveolar macrophages is a consistent histological feature. In human lung tissue, viral antigen is found in multinucleated giant cells located in the alveolar space.[71] Multinucleated giant cell formation is a product not only of alveolar macrophage fusion, which is generally a prominent feature of chronic inflammatory conditions, but also of NiV-induced syncytia formation. Transmigration of infected alveolar macrophages may serve as a "Trojan horse" for the virus to gain systemic access via the microvasculature. Cell-free and cell-associated viremia then result in systemic infection.[91]

Ephrin-B3 expression is mostly restricted to the central nervous system (e.g., brainstem), which correlates with the observation of antemortal brainstem dysfunction noted during henipavirus encephalitis.[45,81] Henipaviruses likely gain access to the brain via basolateral release from brain microvascular endothelial cells, disruption of the blood-brain barrier as a result of cell-cell fusion and vasculitis, and transmigration of "Trojan horse" inflammatory macrophages. It is also possibly that henipaviruses access the central nervous system more directly via infection of the olfactory epithelium and resultant spread along the olfactory neurons.[92,93]

There are clear differences between HeV and NiV infections in regard to the localization of initial infection in animal models despite their use of the same entry receptors,[43,44] which has yet to be understood. The mechanism of foodborne NiV transmission also is unclear since

digestive tract epithelium does not express ephrin-B2 or -B3.[70] Virus infection most likely occurs via accessible and susceptible cells in the oropharyngeal mucosa, such as those of tonsilar tissues and salivary glands.

The henipaviruses partly owe their virulence to effective antagonism of host immune responses. Interferons (messengers of innate immunity that trigger extensive anti-viral responses) bind extracellularly to interferon receptors, which usually triggers an intracellular signal cascade that includes the critical immune signaling factor signal transducer and activator of transcription 1 (STAT1). Like other paramyxoviruses, HeV and NiV encode several nonstructural proteins from their P gene, the C, V, and W proteins, which antagonize innate immune signaling. The P, V, and W proteins have identical N-termini that bind and inhibit STAT1, partly by sequestering STAT1 and thus inhibiting transcription of interferon-inducible genes.[94-97] The P gene products also antagonize signaling from other intracellular sensors of infection, such as TLR3 and Mda-5,[98-100] which sense double-stranded RNA (an intermediate of viral replication) in endosomes and the cytoplasm, respectively.

In contrast to the host species-specific inhibition of interferon signaling induced by some paramyxoviruses,[101] NiV can inhibit interferon signaling in cells from a number of tested mammals,[102] consistent with the ability to cause disease in a wide range of hosts. The high virulence of henipaviruses in the "wrong" host may therefore be a function of their broad tissue tropism *in vivo*, their ability to gain systemic access, and their inhibitory effect on immune responses.

HENIPAVIRUSES AND BIOLOGICAL WEAPONS

HeV and NiV are classified as CDC Category C Bioterrorism agents due to their (1) availability, (2) ease of production and dissemination, and (3) potential for high morbidity and lethality.

Availability

HeV and NiV are readily available from tissues or fluids from patients during frequent, recurring disease outbreaks as well as by isolation from their natural bat reservoirs. Further, reverse genetics systems are available in biosafety level 4 laboratories for the rescue of henipaviruses directly from plasmids.[103,104] *De novo* access to, and modification of, henipaviruses can therefore be accomplished by a determined hostile group with access to resources and the relevant technical expertise.

Ease of Production and Dissemination

Henipaviruses can be grown to very high titers, up to 10^8 $TCID_{50}$/ml or PFU/ml,[105] in a wide range of cell lines.[106] Although henipaviruses are highly sensitive to temperature variation and dessication, henipaviruses can persist for days under certain conditions.[108] It is possible, therefore, that under optimal conditions henipaviruses could be maintained at high titer for extended periods of time. Henipaviruses infect a wide range of hosts, including domestic animals such as dogs and livestock that could serve as amplifying vessels to further spread infection. Although NiV and HeV clearly have the potential to infect through aerosol, this has not been conclusively shown, either experimentally or from the natural history[88,108]; limited epidemiological evidence suggests, however, that some human cases of NiV infection in Bangladesh may have resulted from exposure to coughing.[55,109] Also restricting the biological weapons potential of henipaviruses is the lack of sustained human-to-human transmission: the longest documented chain of transmission was five generations.[54,55] A naturally occurring or intentionally mutated strain with higher transmission efficiency would be required to sustain an epidemic; an expanding pandemic, however, might not be a required or desired goal of a bioterror attack.

Potential for High Morbidity and Lethality

HeV and NiV cause disease with very high case fatality rates, ranging from 40-100% in recent outbreaks.[28] Survivors of disease or asymptomatically infected people may present years later with relapsing or late onset encephalitis, indicating occasional persistence of viral infection.[62]

DIAGNOSIS

In a bioweapons attack or other mass casualty scenario, rapid diagnostic methods must be employed to identify the causative agent(s), and these methods may be differentiated by whether or not the specific agent must be suspected prior to testing, and how quickly the results can be obtained. Under normal circumstances, henipavirus etiology would not be suspected without exposure to risk factors (contact with bats, ill persons or domestic animals, or consumption of raw date palm sap) in the currently affected areas of Southeast Asia and Australia. Henipavirus etiology might also be considered throughout the known geographic range of bats known to harbor henipaviruses (Figure 1-1) if the responsible agent is unknown, with the initial misdiagnosis of NiV as Japanese encephalitis virus remaining a cautionary tale. These factors do not apply in a bioweapons or bioterrorism event, however. The clinical presentation of henipaviruses with encephalitic and/or respiratory symptoms cannot be readily distinguished from other viral and nonviral causes of encephalitis, and diagnosis would require epidemiological and laboratory investigation. Given the broad host range of henipaviruses, the involvement of sick domestic or local animals might suggest potential henipavirus etiology.

Detailed, recent reviews of henipavirus diagnosis may be found elsewhere[105,110,111]; the available methods are discussed below.

RT-PCR. If henipaviruses are suspected, henipavirus-specific polymerase chain reaction (PCR) or real-time PCR should be performed on RNA extracted from patient samples. Prospective samples include serum, whole blood (detectable viremia may be cell-associated[91]), urine, nasopharyngeal aspirates, throat swabs, cerebrospinal fluid, or tissue samples from highly affected tissues such as brain, lung, kidney, or spleen.

Detection of Henipavirus Antigens. Characterized anti-henipavirus antibodies can be used to detect viral antigens in formalin-fixed tissues. Similarly, immunofluorescence with anti-henipavirus antibodies can be performed on infected cell cultures.

Detection of Anti-henipavirus Immune Responses. A number of methods exist for detection of anti-henipavirus antibodies in sera of infected patients. Specific IgM responses develop in virtually all patients by the third day postexposure, and the slower IgG response encompasses virtually all patients by after two weeks of infection.[29,112] Detection of serum antibodies is very useful for diagnostics as antibodies are more stable than viral RNA over time and under different conditions. Furthermore, viremia can be difficult to detect when patients are symptomatic. Serum neutralization of replicating virus is considered the gold standard serological test, although this test requires BSL-4 containment.[105] Surrogate neutralization tests, which can be performed at BSL-2 conditions, offer a combination of high sensitivity and high specificity. Such tests include the use of vesicular stomatitis Indiana virus pseudotyped with the henipavirus envelope proteins[113-115] or a Luminex platform-based assay assessing the ability of sera to inhibit the binding of the henipavirus receptor to microbeads coated with henipavirus attachment protein.[116] Enzyme-linked immunosorbent assay (ELISA) variations on this test using infected cell lysate or recombinant henipavirus proteins have been commonly used as a frontline assay due to simplicity and affordability, but typically have a relatively high false positive rate.[105]

Virus Isolation. Viral etiology may be suspected if cells incubated with filtered patient samples develop cytopathic effects. Henipaviruses grow efficiently in a wide range of cell lines, including Vero E6 cells.[117] Syncytia formation in cell culture would implicate enveloped viruses with a pH-independent fusion mechanism, which include the henipaviruses (Figure 1-5). Electron microscopy on viral preparations and infected cells could implicate a henipavirus as the potential agent. As new or modified henipaviruses may have different characteristics, however, any final diagnosis requires multiple routes of confirmation. In contrast to sequencing, virus isolation is a days-long process (2–5 days usually pass until cytopathic effects become visible), and two rounds of 5 days each are recommended before virus recovery is judged unsuccessful.[105,110] Furthermore, for an outbreak suspected to be caused by a highly virulent

agent, virus isolation attempt should be performed under high-level biosafety containment. Nevertheless, isolation and characterization of the agent remains the most conclusive demonstration of etiology.

Next-generation Sequencing. Next-generation sequencing (NGS) is slowly becoming more widely available and will enable the identification of known and unknown henipaviruses. As the cost and speed of NGS continue to decrease, a rapid and routine measure using NGS in a suspected outbreak is increasingly possible following RNA extraction and RT-PCR.[105] Since henipaviruses only rarely infect humans, detection of henipavirus sequences would not normally be expected, and an appreciable presence of henipavirus sequence in multiple samples would suggest potential henipavirus etiology. Henipavirus-specific NGS is already becoming routinely used during post-outbreak investigations to determine the characteristics of new henipavirus isolates.[105,118]

MEDICAL MANAGEMENT

Licensed therapeutics for treatment of henipavirus infection in humans are not available. Thus, medical management of henipavirus infections is supportive. Mechanical ventilation is required if the patient becomes comatose or develops acute respiratory distress syndrome. Appropriate measures should be taken as for any potentially highly contagious pathogen, including quarantine and use of PPE and engineering controls such as negative air flow, if available; careful handling of clinical specimens; and rapid epidemiological investigation (with particular attention paid to potential spread via domestic animals) and identification of high-risk contacts. Despite the lack of specifically recommended therapeutics, a number of potential treatments with varying levels of supporting evidence should be considered in the event of a bioweapons or mass casualty event. Some of the proposed therapeutic interventions discussed below may also be appropriate in the case of accidental exposure or as prophylaxis for frontline responders to a potential outbreak.

Passive Immunotherapy

Active vaccination is highly effective in animal models[83] and was the basis for the recently approved Equivac HeV® vaccine for horses. This vaccine contains a soluble version of the HeV attachment envelope protein, which stimulates the production of neutralizing anti-HeV antibodies and thus provides protection against HeV infection.[119] However, an active vaccination approach for henipaviruses is unlikely to be a practical strategy on a population-wide basis in humans for a number of reasons. Compared to veterinary vaccines, human vaccines have higher regulatory hurdles. In addition, such vaccines would be truly useful only for a few people. Few cases have occurred during natural outbreaks, and the likelihood that populations outside of affected locations will be exposed to a pathogenic henipavirus is low. However, the risk-benefit calculations may be different for frontline responders to suspected outbreaks.

Passive immunotherapy may be highly efficacious as postexposure treatment. In recent postexposure prophylaxis studies, ferrets and grivets received 1–2 doses of a human monoclonal antibody with neutralizing activity against HeV and NiV attachment proteins 10–72 hours after virus challenge, which completely protected the animals from disease.[120,121] The antibody has been offered to individuals with high risk of HeV exposure and will be evaluated for safety in a human clinical trial in Australia.[122] Although further development of this strategy may not be economically viable if left to the market, such monoclonal antibodies warrant serious consideration as a stockpiled resource that can be used in a limited outbreak or bioweapons attack.

Ribavirin

Ribavirin, a guanosine analog first synthesized in 1970, has long been known to have broad-spectrum activity against many RNA and DNA viruses. Today, ribavirin is mainly used against human respiratory syncytial virus and to treat persistent hepatitis C virus infections.[123,124]

Ribavirin has several potential antiviral properties, which may differ in importance for different viruses.[125]

Because of its broad-spectrum effect, ribavirin was used in an off-label, non-randomized, unblinded trial during the first Malaysia outbreak of NiV encephalitis, despite the known adverse effects (primarily hemolytic anemia at high dose).[126] The lethality in the treated group was reduced by 40%, without affecting the rate of anemia. Follow-up studies revealed that ribavirin inhibits HeV and NiV replication *in vitro*.[127-130] Results from *in vivo* studies examining the efficacy of ribavirin in the hamster[127,128] and grivet[131] animal models consistently found that ribavirin extends time to death. These animal models may represent particularly susceptible models for HeV and NiV pathogenesis because of the reproducibility of human disease.[88] One concern has been that ribavirin only inefficiently crosses the blood brain barrier, which is particularly consequential for an encephalitic disease. Modifications to the drug administration method, however, have the potential to overcome this hurdle.[132-135]

Current treatment of chronic hepatitis C involves the combination of type I interferon (discussed further in the next section) and ribavirin, which act synergistically.[136] Ribavirin may therefore be evaluated in combination with other promising therapeutics in the case of henipavirus infection.

Innate Immune Therapy

Henipavirus inhibition of cellular production of interferon and of cellular responses to exogenous interferon is incomplete.[137,138] Therefore, a clear opportunity is available to inhibit HeV and NiV pathogenesis by augmenting the innate immune response *in vivo*. The investigational double-stranded RNA compound poly(I)-poly($C_{12}U$), which stimulates type I interferon production, is highly effective against NiV in the hamster model when administered immediately after challenge.[128] However, follow-up studies need to address the postexposure therapeutic window. Further, despite undergoing Phase III clinical trials for treatment of

chronic fatigue syndrome, poly(I)-poly(C_{12}U) (Rintatolimod, by Hemispherx Biopharma) has not been FDA-approved.

Recombinant and modified type I interferons (e.g., PEGylated interferon-α), on the other hand, have been FDA-approved for multiple uses, including the treatment of chronic hepatitis B and C. Exogenous interferon inhibits henipavirus replication *in vitro*[138] and would be a more direct approach to treat henipavirus infections than stimulating interferon production with compounds like poly(I)-poly(C_{12}U). However, these compounds have yet to be evaluated against henipaviruses *in vivo*.

"Off-the-shelf" Therapies Evaluated *In Vitro*

Numerous potential therapies for the treatment of henipavirus infections are in varying stages of development (reviewed elsewhere).[139,140] Here, promising therapies that are already available for off-label use against henipaviruses, yet have not been evaluated for efficacy *in vivo*, are briefly described.

As NiV M protein requires ubiquitinylation as part of its intracellular trafficking pathway, proteasome inhibitors, which deplete the intracellular pool of free ubiquitin, are potent inhibitors of NiV replication *in vitro*.[141] Next-generation proteasome inhibitors with improved pharmacokinetics, such as the FDA-approved carfilzomib or orally bioavailable analogs such as oprozomib (currently in Phase I/II oncology trials), have even greater efficacies against henipaviruses *in vitro* (Benhur Lee, personal observation, 2014). If these effects on henipaviruses can be translated into *in vivo* potency, the possibility of using potential FDA-approved proteasome inhibitors for off-label use will be a significant and realistic option for exposed or infected frontline responders.

A number of clinically available drugs were found to inhibit henipavirus replication *in vitro* in the low micromolar range, including the alpha blocker phenoxybenzamine as well as the beta blocker propranolol, the antifungal clotrimazole, and the estrogen receptor antagonist

tamoxifen.[142] However, it is unclear if any of these therapies can achieve viral inhibitory concentrations *in vivo*.

SUMMARY

The recent emergence, high virulence, and pandemic potential of HeV and NiV have fueled public concern, even leading to repeated public calls in Australia for culling of their reservoir hosts, the flying foxes. The world-wide discovery of numerous henipaviruses of unknown pathogenicity, including evidence of a potential spillover event to humans in Africa, further emphasizes the need for continued investigations into all aspects of henipavirus ecology, molecular biology, and pathogenesis. Although HeV and NiV do not appear efficiently transmissible at this time, vigilance for variants (or other henipaviruses) with enhanced transmissibility should be maintained. Significant progress in the development and identification of effective therapeutics for henipaviruses will alleviate the risks involved in managing future outbreaks.

FIGURES

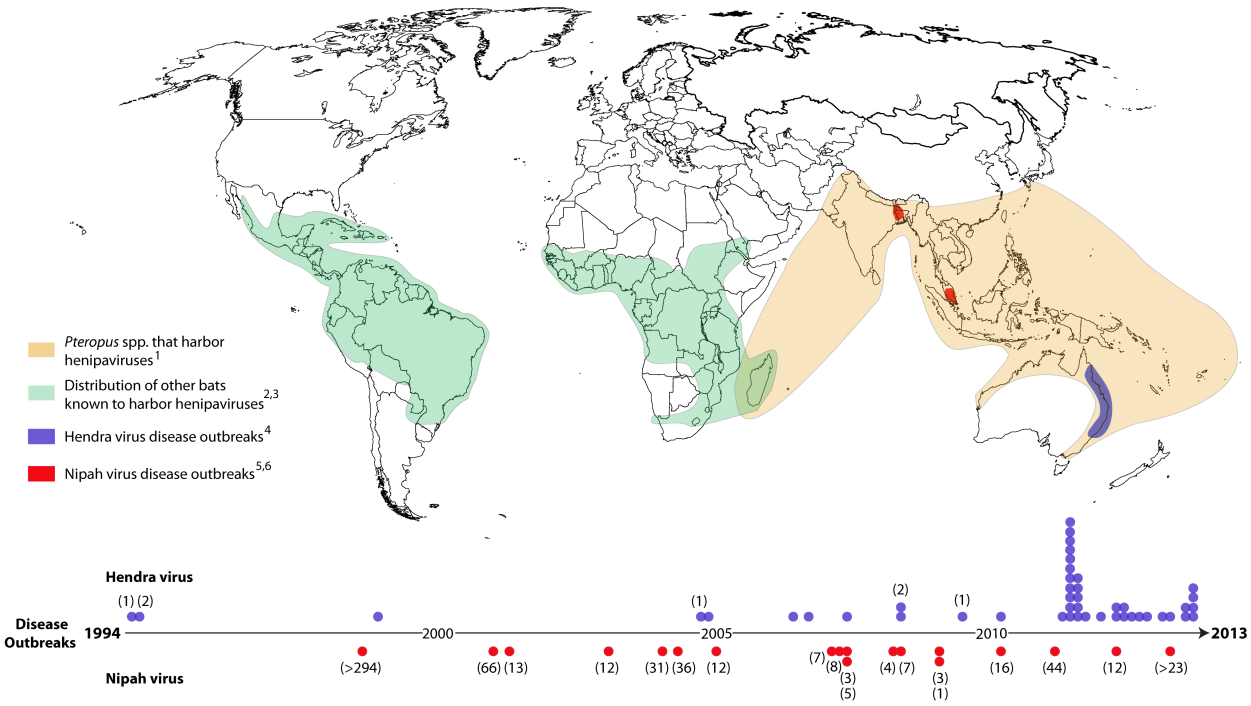

The number of human cases, if any, in each outbreak is indicated in parentheses, e.g. (#)

Figure 1-1. Distribution of henipaviruses and disease outbreaks. The bats that harbor henipaviruses, including Hendra virus and Nipah virus, have widespread distribution. However, outbreaks of HeV and NiV disease have been limited to Australia and Malaysia/Bangladesh, respectively.

Sources: (1) Eaton BT, Broder CC, Middleton D, Wang LF. Hendra and Nipah viruses: different and dangerous. *Nat Rev Microbiol*. 2006;4(1):23-35. (2) Drexler JF, Corman VM, Muller MA, et al. Bats host major mammalian paramyxoviruses. *Nat Commun*. 2012;3:796. (3) Breed AC, Meers J, Sendow I, et al. The distribution of henipaviruses in Southeast Asia and Australasia: is Wallace's line a barrier to Nipah virus? *PLoS One*. 2013;8(4):e61316. (4) Australian Veterinary Association. Hendra virus. http://www.ava.com.au/hendra-virus. Accessed February 13, 2014. (5) World Health Organization Regional Office for South-East Asia. Nipah virus outbreaks in the WHO South-East Asia Region. http://www.searo.who.int/entity/emerging_diseases/links/nipah_virus_outbreaks_sear/en/. Accessed February 13, 2014. (6) World Health Organization Regional Office for South-East Asia. Surveillance and outbreak alert: Nipah virus. http://www.searo.who.int/entity/emerging_diseases/links/nipah_virus/en/. Accessed February 13, 2014.

Figure 1-2. One of the reservoirs of Hendra virus: a spectacled flying fox (*Pteropus conspicillatus*) near Cairns, Australia. Photograph: Courtesy of Pål A. Olsvik, Bergen, Norway.

Figure 1-3. An effective countermeasure against Nipah virus spillover in Bangladesh. (*Left*) In Bangladesh, fresh date palm sap is collected by shaving the date palm tree, placing a tap, and collecting the sap in a clay pot overnight. Fruit bats are known to lick the sap stream and even urinate or defecate into the clay pots, thus potentially contaminating the raw sap with infectious Nipah virus. (*Right*) Covering the sap stream with a bamboo skirt is highly effective at preventing contamination. Photographs: Courtesy of Nazmun Nahar, International Centre for Diarrhoeal Disease Research, Bangladesh.

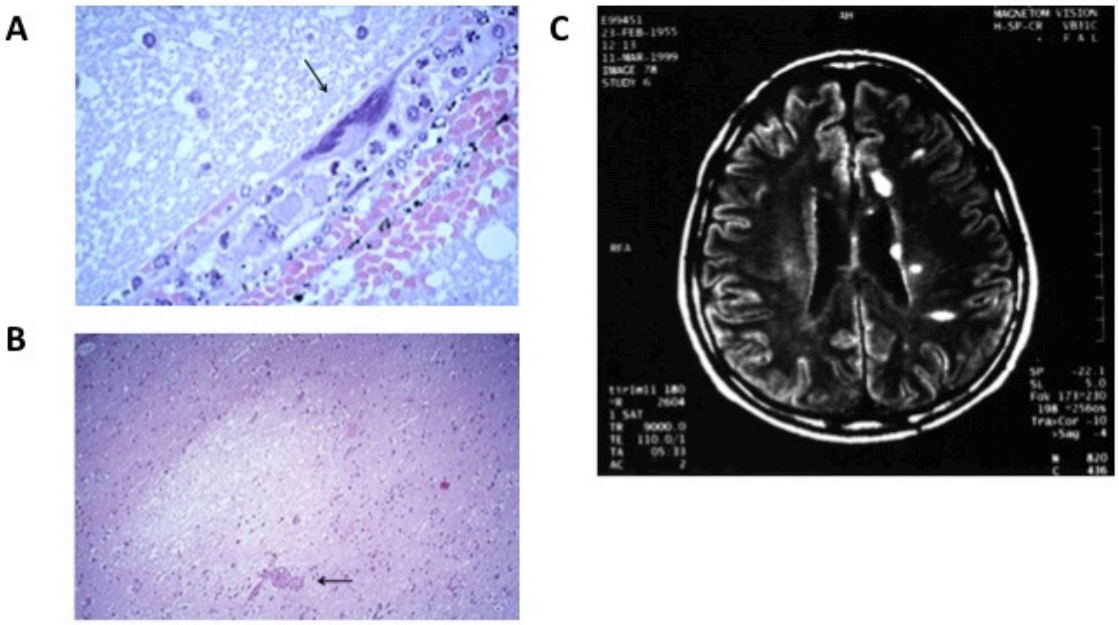

Figure 1-4. Pathology of henipavirus infection. (A) Multinucleated endothelial syncytium (arrow) in brain with perivascular hemmorrhage, H&E stain. **(B)** Necrotic plaque in cerebral parenchyma with adjacent thrombosis (arrow), H&E stain. **(C)** Typical MRI for acute henipavirus encephalitis, with discrete, hyperintense lesions.
Photographs: Courtesy of K. T. Wong, University of Malaya, Kuala Lumpur, Malaysia, with permission from Elsevier (A and B) and *Neurology Asia* (C).

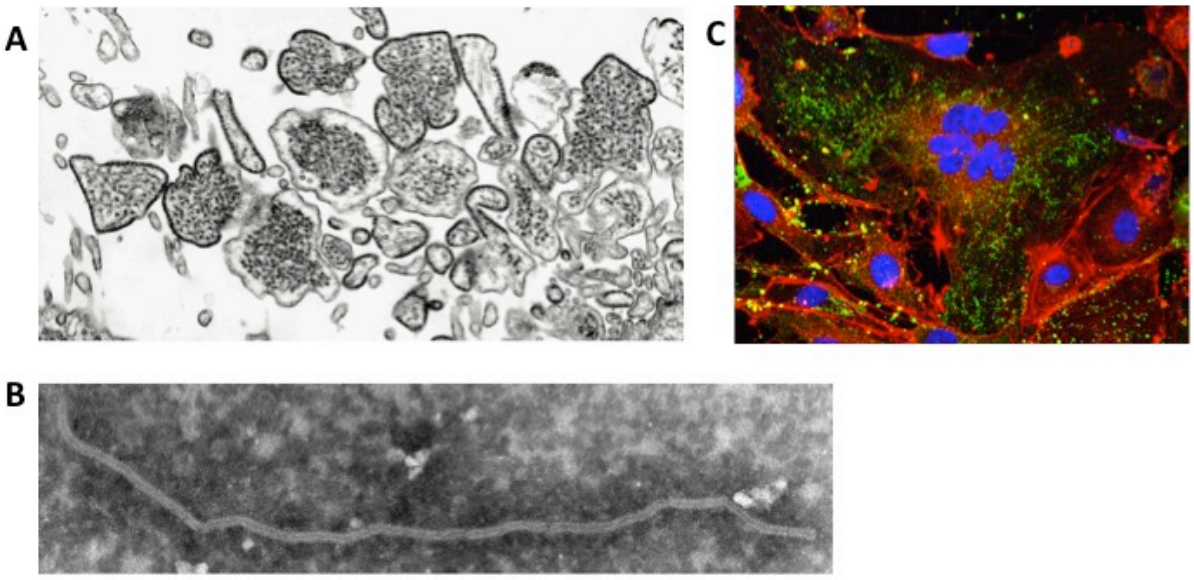

Figure 1-5. Characteristic features of Nipah virus. (A) Nipah virus virions produced from infected Vero E6 cells. **(B)** Nipah virus nucleocapsid, with the herringbone appearance characteristic of paramyxoviruses. **(C)** Multinucleated Nipah virus-induced syncytium in HUVEC cells. Blue represents nuclei; red represents actin filaments and illustrates cell boundaries; and green represents Nipah virus matrix protein.
Photographs: (A and B) Courtesy of Cynthia Goldsmith, Centers for Disease Control and Prevention, Atlanta, Georgia. (C) Courtesy of Arnold Park, University of California Los Angeles, Los Angeles, California.

REFERENCES

1. Drexler JF, Corman VM, Muller MA, et al. Bats host major mammalian paramyxoviruses. *Nat Commun*. 2012;3:796.

2. Peel AJ, Sargan DR, Baker KS, et al. Continent-wide panmixia of an African fruit bat facilitates transmission of potentially zoonotic viruses. *Nat Commun*. 2013;4:2770.

3. Pernet O, Beaty SM, Lebreton M, Schneider B, Wolfe N, Lee B. Evidence for Henipavirus spillover into human populations in Africa. Paper presented at: XV International Conference on Negative Strand Viruses; June 16-21, 2013; Granada, Spain.

4. Field H, Crameri G, Kung NY, Wang LF. Ecological aspects of hendra virus. *Curr Top Microbiol Immunol*. 2012;359:11-23.

5. Selvey LA, Wells RM, McCormack JG, et al. Infection of humans and horses by a newly described morbillivirus. *Med J Aust*. 1995;162(12):642-645.

6. Murray K, Selleck P, Hooper P, et al. A morbillivirus that caused fatal disease in horses and humans. *Science*. 1995;268(5207):94-97.

7. Wang LF, Yu M, Hansson E, et al. The exceptionally large genome of Hendra virus: support for creation of a new genus within the family Paramyxoviridae. *J Virol*. 2000;74(21):9972-9979.

8. O'Sullivan JD, Allworth AM, Paterson DL, et al. Fatal encephalitis due to novel paramyxovirus transmitted from horses. *Lancet*. 1997;349(9045):93-95.

9. Australian Veterinary Association. Hendra virus. http://www.ava.com.au/hendra-virus. Accessed February 13, 2014.

10. Field H, Kung N. Henipaviruses-unanswered questions of lethal zoonoses. *Curr Opin Virol*. 2011;1(6):658-661.

11. Field H, Young P, Yob JM, Mills J, Hall L, Mackenzie J. The natural history of Hendra and Nipah viruses. *Microbes Infect*. 2001;3(4):307-314.

12. Murray K, Rogers R, Selvey L, et al. A novel morbillivirus pneumonia of horses and its transmission to humans. *Emerg Infect Dis*. 1995;1(1):31-33.

13. Rogers RJ, Douglas IC, Baldock FC, et al. Investigation of a second focus of equine morbillivirus infection in coastal Queensland. *Aust Vet J*. 1996;74(3):243-244.

14. Ward MP, Black PF, Childs AJ, et al. Negative findings from serological studies of equine morbillivirus in the Queensland horse population. *Aust Vet J*. 1996;74(3):241-243.

15. Young PL, Halpin K, Selleck PW, et al. Serologic evidence for the presence in Pteropus bats of a paramyxovirus related to equine morbillivirus. *Emerg Infect Dis*. 1996;2(3):239-240.

16. Halpin K, Young PL, Field HE, Mackenzie JS. Isolation of Hendra virus from pteropid bats: a natural reservoir of Hendra virus. *J Gen Virol.* 2000;81(Pt 8):1927-1932.

17. Chua KB. Nipah virus outbreak in Malaysia. *J Clin Virol.* 2003;26(3):265-275.

18. van den Hurk AF, Ritchie SA, Mackenzie JS. Ecology and geographical expansion of Japanese encephalitis virus. *Annu Rev Entomol.* 2009;54:17-35.

19. Chua KB. Epidemiology, surveillance and control of Nipah virus infections in Malaysia. *Malays J Pathol.* 2010;32(2):69-73.

20. Paton NI, Leo YS, Zaki SR, et al. Outbreak of Nipah-virus infection among abattoir workers in Singapore. *Lancet.* 1999;354(9186):1253-1256.

21. Chua KB. Introduction: Nipah virus--discovery and origin. *Curr Top Microbiol Immunol.* 2012;359:1-9.

22. Chua KB. The discovery of Nipah virus: A personal account. *Neurology Asia.* 2004;9:59-63.

23. Ksiazek TG, Rota PA, Rollin PE. A review of Nipah and Hendra viruses with an historical aside. *Virus Res.* 2011;162(1-2):173-183.

24. Wong KT, Shieh WJ, Zaki SR, Tan CT. Nipah virus infection, an emerging paramyxoviral zoonosis. *Springer Semin Immunopathol.* 2002;24(2):215-228.

25. Tan CT, Goh KJ, Wong KT, et al. Relapsed and late-onset Nipah encephalitis. *Ann Neurol.* 2002;51(6):703-708.

26. Chua KB, Bellini WJ, Rota PA, et al. Nipah virus: a recently emergent deadly paramyxovirus. *Science.* 2000;288(5470):1432-1435.

27. Mohd Nor MN, Gan CH, Ong BL. Nipah virus infection of pigs in peninsular Malaysia. *Rev Sci Tech.* 2000;19(1):160-165.

28. World Health Organization Regional Office for South-East Asia. Nipah virus outbreaks in the WHO South-East Asia Region. http://www.searo.who.int/entity/emerging_diseases/links/nipah_virus_outbreaks_sear/en/. Accessed February 13, 2014.

29. Hossain MJ, Gurley ES, Montgomery JM, et al. Clinical presentation of nipah virus infection in Bangladesh. *Clin Infect Dis.* 2008;46(7):977-984.

30. Luby SP, Gurley ES. Epidemiology of henipavirus disease in humans. *Curr Top Microbiol Immunol.* 2012;359:25-40.

31. Luby SP, Rahman M, Hossain MJ, et al. Foodborne transmission of Nipah virus, Bangladesh. *Emerg Infect Dis.* 2006;12(12):1888-1894.

32. Marsh GA, de Jong C, Barr JA, et al. Cedar virus: a novel Henipavirus isolated from Australian bats. *PLoS Pathog.* 2012;8(8):e1002836.

33. Weiss S, Nowak K, Fahr J, et al. Henipavirus-related sequences in fruit bat bushmeat, Republic of Congo. *Emerg Infect Dis*. 2012;18(9):1536-1537.

34. Field HE, Mackenzie JS, Daszak P. Henipaviruses: emerging paramyxoviruses associated with fruit bats. *Curr Top Microbiol Immunol*. 2007;315:133-159.

35. Middleton DJ, Weingartl HM. Henipaviruses in their natural animal hosts. *Curr Top Microbiol Immunol*. 2012;359:105-121.

36. Halpin K, Hyatt AD, Fogarty R, et al. Pteropid bats are confirmed as the reservoir hosts of henipaviruses: a comprehensive experimental study of virus transmission. *Am J Trop Med Hyg*. 2011;85(5):946-951.

37. Middleton DJ, Morrissy CJ, van der Heide BM, et al. Experimental Nipah virus infection in pteropid bats (Pteropus poliocephalus). *J Comp Pathol*. 2007;136(4):266-272.

38. Williamson MM, Hooper PT, Selleck PW, et al. Transmission studies of Hendra virus (equine morbillivirus) in fruit bats, horses and cats. *Aust Vet J*. 1998;76(12):813-818.

39. Williamson MM, Hooper PT, Selleck PW, Westbury HA, Slocombe RF. Experimental hendra virus infection in pregnant guinea-pigs and fruit Bats (Pteropus poliocephalus). *J Comp Pathol*. 2000;122(2-3):201-207.

40. Chua KB, Chua BH, Wang CW. Anthropogenic deforestation, El Nino and the emergence of Nipah virus in Malaysia. *Malays J Pathol*. 2002;24(1):15-21.

41. Field H, de Jong C, Melville D, et al. Hendra virus infection dynamics in Australian fruit bats. *PLoS One*. 2011;6(12):e28678.

42. Selvey L, Taylor R, Arklay A, Gerrard J. Screening of bat carers for antibodies to equine morbillivirus. *Commun Dis Intell*. 1996;20(22):477-478.

43. Dhondt KP, Mathieu C, Chalons M, et al. Type I interferon signaling protects mice from lethal henipavirus infection. *J Infect Dis*. 2013;207(1):142-151.

44. Rockx B, Brining D, Kramer J, et al. Clinical outcome of henipavirus infection in hamsters is determined by the route and dose of infection. *J Virol*. 2011;85(15):7658-7671.

45. Goh KJ, Tan CT, Chew NK, et al. Clinical features of Nipah virus encephalitis among pig farmers in Malaysia. *N Engl J Med*. 2000;342(17):1229-1235.

46. Parashar UD, Sunn LM, Ong F, et al. Case-control study of risk factors for human infection with a new zoonotic paramyxovirus, Nipah virus, during a 1998-1999 outbreak of severe encephalitis in Malaysia. *J Infect Dis*. 2000;181(5):1755-1759.

47. Tan KS, Tan CT, Goh KJ. Epidemiological aspects of Nipah virus infection. *Neurological Journal of Southeast Asia*. 1999;4:77-81.

48. Mills JN, Alim AN, Bunning ML, et al. Nipah virus infection in dogs, Malaysia, 1999. *Emerg Infect Dis*. 2009;15(6):950-952.

49. Mounts AW, Kaur H, Parashar UD, et al. A cohort study of health care workers to assess nosocomial transmissibility of Nipah virus, Malaysia, 1999. *J Infect Dis*. 2001;183(5):810-813.

50. Chua KB, Lam SK, Goh KJ, et al. The presence of Nipah virus in respiratory secretions and urine of patients during an outbreak of Nipah virus encephalitis in Malaysia. *J Infect*. 2001;42(1):40-43.

51. Aziz J, Olson J, Lee OB, et al. Nipah virus infection of animals in Malaysia. Paper presented at: XIth International Congress of Virology; August 9-13, 1999; Sydney, Australia.

52. Harcourt BH, Lowe L, Tamin A, et al. Genetic characterization of Nipah virus, Bangladesh, 2004. *Emerg Infect Dis*. 2005;11(10):1594-1597.

53. Lo MK, Lowe L, Hummel KB, et al. Characterization of Nipah virus from outbreaks in Bangladesh, 2008-2010. *Emerg Infect Dis*. 2012;18(2):248-255.

54. Blum LS, Khan R, Nahar N, Breiman RF. In-depth assessment of an outbreak of Nipah encephalitis with person-to-person transmission in Bangladesh: implications for prevention and control strategies. *Am J Trop Med Hyg*. 2009;80(1):96-102.

55. Gurley ES, Montgomery JM, Hossain MJ, et al. Person-to-person transmission of Nipah virus in a Bangladeshi community. *Emerg Infect Dis*. 2007;13(7):1031-1037.

56. Chadha MS, Comer JA, Lowe L, et al. Nipah virus-associated encephalitis outbreak, Siliguri, India. *Emerg Infect Dis*. 2006;12(2):235-240.

57. Hsu VP, Hossain MJ, Parashar UD, et al. Nipah virus encephalitis reemergence, Bangladesh. *Emerg Infect Dis*. 2004;10(12):2082-2087.

58. ICDDRB. Outbreaks of encephalitis due to Nipah/Hendra-like viruses, Western Bangladesh. *Health and Science Bulletin*. 2003;1(5):1-6.

59. Luby SP, Gurley ES, Hossain MJ. Transmission of human infection with Nipah virus. *Clin Infect Dis*. 2009;49(11):1743-1748.

60. Nahar N, Sultana R, Gurley ES, Hossain MJ, Luby SP. Date palm sap collection: exploring opportunities to prevent Nipah transmission. *EcoHealth*. 2010;7(2):196-203.

61. Nahar N, Mondal UK, Sultana R, et al. Piloting the use of indigenous methods to prevent Nipah virus infection by interrupting bats' access to date palm sap in Bangladesh. *Health Promot Int*. 2013;28(3):378-386.

62. Wong KT, Tan CT. Clinical and pathological manifestations of human henipavirus infection. *Curr Top Microbiol Immunol*. 2012;359:95-104.

63. Wong KT, Ong KC. Pathology of acute henipavirus infection in humans and animals. *Patholog Res Int*. 2011;2011:567248.

64. Playford EG, McCall B, Smith G, et al. Human Hendra virus encephalitis associated with equine outbreak, Australia, 2008. *Emerg Infect Dis*. 2010;16(2):219-223.

65. Chong HT, Kunjapan SR, Thayaparan T, et al. Nipah encephalitis outbreak in Malaysia, clinical features in patients from Seremban. *Neurological Journal of Southeast Asia*. 2000;5:61-67.

66. Lee KE, Umapathi T, Tan CB, et al. The neurological manifestations of Nipah virus encephalitis, a novel paramyxovirus. *Ann Neurol*. 1999;46(3):428-432.

67. Sejvar JJ, Hossain J, Saha SK, et al. Long-term neurological and functional outcome in Nipah virus infection. *Ann Neurol*. 2007;62(3):235-242.

68. Siva SR, Chong HT, Tan CT. Ten year clinical and serological outcomes of Nipah virus infection. *Neurology Asia*. 2009;14:53-58.

69. Chong HT, Kunjapan SR, Thayaparan T, et al. Nipah encephalitis outbreak in Malaysia, clinical features in patients from Seremban. *Can J Neurol Sci*. 2002;29(1):83-87.

70. Pernet O, Wang YE, Lee B. Henipavirus receptor usage and tropism. *Curr Top Microbiol Immunol*. 2012;359:59-78.

71. Wong KT, Shieh WJ, Kumar S, et al. Nipah virus infection: pathology and pathogenesis of an emerging paramyxoviral zoonosis. *Am J Pathol*. 2002;161(6):2153-2167.

72. Wong KT. Emerging epidemic viral encephalitides with a special focus on henipaviruses. *Acta Neuropathol*. 2010;120(3):317-325.

73. Wong KT, Robertson T, Ong BB, et al. Human Hendra virus infection causes acute and relapsing encephalitis. *Neuropathol Appl Neurobiol*. 2009;35(3):296-305.

74. Goldsmith CS, Whistler T, Rollin PE, et al. Elucidation of Nipah virus morphogenesis and replication using ultrastructural and molecular approaches. *Virus Res*. 2003;92(1):89-98.

75. Hyatt AD, Zaki SR, Goldsmith CS, Wise TG, Hengstberger SG. Ultrastructure of Hendra virus and Nipah virus within cultured cells and host animals. *Microbes Infect*. 2001;3(4):297-306.

76. Rota PA, Lo MK. Molecular virology of the henipaviruses. *Curr Top Microbiol Immunol*. 2012;359:41-58.

77. Eaton BT, Broder CC, Middleton D, Wang LF. Hendra and Nipah viruses: different and dangerous. *Nat Rev Microbiol*. 2006;4(1):23-35.

78. Lee B, Ataman ZA. Modes of paramyxovirus fusion: a Henipavirus perspective. *Trends Microbiol*. 2011;19(8):389-399.

79. Bonaparte MI, Dimitrov AS, Bossart KN, et al. Ephrin-B2 ligand is a functional receptor for Hendra virus and Nipah virus. *Proc Natl Acad Sci U S A*. 2005;102(30):10652-10657.

80. Negrete OA, Levroney EL, Aguilar HC, et al. EphrinB2 is the entry receptor for Nipah virus, an emergent deadly paramyxovirus. *Nature*. 2005;436(7049):401-405.

81. Negrete OA, Chu D, Aguilar HC, Lee B. Single amino acid changes in the Nipah and Hendra virus attachment glycoproteins distinguish ephrinB2 from ephrinB3 usage. *J Virol*. 2007;81(19):10804-10814.

82. Negrete OA, Wolf MC, Aguilar HC, et al. Two key residues in ephrinB3 are critical for its use as an alternative receptor for Nipah virus. *PLoS Pathog*. 2006;2(2):e7.

83. Broder CC, Geisbert TW, Xu K, et al. Immunization strategies against henipaviruses. *Curr Top Microbiol Immunol*. 2012;359:197-223.

84. Bossart KN, Tachedjian M, McEachern JA, et al. Functional studies of host-specific ephrin-B ligands as Henipavirus receptors. *Virology*. 2008;372(2):357-371.

85. Tanimura N, Imada T, Kashiwazaki Y, Sharifah SH. Distribution of viral antigens and development of lesions in chicken embryos inoculated with nipah virus. *J Comp Pathol*. 2006;135(2-3):74-82.

86. Pager CT, Craft WW, Jr., Patch J, Dutch RE. A mature and fusogenic form of the Nipah virus fusion protein requires proteolytic processing by cathepsin L. *Virology*. 2006;346(2):251-257.

87. Pager CT, Dutch RE. Cathepsin L is involved in proteolytic processing of the Hendra virus fusion protein. *J Virol*. 2005;79(20):12714-12720.

88. Geisbert TW, Feldmann H, Broder CC. Animal challenge models of henipavirus infection and pathogenesis. *Curr Top Microbiol Immunol*. 2012;359:153-177.

89. Escaffre O, Borisevich V, Carmical JR, et al. Henipavirus pathogenesis in human respiratory epithelial cells. *J Virol*. 2013;87(6):3284-3294.

90. Williamson MM, Torres-Velez FJ. Henipavirus: a review of laboratory animal pathology. *Vet Pathol*. 2010;47(5):871-880.

91. Mathieu C, Pohl C, Szecsi J, et al. Nipah virus uses leukocytes for efficient dissemination within a host. *J Virol*. 2011;85(15):7863-7871.

92. Dups J, Middleton D, Yamada M, et al. A new model for Hendra virus encephalitis in the mouse. *PLoS One*. 2012;7(7):e40308.

93. Munster VJ, Prescott JB, Bushmaker T, et al. Rapid Nipah virus entry into the central nervous system of hamsters via the olfactory route. *Sci Rep*. 2012;2:736.

94. Rodriguez JJ, Cruz CD, Horvath CM. Identification of the nuclear export signal and STAT-binding domains of the Nipah virus V protein reveals mechanisms underlying interferon evasion. *J Virol*. 2004;78(10):5358-5367.

95. Rodriguez JJ, Parisien JP, Horvath CM. Nipah virus V protein evades alpha and gamma interferons by preventing STAT1 and STAT2 activation and nuclear accumulation. *J Virol.* 2002;76(22):11476-11483.

96. Rodriguez JJ, Wang LF, Horvath CM. Hendra virus V protein inhibits interferon signaling by preventing STAT1 and STAT2 nuclear accumulation. *J Virol.* 2003;77(21):11842-11845.

97. Shaw ML, Garcia-Sastre A, Palese P, Basler CF. Nipah virus V and W proteins have a common STAT1-binding domain yet inhibit STAT1 activation from the cytoplasmic and nuclear compartments, respectively. *J Virol.* 2004;78(11):5633-5641.

98. Andrejeva J, Childs KS, Young DF, et al. The V proteins of paramyxoviruses bind the IFN-inducible RNA helicase, mda-5, and inhibit its activation of the IFN-beta promoter. *Proc Natl Acad Sci U S A.* 2004;101(49):17264-17269.

99. Childs K, Stock N, Ross C, et al. mda-5, but not RIG-I, is a common target for paramyxovirus V proteins. *Virology.* 2007;359(1):190-200.

100. Shaw ML, Cardenas WB, Zamarin D, Palese P, Basler CF. Nuclear localization of the Nipah virus W protein allows for inhibition of both virus- and toll-like receptor 3-triggered signaling pathways. *J Virol.* 2005;79(10):6078-6088.

101. Basler CF. Nipah and hendra virus interactions with the innate immune system. *Curr Top Microbiol Immunol.* 2012;359:123-152.

102. Hagmaier K, Stock N, Goodbourn S, Wang LF, Randall R. A single amino acid substitution in the V protein of Nipah virus alters its ability to block interferon signalling in cells from different species. *J Gen Virol.* 2006;87(Pt 12):3649-3653.

103. Conzelmann KK. Reverse genetics of mononegavirales. *Curr Top Microbiol Immunol.* 2004;283:1-41.

104. Yoneda M, Fujita K, Sato H, Kai C. Reverse genetics of Nipah virus to probe viral pathogenicity. *Methods Mol Biol.* 2009;515:329-337.

105. Wang LF, Daniels P. Diagnosis of henipavirus infection: current capabilities and future directions. *Curr Top Microbiol Immunol.* 2012;359:179-196.

106. Aljofan M, Saubern S, Meyer AG, Marsh G, Meers J, Mungall BA. Characteristics of Nipah virus and Hendra virus replication in different cell lines and their suitability for antiviral screening. *Virus Res.* 2009;142(1-2):92-99.

107. Fogarty R, Halpin K, Hyatt AD, Daszak P, Mungall BA. Henipavirus susceptibility to environmental variables. *Virus Res.* 2008;132(1-2):140-144.

108. de Wit E, Bushmaker T, Scott D, Feldmann H, Munster VJ. Nipah virus transmission in a hamster model. *PLoS Negl Trop Dis.* 2011;5(12):e1432.

109. Homaira N, Rahman M, Hossain MJ, et al. Nipah virus outbreak with person-to-person transmission in a district of Bangladesh, 2007. *Epidemiol Infect*. 2010;138(11):1630-1636.

110. Rota PA, Mungall B, Halpin K. Nipah virus. In: Liu D, ed. *Molecular detection of human viral pathogens*. Boca Raton, FL: CRC Press; 2011:545-556.

111. Rollin PE, Rota PA, Zaki S, Ksiazek TG. Hendra and Nipah viruses. In: Versalovic J, ed. *Manual of Clinical Microbiology*. Vol 2. 10 ed: ASM Press; 2011:1479-1487.

112. Ramasundrum V, Tan CT, Chua KB, et al. Kinetics of IgM and IgG seroconversion in Nipah virus infection. *Neurological Journal of Southeast Asia*. 2000;5:23-28.

113. Kaku Y, Noguchi A, Marsh GA, et al. Second generation of pseudotype-based serum neutralization assay for Nipah virus antibodies: sensitive and high-throughput analysis utilizing secreted alkaline phosphatase. *J Virol Methods*. 2012;179(1):226-232.

114. Kaku Y, Noguchi A, Marsh GA, et al. A neutralization test for specific detection of Nipah virus antibodies using pseudotyped vesicular stomatitis virus expressing green fluorescent protein. *J Virol Methods*. 2009;160(1-2):7-13.

115. Tamin A, Harcourt BH, Lo MK, et al. Development of a neutralization assay for Nipah virus using pseudotype particles. *J Virol Methods*. 2009;160(1-2):1-6.

116. Bossart KN, McEachern JA, Hickey AC, et al. Neutralization assays for differential henipavirus serology using Bio-Plex protein array systems. *J Virol Methods*. 2007;142(1-2):29-40.

117. Goldsmith CS, Ksiazek TG, Rollin PE, et al. Cell culture and electron microscopy for identifying viruses in diseases of unknown cause. *Emerg Infect Dis*. 2013;19(6):886-891.

118. Smith I, Broos A, de Jong C, et al. Identifying Hendra virus diversity in pteropid bats. *PLoS One*. 2011;6(9):e25275.

119. Middleton D, Pallister J, Klein R, et al. Hendra Virus Vaccine, a One Health Approach to Protecting Horse, Human, and Environmental Health. *Emerg Infect Dis*. 2014;20(3).

120. Bossart KN, Zhu Z, Middleton D, et al. A neutralizing human monoclonal antibody protects against lethal disease in a new ferret model of acute nipah virus infection. *PLoS Pathog*. 2009;5(10):e1000642.

121. Bossart KN, Geisbert TW, Feldmann H, et al. A neutralizing human monoclonal antibody protects african green monkeys from hendra virus challenge. *Sci Transl Med*. 2011;3(105):105ra103.

122. Springborg L. World-first Hendra treatment one step closer. In: government Q, ed2013.

123. Olszewska W, Openshaw P. Emerging drugs for respiratory syncytial virus infection. *Expert Opin Emerg Drugs*. 2009;14(2):207-217.

124. Snell NJ. Ribavirin--current status of a broad spectrum antiviral agent. *Expert Opin Pharmacother*. 2001;2(8):1317-1324.

125. Parker WB. Metabolism and antiviral activity of ribavirin. *Virus Res*. 2005;107(2):165-171.

126. Chong HT, Kamarulzaman A, Tan CT, et al. Treatment of acute Nipah encephalitis with ribavirin. *Ann Neurol*. 2001;49(6):810-813.

127. Freiberg AN, Worthy MN, Lee B, Holbrook MR. Combined chloroquine and ribavirin treatment does not prevent death in a hamster model of Nipah and Hendra virus infection. *J Gen Virol*. 2010;91(Pt 3):765-772.

128. Georges-Courbot MC, Contamin H, Faure C, et al. Poly(I)-poly(C12U) but not ribavirin prevents death in a hamster model of Nipah virus infection. *Antimicrob Agents Chemother*. 2006;50(5):1768-1772.

129. Wright PJ, Crameri G, Eaton BT. RNA synthesis during infection by Hendra virus: an examination by quantitative real-time PCR of RNA accumulation, the effect of ribavirin and the attenuation of transcription. *Arch Virol*. 2005;150(3):521-532.

130. Aljofan M, Porotto M, Moscona A, Mungall BA. Development and validation of a chemiluminescent immunodetection assay amenable to high throughput screening of antiviral drugs for Nipah and Hendra virus. *J Virol Methods*. 2008;149(1):12-19.

131. Rockx B, Bossart KN, Feldmann F, et al. A novel model of lethal Hendra virus infection in African green monkeys and the effectiveness of ribavirin treatment. *J Virol*. 2010;84(19):9831-9839.

132. Jeulin H, Venard V, Carapito D, Finance C, Kedzierewicz F. Effective ribavirin concentration in mice brain using cyclodextrin as a drug carrier: evaluation in a measles encephalitis model. *Antiviral Res*. 2009;81(3):261-266.

133. Gilbert BE, Wyde PR, Wilson SZ, Robins RK. Aerosol and intraperitoneal administration of ribavirin and ribavirin triacetate: pharmacokinetics and protection of mice against intracerebral infection with influenza A/WSN virus. *Antimicrob Agents Chemother*. 1991;35(7):1448-1453.

134. Patel MM, Goyal BR, Bhadada SV, Bhatt JS, Amin AF. Getting into the brain: approaches to enhance brain drug delivery. *CNS Drugs*. 2009;23(1):35-58.

135. Colombo G, Lorenzini L, Zironi E, et al. Brain distribution of ribavirin after intranasal administration. *Antiviral Res*. 2011;92(3):408-414.

136. Reddy KR, Nelson DR, Zeuzem S. Ribavirin: current role in the optimal clinical management of chronic hepatitis C. *J Hepatol*. 2009;50(2):402-411.

137. Lo MK, Miller D, Aljofan M, et al. Characterization of the antiviral and inflammatory responses against Nipah virus in endothelial cells and neurons. *Virology*. 2010;404(1):78-88.

138. Virtue ER, Marsh GA, Wang LF. Interferon signaling remains functional during henipavirus infection of human cell lines. *J Virol.* 2011;85(8):4031-4034.

139. Aguilar HC, Lee B. Emerging paramyxoviruses: molecular mechanisms and antiviral strategies. *Expert Rev Mol Med.* 2011;13:e6.

140. Vigant F, Lee B. Hendra and nipah infection: pathology, models and potential therapies. *Infect Disord Drug Targets.* 2011;11(3):315-336.

141. Wang YE, Park A, Lake M, et al. Ubiquitin-regulated nuclear-cytoplasmic trafficking of the Nipah virus matrix protein is important for viral budding. *PLoS Pathog*. 2010;6(11):e1001186.

142. Aljofan M, Lo MK, Rota PA, Michalski WP, Mungall BA. Off Label Antiviral Therapeutics for Henipaviruses: New Light Through Old Windows. *J Antivir Antiretrovir*. 2010;2(1):1-10.

CHAPTER 1.2

THE ESSENTIAL ROLE OF THE PARAMYXOVIRUS MATRIX PROTEIN IN VIRAL ASSEMBLY AND BUDDING

ROLE OF MATRIX IN THE VIRAL LIFECYCLE

Viruses of the family *Paramyxoviridae* (otherwise known as "paramyxoviruses"), like other members of *Mononegavirales* order, are enveloped viruses with a single-stranded RNA genome of negative (non-coding) sense. The paramyxoviruses include many longstanding human pathogens such as measles virus, mumps virus, and the human parainfluenza viruses (Figure 1-6). The paramyxovirus matrix protein associates with and underlies the cellular plasma membrane during the final assembly and budding step of the viral lifecycle. Matrix interfaces between the viral envelope proteins and the inner core of the virus, the viral genome with its associated nucleocapsid and replicative complex (Figure 1-7). With all the viral components thus assembled, matrix drives deformation of the plasma membrane and the pinching off of membrane buds, which are then the virions that may transmit infection to further host cells.[1,2]

The Essential Role of Matrix Protein

Beyond the intuitive sense that the viral component underlying the lipid bilayer and forming the "backbone" of the virus would be essential for its budding process, two lines of evidence suggest that the matrix protein is critical for viral budding. First, paramyxoviruses with deleterious mutations (either naturally occurring and intentionally introduced) in the matrix protein are highly defective in, if not incapable of, viral particle production. As a naturally occurring example, hypermutated or highly unstable matrix proteins are characteristic of subacute sclerosing panencephalitis (SSPE), a progressively fatal condition that results from measles virus (MeV) persistence and reemergence in the central nervous system. In the absence of functional matrix, these SSPE MeV variants lack virion production and spread via cell-to-cell contact, which allows the virus to evade the typically high levels of neutralizing antibodies in SSPE patients.[3] Intentionally mutated paramyxoviruses can also be generated via reverse genetics, which involves the "rescue" of replication-competent virus from cDNAs introduced into cells. Although paramyxoviruses with the matrix gene removed from their genomes can be rescued if matrix protein is temporarily supplied *in trans*, the resulting virus is incapable of

subsequent virion formation.[4,5] In our experience, the essential role of matrix protein holds true for the henipaviruses as well: Nipah virus with the matrix gene removed can be rescued with Nipah virus matrix protein (NiV-M) supplied *in trans*; the subsequently infected cells, however, do not produce further virus due to a lack of NiV-M production (Tatyana Yun, UTMB-Galveston, personal observation, 2014).

The second line of evidence for the critical role of matrix in budding is that it is often capable of budding on its own, forming virus-like particles (VLPs) that morphologically resemble true pleiomorphic virions by electron microscopy, though without the envelope protein spikes. For some paramyxovirus matrix proteins, matrix-driven VLP release is enhanced by co-expression of other viral components such as nucleocapsid or fusion protein[6-9]; for NiV-M, however, envelope protein or nucleocapsid co-expression does not enhance its already relatively efficient VLP budding.[10]

MOLECULAR MECHANISMS OF MATRIX TRAFFICKING AND BUDDING

The intracellular trafficking of paramyxovirus matrix proteins and the molecular mechanisms of paramyxovirus budding are not well understood. It is still unclear, for example, whether paramyxovirus matrix proteins traffick on defined intracellular pathways, or whether they diffuse through the cytoplasm, only associating with the membrane upon contact or in response to a specific cue. Paramyxoviruses that target epithelial cells for infection preferentially bud from the apical side, and the cause of this preference, where determined, is known to be the matrix protein.[1,2] Sendai virus (SeV), the prototypic mouse virus that is a common scourge of laboratory mouse colonies, provides a naturally occurring example: while the typical SeV infects the airway epithelium and then buds apically back into the lumen, thus resulting in a localized infection restricted to the airway, the F1-R mutant has a mutated matrix protein that results in bipolar viral budding, thus aiding the establishment of systemic infection.[11] The MeV fusion and attachment proteins traffick to the basolateral side in the absence of the matrix protein; in the

presence of matrix protein, however, these envelope proteins co-migrate to the apical side.[12] The molecular determinants of paramyxovirus matrix polarized trafficking are not known; it is even possible that matrix is not specifically trafficked to the apical side, but that an apical factor has the requisite binding surface to recruit the matrix protein.

The demonstrated physical association of the matrix proteins of SeV and Newcastle Disease virus (NDV) with actin, as well as the described presence of actin in SeV, MeV, and NDV virions,[1,13] suggests involvement of the cytoskeleton in the trafficking or budding process. Treatment with cytochalasin D, which disrupts actin filaments, inhibits SeV budding[14]; however, the same treatment had no effect on another paramyxovirus, human parainfluenza virus type 3, for which microtubule integrity appeared to be more significant.[15] The cytoskeleton may therefore play different roles for the various paramyxoviruses, and in any case, the molecular mechanisms of these roles have yet to be described for any paramyxovirus.

The final budding step for enveloped viruses, the constriction and pinching off of the neck of the viral bud, often requires the recruitment and assistance of the cellular ESCRT (endosomal sorting complexes required for transport) machinery. The ESCRT pathway catalyzes membrane fission events in which cytoplasmic factors have access to the *inside* of the constricting neck (such as during cytokinesis or multivesicular body formation) vs. the opposite topology of access to the *outside* of the constricting neck (such as dynamin during endocytosis).[16-18] HIV-1, the first-described and classic example of an ESCRT-dependent virus, recruits the ESCRT components Tsg101 and Alix via specific motifs on its Gag protein, which fulfills a similar function to the paramyxovirus matrix protein. Some viruses, however, appear to bud independently of ESCRT, and with few exceptions, it remains unclear for most whether they recruit an unknown cellular pathway to catalyze membrane fission or encode their own fission machinery.[19,20] Only one paramyxovirus, human parainfluenza virus type 1, has been shown to be negatively affected by ESCRT inhibition in a live virus context,[21] while SeV, also in the

Respirovirus genus, has had conflicting reports.[22-24] Other paramyxoviruses have been suggested to be ESCRT-independent, including MeV and NiV.[25,26]

The Biology of Henipavirus Matrix Proteins

As the henipaviruses have only been recently identified, their matrix proteins have received only limited attention. Two studies showed that mutations in NiV matrix motifs resembling known ESCRT-interacting motifs abrogated virus-like particle budding[26,27]; far from demonstrating a block at final step of viral budding, however, these matrix mutants were trapped in the nucleus. A follow-up experiment found that wild-type NiV matrix virus-like particle budding was not inhibited by a dominant-negative ESCRT component, suggesting that NiV budding may be ESCRT-independent.[26] Only one potential henipavirus matrix-interacting host factor has been described, the nuclear factor ANP32B, the overexpression of which led to nuclear accumulation of HeV and NiV matrix. Knockdown of ANP32B, however, did not appear to affect viral replication, leaving the functional significance of this interaction unclear.[28] Finally, a study of NiV matrix and envelope protein trafficking in polarized epithelial MDCK (Madin-Darby canine kidney) cells found that matrix appeared to traffick to the apical side, irrespective of the presence or absence of other viral components.[29]

AIMS OF THE DISSERTATION

To gain deeper insight into the molecular mechanisms behind the trafficking and budding of Nipah virus matrix protein, we mutated conserved motifs in the matrix protein, identified and examined the significance of cellular matrix-interacting proteins, and discovered that another viral component that interacts with matrix, the C protein, is required for efficient viral release via recruitment of cellular factors. Further, to establish critical tools for these investigations that allow modification and modulation of both virus and host factors, we established and improved reverse genetics systems for Nipah virus and other paramyxoviruses, and we also pioneered a method to rapidly downregulate host factors at the protein level.

FIGURES

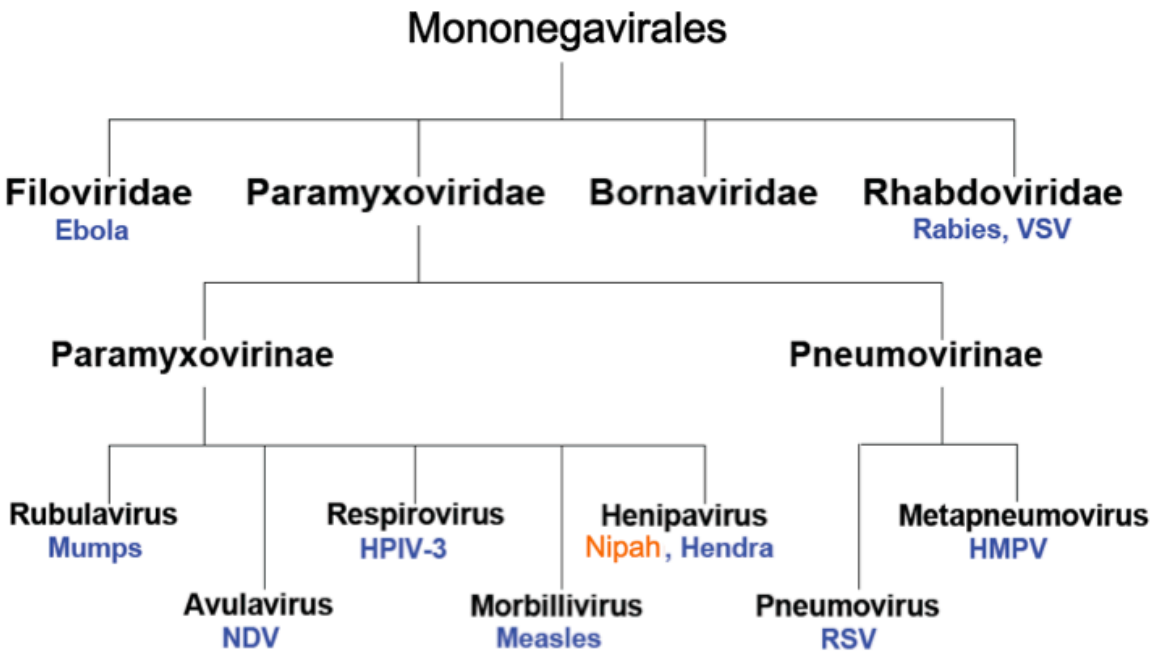

Figure 1-6. Nipah and Hendra viruses are the deadliest members of the *Paramyxoviridae* family. Order *Mononegavirales*, representing the enveloped viruses with negative-sense, single-stranded RNA genomes, comprises many well-known pathogens of biomedical and agricultural importance. VSV, vesicular stomatitis virus; NDV, Newcastle disease virus; HPIV-3, human parainfluenza virus type 3; RSV, respiratory syncytial virus; HMPV, human metapneumovirus.

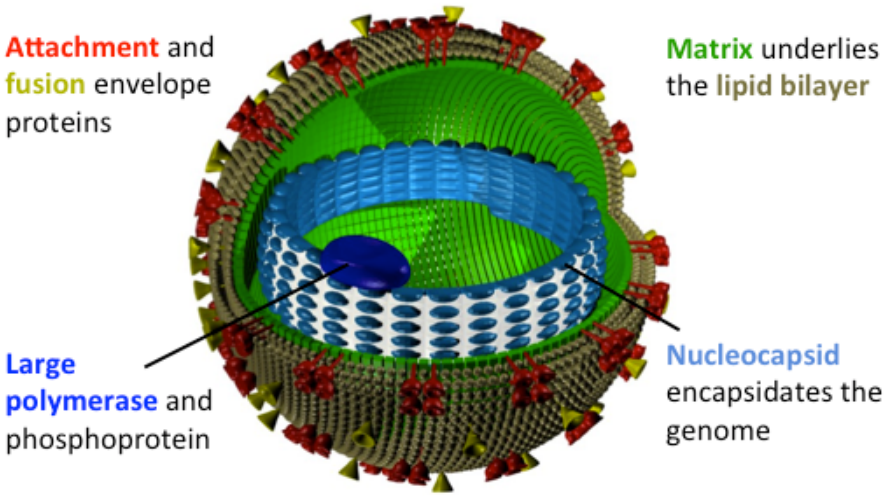

Figure 1-7. Matrix underlies the lipid bilayer and mediates intra-virion interactions. Matrix is responsible for viral assembly and budding, while the coordinated action of the attachment and fusion proteins mediate entry into target cells. The nucleocapsid encapsidates the genome (shown as a white ring). The large polymerase and phosphoprotein jointly form the RNA-dependent RNA polymerase, and together with the encapsidated genome form the ribonucleoprotein complex (RNP).

REFERENCES

1. Harrison MS, Sakaguchi T, Schmitt AP. Paramyxovirus assembly and budding: building particles that transmit infections. *The international journal of biochemistry & cell biology*. 2010;42(9):1416-1429.

2. Takimoto T, Portner A. Molecular mechanism of paramyxovirus budding. *Virus research*. 2004;106(2):133-145.

3. Rima BK, Duprex WP. Molecular mechanisms of measles virus persistence. *Virus research*. 2005;111(2):132-147.

4. Cathomen T, Mrkic B, Spehner D, et al. A matrix-less measles virus is infectious and elicits extensive cell fusion: consequences for propagation in the brain. *The EMBO journal*. 1998;17(14):3899-3908.

5. Inoue M, Tokusumi Y, Ban H, et al. A new Sendai virus vector deficient in the matrix gene does not form virus particles and shows extensive cell-to-cell spreading. *Journal of virology*. 2003;77(11):6419-6429.

6. Takimoto T, Murti KG, Bousse T, Scroggs RA, Portner A. Role of matrix and fusion proteins in budding of Sendai virus. *Journal of virology*. 2001;75(23):11384-11391.

7. Sugahara F, Uchiyama T, Watanabe H, et al. Paramyxovirus Sendai virus-like particle formation by expression of multiple viral proteins and acceleration of its release by C protein. *Virology*. 2004;325(1):1-10.

8. Schmitt AP, Leser GP, Waning DL, Lamb RA. Requirements for budding of paramyxovirus simian virus 5 virus-like particles. *Journal of virology*. 2002;76(8):3952-3964.

9. Li M, Schmitt PT, Li Z, McCrory TS, He B, Schmitt AP. Mumps virus matrix, fusion, and nucleocapsid proteins cooperate for efficient production of virus-like particles. *Journal of virology*. 2009;83(14):7261-7272.

10. Patch JR, Crameri G, Wang LF, Eaton BT, Broder CC. Quantitative analysis of Nipah virus proteins released as virus-like particles reveals central role for the matrix protein. *Virology journal*. 2007;4:1.

11. Tashiro M, McQueen NL, Seto JT, Klenk HD, Rott R. Involvement of the mutated M protein in altered budding polarity of a pantropic mutant, F1-R, of Sendai virus. *Journal of virology*. 1996;70(9):5990-5997.

12. Naim HY, Ehler E, Billeter MA. Measles virus matrix protein specifies apical virus release and glycoprotein sorting in epithelial cells. *The EMBO journal*. 2000;19(14):3576-3585.

13. Giuffre RM, Tovell DR, Kay CM, Tyrrell DL. Evidence for an interaction between the membrane protein of a paramyxovirus and actin. *Journal of virology*. 1982;42(3):963-968.

14. Miazza V, Mottet-Osman G, Startchick S, Chaponnier C, Roux L. Sendai virus induced cytoplasmic actin remodeling correlates with efficient virus particle production. *Virology*. 2011;410(1):7-16.

15. Bose S, Malur A, Banerjee AK. Polarity of human parainfluenza virus type 3 infection in polarized human lung epithelial A549 cells: role of microfilament and microtubule. *Journal of virology*. 2001;75(4):1984-1989.

16. Carlton JG, Martin-Serrano J. Parallels between cytokinesis and retroviral budding: a role for the ESCRT machinery. *Science*. 2007;316(5833):1908-1912.

17. Hanson PI, Shim S, Merrill SA. Cell biology of the ESCRT machinery. *Current opinion in cell biology*. 2009;21(4):568-574.

18. Williams RL, Urbe S. The emerging shape of the ESCRT machinery. *Nature reviews Molecular cell biology*. 2007;8(5):355-368.

19. Chen BJ, Lamb RA. Mechanisms for enveloped virus budding: can some viruses do without an ESCRT? *Virology*. 2008;372(2):221-232.

20. Votteler J, Sundquist WI. Virus budding and the ESCRT pathway. *Cell host & microbe*. 2013;14(3):232-241.

21. Boonyaratanakornkit J, Schomacker H, Collins P, Schmidt A. Alix serves as an adaptor that allows human parainfluenza virus type 1 to interact with the host cell ESCRT system. *PloS one*. 2013;8(3):e59462.

22. Sakaguchi T, Kato A, Sugahara F, et al. AIP1/Alix is a binding partner of Sendai virus C protein and facilitates virus budding. *Journal of virology*. 2005;79(14):8933-8941.

23. Irie T, Nagata N, Yoshida T, Sakaguchi T. Recruitment of Alix/AIP1 to the plasma membrane by Sendai virus C protein facilitates budding of virus-like particles. *Virology*. 2008;371(1):108-120.

24. Gosselin-Grenet AS, Marq JB, Abrami L, Garcin D, Roux L. Sendai virus budding in the course of an infection does not require Alix and VPS4A host factors. *Virology*. 2007;365(1):101-112.

25. Salditt A, Koethe S, Pohl C, et al. Measles virus M protein-driven particle production does not involve the endosomal sorting complex required for transport (ESCRT) system. *The Journal of general virology*. 2010;91(Pt 6):1464-1472.

26. Patch JR, Han Z, McCarthy SE, et al. The YPLGVG sequence of the Nipah virus matrix protein is required for budding. *Virology journal*. 2008;5:137.

27. Ciancanelli MJ, Basler CF. Mutation of YMYL in the Nipah virus matrix protein abrogates budding and alters subcellular localization. *Journal of virology*. 2006;80(24):12070-12078.

28. Bauer A, Neumann S, Karger A, et al. ANP32B is a nuclear target of henipavirus M proteins. *PloS one*. 2014;9(5):e97233.

29. Lamp B, Dietzel E, Kolesnikova L, et al. Nipah virus entry and egress from polarized epithelial cells. *Journal of virology*. 2013;87(6):3143-3154.

CHAPTER 2

HENIPAVIRUS REVERSE GENETICS

CHAPTER 2.1

REVERSE GENETICS AS A CRITICAL TOOL FOR MOLECULAR AND FUNCTIONAL INVESTIGATIONS

As opposed to *forward* genetics, in which the genetic basis for an observed phenotype is examined, *reverse* genetics seeks to examine the functional outcome of a specific genetic mutation or variation. As applied to virology, reverse genetics technology represents the ability to rescue replication-competent virus upon introduction of cloned DNAs into cells. The first successful rescue of a virus from order *Mononegavirales* (enveloped viruses with nonsegmented, negative-sense RNA genomes) was that of rabies virus (family *Rhabdoviridae*) in 1994.[1] This success was followed in quick succession by rescue of vesicular stomatitis virus (also family *Rhabdoviridae*) as well as the paramyxoviruses SeV, MeV, and respiratory syncytial virus.[2-6] Today, reverse genetics systems are widespread for numerous members of *Mononegavirales*, although these systems are still beset by difficulties with rescue efficiency.[7]

REVERSE GENETICS AND THE VIRUS LIFECYCLE

A schematic of the paramyxovirus life cycle is shown in Figure 2-1. Upon viral entry, the negative-sense viral genome is transcribed into both positive-sense mRNAs, which encode for the viral proteins, and positive-sense full-length antigenome. The regulatory decision for transcription of distinct mRNAs vs. full-length antigenome may be dictated by the intracellular concentration of the nucleocapsid protein, which encapsidates the full-length RNAs.[8] In this way, viral protein production can be initially favored, but full-length genome production can be subsequently favored when the levels of viral protein are high. Full-length antigenome can then serve as a template to amplify transcription of negative-sense viral genome. Finally, viral genome is packaged into the virion with other viral components.

Reverse genetics for *Mononegavirales* involves the introduction of DNA that serves as a template for transcription of full-length positive-sense RNA antigenome, along with constructs expressing nucleocapsid (N), phosphoprotein (P), and large RNA-dependent RNA polymerase (L), which together comprise the necessary viral replicative complex to initiate replication of the antigenome into the negative-sense genome.[7] Initial efforts to rescue virus with transcription of

negative-sense genome failed, likely because the positive-sense mRNAs for N, P and L could anneal to the complementary negative-sense transcript, impeding the initiation of replication and perhaps also triggering antiviral responses via cellular sensing of dsRNA.[7]

EXISTING METHODOLOGY AND CHALLENGES

The predominant method of transcribing the full-length antigenome as well as the N, P, and L mRNAs involves the use of T7 RNA polymerase. Because the wild-type bacteriophage T7 gene is not codon-optimized for mammalian expression and expresses poorly, sufficient levels of T7 polymerase are usually obtained via simultaneous infection with a highly attenuated vaccinia virus modified to express T7 polymerase,[9-11] or use of a hamster cell line that stably expresses T7 polymerase.[12] Both strategies have their drawbacks: the use of vaccinia requires extensive measures to separate the rescued virus from the vaccinia, depending on the strain of vaccinia used, and the use of vaccinia has been increasingly discouraged due to safety concerns; regarding the hamster cell line, certain functional studies may require rescue in cell types more relevant to the pathogenesis of the virus, and would thus be limited by use of a single cell line of a given species and expression pattern. In our studies, therefore, we codon-optimized the T7 polymerase gene for mammalian expression, which can then be simply introduced along with the DNAs encoding the viral antigenome and the N, P and L genes.

Another challenge facing reverse genetics of *Mononegavirales* involves the production of enough viral antigenome to efficiently initiate replication. The T7 promoter is most efficient with three guanines at its 3' end, which are incorporated into 5' end of the transcript. Addition of these guanines, however, impedes efficient virus rescue, leading to extensive efforts for specific viruses to determine the number of guanines that leads to the most efficient rescue. The optimal number of guanines represents a balance between adequate transcription of virus antigenome vs. the impeding guanines, which must be lost from the subsequently replicating genome.[7] In the subsequent chapter on henipavirus reverse genetics, we insert a hammerhead ribozyme in

between the optimal T7 promoter and the start of the Nipah virus antigenome, thus allowing both high levels of transcription and avoidance of the inhibitory guanines, thus improving rescue efficiency and the robustness of the system.

The efficiency of rescue for viruses in *Mononegavirales* has been typically highly inefficient, with one recovery event in 10^5 transfected cells representing the highest reported efficiency for any member of *Mononegavirales* until more recently,[7,13] with the advent of the hammerhead ribozyme insertion strategy that was first employed with rabies virus.[14] Such low efficiency for rescue of wild-type virus only emphasizes the difficulty experienced with rescue of mutant and attenuated viruses, for which the lack of rescue may indicate either an inefficient reverse genetics system or a complete inability to rescue. In Chapter 2.3, therefore, we expand the use of codon-optimized T7 polymerase and the hammerhead ribozyme to achieve more efficient viral rescue for paramyxoviruses representing all five major genera of *Paramyxovirinae*.

REVERSE GENETICS AS A CRITICAL TOOL FOR FUNCTIONAL INVESTIGATIONS

Only with reverse genetics can mutations, reporter genes, and other modifications be introduced into the replication-competent virus. Our findings in subsequent chapters throughout this work highlight functional investigations that have made use of modified paramyxoviruses generated by reverse genetics.

FIGURES

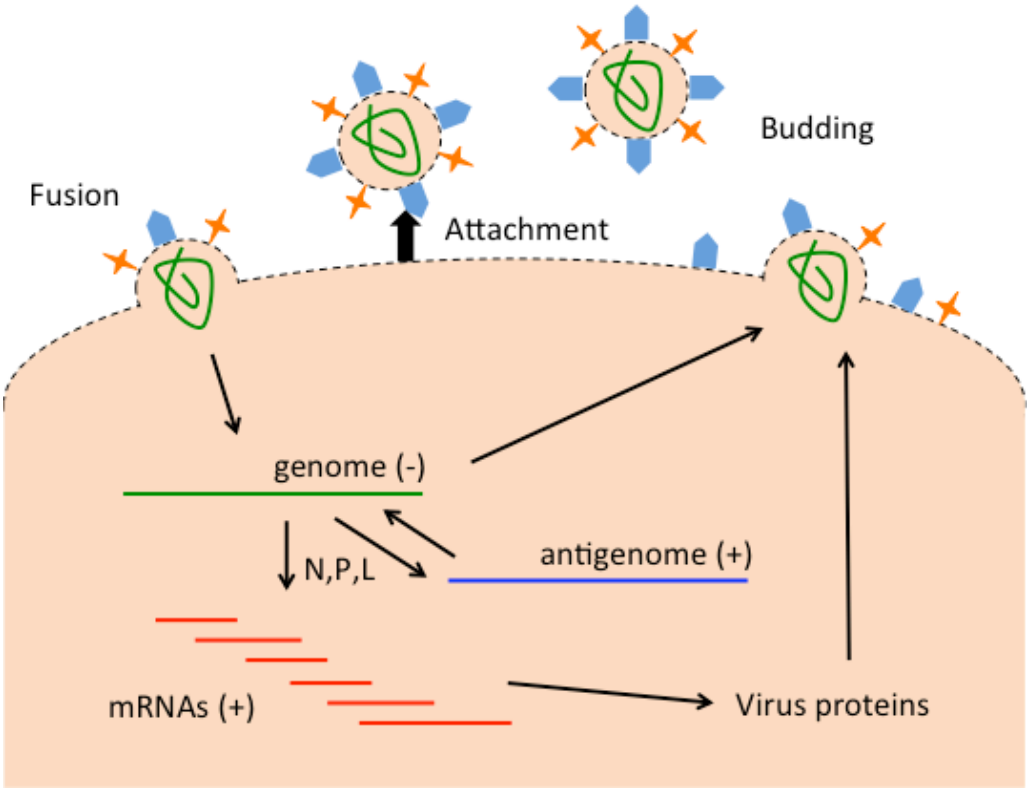

Figure 2-1. Schematic overview of the paramyxoviral life cycle. The viral RNA-dependent RNA polymerase transcribes the negative-sense genome into either positive-sense mRNAs or positive-sense full-length antigenome. The antigenome can then serve as a template for transcription of further negative-sense genome, again mediated by the viral RNA-dependent RNA polymerase. N, nucleocapsid; P, phosphoprotein; L, large polymerase (see Chapter 1.2).

REFERENCES

1. Schnell MJ, Mebatsion T, Conzelmann KK. Infectious rabies viruses from cloned cDNA. *The EMBO journal*. 1994;13(18):4195-4203.

2. Collins PL, Hill MG, Camargo E, Grosfeld H, Chanock RM, Murphy BR. Production of infectious human respiratory syncytial virus from cloned cDNA confirms an essential role for the transcription elongation factor from the 5' proximal open reading frame of the M2 mRNA in gene expression and provides a capability for vaccine development. *Proceedings of the National Academy of Sciences of the United States of America*. 1995;92(25):11563-11567.

3. Garcin D, Pelet T, Calain P, Roux L, Curran J, Kolakofsky D. A highly recombinogenic system for the recovery of infectious Sendai paramyxovirus from cDNA: generation of a novel copy-back nondefective interfering virus. *The EMBO journal*. 1995;14(24):6087-6094.

4. Lawson ND, Stillman EA, Whitt MA, Rose JK. Recombinant vesicular stomatitis viruses from DNA. *Proceedings of the National Academy of Sciences of the United States of America*. 1995;92(10):4477-4481.

5. Radecke F, Spielhofer P, Schneider H, et al. Rescue of measles viruses from cloned DNA. *The EMBO journal*. 1995;14(23):5773-5784.

6. Whelan SP, Ball LA, Barr JN, Wertz GT. Efficient recovery of infectious vesicular stomatitis virus entirely from cDNA clones. *Proceedings of the National Academy of Sciences of the United States of America*. 1995;92(18):8388-8392.

7. Conzelmann KK. Reverse genetics of mononegavirales. *Current topics in microbiology and immunology*. 2004;283:1-41.

8. Whelan SP, Barr JN, Wertz GW. Transcription and replication of nonsegmented negative-strand RNA viruses. *Current topics in microbiology and immunology*. 2004;283:61-119.

9. Fuerst TR, Niles EG, Studier FW, Moss B. Eukaryotic transient-expression system based on recombinant vaccinia virus that synthesizes bacteriophage T7 RNA polymerase. *Proceedings of the National Academy of Sciences of the United States of America*. 1986;83(21):8122-8126.

10. Sutter G, Ohlmann M, Erfle V. Non-replicating vaccinia vector efficiently expresses bacteriophage T7 RNA polymerase. *FEBS letters*. 1995;371(1):9-12.

11. Wyatt LS, Moss B, Rozenblatt S. Replication-deficient vaccinia virus encoding bacteriophage T7 RNA polymerase for transient gene expression in mammalian cells. *Virology*. 1995;210(1):202-205.

12. Buchholz UJ, Finke S, Conzelmann KK. Generation of bovine respiratory syncytial virus (BRSV) from cDNA: BRSV NS2 is not essential for virus replication in tissue culture, and

the human RSV leader region acts as a functional BRSV genome promoter. *Journal of virology*. 1999;73(1):251-259.

13. Kato A, Sakai Y, Shioda T, Kondo T, Nakanishi M, Nagai Y. Initiation of Sendai virus multiplication from transfected cDNA or RNA with negative or positive sense. *Genes to cells : devoted to molecular & cellular mechanisms*. 1996;1(6):569-579.

14. Ghanem A, Kern A, Conzelmann KK. Significantly improved rescue of rabies virus from cDNA plasmids. *European journal of cell biology*. 2012;91(1):10-16.

CHAPTER 2.2

EFFICIENT HENIPAVIRUS REVERSE GENETICS FACILITATES ISOGENIC COMPARISONS OF MATRIX AND GLYCOPROTEINS AND ENABLES REAL-TIME MONITORING OF VIRAL SPREAD IN SMALL ANIMAL MODELS OF HENIPAVIRUS INFECTION

ABSTRACT

Nipah (NiV) and Hendra (HeV) viruses are closely related henipaviruses of the *Paramyxovirinae*. Spillover from their fruit bat reservoirs can cause severe disease in humans and livestock. Despite their high sequence similarity, NiV and HeV exhibit apparent differences in receptor and tissue tropism, envelope-mediated fusogenicity, replicative fitness, and other pathophysiologic manifestations. To investigate the molecular basis for these differences, we first established a highly efficient reverse genetics system that increased rescue titers by ≥3 logs, which offset the difficulty of generating multiple recombinants under constraining BSL-4 conditions. We then substituted singly and in combination, the matrix (M), fusion (F), and attachment glycoprotein (G) genes in mCherry-expressing recombinant NiV (rNiV) with their HeV counterparts. These chimeric but isogenic rNiVs replicated well in primary human endothelial cells and neurons, indicating efficient heterotypic complementation. The determinants of budding efficiency, fusogenicity, and replicative fitness were dissociable: HeV-M budded more efficiently than NiV-M, accounting for the early higher replicative titers of HeV-M-bearing chimeras, while the enhanced fusogenicity of NiV-G-bearing chimeras did not correlate with increased replicative fitness. Furthermore, to facilitate spatiotemporal studies on henipavirus pathogenesis, we generated a Firefly luciferase-expressing NiV and monitored virus replication and spread in infected interferon-α/β receptor knockout mice via bioluminescence imaging. While intraperitoneal inoculation resulted in neuroinvasion following systemic spread and respiratory tract replication, intranasal inoculation resulted in confined spread to regions corresponding to olfactory bulbs and salivary glands before subsequent neuroinvasion. This optimized henipavirus reverse genetics system will facilitate future investigations into the growing numbers of novel henipa-like viruses.

IMPORTANCE

Nipah (NiV) and Hendra (HeV) viruses are recently emergent, zoonotic, and highly lethal pathogens with pandemic potential. Although differences have been observed between NiV and HeV replication and pathogenesis, the molecular basis for these differences has not been examined. In this study, we established a highly efficient system to reverse engineer changes into replication-competent NiV and HeV, which facilitated generation of reporter-expressing viruses and recombinant NiV-HeV chimeras substituted in the genes responsible for viral exit (M, critical for assembly and budding) and viral entry (attachment (G) and fusion (F)). These chimeras revealed differences in the budding and fusogenic properties of the M and G proteins, respectively, which help explain previously observed differences between NiV and HeV. Finally, to facilitate future *in vivo* studies, we monitored replication and spread of a bioluminescent reporter-expressing NiV in susceptible mice, the first time such *in vivo* imaging has been performed under BSL-4 conditions.

INTRODUCTION

Nipah virus (NiV) and the closely related Hendra virus (HeV) are recently emergent, highly pathogenic paramyxoviruses that have the ability to cause severe and often fatal infections in humans and livestock, with clinical manifestations including acute febrile encephalitis and pulmonary syndromes. NiV has caused hundreds of cases in recurrent outbreaks in Southeast Asia with high case fatality rates (ranging from 40-100%),[1] and 4 of 7 documented cases of HeV in Australia were fatal.[2] These zoonotic viruses have repeatedly spilled over from their animal reservoir, the *Pteropus* spp. fruit bats, either directly (i.e., consumption of raw date palm sap contaminated with NiV-containing fluids) or via a domestic animal intermediate (i.e., pigs for NiV, or horses for HeV).[3] Because of their extreme pathogenicity and the absence of licensed human vaccines and antiviral therapeutics, handling of henipaviruses is restricted to high containment Biosafety level 4 (BSL-4) laboratories.

Until recently, NiV and HeV were the sole known members of the *Henipavirus* genus within the *Paramyxoviridae*, a family of RNA viruses with negative-sense, non-segmented genomes. In the past two years, an examination of bats within and beyond the *Pteropus* genus has uncovered a multitude of previously undescribed henipaviruses of unknown virulence and implications for human health.[4-7] The more widespread prevalence of henipaviruses, the documented human-to-human transmission of some strains,[8-10] along with recent evidence of potential henipavirus-like spillover events in Africa,[11] suggest that increased global surveillance efforts directed at detecting henipavirus spillover events are warranted. Indeed, the pandemic potential of NiV has been proposed.[12] These findings underscore the urgency of understanding the molecular determinants of henipavirus pathogenesis and transmission.

NiV and HeV infections cause similar disease symptoms and pathology; it appears that virus transmitted through the oronasal-oropharyngeal routes leads to systemic infection that results in end-organ vasculitis, respiratory distress, and acute encephalitis.[13] Both viruses use the highly conserved ephrin-B2 and -B3 receptor tyrosine kinases as host cell entry receptors, explaining their common preferential tropism for the vascular endothelium, lungs, and brain, all of which express high levels of cellular receptor.[14] Although the paucity of known human cases of HeV infection makes it difficult to compare NiV and HeV, it is intriguing that the case history suggests that HeV is difficult to contract, despite extensive exposure to infected aerosols and fluids from sick horses.[3,15] In contrast, the history of NiV outbreaks in Southeast Asia suggests that NiV may be easier to contract than HeV, with human-to-human transmission clearly documented in Bangladesh as well.[3]

Although NiV and HeV present grossly similar outcomes in human cases and established animal models,[13,16,17] the few studies that have directly compared NiV and HeV replication and pathogenesis *in vitro* and *in vivo* have shown significant but variable differences,[18-20] also depending on the animal model used. Upon intranasal (IN) inoculation in the Syrian golden

hamster model, Rockx *et al.* found that HeV infection was restricted to the lower airways, whereas NiV could also replicate in the upper respiratory tract.[19] The authors suggested that this tropism for the lower airway might explain the relative lack of HeV transmission in the natural case history. However, HeV infection induced lesions and disseminated more quickly than NiV in the hamster model, leading to a faster progression of disease. In contrast, interferon-α/β receptor knockout (IFNAR KO) did not develop clinical signs of disease upon IN inoculation with HeV, although they were clearly susceptible to NiV infection via the same route.[20] Finally, some strains of aged immunocompetent mice appeared to be susceptible to HeV-induced encephalitis, whereas NiV infection resulted in only limited subclinical infection of the lungs.[21,22]

In summary, these studies all found significant differences in NiV and HeV tissue tropism and virulence. HeV appeared to cause more systemic infection or fatal encephalitis than NiV in the hamster model and in aged immunocompetent mice, while the reverse was true in IFNAR KO mice. Importantly, the differential pathology between NiV and HeV in the IFNAR KO mouse model suggests that these differences may derive at least partly from the matrix, fusion, and attachment proteins, as opposed to the anti-innate immune functions of the phosphoprotein gene and its associated alternative gene products. Indeed, HeV may not use ephrin-B2 and/or -B3 as efficiently as NiV,[23,24] although these putative differences attributable to the envelope attachment glycoprotein have not been appropriately examined in the context of a replication-competent virus.

To identify the molecular determinants contributing to the differences in pathobiology between NiV and HeV, we used reverse genetics to engineer chimeric NiV viruses with the matrix and surface envelope genes replaced by their HeV counterparts, either singly or in combination. To construct such a large panel of chimeras, we first took steps to improve the robustness and efficiency of viral rescue, critical considerations for work performed under BSL-4 conditions. A combination of technical strategies allowed for a pure transfection protocol that resulted in a 3-log improvement in viral rescue titers. We used this improved system to rescue

recombinant NiV (Malaysia strain), HeV (prototype strain), and a panel of isogenic chimeras, all expressing a mCherry reporter. *In vitro* characterization revealed previously unknown differences in the budding and fusion properties of the henipavirus matrix protein and envelope glycoproteins, respectively. Finally, we also engineered a recombinant NiV expressing Firefly luciferase, which is suitable for *in vivo* bioluminescence imaging. Using the recently published IFNAR KO mouse model, we were able to monitor incipient and ongoing viral spread *in vivo*. Our robust and efficient reverse genetics system for rescuing recombinant henipaviruses presents a unique opportunity to dissect the molecular determinants of henipavirus pathogenesis, not only for NiV and HeV, but also the increasing numbers of henipaviruses being discovered.

MATERIALS AND METHODS

Cells and Viruses

VeroE6 (ATCC, CRL1586), Vero (ATCC, CCL-81), permissive HeLa (ATCC, CCL-2), 293T, and BSR-T7 cells were propagated in Dulbecco's modified Eagle's medium (DMEM; Gibco, Invitrogen) supplemented with 10% fetal bovine serum (FBS; Sigma), 100 U/mL penicillin (Sigma), 100 μg/mL streptomycin (Sigma) and 1% sodium pyruvate (Cellgro). BSR-T7 cells were also maintained in 1 mg/mL G418. Virus-infected cells were maintained at 37°C in 5% CO_2 in DMEM supplemented with 2% FBS, 100 U/mL penicillin and 100 μg/mL streptomycin. Human umbilical vein endothelial cells (HUVEC; Lonza) were maintained in EGM-2 MV medium, supplemented with 2% FBS, hydrocortisone, human epidermal growth factor, gentamicin, amphotecerin-B, vascular endothelial growth factor, human fibroblast growth factor, fibroblast growth factor basic, R3 insulin-like growth factor 1, ascorbic acid, and heparin, provided through the EGM-2 BulletKit. For human fetal brain neural stem cells (NSCs), the line K048 (generously provided by C. N. Svendsen) was utilized as previously described.[25]

Nipah virus (199901924 Malaysia prototype strain) was kindly provided by the Special Pathogens Branch (Centers for Disease Control and Prevention, GA, USA), and Hendra virus (prototype strain) was kindly provided by the Special Pathogens Program National Microbiology Laboratory Canadian Science Centre for Human and Animal Health (Winnipeg, Canada). Nipah virus used in this study had been passaged a total of six times in Vero cells, and Hendra virus was passaged four times in Vero cells. Viral stocks were prepared by infecting VeroE6 cells. For titrations, confluent monolayers of Vero cells were infected with 100 μL of serial ten-fold dilutions of virus-containing cell supernatant. After 1 hr incubation at 37°C and 5% CO_2, the inocula were removed and wells overlaid with a mixture of one part 1.0% methylcellulose (Fisher Scientific) and one part 2xMEM (Gibco) supplemented with 2% FBS and 2% penicillin/streptomycin. The plates were incubated at 37°C and 5% CO_2 for 3 days, then stained with 0.25% crystal violet in 10% buffered formalin. Plates were washed, plaques enumerated, and concentrations of pfu/mL in the cell culture supernatant calculated. All work with live virus was carried out under Biosafety level 4 conditions in the Robert E. Shope and the Galveston National Laboratory at the University of Texas Medical Branch (UTMB).

Ribozyme cleavage assay

Ribozyme test constructs (see Figure 1B, insert as shown between the NdeI and HindIII sites in pcDNA3.1(-)) were transfected into BSR-T7 cells in 6-well format using Lipofectamine 2000 (Invitrogen). Tested hammerhead ribozyme sequences were derived and modified from a number of publications as indicated in Figure 2-2 (panel A).[26-31] Two hours post-transfection, cells were collected in TRIzol (Invitrogen), and RNA extracted following the manufacturer's instructions. Samples were treated with DNase (Invitrogen) at 1 mM $MgCl_2$, EDTA-treated, and then reverse-transcribed at 1 mM $MgCl_2$ with the SuperScript III First-Strand Synthesis System (Invitrogen). qPCR was performed with the SensiFAST SYBR & Fluorescein Kit (Bioline), and the primers used were positioned as indicated in Figure 2-2 (panel B). Standard curves were generated by using the RbzA test construct as template.

Construction of rNiV$_{RbzA}$-mCherry-P2A-M

A list of the constructs in this study with nomenclature explanation is provided in Table 1. A T7-driven positive-sense NiV "minigenome", between the NdeI and HindIII restriction sites in pcDNA3.1(-), was previously synthesized with the following elements: T7 promoter, 3'leader, N 5'UTR, RFP, N 3'UTR, M 5'UTR, M, M 3'UTR, F 5'UTR, F, F 3'UTR, G 5'UTR, G, G 3'UTR, 5'trailer, HDV ribozyme, T7 terminator. NiV-N, -P, and -L were amplified from the previously described pTM1-based accessory plasmids.[32] The P and L 5' and 3' UTRs were synthesized by Genscript. The full-length construct displayed in Figure 2-3 (panel A) was assembled by serial modification of the original minigenome construct by use of overlapping PCRs to join DNA fragments with Velocity DNA Polymerase (Bioline), with subsequent insertion into the construct at unique restriction sites by restriction digest/ligation or In-Fusion (Clontech). All cloning was performed with Stbl2 *E. coli* (Invitrogen) with growth at 30°C. The NiV sequence matches NCBI NC_002728.1 except for one silent mutation in N, A649G (position in the NCBI sequence).

Subsequent modifications to rNiV

All mutagenesis and modification was performed using standard overlapping PCR with Velocity DNA Polymerase (Bioline), with the ends of the final DNA product compatible with the use of In-Fusion (Clontech) for insertion into the desired restriction sites in rNiV. Existing restriction sites were sufficient, and it was not necessary to introduce artificial restriction sites (except for a single introduced site usually flanking the 3' end of the reporter gene for cloning convenience). Insertion into digested rNiV was performed by restriction digest/ligation or In-Fusion (Clontech). The ligation or In-Fusion reaction was transformed into Stbl2s (Invitrogen) and selected on LB ampicillin at 30°C overnight. Clones were grown in TB ampicillin at 30°C, screened by restriction digest and fully sequenced. <u>rNiV-HeV chimeras:</u> The HeV-M, -F, and -G ORFs were amplified from HeV cDNA (see below) and used to replace the corresponding NiV genes in rNiV$_{RbzA}$-mCherry-P2A-M in various combinations (see Figure 2-3, panel A). <u>rNiV-</u>

EGFP^{NP} and rNiV-Fluc^{NP}: The EGFP and Firefly luciferase ORFs were inserted between N and P, with duplication of the N to P intergenic region.

Construction of rHeV$_{RbzA}$-mCherry-P2A-M

Positive-sense cDNA was amplified from HeV (prototype strain; AF017149) RNA using AccuScript High Fidelity 1st Strand cDNA Synthesis Kit (Agilent). DNA fragments were amplified from cDNA using Velocity DNA Polymerase (Bioline) and cloned into rNiV$_{RbzA}$-mCherry-P2A-M-(HeV-M/F/G) by serial replacement, first between MluI and NotI, then between NotI and AgeI, and finally with simultaneous insertion of two fragments between AgeI and PmeI using In-Fusion (Clontech). The HHrbz sequence in Stem I designed to anneal to the NiV 3' leader, "TTGGT", was mutated to "TCGGT" to match the HeV 3' leader. For the support plasmids, HeV-N, -P, and -L were cloned into pTM1 as previously described for NiV,[32] with the two C ORF start codons mutated in P (from ATGATG to ACGACG) to prevent potential inhibition of rescue.[33]

Recovery of recombinant viruses from cDNA

The recovery of recombinant viruses was slightly modified from previously described protocols.[34,35] 293T cells were seeded into 12-well plates (1.5 x 10^5 cells per well). Cells were transfected the following day with the rNiV antigenomic construct (3.5 μg), codon-optimized T7 RNA polymerase in pCAGGS (1 μg), and the previously published support plasmids[32] NiV-N (1 μg), NiV-P (0.2 μg), and NiV-L (0.4 μg), using TransIT-LT1 transfection reagent (Mirus) according to the manufacturer's recommendations. After 4 days, syncytia formation and expression of fluorescent reporter genes could be detected by microscopy. Supernatant was collected at 4 days post-transfection and stored at -80°C for subsequent preparation of virus stocks and determination of virus titer by plaque assay with Vero cells.

Virus growth kinetics

Cells in 12-well format were infected at a multiplicity of infection (MOI) of 0.1 or 1.0, and supernatants were collected and replenished every 12 hours post-infection (hpi). Samples were stored at -80°C until subsequent determination of viral titer by plaque assay with Vero cells.

Immunofluorescence staining

HUVECs on coverslips were infected at MOI 0.1. At 24 hpi, cells were fixed with 10% formalin for a minimum of 24 hours prior to removal from the BSL-4 laboratory. Samples were washed 3 times with PBS, incubated in blocking buffer (0.5% saponin, 3% BSA in PBS), then incubated with 1:250 Alexa Fluor 647 phalloidin (Invitrogen) in blocking buffer. After 3 washes with 0.5% saponin in PBS, samples were incubated with DAPI to stain nuclei before mounting on slides. Confocal imaging was performed on a Leica SP5 confocal microscope.

qPCR of transcriptional gradient

HUVECs were infected with wild-type NiV or rNiV-mCh^{M} at MOI 0.1. RNA was isolated from TRIzol (Invitrogen) samples collected 12 hpi. mRNAs were purified from total RNA using the Dynabeads mRNA Purification Kit (Invitrogen) and reverse-transcribed into cDNA with oligo(dT) primer and the Tetro cDNA Synthesis Kit (Bioline). QPCR using the SensiFAST SYBR & Fluorescein Kit (Bioline) was performed using gene-specific primers, and standard curves for each gene were generated by a shared serial dilution of the full-length rNiV plasmid.

Immunoblotting

For comparison of NiV-M and HeV-M budding, 3XFLAG-tagged codon-optimized matrix[36] in pCMV-3Tag-1A (Agilent) was transfected into 293T cells with BioT transfection reagent (Bioline) according to manufacturer recommendations. Media was changed at 4 hpt, and cell lysates and supernatants were collected at 18 hpt. Supernatants were clarified and ultracentrifuged through 20% sucrose at 145k x g for 1.5 hrs to pellet virus-like particles. Samples in SDS Laemmli were boiled and run on 10% Tris-glycine SDS-PAGE. Upon transfer to PVDF (Immobilon-FL, Millipore), membranes were incubated in Odyssey Blocking Buffer (LI-COR Biosciences) overnight at 4°C, then incubated in mouse anti-FLAG M2 antibody (1:50,000, Strategene) or rabbit anti-COX IV antibody (1:2000, LI-COR Biosciences) for 1 hr at room temperature, followed by fluorescent secondary antibody (1:10,000 of goat anti-mouse IRDye

800CW or goat anti-rabbit IRDye 680LT, LI-COR Biosciences). Fluorescence images were obtained on a LI-COR Odyssey imaging system.

For detection of NiV-M in virus-infected cells, HUVECs (approx. 2.5 x 10^5 cells/well of a 12-well plate) were infected with wild-type NiV (Malaysia strain), rNiV-mCherry-P2A-M, or the P2A-optimized rNiV-mCherry-P2A-M at a MOI of 0.1. The cells were harvested at 24, 36, and 48 hpi in 2xSDS Laemmli buffer, boiled, and run on denaturing 12% SDS-PAGE. Upon transfer to PVDF, the membrane was blocked overnight at 4°C in PBS-T buffer with 5% milk, then incubated with rabbit polyclonal anti-NiV-M antibody [36] (1:1000) or mouse monoclonal anti-mCherry (1:2000, Abcam) for 1 hr at room temperature. Membranes were washed three times with PBS-T buffer, then incubated with a horseradish peroxidase-conjugated goat anti-rabbit or goat anti-mouse secondary antibody (1:10,000, Santa Cruz Biotechnology). Luminescence was detected through autoradiography using an enhanced chemiluminescent substrate (SuperSignal West Pico Chemiluminescent Substrate, Pierce).

***In vivo* imaging**

Interferon-α/β receptor knockout (IFNAR KO) mice (5-7 weeks old, 129/Sv background; obtained from the laboratory colony of Dr. Paessler at UTMB[37]) were utilized for *in vivo* bioluminescence imaging (IVIS) at BSL-4 containment. Prior to inoculation, mice were shaved to maximize detection of the bioluminescent signal. Mice were anesthetized with 2% isoflurane and inoculated with 8x10^5 pfu/100µl/mouse of rNiV-Fluc^{NP} via the intraperitoneal (IP) route, or 8x10^4 pfu/50µl/mouse via the intranasal (IN) route. Prior to imaging, mice were given D-luciferin (Caliper) through the IP route (150 mg/kg). Bioluminescence was measured using an IVIS Spectrum platform, which was equipped with a CCD camera system. Images were analyzed with the Living Image 4.3.1 software package. Acquisition time was set to auto for each image, with fixed f/stop at F1, and medium binning.

RESULTS

Improved henipavirus reverse genetics with optimized self-cleaving hammerhead ribozyme

Paramyxovirus rescue systems typically incorporate a "GGG" sequence between the minimal T7 promoter and the 5' end of the antigenome, thus allowing relatively efficient transcription by T7 polymerase, yet impeding efficient rescue because the Gs must be lost from the genomic transcript to maintain the rule of six and the appropriate terminal sequence. With the aim of improving the reliability and efficiency of reverse genetics for use in relatively onerous BSL-4 conditions, we evaluated whether the inclusion of a self-cleaving hammerhead ribozyme (HHrbz) at the 5' end of the antigenome would increase rescue efficiency by (i) providing the exact genomic terminus required for efficient replication, and (ii) thus allowing the inclusion of the transcript-initiating "GGG" sequence in the optimal T7 promoter. We modified and screened seven HHrbz motifs for cleavage efficiency at the 5' end of the NiV antigenome (Figure 2-2, panel A). RbzA represents a standard HHrbz, whereas the other HHrbzs are thought to retain efficient cleavage at the low magnesium concentrations reflective of the intracellular environment (submillimolar Mg^{2+}). Using a qRT-PCR-based assay to detect cleavage of RNA isolated from transfected cells (Figure 2-2, panel B), we found that three ribozymes (D, F, and G) self-cleaved with similar or greater efficiency than RbzA, and of these, RbzF resulted in essentially complete cleavage (Figure 2-2, panel C). Surprisingly, even RbzA, the standard HHrbz unoptimized for low Mg^{2+}, resulted in nearly 90% cleavage. We then chose to evaluate whether RbzA and RbzF would improve the rescue efficiency of full-length recombinant NiV.

We therefore constructed a full-length NiV cDNA (based on the Malaysia strain) with a T7-driven antigenome flanked at the 3' end by a hepatitis delta ribozyme, and we inserted a mCherry fluorescent reporter upstream of the matrix protein (M) gene, linked to M via a P2A ribosomal skipping sequence. As has been previously suggested, incorporating the reporter as part of an existing ORF may better preserve the natural polar transcriptional gradient of the virus.[38] Four versions were made, with (i) no additional Gs ($T7_{min}$), (ii) 3 Gs ($T7_{3G}$), (iii) RbzA

($T7_{3G(+)}$ HH_{RbzA}), or (iv) RbzF ($T7_{3G}$ HH_{RbzF}) following the minimal T7 promoter (Figure 2-2, panel D). These constructs were individually co-transfected with the essential support plasmids (codon-optimized T7 polymerase and T7-driven NiV nucleoprotein (N), phosphoprotein (P), and RNA-dependent RNA polymerase (L)) into 293T cells. Titering of cell culture supernatants collected 4-5 days post-transfection revealed that inclusion of RbzA, and to a lesser extent RbzF, resulted in a ≥3 log increase in rescue viral titers compared to the constructs without a HHrbz (Figure 2-2, panel D). We therefore chose to include RbzA in our future reverse genetics constructs. Furthermore, this rescue system was robust, as over 80% of the recombinant viruses we have successfully rescued thus far have rescued on the first attempt (unpublished observations). Use of the codon-optimized T7-RNAP (T7opt) was critical: it obviates the need for vaccinia-driven T7-RNAP, which has unavoidable cytopathic effects, and it also removes the cryptic splice sites present in bacteriophage-derived T7-RNAP. This robust and efficient HHrbz-T7opt-based reverse genetics system enabled us to generate multiple recombinant henipaviruses for more refined studies on henipavirus replication and pathogenesis.

Chimeric recombinant NiV-HeV viruses reveal that the henipavirus matrix and envelope proteins exhibit heterologous cross-complementation

To determine if the viral envelope fusion (F) and attachment (G) glycoproteins, as well as the matrix (M) protein, contribute to the pathogenic differences described in NiV and HeV infections, we generated a panel of chimeric henipaviruses in an isogenic $rNiV_{RbzA}$-mCherry-P2A-M (rNiV-mCh^{M}) background (Figure 2-3, panel A, see Table 1 for additional details). We substituted, singly or in combination, the M, F, and G genes in rNiV-mCh^{M} with their HeV counterparts. In addition, we generated the full-length recombinant HeV counterpart, $rHeV_{RbzA}$-mCherry-P2A-M (rHeV-mCh^{M}). All recombinant viruses were successfully rescued and replicated well, albeit to varying degrees, in human neuron/astrocyte cultures derived from fetal cortical neural stem cells (hNSC-derived neurons/astrocytes), as well as in primary human

umbilical vein endothelial cells (HUVECs), plateauing at 36 – 48 hpi (Figure 2-3, panels B and C).

The NiV and HeV F and G glycoproteins are known to functionally cross-complement each other in cell-cell fusion assays and viral pseudotype entry assays,[23,39] which both require overexpression of F and G genes. Whether such heterotypic envelope cross-complementation will occur in the context of a replication-competent virus has not been examined. Here, the efficient replication of chimeric viruses rNiV-mCh^{M}-HeV-F and rNiV-mCh^{M}-HeV-G (Figure 2-3, right side of panels B and C) confirms that heterotypic complementation occurs in a biologically relevant context. Interestingly, we also found that the matrix proteins of NiV and HeV can support functional incorporation of the heterotypic envelope glycoproteins (rNiV-mCh^{M}-HeV-F/G and rNiV-mCh^{M}-HeV-M, respectively) (Figure 2-3, right side of panels B and C). Further highlighting the genetic relatedness of NiV and HeV, the replication of rNiV-mCh^{M}-HeV-M also demonstrates that HeV-M, in its role as the central organizer of viral assembly and budding, can functionally interface with the heterotypic NiV N-P-L replication complex.

HeV-M buds more efficiently than NiV-M

Unexpectedly, at early time points (12 and 24 hpi) in both hNSC-derived neurons/astrocytes and HUVECs (Figure 2-3, right side of panels B and C), the chimeras bearing either HeV-M or HeV-M/F/G replicated to higher titers than the parental rNiV-mCh^{M} or any of the other chimeras *lacking* HeV-M. Quantitative Western blotting for matrix in a virus-like particle budding assay indicated that HeV-M buds about 2.5-fold more efficiently than NiV-M (Figure 2-3, panels D and E), thus providing a potential explanation for the increased titers seen for the HeV-M-bearing chimeras at early time points.

Fusogenicity is not a correlate of replicative fitness

Furthermore, our data shows that the HeV-G-bearing viruses are less fusogenic than their NiV-G-bearing counterparts. The presence of HeV-G, whether in a rNiV-mCh^{M} chimera (#4 to #6), or in a full-length recombinant HeV (rHeV-mCh^{M}, #7), resulted in less syncytia formation at 24

hpi relative to viruses that expressed NiV-G (#1 to #3) (Figure 2-4, panels A and B). Consistent with this observation, both homotypic NiV-F/G viruses (#1 and #2) exhibited more syncytia formation at 24 hpi than the homotypic HeV-F/G viruses (#5 to #7) (Figure 2-4, panels A and B). This differential fusogenicity was not an artifact of the recombinant genetic background used, as wild-type NiV also formed more numerous syncytia than wild-type HeV during infection of the same primary cell types (HUVECs, data not shown). Yet despite this apparently greater fusogenicity of the NiV-F/G-bearing viruses, they plateaued at similar or lower titers than their isogenic HeV-F/G-bearing counterparts, suggesting that fusogenicity is not a correlate of replicative fitness, at least *in vitro* (see Figure 2-3, panels B and C).

Insertion of an ORF in between the N and P genes does not affect the NiV transcriptional gradient

In our initial chimera constructs, we inserted the mCherry ORF upstream of the matrix gene via a P2A ribosomal skipping sequence to avoid disturbing the natural polar transcriptional gradient. Indeed, our quantitative comparison of viral mRNA transcripts upon infection with either wild-type NiV or rNiV-mCh^{M} showed similar transcriptional gradients: mRNA levels were stable for the first three genes (N, P, and M), but decreased exponentially thereafter, about 3-fold for each subsequent gene (Figure 2-5, panel A). The transcriptional gradient drop-off for HeV also occurs right after the M gene.[40] Despite the similar transcriptional gradients between wild-type NiV and rNiV-mCh^{M}, we observed that rNiV-mCh^{M} had slower replication kinetics *in vitro*, in primary human cells such as hNSC-derived neurons/astrocytes and HUVECs (Figure 2-3, left side of panels B and C) and even in permissive cell lines such as HeLa and Vero cells (Figure 2-5, panel B for Vero cells). Indeed, rHeV-mCh^{M} was similarly attenuated compared to wild-type HeV (Figure 2-3, left side of panels B and C).

A large N-terminal fusion is known to impede the budding function of NiV-M.[36] We hypothesized that inefficient P2A peptide-mediated ribosomal skipping may result in an apparent wild-type transcriptional gradient, yet affect virus replication and budding in a post-

transcriptional manner. Western blotting for NiV-M in cell lysates from HUVECs infected with rNiV-mCh^{M} revealed that P2A ribosomal skipping was indeed inefficient, with about a third of the M protein present as a mCherry fusion protein (Figure 2-5, panel C, see lanes 2 at various time points). We therefore added a short GSG linker upstream of the P2A sequence, which has been reported to result in more efficient ribosome skipping.[41,42] Indeed, this modification to rNiV-mCh^{M} resulted in essentially complete ribosomal skipping (Figure 2-5, panel C, compare lanes 2 and 3), which in turn corresponded to improved growth kinetics *in vitro* (Figure 2-5, panel D). Nevertheless, the peak titer of rNiV-mCh^{M} remained below that of wild-type NiV. The P2A ribosomal skipping sequence appends a proline to the N-terminus of the second protein, and it may be the case that despite efficient ribosomal skipping, this additional amino acid attenuates matrix function.

While our mCherry-P2A-matrix reporter strategy had been useful in revealing the differential determinants of budding and fusogenicity between NiV and HeV in isogenic comparisons *in vitro*, we sought a reporter insertion strategy that would more closely reflect wild-type NiV replication kinetics. We therefore rescued a recombinant NiV with EGFP inserted between the N and P genes, with duplication of the N-to-P intergenic region (rNiV-EGFP^{NP}, see Table 1), similar to the strategy reported by Yoneda *et al.*[35] Since the transcriptional gradient attenuates only after the M gene, insertion of an ORF upstream of the M gene may not disturb the transcriptional gradient. Indeed, the transcriptional gradient of rNiV-EGFP^{NP} was similar to that of rNiV-mCh^{M} (Figure 2-5, panel A), but the *in vitro* growth of rNiV-EGFP^{NP} was now indistinguishable from that of wild-type NiV (Figure 2-5, panel B).

Fluc-expressing rNiV allows real-time monitoring of virus replication and spread in the IFNAR KO mouse

To our knowledge, henipavirus spread and pathogenesis has only been examined in autopsy series or in serial sacrifice studies of experimentally infected animals. To complement the future use of our NiV-HeV chimeras for examining the pathogenic symptomology in animal models, we

generated a Firefly luciferase (Fluc)-expressing rNiV using the N-P intergenic insertion strategy described above (rNiV-Fluc^{NP}, see Table 1). Viral expression of the Fluc reporter will allow for real-time monitoring of bioluminescence at sites of viral replication. As expected, growth of rNiV-Fluc^{NP} was similar to wild-type NiV in HUVECs (data not shown). We then infected IFNAR KO mice with rNiV-Fluc^{NP}, and monitored the spatial and temporal progression of viral replication as presented in Figure 2-6. Two groups of IFNAR KO mice (two females and two males per group) were infected via IN ($8x10^4$ pfu/animal) or IP ($8x10^5$ pfu/animal) routes, respectively, and mice were imaged daily starting at 2 days post-infection (dpi) using the *in vivo* imaging system (IVIS) at BSL-4.

IN inoculation resulted in viral replication primarily confined to the upper respiratory tract (Figure 2-6, panel A). All peripheral organs in the IN group lacked luminescence signals throughout the duration of the study, except for a transient, weak signal in the spleen in three out of four mice at 4 dpi. Interestingly, serial sacrifice studies of NiV-infected Syrian golden hamsters[19] also detected transient viral replication in the spleen. Bioluminescence remained confined to the oropharyngeal/oronasal areas at 3-5 dpi, including regions anatomically consistent with the location of the major salivary glands. In mice, the bilateral submandibular, sublingual and parotid glands form a contiguous structure across the anterior and lateral neck.[43] Mice presented with a hunched posture at 6 and 7 dpi, consistent with bioluminescence signals observed in the CNS, but the majority survived until the end of the study at 21 dpi with no overt symptoms.

By contrast, IP inoculation resulted in systemic infection by 2 dpi as indicated by low levels of bioluminescence throughout the main body cavity (Figure 2-6, bottom of panel B), with virus replication (bioluminescence) highest in the spleen (Figure 2-6, top of panel B). At 3 to 4 dpi, NiV progressively spread to the lungs, the respiratory tract and nasal turbinates. By 5 to 6 dpi, increasing bioluminescence in the olfactory bulb and invasion of the brain were obvious, coinciding with development of clinical signs of disease, such as hunched posture, hyperreflexia,

lethargy, seizures, and ataxic behavior. These results expand upon the report by Dhondt *et al.*[20] by providing evidence that even with IP infection in this animal model, invasion of the brain may result at least in part from respiratory transmission to the olfactory bulb. All IP-inoculated mice developed robust infection and were euthanized between 6 to 8 dpi. Moribund mice after IP infection had luminescence signals present in the upper respiratory tract (including regions of the salivary glands) and urinary (kidneys and bladder) tracts (Figure 2-6, bottom of panel B, Day 6), consistent with presumed modes of HNV transmission via saliva and urine. *Ex vivo* imaging of fresh, non-fixed whole brains from moribund mice after IP infection revealed infection of the olfactory bulb and olfactory tubercle, frontal cortex and cerebellum (Figure 2-6, panel C). Coronal brain slices further revealed bioluminescence signals in deeper brain structures such as the olfactory nucleus, the anterior commissure, nucleus accumbens, basal forebrain, and the amygdala nuclei (Figure 2-6, panel D).

Overall, these data demonstrate the applicability of Fluc-expressing henipaviruses to allow for sensitive detection and identification of early replication sites, spread and development of disease, with the ultimate goal of identifying the molecular determinants of henipavirus-induced pneumonia and encephalitis.

DISCUSSION

Reverse genetics systems for *Mononegavirales*, or the viruses with negative sense, non-segmented RNA genomes, have been typically fraught with inefficiency,[44] making their use under BSL-4 conditions an even greater difficulty. Although the addition of a hammerhead ribozyme between the optimal T7 promoter and the 5' end of the antigenome has been shown to improve rescue for certain negative strand RNA viruses such as rabies virus,[45] we demonstrate here that this strategy also significantly improves rescue for henipaviruses. While Lo *et al.*[38] recently reported rescue of NiV using a HHrbz, it is unclear whether (or by how much) inclusion of their HHrbz improves rescue, as no comparative data on the rescue efficiencies achieved was

reported. In light of the known sequence-dependent efficiency of ribozyme cleavage,[46] we screened seven HHrbz designs, three of which cleaved at equivalent or better efficiencies than the "standard" RbzA. These other HHrbz designs may be useful in a sequence-dependent context for the rescue of other negative-sense RNA viruses that require exact 5' and 3' termini.

Additionally, we also developed a one-step transfection protocol using a custom-designed codon-optimized T7 RNA polymerase expression plasmid, rather than recombinant vaccinia, as the source for T7 polymerase. A vaccinia-free rescue system alleviates the cytopathic effect and other technical complications associated with vaccinia infections, such as blind passaging on vaccinia non-permissive cells to isolate and/or purify the recombinant paramyxovirus, while codon optimization of the bacteriophage T7 gene significantly improves T7 expression and viral rescue.[47] Thus, our hammerhead ribozyme design strategy, in combination with our codon-optimized T7 polymerase, resulted in a highly efficient and robust rescue system that allowed for recovery of recombinant NiV and HeV directly from transfected producer cells without the need for blind passaging or addition of permissive cells for amplification of the rescued virus.

As mentioned above, NiV and HeV exhibit differential tissue tropisms and pathogenic characteristics. To identify the genetic determinants of these differences between NiV and HeV, we rescued an isogenic panel of rNiV-HeV chimeras with substitutions of the NiV M, F and G genes, singly and in combination, with their HeV counterparts. All chimeras resulted in efficiently replicating viruses, highlighting the phylogenetic relatedness of NiV and HeV. The ability of HeV-M to functionally interface with the heterologous NiV N/P/L replication complex and F/G envelope glycoproteins underscores a particularly close genetic relationship between NiV and HeV. The M and F/H envelope genes of the Peste-des-petits-ruminants virus have also shown to be functional in the genetic background of a vaccine strain of Rinderpest virus, a closely related morbillivirus[48]; however, it was not the intention of that study, which used a

smaller set of chimeras, to dissect the genetic determinants of budding or fusogenicity between the two morbilliviruses.

Consistent with previous observations that HeV is slower to form syncytia than NiV[18,49,50] and that HeV-G may bind ephrin-B2 and -B3 less efficiently than NiV-G,[23,24] our results show in the context of live recombinant virus infection that the HeV-G (attachment) glycoprotein is less fusogenic than NiV-G: all heterotypic and homotypic HeV-G bearing chimeras (Figure 2-4, panels A and B, constructs 4-7) form smaller and less numerous syncytia than their isogenic heterotypic and homotypic NiV-G bearing counterparts (Figure 2-4, panels A and B, constructs 1-3). This decreased fusogenicity associated with HeV-G (relative to NiV-G) might contribute, in part, to observed differences in HeV versus NiV transmissibility or tropism. We anticipate that future *in vivo* experiments with our NiV-HeV chimeras will shed further light on this question. In addition, our results showing higher titers of HeV-M-bearing viruses at early time points—particularly apparent in the infections of primary hNSC-derived neurons/astrocytes (Figure 2-3, panel B)—are consistent with the aforementioned faster dissemination of HeV in the hamster model once infection has taken place.[19]

Our reporter insertion strategy, linking the reporter to the matrix gene via a P2A ribosomal sequence, maintained the natural polar transcriptional gradient. Interestingly, the NiV mRNA gradient resembled the previously published HeV gradient,[40] with the initial sharp attenuation in transcript levels occurring at the M-F junction. Nevertheless, the wild-type transcriptional gradient observed for our initial rNiV-mCh^{M} infectious clone was insufficient to confer wild-type replication (Figure 2-3, panels B and C, and also Figure 2-5, panel B). The P2A ribosomal skipping peptide sequence we chose appears to be the most efficient of the major "2A" peptide sequences in widespread use.[51,52] Lo *et al.* used a F2A sequence to generate an infectious NiV reporter in a similar strategy to ours,[38] but no analysis of "cleavage" or comparison with wild-type virulence was presented. By adding a GSG linker upstream of the P2A sequence, we improved the efficiency of the P2A-mediated ribosomal skipping and correspondingly improved

the *in vitro* growth kinetics of our recombinant NiV (Figure 2-5, panel E). Nevertheless, the recombinant NiV remained attenuated, perhaps due to the unnatural attachment of proline to the N-terminus of matrix from the P2A sequence. Our finding that attenuation in transcript levels only occurs after the M gene led us to consider whether insertion of an ORF upstream of the M gene would even in fact disturb the transcriptional gradient. Insertion of EGFP in between the N and P genes, corresponding to the first described design for NiV reverse genetics,[35] also did not affect the transcriptional gradient (Figure 2-5, panel A), but this recombinant virus replicated similar to wild-type NiV (Figure 2-5, panel B).

To evaluate our ability to monitor the spatial and temporal progression of viral spread *in vivo*, we used a Firefly luciferase-expressing NiV in the recently established IFNAR KO mouse model.[20] IP and IN infections resulted in outcomes that were consistent with the previous report by Dhondt *et al.*,[20] but real-time bioluminescence imaging shed light on the dynamic processes of viral pathogenesis and transmission. Evidence of viral replication in the respiratory and urinary tracts in moribund animals provides strong evidence for the presumed modes of henipavirus transmission via respiratory secretions and urine. The spread of luminescence in IP-inoculated mice suggested that despite systemic infection in the body cavity, invasion of the brain might have followed viral spread to the respiratory tract and subsequent infection of the olfactory bulb, perhaps via aerosolized virus that infected olfactory receptors. While it is possible that breach of the blood-brain barrier was also involved, the relative contributions of these mechanisms of CNS invasion deserve further investigation. IN infection, on the other hand, resulted in viral spread that was limited to the upper respiratory tract, and CNS invasion again appeared to follow replication in the olfactory bulb, likely from direct infection of olfactory neurons as a result of the route of inoculation.

Our efficient and robust henipavirus reverse genetics system will enable the generation of multiple reporter viruses that will facilitate more refined *in vitro* and *in vivo* studies of henipavirus pathogenesis and spread, as well as the evaluation of vaccines and antivirals. For

example, we have designed other reporter-expressing viruses with their own unique advantages for *in vivo* studies, such as a NiV with a secreted *Gaussia* luciferase-P2A-eGFP dual expression cassette that can be used to monitor viral load directly in tissues by bioluminescence imaging or indirectly by measuring Gaussia luciferase activity in serum.[11] Future *in vivo* studies with these reporter constructs and recombinant henipavirus chimeras will not only reveal insights into NiV and HeV pathogenesis, but also open the door to similar investigations into different NiV strains (e.g., the Malaysian strain vs. the more diverse Bangladeshi strains, which also appear to have significant differences both epidemiologically and experimentally[53-55]), and newly discovered henipaviruses (such as Cedar virus and the African Gh-M74a[4,5]).

FIGURES

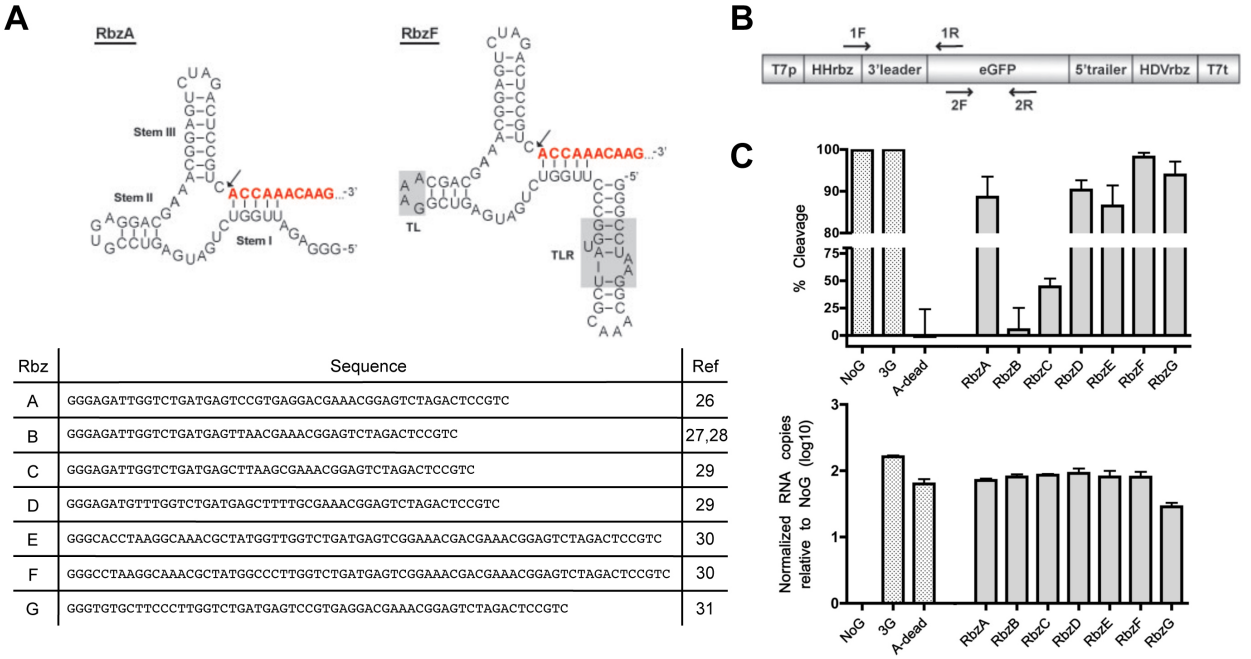

Rbz	Sequence	Ref
A	GGGAGATTGGTCTGATGAGTCCGTGAGGACGAAACGGAGTCTAGACTCCGTC	26
B	GGGAGATTGGTCTGATGAGTTAACGAAACGGAGTCTAGACTCCGTC	27,28
C	GGGAGATTGGTCTGATGAGCTTAAGCGAAACGGAGTCTAGACTCCGTC	29
D	GGGAGATGTTTGGTCTGATGAGCTTTTGCGAAACGGAGTCTAGACTCCGTC	29
E	GGGCACCTAAGGCAAACGCTATGGTTGGTCTGATGAGTCGGAAACGACGAAACGGAGTCTAGACTCCGTC	30
F	GGGCCTAAGGCAAACGCTATGGCCCTTGGTCTGATGAGTCGGAAACGACGAAACGGAGTCTAGACTCCGTC	30
G	GGGTGTGCTTCCCTTGGTCTGATGAGTCCGTGAGGACGAAACGGAGTCTAGACTCCGTC	31

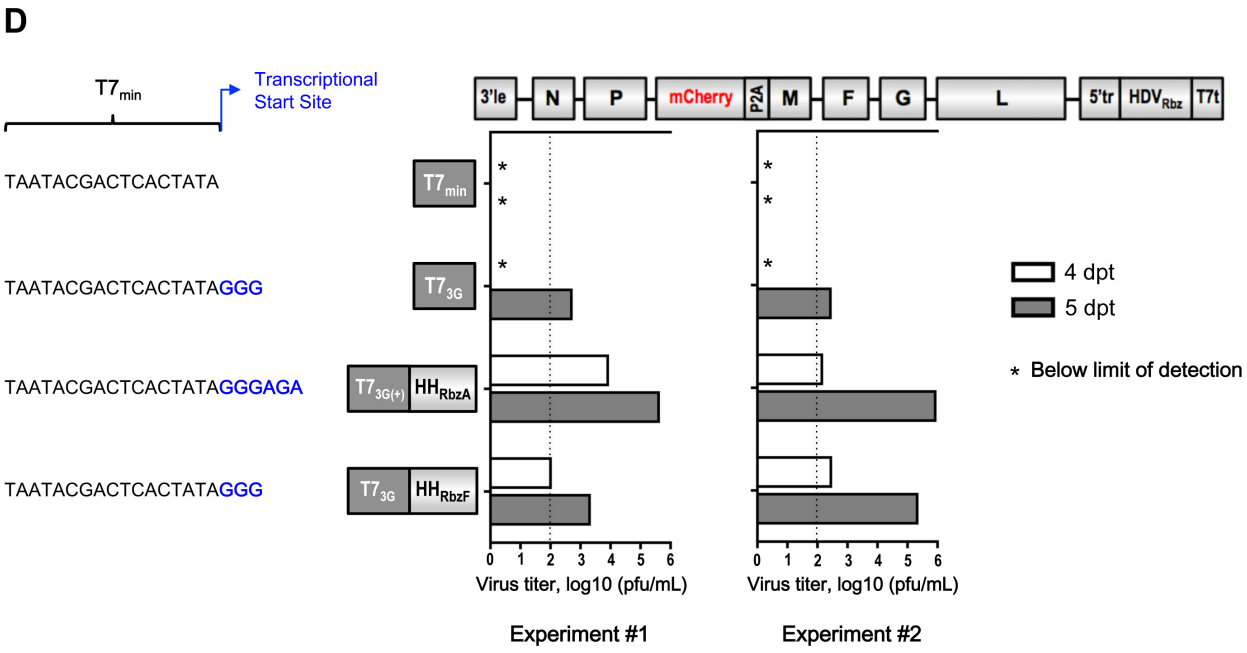

(*Previous page*)

Figure 2-2. Optimization of hammerhead ribozyme for 5' end of antigenome. (A) The sequence and structure of the two hammerhead ribozymes (HHrbzs) ultimately tested in NiV rescue are shown, with the NiV antigenome shown bolded in red. RbzA is a standard HHrbz ribozyme unoptimized for low Mg^{2+}, and RbzF is a modified version of a HHrbz optimized for low Mg^{2+}. (Arrow, autocleavage site; TL, tetraloop; TLR; tetraloop receptor.) **(B)** Following transfection and RNA collection as described in Materials and Methods, qRT-PCR was performed to detect PCR product 1 (lost upon cleavage due to lack of 1F primer binding) and PCR product 2 (always detected, regardless of HHrbz cleavage). % cleavage was determined as 100*((product 2 – product 1)/product 2). **(C)** The NoG and 3G constructs appear completely "cleaved" because they lack the HHrbz sequence that binds primer 1F. By contrast, A-dead, in which RbzA was rendered nonfunctional with a poison pill mutation, displays a lack of cleavage. Overall expression was determined by normalizing PCR product 2 to the hamster GAPDH gene. Error bars represent SD from 3 independent experiments. **(D)** Rescue of rNiV-mCh^{M} full-length antigenomic constructs with different T7 promoters and ribozymes as shown was performed as described in Materials and Methods. See also Table 1 for explanation of differences in the T7 promoter. Supernatants were collected at 3, 4, and 5 days post-transfection (dpt) for subsequent titering by plaque assay. No viral titer was detected for any condition at 3 dpt, but titers were detected for the ribozyme-bearing constructs starting at 4 dpt. The lower limit of detection, 100 pfu/mL, is indicated by the dotted lines. The results of two representative independent experiments are shown to illustrate the reproducibility of our rescue protocol.

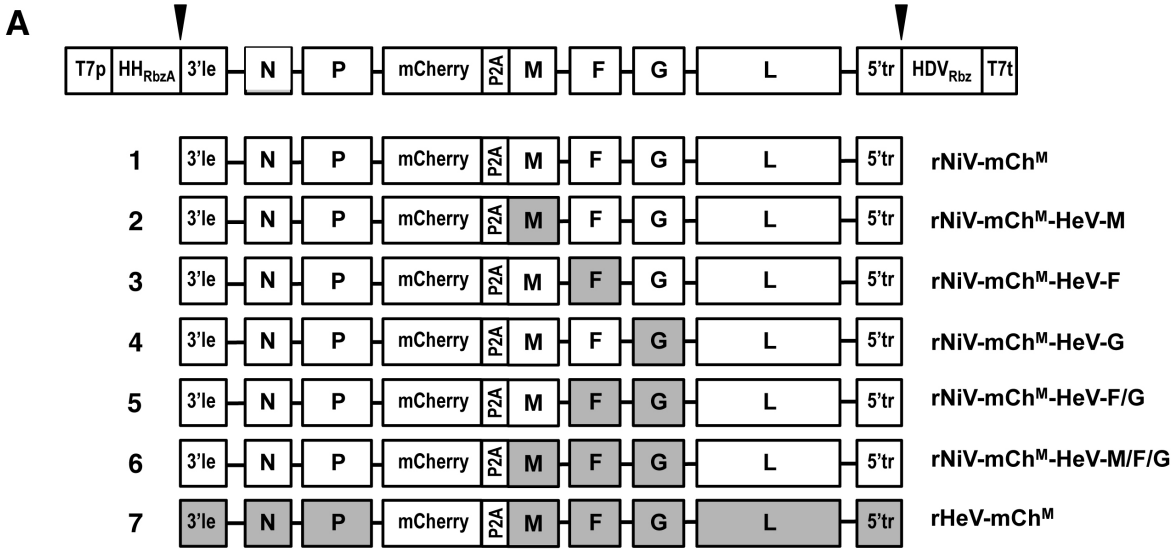
A
T7p
HHRbzA
3'le
N
P
mCherry
P2A
M
F
G
L
5'tr
HDVRbz
T7t
1
rNiV-mChM
2
rNiV-mChM-HeV-M
3
rNiV-mChM-HeV-F
4
rNiV-mChM-HeV-G
5
rNiV-mChM-HeV-F/G
6
rNiV-mChM-HeV-M/F/G
7
rHeV-mChM

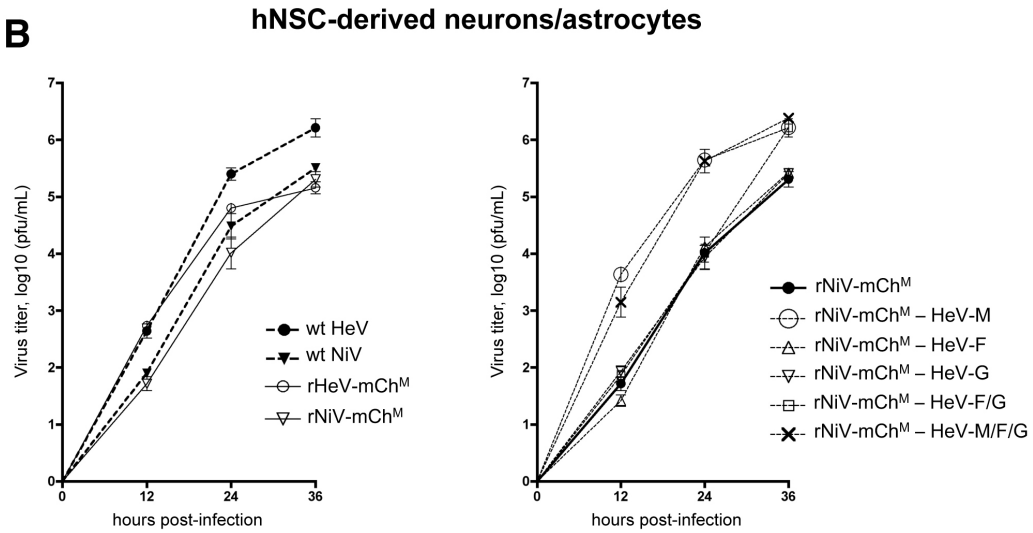
B
hNSC-derived neurons/astrocytes
Virus titer, log10 (pfu/mL)
hours post-infection
wt HeV
wt NiV
rHeV-mChM
rNiV-mChM
rNiV-mChM – HeV-M
rNiV-mChM – HeV-F
rNiV-mChM – HeV-G
rNiV-mChM – HeV-F/G
rNiV-mChM – HeV-M/F/G

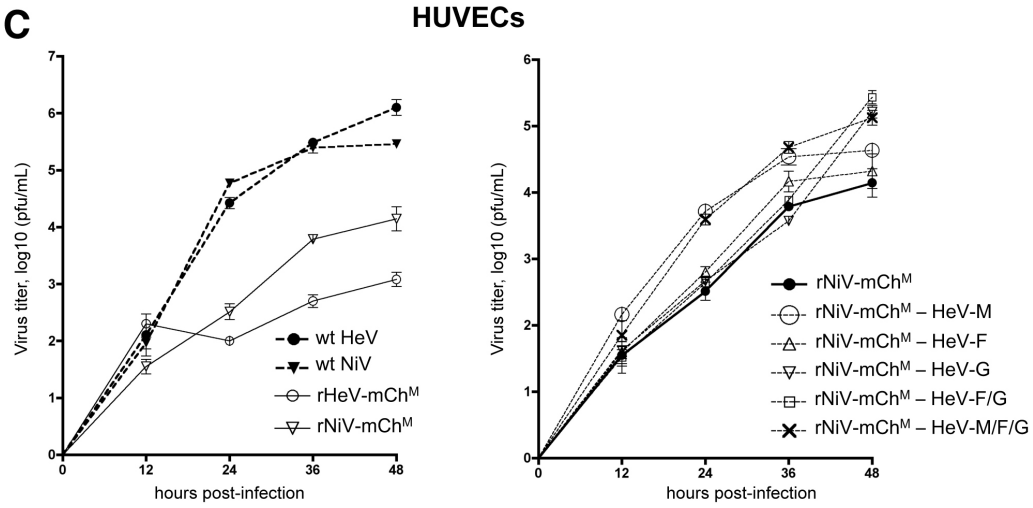
C
HUVECs
Virus titer, log10 (pfu/mL)
hours post-infection
wt HeV
wt NiV
rHeV-mChM
rNiV-mChM
rNiV-mChM – HeV-M
rNiV-mChM – HeV-F
rNiV-mChM – HeV-G
rNiV-mChM – HeV-F/G
rNiV-mChM – HeV-M/F/G

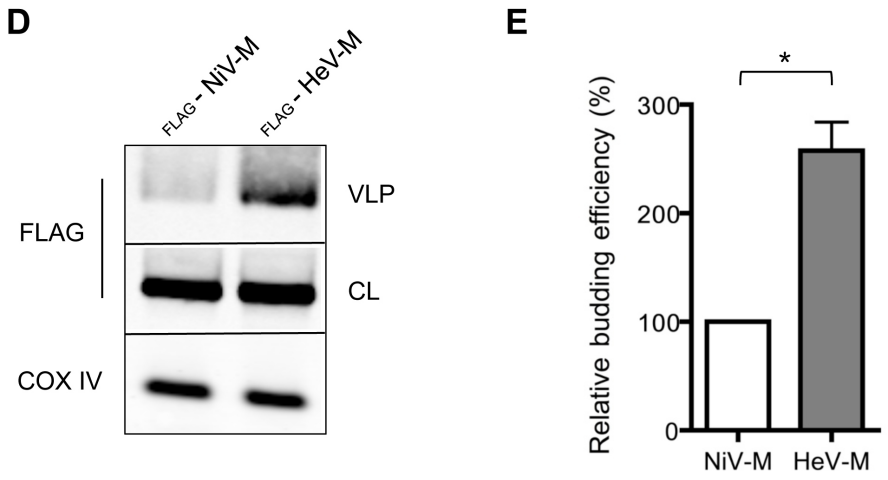

Figure 2-3. Replication kinetics of rNiV-HeV chimeric viruses reveals heterologous cross-complementation of henipavirus matrix and envelope proteins and demonstrates that HeV-M buds more efficiently than NiV-M. (A) The parental rNiV-mCh^{M} construct and relevant rNiV-HeV chimeras generated and rescued in this study are schematically diagrammed. Genetic components from NiV and HeV are indicated in orange and blue, respectively. T7p, T7 promoter; 3'le, 3' leader; 5'tr, 5' trailer; T7t, T7 terminator. The arrowheads indicate where the hammerhead ribozyme (HH_{Rbz}) and hepatitis delta virus ribozyme (HDV_{Rbz}) self-cleave. **(B)** hNSC-derived neurons/astrocytes and **(C)** HUVECs were infected with the indicated wild-type and recombinant viruses at MOI 0.1, and the growth kinetics were monitored as described in Materials and Methods. A representative experiment is shown, with error bars representing SD of triplicate samples. Two-way ANOVA followed by Bonferroni post-tests shows that both HeV-M-bearing chimeras have significantly higher titers than all other NiV-M-bearing rNiVs at 24 hpi for both HUVECs and hNSC-derived neurons/astrocytes, $p < 0.001$. **(D-E)** HeV-M buds more efficiently than NiV-M. **(D)** FLAG-tagged NiV-M and HeV-M were transfected into 293T cells. 18 hours post-transfection, cell lysates (CL) and virus-like particles (VLPs) in supernatants were collected and Western blotted for matrix (anti-FLAG) as described in Materials and Methods. A representative comparison of NiV-M vs. HeV-M in CL and VLP is shown. COX IV was used as the cell lysate loading control. **(E)** For each experiment, a titration of NiV-M was transfected to determine a best-fit NiV-M budding curve of relative matrix in CL (x variable) vs. relative matrix in VLP (y variable), as determined by quantitative fluorescent Western blots. In the same experiment, the relative budding efficiency of HeV-M was determined by comparison to this best-fit NiV-M budding curve. Error bar represents SD from 3 independent experiments; *, $p=0.0265$, 2-tailed paired Student's t-test.

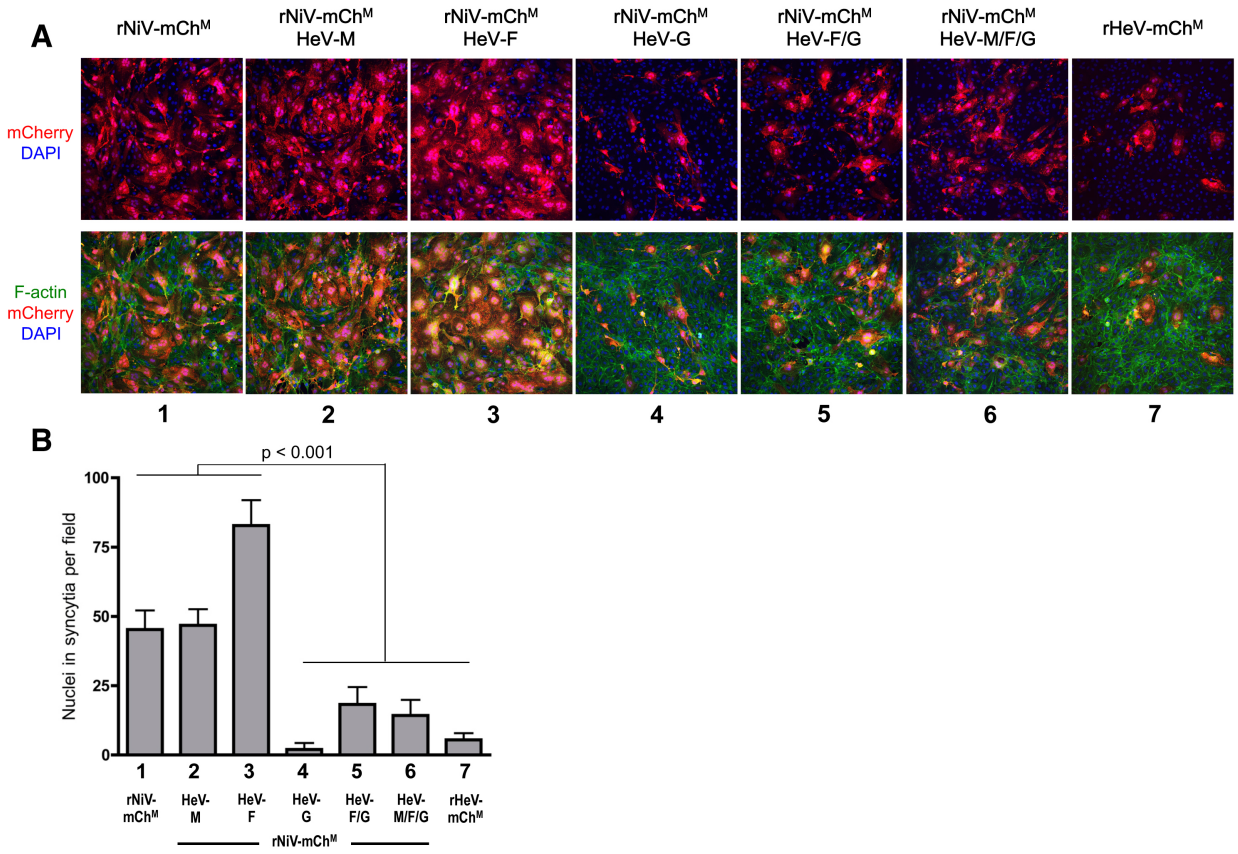

Figure 2-4. Fusogenicity of recombinant NiV-HeV chimeras in infected HUVECs. **(A-B)** Immunofluorescence imaging of syncytia formation in infected HUVECs shows differential fusogenicity of recombinant NiV-HeV chimeras. **(A)** HUVECs on coverslips were infected with the indicated mCherry-expressing viruses at MOI 0.1. At 24 hours post-infection, coverslips were fixed in formalin and stained with DAPI (in blue, for nuclei) and Alexa Fluor 647 phalloidin (in green, for F-actin). 20X confocal z-stacks were obtained, and a representative extended focus image for each virus is shown. **(B)** Nuclei within syncytia (3 or more nuclei within a mCherry-positive cell) were counted in 4 independent 40X fields per virus. Error bars represent SD. One-way ANOVA followed by a Tukey's multiple pairwise comparison test shows that all HeV-G-bearing viruses result in significantly less syncytia formation than all NiV-G-bearing viruses ($p < 0.001$).

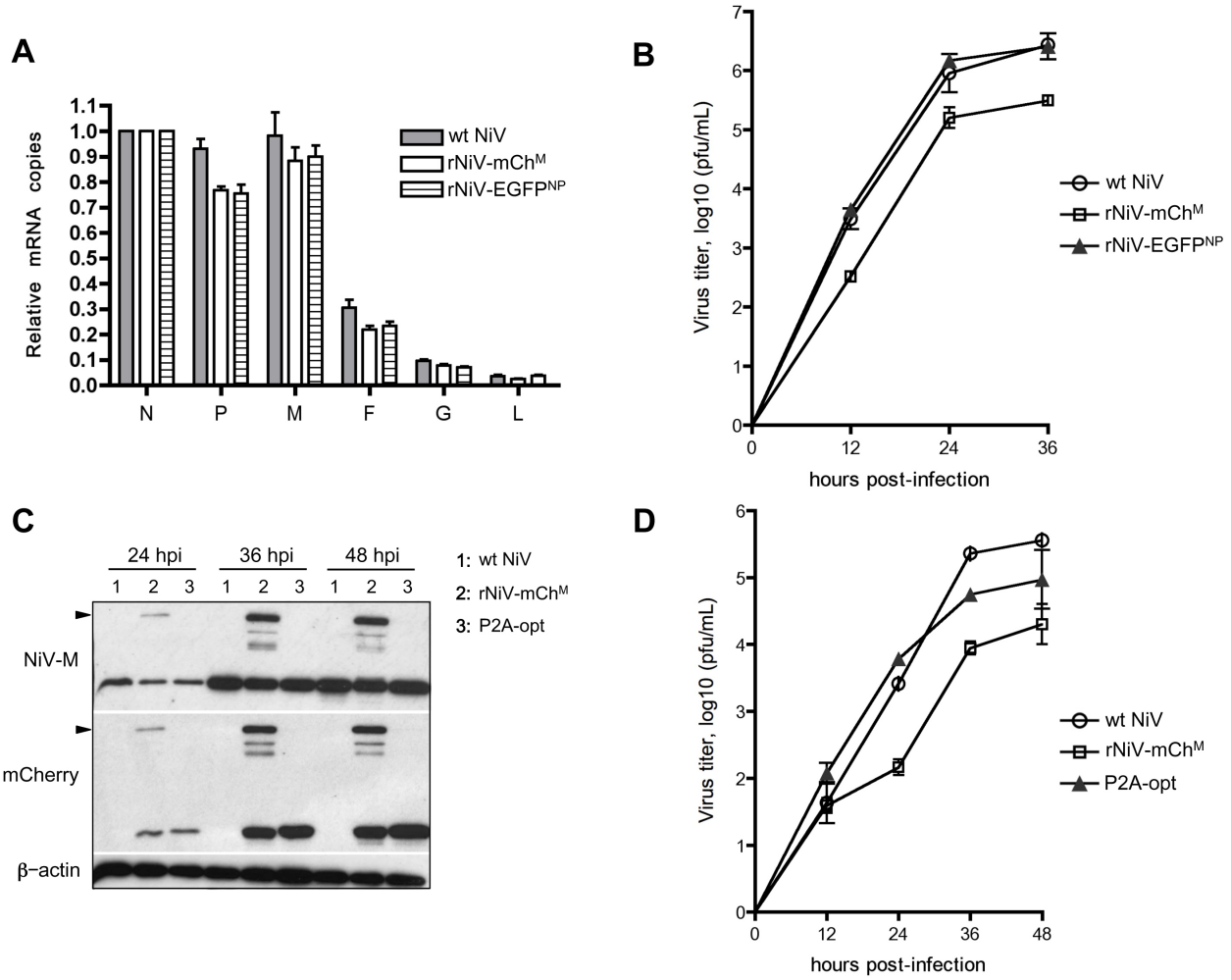

Figure 2-5. Insertion of an ORF between the N and P genes does not affect the NiV transcriptional gradient. (A) Wild-type and recombinant NiV have similar transcriptional gradients. HUVECs were infected with the indicated viruses at MOI 0.1, and RNA was isolated from samples collected at 24 hpi. mRNAs were selectively purified using oligo(dT) magnetic beads. qRT-PCR was performed for the viral genes, with standard curves generated by a shared serial dilution of the full-length rNiV plasmid. Error bars represent SD, representative of 3 independent experiments. **(B)** Vero cells were infected with the indicated viruses at MOI 1, and the growth kinetics were monitored as described in Materials and Methods. Error bars represent SD of 3 replicates. **(C)** HUVECs were infected with the indicated viruses at MOI 0.1, and cell lysates were collected at indicated time points. P2A-opt refers to a rNiV-mCh^M virus with a GSG linker inserted in front of the P2A sequence. Western analysis with anti-NiV-M and anti-mCherry shows that P2A ribosomal skipping in the mCherry-P2A-M cassette was inefficient for the original rNiV-mCh^M virus, and that insertion of the GSG linker results in essentially complete ribosomal skipping. The arrowheads indicate the uncleaved fusion product. **(D)** HUVECs were infected with the indicated viruses at MOI 0.1, and the growth kinetics were monitored as described in Materials and Methods.

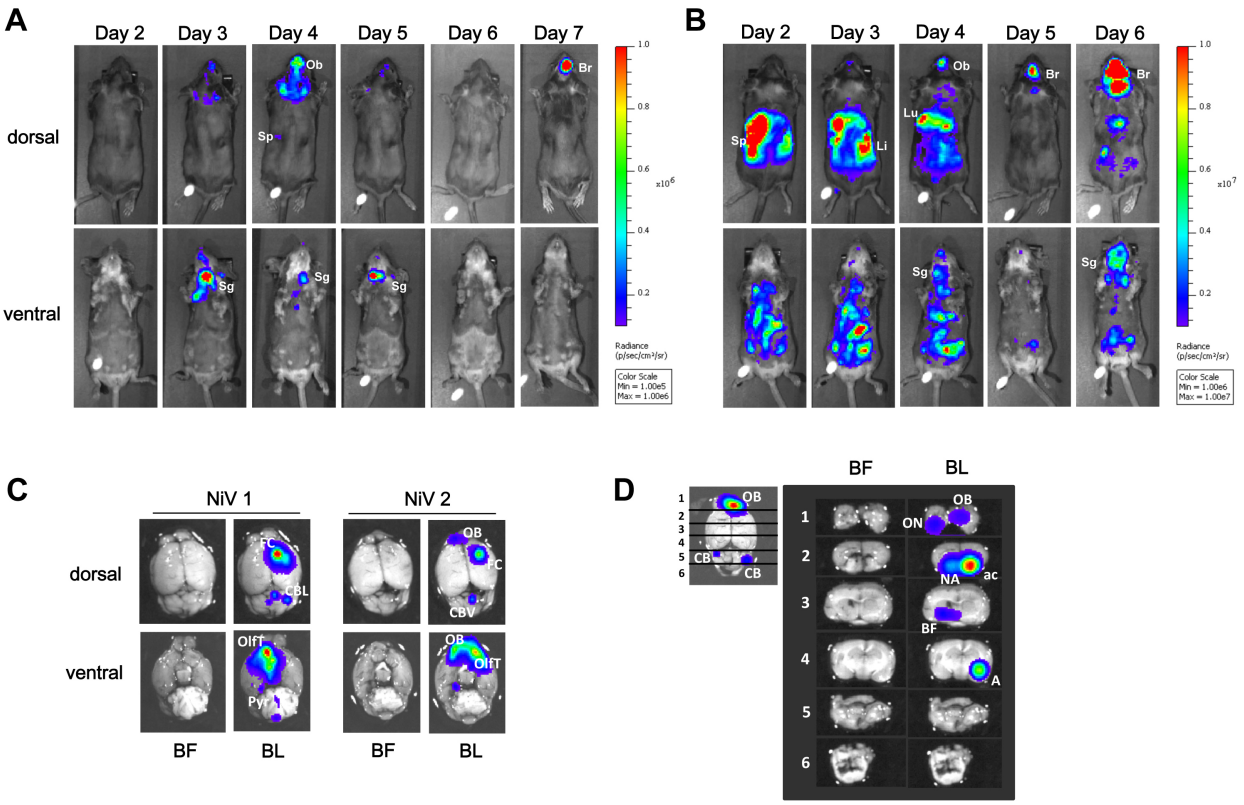

Figure 2-6. Spatial and temporal dynamics of recombinant Nipah virus infection monitored by *in vivo* bioluminescence imaging in IFNAR KO mice. Groups of four IFNAR KO mice each were infected with rNiV-Fluc^{NP} via the **(A)** intranasal (IN) ($8x10^4$ pfu/animal) or **(B)** intraperitoneal (IP) ($8x10^5$ pfu/animal) route, respectively. Infected animals were imaged at indicated time points as described in Materials and Methods. One representative female mouse is shown for each inoculation route. The data are displayed as radiance (bioluminescence intensity) on a rainbow log scale with a range of $1x10^5$ (blue) to $1x10^6$ (red) photons/s/cm^2/steradian for the IN mouse, and $1x10^6$ to $1x10^7$ for the IP mouse. Organs with positive bioluminescence signals are labeled as follows: Br, brain; Li, liver; Lu, lung; Ob, olfactory bulb; Sg, salivary gland; Sp, spleen. **(C)** *Ex vivo* imaging of fresh brains from moribund IP-infected mice at day 8 post-infection (identified as NiV 1 and NiV 2). BF, brightfield modus; BL, bioluminescence modus. Brain substructures with positive bioluminescence signals are labeled as follows: CBL, cerebellum - lateral hemisphere; CBV, cerebellum - vermis; FC, frontal cortex; OB, olfactory bulb; OlfT, olfactory tubercle; Pyr, pyramids. **(D)** Gross cross sections were prepared from a fresh brain from a moribund IP-infected mouse at day 6 post-infection. The numbered levels shown in the panel for the entire brain correspond to the labeled levels in cross section panels. Brain substructures with positive bioluminescence signals are labeled as follows: ac, anterior commissure; A, amygdala nuclei; BF, basal forebrain; CB, cerebellum; NA, nucleus accumbens; OB, olfactory bulb; ON, olfactory nucleus.

Name of Antigenomic Construct	Abbreviated Name	Descriptive Nomenclature[a,b]	T7 Promoter
$rNiV_{noG}$-mCherry-P2A-M	$rNiV_{noG}$-mCh^{M}	$[NiV_{Mal}]$ $T7_{P\text{-}min}$ (mCherry-P2A-M)	TAATACGACTCACTATA
$rNiV_{3G}$-mCherry-P2A-M	$rNiV_{3G}$-mCh^{M}	$[NiV_{Mal}]$ $T7_{P\text{-}3G}$ (mCherry-P2A-M)	TAATACGACTCACTATAGGG
$rNiV_{RbzA}$-mCherry-P2A-M	rNiV-mCh^{M}	$[NiV_{Mal}]$ $T7_{P\text{-}3G(+)}$ 5'RbzA-(mCherry-P2A-M)	TAATACGACTCACTATAGGGAGA
$rNiV_{RbzF}$-mCherry-P2A-M	$rNiV_{RbzF}$-mCh^{M}	$[NiV_{Mal}]$ $T7_{P\text{-}3G}$ 5'RbzF-(mCherry-P2A-M)	TAATACGACTCACTATAGGG
$rNiV_{RbzA}$-mCherry-P2A-M: HeV-M	rNiV-mCh^{M}-HeV-M	$[NiV_{Mal}]$ $T7_{P\text{-}3G(+)}$ 5'RbzA-(mCherry-P2A-M)^{1}-(M > $M_{HeV\text{-}Aus}$)^{2}	TAATACGACTCACTATAGGGAGA
$rNiV_{RbzA}$-mCherry-P2A-M: HeV-F	rNiV-mCh^{M}-HeV-F	$[NiV_{Mal}]$ $T7_{P\text{-}3G(+)}$ 5'RbzA-(mCherry-P2A-M)^{1}-(F > $F_{HeV\text{-}Aus}$)^{2}	TAATACGACTCACTATAGGGAGA
$rNiV_{RbzA}$-mCherry-P2A-M: HeV-G	rNiV-mCh^{M}-HeV-G	$[NiV_{Mal}]$ $T7_{P\text{-}3G(+)}$ 5'RbzA-(mCherry-P2A-M)^{1}-(G > $G_{HeV\text{-}Aus}$)^{2}	TAATACGACTCACTATAGGGAGA
$rNiV_{RbzA}$-mCherry-P2A-M: HeV-F/G	rNiV-mCh^{M}-HeV-F/G	$[NiV_{Mal}]$ $T7_{P\text{-}3G(+)}$ 5'RbzA-(mCherry-P2A-M)^{1}-(F/G > F/$G_{HeV\text{-}Aus}$)^{2}	TAATACGACTCACTATAGGGAGA
$rNiV_{RbzA}$-mCherry-P2A-M: HeV-M/F/G	rNiV-mCh^{M}-HeV-M/F/G	$[NiV_{Mal}]$ $T7_{P\text{-}3G(+)}$ 5'RbzA-(mCherry-P2A-M)^{1}-(M/F/G > M/F/$G_{HeV\text{-}Aus}$)^{2}	TAATACGACTCACTATAGGGAGA
$rNiV_{RbzA}$-N_eGFP_P	rNiV-$eGFP^{NP}$	$[NiV_{Mal}]$ $T7_{P\text{-}3G(+)}$ 5'RbzA-(N_eGFP_P)	TAATACGACTCACTATAGGGAGA
$rNiV_{RbzA}$-N_Fluc_P	rNiV-$Fluc^{NP}$	$[NiV_{Mal}]$ $T7_{P\text{-}3G(+)}$ 5'RbzA-(N_Fluc_P)	TAATACGACTCACTATAGGGAGA
$rHeV_{RbzA}$-mCherry-p2A-M	rHeV-mCh^{M}	$[HeV_{Aus}]$ $T7_{P\text{-}3G(+)}$ 5'RbzA-(mCherry-P2A-M)	TAATACGACTCACTATAGGGAGA

[a] Descriptive nomenclature: i) Virus and strain are in square brackets, with strain in subscript; ii) The type of promoter and 5' HHrbz, if any, are indicated; iii) Major features are within parentheses. For multiple features, each one is labeled with a superscript number; iv) Within a feature, "-" indicates direct connection (i.e., mCherry-P2A-M), whereas "_" indicates context (i.e., N_eGFP_P).

[b] $T7_{P\text{-}min}$ is the minimal T7 promoter without additional Gs to drive higher levels of transcription; $T7_{P\text{-}3G}$ has 3 additional Gs to drive higher levels of transcription; and $T7_{P\text{-}3G(+)}$ has an additional "AGA" sequence that is part of the optimal T7 promoter.

Table 2-1. Henipavirus reverse genetics constructs described in Chapter 2.2. See Materials and Methods for details on plasmid construction and virus rescue.

REFERENCES

1. SEARO. Surveillance and outbreak alert: Nipah virus outbreaks in the WHO South-East Asia Region. 2013; http://www.searo.who.int/entity/emerging_diseases/links/nipah_virus_outbreaks_sear/en/index.html. Accessed December 15, 2013.

2. Field H, Crameri G, Kung NY, Wang LF. Ecological aspects of hendra virus. *Curr Top Microbiol Immunol.* 2012;359:11-23.

3. Luby SP, Gurley ES. Epidemiology of henipavirus disease in humans. *Curr Top Microbiol Immunol.* 2012;359:25-40.

4. Drexler JF, Corman VM, Muller MA, et al. Bats host major mammalian paramyxoviruses. *Nat Commun.* 2012;3:796.

5. Marsh GA, de Jong C, Barr JA, et al. Cedar virus: a novel Henipavirus isolated from Australian bats. *PLoS Pathog*. 2012;8(8):e1002836.

6. Muleya W, Sasaki M, Orba Y, et al. Molecular Epidemiology of Paramyxoviruses in Frugivorous Eidolon helvum Bats in Zambia. *The Journal of veterinary medical science / the Japanese Society of Veterinary Science*. 2013.
7. Wu Z, Yang L, Yang F, et al. Novel Henipa-like virus, Mojiang Paramyxovirus, in rats, China, 2012. *Emerging Infectious Diseases*. 2014;20(6).

8. Blum LS, Khan R, Nahar N, Breiman RF. In-depth assessment of an outbreak of Nipah encephalitis with person-to-person transmission in Bangladesh: implications for prevention and control strategies. *Am J Trop Med Hyg*. 2009;80(1):96-102.

9. Chadha MS, Comer JA, Lowe L, et al. Nipah virus-associated encephalitis outbreak, Siliguri, India. *Emerg Infect Dis*. 2006;12(2):235-240.

10. Gurley ES, Montgomery JM, Hossain MJ, et al. Person-to-person transmission of Nipah virus in a Bangladeshi community. *Emerg Infect Dis*. 2007;13(7):1031-1037.

11. Pernet O, Beaty SM, Lebreton M, Schneider B, Wolfe N, Lee B. Evidence for Henipavirus spillover into human populations in Africa. XV International Conference on Negative Strand Viruses; 2013; Granada, Spain.

12. Luby SP. The pandemic potential of Nipah virus. *Antiviral Res*. 2013;100(1):38-43.

13. Wong KT, Tan CT. Clinical and pathological manifestations of human henipavirus infection. *Curr Top Microbiol Immunol.* 2012;359:95-104.

14. Pernet O, Wang YE, Lee B. Henipavirus receptor usage and tropism. *Curr Top Microbiol Immunol.* 2012;359:59-78.

15. Field HE, Mackenzie JS, Daszak P. Henipaviruses: emerging paramyxoviruses associated with fruit bats. *Curr Top Microbiol Immunol.* 2007;315:133-159.

16. Geisbert TW, Feldmann H, Broder CC. Animal challenge models of henipavirus infection and pathogenesis. *Curr Top Microbiol Immunol.* 2012;359:153-177.

17. Wong KT, Ong KC. Pathology of acute henipavirus infection in humans and animals. *Patholog Res Int.* 2011;2011:567248.

18. Aljofan M, Saubern S, Meyer AG, Marsh G, Meers J, Mungall BA. Characteristics of Nipah virus and Hendra virus replication in different cell lines and their suitability for antiviral screening. *Virus Res.* 2009;142(1-2):92-99.

19. Rockx B, Brining D, Kramer J, et al. Clinical outcome of henipavirus infection in hamsters is determined by the route and dose of infection. *Journal of virology.* 2011;85(15):7658-7671.

20. Dhondt KP, Mathieu C, Chalons M, et al. Type I interferon signaling protects mice from lethal henipavirus infection. *J Infect Dis.* 2013;207(1):142-151.

21. Dups J, Middleton D, Long F, Arkinstall R, Marsh GA, Wang LF. Subclinical infection without encephalitis in mice following intranasal exposure to Nipah virus-Malaysia and Nipah virus-Bangladesh. *Virology journal.* 2014;11(1):102.

22. Dups J, Middleton D, Yamada M, et al. A new model for Hendra virus encephalitis in the mouse. *PLoS One.* 2012;7(7):e40308.

23. Negrete OA, Chu D, Aguilar HC, Lee B. Single amino acid changes in the Nipah and Hendra virus attachment glycoproteins distinguish ephrinB2 from ephrinB3 usage. *Journal of virology.* 2007;81(19):10804-10814.

24. Bossart KN, McEachern JA, Hickey AC, et al. Neutralization assays for differential henipavirus serology using Bio-Plex protein array systems. *J Virol Methods.* 2007;142(1-2):29-40.

25. Wu P, Tarasenko YI, Gu Y, Huang LY, Coggeshall RE, Yu Y. Region-specific generation of cholinergic neurons from fetal human neural stem cells grafted in adult rat. *Nat Neurosci.* 2002;5(12):1271-1278.

26. Price SR, Ito N, Oubridge C, Avis JM, Nagai K. Crystallization of RNA-protein complexes. I. Methods for the large-scale preparation of RNA suitable for crystallographic studies. *J Mol Biol.* 1995;249(2):398-408.

27. Conaty J, Hendry P, Lockett T. Selected classes of minimised hammerhead ribozyme have very high cleavage rates at low Mg2+ concentration. *Nucleic Acids Res.* 1999;27(11):2400-2407.

28. McCall MJ, Hendry P, Mir AA, Conaty J, Brown G, Lockett TJ. Small, efficient hammerhead ribozymes. *Mol Biotechnol.* 2000;14(1):5-17.

29. Persson T, Hartmann RK, Eckstein F. Selection of hammerhead ribozyme variants with low Mg2+ requirement: importance of stem-loop II. *Chembiochem.* 2002;3(11):1066-1071.

30. Fedoruk-Wyszomirska A, Szymanski M, Wyszko E, Barciszewska MZ, Barciszewski J. Highly active low magnesium hammerhead ribozyme. *J Biochem*. 2009;145(4):451-459.

31. Burke DH, Greathouse ST. Low-magnesium, trans-cleavage activity by type III, tertiary stabilized hammerhead ribozymes with stem 1 discontinuities. *BMC Biochem*. 2005;6:14.

32. Halpin K, Bankamp B, Harcourt BH, Bellini WJ, Rota PA. Nipah virus conforms to the rule of six in a minigenome replication assay. *J Gen Virol*. 2004;85(Pt 3):701-707.

33. Sleeman K, Bankamp B, Hummel KB, Lo MK, Bellini WJ, Rota PA. The C, V and W proteins of Nipah virus inhibit minigenome replication. *J Gen Virol*. 2008;89(Pt 5):1300-1308.

34. Ciancanelli MJ, Volchkova VA, Shaw ML, Volchkov VE, Basler CF. Nipah virus sequesters inactive STAT1 in the nucleus via a P gene-encoded mechanism. *Journal of virology*. 2009;83(16):7828-7841.

35. Yoneda M, Guillaume V, Ikeda F, et al. Establishment of a Nipah virus rescue system. *Proc Natl Acad Sci U S A*. 2006;103(44):16508-16513.

36. Wang YE, Park A, Lake M, et al. Ubiquitin-regulated nuclear-cytoplasmic trafficking of the Nipah virus matrix protein is important for viral budding. *PLoS Pathog*. 2010;6(11):e1001186.

37. Yun NE, Poussard AL, Seregin AV, et al. Functional interferon system is required for clearance of lassa virus. *Journal of virology*. 2012;86(6):3389-3392.

38. Lo MK, Peeples ME, Bellini WJ, Nichol ST, Rota PA, Spiropoulou CF. Distinct and overlapping roles of Nipah virus P gene products in modulating the human endothelial cell antiviral response. *PLoS One*.7(10):e47790.

39. Bossart KN, Wang LF, Flora MN, et al. Membrane fusion tropism and heterotypic functional activities of the Nipah virus and Hendra virus envelope glycoproteins. *Journal of virology*. 2002;76(22):11186-11198.

40. Wright PJ, Crameri G, Eaton BT. RNA synthesis during infection by Hendra virus: an examination by quantitative real-time PCR of RNA accumulation, the effect of ribavirin and the attenuation of transcription. *Arch Virol*. 2005;150(3):521-532.

41. Holst J, Vignali KM, Burton AR, Vignali DA. Rapid analysis of T-cell selection in vivo using T cell-receptor retrogenic mice. *Nat Methods*. 2006;3(3):191-197.

42. Szymczak AL, Workman CJ, Wang Y, et al. Correction of multi-gene deficiency in vivo using a single 'self-cleaving' 2A peptide-based retroviral vector. *Nat Biotechnol*. 2004;22(5):589-594.

43. Amano O, Mizobe K, Bando Y, Sakiyama K. Anatomy and histology of rodent and human major salivary glands: -overview of the Japan salivary gland society-sponsored workshop. *Acta histochemica et cytochemica*. 2012;45(5):241-250.

44. Conzelmann KK. Reverse genetics of mononegavirales. *Curr Top Microbiol Immunol.* 2004;283:1-41.

45. Ghanem A, Kern A, Conzelmann KK. Significantly improved rescue of rabies virus from cDNA plasmids. *Eur J Cell Biol.* 2012;91(1):10-16.

46. Eckstein F, Kore AR, Nakamaye KL. In vitro selection of hammerhead ribozyme sequence variants. *Chembiochem.* 2001;2(9):629-635.

47. Beaty SM, Park A, Yun T, et al. Efficient rescue and reverse genetics of viruses from all Paramyxovirinae genera without the use vaccinia-driven T7 polymerase. XV International Conference on Negative Strand Viruses; 2013; Granada, Spain.

48. Mahapatra M, Parida S, Baron MD, Barrett T. Matrix protein and glycoproteins F and H of Peste-des-petits-ruminants virus function better as a homologous complex. *J Gen Virol.* 2006;87(Pt 7):2021-2029.

49. Wang LF, Daniels P. Diagnosis of henipavirus infection: current capabilities and future directions. *Curr Top Microbiol Immunol.* 2012;359:179-196.

50. Escaffre O, Borisevich V, Carmical JR, et al. Henipavirus pathogenesis in human respiratory epithelial cells. *Journal of virology.* 2013;87(6):3284-3294.

51. Szymczak-Workman AL, Vignali KM, Vignali DA. Design and construction of 2A peptide-linked multicistronic vectors. *Cold Spring Harbor protocols.* 2012;2012(2):199-204.

52. Kim JH, Lee SR, Li LH, et al. High cleavage efficiency of a 2A peptide derived from porcine teschovirus-1 in human cell lines, zebrafish and mice. *PloS one.* 2011;6(4):e18556.

53. Luby SP, Gurley ES, Hossain MJ. Transmission of human infection with Nipah virus. *Clin Infect Dis.* 2009;49(11):1743-1748.

54. Clayton BA, Middleton D, Bergfeld J, et al. Transmission routes for nipah virus from Malaysia and Bangladesh. *Emerg Infect Dis.* 2012;18(12):1983-1993.

55. DeBuysscher BL, de Wit E, Munster VJ, Scott D, Feldmann H, Prescott J. Comparison of the pathogenicity of Nipah virus isolates from Bangladesh and Malaysia in the Syrian hamster. *PLoS Negl Trop Dis.* 2013;7(1):e2024.

CHAPTER 2.3

EFFICIENT REVERSE GENETICS FOR THE *PARAMYXOVIRINAE* SUBFAMILY

INTRODUCTION

Reverse genetics systems have been described for multiple members of the *Paramyxovirinae* subfamily.[1-10] Although the method for determining rescue efficiency varies widely between reports, the longstanding rescue efficiency for paramyxoviruses appears to be one in 10^5 transfected cells or less.[2,11] To determine whether our use of codon-optimized T7 polymerase and the hammerhead ribozyme could improve rescue efficiencies across the *Paramyxovirinae*, we accordingly modified existing reverse genetics systems for representative members of the major genera: Sendai virus (*Respirovirus*), Newcastle disease virus (*Avulavirus*), mumps virus (*Rubulavirus*), and measles virus (*Morbillivirus*). Reverse genetics for the henipaviruses, having been described in Chapter 2.2, is not further discussed here.

MATERIALS AND METHODS

Plasmids

The wild-type T7 bacteriophage gene in pCAGGS is as described.[12,13] The codon-optimized T7 gene (Genscript) was cloned into pCAGGS to match the wild-type construct.

Sendai virus (*SeV*). T7-driven SeV antigenome, Fushimi strain, as well as the T7-driven SeV-N, -P, and -L plasmids, were the kind gift of Dr. Nancy McQueen. The full-length SeV incorporates specific F1-R strain mutations in the SeV-F and SeV-M genes that allow trypsin-independent growth, as replication of wild-type SeV requires a cellular protease for F protein cleavage and maturation that is not present in common mammalian cell lines.[14] We further modified this construct to insert EGFP between the N and P genes, with duplication of the N-to-P intergenic region.

Newcastle disease virus (*NDV*). T7-driven NDV antigenome, La Sota strain, as well as the T7-driven NDV-N, -P, and -L plasmids, were the kind gift of Dr. Elankumaran Subbiah. Similar to wild-type SeV, wild-type NDV is restricted by the lack of the required protease in common mammalian cell lines and requires addition of exogenous trypsin for growth. We therefore

modified the full-length construct to convert the F protein cleavage site to a urokinase-type plasminogen activator (uPA) cleavage site: uPA is a serine protease associated with cancer malignancy and is thus expressed by some common cell lines. We note that HEK-293 cells express minimal endogenous uPA, and that although we perform our rescue experiments in 293T cells, the rescued NDV does not expand on this cell line. We further modified this construct to insert EGFP between the N and P genes, with duplication of the N-to-P intergenic region.

Mumps virus (*MuV*). T7-driven MuV antigenome, Jeryl Lynn strain, as well as the T7-driven MuV-N, -P, and -L plasmids, were the kind gift of Dr. Paul Duprex. EGFP is present as an inserted ORF upstream of the N gene.

Measles virus (*MeV*). T7-driven MeV antigenome, Edmonston B strain, as well as the T7-driven MeV-N, -P, and -L plasmids, were the kind gift of Dr. Paul Duprex. We modified the full-length construct to insert EGFP between the N and P genes, with duplication of the N-to-P intergenic region.

Immunoblotting

BSR-T7 cells[15] stably expressing T7 polymerase or 293T cells were transfected with empty pCAGGS vector, wild-type T7 polymerase, or codon-optimized T7 polymerase using either Lipofectamine LTX (Invitrogen) for BSR-T7 cells, or BioT (Bioland) for 293T cells, according to manufacturers' instructions. Cells were collected in PBS with 10mM EDTA, and boiled 1:1 with 2X Laemmli SDS sample buffer with 5% 2-mercaptoethanol. Samples were run on 10% Tris-glycine SDS-PAGE, transferred to Immobilon-FL PVDF membranes (Millipore), and detected with either mouse anti-T7 (TB244, Novagen) or rabbit anti-b-tubulin (2128, Cell Signaling), followed by anti-mouse 800CW or anti-rabbit 680LT (LI-COR Biosciences), respectively. Fluorescence images were obtained on a LI-COR Odyssey imaging system.

Recovery of recombinant viruses from cDNA

1 x 10^6 293T cells/6-well were plated to achieve about 50% confluency the following day. For transfection, specific amounts of full-length antigenome, helper plasmids, and T7 polymerase were transfected with Lipofectamine LTX (Invitrogen) according to manufacturer's instructions. Amounts of T7 polymerase are as indicated in the Results. For a given virus, the ratio of genomic plasmid to individual helper plasmids was previously optimized by the gifting lab, and was not modified further. For SeV, 4 ug genome, 1.44 ug T7-N, 0.77 ug T7-P, and 0.07 ug of T7-L were transfected per 6-well; for NDV, 0.8 ug genome, 0.4 ug T7-N, 0.2 ug T7-P, and 0.2 ug T7-L; for MuV, 5 ug genome, 0.3 ug T7-N, 0.1 ug T7-P, 0.2 ug T7-L; for MeV, 5 ug genome, 1.2 ug T7-N, 1.2 ug T7-P, and 0.4 ug T7-L. For determination of rescue efficiency by flow cytometry (%GFP+), cells were collected at day 2 post-transfection in 2% paraformaldehyde.

RESULTS

Codon-optimized T7 polymerase is expressed more highly than wild-type T7

We first confirmed that codon-optimization of the bacteriophage T7 gene, which is not optimized for mammalian expression and contains cryptic splice sites, improves T7 expression in mammalian cell lines. Transfection of 293T cells showed that the optimized gene expressed more highly than the wild-type gene (Figure 2-7). We also considered if transfection of the optimized T7 gene might enable even higher expression of T7 in BSR-T7 cells, which have stable expression of T7 polymerase. Indeed, the higher expression of T7 upon transfection (Figure 2-7) raises the possibility that rescue efficiency even in this cell line might be improved with additional T7 expression.

GFP-positive cells at day 2 post-transfection as a metric for rescue efficiency

Since all our recombinant viruses have an EGFP reporter, we sought to use this reporter to establish a straightforward metric for the efficiency of viral rescue. First, we noticed that for all the viruses, EGFP fluorescence became clearly visible at day 2 post-transfection, indicating production of viral proteins and thus initiation of the replication cycle. As a control, the same

transfection but with the sole omission of the T7-L plasmid resulted in no EGFP fluorescence (data not shown). Further, as an indication that all EGFP-positive cells at day 2 post-transfection represent original rescue cells and not cells subsequently infected by rescued virus, we determined that no virus was detectable in the supernatant at this time point (shown for SeV in Figure 2-8, panel A). We therefore used GFP-positive cells/10^5 cells at day 2 post-transfection, determined by percent GFP-positive at this time point by flow cytometry, as a metric for rescue efficiency. To additionally confirm that this metric was representative of virus rescue, we correlated the metric with the supernatant virus titer at day 6 post-transfection for different conditions that gave different rescue efficiencies (differing amounts of wild-type or codon-optimized T7 polymerase). We found a strong correlation between these two measures (Figure 2-8, panel B).

Codon-optimized T7 and insertion of a hammerhead ribozyme synergistically enhance virus rescue

For all the viruses, we used the existing construct or inserted a hammerhead ribozyme (described in Chapter 2.2) between the T7 promoter and the start of the antigenome. Use of the hammerhead ribozyme allowed insertion of the three guanines allowing optimal T7 transcription for the MeV and MuV antigenomic constructs; the SeV and NDV constructs already included the guanines. For all viruses, use of codon-optimized T7 vs. wild-type T7, or the hammerhead ribozyme vs. without, increased rescue efficiency (Figure 2-9). The highest rescue efficiency was obtained when both codon-optimized T7 and the hammerhead ribozyme were used in conjunction.

DISCUSSION

Although our focus remains on the emergent henipaviruses, our analyses of conserved or non-conserved features of these viruses will involve comparative studies with the related paramyxoviruses. We therefore obtained and improved reverse genetics systems for prototypical

paramyxoviruses from each of the major genera of the *Paramyxovirinae* subfamily (Figure 2-10). It was surprising to see that the best rescue efficiency obtained for MeV was still only one in 10^5 cells; we have recently found, however, that use of MeV helper plasmids with gene sequences derived from a more wild-type MeV, vs. the attenuated Edmonston vaccine strain, dramatically improves MeV rescue efficiency. This finding only emphasizes that despite our improvement of a major roadblock to rescue efficiency, many factors contribute to the overall efficiency of virus rescue.

FIGURES

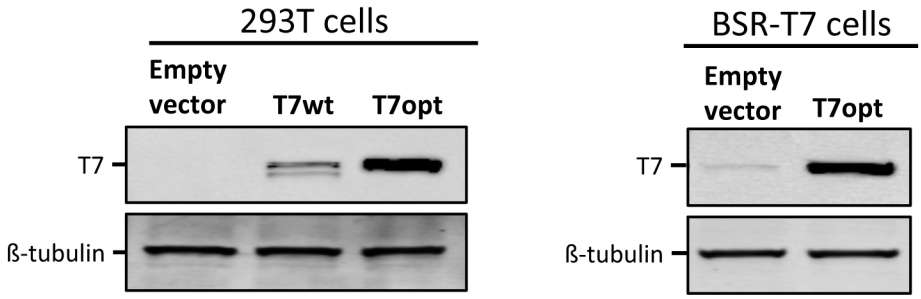

Figure 2-7. Codon-optimized T7 polymerase expresses more highly than wild-type T7 polymerase. Codon-optimization of the T7 gene sequence for mammalian expression led to improvement in T7 expression in 293T cells. Transfection of the BSR-T7 cell line that stably expresses T7 shows that T7 expression can be substantially increased. In the subsequent experiments in 293T cells, we show that use of the optimized construct leads to more efficient virus rescue.

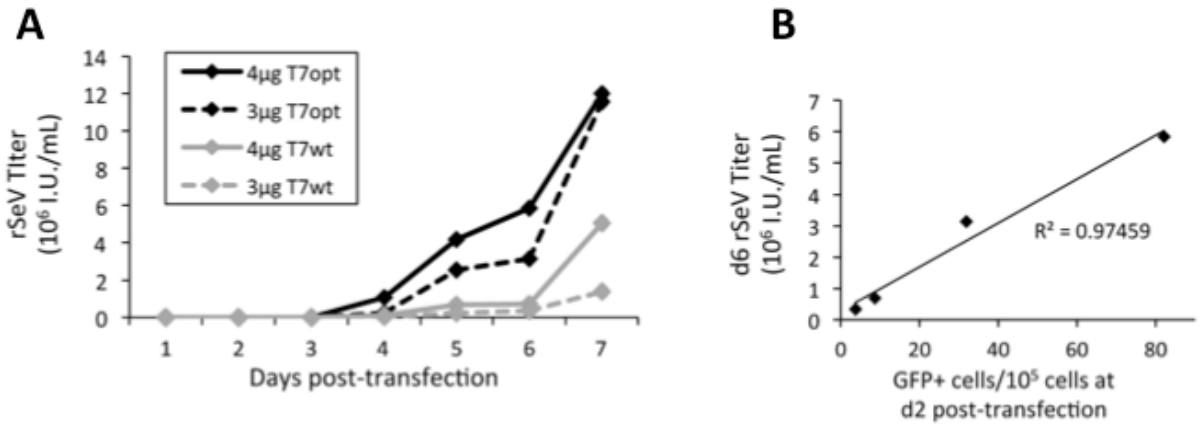

Figure 2-8. GFP-positive cells at day 2 post-transfection correlates with rescued virus titers at a later time point. (A) After transfection with the full-length SeV construct, N, P, L, and the indicated amounts of wild-type or codon-optimized T7 plasmid, supernatants were collected and replenished each day, and subsequently titered. **(B)** Cells treated identically in parallel were collected for flow cytometry at day 2 post-transfection. The GFP+ count for each condition was then correlated to the day 6 infectious titer for each condition (from panel A).

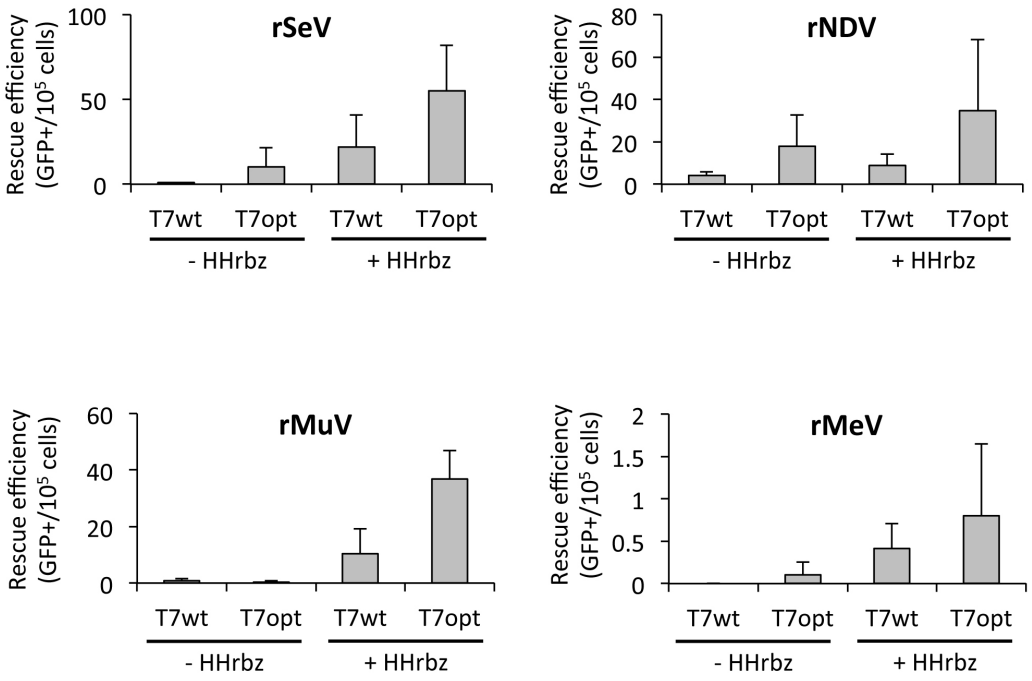

rSeV	No Hh-Rbz	With Hh-Rbz	Fold increase (+/- HhRbz)
T7wt	1.0	22.0	**22.0**
T7opt	10.2	55.3	**5.4**
Fold increase (T7wt vs T7opt)	**10.2**	**2.5**	

Figure 2-9. Codon-optimized T7 polymerase and the hammerhead ribozyme synergistically improve rescue efficiency. Virus rescue was performed as indicated in Materials and Methods. The amount of T7 used for each virus was based on previous optimization: 4 ug for SeV, 0.4 ug for NDV, 2 ug for MuV, and 3 ug for MeV. To illustrate the synergistic effect of using codon-optimized T7 and the hammerhead ribozyme (HhRbz), the fold change in rescue efficiency is shown for Sendai virus, with both improvements together leading to an over 50-fold increase in efficiency.

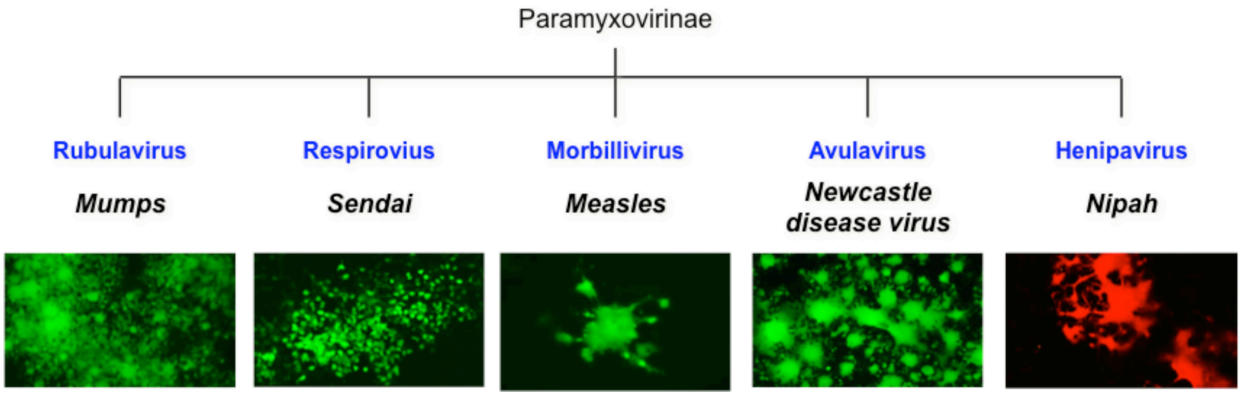

Figure 2-10. Example fluorescent images of each recombinant virus in cell culture. The cell types shown are: 293T for mumps, Sendai, and measles; BSR-T7 for Newcastle disease virus; human umbilical vein endothelial cells for Nipah.

REFERENCES

1. Clarke DK, Sidhu MS, Johnson JE, Udem SA. Rescue of mumps virus from cDNA. *Journal of virology.* 2000;74(10):4831-4838.

2. Conzelmann KK. Reverse genetics of mononegavirales. *Current topics in microbiology and immunology.* 2004;283:1-41.

3. Durbin AP, Hall SL, Siew JW, Whitehead SS, Collins PL, Murphy BR. Recovery of infectious human parainfluenza virus type 3 from cDNA. *Virology.* 1997;235(2):323-332.

4. Garcin D, Pelet T, Calain P, Roux L, Curran J, Kolakofsky D. A highly recombinogenic system for the recovery of infectious Sendai paramyxovirus from cDNA: generation of a novel copy-back nondefective interfering virus. *The EMBO journal.* 1995;14(24):6087-6094.

5. Hoffman MA, Banerjee AK. An infectious clone of human parainfluenza virus type 3. *Journal of virology.* 1997;71(6):4272-4277.

6. Marsh GA, Virtue ER, Smith I, et al. Recombinant Hendra viruses expressing a reporter gene retain pathogenicity in ferrets. *Virology journal.* 2013;10:95.

7. Peeters BP, de Leeuw OS, Koch G, Gielkens AL. Rescue of Newcastle disease virus from cloned cDNA: evidence that cleavability of the fusion protein is a major determinant for virulence. *Journal of virology.* 1999;73(6):5001-5009.

8. Radecke F, Spielhofer P, Schneider H, et al. Rescue of measles viruses from cloned DNA. *The EMBO journal.* 1995;14(23):5773-5784.

9. Romer-Oberdorfer A, Mundt E, Mebatsion T, Buchholz UJ, Mettenleiter TC. Generation of recombinant lentogenic Newcastle disease virus from cDNA. *The Journal of general virology.* 1999;80 (Pt 11):2987-2995.

10. Yoneda M, Guillaume V, Ikeda F, et al. Establishment of a Nipah virus rescue system. *Proceedings of the National Academy of Sciences of the United States of America.* 2006;103(44):16508-16513.

11. Kato A, Sakai Y, Shioda T, Kondo T, Nakanishi M, Nagai Y. Initiation of Sendai virus multiplication from transfected cDNA or RNA with negative or positive sense. *Genes to cells : devoted to molecular & cellular mechanisms.* 1996;1(6):569-579.

12. Kobasa D, Rodgers ME, Wells K, Kawaoka Y. Neuraminidase hemadsorption activity, conserved in avian influenza A viruses, does not influence viral replication in ducks. *Journal of virology.* 1997;71(9):6706-6713.

13. Niwa H, Yamamura K, Miyazaki J. Efficient selection for high-expression transfectants with a novel eukaryotic vector. *Gene.* 1991;108(2):193-199.

14. Hou X, Suquilanda E, Zeledon A, et al. Mutations in Sendai virus variant F1-R that correlate with plaque formation in the absence of trypsin. *Medical microbiology and immunology.* 2005;194(3):129-136.

15. Buchholz UJ, Finke S, Conzelmann KK. Generation of bovine respiratory syncytial virus (BRSV) from cDNA: BRSV NS2 is not essential for virus replication in tissue culture, and the human RSV leader region acts as a functional BRSV genome promoter. *Journal of virology.* 1999;73(1):251-259.

CHAPTER 2.4

TIMING OF GALECTIN-1 EXPOSURE DIFFERENTIALLY MODULATES NIPAH VIRUS ENTRY AND SYNCYTIA FORMATION IN ENDOTHELIAL CELLS

ABSTRACT

Nipah virus (NiV) is a deadly emerging enveloped virus that targets human endothelial cells. Endothelial cells express the innate immune effector galectin-1, which we have previously shown can bind to specific N-glycans on the NiV envelope fusion glycoprotein (F). NiV-F mediates fusion of infected endothelial cells into syncytia, resulting in endothelial disruption and hemorrhage. Galectin-1 is an endogenous carbohydrate-binding protein that binds to specific glycans on NiV-F to reduce endothelial cell fusion, an effect that may reduce pathophysiologic sequelae of NiV infection. However, galectins play multiple roles in regulating host-pathogen interactions: for example, galectins can facilitate attachment of HIV and HSV-1 to target cells and thus promote infection, yet can inhibit influenza entry into airway epithelial cells. In the present study, we demonstrate that galectin-1 can enhance NiV attachment to and infection of human endothelial cells by bridging glycans on the viral envelope to host cell glycoproteins. In order to exhibit an enhancing effect, galectin-1 must be present during the initial phase of virus attachment; in contrast, addition of galectin-1 post-infection results in reduced production of progeny virus and syncytia formation. Thus, galectin-1 can have dual and opposing effects on NiV infection of human endothelial cells. While various roles for galectin family members in microbial-host interactions have been described, this is the first report of opposing effects of the same galectin family member on a specific virus, with the timing of exposure during the viral life cycle determining the outcome.

INTRODUCTION

Nipah virus (NiV) is an emerging zoonotic paramyxovirus that targets endothelial and neural cells. Infection with NiV may result in a severe encephalitic syndrome with mortality rates from 40-100% in humans.[1,2] While initial outbreaks involved transmission from bats-to-pigs, and then from pigs-to-humans, more recent outbreaks have been shown to involve human-to-human virus transmission.[2] There are currently no approved vaccines or anti-viral agents targeting NiV for human cases, and quarantine has been the predominant measure to restrain the spread of the virus.[3]

NiV preferentially infects microvasculature endothelial cells that express the entry receptor ephrinB2.[4] The NiV attachment protein NiV-G binds to ephrinB2 on the host cell plasma membrane, triggering the NiV fusion protein, NiV-F, to execute fusion of the viral envelope with the host cell membrane. Infected microvascular endothelial cells produce NiV-F and NiV-G which results in fusion of the cells into syncytia,[5] and this syncytia formation contributes to vascular compromise and hemorrhage, two hallmarks of Nipah virus infection.[6]

Endothelial cells respond to viral infection by producing inflammatory mediators including cytokines, which regulate leukocyte trafficking into adjacent tissues, and by presenting viral antigens.[7] Among the inflammatory mediators produced by endothelial cells are the galectins, a family of mammalian lectins implicated in immune regulation. Vascular endothelial cells express several galectin family members, including galectins-1 and -9. For example, infection of vascular endothelial cells with Ebola virus results in endothelial cell activation[8] and increased expression of galectin-1.[9,10] Infection of endothelial cells with Dengue virus induces expression of galectin-9,[11] as does binding of double-stranded RNA to TLR-3 on endothelial cells.[12]

Galectins play several roles in modulating host-pathogen interactions. Galectins can participate in innate immune recognition and clearance of pathogens, however pathogens can also use galectins as attachment receptors. Galectins specifically recognize a subset of microbes

based on binding to pathogen-specific polysaccharides.[13] For example, galectin-4 and galectin-8 bind and directly kill human blood group B-expressing *Escherichia coli*,[14] and galectin-3 binds and directly kills *Candida albicans*[15] in the absence of immunoglobulin or complement. In contrast, *Pseudomonas aeruginosa* and *Trypanosoma cruzi* use galectin-3 to bind and infect human cells, and galectin-1 on human cervical epithelial cells is an attachment factor for *Trichomonas vaginalis*.[16-18] Similarly, galectin-1, which preferentially recognizes LacNAc (Galb1,4GlcNAc) containing glycans, increases HIV infection of monocyte-derived macrophages through stabilization of virus attachment,[19-21] and galectin-9 promotes HIV infection of T cells by regulating the cell surface redox status.[22] Thus, different galectins can have pleiotropic and sometimes opposing roles in the etiology and pathophysiology of microbial infections. However, opposing effects of a single galectin on a specific virus have not been reported.

We have previously shown that galectin-1 produced by endothelial cells can inhibit endothelial cell syncytia formation mediated by NiV-F and NiV-G.[10,23] Galectin-1 reduced NiV-F mediated fusion of endothelial cells by interfering with NiV-F maturation, reducing lateral mobility of NiV-F on the plasma membrane, and inhibiting the conformational change in NiV-F triggered by receptor binding to NiV-G that is necessary for cell-cell fusion.[10] While galectin-1 produced by endothelial cells can clearly inhibit post-infection cell-cell fusion triggered by NiV-F, the effect of galectin-1 on NiV attachment and entry into host cells is not known. In the present study, we found that galectin-1 can enhance NiV attachment to and infection of endothelial cells by bridging glycans on the viral envelope to cell surface glycoproteins. While the presence of galectin-1 enhances NiV entry, galectin-1 also inhibits syncytia formation of infected cells. In both cases, a specific N-linked glycan site on NiV-F plays a critical role in mediating galectin-1's effects. Our results highlight the complex roles galectin-1 may play in viral pathogenesis.

MATERIALS AND METHODS

Cells, virus, and reagents

Vero cells (ATCC) were maintained in MEM alpha (Invitrogen) with 10% FBS (Hyclone) and 2mM Glutamax in 5% CO2 at 37°C. 293T cells were maintained in DMEM (Invitrogen) with 10% FBS (Hyclone) and 2mM Glutamax. VeroCCL-81 cells were maintained in DMEM (Gibco) with 10% FBS (Hyclone). HUVECs (BD Biosciences) were maintained in MDCB-131 complete media with fetal bovine serum and antibiotics (VEC Technologies, INC). HUVECs (LONZA) were maintained in Endothelial Basal Medium-2 (EGM-2) with EGM-2 SingleQuots.

Recombinant human galectin-1 was expressed in *E. coli* and purified by affinity chromatography on lactosyl-Sepharose, as described[24]; in all assays, buffer controls are PBS with 1.2 mM dithiothreitol (DTT), as galectin-1 is prepared and stored in PBS with DTT.

NiV-F and -G were pseudotyped onto a reporter vesicular stomatitis virus (VSV) expressing *Renilla* luciferase as described.[25] Nipah virus (NiV) strain Malaysia (NiV-$_{MAL}$) was kindly provided by the Special Pathogens Branch, CDC, Atlanta, GA, and propagated in VeroE6 cells. Stock virus was harvested 48 hr post-infection and virus titer determined by plaque assay using VeroCCL-81 cells.

Quantitation of viral entry

Cells plated in 48-well plates were infected with pseudotyped virions in PBS plus 1% FBS for 2 hr at 25°C at 2000 rpm (spinoculation). After 2 hr, cells were washed, appropriate growth medium was added, and cells were incubated at 37°C. At 24 hr post-infection, cells were lysed and luciferase activity was measured as relative light units (RLU) using a *Renilla* luciferase detection system (Promega, Madison, WI) and a Veritas microplate luminometer (Turner Biosystems, Sunnyvale, CA). Galectin-1, buffer control, 100 mM lactose and 100 mM sucrose were added just prior to spinoculation.

Reduction in complex N-glycans

Cells (Vero, 293T, HUVECs) were treated with kifunensine (2 ug/ml) for 24 hr. To confirm loss of complex N-glycans on the cell surface, cells were suspended in PBS with 5 mM ethylenediaminetetraacetic acid (EDTA), washed, and resuspended in biotinlyated L-PHA in PBS (1:1000) plus 1% bovine serum albumin (BSA) (Gemini Scientific) for 1 hr at 4°C. Cells were washed in PBS and bound PHA detected with a FITC-conjugated streptavidin (SA) (1:60) in PBS plus 1% BSA, for 1 hr at 4°C. Cells were washed in PBS with 1% BSA and flow cytometric analysis was performed on a FACScan, using CellQuest software (Becton-Dickenson). Pseudotyped VSV expressing NiV-G and NiV-F were produced by infecting kifunensine-treated or control cells with VSV-rLuc virions for 24 hr. Supernatants were collected and virions purified by centrifugation through 20% sucrose in NTE buffer. To examine loss of N-glycan processing by immunoblot, NiV-G and NiV-F were separated and detected as previously described.[23]

Recombinant Nipah virus (NiV) production and *in vitro* luciferase assay

rNiV Rbz NP Gluc-p2A-eGFP was rescued in Galveston National Laboratory, TX, USA. Virus stock was prepared by infecting Vero CCL-81 cells and collecting supernatant at 48 hours post-infection. Virus titer in the supernatant was determined by plaque assay using VeroCCL-81 cells. HUVECs were infected with rNiV Rbz NP Gluc-p2A-eGFP at different MOIs and cells supernatants were collected at regular intervals. Luciferase assay were performed using BioLux Gaussia Luciferase assay kit (New England BioLabs) according to the manufacturer's protocol and expression was measured on Modulus Luminometer (Turner BioSystems, Inc).

NiV live virus plaque titrations

For titrations, confluent monolayers of VeroCCL-81 cells were infected with 100 µl of serial ten-fold dilutions of virus-containing cell supernatant. After 1 hr incubation at 37°C and 5% CO_2, the inocula were removed and wells overlaid with a mixture of one part 1.0% methylcellulose (Fisher Scientific) and one part 2xMEM (Gibco, Invitrogen) supplemented with 2% FBS and 2% penicillin/streptomycin. The plates were incubated at 37°C and 5% CO_2 for 3 days and stained with 0.25% crystal violet in 10% buffered formalin. Plates were washed and plaques

enumerated. All work with live virus was carried out under Biosafety Level 4 (BSL4) conditions in the Robert E. Shope BSL-4 Laboratory and in the Galveston National Laboratory BSL-4 laboratories at the University of Texas Medical Branch (UTMB).

NiV live virus galectin-1 experiments

HUVECs were infected with NiV-$_{MAL}$ at a multiplicity of infection of 0.1 for 1 hr at 37°C. Infections were performed either in the presence of various galectin-1 concentrations (1, 7, and 20 μM) or cells were treated with galectin-1 post-infection. In the case of infections performed in the presence of galectin-1, the inoculum was removed 1 hr post-infection and cells were washed three times with 0.1 M *β*-Lactose, followed by incubation in complete EGM-2 media. Cells infected only with NiV were washed three times with media and incubated in complete EGM-2 media containing different concentrations of galectin-1 (1, 7 or 20 μM). Supernatant aliquots were harvested at 1, 12, 24 and 36 hpi and stored at -80°C until titration. DTT was used as negative control and experiments were performed in triplicates.

For DAPI staining, HUVECs were grown in 12-well plates and incubated with NiV for 1 hr at 37°C. Galectin-1 treatment was performed as described above. At 24 hpi, cells were fixed in 10% buffered formalin and nuclei stained with 20 μg/ml DAPI (Sigma) before analysis by fluorescence microscopy.

RESULTS

Galectin-1 increases viral infection of endothelial cells

Galectin-1 inhibits endothelial cell syncytia formation mediated by NiV envelope glycoproteins.[10] Although galectin-1 can bind to both NiV-F and -G, we showed that inhibition of cell-cell fusion was mediated largely by galectin-1 binding to abundant and accessible lactosamine moieties on complex N-glycans at the "F3" N-glycan site (^{93}NNT^{101}) on NiV-F.[10,23] The F3 N-glycan site is close to the cathepsin L cleavage site ^{103}DLVGDVR^{109}. Binding of dimeric galectin-1 to F3 N-glycans on different NiV-F protomers likely accounts for the suite of inhibitory activities that

galectin-1 exerts on NiV-F-mediated fusion.[10] We therefore expected galectin-1 to inhibit NiV infection just as potently. Surprisingly, when we examined the function of galectin-1 in Nipah virus entry using NiV-F/G-pseudotyped particles (NiVpp),[26] we found that addition of recombinant galectin-1 significantly increased infection of target cells in a concentration-dependent manner (Figure 2-11, panel A).

We confirmed that the galectin-1-mediated increase in infection was carbohydrate-dependent. Lactose, but not sucrose, specifically abrogated the galectin-1 mediated increase in infection, while lactose alone in the absence of galectin-1 had no effect (Figure 2-11, panel B). Thus, exogenous galectin-1 increased viral infection in a dose-dependent and carbohydrate binding-dependent manner.

Galectin-1 increases viral attachment to host cells

Viral entry requires two steps, viral attachment to the target cell surface mediated by NiV-G followed by membrane fusion mediated by NiV-F. Viral attachment is largely energy-independent while virus-cell fusion is an energy-dependent process.[27] To examine the point at which galectin-1 enhancement occurs, NiVpp was centrifuged onto target cells in the presence or absence of galectin-1 for 2 hours at 4^{o}C, to allow viral attachment, but not virus-target cell fusion, before shifting to 37^{o}C to permit fusion. Alternatively, virus was centrifuged onto target cells in the absence of galectin-1, then incubated with or without galectin-1 for 1 hour at 37^{o}C to permit fusion. As shown in Figure 2-11 (panel C), galectin-1 present during the 4^{o}C spinoculation step clearly enhanced viral entry. In contrast, galectin-1 added after spinoculation at 4^{o}C and present only during the 37^{o}C fusion step did not increase viral entry. These experiments suggest that galectin-1 increased infection by enhancing viral attachment to host cells. Moreover, that no inhibition was seen suggests that there are functional NiV-F envelope spikes on the virion particles that are not bound by galectin-1 and are still capable of being triggered by receptor binding to NiV-G.

Galectin-1 bridges N-glycans on viral envelope glycoproteins to glycoproteins on target cells

Galectin-1 stabilizes HIV-1 attachment and adsorption to host cells by binding specifically to clustered complex N-glycans on gp120 and CD4, bridging the virus to the target cell.[19-21] We asked if complex N-glycans, which bear glycan ligands recognized by galectin-1, were involved in the galectin-1-mediated increase in viral entry of NiVpp. To eliminate complex N-glycans from viral envelope glycoproteins, virus was produced in 293T cells treated with kifunensine, which blocks processing of high-mannose N-glycan precursors into complex N-glycans.[28] We detected equivalent expression levels of NiV-F by immunoblot from cells treated with and without kifunensine (data not shown). We confirmed that kifunensine blocked N-glycan processing in 293T cells by flow cytometry with the lectin L-PHA (Figure 2-12, panel A); loss of L-PHA binding indicates loss of complex N-glycans.

Vero cells were infected with control virus, with virus lacking complex N-glycans from kifunensine-treated 293T cells, or with virus specifically lacking the F3 N-glycan in the presence or absence of exogenous galectin-1 (Figure 2-12, panel B). As expected, addition of galectin-1 resulted in a 12.6-fold increase in target cell infection of virus with a full complement of complex N-glycans (Figure 2-12, panel B, "wt NiVpp"). Remarkably, the loss of the F3 N-glycan site on NiV-F resulted in a >80% reduction in galectin-1 mediated enhancement (3.2-fold vs 12.6-fold enhancement for NiV-F3pp vs wt NiVpp, respectively), underscoring the contribution of the complex N-glycan at the F3 site in the enhancement of virus entry as well as fusogenicity.[10,25] However, the galectin-1-mediated increase was further reduced (~95% reduction) when cells were infected with virus lacking complex N-glycans (Figure 2-12, panel B, "Complex N-glycanless NiVpp"), indicating that other complex N-glycans on NiV-F or NiV-G also contributed to the galectin-1 enhancement effect.

To examine the role of host cell complex N-glycans in galectin-1-mediated enhancement of viral infection, we treated uninfected Vero cells with kifunensine to reduce complex N-glycans

on the target cells. Loss of complex N-glycans was confirmed by flow cytometry with L-PHA, as described above (Figure 2-12. panel C). Loss of complex N-glycans from target Vero cells reduced galectin-1-mediated enhancement of infection by approximately 30% (Figure 2-12, panel D). Thus, complex N-glycans on host cell glycoproteins participate in the galectin-1 enhancement of viral infection; however, as loss of complex N-glycans on kifunensine-treated host cells partially reduced the galectin-1 enhancement effect, other host cell glycans, likely O-glycans, may also play a role on the host cell side.[29] Collectively, the data in Figure 2-12 demonstrate that glycans on both the viral envelope and on the target cell surface are important for galectin-1 enhancement. Our results support a model in which the enhancement effect results from dimeric galectin-1 acting as a bridge or bivalent attachment factor between the virus and the target cell, with complex N-glycans important for attachment on both the virus and the host cell.

Galectin-1 enhances Nipah virus infection of human endothelial cells

Endothelial cells are primary targets of NiV infection *in vivo*, due to expression of the viral attachment receptor ephrinB2.[4] To determine if galectin-1 would enhance Nipah virus infection of physiologically relevant target cells, we infected human umbilical vein endothelial cells (HUVECs) with NiVpp (Figure 2-13) in the presence or absence of exogenous galectin-1. The addition of galectin-1 resulted in a 6-fold increase in infection of HUVECs, similar to the effect we had observed with Vero cells as targets of infection.

Thus far, we used NiVpp, rather than replication-competent native virus. NiVpp is a VSV-based pseudotyped virus capable only of single cycle of infection, and the bullet-shaped VSV-based particles may not fully recapitulate the morphology or envelope glycoprotein densities present on native pleomorphic paramyxovirus particles.[30] To determine if galectin-1 modulates infection by replication-competent NiV, we first generated and rescued, under BSL4 conditions, a recombinant NiV expressing secreted *Gaussia* luciferase (rNiV-GLuc) (see Materials and Methods). To facilitate the generation of additional recombinant NiVs such as the

one bearing the F3 N-glycan, we also developed an efficient and robust reverse genetics system for henipaviruses. The salient points of thie improved genetic system are described in Figure 2-14.

This rNiV-GLuc replicated to the same end-point titers as the parental NiV Malaysia strain (data not shown) and was pathogenic in a lethal hamster challenge model (Chapter 2.5); using rNiV-GLuc allowed us to accurately quantify enhancement or inhibition of live virus entry by sampling the infected cell culture supernatant for GLuc activity. We first asked if rNiV-GLuc would also exhibit enhanced infection of endothelial cells in the presence of galectin-1. HUVEC cells infected at an MOI of 0.05 with rNiV-GLuc showed a dose-dependent enhancement of infection in the presence of galectin-1 at 24 hours post-infection. The enhancement effect plateaued at 7-10 mM galectin-1, with a 6-fold increase in infection compared to controls lacking exogenous galectin-1 (Figure 2-15, panel A). This level of enhancement was similar to that observed for NiVpp in HUVECs, albeit in the presence of 20 mM galectin-1.

Next, we reasoned that if galectin-1 was bridging virions to the cell surface, as suggested by the data in Figure 2-12, then the relative level of enhancement should be increased when the amount of viral inoculum was decreased. That is, when the number of infectious viral particles is more limiting, the effect of galectin-1 on bridging viruses to the cell surface should become more apparent. Thus, we reduced the viral inoculum by 5-fold and quantified the corresponding effect of galectin-1 on virus infection. Indeed, at a MOI of 0.01, 10 mM of galectin-1 enhanced rNiV-GLuc infection by up to 40-fold (Figure 2-15, panel B, black bars) compared to the 6-fold enhancement seen with an equivalent dose of galectin-1 when a higher viral inoculum (MOI of 0.05) was used (Figure 2-15, panel A).

Galectin-1 enhances rNiV-GLuc virus infection by bridging complex N-Glycans

To confirm that galectin-1 enhances rNiV-GLuc infection by bridging complex N-glycans present on virions and the endothelial cell surface, as we had seen in infection of Vero cells with NiVpp (Figure 2-12), we generated either HUVECs or viruses deficient in complex N-glycans by

treating HUVECs with kifunensine (Cells Kif+) or producing rNiV-GLuc viral stocks in the presence of kifunensine (Virus Kif+). Complex N-glycanless Nipah virus (Virus Kif+) was equally infectious when titered on Vero cells (data not shown). As shown in Figure 2-15 (panel B), depletion of complex N-glycans on target cells (Cells Kif+) moderately reduced galectin-1-enhanced rNiV-GLuc infection of HUVECs (black bars versus dark grey bars), as we had seen with Vero cells. Depleting virus of complex N-glycans (Virus Kif+) also reduced galectin-1 enhancement of infection (light grey bars) more significantly, as we had seen with NiVpp. When both virus and HUVECs lack complex N-glycans (Virus Kif+/Cells Kif+), galectin-1 had the least enhancement effect (white bars). *In toto*, our data reveal that galectin-1 enhanced infection of both rNiV-GLuc and NiVpp by the same mechanism, i.e. the interaction between galectin-1 and Nipah virus results primarily from galectin-1 binding to complex N-glycans on NiV envelope glycoproteins, and that enhancement of infection involves galectin-1-mediated bridging of viral glycans to glycans on the host cell surface. The remaining degree of galectin-1-mediated enhancement seen with kifunensine-treated cells and virus suggest that lactosamine residues on O-linked glycans might also serve as bridging receptors for galectin-1's infection enhancement effect. However, the role of these putative O-glycans may only be unmasked when cognate complex N-glycans are limiting.

Timing of galectin-1 exposure has opposing effects in Nipah virus replication

Previous work in our labs has shown that galectin-1 inhibited NiV-F and -G-mediated syncytia formation by endothelial cells.[10,23] Galectin-1 reduced NiV-F-mediated fusion by retarding NiV-F maturation, reducing the lateral mobility of NiV-F in the plasma membrane, and inhibiting triggering of NiV-F that results in fusion of the virus with the host cell plasma membrane. Moreover, endogenous galectin-1 produced by endothelial cells was sufficient to inhibit syncytia formation.[10] Importantly, all of the galectin-1-mediated effects that we had previously analyzed would occur following Nipah virus infection, and were studied only in a cell-cell fusion context. Thus, while the data presented demonstrate that galectin-1 enhances viral entry when present at

initial infection, we asked if downstream events, i.e. syncytia formation and viral replication in human endothelial cells infected with NiV_{MAL}, were affected by the presence of galectin-1.

To examine the effect on viral replication, HUVECs infected with the Nipah virus strain Malaysia (NiV_{MAL}) were incubated post-infection with galectin-1 or buffer control. The presence of exogenous galectin-1 post-infection at early time points (12 and 24 hpi) inhibited virus replication titers below the limit of detection, effectively reducing viral titers by >3 logs at 24 hpi. This inhibitory effect of galectin-1 persisted at 36 hpi as a 15-fold reduction in viral titers (Figure 2-16, panel A).

To examine the effect of galectin-1 on syncytia formation, wild type NiV_{MAL}-infected HUVECs were analyzed microscopically in three conditions: no exogenous galectin-1, galectin-1 added before infection, or galectin-1 added post-infection. Addition of exogenous galectin-1 before infection enhanced syncytia formation (Figure 2-16, panel B, image 2), consistent with the effect of galectin-1 on increasing NiV infection of endothelial cells (Figure 2-15). In contrast, addition of exogenous galectin-1 after NiV infection essentially abrogated syncytia formation (Figure 2-16, panel B, image 3). This inhibitory effect of galectin-1 on fusion (quantified in Figure 2-16, panel C) is consistent with our previous observation using pseudotyped virus.[10]

To determine if the NiV-F3 N-glycan contributes to the differential effect of galectin-1 on syncytia formation in the context of live virus infection, we generated and rescued a rNiV-GLuc bearing the NiV-F3 N-glycan mutant. Infection with the rNiV-GLuc F3 N-glycan mutant virus resulted in an overall increase in syncytia formation, compared to wild-type NiV-$_{MAL}$ (Figure 2-16, panel B), consistent with the hyperfusogenic phenotype previously observed for the NiV-F3 mutant.[25] However, addition of galectin-1 before infection no longer enhanced syncytia formation, in contrast to the enhancement seen with the wild-type virus in the presence of galectin-1 (Figure 2-16, panel C). Galectin-1 was still able to inhibit syncytia formation of the mutant virus when added after infection, although lack of N-glycans at the F3 site made the mutant virus more resistant to the inhibitory effect of galectin-1 (Figure 2-16, panel C).

Collectively, our data indicate that the timing of galectin-1 exposure differentially modulates Nipah virus entry, syncytia formation and replicative spread in endothelial cells. Galectin-1 present at the attachment/entry step of viral infection enhanced viral entry into endothelial cells and also enhanced syncytia formation, likely due to increased virus envelope production in initially infected cells. In contrast, galectin-1 added after NiV infection of endothelial cells inhibited both syncytia formation and the replicative spread of progeny virus.

DISCUSSION

Innate immune mediators such as galectins have many functions, including triggering endothelial activation, inducing cytokine production and release, promoting leukocyte infiltration of infected tissues, and mediating pathogen clearance.[9,13,15,31,32] As galectin-1 can recognize both self (mammalian) and non-self (pathogen) glycans, depending on factors such as glycan ligand density and presentation,[33] galectin-1 has been proposed to be both a damage-associated molecular pattern (DAMP) that is released from injured cells, and a pattern recognition receptor (PRR), recognizing pathogen associated molecular patterns (PAMPs), such as specific viral glycans.[10] Thus, galectin-1 can have dual functions in innate immunity.[34] Our current data also demonstrate that galectin-1 has complex and dual roles in NiV infection. Galectin-1 enhanced initial NiV attachment to and entry into human endothelial target cells (Figure 2-15), while subsequently inhibiting cell syncytia formation (Figure 2-16),[10,23] a key sequel of viral replicative spread. The ability of galectin-1 to produce these divergent effects depends on when it is present during the viral replicative life cycle.

There are several examples of galectin-1 having complex or opposing roles in different viral infections, via binding to glycan ligands on both the virus and the target cell. Galectin-1 bound to influenza virus reduced virus entry into host cells; moreover, intranasal administration of galectin-1 enhanced survival of mice infected with a lethal dose of influenza virus, and galectin-1-null mice were more susceptible to influenza virus infection than wildtype mice.[35] In

contrast, galectin-1 increased HIV-1 infection of monocyte-derived macrophages through stabilization of virus attachment and adsorption.[19,20] That galectin-1 stabilized HIV adsorption to macrophages suggests that dimeric galectin-1 can act as a bridge between virus glycans and host cell surface glycans, although this was not directly demonstrated in those studies.

Here we examined whether galectin-1 formed a bridge between viral particles and host cells to enhance infection. The enhancement effect was clearly glycan-dependent, as the specific inhibitor lactose, but not the non-cognate disaccharide sucrose, blocked the enhancement of viral infection (Figure 2-11, panel B). To specifically address the step at which galectin-1 binding promoted infection, we bound virus to host cells at 4°C and initiated viral entry at 37°C (Figure 2-11, panel C). Galectin-1 added only during the attachment step at 4°C enhanced infection, while galectin-1 added after viral attachment, but during fusion at 37°C, did not enhance infection. These data support a model whereby galectin-1 enhancement occurs as a result of bridging glycoproteins on the virus to glycoproteins on the host cell. To determine whether the essential glycans recognized by galectin-1 were on the virus, the host cell, or both, we eliminated complex N-glycans on viral particles and on the surface of the target cells by treatment with the a-mannosidase I inhibitor kifunensine. Complex N-glycans on viral glycoproteins were clearly required for galectin-1 enhancement of infection (Figure 2-12, panel B and also Figure 2-15, panel B). We have previously demonstrated that galectin-1 specifically interacts with the F3 N-glycan on the NiV-F glycoprotein, and that the F3 N-glycan site is occupied by complex N-glycans that bears cognate ligands for galectin-1.[10,25] In the present report, we show that this F3 glycan was the most significant viral determinant of galectin-1-mediated enhancement of infection (Figure 2-12, panel B, and also Figure 2-16, panel C). On the target cells, both complex N-glycans and O-glycans may contribute to galectin-1 enhancement of infection (Figure 2-12, panel D, and also Figure 2-15, panel B).[36]

Lectin-glycan interactions play complex roles in virus-host pathogenesis, and other types of innate immune lectins have apparently dichotomous roles in viral pathogenesis. For example,

mannan-binding lectin (MBL), a soluble innate immune lectin, binds to influenza A virus and leads directly to virus inactivation.[37] In contrast, another mannose-binding human lectin, macrophage mannose receptor (MMR) potentiates HIV binding to target cells,[38-40] and MMR can also potentiate infection of macrophages by influenza virus,[41] so that different mannose-binding lectins can bind to viruses to either reduce or potentiate infection. Considering the long-standing evolutionary relationship between virus and host, it is not entirely surprising that viruses have learned to co-opt host innate immune defenses for increased target cell entry and replication.

In the present study, we demonstrate that galectin-1 enhanced infection of endothelial cells by live NiV (Figure 2-15, panel B); as inflammation is known to increase endothelial cell production of galectin-1,[10] we speculate that, *in vivo*, galectin-1 produced by endothelial cells may increase target cell infection. However, galectin-1 can also inhibit syncytia formation among endothelial cells infected with NiV *in vitro* (Figure 2-16). This effect may limit the extent or severity of NiV pathogenicity *in vivo*, potentially reducing endothelial cell damage and the resulting hemorrhagic diathesis. It is remarkable that complex N-glycans on a specific site in NiV-F (F3) can account for the majority of galectin-1's effect. To gain further insight into how galectin-1 binding to F3 N-glycan mediates its dual role in NiV infection and spread, we modeled a trimeric spike with the cognate N-glycans at the relevant sites. Figure 2-17 (panel A) shows that the F3 N-glycan (red) is positioned right "above" the fusion peptide (blue), and proximal to the putative target cell membrane. The distance between glycan-binding sites on the dimeric galectin-1 is ~50Å (Figure 2-17, panel B), which is too short to span the F3 N-glycans between any two F protomers on the same trimeric NiV-F spike. Thus, galectin-1 likely binds to the F3 N-glycans on NiV-F protomers from distinct F spikes, forming a glycoprotein lattice that blocks the triggering of the fusion peptide (Figure 2-17, panel A, legend). We propose that glycoprotein lattice formation predominates when galectin-1 binds to NiV-F expressed on infected cells, thereby inhibiting syncytia formation.[10] However, on the virion surface that is tightly packed

with envelope glycoproteins, glycoprotein lattice formation may be less efficient, and the ability of galectin-1 to bridge virus predominates. This bridging can lead to an enhancement of infection when receptor binding triggers fusion by the other virion-associated F spikes that are not bound by galectin-1.

This study further characterizes the complex interaction between galectin-1 and NiV. While other lectins have been shown to have effects both beneficial and detrimental to the host in microbial infections,[19,20,32,35] we believe this is the first report of these opposing effects for a single virus, NiV, and a single lectin, galectin-1, in the same host cell. These studies may help to explain the range of clinical outcomes of NiV infection, as some patients recover fully after infection, while other patients succumb. Perhaps differential expression of galectin-1 in different individuals at different time points during infection either promotes virus-endothelial cell interactions or prevents endothelial cell damage. The present work suggests a complex spatiotemporal interplay between an immune regulator and a virus that may ultimately determine the outcome of infection.

FIGURES

A.

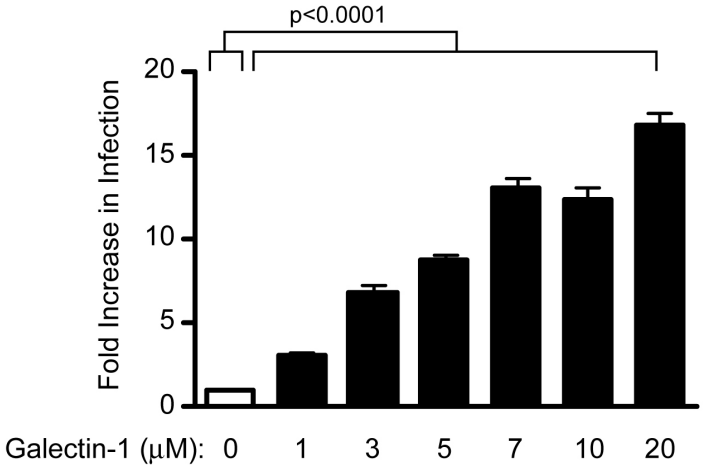
p<0.0001
Fold Increase in Infection
20
15
10
5
0
Galectin-1 (μM): 0 1 3 5 7 10 20

B.

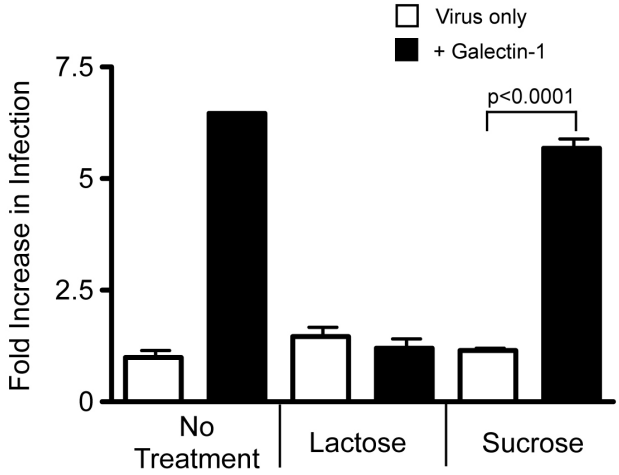
Virus only
+ Galectin-1
p<0.0001
Fold Increase in Infection
7.5
5
2.5
0
No Treatment
Lactose
Sucrose

C.

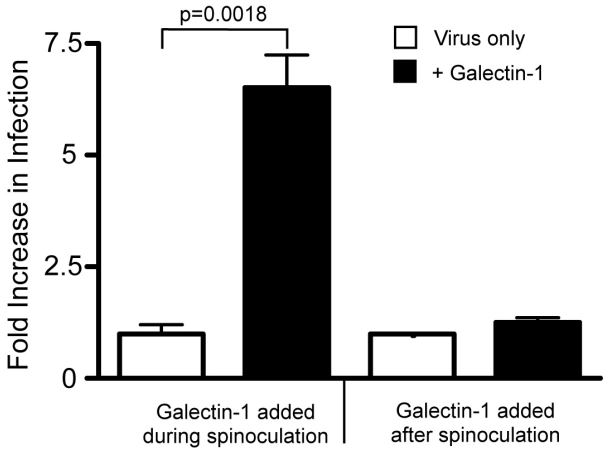
p=0.0018
Virus only
+ Galectin-1
Fold Increase in Infection
7.5
5
2.5
0
Galectin-1 added during spinoculation
Galectin-1 added after spinoculation

(*Previous page*)

Figure 2-11. Galectin-1 enhances infection of NiVpp in a carbohydrate binding-dependent manner. (A) Quantification of galectin-1 enhancement of NiVpp infection. NiVpp was titrated such that viral inoculum that gave luciferase activity in the linear range at 24 hpi was used. NiVpp was added to monolayers of Vero cells, and virus entry in the absence (white bars) and presence (black bars) of increasing concentrations of galectin-1 was quantified by measuring luciferase activity in infected cell lysate 24 hpi as described in Materials and Methods. Data from one of three replicate experiments are presented as mean fold-increase (+/- SD of triplicate samples) over the virus only (no galectin-1) condition. Significant p-value determined by two-way ANOVA. (**B)** Galectin-1 enhancement of NiVpp infection is carbohydrate binding-dependent. NiVpp (white bars) and 10 mM galectin-1 (black bars) was added to Vero cells in the presence of 100 mM lactose or 100 mM sucrose. Data are presented as in (A); mean +/- SD of triplicate samples from one of three replicate experiments is shown. **(C)** Galectin-1 added during spinoculation (at 4°C) shows an increase in NiVpp infection on Vero cells. NiVpp infection in the absence (white bars) or presence (black bars) of 10 mM galectin-1 added during or after spinoculation, i.e. during or after attachment of virus to cells. Data are mean +/- SD of triplicate samples from one of three replicate experiments. Significant p-value determined by Student's t-test.

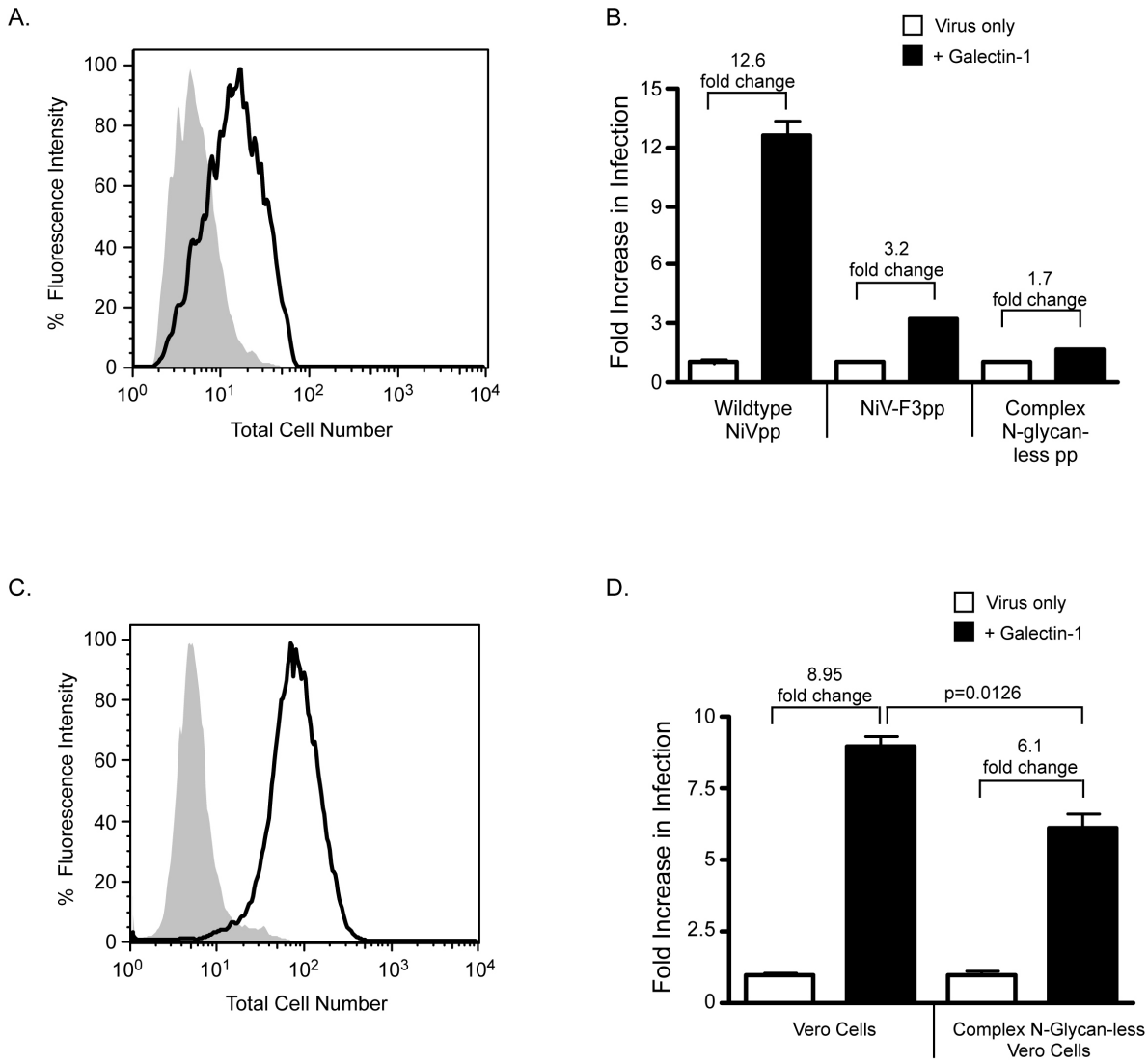

Figure 2-12. Galectin-1 enhances infection of NiVpp by bridging the virus to the cell through binding of viral surface and cell surface complex N-glycans. Flow cytometric analysis of L-PHA binding to 293T cells **(A)** or Vero cells **(C)** treated with kifunensine (grey filled histograms) shows loss of cell surface complex N-glycans when compared to L-PHA binding to untreated parental cells (bold outlined histograms). **(B)** Galectin-1-mediated enhancement of NiVpp infection is dependent upon complex N-glycans found on the surface of the virus. Virus infection of Vero cells in the absence (white) or presence of 20mM galectin-1 (black) is shown for NiVpp bearing three types of envelope glycoproteins; wild type NiV-F + -G, NiV-F3 mutant (+ wild type G), or NiV-F + -G devoid of complex N-glycans. Data from one of three replicate experiments are presented as mean fold-increase in infection (+/- SD of triplicate samples) over the virus only (no galectin-1) condition. **(D)** Galectin-1-mediated enhancement of NiVpp infection is dependent upon complex N-glycans on the surface of Vero cells. Virus infection in the absence (white bars) or presence (black bars) of 20 mM galectin-1 is shown for wild-type Vero cells and Vero cells devoid of complex N-glycans. Data (mean +/- SD of triplicate samples) from one of three replicate experiments are presented exactly as described for (B).

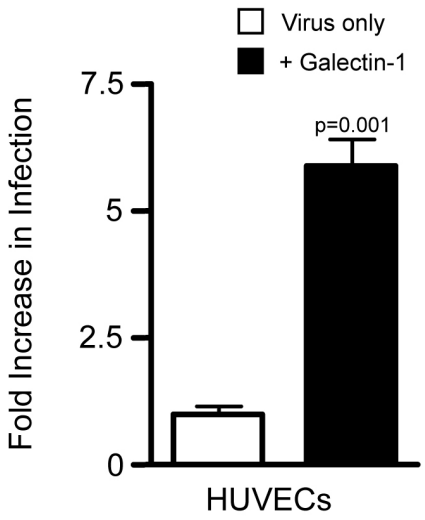

Figure 2-13. Galectin-1 enhances NiVpp infection of HUVECs. NiVpp was added to monolayers of HUVECS in the absence (white bar) and presence (black bars) of 20 mM of galectin-1 for 1 hour, and infection was quantified by measuring *Renilla* luciferase activity at 24 hpi. Data are presented as mean fold-increase (+/- SD of triplicate samples) in infection over the virus only (no galectin-1) condition. One of three replicate experiments is shown.

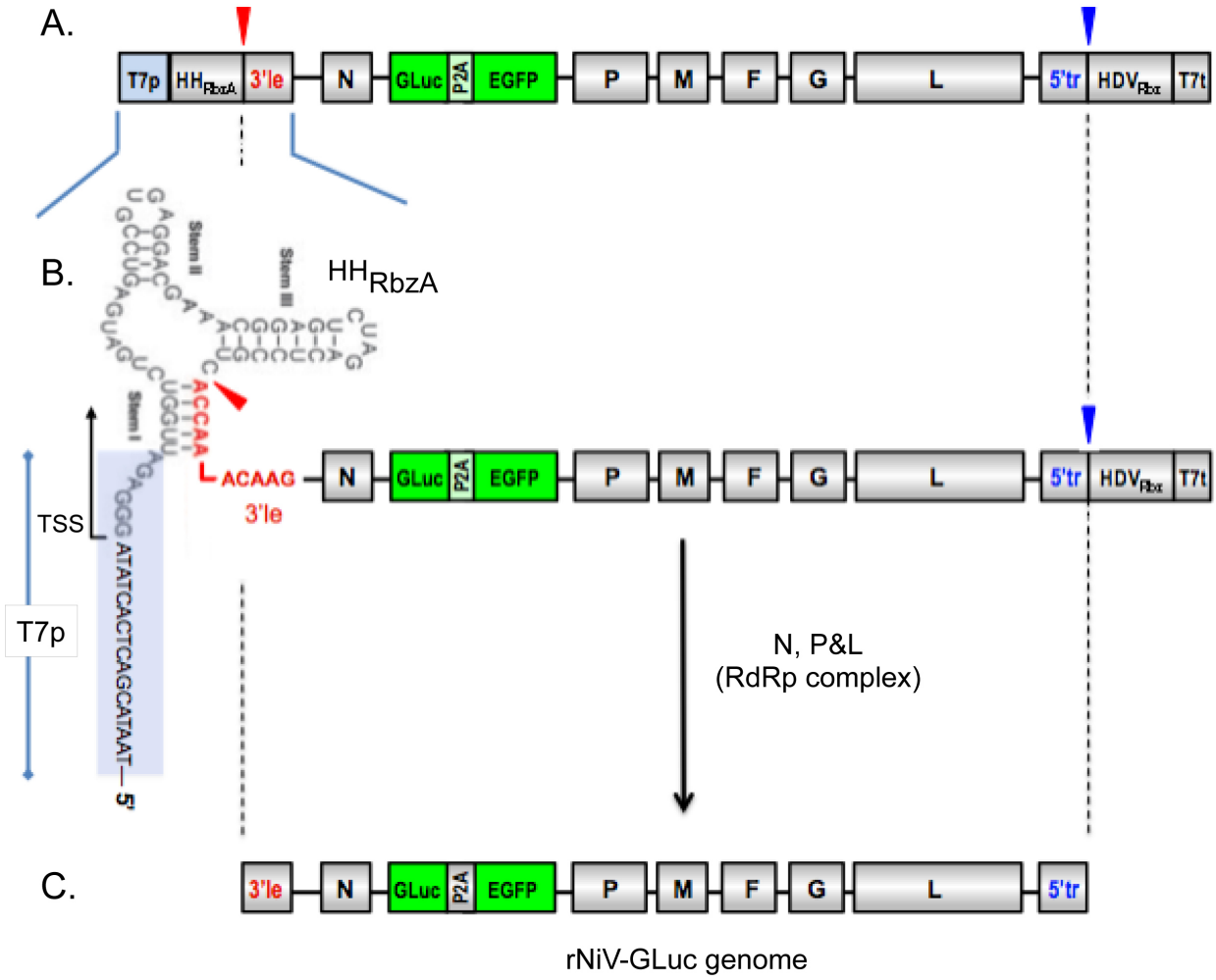

Figure 2-14. Design of recombinant Nipah virus *Gaussia* Luciferase (rNiV-GLuc) reporter virus for efficient reverse genetics. (A) Schematic of a T7 promoter (T7p)-driven (anti)genomic construct of rNiV-GLuc. The reporter genes GLuc and EGFP are linked by a P2A ribosomal skipping sequence and inserted as an extra open reading frame via duplication of the N-to-P intergenic region. The HDV ribozyme (HDV_{Rbz}) is a standard tool designed to cleave and generate the exact 5' trailer (5'tr) sequence of the NiV genome. The hammerhead ribozyme (HH_{RbzA}) is a novel application of thie cis-acting ribozyme to cleave and generate the 3' leader (3'le) sequence T7t, T7-terminator sequence. **(B)** The T7 polymerase-derived antigenomic transcript of rNiV-GLuc is shown with the 5' end expanded to illustrate the cleavage context that gives rise to the exact 3' le sequence. The HH_{RbzA} also allows for use of the full T7 promoter (T7p, shaded in light blue), which includes the triple GGG sequence that serves as the transcriptional start-site (TSS) for the full T7p. **(C)** The N, P, and L gene products form a RNA-dependent RNA polymerase complex (RdRp). Genome transcription and replication requires recognition of the exact 3'le and 5'tr sequences and encapsidation by the RdRp complex. In (A) and (B), cleavage by the HH_{RbzA} and HDV_{Rbz} to generate these exact 3' and 5' termini sequences are represented by the red and blue arrowheads, respectively.

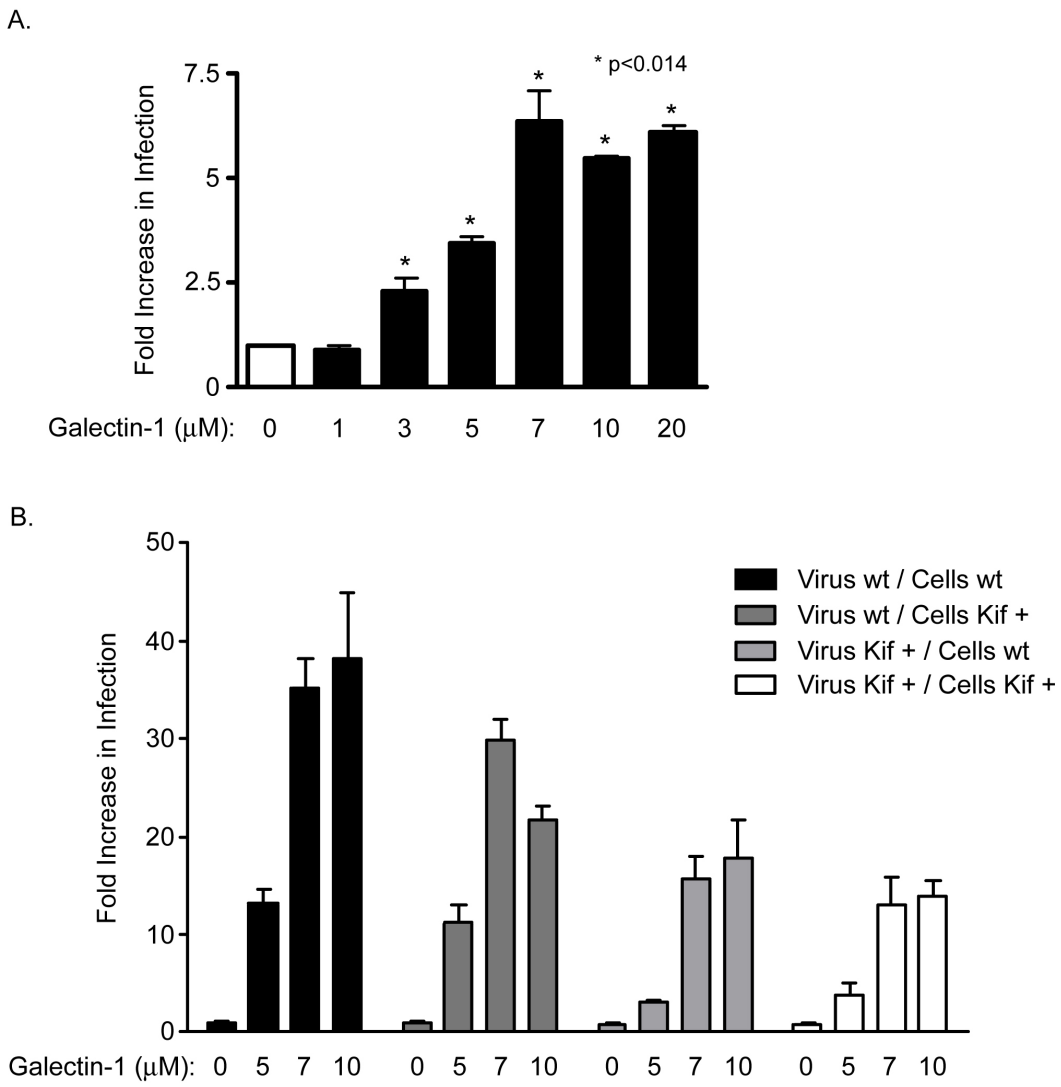

Figure 2-15. Galectin-1 enhances NiVpp and live Nipah virus infection of HUVECs. **(A)** Quantification of galectin-1 enhancement of recombinant GLuc reporter NiV (rNiV-GLuc) infection of HUVECs. rNiV-GLuc was added to monolayers of HUVECs in the absence (white bar) and presence (black bars) of the indicated amounts of galectin-1 for 1 hour, and infection was quantified by measuring *Gaussia* luciferase activity. Data are presented as mean fold-increase (+/- SD of triplicate samples) in infection over the virus only (no galectin-1) condition. One of three replicate experiments is shown. **(B)** Galectin-1 mediated enhancement of rNiV-GLuc infection is dependent upon complex N-glycans on the surface of HUVECs and on the surface of the virus. Virus or HUVECs deficient in complex N-glycans were made in the presence of 20 mM kifunensine (Virus Kif+ and Cells Kif+, respectively). rNiV-GLuc infection in the absence or presence of increasing concentrations of galectin-1 is shown for wild type rNiV-GLuc and HUVECs (Virus wt/Cells wt, black bars), wild type rNiV-GLuc and complex N-glycan-deficient HUVECs (Virus wt/Cells Kif+, dark grey bars), complex N-glycan-deficient rNiV-GLuc and wild type HUVECs (Virus Kif+/Cells wt, light grey bars), and complex N-glycan-deficient rNiV-GLuc and HUVECs (Virus Kif+/Cells Kif+, white bars). Data represent the average fold-increase in infection determined as in (A), and presented as mean +/- SD of triplicate samples from one of three replicate experiments.

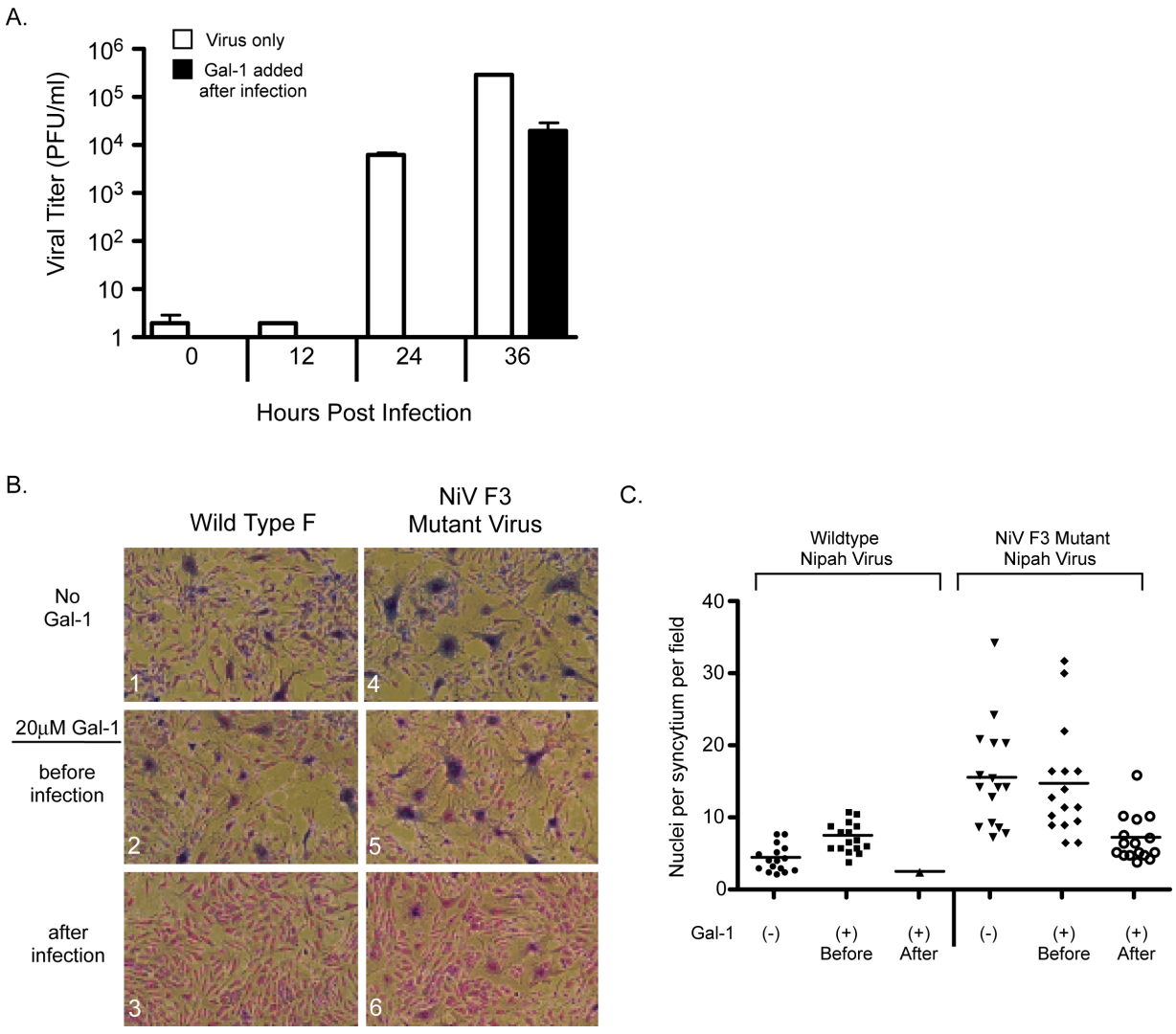

Figure 2-16. Galectin-1 can have opposing effects on Nipah virus production and syncytia formation. (A) Effect of galectin-1 added post-infection on the replicative spread of Nipah virus. HUVECs were infected with NiV_{MAL} for 1 hour at 37 C, washed to remove excess virus, and 20 mM galectin-1 (black bars) or buffer (virus only, white bars) added to the media only post-infection. Viral titers (log scale) were quantified by plaque assay after 0, 12, 24, and 36 hours post infection. **(B)** Syncytia formation induced by NiV infection. HUVECs infected with live NiV_{MAL} or NiV_{MAL} F3 mutant virus in the absence (no galectin-1), presence of galectin-1 added before infection, or presence of galectin-1 added after infection. Cells were fixed at 24 hpi and stained with DAPI to reveal nuclei. **(C)** Quantitation of panel B. Nuclei per syncytium per field were enumerated for the three separate conditions.

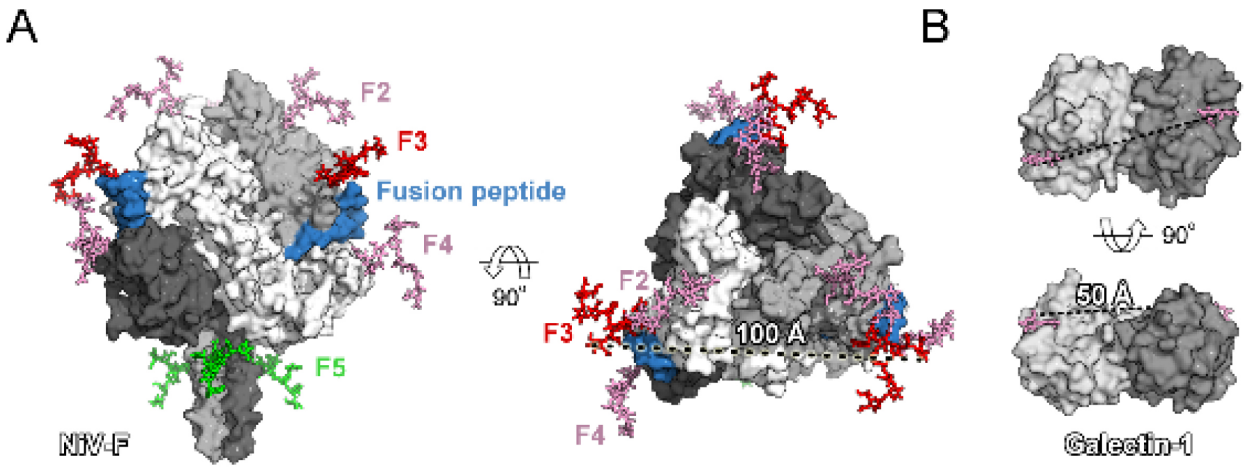

Figure 2-17. Modeling of the glycosylated pre-fusion trimeric NiV-F spike and galectin-1. (A) A model of the glycosylated NiV-F ectodomain in the prefusion state was created with the SWISS-MODEL server[42] using the structure of the parainfluenza virus 5 F protein in the metastable, prefusion conformation (PDB accession number 2B9B)[43] as a template. The model of the NiV-F ectodomain is shown in the surface representation, with each protomer colored a different shade of gray. For each protomer, structures of complex-type glycans[44] were placed at N-linked glycosylation sites F2-F4 and oligomannose-type glycans[45] were placed at F5. Glycans at sites F2 and F4 are colored pink, F3 are colored red, and at F5 are colored green. Residues corresponding to the putative fusion peptide (residues 103-128) are colored blue. The distance between equivalent F3 glycans is approximately 100Å. **(B)** Homo-dimeric crystal structure of C2S human galectin-1 in complex with lactose (PDB accession number 1W60).[46] Galectin-1 is shown as a surface representation with the two protomers colored different shades of gray. b-lactose is bound to both protomers and is shown as pink sticks. The distance between equivalent binding sites is approximately 50Å. Structures and models were rendered with pymol (www.pymol.org).

REFERENCES

1. Hsu VP, Hossain MJ, Parashar UD, et al. Nipah virus encephalitis reemergence, Bangladesh. *Emerg Infect Dis*. 2004;10(12):2082-2087.

2. Stone R. Epidemiology. Breaking the chain in Bangladesh. *Science*. 2011;331(6021):1128-1131.

3. Nahar N, Mondal UK, Hossain MJ, et al. Piloting the promotion of bamboo skirt barriers to prevent Nipah virus transmission through date palm sap in Bangladesh. *Glob Health Promot*. 2014.

4. Negrete OA, Levroney EL, Aguilar HC, et al. EphrinB2 is the entry receptor for Nipah virus, an emergent deadly paramyxovirus. *Nature*. 2005;436(7049):401-405.

5. Aguilar HC, Iorio RM. Henipavirus membrane fusion and viral entry. *Curr Top Microbiol Immunol*. 2012;359:79-94.

6. Maisner A, Neufeld J, Weingartl H. Organ- and endotheliotropism of Nipah virus infections in vivo and in vitro. *Thromb Haemost*. 2009;102(6):1014-1023.

7. Behling-Kelly E, Czuprynski CJ. Endothelial cells as active participants in veterinary infections and inflammatory disorders. *Anim Health Res Rev*. 2007;8(1):47-58.

8. Wahl-Jensen VM, Afanasieva TA, Seebach J, Stroher U, Feldmann H, Schnittler HJ. Effects of Ebola virus glycoproteins on endothelial cell activation and barrier function. *J Virol*. 2005;79(16):10442-10450.

9. Thijssen VL, Postel R, Brandwijk RJ, et al. Galectin-1 is essential in tumor angiogenesis and is a target for antiangiogenesis therapy. *Proc Natl Acad Sci U S A*. 2006;103(43):15975-15980.

10. Garner OB, Aguilar HC, Fulcher JA, et al. Endothelial galectin-1 binds to specific glycans on nipah virus fusion protein and inhibits maturation, mobility, and function to block syncytia formation. *PLoS Pathog*. 2010;6(7):e1000993.

11. Warke RV, Xhaja K, Martin KJ, et al. Dengue virus induces novel changes in gene expression of human umbilical vein endothelial cells. *J Virol*. 2003;77(21):11822-11832.

12. Imaizumi T, Yoshida H, Nishi N, et al. Double-stranded RNA induces galectin-9 in vascular endothelial cells: involvement of TLR3, PI3K, and IRF3 pathway. *Glycobiology*. 2007;17(7):12C-15C.

13. Stowell SR, Arthur CM, McBride R, et al. Microbial glycan microarrays define key features of host-microbial interactions. *Nat Chem Biol*. 2014;10(6):470-476.

14. Stowell SR, Arthur CM, Dias-Baruffi M, et al. Innate immune lectins kill bacteria expressing blood group antigen. *Nature medicine*. 2010;16(3):295-301.

15. Kohatsu L, Hsu DK, Jegalian AG, Liu FT, Baum LG. Galectin-3 induces death of Candida species expressing specific beta-1,2-linked mannans. *J Immunol.* 2006;177(7):4718-4726.

16. Gupta SK, Masinick S, Garrett M, Hazlett LD. Pseudomonas aeruginosa lipopolysaccharide binds galectin-3 and other human corneal epithelial proteins. *Infect Immun.* 1997;65(7):2747-2753.

17. Moody TN, Ochieng J, Villalta F. Novel mechanism that Trypanosoma cruzi uses to adhere to the extracellular matrix mediated by human galectin-3. *FEBS Lett.* 2000;470(3):305-308.

18. Kleshchenko YY, Moody TN, Furtak VA, Ochieng J, Lima MF, Villalta F. Human galectin-3 promotes Trypanosoma cruzi adhesion to human coronary artery smooth muscle cells. *Infect Immun.* 2004;72(11):6717-6721.

19. Ouellet M, Mercier S, Pelletier I, et al. Galectin-1 acts as a soluble host factor that promotes HIV-1 infectivity through stabilization of virus attachment to host cells. *J Immunol.* 2005;174(7):4120-4126.

20. Mercier S, St-Pierre C, Pelletier I, Ouellet M, Tremblay MJ, Sato S. Galectin-1 promotes HIV-1 infectivity in macrophages through stabilization of viral adsorption. *Virology.* 2008;371(1):121-129.

21. St-Pierre C, Manya H, Ouellet M, et al. Host-soluble galectin-1 promotes HIV-1 replication through a direct interaction with glycans of viral gp120 and host CD4. *J Virol.* 2011;85(22):11742-11751.

22. Bi S, Hong PW, Lee B, Baum LG. Galectin-9 binding to cell surface protein disulfide isomerase regulates the redox environment to enhance T-cell migration and HIV entry. *Proc Natl Acad Sci U S A.* 2011;108(26):10650-10655.

23. Levroney EL, Aguilar HC, Fulcher JA, et al. Novel innate immune functions for galectin-1: galectin-1 inhibits cell fusion by Nipah virus envelope glycoproteins and augments dendritic cell secretion of proinflammatory cytokines. *J Immunol.* 2005;175(1):413-420.

24. Pace KE, Lee C, Stewart PL, Baum LG. Restricted receptor segregation into membrane microdomains occurs on human T cells during apoptosis induced by galectin-1. *J Immunol.* 1999;163(7):3801-3811.

25. Aguilar HC, Matreyek KA, Filone CM, et al. N-glycans on Nipah virus fusion protein protect against neutralization but reduce membrane fusion and viral entry. *J Virol.* 2006;80(10):4878-4889.

26. Tamin A, Harcourt BH, Lo MK, et al. Development of a neutralization assay for Nipah virus using pseudotype particles. *J Virol Methods.* 2009;160(1-2):1-6.

27. Stachowiak JC, Brodsky FM, Miller EA. A cost-benefit analysis of the physical mechanisms of membrane curvature. *Nat Cell Biol.* 2013;15(9):1019-1027.

28. Elbein AD, Tropea JE, Mitchell M, Kaushal GP. Kifunensine, a potent inhibitor of the glycoprotein processing mannosidase I. *J Biol Chem*. 1990;265(26):15599-15605.

29. Nguyen JT, Evans DP, Galvan M, et al. CD45 modulates galectin-1-induced T cell death: regulation by expression of core 2 O-glycans. *J Immunol*. 2001;167(10):5697-5707.

30. Wolf MC, Wang Y, Freiberg AN, Aguilar HC, Holbrook MR, Lee B. A catalytically and genetically optimized beta-lactamase-matrix based assay for sensitive, specific, and higher throughput analysis of native henipavirus entry characteristics. *Virol J*. 2009;6:119.

31. Liu FT, Yang RY, Hsu DK. Galectins in acute and chronic inflammation. *Ann N Y Acad Sci*. 2012;1253:80-91.

32. Cerliani JP, Stowell SR, Mascanfroni ID, Arthur CM, Cummings RD, Rabinovich GA. Expanding the universe of cytokines and pattern recognition receptors: galectins and glycans in innate immunity. *J Clin Immunol*. 2011;31(1):10-21.

33. Dam TK, Brewer CF. Lectins as pattern recognition molecules: the effects of epitope density in innate immunity. *Glycobiology*. 2010;20(3):270-279.

34. Sato S, St-Pierre C, Bhaumik P, Nieminen J. Galectins in innate immunity: dual functions of host soluble beta-galactoside-binding lectins as damage-associated molecular patterns (DAMPs) and as receptors for pathogen-associated molecular patterns (PAMPs). *Immunol Rev*. 2009;230(1):172-187.

35. Yang ML, Chen YH, Wang SW, et al. Galectin-1 binds to influenza virus and ameliorates influenza virus pathogenesis. *J Virol*. 2011;85(19):10010-10020.

36. Earl LA, Bi S, Baum LG. N- and O-glycans modulate galectin-1 binding, CD45 signaling, and T cell death. *J Biol Chem*. 2010;285(4):2232-2244.

37. Kase T, Suzuki Y, Kawai T, et al. Human mannan-binding lectin inhibits the infection of influenza A virus without complement. *Immunology*. 1999;97(3):385-392.

38. Nguyen DG, Hildreth JE. Involvement of macrophage mannose receptor in the binding and transmission of HIV by macrophages. *Eur J Immunol*. 2003;33(2):483-493.

39. Liu Y, Liu H, Kim BO, et al. CD4-independent infection of astrocytes by human immunodeficiency virus type 1: requirement for the human mannose receptor. *J Virol*. 2004;78(8):4120-4133.

40. Lai J, Bernhard OK, Turville SG, Harman AN, Wilkinson J, Cunningham AL. Oligomerization of the macrophage mannose receptor enhances gp120-mediated binding of HIV-1. *J Biol Chem*. 2009;284(17):11027-11038.

41. Upham JP, Pickett D, Irimura T, Anders EM, Reading PC. Macrophage receptors for influenza A virus: role of the macrophage galactose-type lectin and mannose receptor in viral entry. *J Virol*. 2010;84(8):3730-3737.

42. Arnold K, Bordoli L, Kopp J, Schwede T. The SWISS-MODEL workspace: a web-based environment for protein structure homology modelling. *Bioinformatics*. 2006;22(2):195-201.

43. Yin HS, Wen X, Paterson RG, Lamb RA, Jardetzky TS. Structure of the parainfluenza virus 5 F protein in its metastable, prefusion conformation. *Nature*. 2006;439(7072):38-44.

44. Crispin M, Yu X, Bowden TA. Crystal structure of sialylated IgG Fc: implications for the mechanism of intravenous immunoglobulin therapy. *Proc Natl Acad Sci U S A*. 2013;110(38):E3544-3546.

45. Crispin M, Bowden TA, Coles CH, et al. Carbohydrate and domain architecture of an immature antibody glycoform exhibiting enhanced effector functions. *J Mol Biol*. 2009;387(5):1061-1066.

46. Lopez-Lucendo MF, Solis D, Andre S, et al. Growth-regulatory human galectin-1: crystallographic characterisation of the structural changes induced by single-site mutations and their impact on the thermodynamics of ligand binding. *J Mol Biol*. 2004;343(4):957-970.

CHAPTER 2.5

EVIDENCE FOR HENIPAVIRUS SPILLOVER INTO HUMAN POPULATIONS IN AFRICA

ABSTRACT

Zoonotic transmission of lethal Henipaviruses (HNV) from their natural fruit bat reservoirs to humans has only been reported in Australia and South/Southeast Asia. However, a recent study discovered numerous HNV clades in African bat samples. To determine the potential for HNV spillover events among humans in Africa, we examined well-curated sets of bat (*Eidolon helvum,* n=44) and human (n=497) serum samples from Cameroon for Nipah virus (NiV) cross-neutralizing antibodies (NiV-X-Nabs). Using a VSV-based pseudoparticle seroneutralization assay, we detected NiV-X-Nabs in 48% and 3-4% of the bat and human samples, respectively. Seropositive human samples were found almost exclusively in individuals that reported butchering bats for bushmeat. Seropositive human sera also neutralized Hendra virus and Gh-M74a (an African HNV) pseudoparticles, as well as live NiV. Butchering bat meat and living in areas undergoing deforestation were the most significant risk factors associated with seropositivity. Evidence for HNV spillover events warrants increased surveillance efforts.

INTRODUCTION

Nipah and Hendra viruses are highly pathogenic paramyxoviruses of the henipavirus genus that cause acute encephalitis and respiratory illness. Their mortality rate in humans can be greater than 90%[1,2] and they are the only paramyxoviruses that are classified as biosafety level 4 (BSL-4) pathogens. Until recently, the *Henipavirus* genus contained only two species — Hendra (HeV) and Nipah (NiV) viruses — which are phylogenetically closely related and exhibit serological cross-reactivity.[3] Fruit bats within the suborder *Megachiroptera*, particularly those of the genus *Pteropus,* have been identified as the natural reservoir for HNVs.[4-7] The geographical distribution of these reservoir bats partially coincides with the distribution of HNV outbreaks and spillovers events around the Indian Ocean, reaching from Australia (HeV) to Southeast Asia and the Indian subcontinent (NiV). Ecological studies[8] have revealed several characteristics common to all regions of HNV outbreaks: i) they are the natural habitat of Pteropid bats

(*Pteropus spp.*), ii) bat habitats in the region have been dramatically altered by the introduction of domestic plant and animal species and concomitant deforestation of the natural landscape,[9] and iii) humans or domestic animals have direct contact with bats in the area. While these characteristics can be observed in other locations around the world, to date, HNV outbreaks and spillovers into human populations have only been recognized in Australasia and South Asia.

The geographic distribution of *Pteropus* and other Pteropodids (Old World fruit bats) extends well beyond areas with documented HeV and NiV outbreaks. In 2007, a survey of Pteropodid species in Madagascar[10] reported that 2.3% and 19.2% of serum samples from *Pteropus rufus* and *Eidolon dupreanum*, respectively, tested positive for cross-reactive anti-HNV antibodies. Malagasy fruit bats share ecological niches, either roosting in the same caves or feeding in the same fruit trees. Since *Eidolon* species are extremely mobile (they can fly up to 2500km per year[11,12]) and are present all around sub-Saharan Africa, Iehlé *et al.* raised the possibility of lateral transfer of HNV from or to other *Eidolon* species on mainland Africa and hypothesized a much wider distribution of HNV.[10] Indeed, anti-HNV antibodies were soon found in *Eidolon helvum* (the common straw-colored African fruit bat) from Ghana[13] on the west coast of Africa, and more recently on Annobón island[14] in the Gulf of Guinea. Furthermore, HNV-like RNA sequences have been identified in fecal droppings of urban roosting bats in Ghana,[15] and more ominously, in fruit bat bushmeat in the Republic of Congo.[16]

Recently, sequence analysis of a larger sample set collected from western and southern Africa revealed a surprising diversity of paramyxoviruses in African bats, including 19 new species of HNV-like viruses distinct from the Nipah and Hendra viruses found in Southeast Asia and Australia.[17] However, only one almost complete African HNV-like genome sequence (Gh-M74a clone) has been published to date, and the corresponding viral isolate has not reported. This sequence was derived from a bat specimen originating in Ghana. We will refer to this putative HNV-like virus as the Ghana Virus (GhV), and GhV-F and GhV-G when referring to its fusion (F) and attachment (G) envelope glycoproteins, respectively. In contrast to the 80-90%

sequence identity shared between the F and G envelope glycoproteins of NiV and HeV, GhV-F and GhV-G share only about 70% and 40% sequence homology and even lower sequence identity (56% and 26%) with their respective NiV and HeV counterparts. Given this poor overall sequence conservation, it is unclear whether humoral responses elicited against the F/G proteins from African clades of HNV-like viruses would cross-react with F/G from NiV or HeV. This sequence divergence highlights the limitations faced by current seroprevalence studies that rely mostly on ELISA or Luminex based assays using recombinant NiV-G or HeV-G proteins as the target antigen.[10,13,14,18]

ELISA-based screening assays, while efficient, can yield high false positive and false negative rates compared to functional seroneutralization assays.[19] Thus, whenever possible, ELISA/Luminex-positive samples are confirmed by a seroneutralization (SN) assay. Although SN assays are considered a gold standard for seroprevalence studies,[19-21] follow-up confirmation with live virus SN assays is limited by the amount of sample available, and the requirement to work with live HNV in a high containment facility (BSL-4). Consequently, in many prior studies, only ELISA/Luminex positive samples, and often, only a small subset such as those with the highest binding activity, were confirmed with a biological or surrogate SN assay (reviewed in LF Wang et al., 2012[21]; for example AJ Peel *et al.*).[22] The latter is based on serum antibody competition of soluble receptor (sEphrinB2-Fc) binding to recombinant NiV-G or HeV-G conjugated to Luminex beads.[18] While these procedures can guard against false positives, they do not address the loss of potential false negatives.[10,13,14]

Given the recent reports that a diversity of HNV-like viruses are present and may be widely distributed in the bat reservoir host population across Africa,[17,22] we sought to evaluate the seroprevalence of HNV-like infections in both the bat and proximate human populations in Cameroon, and to assess risk factors that might be associated with any putative zoonotic transmission of African HNV-like viruses. To avoid the specificity and sensitivity issues associated with ELISA based assays, as well as the impracticalities of using a live virus SN assay

in BSL-4 as a screening test, we developed a VSV-based HNV envelope pseudotype particle (VSV-HNVpp) infectious SN assay[20] which can be used at BSL2 conditions as a primary screen for anti-NiV cross-neutralizing antibodies (anti-NiV-X-Nabs). Wang and Daniels raised the possibility that the high sensitivity and specificity of the pseudotyped particle platform may allow for the combination of screening and confirmatory tests in a single assay.[21] Thus, we screened serum samples from hunted bats (*E. helvum*) in an urban area in Yaoundé, Cameroon, and from almost 500 humans living in various villages across the south of Cameroon. The specificity, breath, and potency of anti-NiV-X-Nabs were confirmed using numerous specificity controls unique to our infectious SN assay, including isogenic viruses pseudotyped with irrelevant (VSV-G) or related HNV envelopes (HeV and GhV), and follow-up confirmation with a recombinant replication-competent reporter NiV specifically engineered for high sensitivity detection of anti-NiV-X-Nabs. Remarkably, the seropositive human samples were found almost exclusively in individuals that reported butchering bats for bushmeat. The geographical and temporal clustering of these seropositive cases provides evidence for recent HNV-like spillover events into the human population in this part of Africa.

MATERIALS AND METHODS

Mapping the putative GhV-G-ephrin binding interface

Based upon sequence similarity with the NiV (24%) and HeV (25%) attachment glycoproteins, the C-terminal 430 amino acids of GhV-G are predicted to comprise a globular six-bladed b-propeller domain.[23] To predict if the GhV-G b-propeller also shares receptor-binding specificity for ephrinB2 and ephrinB3, sequence conservation between GhV-G and NiV-G was mapped onto the crystal structure of NiV-G in complex with ephrinB2 (PDB accession number 2VSM).[24] NiV-G residues involved in ephrin binding were identified with the PISA EBI server[25] and a structure-based sequence alignment of NiV-G, HeV-G, and GhV-G was calculated with

ClustalW[26] and plotted with ESPript[27]. Residue conservation mapping and image rendering was performed with the program PyMOL (www.pymol.org).

Bat serum samples

Blood samples were obtained from wild *E. helvum* fruit bats (n=45) hunted by local hunters in Yaoundé, Cameroon between 8 May 2004 and 9 June 2007 in accordance with approvals from the Cameroon government and Johns Hopkins University IACUC approvals (FS03M221 and FS06H205). No payments were made in relation to the collection of samples to ensure no increased hunting of bats occurred as a results of this research. Dead bats were bled by cardiac puncture shortly after death with a 3 ml syringe. The blood was transferred to EDTA (plasma) or CAT Plus (serum) vaccutainer and centrifuged at 300×g / 1300 rpm for 15 min. Normal bat serum samples were obtained from *Pteropus hypomelanus* that were born and raised in captivity in the United States (a kind gift from the Brevard Zoo, Melbourne, Florida). Serum was collected during a routine check-up of the animals in fall 2011.

Human serum samples

Participation in the study was voluntary. Description of the study, informed consent procedures and questionnaire administration were done orally in either French or English, which are widely spoken as second languages in study villages. Participants were offered compensation approximately equivalent to 1 day of work, since participation precluded farm work on that day. The study protocol was approved by the Johns Hopkins Committee for Human Research, the Cameroon National Ethics Committee, and the HIV Tri-Services Secondary Review Board. In addition, a single project assurance was obtained from the Cameroonian Ministry of Health and accepted by the National Institutes of Health Office for Protection from Research Risks. The UCLA Internal Research Board (IRB) confirmed that the use of these anonymized archival serum samples did not constitute “human subjects” research and thus no independent IRB review was required. Human blood samples were collected by on site Global Viral / Metabiota (previously known as GVFI) team from 497 participants between 2001 and 2003 in 13 different

areas around southern Cameroon. Once drawn, the blood was transferred to EDTA (plasma) or CAT Plus (serum) vaccutainer and centrifuged at 300×g / 1300 rpm for 15 min. Sera were store at -80°C until processing for utilization in assays.

Serum sample handling and preparation

All bat and human serum samples were handled according to proposed WHO guidelines for working safely with diagnostic field specimens.[19] Sera were first heat inactivated at 56°C for 30 minutes, and then treated with Triton X-100 under BSL-2 conditions to ensure pathogen inactivation. All procedures were approved by the UCLA Institutional Biosafety Committee.

Production of vesicular stomatitis virus-based pseudoparticles (VSVpp)

Vesicular stomatitis virus (VSV)–based pseudoparticles were produced following established protocols.[20] Briefly, recombinant VSV with a *Renilla* luciferase reporter gene engineered in place of its native envelope glycoprotein (VSV-DG-rLuc) was pseudotyped with either its own G protein (**VSV-Gpp**), or the F and G envelope glycoproteins of NiV (**NiVpp**) (Genbank Accession: NC_002728.1 GI:13559808), HeV (**HeVpp**) (Genbank Accession: NC_001906.3 GI:529283690), or the newly described African HNV from Ghana (**GhVpp**) (Clone Gh-M74a,[17] Genbank Accession: HQ660129.1 GI:384476032). Pseudotyping was accomplished by transfecting 293T cells with codon-optimized expression plasmids for the F and G envelope glycoproteins of NiV and HeV, or for the VSV-G glycoprotein itself, and then infecting with VSV-DG-rLuc (complemented with VSV-G). At 24 hpi, pseudotypes containing media were clarified from cells debris by centrifugation at 1500 rpm for 5 min. Supernatants were then loaded on a 20% sucrose cushion and ultracentrifuged for 2 hours at 110,000×g. The pellet of concentrated pseudoparticles was then resuspended in Opti-MEM (Life Technologies), aliquoted and stored at -80°C.

GhV-F sequence rectification

Sequence inspection and bioinformatics analysis indicated that the GhV-F sequence in Genbank (Accession no. AFH96010.1) is likely incorrect due to a single nucleotide deletion near the N-

terminus which resulted in an extra-long N-terminus with no predicted signal peptide. The details, rationale, and functional evidence for sequence rectification of the GhV-F gene are provided in the accompanying manuscript.[28]

Generation of recombinant Sendai virus (rSeV) and Nipah virus (rNiV)

The rSeV is a modified version of RGV0 (a kind gift of Nancy McQueen), a Fushimi strain construct with F1-R strain mutations in F and M as described by Hou *et al.*[29] We inserted an eGFP reporter between the N and P genes and made further modifications to increase rescue efficiency.[30]

Recombinant NiV (reference Malaysia strain, Genbank Accession: NC_002728.1 GI:13559808), rNiV-GLuc, was engineered to express secreted *Gaussia* Luciferase (descriptive name: NiV_{MAL} $T7_{P\text{-}3G}$ 3'Ribozyme A-(N_GLuc-p2A-eGFP_P) as described in Chapter 2.2. The Gaussia Luciferase (GLuc) ORF was modified with 2 mutations that provide greater signal and stability, M60L and M127L[31,32] (these references refer to corresponding residues M43 and M110 due to removal of the 17a.a. secretion signal peptide). Rescue of rNiV-GLuc and seroneutralization assays were performed at the UTMB Galveston National Laboratory BSL-4 laboratory.

Optimization and validation of VSVpp seroneutralization (SN) assay

Using a reference panel of human and pig sera, we and our collaborators at the United States Centers for Disease Control, Canadian Food Inspection Agency, and Merial Sanofi (Lyon, France), previously validated our NiVpp SN assay to have a specificity of 94-100%, and an equivalent or lower sensitivity when measured against a standard live NiV plaque reduction neutralization test as the gold standard.[20]

For our current study, we first determined the linear dynamic range of each pseudoparticle preparation, and a fixed amount of virus within the linear range (corresponding to the luciferase reporter output of ~20,000 RLU at 24 hpi) was chosen for subsequent SN assays (Figure 2-18, panel A). Next, the optimal serum dilution to be used was determined by

comparing the SN activity of a well-characterized hyper-immune rabbit sera made against Nipah viral-like particles bearing both the NiV fusion (F) and attachment (G) envelope glycoproteins,[33] and its pre-immune counterpart. Significant differences were observed for dilutions between 1:100 and 1:10,000 (Figure 2-18, panel B). Based on these data, we diluted bat and human sera 1:100 for all our SN assays. Use of high serum dilutions (>1:20) might also mitigate putative serum-induced cytotoxicity effects that often occur at high serum concentrations, which can confound SN results.[34,35] As an additional specificity control, we used an isogenic VSV-DG-rLuc pseudoparticle containing the envelope glycoprotein of Vesicular Stomatitis virus itself (VSVpp) (Figure 2-19 and Figure 2-21). VSV is endemic to the Americas, and has not been reported in Africa since 1900,[36,37] so any serum samples that show inhibition of both VSVpp and NiVpp infection was considered non-specific or cytotoxic, and was discarded from further analysis. 1/45 and 10/497 bat and human samples, respectively, strongly inhibited both VSVpp and NiVpp infection and were discarded from analysis.

For the valid samples, SN assays were performed in DMEM (Invitrogen) containing 1:100 dilution of sera and an optimized amount of pseudotyped virus inoculum (VSV-Gpp, NiVpp, HeVpp, or GhVpp) that will result in ~20,000 RLU of luciferase activity at 24 hpi. The medium containing infectious virus and serum was transferred to a monolayer of Vero cells and incubated at 37°C for 2h before removal and replacement with fresh DMEM containing 10% fetal calf serum (FCS). Cells were incubated at 37°C for another 24 hours before processing for detection of *Renilla* luciferase activity according to manufacturer's directions (Promega). SN titers were performed using identical procedures except that the viral inoculum (NiVpp) was pre-mixed with serial 5-fold dilution of sera from 1:50 to 1:31,250. All infections were performed in quadruplicates.

Live virus seroneutralization assay

The relevant bat and human serum samples were also tested for neutralizing antibodies using the replication-competent recombinant paramyxoviruses (rSeV-eGFP or rNiV-GLuc) generated

as described above. Seroneutralization of live rSeV-eGFP and rNiV-GLuc infection was performed in an identical fashion as VSVpp (the latter under BSL-4 conditions), except that rSeV-eGFP infection was detected by FACS analysis and rNiV-GLuc infection was detected by quantifying GLuc activity (BioLux *Gaussia* Luciferase Assay, New England Biolabs) in 10% (v/v) of infected cell culture supernatant at 24 hpi.

FCS and hyper-immune rabbit anti-NiV serum[33] were used as negative and positive controls, respectively. Additional negative controls included normal human sera (NHS) from Los Angeles blood donors (blood samples obtained from the virology core at the UCLA AIDS Institute) and normal bat sera (NBS) from captive-bred bats (generously provided by Brevard Zoo, Melbourne, Florida). All SN assays were performed in quadruplicates.

Geographical data

Raw geographical data were extract from www.openstreetmap.org (© OpenStreetMap contributors) and are available under the Open Database License. Maps were then built and modified with JOSM, Merkaartor, and Inkscape softwares. Forest cover and deforestation was determined by onsite collaborators and documented in field reports.

Statistical Methods

SN assay results for quadruplicates were grouped for statistical analysis. Tests between groups were done using Dunnett's test, a multiple comparison procedure for testing groups against a single control. Categorical data were tested and confidence intervals were estimated using Fisher's Exact test. The strengths of association of seropositivity with bat contact and butchering were also estimated using two-tailed Fisher's exact test. Because no exposure was observed in the unexposed, a value of 0.5 was added to all cells to allow the odds ratios to be calculated.[38,39] Statistical tests were performed using R version 2.15.1 for Mac and version 3.0.1 for GNU Linux with the *multcomp* package. A modified R script was written to allow for use of non-integers in the Fisher's Exact test.

RESULTS

Prevalence of anti-Nipah virus cross-neutralizing antibodies in bat serum samples

Despite the overall low sequence homology between GhV-G and NiV-G/HeV-G, mapping of the GhV-G sequence onto the crystal structure of NiV-G complexed with ephrinB2[24] indicated that the vast majority of the sequence conservation was located at the receptor-binding interface, suggesting that GhV-G may also use ephrinB2 (and likely ephrinB3) as receptors for cell entry (Figure 2-20). The clustering of conserved sequences around the receptor-binding site raises the possibility of biologically significant anti-NiV *cross-neutralizing* antibodies (anti-NiV-X-Nabs) in African bats exposed to African clades of HNV-like viruses despite their overall low sequence identity with NiV. To determine the prevalence of anti-NiV-X-Nabs in that geographically proximate part of Western Africa, we screened fruit bat (*E. helvum*) serum samples from Cameroon, collected and curated by Global Viral/Metabiota. To conserve the use of such sera, we further optimized a previously validated VSV-based (VSV-DG-rLuc) NiV envelope pseudotyped particle (NiVpp) seroneutralization (SN) assay for high specificity screening, and established appropriate control sera as described in Materials and Methods (Figure 2-18).

In our screen of bat serum samples, ~48% (21/44) were classified as being positive for anti-NiV cross-neutralizing activity (Figure 2-21, panel 4; Figure 2-19, panel A) when compared against the fetal calf serum (FCS) negative control group (Figure 2-21, panel 1) as determined by the Dunnett's test for multiple comparisons against a single control group. The specificity of our NiVpp SN assay is underscored by the lack of inhibition of the relevant serum samples against VSVpp. Furthermore, "normal bat sera" (NBS) from captive-bred bats in the United States did not show significant neutralization activity against NiVpp or VSVpp (Figure 2-21, panel 2).

Anti-Nipah virus cross-neutralizing antibodies in human serum samples from Cameroon

The relatively high prevalence of anti-NiV-X-Nabs in the bat populations surrounding Yaoundé in southern Cameroon prompted us to examine archival *human* sera collected from this region

of Africa for the presence of similar anti-NiV-X-Nabs, which might indicate potential spillover event(s). Thus, we analyzed almost 500 blood samples collected from healthy adults by Global Viral/Metabiota in southern Cameroon between February 2001 and January 2003 in 13 different locations. All samples were collected in rural areas, but represent different habitats (savanna, gallery forest, and lowland forest) supporting wild game populations that provided a source for the bushmeat trade (Figure 2-26 below).

The careful curation of samples allowed us to segregate the sera into various dichotomous groups such as those who reported contacts with bats and those that did not. Sera were analyzed using the same SN assay and criteria as described for the bat serum analysis except that normal human sera (NHS) from blood donors were used as complementary negative controls to FCS. Using the Dunnett's test as a stringent measure of significance, 7/227 samples (~3%) in the bat-exposed group were considered to have significant anti-NiVpp cross-neutralizing activity when compared against the FCS group (Figure 2-22, panel 4; Figure 2-19, panel B; and Table 2-2). The same 7 samples were identified as statistically different if the NHS was used as the control group (data not shown). On the other hand, none of the 260 samples in the non-bat exposed group were statistically different from the FCS control group (Figure 2-22, panel 5; Figure 2-19, panel C; and Table 2-2). Seropositive samples exhibited different neutralizing potencies. One seropositive sample gave an IC50 titer of ~ 1:1,000 whereas the other only achieved ~40% inhibition at 1:50 (the lowest serum dilution tested) (Figure 2-19, panel G). As expected, our hyperimmune anti-NiV control serum exhibited the highest IC50 titer of ~1:15,000. Interestingly, representative seronegative samples showed a slight enhancing effect as serum concentrations were increased, suggesting that we may even have underestimated the number of true positives.

Specificity of anti-NiV cross-neutralizing antibodies in human serum samples

To further confirm the specificity of the human sera positive for anti-NiV-X-Nabs, and to determine the potential breadth of cross-reactivity of these antibodies, we chose two

seropositive samples and tested them in our SN assay against three HNV pseudoparticles: NiVpp, HeVpp and GhVpp, the latter bearing F and G from the Gh-M74a clone reported by Drexler *et al.*,[17] and an eGFP-expressing recombinant Sendai virus (rSeV-eGFP). SeV is a murine paramyxovirus (*Respirovirus* genus) not normally found in humans that enter cells via a pH-independent pathway using sialic acid-based receptors, and thus, should not be enhanced nor inhibited by the seropositive human samples identified in Figure 2-22. Indeed, neither the seropositive human Cameroon sera nor the hyper-immune rabbit anti-NiV serum inhibited the pH-independent entry of rSeV-eGFP (Figure 2-23, blue bars). In contrast, seropositive human Cameroon samples inhibited NiVpp, HeVpp and GhVpp to varying degrees (Figure 2-23, red, orange, and grey bars, respectively). Interestingly, our hyper-immune anti-NiV sera showed good to moderate (50-80%) inhibition of NiVpp and HeVpp infection but only minimal inhibition (~10-15%) of GhVpp infection. The implications of these results will be discussed.

As a final confirmation regarding the specificity of the anti-NiV-X-Nabs that we detected in the seropositive human samples, we repeated the SN assay with live NiV under BSL-4 conditions. In order to conserve the use of these archival sera, which were only available in small amounts, we generated and rescued a recombinant NiV expressing secreted *Gaussia* Luciferase (rNiV-Gluc) (see Materials and Methods and also Figure 2-24, panel A). *In vitro* growth kinetics of rNiV-GLuc was comparable to the parental NiV Malaysia strain and pathogenicity was demonstrated in the hamster model where bioluminescence in *ex vivo* harvested organs from the moribund animal correlated well with viral titers measured by traditional plaque assays (Figure 2-24, panel B). rNiV-GLuc allowed us a highly sensitive and dynamic method to monitor NiV infection (or inhibition thereof) in cell culture by sampling infected cell culture supernatant for *Gaussia* luciferase activity. Thus, we chose four seropositive and two seronegative human samples from our Cameroon cohort, and performed our SN assay with rNiV-GLuc along with the other appropriate negative and positive controls.

Figure 2-25 shows that only the seropositive samples significantly inhibited rNiV-GLuc

infection, albeit with varying degrees of potency (15 to 65% reduction in GLuc activity). A relatively high inoculum was used (MOI = 1), and raw luciferase activity values (>10^7 RLU) are presented to demonstrate the robustness of our assay. Seronegative samples showed no significant inhibition of rNiV-GLuc infection, and the GLuc activity detected was no different from the FSC or NHS negative controls. As expected, the hyper-immune rabbit anti-NiV serum inhibited rNiV-GLuc infection by close to 90%.

Risk factor analysis. The questionnaire filled out by the participants before blood sample collection covered their contacts with some animals known to be HNV hosts, some of their "at risk" activities, and the location of the village with its associated environmental features. We analyzed their answers to uncover any risk factors that might be associated with seropositivity. Table 2-2 shows that all of the seropositive samples came from the group that reported contact with bats in one form or another with those exposed to bats being 17 times more likely to be HNV seropositive (OR=17.72, P=0.0021, two-tailed Fisher's Exact test with zero-cell correction[38,39]). The highly statistically significant difference between seroprevalence rates in the bat exposed (7/227, 3%) versus non-exposed groups (0/260) (P=0.0045, Fisher's Exact test) supports the hypothesis that contact with bats increases one's risk of being infected by an antigenically related African HNV-like virus.

We next tried to determine whether a particular type of bat exposure was more significantly associated with seropositivity. The detailed questionnaire allowed us to segregate the tested serum samples into other dichotomous groups such as those that butchered bats (or not), those that hunted bats (or not), and those that remembered bites/scratches from bats (or not). Intriguingly, hunting bats alone was not a sufficient risk factor; however, those butchering bats were 29 times more likely to be seropositive than those not having contact with bats (7/164 (4%) versus 0/316, respectively; P=0.0002; Table 2-2). While there was no statistically significant association with gender, there appears to be one with associated with age although the latter association may be due to the age of bat butchers (data not shown).

Finally, we examined environmental and geographic parameters. Figure 2-26 shows a map of the indicated areas of our sample collection sites. The majority of the seropositive participants were from the ND area (4/7), while the others were from MB (C1), M (A2), and HA (F2) areas. Ground reporting from Global Viral/Metabiota staff at the time of collection revealed that seropositive samples came almost invariably from low forest cover areas (Figure 2-26). Indeed, Table 2-2 shows that seroprevalence for HNV-like viruses were significantly higher in samples originating from these four areas compared to those that did not (3.2% versus 0.3%, respectively, p=0.0136). In effect, those living in areas of putative deforestation were 10 times more likely to be HNV-seropositive than those who were not (OR=10.1, P=0.0088). In addition to the seven "true" seropositive samples classified by the Dunnett's test, there were three borderline-positive samples (~ 50% inhibition) in the bat-exposed group (Figure 2-19, panel E, blue) that also came from areas associated with deforestation: ND, MN, and HA (located in C3, A2, and F3, respectively, in Figure 2-26 map). Within the ND area, 3 of the 4 seropositive samples were from the same village, and only 12 persons from this village with known bat contacts volunteered for this study, which would have resulted in a 25% seroprevalence rate amongst the bat-exposed group if this village were considered alone.

DISCUSSION

In this study, we provide multiple lines of evidence that suggest HNV-like spillover events from its natural bat reservoir into the human population in southern Cameroon. Using our optimized pseudotyped virus SN assay as a primary screen for almost 500 human serum samples, we confidently identified at least 7 HNV seropositive based on stringent statistical criteria, internal specificity controls for both the virus and the sera, and follow-up confirmation with live recombinant NiV (rNiV-GLuc) or SeV, a paramyxovirus from a different genus. Together these precautions enabled the risk factor analysis that revealed highly significant associations of seropositivity with the behavioral and environmental parameters that are known to facilitate

zoonotic emergence.[40-43]

By combining behavioral, geographic and serological data, we can provide more conclusive results than that which would be available from inclusion of one set of data alone. For example, that seropositivity was exclusively and most significantly associated with intimate bat exposure (p=0.0006), such as the slaughtering of bats for bushmeat (Table 2-2), is more informative than results from a SN assay with perfect sensitivity and specificity unlinked to an exposure risk. As for environmental factors, all seropositive samples come from villages located near open savannah lands or areas of deforestation as documented by our local field staff. *In toto*, we provide a strong body of evidence indicating spillover of HNV-like viruses into the human population in Africa.

In recent years, several groups have detected henipavirus-like sequences in African wildlife (bat) and domesticated pig populations.[10,14-17] A more recent study[22] *provides* evidence for continent-wide panmixia of the HNV reservoir host, the common straw-colored African fruit bat (E. helvum), and reports an average seroprevalance of ~42% for cross-reactive NiV-G binding antibodies using the Luminex assay. This is close to the 48% seroprevalance rate we found in our cohort of *E. helvum* serum samples using our SN assay. However, the former study reported a much lower seroprevalance rate (~5% in Tanzania and ~15% in Ghana) when using their Luminex-based serum antibody/sEphrinB2 competition assay as a surrogate viral neutralization test. These contrasting results suggest that our infectious NiVpp SN assay has increased sensitivity, perhaps due to the ability of our SN assay to detect neutralizing anti-F antibodies as well as neutralizing anti-G antibodies that do not compete for sEphrinB2 binding.[44]

The ability of seropositive bat sera to cross-neutralize NiVpp infection suggest a close antigenic relationship between the envelope glycoproteins of NiV and that of the putative "Cameroon" HNV strain(s). Drexler et al. also showed that serum from the African bat that was infected with the parental GhV (Gh-M74a) exhibited cross-reactivity with antigens expressed on

NiV infected cells.[17] Mapping the sequence of GhV-G onto the NiV-G crystal structure indicated that despite the low overall sequence identity (~25%) between the two attachment glycoproteins, the ephrinB2 receptor-binding site was relatively conserved, suggesting common receptor usage between these two divergent HNVs (Figure 2-20). Indeed, sEphrinB2-Fc inhibits GhVpp infection, binds to cell surface-expressed GhV-G,[28,45] and immunoprecipitates GhV-G,[46] suggesting that GhV is a related African HNV that also uses ephrinB2 as an entry receptor. Conservation of receptor usage is strong biological evidence that GhV is a bona fide HNV, albeit distantly related to NiV and HeV. Indeed, the ability of a virus to use highly conserved receptors has predictive value when considering the likelihood of viral emergence and cross-species spillover.[42,47]

The results of our SN assay comparing seropositive Cameroon human sera samples with our hyperimmune rabbit anti-NiV serum (Figure 2-23) suggest that GhV, or at least the GhV-F and/or -G, is antigenically closer to the putative HNV common ancestor than NiV or HeV. Antibodies made against a more "ancestral" virus such as the presumptive African HNV-like virus that infected the seropositive individuals, have a greater breadth of cross-neutralization than antibodies made against a more divergent lineage isolated by genetic drift (e.g. anti-NiV), which does not neutralize GhVpp well, if at all. Note that the putative "Cameroon" HNV strains that infected and elicited the anti-NiV-X-Nabs from the seropositive individuals were not even likely to be the same strain as GhV itself, and yet elicited antibodies that cross-neutralized NiV, HeV, and GhV. These results have implications for a broad-coverage vaccine strategy: the use of envelope glycoproteins from a more "ancestral" African HNV clade could induce more potent cross- neutralizing antibodies against emerging HNV-like viral strains. The increased breadth of cross-neutralization elicited by more ancestral viral envelopes have already been documented for HIV[48] and influenza virus[49], and forms the basis of vaccine strategies to elicit broadly neutralizing antibodies.

Given the relative ubiquity of HNVs or HNV-like viral agents in Africa, the commonality

of the bushmeat trade in the resource poor areas under study, and the presence of HNV-like sequences in up to one-third of E. helvum sold as bushmeat in neighboring Brazzaville, Congo,[16] we surmised that the conditions were alarmingly optimal for zoonotic transmission of African HNVs from a bat reservoir host to the human population group at highest risk for such zoonoses. If we classify all 487 serum samples by those that reported butchering bats (n=171) and those that did not (n=316), the seroprevalence rate for anti-NiV-X-Nabs amongst bat batchers is ~4% (7/171, Table 2-2). As a reference point, HIV-1 prevalence in Cameroon was estimated to be approximately 5% by UNAIDS in 2010.

Although no human HNV encephalitis cases have ever been documented in Africa, this does not preclude the existence of outbreaks or spillovers. Considering the shortage of physicians (1/10,400 according the WHO) and the endemicity of malaria, yellow fever, typhoid fever, and meningococcal meningitis, it is not surprising that an emerging encephalitic virus would remain misdiagnosed and unreported. Indeed, HNV infections have a history of being mis-diagnosed: NiV was initially incorrectly identified as Japanese encephalitis virus when it first appeared in 1998,[50] and the Siliguri outbreak of NiV was originally reported as 'aberrant measles'.[51] It is also possible that some of these African HNV-like viruses are non-pathogenic, not unlike Cedar Virus, a non-pathogenic strain of HNV isolated from Australian bats.[52] In any case, the virulence of African HNV-like viruses awaits experimental confirmation. In all likelihood, the high diversity of HNV-like viruses in Africa suggests a virulence spectrum that is equally diverse.

As humans and/or their domesticated animals encroach upon the ecological niche occupied by the reservoir hosts, increased opportunities for contact with the virus reservoir also increases the risk for cross-species infection.[53,54] The destruction of natural habitats can also lead wildlife to relocate, sometimes within greater proximity to human populations.[41,42,54,55] Our field data indicate that the vast majority of seropositive participants come from the western part of the country (ND, MN, MB), where a lack of forest cover due to natural or human causes was a

noted feature (C3, A2 and C1 in Figure 2-26). The clustering of seropositive participants is particularly striking in a village of the ND area where 3/12 (25%) participants were positive. These 3 participants are all young adults (25 – 35 years old) with documented bat butchering activities. On the other hand, none of the >200 samples from the deep tropical forest locations such as LE and MO (Figure 2-26, F4 and G5, respectively) were positive even though ~50% of these samples came from the bat-exposed group.

Bat hunting in Cameroon – typically by use of firearm, nets, or catapults – do not involve physical contact between bats and hunters. Consistent with these observations, hunting bats per se was not associated with an increased risk for seroconversion. Furthermore, none of the pig owners or hunters (that do not also butcher their catch) enrolled in our study was seropositive. Thus, superficial contact with domestic animals does not appear to increase the risk of a HNV-like infection. In contrast, that butchering bats is the most significantly associated risk factor for HNV seropositivity suggests that close contact with bodily fluids (blood, saliva, excreta) is likely required for successful cross-species transmission.

Until recently, the range of the reservoir hosts was thought to confine HNV spillovers to Asia and Australia. However, there is increasing serological and molecular evidence documenting the widespread occurrence and diversity of HNVs in Africa, mainly in African fruit bat species. Our study now provides evidence for HNV spillover into human population groups in Africa (Cameroon) at high risk for contracting zoonoses. In the various taxonomic schemes proposed for the transitional dynamics of zoonotic pathogens,[41,56] features such as the (i) prevalence and diversity of HNVs in their African reservoir hosts, (ii) the increased opportunities for zoonotic transmission provided by the bushmeat trade, (iii) the unusually broad species tropism of HNVs facilitated by the use of highly conserved receptors, and (iv) the documented human-to-human transmissibility of NiV, justifiably place HNV or HNV-like viruses at or close to the penultimate stage for sustained transmission in human outbreaks. Our data warrants increased surveillance efforts to determine the frequency of similar spillover

events in Africa at large, and highlights the need for international collaborations and cross-disciplinary approaches to determine the virulence spectrum of African HNVs.

FIGURES

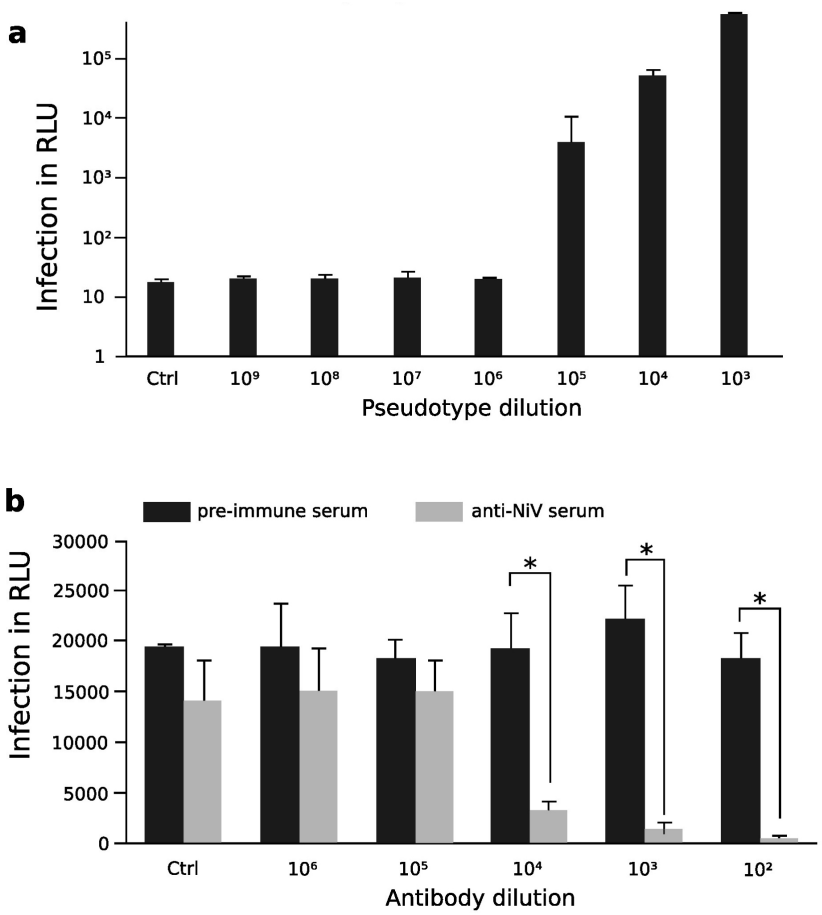

Figure 2-18. Optimization of the seroneutralization assay. (A) Determination of the linear dynamic range of VSV-DG-rLuc reporter NiV pseudotype particle (NiVpp) infection: Vero cells were seeded in a 96-well plate and infected with 10-fold serial dilutions of a NiVpp preparation (10^{-3} to 10^{-9}). At 24 hours post-infection (hpi), cells were lysed and luciferase activity was quantified by luminometry as a measure of NiVpp infection. Mock infection (Ctrl, infection medium only) gave negligible luciferase activity (RLU, relative light units) of less than 50 whereas a linear range of infectivity (~20,000 to ~200,000 RLU) was observed for viral dilutions between 10^{-3} and 10^{-5}. **(B)** Determination of the optimal serum dilution. Vero cells were seeded in a 96-well plate and infected with NiVpp in the presence of serial 10-fold dilutions (10^{-2} to 10^{-6}) of hyperimmune rabbit anti-NiV serum (grey) or its pre-immune counterpart (control, black). 24 hpi, cells were lysed and infection was measured by quantifying luciferase activity in the cell lysate as above. Significant differences (asterisks) between the two sera, indicating specific neutralization activity, were observed for serum dilutions from 10^{-2} to 10^{-4} ($p < 0.0002$; two-tailed Student t-test).

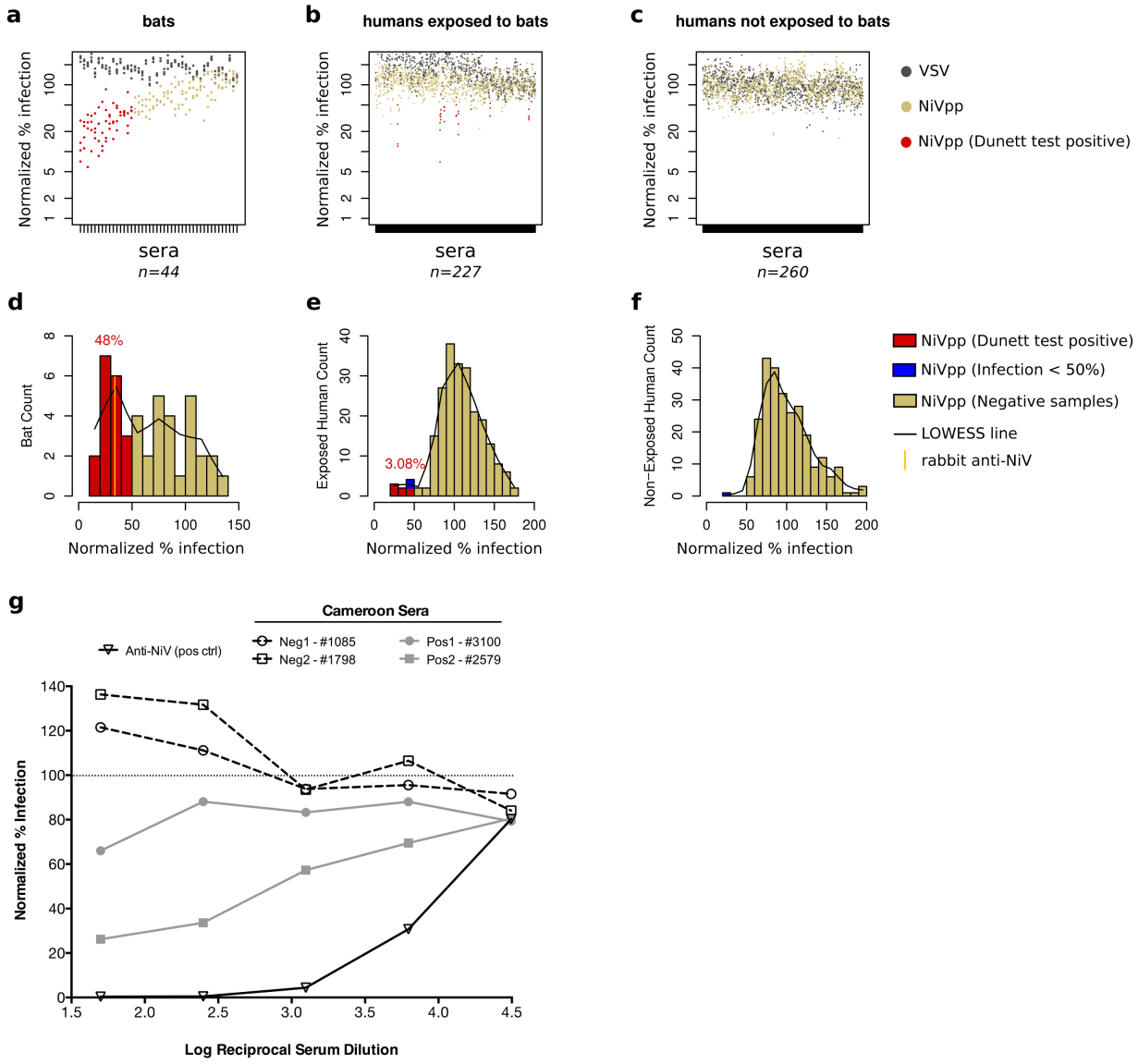

Figure 2-19. Primary data for individual serum samples screened with the infectious pseudotyped particle (VSVpp and NiVpp) seroneutralization assay. Dot plots representing the primary seroneutralization (SN) data for bat sera **(A)**, bat-exposed human sera **(B)**, and non-exposed human sera **(C)**. SN data are presented as normalized % infection with infectivity obtained with NiVpp in the presence of FCS (1:100) set at 100%. Each sample, represented by the tick marks on the x-axis in panel (A), was tested in quadruplicate for NiVpp (gold or red dots) and VSVpp (black dots) inhibition. VSVpp is the isogenic virus control pseudotyped with VSV-G rather than NiV-F/G. Each vertical alignment of 8 dots (4 for NiVpp + 4 for VSVpp) represents the results from a single serum sample. For NiVpp, seropositive samples, i.e., those classified as significantly different from the designated negative control group by the Dunnett's test, are indicated by red dots whereas the remaining seronegative samples are shown as gold dots. For the bat serum samples in panel (A), SN data are presented in order of their neutralization potency from left to right (sample with best SN activity is the first one on the left). For the bat-exposed (B) or non-exposed (C) human samples, SN data are

presented in the order they were performed. The apparent enhancement of VSVpp infection seen with serum from the bat-exposed group (B), but not from the bat non-exposed group (C), is likely due to different shipment conditions: the former was exposed to long periods of dry-ice which resulted in carbon dioxide mediated acidification of the serum, thus enhancing entry by pH-dependent VSVpp, but having no such effect on pH-independent NiVpp entry. **(D-F)** The NiVpp SN data for the bat sera **(D)**, bat-exposed human sera **(E)**, and non-exposed human sera **(F)** were converted into frequency distribution histograms by grouping together samples in intervals of 10% of normalized infection. Seropositive and seronegative samples are indicated by red and gold bars, respectively. The LOWESS (Locally Weighted Scatterplot Smoothing**)** lines (in black) superimposed on the histograms identify two populations in panels (D) and (E), in agreement with the results from the Dunnett's test. The percentage of seropositive samples according to the Dunnett's test is indicated in red. In (B), serum samples (n=3) with ≥50% seroneutralization activity but not classified as seropositive by the stringent Dunnett's test appear in blue in panel (E). Lastly, seroneutralization titers (SNTs) performed on representative seropositive and seronegative samples from the bat-exposed group are shown in panel **(G)**. The SN assay was performed exactly as in (B) except that the viral inoculum was pre-mixed with 5-fold serial dilution of the indicated sera (1:50 to 1:31,250). SN data are presented as normalized % infection (mean values) with infectivity in 1:100 FCS set at 100% (dotted line) plotted against the log reciprocal serum dilution on the x-axis. Hyperimmune rabbit anti-NiV served as the positive control (inverted triangles). Infections were performed in quadruplicates. Mean values are shown without error bars for clarity.

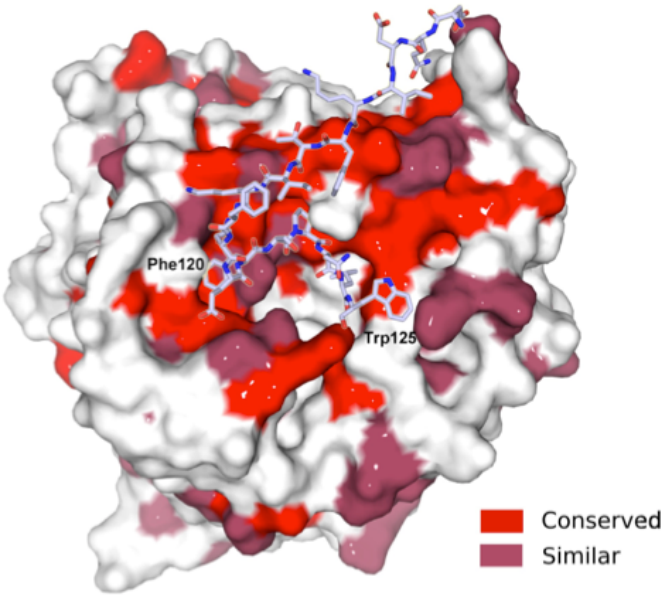

Figure 2-20. Mapping sequence conservation of GH-M74a onto the surface of NiV-G. NiV-G surface is colored according to residue conservation with GH-M74a: red, conserved; maroon, similar; white, no sequence conservation. EphrinB2 residues 107-127 are represented as sticks. Although NiV-G shares relatively low sequence conservation with GhV-G (approximately 25%), it shares greater sequence conservation (45%) in residues that make up the receptor-binding site (calculation performed with PISA EBI server).

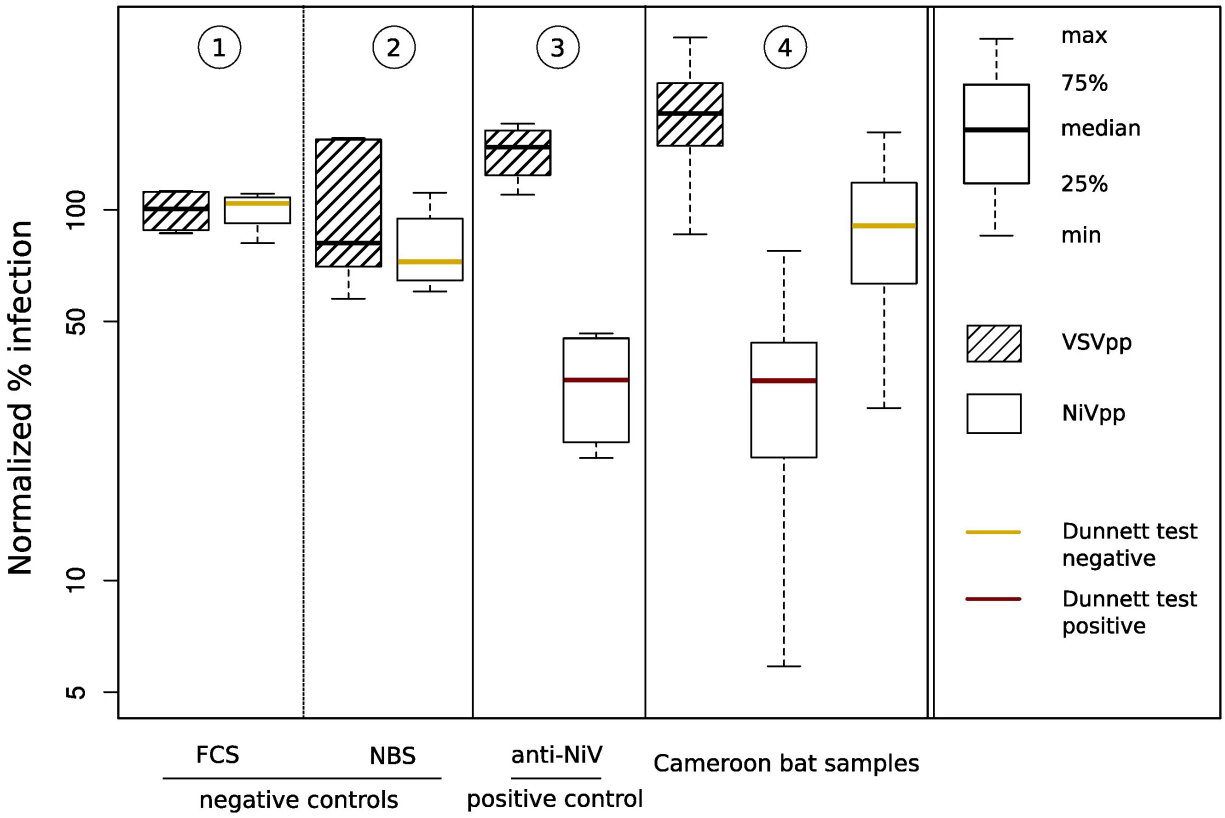

Figure 2-21. Prevalence of anti-NiV cross-neutralizing antibodies in bat sera from Cameroon. Box-and-whisker plots showing the infection (normalized to the negative control Fetal Calf Serum, FCS) of Vero cells by VSVpp (isogenic control, striped pattern box) and NiVpp (white box) in presence of 100X diluted sera from different groups: **Panel 1** (FCS) and **Panel 2** (NBS, normal bat sera), negative control sera; **Panel 3** (rabbit anti-NiV), positive control; **Panel 4**, bat sera from Cameroon (n=44). Seropositive (n = 21, median bar in red) and seronegative (n = 23, median bar in yellow) bat sera in panel 4 were segregated based on the Dunnett's test for significance using the FCS control group. The boxes represent the first and the third quartiles, and the solid horizontal lines within the box represent the median values. The whiskers represent the lowest and highest value. Each sample was tested in quadruplicate. The data for each serum sample are shown in Figure 2-19, panel A.

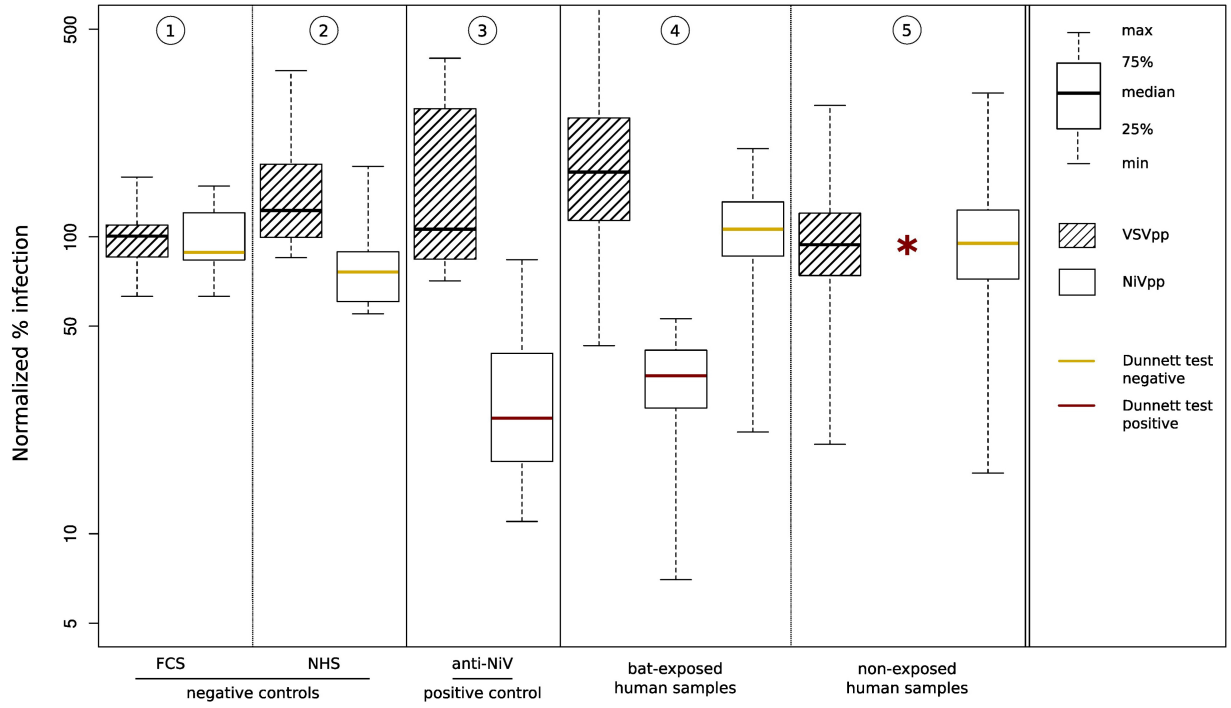

Figure 2-22. Seroneutralization activity of NiV pseudoparticle infection by human sera collected from Cameroon villagers with documented differential exposure to bats. Box-and-whisker plots showing the normalized % infection of Vero cells by VSVpp (isogenic control, striped pattern box) and NiVpp (white box) in presence of sera diluted 1:100 from the indicated sample groups (Panels 1 -5). **Panel 1**, all infections were normalized to the infectivity observed for NiVpp in the presence of the fetal calf serum (FCS) negative control (set at 100%); **Panel 2**, Normal Human Sera (NHS) from Los Angeles blood donors served as additional negative controls; **Panel 3**, hyperimmune rabbit anti-NiV sera (positive control); **Panels 4 and 5**, human sera from the bat-exposed (n = 227) or non-exposed (n= 260) cohort of Cameroon villagers, respectively. For the bat-exposed group, the Dunnett's test could stratify the NiVpp SN results into seropositive (n=7, median bar in red) and seronegative (n=220, median bar in yellow) subsets. In contrast, in the non bat-exposed group, the Dunnett's test could not identify any serum sample as being significantly different from the negative control group (FCS) (Panel 5, asterisk indicates no seropositive samples). Boxes encompass the first and the third quartiles, and the solid horizontal lines within the boxes represent the median values. The whiskers represent the lowest and highest values in each sample group. The data for individual serum samples (n=487), each tested in quadruplicates, are shown in Figure 2-19, panels B and C.

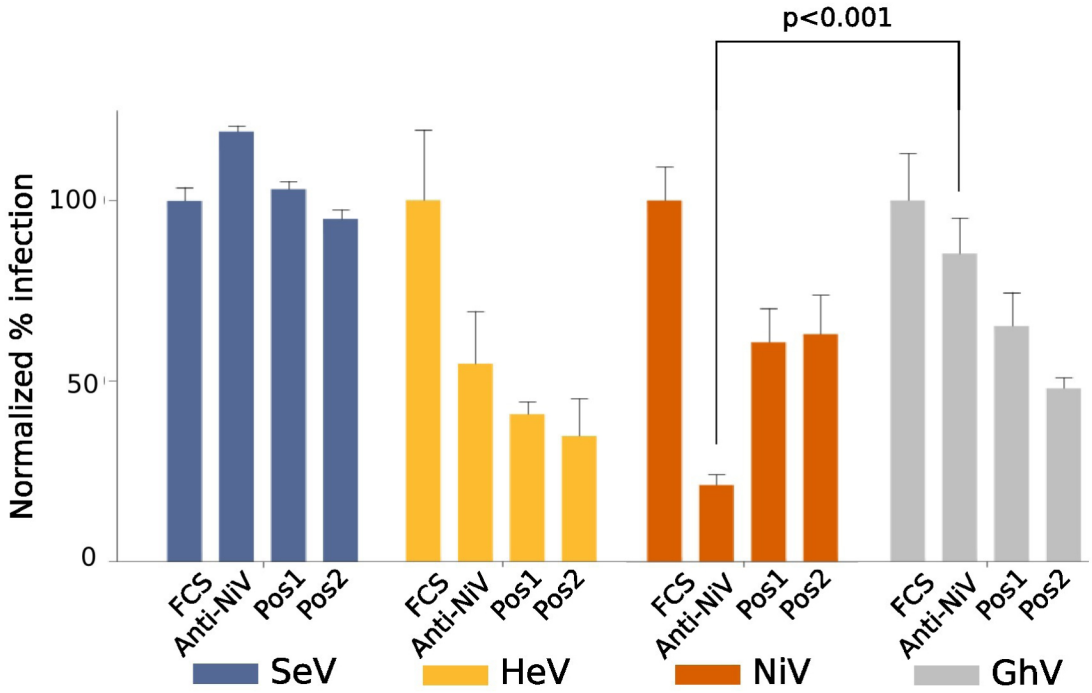

Figure 2-23. Characterization of seropositive human sera for anti-henipavirus cross-neutralizing antibodies. Two seropositive human samples (*Pos1* and *Pos2*) from the bat-exposed group were tested for seroneutralization activity against different HNV pseudoparticles: Hendra Virus (HeV, yellow), Nipah Virus (NiV, orange), and Ghana Virus (GhV, grey). Infection of Vero cells was performed in presence of the indicated sera diluted 1:100 as in Figure 2-22. As a specificity control for the virus, we used a recombinant Sendai virus expressing eGFP (SeV, blue). Data is presented as normalized % infection (mean +/- S.D. from three independent replicates) as in Figure 2-22. FCS, fetal calf serum; anti-NiV, hyperimmune rabbit anti-NiV serum. Significant differences (asterisks) of inhibition was observed between the NiVpp and GhVpp for the anti-NiV serum (two-tailed Student t-test, $p < 0.001$).

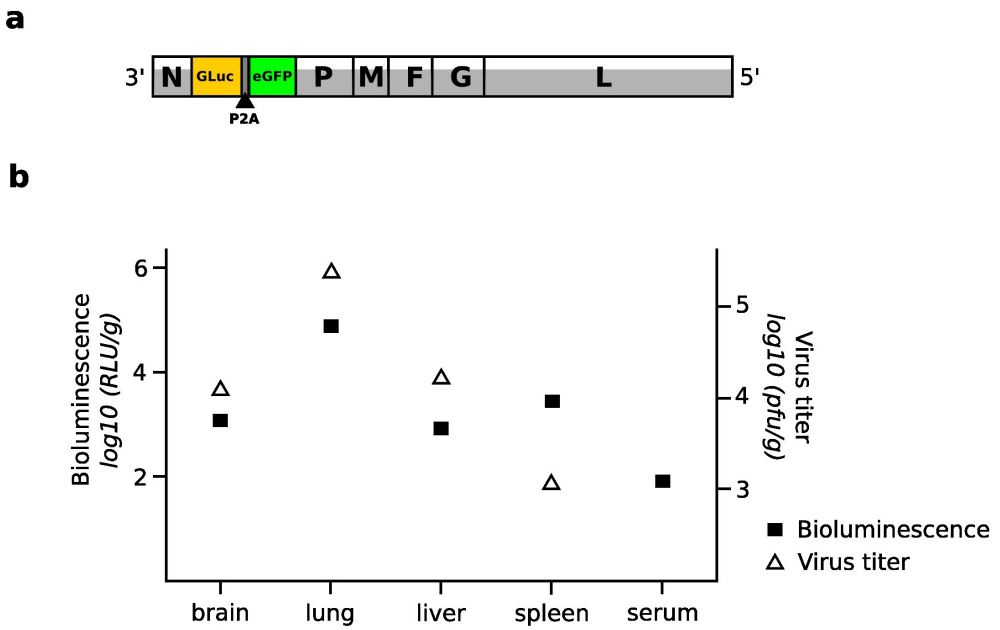

Figure 2-24. The recombinant NiV construct and the detection of secreted *Gaussia* Luciferase in different tissues. (A) Schematic representation of the reverse genetics construct used to rescue the recombinant NiV expressing eGFP and secreted *Gaussia* Luciferase, which we term rNiV-GLuc. The GLuc-P2A-eGFP reporter cassette was inserted between a duplicated N-P intergenic region and the recombinant construct was rescued as described in Chapter 2.2. Stocks of rNiV-GLuc were then expanded and tittered on Vero cells. **(B)** A hamster was challenged with 1,500 pfu of the rescued rNiV-GLuc virus (LD_{50} of NiV_{Mal} in hamsters ~250 pfu),[57] and the moribund animal was euthanized 6 days post-infection. Major organs (brain, liver, spleen, and lung) were collected and homogenized in PBS. GLuc activity was measured in clarified organ homogenates and presented as relative light units (RLU)/gram of tissue (or per ml of serum). Note that viremia is almost never detected in moribund animals as viral replication at that point occurs mostly in the brain and lungs.[58] Thus, the detection of secreted *Gaussia* luciferase activity in serum in the absence of detectable viral titers further underscores the sensitivity of this reporter for productive viral infection.

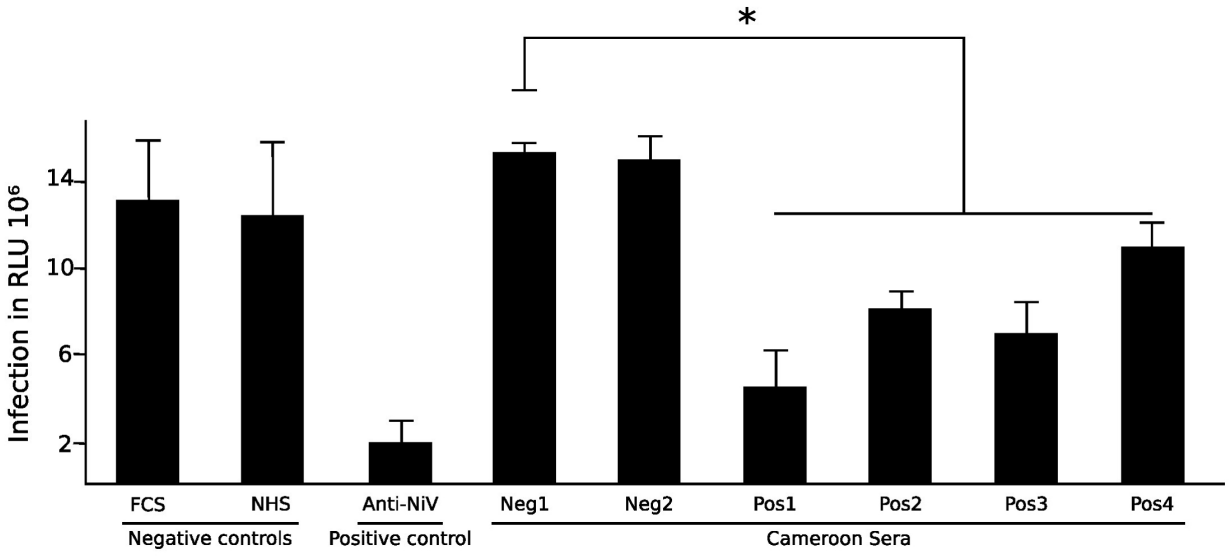

Figure 2-25. Seropositive human samples neutralize live recombinant NiV infection. Infection of Vero cells by live recombinant NiV expressing secreted *Gaussia* luciferase (rNiV-GLuc, MOI=1) in the presence of 1:100 dilution of the indicated sera: FCS (fetal calf serum, negative control), NHS (normal human serum, negative control), rabbit anti-NiV (positive control), two seronegative samples (picked randomly among the 480 seronegative samples), and four seropositive samples. 20 µL (out of 150 µL) of infected cell culture supernatant was collected and analyzed for *Gaussia* luciferase activity at 24 hpi. Infectivity data is presented as mean relative light units (RLU) +/- S.D. from 3 independent replicates. Significant differences (asterisk) were observed between seropositive and seronegative sera ($p < 0.05$; one-tailed Student t-test followed by the Holm step-down procedure for multiple comparisons).

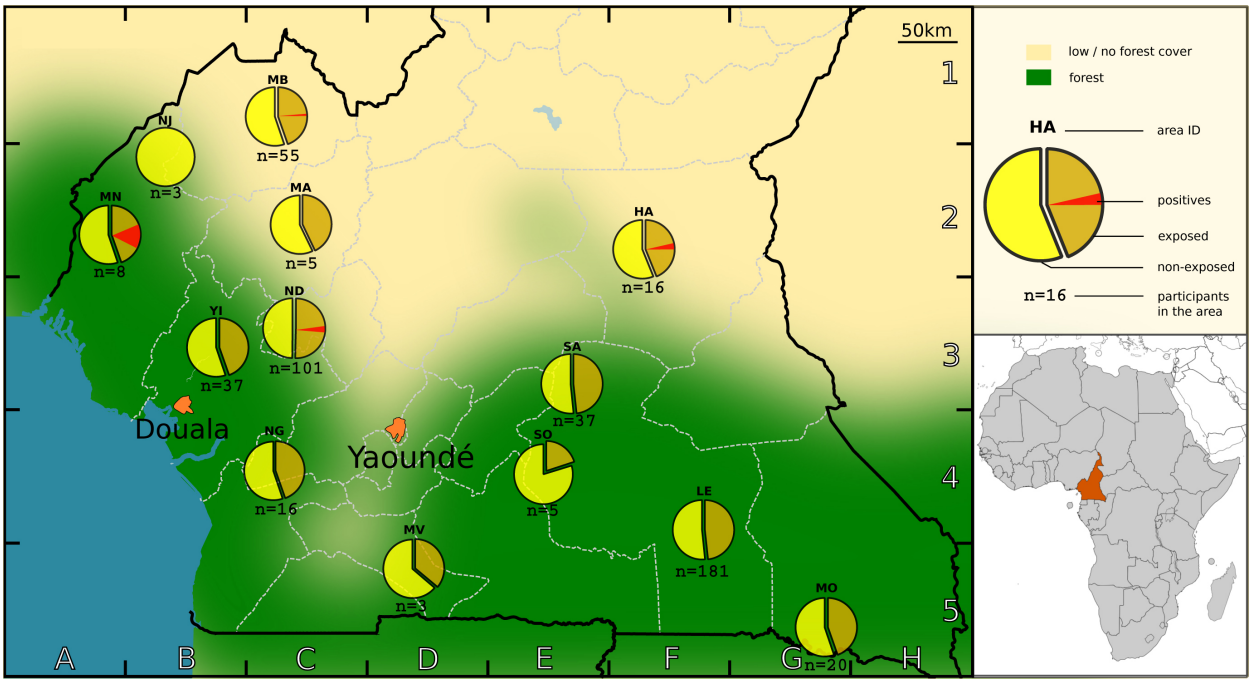

Figure 2-26. Map of collection sites in southern Cameroon. For each location, the proportion of participants with self-reported contacts with bats (exposed) or not (non-exposed) is indicated, respectively, by the brown or yellow segment of the accompanying pie-chart. The superimposed red segments in some pie-charts represent the seropositive samples identified in Figure 2-23 (also Figure 2-19, panel B). The number of participants from each location is shown below the corresponding pie chart. Green or beige shaded areas represent regions with high or low/no forest cover, respectively (see “geographical data” section in Methods and Materials for further details).

Risk Factor		Total (n)	Seronegative (n)	Seropositive (n)	Seroprevalence (%)	P value*	Odds Ratio§ (95% CI)	P value
Contact with bats	Yes	227	220	7	3.1%	**0.0045**	**17.7**	**0.0021**
	No	260	260	0	0%		(1.0 to 312)	
	Total	487						
Butchering Bats	Yes	171	164	7	4.1%	**0.0006**	**28.9**	**0.0002**
	No	316	316	0	0%		(1.6 to 508)	
	Total	487						
Hunting Bats	Yes	99	96	3	3.0%	0.1523	3.0	0.1357
	No	388	384	4	1.0%		(0.7 to 13.6)	
	Total	487						
Low Forest Cover/ Deforestation	Yes	185	179	6	3.2%	**0.0136**	**10.1**	**0.0088**
	No	302	301	1	0.3%		(1.2 to 84.5)	
	Total	487						

* two-tailed Fisher's Exact test

§ 0.5 added to all cells where there is a zero cell count, see statistical methods

Table 2-2. Risk factors for seroconversion. Contact with bats, butchering bats, and deforestation were all significantly associated with seroconversion.

REFERENCES

1. Luby SP, Gurley ES. Epidemiology of henipavirus disease in humans. *Current topics in microbiology and immunology*. 2012;359:25-40.

2. Marsh GA, Wang LF. Hendra and Nipah viruses: why are they so deadly? *Current opinion in virology*. 2012;2(3):242-247.

3. Zhu Z, Bossart KN, Bishop KA, et al. Exceptionally potent cross-reactive neutralization of Nipah and Hendra viruses by a human monoclonal antibody. *The Journal of infectious diseases*. 2008;197(6):846-853.

4. Field HE. Bats and emerging zoonoses: henipaviruses and SARS. *Zoonoses and public health*. 2009;56(6-7):278-284.

5. Field HE, Mackenzie JS, Daszak P. Henipaviruses: emerging paramyxoviruses associated with fruit bats. *Current topics in microbiology and immunology*. 2007;315:133-159.

6. Halpin K, Hyatt AD, Fogarty R, et al. Pteropid bats are confirmed as the reservoir hosts of henipaviruses: a comprehensive experimental study of virus transmission. *The American journal of tropical medicine and hygiene*. 2011;85(5):946-951.

7. Hasebe F, Thuy NT, Inoue S, et al. Serologic evidence of nipah virus infection in bats, Vietnam. *Emerg Infect Dis*. 2012;18(3):536-537.

8. Smith I, Wang LF. Bats and their virome: an important source of emerging viruses capable of infecting humans. *Current opinion in virology*. 2013;3(1):84-91.

9. Hahn MB, Gurley ES, Epstein JH, et al. The Role of Landscape Composition and Configuration on Pteropus giganteus Roosting Ecology and Nipah Virus Spillover Risk in Bangladesh. *The American journal of tropical medicine and hygiene*. 2013.

10. Iehle C, Razafitrimo G, Razainirina J, et al. Henipavirus and Tioman virus antibodies in pteropodid bats, Madagascar. *Emerging infectious diseases*. 2007;13(1):159-161.

11. Richter HV, Cumming GS. Food availability and annual migration of the straw-colored fruit bat (Eidolon helvum). *Journal of Zoology (London)*. 2006;268(1):35-44.

12. Richter HV, Cumming GS. First application of satellite telemetry to track African straw-coloured fruit bat migration. *Journal of Zoology (London)*. 2008;275(2):172-176.

13. Hayman DT, Suu-Ire R, Breed AC, et al. Evidence of henipavirus infection in West African fruit bats. *PloS one*. 2008;3(7):e2739.

14. Peel AJ, Baker KS, Crameri G, et al. Henipavirus neutralising antibodies in an isolated island population of African fruit bats. *PloS one*. 2012;7(1):e30346.

15. Drexler JF, Corman VM, Gloza-Rausch F, et al. Henipavirus RNA in African bats. *PloS one*. 2009;4(7):e6367.

16. Weiss S, Nowak K, Fahr J, et al. Henipavirus-related sequences in fruit bat bushmeat, Republic of Congo. *Emerging infectious diseases*. 2012;18(9):1536-1537.

17. Drexler JF, Corman VM, Muller MA, et al. Bats host major mammalian paramyxoviruses. *Nature communications*. 2012;3:796.

18. Bossart KN, McEachern JA, Hickey AC, et al. Neutralization assays for differential henipavirus serology using Bio-Plex protein array systems. *Journal of virological methods*. 2007;142(1-2):29-40.

19. Daniels P, Ksiazek T, Eaton BT. Laboratory diagnosis of Nipah and Hendra virus infections. *Microbes and infection / Institut Pasteur*. 2001;3(4):289-295.

20. Tamin A, Harcourt BH, Lo MK, et al. Development of a neutralization assay for Nipah virus using pseudotype particles. *Journal of virological methods*. 2009;160(1-2):1-6.

21. Wang LF, Daniels P. Diagnosis of henipavirus infection: current capabilities and future directions. *Current topics in microbiology and immunology*. 2012;359:179-196.

22. Peel AJ, Sargan DR, Baker KS, et al. Continent-wide panmixia of an African fruit bat facilitates transmission of potentially zoonotic viruses. *Nature communications*. 2013;4:2770.

23. Bowden TA, Crispin M, Jones EY, Stuart DI. Shared paramyxoviral glycoprotein architecture is adapted for diverse attachment strategies. *Biochemical Society transactions*. 2010;38(5):1349-1355.

24. Bowden TA, Aricescu AR, Gilbert RJ, Grimes JM, Jones EY, Stuart DI. Structural basis of Nipah and Hendra virus attachment to their cell-surface receptor ephrin-B2. *Nature structural & molecular biology*. 2008;15(6):567-572.

25. Krissinel E, Henrick K. Inference of macromolecular assemblies from crystalline state. *Journal of molecular biology*. 2007;372(3):774-797.

26. Chenna R, Sugawara H, Koike T, et al. Multiple sequence alignment with the Clustal series of programs. *Nucleic acids research*. 2003;31(13):3497-3500.

27. Gouet P, Courcelle E, Stuart DI, Metoz F. ESPript: analysis of multiple sequence alignments in PostScript. *Bioinformatics*. 1999;15(4):305-308.

28. Pernet O, Beaty SM, Lee B. Functional rectification of the newly described African Henipavirus fusion glycoprotein (Gh-M74a) *Journal of Virology*. in submission.

29. Hou X, Suquilanda E, Zeledon A, et al. Mutations in Sendai virus variant F1-R that correlate with plaque formation in the absence of trypsin. *Medical microbiology and immunology*. 2005;194(3):129-136.

30. Beaty SM, Park A, Yun TE, et al. Efficient rescue and reverse genetics of viruses from all Paramyxovirus genera without the use of vaccinia driven T7 polymerase. XV International Conference on Negative Strand Virus; 2013; Grenada, Spain.

31. Welsh JP, Patel KG, Manthiram K, Swartz JR. Multiply mutated Gaussia luciferases provide prolonged and intense bioluminescence. *Biochemical and biophysical research communications*. 2009;389(4):563-568.

32. Maguire CA, Deliolanis NC, Pike L, et al. Gaussia luciferase variant for high-throughput functional screening applications. *Analytical chemistry*. 2009;81(16):7102-7106.

33. Aguilar HC, Matreyek KA, Filone CM, et al. N-glycans on Nipah virus fusion protein protect against neutralization but reduce membrane fusion and viral entry. *Journal of virology*. 2006;80(10):4878-4889.

34. Yob JM, Field H, Rashdi AM, et al. Nipah virus infection in bats (order Chiroptera) in peninsular Malaysia. *Emerging infectious diseases*. 2001;7(3):439-441.

35. Rahman SA, Hassan L, Epstein JH, et al. Risk Factors for Nipah virus infection among pteropid bats, Peninsular Malaysia. *Emerging infectious diseases*. 2013;19(1):51-60.

36. (OIE) WOfAH. World Animal Health Information Database (WAHID). 2012, 2013.

37. Hanson RP. The natural history of vesicular stomatitis. *Bacteriol Rev*. 1952;16(3):179-204.

38. Parzen M, Lipsitz SR, Ibrahim JG, Lipshultz S. A weighted estimating equation for linear regression with missing covariate data. *Statistics in medicine*. 2002;21(16):2421-2436.

39. Sweeting MJ, Sutton AJ, Lambert PC. What to add to nothing? Use and avoidance of continuity corrections in meta-analysis of sparse data. *Statistics in medicine*. 2004;23(9):1351-1375.

40. Keesing F, Belden LK, Daszak P, et al. Impacts of biodiversity on the emergence and transmission of infectious diseases. *Nature*. 2010;468(7324):647-652.

41. Lloyd-Smith JO, George D, Pepin KM, et al. Epidemic dynamics at the human-animal interface. *Science*. 2009;326(5958):1362-1367.

42. Wolfe ND. Bushmeat Hunting, Deforestation, and Prediction of Zoonotic Disease Emergence. *Emerg Infect Dis*. 2005;11(12):1822-1827.

43. Woolhouse M. How to make predictions about future infectious disease risks. *Philosophical transactions of the Royal Society of London Series B, Biological sciences*. 2011;366(1573):2045-2054.

44. Aguilar HC, Ataman ZA, Aspericueta V, et al. A novel receptor-induced activation site in the Nipah virus attachment glycoprotein (G) involved in triggering the fusion glycoprotein (F). *The Journal of biological chemistry*. 2009;284(3):1628-1635.

45. Pernet O, Beaty SM, B.S. S, et al. Evidence of Henipavirus spillover in African Populations. XV Conference on Negative Strand Virus; 2013; Grenada, Spain.

46. Kruger N, Hoffmann M, Weis M, et al. Surface glycoproteins of an African henipavirus induce syncytium formation in a cell line derived from an African fruit bat, Hypsignathus monstrosus. *Journal of virology*. 2013.

47. Holmes EC. What can we predict about viral evolution and emergence? *Current opinion in virology*. 2013;3(2):180-184.

48. Kothe DL, Li Y, Decker JM, et al. Ancestral and consensus envelope immunogens for HIV-1 subtype C. *Virology*. 2006;352(2):438-449.

49. Ducatez MF, Bahl J, Griffin Y, et al. Feasibility of reconstructed ancestral H5N1 influenza viruses for cross-clade protective vaccine development. *Proceedings of the National Academy of Sciences of the United States of America*. 2011;108(1):349-354.

50. Chua KB. Introduction: Nipah virus--discovery and origin. *Current topics in microbiology and immunology*. 2012;359:1-9.

51. Chadha MS, Comer JA, Lowe L, et al. Nipah virus-associated encephalitis outbreak, Siliguri, India. *Emerging infectious diseases*. 2006;12(2):235-240.

52. Marsh GA, de Jong C, Barr JA, et al. Cedar virus: a novel Henipavirus isolated from Australian bats. *PLoS pathogens*. 2012;8(8):e1002836.

53. Weiss RA, McMichael AJ. Social and environmental risk factors in the emergence of infectious diseases. *Nature medicine*. 2004;10(12 Suppl):S70-76.

54. Daszak P, Zambrana-Torrelio C, Bogich TL, et al. Interdisciplinary approaches to understanding disease emergence: the past, present, and future drivers of Nipah virus emergence. *Proceedings of the National Academy of Sciences of the United States of America*. 2013;110 Suppl 1:3681-3688.

55. Murray KA, Daszak P. Human ecology in pathogenic landscapes: two hypotheses on how land use change drives viral emergence. *Current opinion in virology*. 2013;3(1):79-83.

56. Wolfe ND, Dunavan CP, Diamond J. Origins of major human infectious diseases. *Nature*. 2007;447(7142):279-283.

57. Wong KT, Grosjean I, Brisson C, et al. A golden hamster model for human acute Nipah virus infection. *The American journal of pathology*. 2003;163(5):2127-2137.

58. Geisbert TW, Feldmann H, Broder CC. Animal challenge models of henipavirus infection and pathogenesis. *Current topics in microbiology and immunology*. 2012;359:153-177.

CHAPTER 3

FUNCTION OF CONSERVED MATRIX MOTIFS

CHAPTER 3.1

MUTATIONS IN CONSERVED RESIDUES OF NIPAH VIRUS MATRIX REVEAL DEFECTS IN ITS BUDDING PATHWAY

INTRODUCTION

The matrix protein is relatively conserved among the paramyxovirus proteins. A comparison of Nipah virus matrix with other paramyxovirus matrix proteins indicates similarities ranging from 34-63%, comparable with the conservation of the nucleocapsid, fusion protein, and large protein (the RNA-dependent RNA polymerase) (Figure 3-1). The attachment protein and phosphoprotein appear less conserved. Further, the recent crystal structure of the Newcastle disease virus (NDV) matrix protein[1] has allowed homology modelling of related matrix proteins, including NiV-M (Figure 3-2). Despite these similarities, however, an analysis of the significance of conserved residues in the paramyxovirus matrix protein has not been performed. An alignment of matrix protein sequences from representative paramyxoviruses from each of the five major genera within the *Paramyxovirinae* subfamily revealed 12 absolutely conserved amino acid residues (Figures 3-2 and 3-3). With a view to gaining insight into matrix function, we mutated each absolutely conserved residue in NiV-M to the minimal amino acid alanine to disrupt its potential function. We then examined the effect of these mutations on the expression and budding function of NiV-M.

MATERIALS AND METHODS

Alignments and homology modelling

Pairwise sequence alignments were performed using EMBOSS Needle on the EMBL-EBI website. Multiple sequence alignment was performed using ClustalW2 on the EMBL-EBI website. Homology modelling was performed via the Phyre2 Protein Fold Recognition Server (http://www.sbg.bio.ic.ac.uk/phyre2), created by the Structural Bioinformatics Group at Imperial College, London. Structures were visualized using UCSF Chimera. For visualization of surface electrostatic potential, the pdb file was evaluated by APBS (Adaptive Poisson-Boltzmann Software) on www.poissonboltzmann.org, using default settings.

Plasmids

Untagged NiV-M in pcDNA3 and 3XFLAG-NiV-M in pCMV-3Tag-1 are as previously described.[2] Mutations were inserted via standard overlapping PCR with Velocity DNA polymerase (Bioline), digestion of insert and vector with HindIII and XhoI, and ligation with T4 DNA ligase (NEB).

Virus-like particle budding

HEK 293T cells as 70-90% confluency in 6-well dishes were transfected with 0.4 ug wild-type or mutant untagged NiV-M, or a range of wild-type NiV-M from 0.15 to 0.7 ug to generate a wild-type standard budding curve, with pcDNA3 filler DNA to 2 ug total for each condition, using BioT (Bioland) according to manufacturer's instructions. Media was changed at 6 hours post-transfection (hpt), and supernatants and cell lysates were collected at 24 hpt. Cells in PBS were vortexed 1:1 with 2X Laemmli SDS sample buffer with 10% 2-mercaptoethanol, while clarified supernatants were ultracentrifuged through 20% sucrose at 145 x g, with pellets resuspended in 1X Laemmli SDS sample buffer with 5% 2-mercaptoethanol.

Membrane flotation

HEK 293T cells in 6-well dishes were transfected with 0.3 ug wild-type or mutant untagged NiV-M. At 24 hpt, cells were rinsed briefly in PBS, then collected in ice-cold TNE buffer (50 mM Tris-HCl, 150 mM NaCl, 2 mM EDTA, 0.1% 2-mercaptoethanol, protease inhibitor cocktail (Roche)). Resuspended cells were dounce-homogenized, clarified at 3000 rpm for 30 min at 4C, then mixed with 85% sucrose in PBS to 73% final concentration before transfer to the bottom of an ultracentrifuge tube. The sample was layered sequentially with 65% and 10% sucrose before ultracentrifugation at 100k x g for 16 hours at 4C. Eight fractions were collected, and protein from each fraction was isolated via methanol/chloroform extraction before resuspension in 2X Laemmli SDS sample buffer with 5% 2-mercaptoethanol.

Lipid raft isolation

Similar to membrane flotation, transfected HEK 293T cells were collected in TNE buffer and dounce-homogenized before clarification to remove cell debris and nuclei. Triton X-100 was added to a final concentration of 1%, and the sample was incubated 30 min on ice (with all

subsequent steps until post-centrifugation fraction collection being carried out at 4C), then mixed with 60% OptiPrep for 40% final before transfer to the bottom of an ultracentrifuge tube. The sample was layered sequentially with 30% and 5% OptiPrep before ultracentrifugation at 240k x g for 4 hours at 4C. 14 fractions were collected from the top, followed by methanol/chloroform extraction and SDS-PAGE.

Immunofluorescence

HeLa cells on collagen-coated coverslips were transfected with untagged or 3XFLAG-tagged wild-type or mutant NiV-M, using Lipofectamine LTX (Invitrogen) according to manufacturer's recommendations. At 24 hpt, cells were fixed in 2% paraformaldehye, washed 3 times in PBS, incubated in blocking buffer (0.5% saponin, 3% BSA in PBS), then incubated with either 1:3000 rabbit anti-NiV-M or 1:5000 mouse anti-FLAG (clone M2, Stratagene) in blocking buffer. After 3 washes with 0.5% saponin in PBS, cells were incubated with 1:250 Alexa Fluor 647 (Invitrogen) and the appropriate Alexa Fluor 488 anti-rabbit or anti-mouse secondary (Invitrogen). After a further 3 washes, samples were stained with DAPI to stain nuclei before mounting on slides. Confocal imaging was performed on a Leica SP5 confocal microscope. 3D rendering was performed with Volocity software (PerkinElmer).

Acyl-biotin exchange assay for palmitoylation

HEK 293T in two 6-wells were transfected with 0.5 ug untagged NiV-M each (balance pcDNA3, using BioT). At 24 hpt, cells were rinsed briefly with PBS before both wells were collected in 1 mL total ice-cold lysis buffer with N-ethylmaleimide (NEM) (Sigma): 1% NP-40, 50 mM Tris-HCl pH 7.2, 150 mM NaCl, protease inhibitor cocktail (Roche), 5% glycerol, 50 mM NEM. Lysates were passed several times through a 25-gauge needle, then clarified for 13k rpm for 5 min at 4C before incubation with 3 ug rabbit anti-NiV-M antibody, rotating overnight at 4C. The following day, equilibrated protein G agarose was added to the lysates and rotated for 2 hours at 4C. All subsequent washes were performed by centrifuging the agarose at 1800 rpm for 2 min at 4C. The agarose was washed once in lysis buffer (as above, but with 10 mM NEM), then washed

three additional times in lysis buffer with no NEM. The bound beads were split into two equivalent samples, and one sample was incubated in lysis buffer with 1M hydroxylamine (HAM) (Sigma), and the other without HAM, rotating for 1 hour at room temperature. Samples were washed once in lysis buffer pH 6.2, then incubated with 4 uM BMCC-Biotin (Pierce) in lysis buffer pH 6.2, rotating for 1 hour at 4C. After washing once with lysis buffer pH 6.2, then three additional times in lysis buffer pH 7.2, samples were eluted by boiling in 2X Laemmli SDS sample buffer with 5% 2-mercaptoethanol.

Crosslinking assay for oligomerization

HEK 293T cells transfected with 0.3 ug untagged NiV-M per 6-well were washed and resuspended in ice-cold phosphate-buffered saline, pH 8. DSS crosslinker (21655, Pierce) in DMSO was added to the cells at 1 mM final. After 30 min at room temperature, the reaction was quenched with 20 mM Tris, pH 7.5 for 15 min at room temperature. The cells were pelleted, resuspended in cold TNE buffer, and vortexed 1:1 with 2X NuPAGE LDS buffer with 10% 2-mercaptoethanol. After boiling samples for 10 min at 95C, samples were run on 4-12% Bis-Tris SDS-PAGE (Invitrogen).

Immunoprecipitation

HEK 293T in 6-well dishes were transfected with 1 ug 3XFLAG-tagged wild-type or mutant NiV-M (balance pCMV-3Tag-1, using BioT). At 24 hpt, cells were rinsed briefly with PBS before being collected in ice-cold lysis buffer (0.1% NP-40, 100 mM Tris-HCl pH 7.5, 150 mM NaCl, 5% glycerol, 1 mM sodium orthovanadate, 1 mM b-glycerophosphate, 1 mM EDTA, protease inhibitor cocktail (Roche)). Lysates were clarified at 13k for 5 min at 4C, then incubated with anti-FLAG M2 agarose (A2220, Sigma), rotating for 2 hours at 4C. Samples were washed four times with lysis buffer, then eluted with an excess of 3X FLAG peptide in elution buffer (lysis buffer as above except without NP-40).

Immunoblotting

All samples were boiled 10 min at 95C before Tris-glycine SDS-PAGE. Upon transfer to Immobilon-FL PVDF (Millipore), membranes were blocked overnight at 4C (Odyssey Blocking Buffer, LI-COR Biosciences), then incubated with the appropriate primary antibody: rabbit anti-NiV-M, mouse anti-FLAG M2 (Stratagene), rabbit anti-phosphothreonine (9381, Cell Signaling), or IRDye 800CW Streptavidin (LI-COR Biosciences). After incubation with the appropriate IRDye fluorescent secondary antibody (LI-COR Biosciences) if necessary, fluorescence images were obtained on a LI-COR Odyssey imaging system.

Beta-lactamase entry assay

The entry assay was performed as described[3] with a few modifications. Briefly, HEK 293T in a 15-cm dish was transfected with a 1:1:2.5 ratio of AU1-tagged NiV-F, HA-tagged NiV-G, and beta-lactamase-NiV-M fusion protein, using BioT (Bioland) according to manufacturer's instructions. Media was changed at 6 hpt. At 48 hpt, supernatant was collected, clarified, and ultracentrifuged through 20% sucrose at 110k x g for 2 hours. The virus-like particle (VLP) pellet was resuspended in Opti-MEM (Invitrogen) with 5% sucrose before storage at -80C. For the entry assay, HEK 293T at 70-90% confluency in 24-well were mock- or VLP-infected via spinoculation at 2000 rpm at 37C for 1.5 hours. Cells were incubated at 37C for another 30 min, collected via trypsinization, then loaded with the beta-lactamase substrate CCF2-AM using the CCF2-AM loading kit (K1032, Invitrogen). The blue-to-green fluorescence shift catalyzed by beta-lactamase was detected on a TECAN Infinite M1000 PRO microplate reader.

RESULTS

Most mutations in conserved residues result in budding deficiency

Although we mutated all 12 conserved residues in NiV-M to alanine, the K258A mutant (part of the conserved bipartite NLS) will be discussed in detail in Chapter 3.2 and will not be discussed further here. To assess the budding function of our NiV-M alanine mutants, we first developed a semi-quantitative budding assay. As discussed in Chapter 1.2, transfection of NiV-M leads to

release of virus-like particles (VLPs) into the cell culture supernatant (Figure 3-4). Purification and concentration of VLPs by ultracentrifuging and pelleting through a 20% sucrose cushion allows a comparison of NiV-M VLP production to cell lysate expression by Western immunoblotting. Since our mutants were likely to have variable expression, we normalized our results to a titrated transfection of wild-type NiV-M, which was included with each experiment. Comparison of relative VLP production to relative cell lysate expression for this wild-type titration allowed us to plot a wild-type budding curve (Figure 3-5). Our calculated budding efficiency was therefore the percent expected VLP for a given cell lysate expression.

Thus assaying our alanine mutants, we determined that all mutants were strongly budding-deficient (15% or less) except for the C-terminal Q328A mutant, which had wild-type budding efficiency (Figure 3-6). Further, only the three C-terminal mutants displayed cell lysate expression comparable to wild-type (over 60%); the other mutants all displayed poor expression (25% or less). Although poor expression may result from a block in trafficking that leads to degradation, it may also indicate structural dysfunction, misfolding and instability that likewise lead to degradation. We therefore chose to focus our follow-up on those mutants that displayed cell lysate expression comparable to wild-type, and in particular one budding-deficient mutant, C299A (position in threaded structure shown in Figure 3-9), and one apparently wild-type mutant, Q328A (position in structure shown by dotted circle in Figure 3-2, panel B). Although W314A also expressed well and had the interesting phenotype of being clearly at the membrane and in long filopodial extensions despite being completely budding-deficient, it will not be discussed further here.

C299 is a potential site of palmitoylation

The thiol group of cysteines is a potential site of post-translational modification, such as disulfide bonding or lipid attachment. Since disulfides are typically not expected to form in the reducing cytoplasm, and additionally there is no evidence for disulfide bond formation in the NDV-M crystal structure,[1] we evaluated whether C299 might be a potential site of lipid

attachment. The myristoylation of HIV-1 Gag is essential for its function, promoting and regulating the membrane association of Gag;[4,5] no similar lipid attachment has been described for paramyxovirus matrix proteins, however. Although the positively charged membrane-binding surface of the paramyxovirus matrix protein is thought to be sufficient for membrane association, lipid modification may regulate the strength and temporal dynamics of this association. We first assessed whether the C299A mutant had reduced binding to membranes compared to wild-type NiV-M, as would be expected if it had lost a lipid modification. Indeed, membrane flotation revealed that C299A displayed about half the membrane binding of wild-type matrix (Figure 3-7). Lipid modification of cysteines can proceed through S-prenylation (attachment of a farnesyl or geranylgeranyl group) or S-acylation (most often attachment of palmitate, but more rarely stearate or oleate).[6] Since S-prenylation occurs at a C-terminal "CAAX" motif that is not present in NiV-M, we assessed whether NiV-M might be palmitoylated. Further buttressing this possibility was our finding that NiV-M associates with detergent-resistant membranes, or "lipid rafts" (Figure 3-8), and lipid raft association is regulated by palmitoylation for many proteins.[7,8]

Although there is no consensus motif for palmitoylation, we used an algorithmic palmitoylation prediction program, CSS-PALM 3.0, that uses known sites of palmitoylation from the literature to predict potential sites of palmitoylation.[9] Three of the six cysteines in NiV-M, C157, C255, and C299, were predicted as potential sites of palmitoylation (Figure 3-9, red asterisks). Of these, C255 and C299 are close to the predicted membrane-binding surface. To evaluate whether a C255 mutant is budding-deficient, as would be expected if it also represents a site of palmitoylation, we mutated all five remaining cysteines, including C255, to alanine. Of these five mutants, only the budding of C255A was abrogated (Figure 3-10, panel A). As will be discussed in detail in Chapters 3.2 and 3.3, C255 is flanked by both arms of the bipartite nuclear localization sequence (NLS) in NiV-M that is important for viral budding (also compare Figure 3-9 with the orange highlight in Figure 3-2), although the molecular mechanism behind this

importance is still unclear. To ensure that C255A was not interfering with NLS function, we verified that C255A was not excluded from the nucleus (Figure 3-10, panel B).

With these findings consistent with potential palmitoylation of C255 and C299, we assessed NiV-M palmitoylation with the acyl-biotin exchange assay.[10-12] Free thiols on immunoprecipitated NiV-M, representing non-modified cysteines, were first irreversibly blocked with N-ethylmaleimide. Then, potential palmitoyl-thiol linkages were cleaved with hydroxylamine (HAM) at neutral pH, thus liberating thiols at the cysteine residue(s) that were previously palmitoylated. These free cysteines were then labeled with sulfhydryl-reactive biotin, which could then be detected with fluorescent streptavidin by Western immunoblotting. This acyl-biotin exchange assay found that NiV-M is potentially palmitoylated (Figure 3-11). The lack of detectable biotin labeling in the HAM-negative control adds confidence that the biotin labeling was somewhat specific. Nonetheless, confirmation of NiV-M palmitoylation would require a direct palmitate labeling assay using radioactive palmitate or palmitate analogs that can be detected via click chemistry.[13]

Q328A accumulates in large, angular structures that protrude from the cell surface

Despite the absolute conservation of Q328 among paramyxovirus matrix proteins, the Q328A mutation did not result in reduced budding efficiency (Figure 3-6). To determine whether this front-line assay did not capture a deeper defect in virus assembly, we used an established beta-lactamase (bla)-matrix fusion protein VLP budding assay that can assess the ability of matrix to assemble infectious VLPs upon co-expression with the NiV-F and -G envelope proteins.[3] The bla-Q328A fusion was able to assemble the envelope proteins into infectious virus-like particles, as determined by the bla substrate fluorescence shift in the subsequently infected cells (Figure 3-12).

We further examined the Q328A mutant by immunofluorescence to determine if it displayed aberrant cellular localization. We were surprised to find that in contrast to wild-type

NiV-M, which is diffuse throughout the cell with a punctate appearance (Figure 3-13, panel A), the Q328A mutant appeared accumulated in large, angular structures that protruded from the cell surface (Figure 3-13, panel B). The protrusions at the cell surface suggested association of the Q328A mutant with the membrane, and indeed, membrane flotation suggested that the mutant was more concentrated in the membrane fraction than wild-type NiV-M, with almost half of the cellular Q328A associated with membrane (Figure 3-13, panel C).

We then considered if these structures might retain the virus assembly function of wild-type matrix. Continued association with other structural components of the virus might suggest that the structures represent mutant matrix trapped at an intermediate step of the budding process, yet still competent to assemble viral components. We therefore co-expressed NiV-N, NiV-G, and wild-type NiV-M with the Q328A mutant. Nucleocapsid, attachment protein, and wild-type matrix all co-localized with the Q328A structures (Figure 3-14). Of note, the Q328A phenotype was dominant over wild-type M, as Q328A structure formation was not prevented by the presence of wild-type M, but rather the structures recruited wild-type M.

Q328 may mediate the dynamics of matrix multimerization

To assess whether there might be a structural basis for the Q328A phenotype, we examined the solved dimer structure of NDV-M. The side chain of the corresponding glutamine in NDV-M, Q330, has a potential hydrogen bond contact with the side chain of S120 in the other matrix monomer (Figure 3-15). Q328 in NiV-M may therefore mediate the dynamics or structural characteristics of matrix multimerization. Although the Q328A mutant appears to self-associate into the large structures, even recruiting wild-type NiV-M, we confirmed that the Q328A mutation does not abrogate dimer formation by exposing cells expressing mutant or wild-type NiV-M to a 11.4Å membrane-permeable amine-amine crosslinker, then running cell lysates on SDS-PAGE. Western immunoblotting revealed dimer formation by both mutant and wild-type NiV-M (Figure 3-16).

We reasoned that if disrupting the monomer-to-monomer contact with the Q328A mutation was responsible for the Q328 phenotype, mutating the contacting amino acid on the other monomer should result in a similar phenotype. The NDV-M S120 residue corresponds to T120 in NiV-M (Figures 3-3 and 3-15). Like Q328A, the T120A mutant had wild-type budding efficiency (Figure 3-17, panel A), and it also displayed large, angular structures, although in a lesser proportion of transfected cells (Figure 3-17, panel B).

Interestingly, the T120 residue in NiV-M would have been absolutely conserved among the paramyxoviruses except for the presence of a serine at that position in NDV-M (Figures 3-3 and 3-15). Serine and threonine residues share the property of potential phosphorylation, and we hypothesized that phosphorylation (either static or dynamic) of this residue might modulate the interaction between the two monomers. NiV-M has 12 threonine residues, and it was surprising to find that the T120A mutation alone was sufficient to abrogate threonine phosphorylation of NiV-M (Figure 3-18, panel A). Mutation of the flanking threonines T116 and T124 did not likewise abrogate threonine phosphorylation (Figure 3-18, panel B). Although the T120A mutation may indirectly cause loss of phosphorylation for other threonine(s), our findings are nevertheless consistent with potential direct phosphorylation of T120.

In an effort to modulate this potential T120 phosphorylation and thus examine its functional consequence, we evaluated the amino acid sequence of NiV-M for consensus kinase recognition sites with the PhosphoMotif finder (Human Protein Reference Database). Potential kinases for T120 included the PKA and PKC kinases, GRK1 (rhodopsin kinase), casein kinase 1, and casein kinase 2. Circumstantially, we noticed that a E125A mutant was noticeably downshifted relative to wild-type NiV-M on SDS-PAGE, indicating the potential loss of multiple negative charges. E125 is part of a consensus casein kinase 2 (CK2) motif for S123, which, if phosphorylated, would be part of the consensus CK2 motif for T120. Inhibition of CK2 with the specific and potent inhibitor TBCA,[14] however, had no effect on NiV-M threonine phosphorylation (Figure 3-18, panel C).

NiV reverse genetics will further illuminate the significance of Q328

To gain further insight into the functional significance of the large, angular structures formed by this mutant, we introduced the mutation into the rNiV-EGFP^{NP} full-length Nipah virus reverse genetics construct (see Chapter 2.2 for details on this construct). Efforts to rescue this mutant NiV at BSL4 are ongoing.

DISCUSSION

To assay the effect of alanine mutagenesis on absolutely conserved residues in NiV-M, we first established a reliable and semi-quantitative NiV-M budding assay. Traditionally and commonly, the efficiency of virus budding is determined by SDS-PAGE and Western immunoblotting of viral vs. cell lysate samples, and subsequent straightforward division of band densitometry from virus samples vs. cell lysate samples. This method suffers from two faulty assumptions, however: first, it is assumed that the relative changes in densitometry represent relative changes in absolute protein. As is well known but not yet firmly established in practice, this is often not the case, and it is therefore imperative to include a standard curve of sample dilutions on every blot for accurate quantitation. Further compounding this issue is that virus and cell lysate protein samples are typically run on separate blots due to space constraints, and relative changes in densitometry can differ significantly between blots.

The second traditional assumption is that a fold-change in cell lysate expression yields an equivalent fold-change in virus budding. This assumption, in our experience, is false: for example, in the example wild-type NiV-M titration given in Figure 3-5, a 2-fold increase in cell lysate expression (from relative cell lysate “1” to “2”) yields a 5-fold increase in virus-like particle budding (from relative VLP “1” to “5”). Therefore, to better estimate the wild-type behavior of virus budding in relation to cell lysate expression, a titrated transfection of wild-type NiV-M was included with each experiment, with experimental conditions compared to this wild-type behavior.

Using this optimized budding assay, we found that all mutants were deficient in budding except for the C-terminal Q328A (Figure 3-6). Most mutants were also not expressed well compared to wild-type NiV-M. To focus our energies on mutants that were likely not destabilized and degraded due to structural reasons, we decided to investigate in more depth one well-expressed budding-deficient mutant, C299A, as well as one well-expressed budding-normal mutant, Q328A.

Because cysteine residues are often sites of post-translation modification, we wondered if C299 might be a site of palmitoylation. Modification by lipid has not been described for any paramyxovirus matrix protein, or indeed any member of *Mononegavirales*, although palmitoylation of the hepatitis C virus (a positive-sense RNA virus) core protein has been described.[15] Indeed, association of C299A with membrane was reduced as compared to wild-type NiV-M (Figure 3-7), consistent with a potential loss of lipid attachment. *In silico* screening of the NiV-M sequence with a palmitoylation prediction algorithm suggested potential palmitoylation of C157, C255, and C299; of these, C255 and C299 are near the membrane in the threaded structure of NiV-M (Figure 3-9). Interestingly, the region that contains C255 is predicted not only to be a bipartite NLS sequence (discussed further in Chapter 3.2), but also contains a hydrophobic loop that aligns with a membrane-spanning domain by homology modelling in Phyre2. In a potentially analogous finding, a juxta-membrane hydrophobic region in the Ebola virus matrix protein VP40 was recently shown to penetrate into the membrane.[16,17] Consistent with a possible role for C255, a C255A mutant was budding-deficient, while mutation of C157 did not affect budding (Figure 3-10).

The mutant phenotypes of C299A and C255A suggested that NiV-M is palmitoylated at one or both of these cysteine residues, which is consistent with evidence provided by the acyl-biotin exchange assay indicating that wild-type NiV-M is palmitoylated (Figure 3-11). Although this finding should be confirmed with a direct labeling assay using radioactive palmitate or a palmitate analog, lipid modification of NiV-M would help explain our findings in Chapter 3.2, in

which a single point mutant, K258A, loses membrane association despite preservation of much of the membrane-binding surface shown in Figure 3-2. The loss of membrane association of the K258A mutant suggests the involvement of matrix modifications or cellular pathways in matrix membrane association, perhaps involving direct modification of matrix with lipids. Our results raise the exciting possibility that NiV-M palmitoylation and budding may be sensitive to broad-spectrum inhibitors of palmitoylation such as 2-bromopalmitate.

We then examined the effect of mutating conserved residue Q328. Beyond the wild-type budding efficiency of the Q328A mutant, a bla-Q328A fusion protein was able to assemble NiV-F and -G into infectious virus-like particles (Figure 3-12), indicating further wild-type behavior. Immunofluorescence of Q328A in transfected cells, however, revealed the accumulation of Q328A in large, angular structures that protruded from the cell surface and appeared to associate with the cell membrane (Figure 3-13). These structures co-localized with co-expressed viral components such as NiV-N, NiV-G, and wild-type NiV-M (Figure 3-14). Analysis of the corresponding Q330 residue in the solved NDV-M dimer structure suggested that the glutamine side chain might contact S120 in the other monomer, and indeed, mutation of the corresponding T120 residue in NiV-M resulted in a similar phenotype as Q328A (Figure 3-17). Since the Q328A mutation does not affect dimer formation *per se* (Figure 3-16), it potentially modulates the temporal timing or structural dynamics of this process. Potential direct phosphorylation of T120 (Figure 3-18) may represent regulation of this interaction between glutamine and threonine side chains. Although inhibition of a potential T120 kinase, CK2, did not inhibit T120 phosphorylation, further screening of kinase inhibitors to specifically prevent T120 phosphorylation may provide a means to modulate the function of wild-type NiV-M, either on its own or in the context of live virus replication.

Whether the Q328A mutation in the context of NiV reverse genetics allows viral replication, and if so, how the mutation affects NiV-M localization and function within the full virus life cycle will also give critical insight into the functional importance of this conserved

residue. Even if the mutation does not allow full virus replication and spread, our results in Chapter 3.3 for mutant Sendai virus rescue demonstrate that important findings can be revealed by examination of individual cells that display rescue of mutant virus genome replication and protein production. Importantly, for all conserved residues, including C299 and Q328, our development of reverse genetics systems for paramyxoviruses spanning the five major genera allows us to examine the significance of these residues outside of constraining BSL4 conditions.

FIGURES

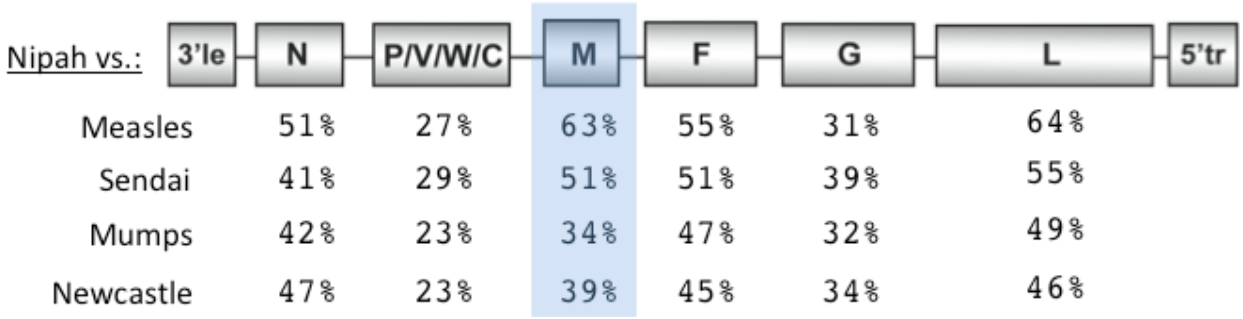

Figure 3-1. Conservation of the matrix protein among the *Paramyxovirinae*. The amino acid sequence of each Nipah virus protein was aligned against the corresponding protein from representative viruses of the other four major *Paramyxovirinae* genera. The percent similarity for each pairwise comparison is reported above. The NCBI reference sequences used for the viruses are: Nipah, NC_002728.1; Measles, NC_001498.1; Sendai, NC_001552.1; Mumps, NC_002200.1; Newcastle, NC_002617.1.

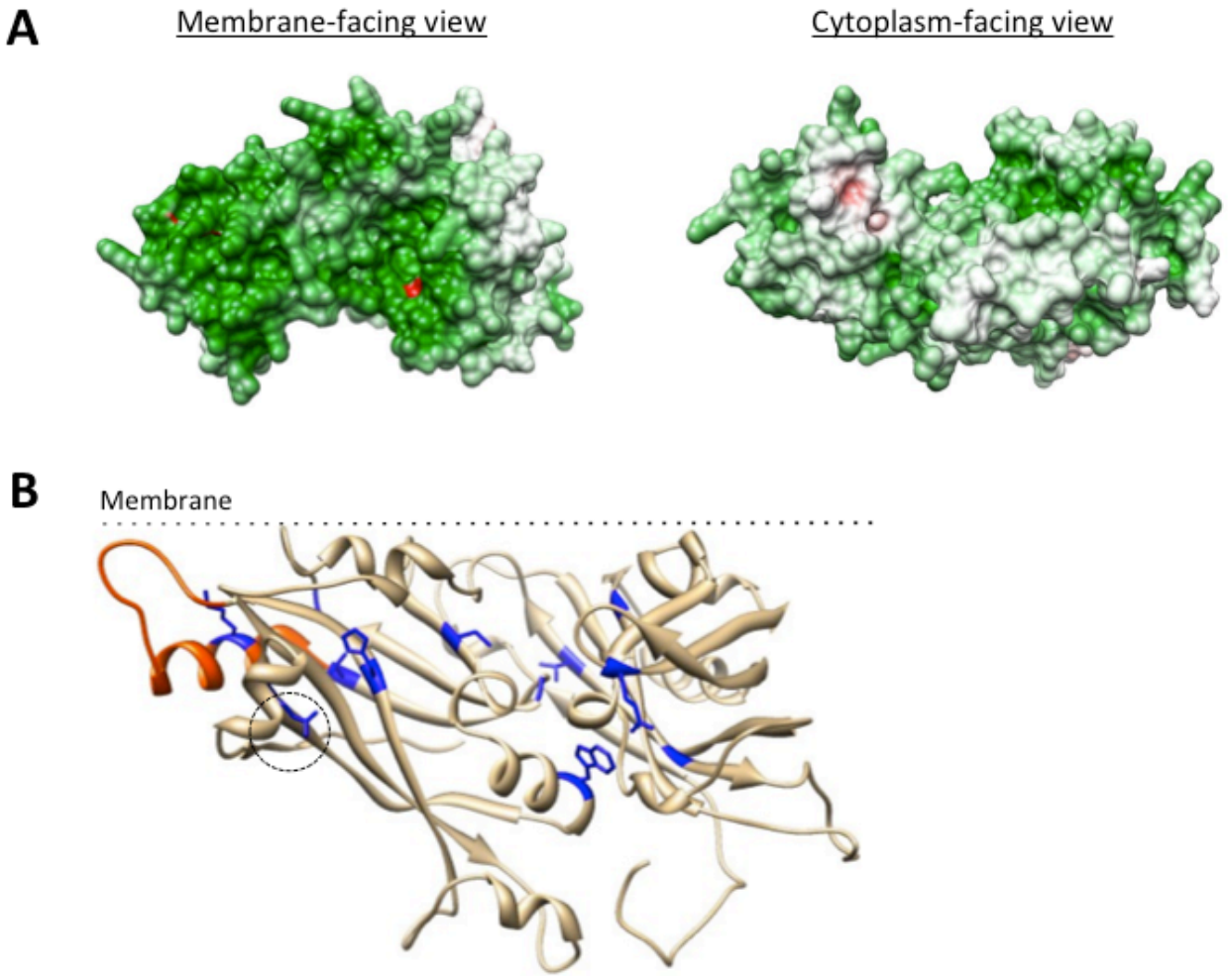

Figure 3-2. Homology structure of NiV-M via threading of the solved NDV-M structure. The NiV-M sequence was evaluated by Phyre2, with surface electrostatic potential calculated by APBS (see Materials and Methods). **(A)** The putative membrane-binding and cytoplasm-facing surfaces are shown for NiV-M, in the orientation suggested for NDV-M. Consistent with this possible orientation, the putative membrane-binding surface is highly positively charged (green), but the opposite face of the structure is less so (negative charge represented by shading to red). **(B)** Residues that are absolutely conserved among the *Paramyxovirinae* are colored blue on the NiV-M structure, with the side chains shown. The bipartite nuclear localization sequence characterized in Chapter 3.2 is colored orange. The Q328 residue is highlighted with a dotted circle. The position of the C299 residue is shown in Figure 3-9.

```
Nipah          MEPDIKSISSE-SMEGVSDFSPSSWEHGGYLDKVEPEIDENGSMIPKYKIYTPGANERKY 59
Measles        ------------MTEIYDFDKSAWDIKGSIAPIQPTTYSDGRLVPQVRVIDPGLGDRKD 47
Sendai         ------------MADIYRFPKFSYEDNGTVEPLPLRTGPDKKAIPHIRIVKVGDPPKHG 47
Mumps          --------MAGSQIKIPLPKPPDSDSQRLNAFPVIMAQEGKGRLLRQIRLRKILSGDPSD 52
Newcastle      -------MDSSRTIGLYFDSAHSSSNLLAFPIVLQDTGDGKKQIAPQYRIQRLDLWTDSK 53


Nipah          NNYMYLICYGFVEDVERTPETG--------KRKKIRTIAAYPLGVGKSASHPQDLLEELC 111
Measles        ECFMYMFLLGVVEDSDPLGPP------------IGRAFGSLPLGVGRSTAKPEELLKEAT 95
Sendai         VRYLDLLLLGFFETPKQTASLGSVSDLTEHTGYSICGSGSLPIGVAKYHGSDQELLKACT 107
Mumps          QQITFVNTYGFIRATPETSEFISES--SQQKVTPVVTACMLSFGAGPVLEDPQHMLKALD 110
Newcastle      EDSVFITTYGFIFQVGNEEATVGIID--DKPKRELLSAAMLCLGSVPNTGDLIELARACL 111
                        *                                  *

Nipah          SLKVTVRRTAGSTEKIVFGSSGPLNHLVPWKKVLTSGSIFNAVKVCRNVDQIQLDKHQAL 171
Measles        ELDIVVRRTAGLNEKLVFYNNTPLTLLTPWRKVLTTGSVFNANQVCNAVNLIPLDTPQRF 155
Sendai         DLRITVRRTVRAGEMIVYMVDSIGAPLLPWSGRLRQGMIFNANKVALAPQCLPVDKDIRF 167
Mumps          QTDIRVRKTASDKEQILFEINRIPNLFRHHQISADHLIQASSDKYVKSPAKLIAGVNYIY 170
Newcastle      TMMVTCKKSATNTERMVFSVVQAPQVLQSCRVVANKYSSVNAVKHVKAPEKIPGSGTLEY 171
                           *

Nipah          RIFFLSITKLNDSGIYMIPRTMLEFRR--NNAIAFNLLVYLKIDADLSKMGIQGSLDKDG 229
Measles        RVVYMSITRLSDNGYYTVPRRMLEFRS--VNAVAFNLLVTLRIDKAIGPGKIIDN--AEQ 211
Sendai         RVVFVNGTSLGAITIAKIPKTLADLAL--PNSISVNLLVTLKTGISTEQKGVLPVLDDQG 225
Mumps          CVTFLSVTVCSASLKFRVARPLLAARSRLVRAVQMEVLLRVTCKKDSQMAKSMLSDPDGE 230
Newcastle      KVNFVSLTVVPKKDVYKIPAAVLKISG--SSLYNLALNVTINVEVDPRSPLVKSLSKSDS 229
                      *

Nipah          FKVASFMLHLGNFV--RRAGKYYSVDYCRRKIDRMKLQFSLGSIGGLSLHIKINGVISKR 287
Measles        LPEATFMVHIGNFR--RKKSEVYSADYCKMKIEKMGLVFALGGIGGTSLHIRSTGKMSKT 269
Sendai         EKKLNFMVHLGLIR--RKVGKIYSVEYCKSKIERMRLIFSLGLIGGISFHVQVTGTLSKT 283
Mumps          GCIASVWFHLCNLCKGRNKLRSYDENYFASKCRKMNLTVSIGDMWGPTILVHAGGHIPTT 290
Newcastle      GYYANLFLHIGLMTTVDRKGKKVTFDKLEKKIRSLDLSVGLSDVLGPSVLVKARGARTKL 289
                      *                    *     *        *        *

Nipah          LFAQMGFQKNLCFSLMDINPWLNRLTWNNSCEISRVAAVLQPS-----IPREFMIYDDVF 342
Measles        LHAQLGFKKTLCYPLMDINEDLNRLLWRSRCKIVRIQAVLQPS-----VPQEFRIYDDVI 324
Sendai         FMGQLAWKRAVCFPLMDVNPHMNLVIWAASVEITDVDAVFQPA-----IPRDFRYYPNVV 338
Mumps          AKPFFNSRGWVCHPIHQSSPSLAKTLWSSGCEIKAASAILQGSDYASLAKTDDIIYSKIK 350
Newcastle      LAPFFSSSGTACYPIANASPQVAKILWSQTACLRSVKIIIQAG---TQRAVAVTADHEVT 346
                         *              *             *

Nipah          IDNTGRILKG---------------- 352
Measles        INDDQGLFKVL--------------- 335
Sendai         AKNIGRIRKL---------------- 348
Mumps          VDKDAANYKGVSWSPFRKSASMSNL 375
Newcastle      STKLEKGHTLAKYNPFKK------- 364
```

Figure 3-3. Multiple sequence alignment of *Paramyxovirinae* matrix proteins. Matrix proteins of representative viruses from all five major *Paramyxovirinae* genera were aligned with ClustalW2. Absolutely conserved residues are marked by an asterisk.

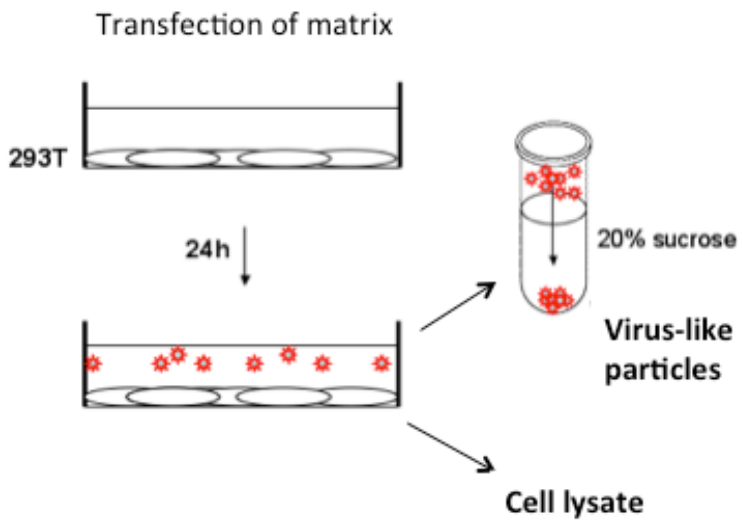

Figure 3-4. Overview of NiV-M virus-like particle budding assay. Transfection of NiV-M alone leads to production of virus-like particles (VLPs) that morphologically resemble NiV virions by electron microscopy (without the visible envelope protein spikes). VLPs can be purified and concentrated by pelleting through a 20% sucrose cushion via ultracentrifugation.

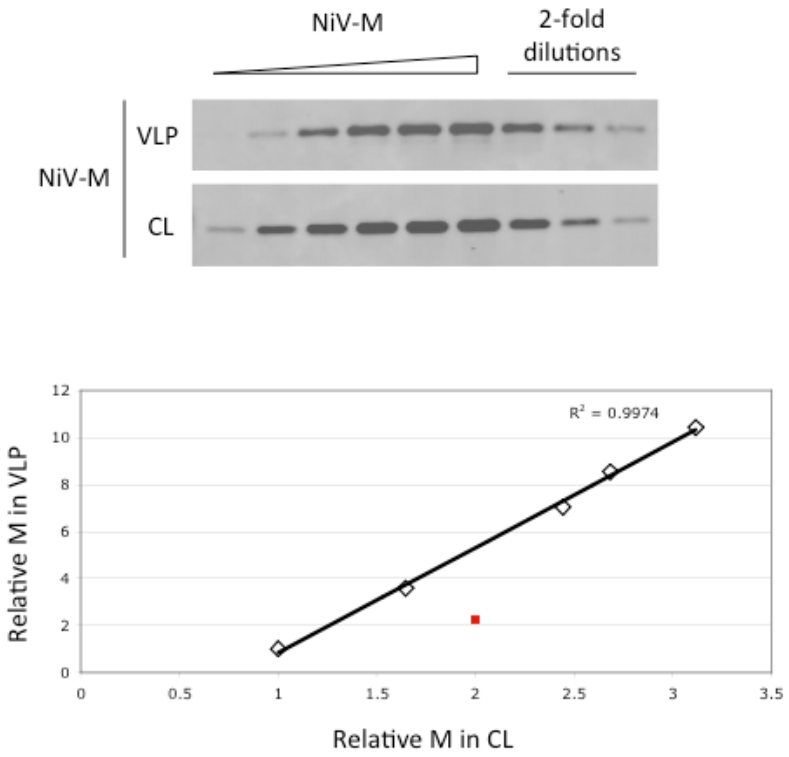

Figure 3-5. Optimization of a semi-quantitative budding assay. An increasing titration of NiV-M transfection allows comparison of relative NiV-M in VLPs versus cell lysate for different levels of cell lysate expression. This titration can be graphed to yield a standard curve of wild-type budding behavior for each experiment. Experimental conditions can then be reported as % expected M in VLP for a given amount of relative M cell lysate expression. For example, the red dot would represent about 40% of expected VLP budding (40% of wild-type).

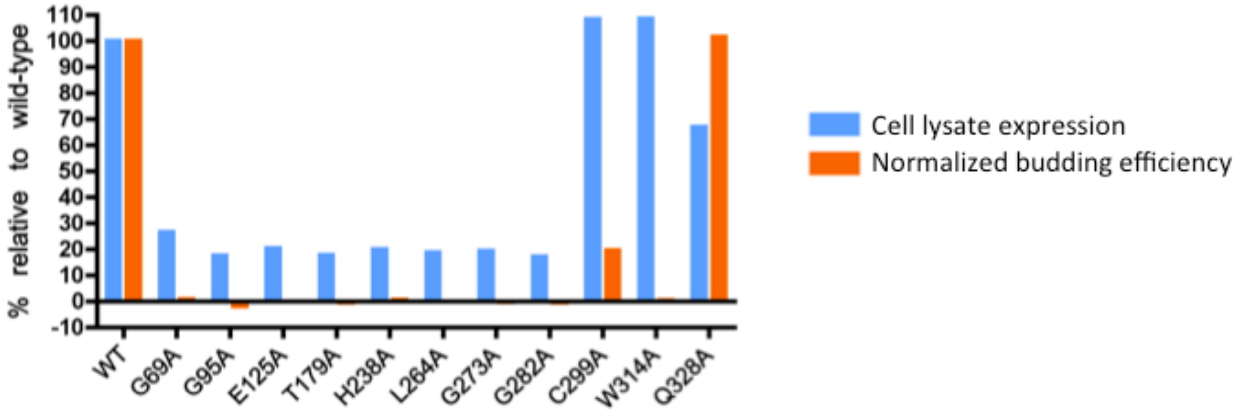

Figure 3-6. Almost all mutations in conserved residues result in budding deficiency. Only the three C-terminal mutations resulted in cell lysate matrix expression comparable to wild-type, and these mutants were both budding-deficient and budding-normal.

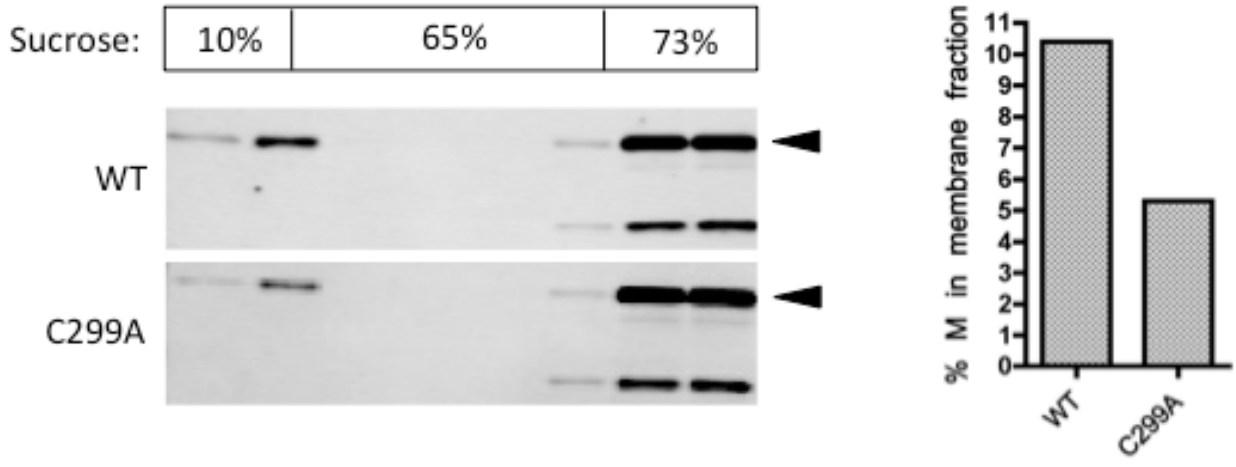

Figure 3-7. The C299A mutant has reduced membrane association. Membrane association was examined by flotation on a discontinuous sucrose gradient as described in Materials and Methods. Membrane fractions float from the dense fraction (73%) to the 10%-65% interface.

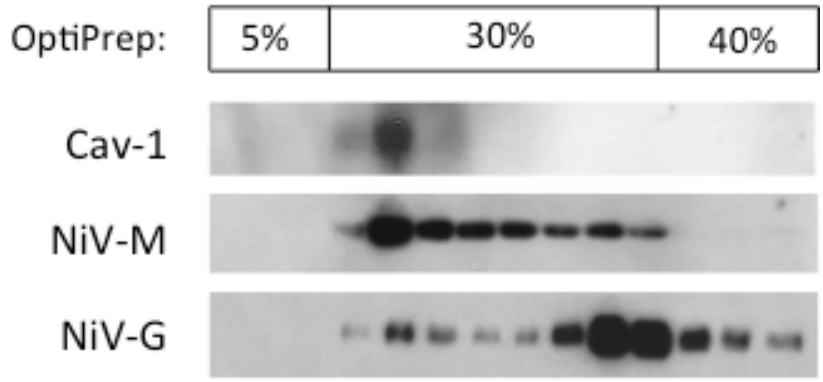

Figure 3-8. NiV-M associates with detergent-resistant lipid rafts. Membrane fractions that resist solubilization by detergent at 4C, representing highly ordered lipid raft domains, float in the discontinuous OptiPrep gradient, similar to the membrane flotation assay in Figure 3-6. The lipid raft fraction is marked by the presence of caveolin-1. NiV-G, in contrast to NiV-M, does not concentrate in the lipid raft fraction.

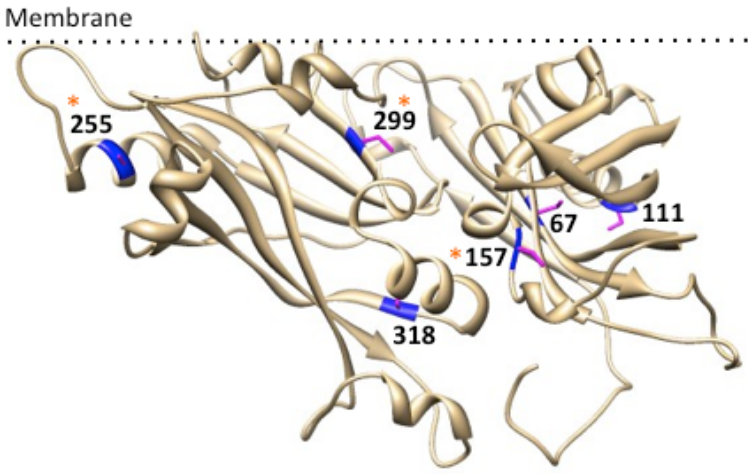

Figure 3-9. C255 and C299 are predicted sites of palmitoylation. Evaluation of the NiV-M sequence in CSS-PALM 3.0 predicted C157, C255, and C299 (marked by asterisks; all six cysteines are highlighted) as potential sites of palmitoylation. Only C255 and C299 are near the membrane-facing surface.

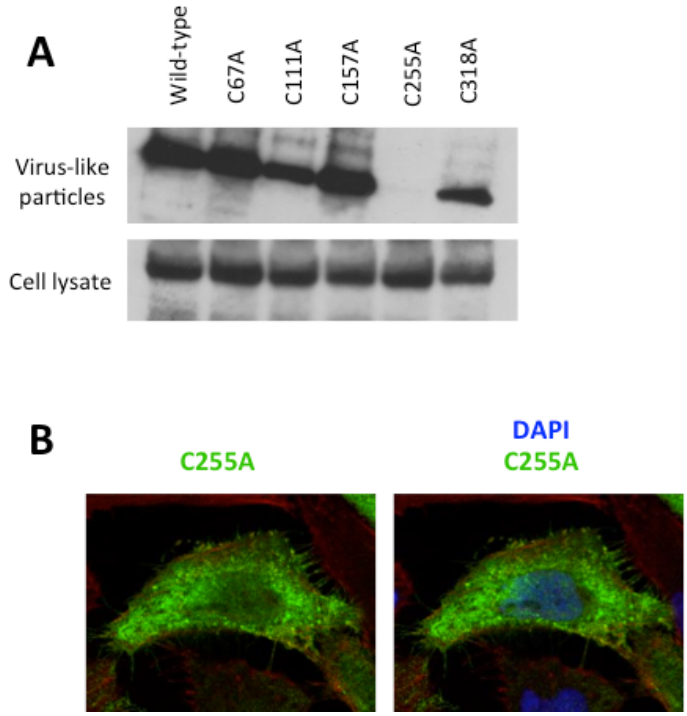

Figure 3-10. C255A is budding-deficient. (A) C255A is budding-deficient, consistent with potential loss of critical palmitoylation. **(B)** The mutation also did not abrogate NLS function (the bipartite NLS that flanks C255 is further described in Chapter 3.2) as shown by the presence of C255A in the nucleus.

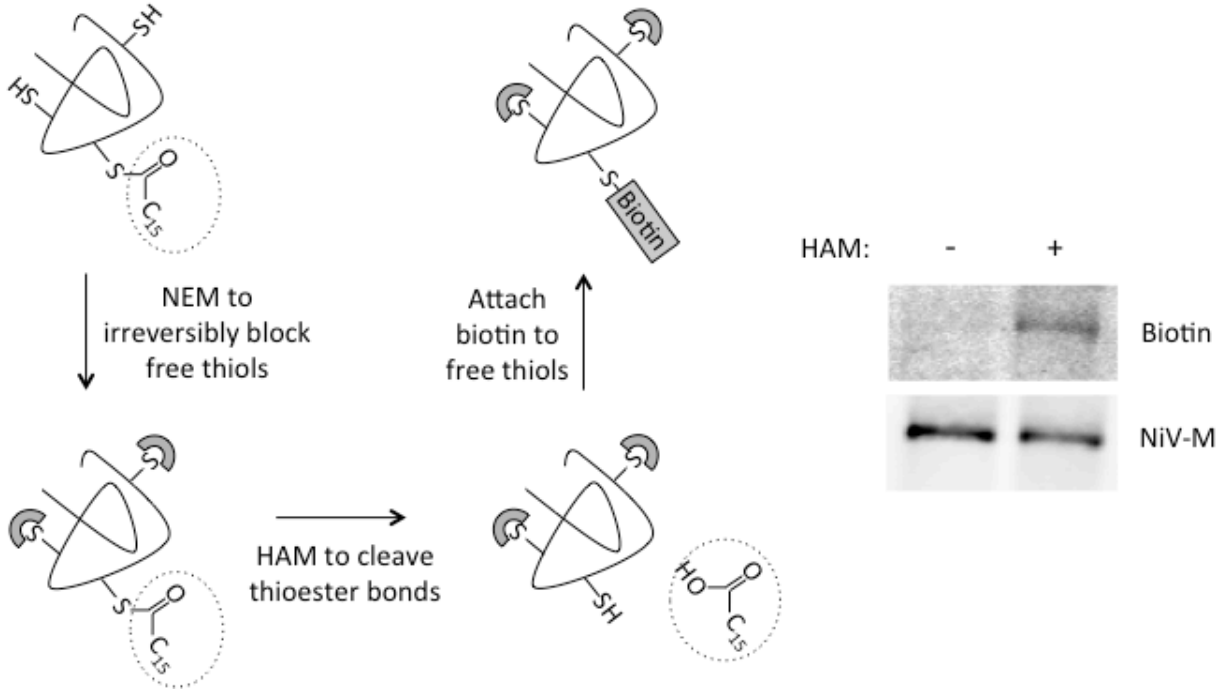

Figure 3-11. Acyl-biotin exchange indicates palmitoylation of NiV-M. The acyl-biotin exchange assay was performed as described in Materials and Methods. The palmitate moiety is shown by a dotted circle. NEM, N-ethylmaleimide; HAM, hydroxylamine; biotin was attached with BMCC-Biotin, a sulfhydryl-reactive biotin. A minus-HAM control does not result in detection of biotinylated NiV-M by Western immunoblot (detected by a fluorescent streptavidin conjugate).

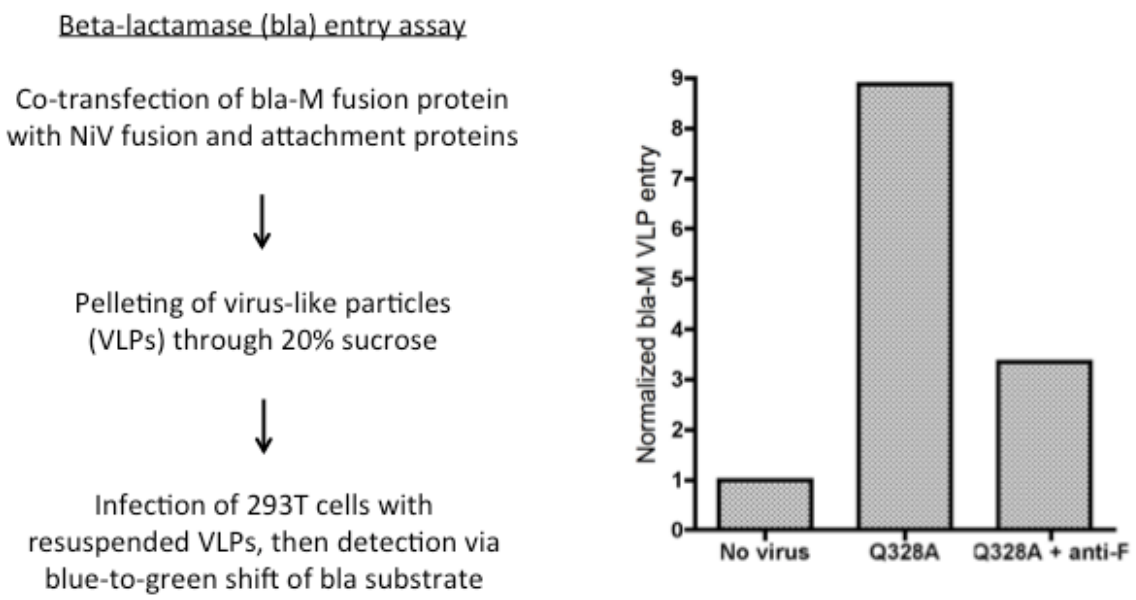

Figure 3-12. A beta-lactamase-Q328A fusion protein can assemble NiV-F and -G into infectious virus-like particles. The assay was performed as described in Materials and Methods, according to the method in Wolf *et al.* (ref. 3). The blue-to-green ratio for each condition was normalized to mock infection. The inclusion of anti-NiV-F neutralizing antibody during infection inhibited VLP entry, as a control for the specificity of the assay for viral entry mediated by the NiV envelope proteins.

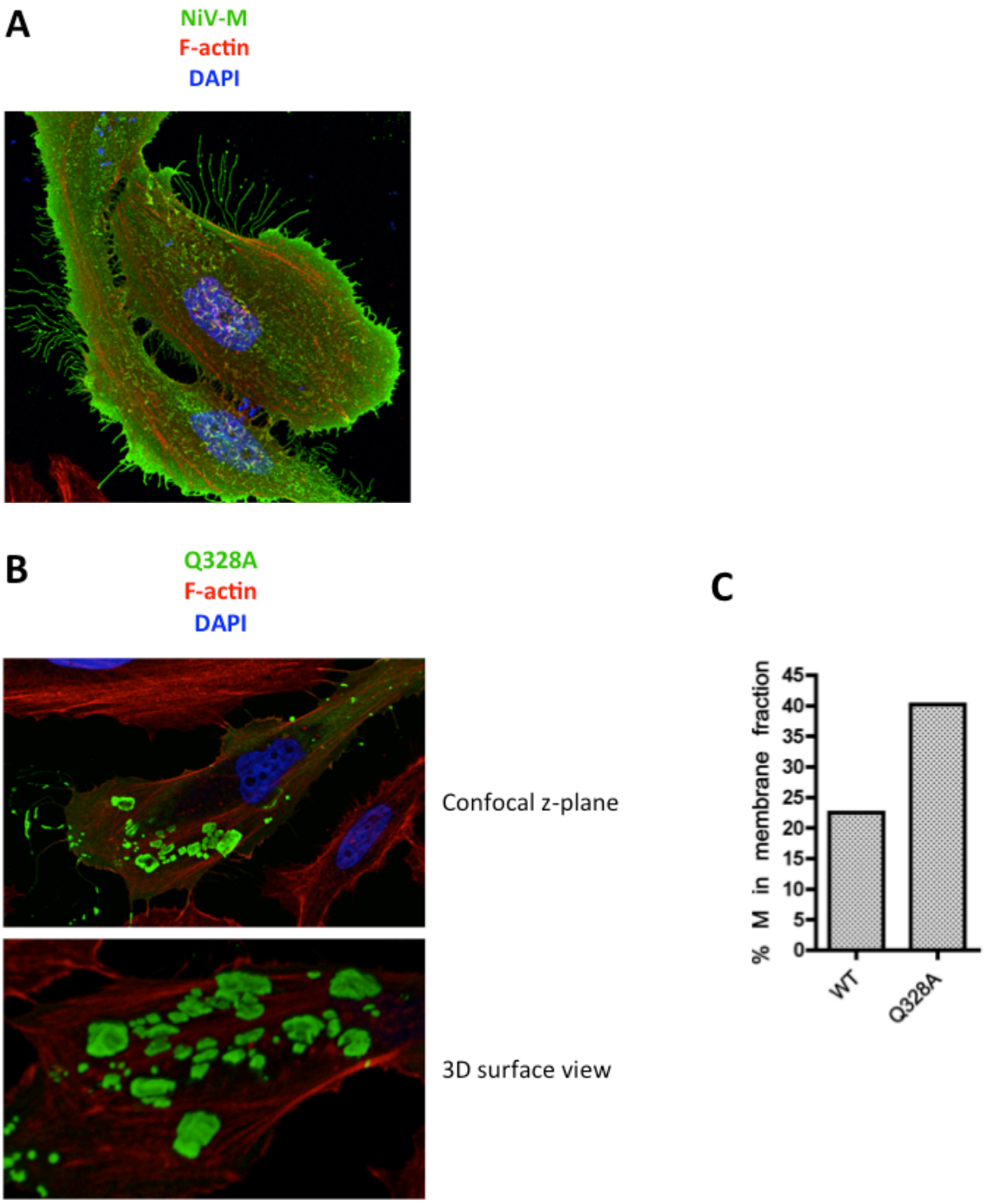

Figure 3-13. The Q328A mutant assembles into large, angular structures that associate with membrane. (A) Wild-type NiV-M is diffuse throughout the cell with a punctate appearance. **(B)** The Q328A mutant forms large, angular structures that protrude from the cell surface. Due to the intensity of staining for these structures, the presence of matrix throughout the rest of the cell is not as apparent. **(C)** Membrane flotation was performed as for Figure 3-7. The higher membrane association of wild-type M in this figure as compared to Figure 3-7 is due to modification of the cell collection protocol (omission of PBS washing step in eppendorfs, which led to the loss of a portion of the membrane fraction, likely due to shearing).

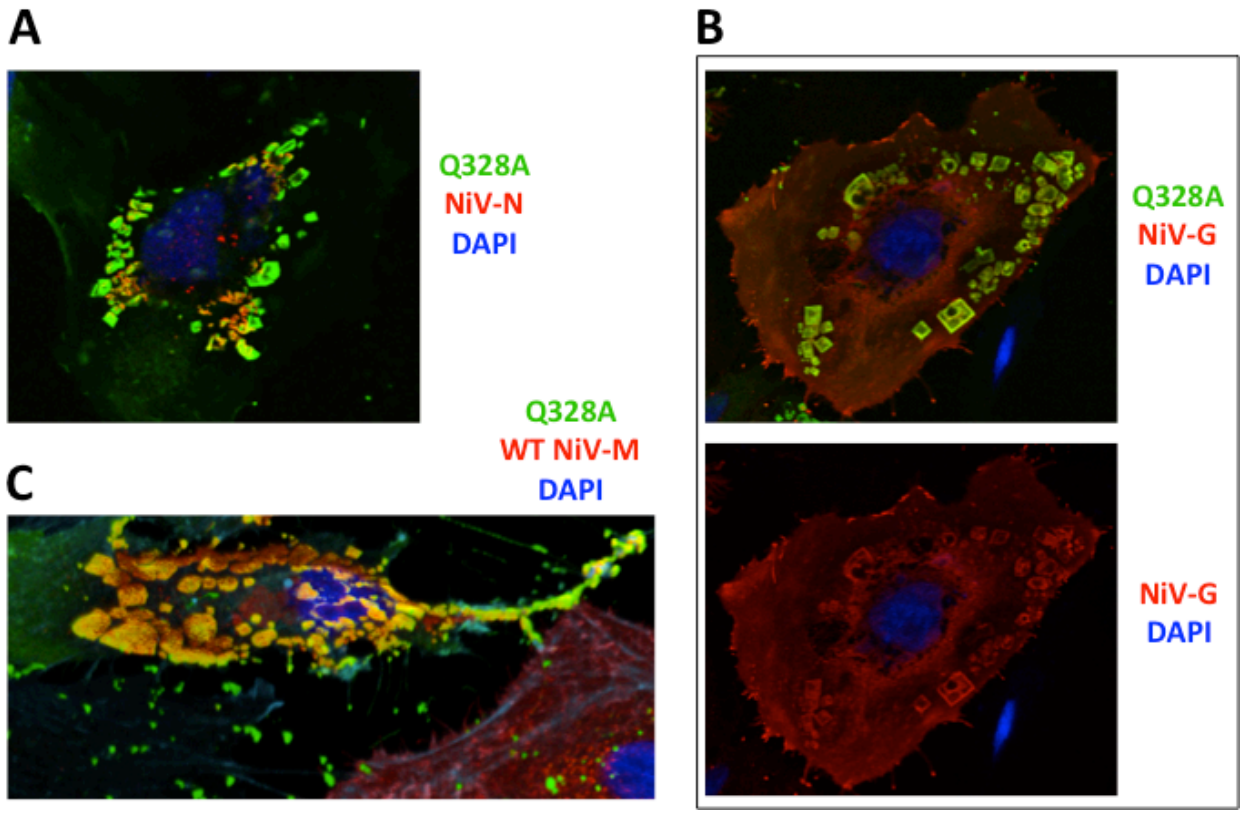

Figure 3-14. The Q328A mutant co-localizes with other NiV proteins. Co-staining for FLAG-Q328A (anti-FLAG) with the indicated NiV protein (anti-HA): **(A)** HA-NiV-N, **(B)** HA-NiV-G, and **(C)** HA-NiV-M. (A) represents extended focus, (B) represents a confocal z-slice, and (C) represents a 3D-reconstructed surface view.

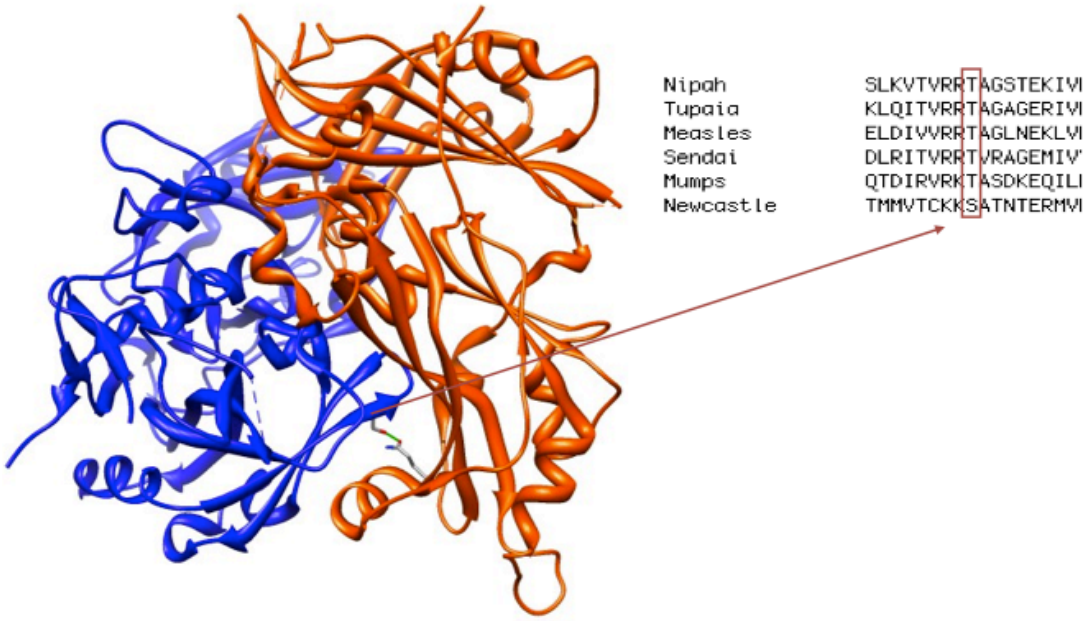

Figure 3-15. Q330 contacts S120 in the NDV-M dimer structure. The Q330 side chain extended from the orange monomer, while the S120 side chain extends from the blue monomer. The hydrogen bond (using the FindHBond function in UCSF Chimera) is indicated by the green line. The paramyxovirus matrix alignment for the residues surrounding NDV-M S120 is shown.

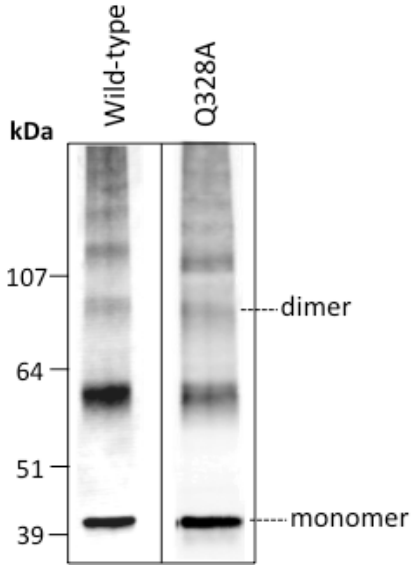

Figure 3-16. The Q328A mutation does not abrogate dimer formation. Wild-type and Q328A mutant NiV-M expressed in HEK 293T cells were crosslinked with a 11.4Å membrane-permeable amine-amine crosslinker (see Materials and Methods), run on SDS-PAGE and examined by Western.

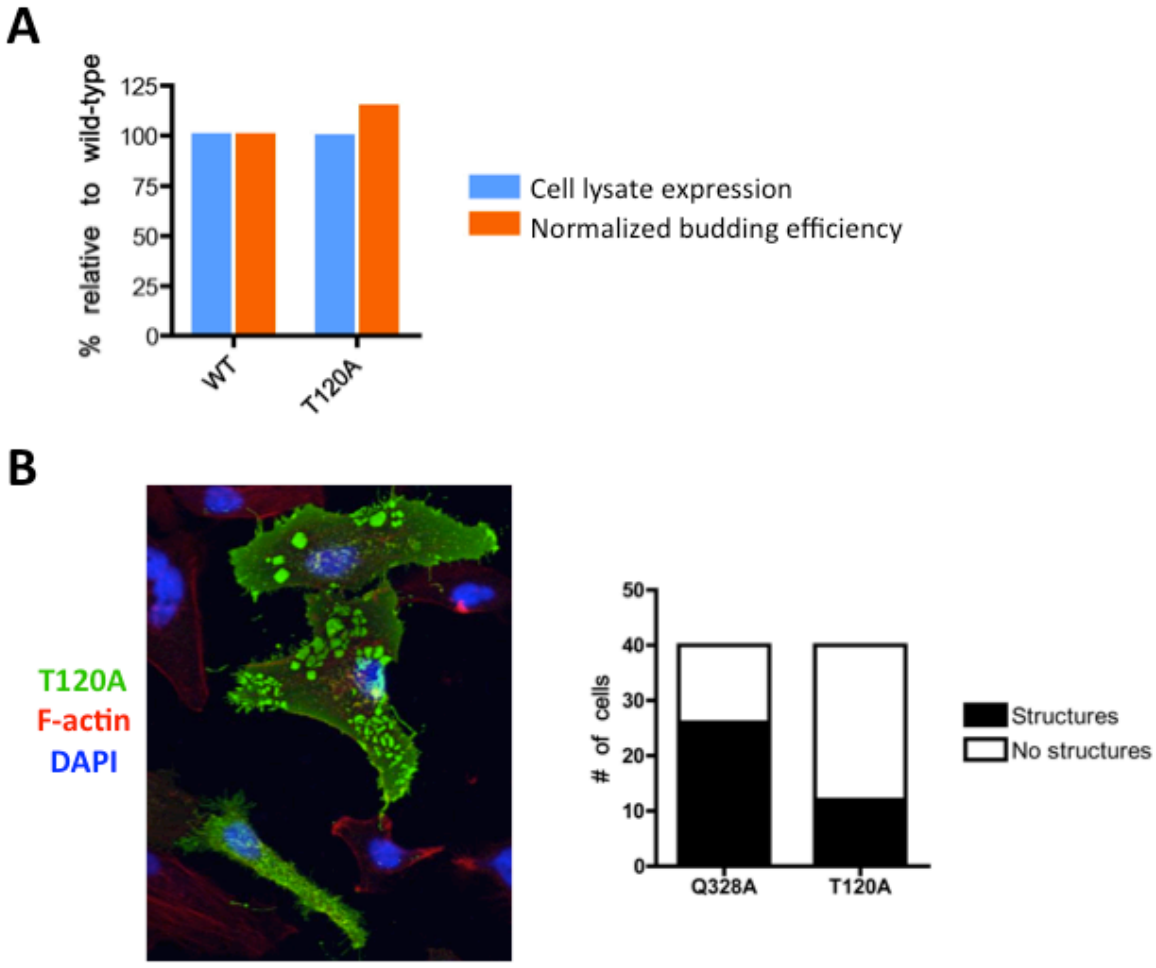

Figure 3-17. Mutation of T120 mimics the phenotype of Q328A. (A) The budding of T120A was examined as in Figure 3-6. **(B)** Random fields of HeLa cells transfected with the Q328A or T120A mutant were imaged, and 40 cells selected at random for each mutant were evaluated for the presence of matrix accumulated in large, angular structures.

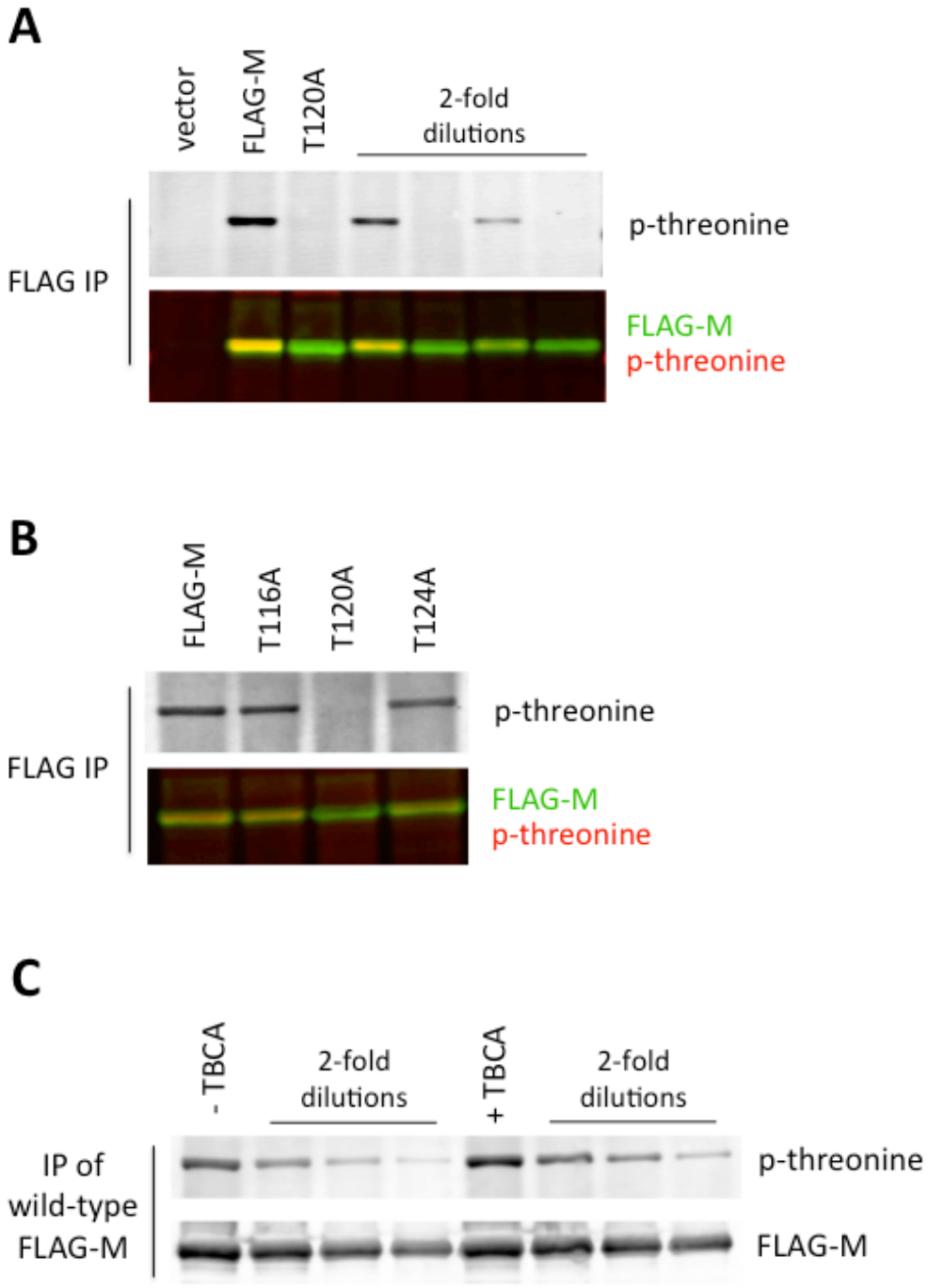

Figure 3-18. T120 may be phosphorylated. (A and B) Wild-type or mutant FLAG-M was immunoprecipitated, run on SDS-PAGE and evaluated for phosphothreonine modification by Western. Only T120A loses phosphothreonine modification. **(C)** Although T120 is a potential CK2 phosphorylation site, inhibition of CK2 with 100 uM TBCA (IC_{50} = 110 nM) did not affect NiV-M threonine phosphorylation (despite observation of known visual effects of TBCA treatment in cell culture, such as cell rounding).

REFERENCES

1. Battisti AJ, Meng G, Winkler DC, et al. Structure and assembly of a paramyxovirus matrix protein. *Proceedings of the National Academy of Sciences of the United States of America*. 2012;109(35):13996-14000.

2. Wang YE, Park A, Lake M, et al. Ubiquitin-regulated nuclear-cytoplasmic trafficking of the Nipah virus matrix protein is important for viral budding. *PLoS pathogens*. 2010;6(11):e1001186.

3. Wolf MC, Wang Y, Freiberg AN, Aguilar HC, Holbrook MR, Lee B. A catalytically and genetically optimized beta-lactamase-matrix based assay for sensitive, specific, and higher throughput analysis of native henipavirus entry characteristics. *Virology journal*. 2009;6:119.

4. Bryant M, Ratner L. Myristoylation-dependent replication and assembly of human immunodeficiency virus 1. *Proceedings of the National Academy of Sciences of the United States of America*. 1990;87(2):523-527.

5. Gottlinger HG, Sodroski JG, Haseltine WA. Role of capsid precursor processing and myristoylation in morphogenesis and infectivity of human immunodeficiency virus type 1. *Proceedings of the National Academy of Sciences of the United States of America*. 1989;86(15):5781-5785.

6. Linder ME, Deschenes RJ. Palmitoylation: policing protein stability and traffic. *Nature reviews Molecular cell biology*. 2007;8(1):74-84.

7. Fukata Y, Fukata M. Protein palmitoylation in neuronal development and synaptic plasticity. *Nature reviews Neuroscience*. 2010;11(3):161-175.

8. Resh MD. Fatty acylation of proteins: new insights into membrane targeting of myristoylated and palmitoylated proteins. *Biochimica et biophysica acta*. 1999;1451(1):1-16.

9. Ren J, Wen L, Gao X, Jin C, Xue Y, Yao X. CSS-Palm 2.0: an updated software for palmitoylation sites prediction. *Protein engineering, design & selection : PEDS*. 2008;21(11):639-644.

10. Brigidi GS, Bamji SX. Detection of protein palmitoylation in cultured hippocampal neurons by immunoprecipitation and acyl-biotin exchange (ABE). *Journal of visualized experiments : JoVE*. 2013(72).

11. Drisdel RC, Alexander JK, Sayeed A, Green WN. Assays of protein palmitoylation. *Methods*. 2006;40(2):127-134.

12. Wan J, Roth AF, Bailey AO, Davis NG. Palmitoylated proteins: purification and identification. *Nature protocols*. 2007;2(7):1573-1584.

13. Martin BR, Wang C, Adibekian A, Tully SE, Cravatt BF. Global profiling of dynamic protein palmitoylation. *Nature methods*. 2012;9(1):84-89.

14. Pagano MA, Poletto G, Di Maira G, et al. Tetrabromocinnamic acid (TBCA) and related compounds represent a new class of specific protein kinase CK2 inhibitors. *Chembiochem : a European journal of chemical biology*. 2007;8(1):129-139.

15. Majeau N, Fromentin R, Savard C, Duval M, Tremblay MJ, Leclerc D. Palmitoylation of hepatitis C virus core protein is important for virion production. *The Journal of biological chemistry*. 2009;284(49):33915-33925.

16. Adu-Gyamfi E, Soni SP, Xue Y, Digman MA, Gratton E, Stahelin RV. The Ebola virus matrix protein penetrates into the plasma membrane: a key step in viral protein 40 (VP40) oligomerization and viral egress. *The Journal of biological chemistry*. 2013;288(8):5779-5789.

17. Soni SP, Adu-Gyamfi E, Yong SS, Jee CS, Stahelin RV. The Ebola virus matrix protein deeply penetrates the plasma membrane: an important step in viral egress. *Biophysical journal*. 2013;104(9):1940-1949.

CHAPTER 3.2

UBIQUITIN-REGULATED NUCLEAR-CYTOPLASMIC TRAFFICKING OF THE NIPAH VIRUS MATRIX PROTEIN IS IMPORTANT FOR VIRAL BUDDING

Ubiquitin-Regulated Nuclear-Cytoplasmic Trafficking of the Nipah Virus Matrix Protein Is Important for Viral Budding

Yao E. Wang[1], Arnold Park[1], Michael Lake[1], Mickey Pentecost[1], Betsabe Torres[1], Tatyana E. Yun[2], Mike C. Wolf[1], Michael R. Holbrook[2,3], Alexander N. Freiberg[2☯], Benhur Lee[1,4,5*☯]

1 Department of Microbiology, Immunology, and Molecular Genetics, UCLA, Los Angeles, California, United States of America, **2** Department of Pathology, University of Texas Medical Branch, Galveston, Texas, United States of America, **3** Integrated Research Facility, National Institutes of Health, National Institute of Allergy and Infectious Diseases, Frederick, Maryland, United States of America, **4** Department of Pathology and Laboratory Medicine, UCLA, Los Angeles, California, United States of America, **5** UCLA AIDS Institute, UCLA, Los Angeles, California, United States of America

Abstract

Paramyxoviruses are known to replicate in the cytoplasm and bud from the plasma membrane. Matrix is the major structural protein in paramyxoviruses that mediates viral assembly and budding. Curiously, the matrix proteins of a few paramyxoviruses have been found in the nucleus, although the biological function associated with this nuclear localization remains obscure. We report here that the nuclear-cytoplasmic trafficking of the Nipah virus matrix (NiV-M) protein and associated post-translational modification play a critical role in matrix-mediated virus budding. Nipah virus (NiV) is a highly pathogenic emerging paramyxovirus that causes fatal encephalitis in humans, and is classified as a Biosafety Level 4 (BSL4) pathogen. During live NiV infection, NiV-M was first detected in the nucleus at early stages of infection before subsequent localization to the cytoplasm and the plasma membrane. Mutations in the putative bipartite nuclear localization signal (NLS) and the leucine-rich nuclear export signal (NES) found in NiV-M impaired its nuclear-cytoplasmic trafficking and also abolished NiV-M budding. A highly conserved lysine residue in the NLS served dual functions: its positive charge was important for mediating nuclear import, and it was also a potential site for monoubiquitination which regulates nuclear export of the protein. Concordantly, overexpression of ubiquitin enhanced NiV-M budding whereas depletion of free ubiquitin in the cell (via proteasome inhibitors) resulted in nuclear retention of NiV-M and blocked viral budding. Live Nipah virus budding was exquisitely sensitive to proteasome inhibitors: bortezomib, an FDA-approved proteasome inhibitor for treating multiple myeloma, reduced viral titers with an IC_{50} of 2.7 nM, which is 100-fold less than the peak plasma concentration that can be achieved in humans. This opens up the possibility of using an "off-the-shelf" therapeutic against acute NiV infection.

Citation: Wang YE, Park A, Lake M, Pentecost M, Torres B, et al. (2010) Ubiquitin-Regulated Nuclear-Cytoplasmic Trafficking of the Nipah Virus Matrix Protein Is Important for Viral Budding. PLoS Pathog 6(11): e1001186. doi:10.1371/journal.ppat.1001186

Editor: Christopher F. Basler, Mount Sinai School of Medicine, United States of America

Received October 6, 2009; **Accepted** October 11, 2010; **Published** November 11, 2010

Funding: This work was supported by the Cellular and Molecular Biology Training grant (T32 GM007185) to A.P., the Molecular Pathogenesis Training Grant and UCLA Warsaw Fellowship to M.C.W. (AI07323), and NIH grants to B.L. (U01 AI070495, U01 AI082100, R01 AI069317), M.R.H. (U01 AI070495, U01 AI082100) and A.N.F. (U01 AI070495, U01 AI082100). B.T. was supported by a National Science Foundation grant (HRD-0603239) and the Maximizing Student Diversity Program (NIH grant GM055052). We also acknowledge support from the Pacific Southwest Regional Center of Excellence for Biodefense & Emerging Infectious Diseases (U54 AI065359) and the UCLA AIDS Institute and CFAR (P30 AI028697). B.L. also thanks the Burroughs Wellcome Fund and the Rockefeller Brothers Fund for providing initial unrestricted funds to explore new fields. The funders had no role in study design, data collection and analysis, decision to publish, or preparation of the manuscript.

Competing Interests: The authors have declared that no competing interests exist.

* E-mail: bleebhl@ucla.edu

☯ These authors contributed equally to this work.

Introduction

Nipah virus (NiV) is a highly pathogenic paramyxovirus that has recently emerged from fruit bats to cause fatal diseases in humans [1,2,3]. It was first identified as the etiologic agent responsible for an outbreak of severe encephalitis in Malaysia and Singapore that began in 1998 and continued into 1999 with a case-fatality rate of 40% [3]. In the initial cases of NiV infection, the virus is thought to have transmitted from pigs to humans, although it is able to infect a broad spectrum of animal hosts under natural and experimental conditions [1,4]. Later outbreaks of NiV encephalitis in Bangladesh were associated with an increased mortality rate (up to 75%), and there has been evidence for direct human-to-human transmission [5]. The high virulence of the viruses and the absence of effective therapeutic modalities and vaccines have led to the classification of NiV and the closely-related Hendra virus (HeV) as Biosafety Level 4 (BSL4) pathogens [1]. Indeed, recent outbreaks of Hendra virus in Queensland, Australia (Aug-Sep 2009) have killed 3 horses and one veterinarian, and led to the quarantine of affected horse farms and potentially infected individuals [6]. Thus, NiV and HeV infections pose an ongoing threat to both agriculture and public health.

NiV and HeV comprise a new genus Henipavirus within the family *Paramyxoviridae*. This is a family of viruses with negative-stranded RNA genomes and lipid envelopes derived from the host cell membrane. The genome contains six principle genes:

Author Summary

Nipah virus (NiV) is a lethal, newly emerging virus that causes fatal inflammation of the brain and has a high death rate in infected humans. NiV and the closely related Hendra virus (HeV) can also infect agriculturally important livestock such as pigs and horses. The lack of effective vaccines and treatments, and the ongoing threat they pose to both agriculture and public health, have led to the classification of NiV and HeV as Biosafety Level 4 (BSL4) pathogens. Paramyxoviruses such as NiV are known to replicate in the cytoplasm and bud from the plasma membrane. Viral assembly and budding is mediated by the matrix structural protein. However, we found, quite unexpectedly, that the matrix protein of NiV needs to transit through the nucleus before gaining the functional ability to localize and bud from the plasma membrane. Although NiV-M has putative nuclear import and export signals, we also found that ubiquitination of a conserved lysine residue in NiV-M is critical for nuclear export, subsequent membrane localization and viral budding. Proteasome inhibitors, which deplete cellular pools of free ubiquitin, potently reduce viral titers during live NiV infection, opening up new possibilities for therapeutics against acute NiV infection.

nucleocapsid (N), phosphoprotein (P), polymerase (L), matrix (M), fusion (F) and attachment (HN, H or G) proteins [7]. Paramyxoviruses are known to replicate in the cytoplasm, and progeny virions are released from the plasma membrane of the host cell. Viral assembly and budding are orchestrated by the matrix protein (M), a major structural protein underlying the viral envelope [7,8,9]. Previous studies have shown that when expressed alone in the cell, NiV-M in itself carries sufficient information for the spontaneous formation and release of viral-like particles (VLPs) in the absence of other viral components [10,11,12]. However, despite the identification of the YMYL motif in NiV-M as a potential late-domain [10] and the YPLGVG motif as another requirement for budding [12], the intracellular trafficking and budding pathways of NiV-M remain poorly defined. In our attempt to characterize the trafficking pathway of NiV-M, we found, quite unexpectedly, that it translocates to the nucleus at early stages of infection before localizing to the plasma membrane, suggesting a previously unappreciated role for the nuclear-cytoplasmic trafficking of the Nipah matrix protein in the viral life cycle.

Though paramyxoviruses replicate in the cytoplasm, nuclear localization of viral accessory proteins has been described before. For example, the W protein of NiV inhibits host interferon response by sequestering STAT1 in the nucleus [13,14,15], and a fraction of the V protein of human parainfluenza virus type 2 can be found in the nucleus [16]. The nuclear localization of viral structural proteins, however, is less expected. Within *Paramyxoviridae*, the matrix protein has been reported to localize to the nuclear compartment in three cases so far: Sendai virus (SeV) [17], Newcastle disease virus (NDV) [18,19,20] and human respiratory syncytial virus (HRSV) [21,22,23]. In SeV and NDV, although the nuclear localization of M was clearly described, the biological function of this nuclear localization remains undefined. Faaberg et al examined more than 10 strains of NDV and found that the degree of M nuclear localization appears unrelated to virulence *per se* [24]. In the case of HRSV, Ghildyal et al showed that nuclear extract from HRSV-infected cells supports in vitro transcription less efficiently compared to mock-infected cells, but it has yet to be demonstrated that this inhibition is directly attributable to M [23]. A recent study on HRSV showed that Crm1-dependent nuclear export of the matrix protein is important for viral assembly and budding, suggesting that nuclear trafficking of M is somehow involved in effectuating proper viral budding [21]. However, it remains unclear why M budding needs a nuclear transit phase or whether M's nuclear localization has additional biological functions.

For proteins larger than 40 kD, efficient transport across the nuclear membrane is mediated by specific import and export signals [25,26]. There are two types of nuclear localization signals (NLSs) that have been well characterized. A monopartite NLS consists of one single cluster of positively charged amino acid residues such as lysine (K) or arginine (R), whereas a bipartite NLS contains two stretches of K/R residues conforming to the consensus (K/R)(K/R)-X_{10-12}-(K/R)(K/R) (where X stands for any amino acid residue) [27,28,29]. Nuclear export signals (NESs) are less well-defined although leucine/isoleucine-rich stretches have been identified as NESs. The most well-defined nuclear export pathway involves the chromosomal region maintenance protein 1 (CRM-1), which recognizes these leucine/isoleucine-rich NESs [30,31]. Additionally, post-translational modifications such as ubiquitination and SUMOylation have also been shown to regulate the nuclear-cytoplasmic trafficking of cellular proteins including p53, NF-kB, PTEN, and NEMO [32,33,34,35,36], although their involvement in viral protein trafficking is less known. Nevertheless, many viruses have evolved to co-opt the cellular ubiquitin/proteasome system as a means of manipulating the host cell cycle, evading the immune system as well as egressing from the infected cell [37,38].

Here, we find in one viral structural protein, the use and convergence of three well known cellular pathways for nuclear-cytoplasmic trafficking. We report that proper nuclear-cytoplasmic trafficking of NiV-M is essential for viral budding, and that NiV-M's nuclear-cytoplasmic trafficking is regulated by a putative bipartite NLS, a leucine-rich NES, as well as potential ubiquitination on a conserved lysine residue located in the bipartite NLS itself. Not only does this lysine play key roles in both nuclear import and export, it is also indispensable for the plasma membrane targeting of NiV-M and its subsequent incorporation into virions. Live Nipah virus budding is exquisitely sensitive to ubiquitin depletion, which leads to the nuclear retention of NiV-M. Our results suggest the clinical use of FDA-approved proteasome inhibitors such as bortezomib (Velcade) as a potential "off-the-shelf" therapeutic against acute NiV infection.

Results

Nipah virus matrix protein transits through the nuclear compartment before it localizes to the plasma membrane

In order to examine the subcellular localization of Nipah virus matrix protein (NiV-M) during the natural course of viral infection, NiV-infected cells were fixed at different time points post-infection and processed for analysis by confocal microscopy. The polyclonal anti-NiV-M antibody used in these experiments was raised by immunizing rabbits with a peptide corresponding to amino acids 29–49 of NiV-M. We verified that this affinity purified antibody was highly specific to NiV-M and had very low background staining in M non-expressing cells (Fig. S1).

At early time points (between 8 and 16 hrs) post-infection, many cells had M protein primarily concentrated in the nuclei and fluorescence followed a discrete punctuate staining pattern (Figs. 1A to C). At later time points (20 to 24 hrs), NiV-M protein

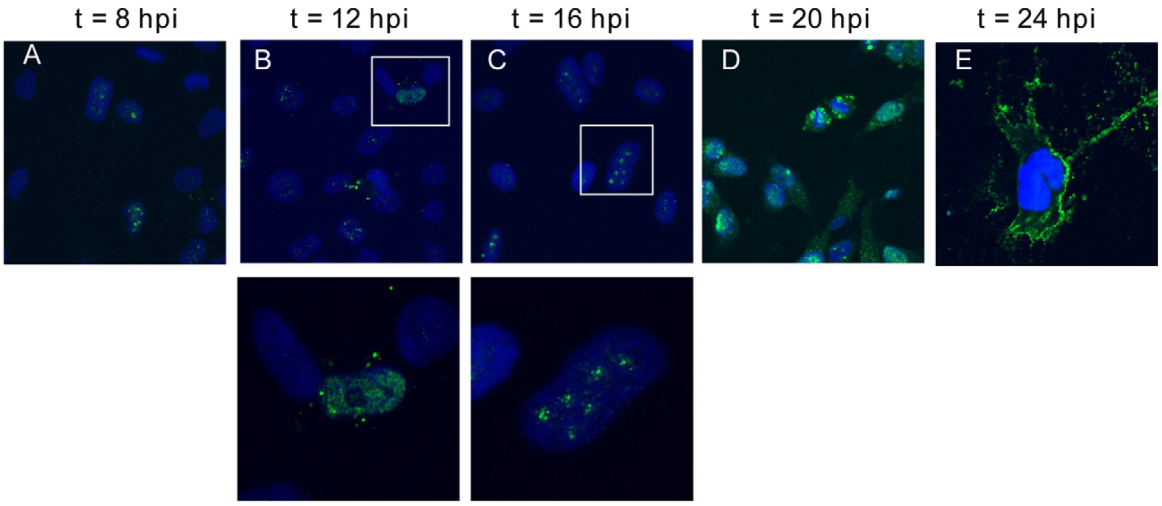

Figure 1. Nuclear-cytoplasmic trafficking of Nipah virus matrix protein (NiV-M) during live viral infection. HeLa cells plated on poly-lysine-coated glass coverslips were incubated with Nipah virus Malaysia strain for 1 hr at 37°C and then fresh growth medium for up to 24 hrs. At (**A**) 8, (**B**) 12, (**C**) 16, (**D**) 20, and (**E**) 24 hpi, cells were fixed with 10% formalin, stained with rabbit anti-M polyclonal antibody and imaged on a confocal fluorescent microscope (63× magnification). DAPI was used for visualization of the nuclei. Insets in (B) and (C) indicate nuclear localization of M in infected cells. Experiments were performed under BSL4 conditions.
doi:10.1371/journal.ppat.1001186.g001

was distributed diffusely in both the cytoplasm and nucleus of infected cells (Figs. 1D and E). At the latest time-point examined (24 hrs), when syncytia have begun to form, NiV-M was more clearly localized to patches on the plasma membrane and filamentous membrane extensions.

To facilitate further biochemical characterizations and mutagenesis studies of NiV-M, we generated an N-terminally triple FLAG-tagged NiV-M expression construct (3XFLAG-M). This tagged protein, when expressed alone in HeLa cells, exhibited similar localization patterns as those seen during the natural course of viral infection. It concentrated in the nuclear compartment before the cytoplasmic staining became prominent (Fig. S2). A GFP-M fusion protein also behaved in a similar manner (data not shown).

Table 1. Alignment of Nipah matrix sequence with known NLSs.

Monopartite NLS consensus	**short stretch of K/R**
SV40 T Antigen	P**KKKRK**V
Histone H2B	G**KKR**S**K**V
NiV matrix	^{82}**KRKK**I**R**^{87}
Bipartite NLS consensus	**(K/R) (K/R) -X_{10-12}- (K/R) (K/R)**
Nucleoplasmin	**KR**PAATKKAGQA**KKKK**LDK
Human p53	**KR**ALPNNTSSSPQP**KKK**P
NiV-M	^{244}**RR**AGKYYSVDYC**RRK**^{258}

(Note: NLS = Nuclear Localization Signal; K = lysine; R = arginine; X = any amino acid residue. The positively-charged amino acid residues in each NLS are in bold.)
doi:10.1371/journal.ppat.1001186.t001

NiV-M possesses a putative bipartite nuclear localization signal (NLS) and a leucine-rich nuclear export signal (NES)

The calculated molecular weight of NiV-M is 39 kD, which is around the upper limit for free diffusion across the nuclear envelope. Efficient nuclear import and export of proteins >20–40 kD usually require nuclear localization signals (NLSs) and nuclear export signals (NESs), respectively [26]. Sequence analysis of NiV-M revealed the presence of one cluster of positively charged amino acids analogous to known monopartite NLSs as well as a potential bipartite NLS consisting of two short stretches of lysines/arginines separated by ten other amino acid residues (Table 1). There are also two leucine/isoleucine-rich stretches in NiV-M that conform to the consensus for NESs (Table 2).

To test whether the NLSs are functional, we performed alanine substitution of key lysine/arginine residues. Subcellular localization of these mutants was examined by immunofluorescence microscopy (Fig. 2A), and quantification of the cytoplasmic/nuclear fluorescence intensity ratio was performed as described in *Materials and Methods*. The monopartite NLS mutant did not give a very obvious phenotype compared to the wild-type matrix protein and showed large cell-to-cell variations. This mutant was therefore excluded from further analysis. Mutating the first part of the

Table 2. Alignment of Nipah matrix sequence with known NESs.

NES consensus	**L-X_{2-3}-L-X_{2-3}-L-X-L**
HIV Rev	**L**PP**L**ER**L**T**L**
Ad5 E1B	**L**YPE**L**RRI**L**T**I**
NiV-M (N-ter)	^{106} **LL**EE**L**C**L**KV^{115}
NiV-M (C-ter)	^{268}**L**GS**I**GG**L**S**L**^{276}

(Note: NES = Nuclear Export Signal; L = Leucine; I = Isoleucine; X = any amino acid residue. The key L/I residues in each NES are in bold.)
doi:10.1371/journal.ppat.1001186.t002

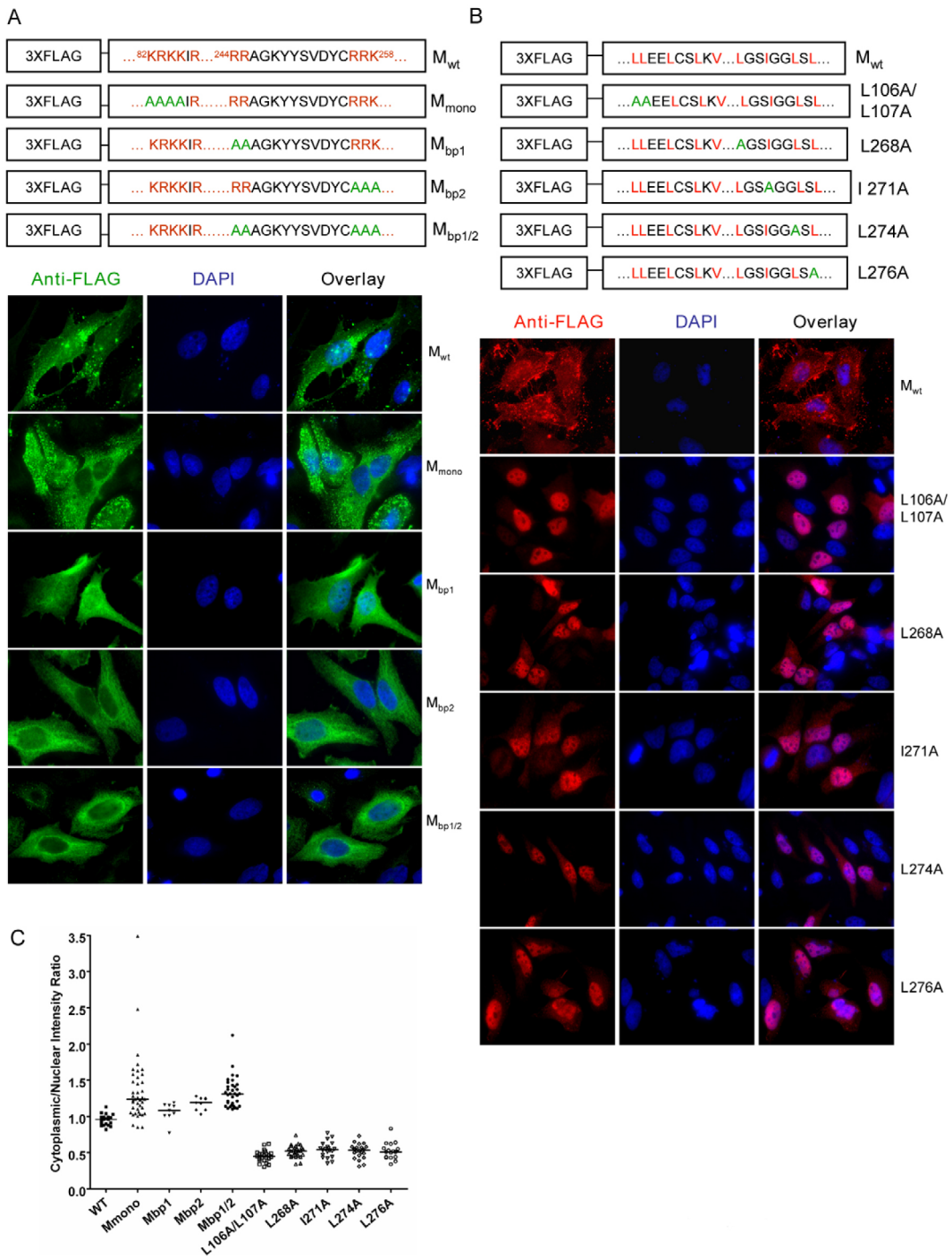

Figure 2. Mutagenesis studies of potential nuclear localization signals (NLSs) and nuclear export signals (NESs) in NiV-M. Positively charged amino acid residues in the predicted monopartite and bipartite NLSs (**A**) or key leucine/isoleucine residues in the potential NESs (**B**) were mutated to alanines using site-directed mutagenesis. HeLa cells expressing the indicated proteins were stained with an anti-FLAG monoclonal antibody as well as DAPI. Representative fields are shown in (A) and (B), and (**C**) shows the quantification of cytoplasmic/nuclear fluorescence intensity (C:N) ratios for ~10–50 individual cells analyzed for each mutant as described in *Materials and Methods*. Compared to Mwt, statistically significant increases in C:N ratios were observed for M_{bp1} ($p<0.01$), M_{bp2} ($p<0.0001$) and $M_{bp1/2}$ ($p<0.0001$) (unpaired t-test).
doi:10.1371/journal.ppat.1001186.g002

bipartite signal (M_{bp1}) led to a mild nuclear exclusion phenotype, whereas mutating the second part (M_{bp2}) had a more apparent effect. When both parts of the bipartite NLS were mutated ($M_{bp1/2}$), nuclear import was most obviously impaired (Fig. 2A). These visual differences were confirmed by the quantification of the cytoplasmic/nuclear fluorescence intensity (C:N) ratios shown in Fig. 2C. Note that M_{bp1}, M_{bp2}, and $M_{bp1/2}$ had statistically significant increases in C:N ratios compared to M_{wt}, indicating increased cytoplasmic retention relative to nuclear import. Interestingly, we also noticed that while M_{wt} localized to punctuate structures in the cytoplasm as well as patches on the plasma membrane, the bi-partite NLS mutants, especially M_{bp2} and $M_{bp1/2,}$ exhibited more diffused localization patterns.

Similarly, the key leucine/isoleucine residues in the potential NESs were mutated to alanines individually. All the NES mutants demonstrated nuclear retention phenotypes (Figs. 2B and C). However, previous studies have shown that deletion of the YMYL motif or the YPLGVG motif, originally thought to be late domain motifs, and neither of which conforms to a classical nuclear export sequence, also resulted in the nuclear retention of NiV-M [10,12]. To test whether the two putative NESs in NiV-M are functional in the context of a heterologous protein, we adopted an experimental system similar to that developed by Henderson *et al* [39]. A fluorescent protein mCherry was fused to the C-terminus of the HIV Rev protein. This fusion protein localized to both the nucleus and the cytoplasm (Fig. 3A, panel a). When the endogenous NES in Rev was mutated (RevΔNES), the resulting fusion protein was restricted to the nuclear compartment (Fig. 3A, panel b), whereas the insertion of a short peptide corresponding to the first putative NES of NiV-M (amino acids 106–117) between RevΔNES and mCherry partially restored nuclear export (Fig. 3A, panel c). Insertion of a peptide corresponding to the second putative NES of NiV-M (amino acids 264–280) did not result in significant nuclear export of the fusion protein (data not shown). As a control, the endogenous Rev NES was inserted in the place of NiV-M NES, which led to significant nuclear export (Fig. 3A, panel d) as reported previously by other groups [39,40]. Fig. 3B provides a semi-quantitative representation of the results in Fig. 3A by counting the relative distribution of the Rev-mCherry fusion proteins in the nucleus vs. cytoplasm of 100 transfected cells. These experiments were done in the presence of 5 μg/ml actinomycin D, which reduces the strength of the endogenous Rev NLS and therefore allows for the detection of relatively weak NESs in this reporter construct [39,41,42].

Our results so far show that NiV-M harbors a putative bi-partite NLS and two leucine/isoleucine-rich stretches that are important for nuclear export as suggested by mutagenesis studies. However, only the first leucine/isoleucine rich motif acts as a *bona fide* nuclear export signal in the context of a heterologous protein. These nuclear import/export phenotypes were recapitulated when we examined the localization of GFP-fused Mwt and NLS/NES mutants (Fig. S3).

Nuclear localization of NiV-M correlates with budding

The most important known function of viral matrix proteins is to mediate viral assembly and budding [7,9]. Indeed, NiV-M, when expressed by itself in the cell, is able to form viral-like particles (VLPs) that spontaneously bud into the supernatant [10,11,12]. We confirmed that both 3XFLAG-tagged M and GFP-M were functional in a VLP budding assay (Figs. S4 and S5), although 3XFLAG-tagged M seemed to bud at reduced levels compared to the untagged M, especially at lower concentrations of transfected DNA. However, at concentrations we normally use for the VLP budding assay (1–2 μg of DNA), the budding index of 3XFLAG-M was not dramatically lower than untagged M. Since NiV-M was first localized to the nucleus before re-localizing to patches on the plasma membrane (Fig. 1), we sought to determine whether the nuclear-cytoplasmic trafficking of M is important for its ability to bud. We first examined the VLP budding of the NLS mutants (Fig. 4A) and found that, interestingly, the nuclear localization of M correlates with its ability to bud. M_{bp1}, which had a mild nuclear exclusion phenotype, formed VLPs at a moderately reduced level compared to wild-type M, whereas M_{bp2} and $M_{bp1/2}$, which were more deficient in nuclear import, were also more severely impaired in their abilities to bud. Fig. 4B shows that all the NES mutants were also deficient in budding, presumably due to their nuclear retention and consequentially their inability to reach the plasma membrane where budding occurs. The budding phenotype of the NLS and NES mutants were quantified by determining their budding index as described in *Materials and Methods* and shown in Fig. 4C and 4D, respectively.

The budding defect exhibited by the NLS and NES mutants is likely due to their nuclear import or export phenotypes rather than the disruption of their conformational integrity, as the budding defective mutants can associate and oligomerize with wild-type M (Fig. S6) and be rescued into VLPs by wild-type M (Fig. S7). Thus far, our data suggest that nuclear-cytoplasmic trafficking contributes to the eventual ability of NiV-M to bud.

A conserved lysine residue plays dual roles in regulating M nuclear-cytoplasmic trafficking

Functional NLSs have been described in the matrix protein of two other paramyxoviruses, namely human respiratory syncytial virus and Newcastle disease virus [18,22]. Our finding that NiV-M possesses a putative NLS spurred us to look at the matrix proteins of other paramyxoviruses to determine the degree to which this motif might be conserved.

We aligned the matrix protein sequences of twelve viruses from different genera within the family *Paramyxoviridae*. Interestingly, in the same region where we identified the bipartite NLS in NiV-M, all twelve viruses had clusters of positively charged amino acids that could potentially function as bipartite NLSs (Fig. 5A). Specifically, the lysine residue in the second part of the bipartite NLS (K258 in NiV-M) was absolutely conserved, suggesting that the lysine itself, and not just the positive charge, might serve important functions. We therefore mutated K258 in NiV-M to an alanine versus an arginine.

As expected, the loss of positive charge impaired the function of the NLS. The K258A mutant was largely excluded from the nucleus, confirming that K258 was a critical part of the bipartite NLS (Fig. 5B). However, the K258R mutant, which retains the positive charge and should therefore have a localization pattern similar to wild-type M, gave a phenotype exactly the opposite of K258A. K258R was retained in the nucleus. This phenomenon was specific to K258, as mutating a nearby non-conserved lysine residue (K263) to arginine did not give an obvious nuclear retention phenotype (Fig. 5B). As in Fig. 2C, the C:N ratios determined for each of these mutants confirmed the visual phenotypes observed (Fig. 5C). Thus, compared to Mwt, the nuclear-excluded K258A mutant had C:N ratios significantly greater than 1 while the nuclear retained K258R mutants had C:N ratios significantly less than 1 ($p<0.0001$ for both comparisons, unpaired t-test). This confirms the importance of the lysine residue itself at position 258 and suggests that potential modification(s) on K258 might be important for nuclear export. When K258 was mutated to arginine, the positive charge still allowed for nuclear import. However, arginines cannot be modified the same way that

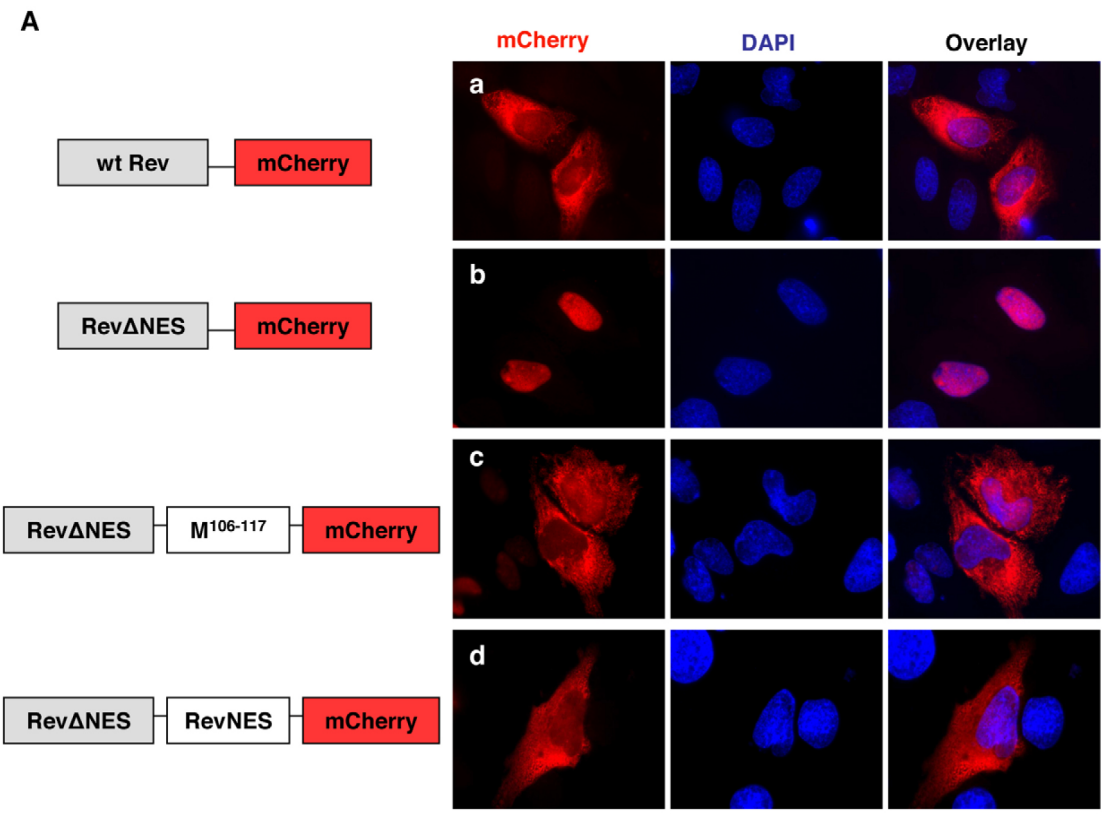

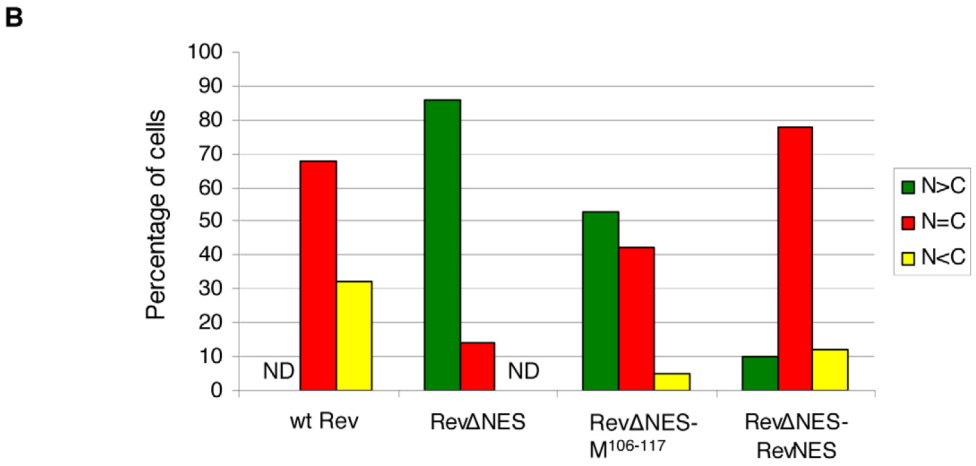

Figure 3. NiV-M NES partially restores nuclear export to an NES-defective HIV Rev. (**A**) HeLa cells were transiently transfected with plasmids encoding Rev-mCherry (panel a), RevΔNES-mCherry (panel b), RevΔNES-$M^{106–117}$-mCherry (panel c), or RevΔNES-RevNES-mCherry (panel d). 24 hrs post transfection, cells were treated with 5 μg/ml actinomycin D for 4 hrs before fixation. Cells were stained with DAPI for visualization of the nuclei and imaged on a fluorescent microscope under 60× magnification. Representative images are shown in (A), and **(B)** shows the quantification of the percentage of cells with the fusion protein localized to only the nucleus (N>C), both the nucleus and the cytoplasm (N=C), or only the cytoplasm (N<C). For each mutant, at least 100 cells were counted. Both $M^{106–117}$ and the endogenous NES from Rev were able to restore nuclear export to the RevΔNES-mCherry fusion protein.
doi:10.1371/journal.ppat.1001186.g003

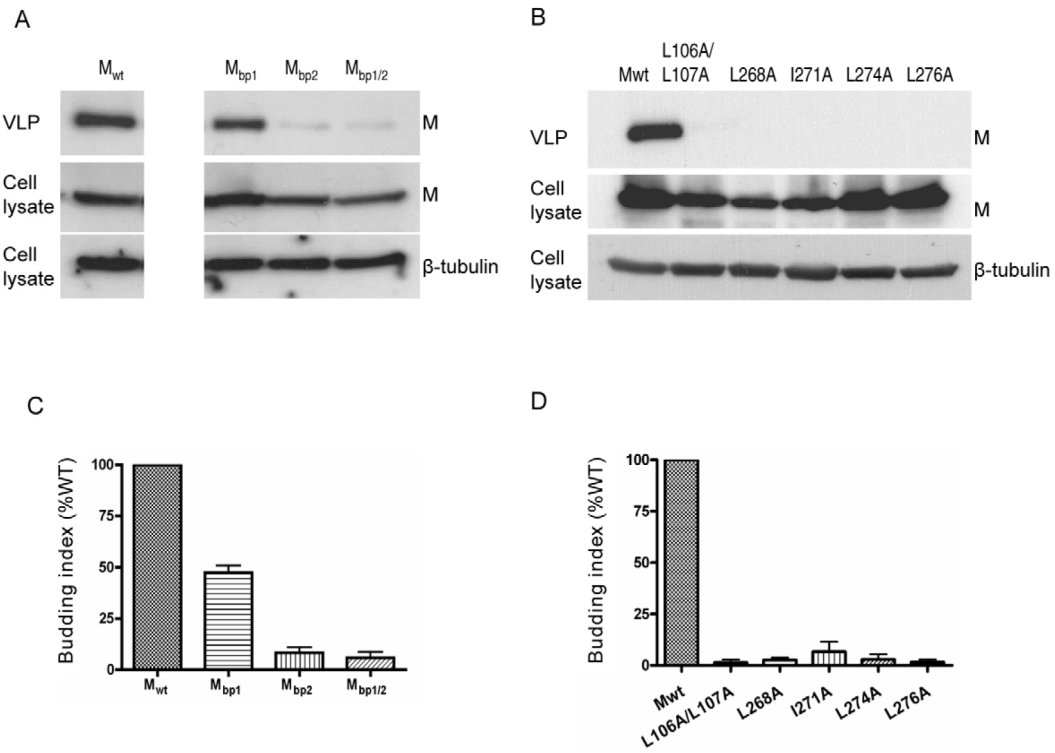

Figure 4. Correlation between the nuclear localization of NiV-M and VLP budding. Viral-like particles were harvested from culture supernatants of cells expressing wild-type NiV-M, NLS mutants (**A**) or NES mutants (**B**) at 24 hpt as described in *Materials and Methods*. VLPs and the corresponding cell lysates were immunoblotted with an anti-FLAG antibody. The cell lysate blots were then stripped and re-probed with an anti-β-tubulin antibody as loading control. Representative results are shown in (A) and (B). (**C**) and (**D**) show the quantification of the budding index for the indicated wild-type and mutant NiV-M proteins as described in *Materials and Methods*. Error bars were calculated from three independent experiments. M mutants that were deficient in either nuclear import or export were also deficient in budding.
doi:10.1371/journal.ppat.1001186.g004

lysines are. Therefore, the K to R mutation could potentially compromise functions associated with the modified K258.

Ubiquitination regulates NiV-M nuclear-cytoplasmic trafficking

Lysine residues could be modified in different ways including ubiquitination, SUMOylation and acetylation. Interestingly, ubiquitination has previously been shown to be involved in the nuclear-cytoplasmic trafficking of cellular proteins such as NF-kB and p53 [35]. Specifically, monoubiquitination on the C-terminus of p53 regulates its nuclear export [32,33]. Thus, we asked if NiV-M might exploit similar pathways for its nuclear-cytoplasmic trafficking behavior.

To test whether ubiquitin was involved, we took advantage of a well-characterized proteasome inhibitor, MG132. MG132 blocks proteasome-dependent degradation of poly-ubiquitinated proteins, thus depleting the cellular pool of free ubiquitin for new conjugations. It has previously been shown to inhibit retroviral budding, presumably because ubiquitin is required for a late step during viral assembly and egress [43,44,45,46].

MG132 treatment resulted in the nuclear retention of GFP-M fusion protein (Fig. 6A, panel b) reminiscent of the phenotype of the K258R mutant (Fig. 5B). Similar results were obtained when another proteasome inhibitor, bortezomib, was used (Fig. S8). Overexpressing an HA-tagged ubiquitin (HA-Ub) in the cells was able to reverse the effect of MG132 (Fig. 6A, panel c), confirming that MG132's effect on the nuclear retention of NiV-M was indeed due to its effect on depleting the cellular pool of free ubiquitin, and suggesting that the ubiquitination of M is important for its nuclear export. As a specificity control, GFP-$M_{bp1/2}$, which is impaired in nuclear import (Fig. S3), did not accumulate in the nucleus upon MG132 treatment (Fig. 6A, panel d).

To biochemically detect the ubiquitinated NiV-M, we co-transfected triple-FLAG tagged M_{wt} or the indicated mutants with HA-Ub. Since polyubiquitination is usually associated with proteasome-dependent protein degradation, whereas monoubiquitination serves regulatory functions, we wanted to specifically look at the monoubiquitinated M species by using a mutated version of ubiquitin in which all the lysine residues are changed to arginines [33]. We immunoprecipitated M with an anti-FLAG antibody and detected the ubiquitinated species with an anti-HA antibody (Fig. 6B). For M_{wt}, there were at least four distinct bands at ~8 kD intervals starting from 60 kD which represents the first monoubiquintinated band above the size of unconjugated 3XFLAG-M (Fig. 6B, arrow). These bands likely represent M monoubiquitinated on four different lysine residues. When the same experiment was performed using K258A or K258R mutant, the banding patterns were different from M_{wt}. The bottom band (indicated by the arrow) was the same for M_{wt} as well as the mutants, likely indicating monoubiquitination on a lysine residue other than K258. The three bands above it, however, were significantly reduced in the mutants compared to the wild-type. These bands likely represent ubiquitinated K258

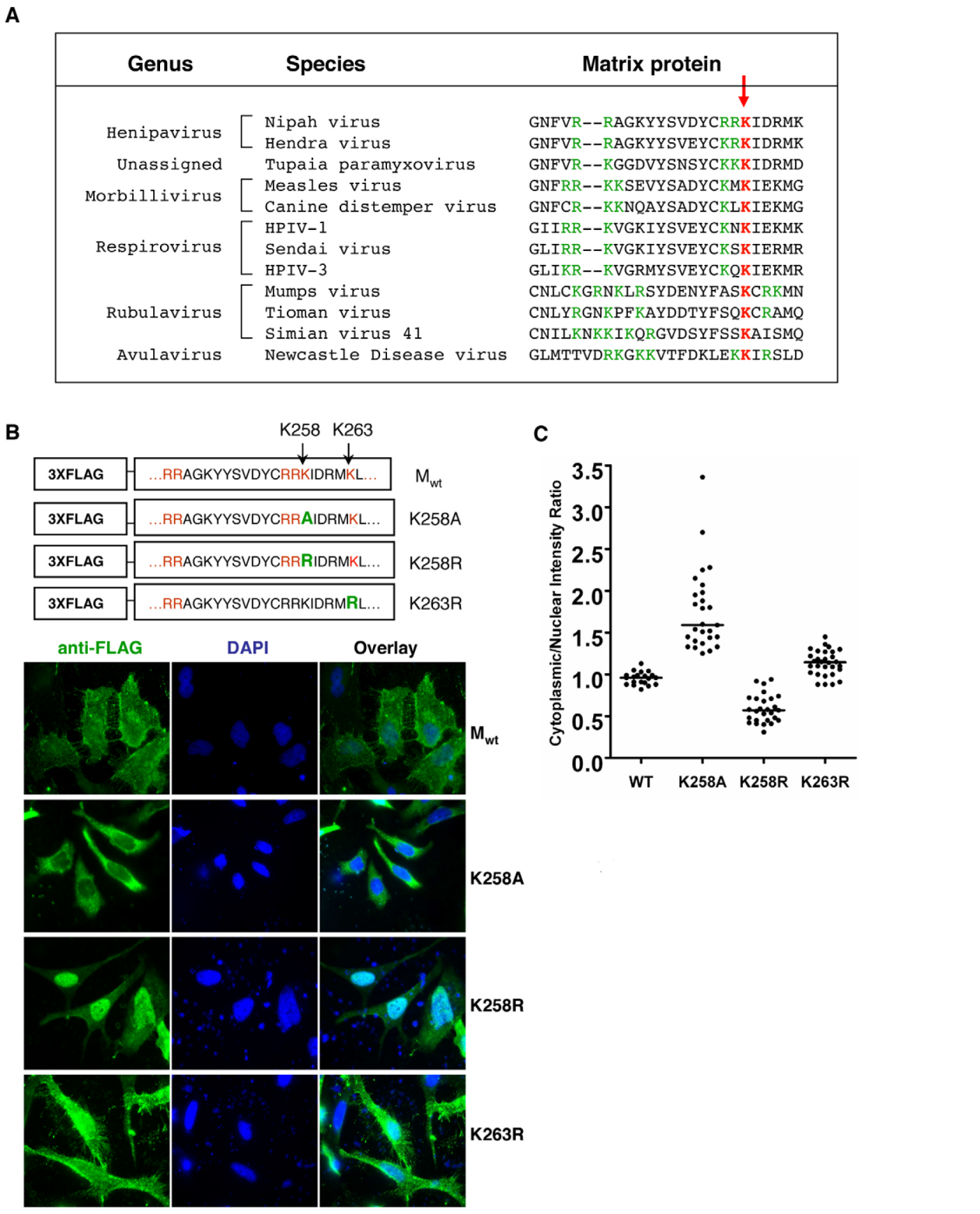

Figure 5. Dual functions of critical residue K258 in regulating NiV-M nuclear-cytoplasmic trafficking. (**A**) The matrix protein sequences of twelve viruses from different genera within the family *Paramyxoviridae* were aligned using CLUSTAL W (version 1.83). Positively charged amino acid residues that conform to the consensus for bipartite NLSs are colored green. The red arrow points to the lysine residue conserved among all twelve viruses. (**B**) K258 in NiV-M was mutated to alanine or arginine using site-directed mutagenesis. As control, K263, a non-conserved lysine in the vicinity

of K258, was also mutated to arginine. HeLa cells transfected with the indicated constructs were stained with mouse anti-FLAG antibody and DAPI. K258A was excluded from the nucleus, whereas K258R was concentrated in the nucleus. The localization of K263R was similar to wild-type M. Quantification of cytoplasmic/nuclear fluorescence intensity ratios is shown in (**C**).
doi:10.1371/journal.ppat.1001186.g005

as well as other lysines whose ubiquitination depends on K258. It was not totally unexpected that the banding patterns of K258A and K258R were not exactly identical. One of them was in the cytoplasm while the other in the nucleus, where distinct ubiquitination machineries might account for the difference. As controls, K263R had the same banding pattern as wild-type, whereas M_{bp2}, in which all three basic amino acid residues in the second part of the bipartite NLS including K258 were simultaneously mutated to alanines, showed a banding pattern similar to K258A.

We therefore hypothesized that ubiquitination on K258 in the nucleus might be necessary for the subsequent nuclear export of NiV-M. The altered subcellular localization of the K258R mutant was likely due to its lack of ubiquitination. To test this hypothesis, we constructed a fusion protein with one copy of ubiquitin fused in-frame to the C-terminus of K258R to mimic monoubiquitination [47,48,49,50]. It has previously been shown that fusion to ubiquitin induces the nuclear export of p53 but had no effect on Max, a nuclear protein known not to be regulated by monoubiquitination [33]. Fusion to ubiquitin was able to restore nuclear export to K258R. While K258R was largely retained in the nucleus, the K258R-Ub fusion protein was clearly more cytoplasmic although in some cells, it was evenly distributed between the nucleus and cytoplasm (Fig. 6C). Fig. 6D quantifies the nuclear:cytoplasmic ratios of K258R and K258R-Ub in ~40–50 cells and confirms the visual phenotypes seen in Fig. 6C.

K258 is important for the membrane association and budding of NiV-M

Since K258 plays key roles in regulating NiV-M trafficking, we asked whether it might also affect the ability of M to bud. We therefore purified viral-like particles (VLPs) from the culture supernatants of HEK293T cells expressing M_{wt}, K258A, K258R, or K263R as control. Both K258A and K258R were deficient in budding, whereas K263R budded at similar levels compared to M_{wt} (Figs. 7A and B). K258R was defective in budding presumably because it was trapped in the nucleus and therefore not able to reach the plasma membrane where budding normally occurs, but it was less intuitively obvious why K258A, which was localized to the cytoplasm, was also budding-deficient.

A closer look at the microscopic images revealed that while M_{wt} localized to patches on the membrane as well as filopodia-like membrane extensions, K258A exhibited a more diffused cytoplasmic localization pattern indicative of a defect in membrane association (Fig. 7C). This was confirmed by a membrane flotation assay (Fig. 7D). While M_{wt} was distributed in both the membrane and non-membrane fractions, the K258A mutant was found almost exclusively in the non-membrane fractions. As controls, wild-type HIV Gag (Gag_{wt}) and a myristoylation site mutant G2A were subjected to the same treatment. Gag_{wt} was in both the membrane and non-membrane fractions, but G2A, which lacks membrane association, was found mainly in the non-membrane fractions as described previously [51,52].

To confirm that the budding defect of K258A was due to its lack of membrane association rather than a conformational defect that prevented its incorporation into the virions, we tried to rescue the budding of K258A by fusing membrane targeting signals to its N-terminus. L10 is the minimal signal required for targeting $p56^{lck}$ to the lipid rafts, whereas S15 from c-Src targets proteins to non-raft membrane compartments [53,54]. Both L10 and S15 were able to rescue the membrane association of K258A, as indicated by the presence of these fusion proteins in the membrane fractions as determined in our membrane flotation assay (Fig. 7E). Fusion to L10 and S15 also restored VLP budding to the K258A mutant (Figs. 7F and G). Indeed, a greater fraction of both L10-K258A and S15-K258A appeared to be in the membrane fractions which correlated with their increased budding index.

Proteasome inhibitors block Nipah virus budding

The proteasome inhibitor MG132, which we have previously shown to inhibit NiV-M nuclear export (Fig. 6A), reduced M VLP budding in a dose-dependent manner (Fig. 8A). This inhibition was not due to potential cytotoxic effect of MG132, as both endogenous (β-tubulin) and exogenous protein (NiV-M) expression levels in the cell lysates were very similar between MG132-treated and untreated samples. The budding inhibition was also seen when a different proteasome inhibitor, bortezomib, was used (Fig. S9). Moreover, the budding inhibition by MG132 could be reversed by overexpressing HA-Ub in the cells (Fig. 8A), confirming that the inhibition was indeed due to the depletion of cellular free ubiquitin. Similar phenotypes were also observed when a different cell line, HeLa, was used instead of HEK293T (Fig. S10), suggesting that this phenomenon is not a cell-type specific effect.

Next, we wanted to confirm the effect of proteasome inhibition on M localization and activity in the context of a live viral infection. MG132 altered M localization during live Nipah virus infection (Fig. 8B), restricting M to the nucleus similar to what we have seen using the transfection system. It also reduced viral titers in a dose-dependent manner, with an IC_{50} of 0.47 nM (Fig. 8C). Under our experimental conditions, at all concentrations tested here, MG132 did not seem to be toxic to the cells as indicated by the cytotoxicity assay (Fig. S11), and the expression levels of cellular (β-actin) and viral (matrix) proteins were very similar between MG132-treated and DMSO-treated cells (Fig. 8C, lower panel). However, MG132 has limited in vivo utility due to its configurational instability [55]. Therefore, we tested another proteasome inhibitor, bortezomib, which is an FDA-approved drug for treating multiple myeloma [56]. A dose response curve for bortezomib indicates that 50% inhibition of viral infection was achieved at 2.7 nM (Fig. 8D), which is 100-fold less than the peak plasma concentration (200–300 nM) that can be reached in humans [57,58].

Discussion

Most negative-stranded RNA viruses, including paramyxoviruses such as Nipah virus (NiV), are known to replicate in the cytoplasm [7]. Quite unexpectedly, we found that the matrix protein of NiV transits through the nuclear compartment before reaching the plasma membrane both during live viral infection and when expressed alone in the cells.

Within the *Paramyxoviridae*, nuclear localization of matrix proteins has previously been described for Newcastle disease virus, Sendai virus and human respiratory syncytial virus [17,20,23]. However, to our knowledge, this phenomenon has not been directly associated with any biological functions. Our

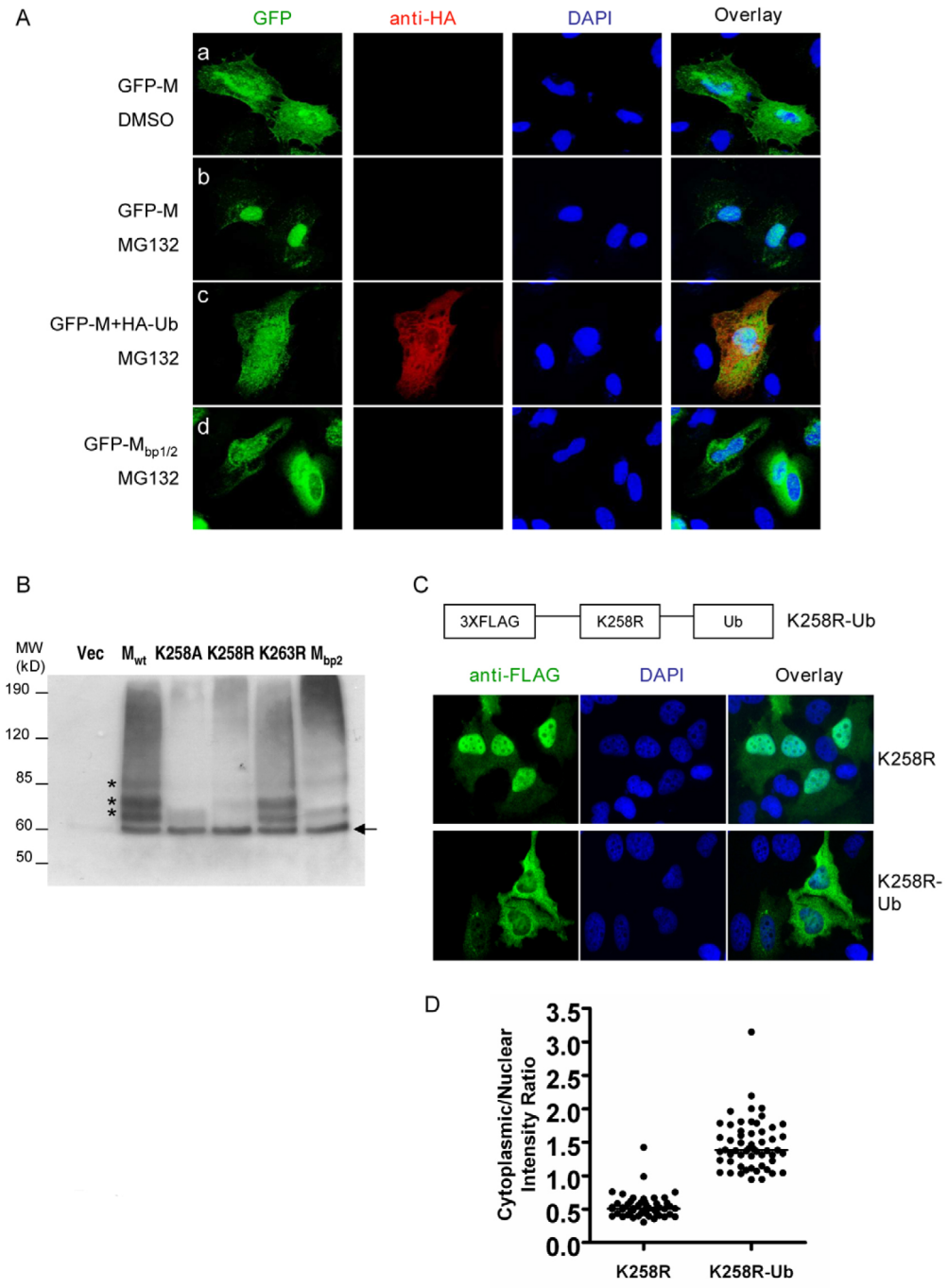

Figure 6. Ubiquitination regulates NiV-M nuclear export. (**A**) Ubiquitin depletion by MG132 treatment inhibits M nuclear export. HeLa cells were transfected with GFP-M alone (panels a and b), GFP-M plus HA-Ub (panel c) or GFP-$M_{bp1/2}$ (panel d). 24 hpt, cells were treated with 50 μM MG132 or DMSO as indicated, fixed 6 hrs later with 2% paraformaldehyde, stained with DAPI as well as a mouse anti-HA antibody followed by Alexa594-conjugated goat-anti-mouse secondary antibody to identify cells expressing HA-Ub, and imaged on a fluorescent microscope. Representative images are shown. (**B**) Ubiquitination patterns of wild-type M and the indicated mutants. HEK293T cells were co-transfected with HA-Ub (in which all the lysines were mutated to arginines to specifically look at monoubiquitination) and the indicated 3XFLAG-tagged M mutants or empty vector as control. M was immunoprecipitated as described in *Materials and Methods* and the ubiquitinated species were detected by immunoblotting using an anti-HA antibody. The banding patterns of K258A, K258R and M_{bp2} were different from Mwt, whereas K263R was similar to Mwt. (**C**) Mimicking monoubiquitination restores nuclear export to K258R. One copy of ubiquitin was fused in frame to the C-terminus of 3XFLAG-K258R, and HeLa cells expressing K258R or K258R-Ub were stained with an anti-FLAG antibody. Quantification of the cytoplasmic/nuclear fluorescence intensity ratio for each mutant is shown in (**D**). There is significant difference between the localization patterns of K258R and K258R-Ub ($p<0.0001$, unpaired t test).

doi:10.1371/journal.ppat.1001186.g006

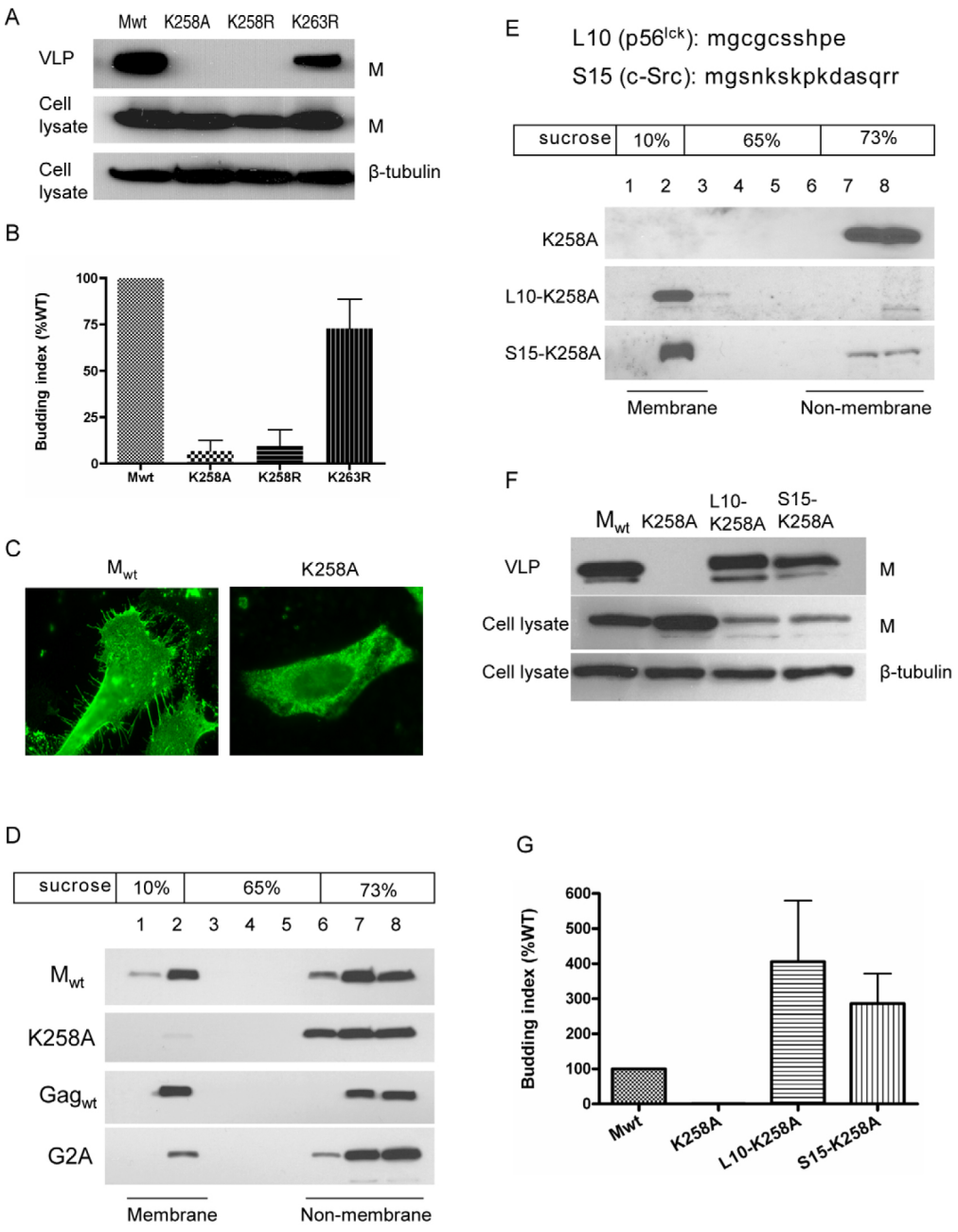

Figure 7. K258 is critical for NiV-M membrane association and budding. (**A**) NiV-M K258 mutants are deficient in VLP budding. VLP and cell lysate samples were prepared from cells expressing wild-type M, K258A, K258R or K263R at 24 hpt as described in *Materials and Methods*. Immunoblotting was performed using an anti-FLAG monoclonal antibody, then the cell lysate blot was stripped and re-probed with an anti-β-tubulin antibody as loading control. Both K258A and K258R were expressed in the cells at similar levels compared to wild-type M, but they were absent from the VLPs. The experiment was repeated three times and representative results are shown. (**B**) Quantification of the budding index for the wild-type and mutant NiV-M proteins shown in (A). (**C**) Wild-type M localized to membrane patches and fine filopodia extensions while the K258A mutant did not. (**D**) K258A is deficient in membrane association. HEK293T cells expressing wild-type NiV-M, K258A, wild-type HIV Gag, or a myristoylation mutant of HIV Gag (G2A) were harvested at 24 hpt. Cell homogenates were loaded at the bottom of a 10–73% discontinuous sucrose gradient and ultracentrifuged for 16 hrs at 100,000×g. Eight fractions were collected from the top, and proteins were extracted using methanol/chloroform prior to immunoblotting with anti-NiV-M (in the case of M_{wt} and K258A) or anti-myc (Gag_{wt} and G2A) antibodies. Membrane-associated proteins were collected at the interface between 10% and 65% sucrose as "fraction 2" as described previously [71]. (**E**) Fusion to L10 or S15, the membrane targeting N-terminal peptide sequence from $p56^{lck}$ and c-Src, respectively, restores membrane association to the K258A mutant. Membrane flotation centrifugation was performed as in (D). (**F**) Rescue of K258A budding by L10 and S15. VLP and cell lysate samples were prepared from HEK293T cells expressing the indicated constructs and examined by immunoblotting using a rabbit anti-NiV-M antibody. The cell lysate blot was also probed with an anti-β-tubulin antibody as loading control. The experiment was repeated three times. Representative blots are shown in (F), and the quantification of the budding indices is shown in (**G**).
doi:10.1371/journal.ppat.1001186.g007

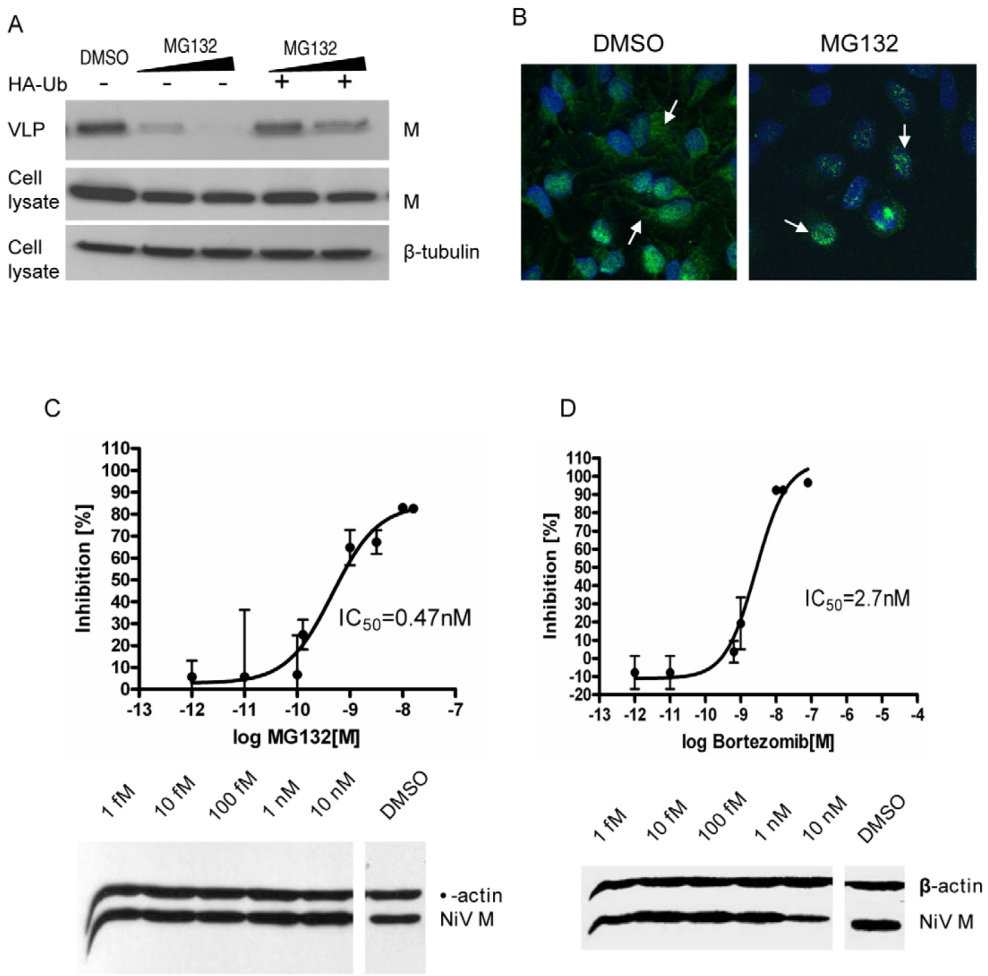

Figure 8. MG132 and bortezomib inhibit NiV-M nuclear export during live viral infection and reduce viral titers. (**A**) NiV-M VLP budding in the presence of MG132. HEK293T cells expressing 3XFLAG-M (left three lanes) or 3XFLAG-M plus HA-Ub (right two lanes) were incubated with DMSO, 10 μM or 50 μM MG132 for 12 hrs, and VLPs produced during this period were harvested as described in *Materials and Methods*. VLPs and cell lysates were immunoblotted with an anti-FLAG antibody, then the cell lysate blot was stripped and re-probed with an anti-β-tubulin antibody as loading control. (**B**) MG132 altered M localization during live viral infection. HeLa cells infected with Nipah virus Malaysia strain were incubated with 50 μM MG132 or DMSO for 8 hrs starting from 15 hpi. Cells were then stained with an anti-M antibody and imaged on a confocal microscope. MG132 restricted M localization to the nuclear compartment. (**C**) and (**D**) Dose-response curves of Nipah viral titers in the presence of MG132 (C) or bortezomib (D). HeLa cells were incubated with NiV for 1 hr at 37°C and then fresh growth medium. 15 hpi, serial dilutions of MG132 or bortezomib were added, yielding final concentrations ranging from 10 nM to 1 fM. Considering the short half-life of bortezomib (9–15 hrs), it was re-added 12 hrs later. Supernatants were collected at 40 hpi and viral titers were determined by plaque assay. To calculate the 50% inhibitory concentration (IC_{50}), the resulting data were fit to the sigmoidal dose-response curve (GraphPad Prism software version 4.00) using the equation: % inhibition = minimal inhibition + (maximal inhibition-minimal inhibition)/(1+10^(LogIC_{50}-Log drug concentration)). Results shown are from two independent experiments with triplicates for each data point. The infected cells were harvested, and the expression of cellular (β-actin) and viral (matrix) proteins was examined by immunoblotting.
doi:10.1371/journal.ppat.1001186.g008

results suggest that the nuclear translocation of NiV-M is important for viral budding, as all the nuclear-excluded mutants are deficient in VLP formation (Figs. 4A, 4C, 7A and 7B). A straightforward explanation would be that post-translational modification(s) occurs in the nucleus which allows NiV-M to interact with the budding machinery once it is exported into the cytoplasm. Indeed, our data support the hypothesis that ubiquitination might be a key regulator of NiV-M intracellular trafficking and function.

The 76-amino-acid protein modifier ubiquitin is involved in the activity of many cellular as well as viral proteins [38,59,60]. Previous studies have shown that the ubiquitin-proteasome machinery is present in both the cytoplasmic and nuclear compartments of the cell [33,61,62], and a role for ubiquitin in protein nuclear/cytoplasmic trafficking has been demonstrated in the cases of cellular proteins including p53, PTEN and NF-kB [32,33,34,35,36]. We found that ubiquitination is important for NiV-M nuclear export as well as budding. Mutation of the putative ubiquitination site K258 altered M subcellular localization (Fig. 5B) and abrogated budding (Fig. 7A). These phenotypes were recapitulated when ubiquitin was depleted from the cells (Fig. 6A and Fig. 8). The involvement of ubiquitin in NiV-M

budding is also reflected in our observation that overexpression of ubiquitin in the cells enhances M budding (Fig. S12). This effect is likely due to the ubiquitination of M *per se* instead of stimulating the cellular budding machinery, as the enhancement was not observed when a ubiquitination-site mutant was used.

Ubiquitin has previously been shown to be required for a late step during retroviral budding, namely the fission of virions from the cellular membrane, a process that involves the interaction between the late-domain in the Gag proteins and the cellular ESCRT complexes [37,43,63]. In the case of NiV-M, however, the dependence on ubiquitin seems to be via a different mechanism. Our finding that the potential ubiquitination-site mutant K258A was not membrane-associated seems to suggest a role for ubiquitin in targeting M to the plasma membrane. Plasma membrane targeting is usually mediated by N-terminal acylations such as the myristoylation of HIV Gag and the palmitoylation of Synaptosomal-associated protein of 25 kDa (SNAP-25) [64,65]. Our sequence analysis of NiV-M did not reveal the presence of such signals, and membrane targeting is unlikely attributed solely to the interaction between M and viral transmembrane glycoproteins such as F and G, as M was able to reach the plasma membrane when expressed alone. It is possible that the ubiquitination of NiV-M might contribute to its recognition by a cellular factor that transports it to the plasma membrane. Fusing a copy of ubiquitin to the C-terminus of the K258R mutant to mimic monoubiquitination restored nuclear export (Fig. 6C), but this fusion protein was still not membrane-associated and failed to bud (data not shown), suggesting that the requirement for ubiquitin in the case of membrane targeting might be context-dependent. However, we cannot rule out the possibility that modifications other than ubiquitination might be involved.

Additionally, we found that membrane targeting positively correlates with budding. L10 and S15 peptides seem to be more potent membrane-targeting signals compared to the endogenous signal in NiV-M, as L10-K258A and S15-K258A were found predominantly in the membrane fractions whereas Mwt was present in both membrane and non-membrane fractions (Figs. 7D and F). The more efficient membrane targeting conferred by L10 and S15 translated to higher levels of budding (Figs. 7G and H).

The cholesterol- and sphingolipid-rich membrane microdomains, or lipid rafts, have been implicated in the budding of some enveloped viruses including a few paramyxoviruses [66,67,68]. The fact that both L10 and S15, which target proteins to lipid raft and non-raft compartments, respectively, were equally capable of restoring NiV-M K258A budding seems to suggest that the budding of NiV-M does not require localization to the lipid rafts. This is also consistent with our observation that NiV-M localized to, but did not concentrate in lipid raft fractions (our unpublished observation). However, no conclusions can be drawn at this point as to where budding occurs during live viral infection.

NiV-M possesses two leucine/isoleucine-rich stretches, both of which are important for nuclear export, as mutating either one resulted in nuclear retention phenotypes (Figs. 2B and C). However, only one of them (amino acids 106–117) is functional in directing the nuclear export of a heterologous protein (Fig. 3). Moreover, the presence of a functional NES seems to be necessary but not sufficient for the nuclear export of NiV-M. This is demonstrated by the nuclear-retained K258R mutant, which still failed to be exported despite the presence of an intact NES. It seems that ubiquitination on K258, in addition to the NES, is required for efficient nuclear export. This is consistent with the hypothesis that ubiquitination changes the conformation of the protein, exposing the NES that is otherwise not accessible to cellular exportins [35,49]. Alternatively, it is possible that K258 needs to be ubiquitinated for recognition by a yet-to-be-identified cellular ubiquitin-binding protein that forms an indispensable part of the nuclear export machinery. Previous studies have indicated that deleting the YMYL and YPLGVG motifs in NiV-M also results in nuclear retention [10,12]. Since those two motifs are in proximity to the NES we identified in NiV-M, it is possible that the altered localization is due to NES masking induced by conformational changes resulting from the deletions.

Nipah virus causes fatal encephalitis in humans with high mortality rates, and there are currently no vaccines or effective therapeutics. We report here that proteasome inhibitors including MG132 and bortezomib potently reduce viral titers during live NiV infection. Bortezomib (marketed as Velcade) is an FDA-approved drug for treating multiple myeloma and mantle cell lymphoma. It is usually given to patients at a dose of 1.3 mg/m^2 twice a week, and the mean maximum plasma concentration of the drug reaches 200–300 nM [57,58]. Our inhibition curve (Fig. 8D) indicates that the IC_{50} of bortezomib is 2.7 nM, well below the clinically achievable plasma concentration, suggesting that it could potentially be used as an anti-viral against acute NiV infection.

Although the nuclear localization of paramyxoviral matrix proteins has been known for quite some time [17,19,20,23], the biological function of this intracellular trafficking behavior remains enigmatic. Here, we provide evidence that, at least for Nipah virus matrix, nuclear transit and possible post-translational modification play critical roles in subsequent matrix-mediated viral budding. The Nipah matrix protein also illustrates the remarkably efficient use of multiple cellular trafficking machineries: that a single lysine residue in the putative bipartite NLS can serve as both a signal for nuclear import and a regulator for subsequent nuclear export. Also, the fact that the homologous lysine residue (K258 in NiV-M) in the bipartite NLS is highly conserved in all 5 genera of *Paramyxoviridae* suggests that the mechanisms described for NiV-M budding may extend to other paramyxoviruses. Finally, our findings suggest the potential use of bortezomib (Velcade) as treatment for acute henipavirus infections, or even prophylaxis in the case of high-risk exposure (such as veterinarians treating symptomatic horses in the Australian Hendra virus outbreaks). Although Velcade is an FDA-approved drug, it is not completely innocuous. However, it has the benefit of well-documented pharmacokinetic and toxicity profiles.

Materials and Methods

Cells and virus

VeroE6, HeLa and HEK293T cells were grown in Dulbecco's modified eagle medium (DMEM, Gibco) supplemented with 10% fetal bovine serum, 100 U/mL penicillin, 100 μg/mL streptomycin, and 1% sodium pyruvate. The Nipah virus (NiV) strain Malaysia (kindly provided by the Special Pathogens Branch, CDC, Atlanta) was propagated in VeroE6 cells. Stock virus was harvested 48 hours post infection (hpi) and virus titer was calculated using the Reed–Muench method [69].

For infection, HeLa cells were incubated with NiV for 1 hr at 37°C, and then fresh medium containing 2% FBS, 100 U/mL penicillin and 100 μg/mL streptomycin was added. For generating the dose-response inhibition curve in Figure 8, serial dilutions of MG132 or bortezomib were added at 15 hpi, yielding final concentrations ranging from 10 nM to 1fM. Considering the short half-life of bortezomib (9–15 hrs), it was re-added 12 hrs later. Supernatants were collected at 40 hpi and viral titers were determined by plaque assay.

For plaque assay, confluent monolayers of Vero cells (seeded in 12-well plates) were infected with 100 µl of serial tenfold dilutions of virus-containing cell supernatant. After 1 hr incubation at 37°C and 5% CO_2, the inocula were removed and wells overlaid with a mixture of one part 1.0% methylcellulose and one part 2xMEM (Gibco, Invitrogen) supplemented with 2% FBS and 2% penicillin/streptomycin. The plates were incubated at 37°C and 5% CO_2 for 3 days and then stained with 0.25% crystal violet in 10% buffered formalin. Plates were then washed and the plaques enumerated. All work with live virus was carried out under Biosafety Level 4 (BSL4) conditions in the Robert E. Shope BSL4 Laboratory, UTMB.

Plasmids and reagents

The open reading frame encoding Nipah virus matrix protein was codon-optimized and synthesized by Geneart Inc. (Regensburg, Germany) to facilitate expression in mammalian cells. NiV-M sequence was then amplified by PCR and inserted between the HindIII and XhoI sites in the pCMV-3Tag-1 vector (Stratagene) to generate 3XFLAG-M. 3XFLAG-tagged M mutants including M_{mono}, M_{bp1}, M_{bp2}, $M_{bp1/2}$, L106A/L107A, L268A, I271A, L274A, L276A, K258A, K258R, R256A/R257A and K263R were generated by QuikChange site-directed mutagenesis (Stratagene). GFP sequence was fused in-frame to the N-terminus of NiV-M by overlapping PCR to generate GFP-M, and untagged NiV-M and mutants were constructed by PCR amplification and insertion into the pcDNA3.1(+) vector (Invitrogen). HA-ubiquitin constructs (wild-type and a mutant in which all the lysines were mutated to arginines) have been described previously [70] and were purchased from Addgene (Addgene plasmids 17608 and 17603). K258R-Ub was generated by fusing one copy of ubiquitin in-frame to the C-terminus of 3XFLAG-K258R. L10 and S15 sequences were fused to the N-terminus of the untagged K258A mutant by PCR using primers 5′-agaagcttgccaccatgggctgtgtctgcagctcaaaccctgaagagcccgacatcaag, 5′- ataagcttgccaccatgggtagcaacaagagcaagcccaaggatgccagccagcggcgcgagcccgacatcaag, and 5′- gtcagcctcgagtcatcagcccttcagg.

Rev-mCherry was constructed by fusing the coding sequence of mCherry at the C-terminus of HIV Rev via a GGS linker followed by a KpnI restriction enzyme site. Amino acids L78 and L81 in Rev were mutated to alanines via site-directed mutagenesis to derive RevΔNES-mCherry. RevΔNES-$M^{106–117}$-mCherry, RevΔNES-$M^{264–280}$-mCherry and RevΔNES-RevNES-mCherry were constructed by inserting sequences corresponding to each NES between the GGS linker and the KpnI site. All the sequences were verified by DNA sequencing. Cell transfection was performed using BioT transfection reagent per manufacturer's instructions. MG132 was purchased from Calbiochem as a 10mM stock solution in DMSO, bortezomib (Velcade) was purchased from ChemieTek, and actinomycin D was purchased from Sigma.

Antibodies

Rabbit anti-NiV-M polyclonal antibodies were raised by immunizing rabbits with a purified peptide corresponding to amino acids 29–49 of NiV matrix protein (21st Century Biochemicals Inc.). Mouse anti-FLAG monoclonal antibody clone M2 was purchased from Stratagene. Mouse anti-HA and anti-myc (9E10) monoclonal antibodies were obtained from Covance and the Developmental Studies Hybridoma Bank at University of Iowa, respectively. Mouse anti-β-tubulin antibody was purchased from Sigma.

Production of viral-like particles (VLPs) and quantification of the budding index

HEK293T cells were transfected with NiV-M or M mutants expression constructs. 24 hpt, culture supernatants were collected and centrifuged at 2000 rpm for 5 min to get rid of contaminating cells. The cleared supernatants were then ultracentrifuged at 30,600 rpm on an AH-650 rotor (Thermo Scientific) for 2 hrs through a 20% (w/v) sucrose cushion. VLPs pelleted at the bottom of the tubes were resuspended in lysis buffer and subjected to immunoblotting. The intensities of the bands were quantified by densitometry with a VersaDoc Imaging System (Bio-Rad), and budding index was defined as the amount of M in the VLPs divided by the amount in the cell lysate and presented as % of wt M which is set as 100%.

Immunoprecipitation and immunoblotting

HEK293T cells expressing NiV-M or M mutants were harvested in a lysis buffer containing 50 mM Tris-HCl, 150 mM NaCl, 1% NP-40, 1 mM EDTA, 0.25% (w/w) sodium deoxycholate, 5 mM N-ethylmaleimide (NEM) and protease inhibitors cocktail (Roche). Cell lysate was clarified by centrifugation at 21,000×g for 5 min before incubation overnight with mouse anti-FLAG antibody crosslinked to protein G-conjugated agarose beads (Pierce) with 10 mg/ml dimethyl pimelimidate (DMP). Beads were then extensively washed, and the bound proteins were eluted by boiling for 10 min in SDS protein loading buffer. Proteins were separated by SDS-PAGE, transferred to PVDF membranes and analyzed using appropriate antibodies.

Immunofluorescence microscopy and image analysis

For the live viral infection experiments, cells infected with NiV were fixed with 10% formalin for 24 hrs and removed from the BSL4. Cells were then permeabilized with 0.2% Triton X-100 in phosphate-buffered saline (PBS) for 5 min at room temperature (RT), washed with PBS and then incubated with rabbit polyclonal anti-NiV-M antibody. After extensive washing with PBS, cells were incubated with Alexa488-conjugated goat anti-rabbit secondary antibody (Invitrogen Molecular Probes) for 30 min at RT. Cells were then counterstained with DAPI. The slides were imaged on a Zeiss LSM 510 confocal microscope in the UTMB optical imaging core. For the cell transfection experiments, HeLa cells transfected with the indicated constructs were fixed with 2% paraformaldehyde, permeabilized with 0.2% Triton in PBS and stained with mouse anti-FLAG antibody followed by Alexa488 or 594-conjugated goat anti-mouse secondary antibodies. Cells were imaged on a Nikon Eclipse TE300 fluorescent microscope with MetaMorph software (Molecular Devices).

Image analysis was performed with MetaXpress software from Molecular Devices using the Enhanced Translocation module. The algorithm identifies nuclei as compartments using DAPI stain. The nuclear region was defined as the central region 20 pixels inset from the nuclear/cytoplasm boundary. The cytoplasmic region was defined as a disc beginning at the nuclear/cytoplasmic boundary and extending 5 pixels into the cytoplasm. Cells were manually included or excluded by inspection to insure that all cells included in the final scoring had the cytoplasm and nuclear regions correctly defined. A minimum cutoff intensity level was applied to ensure NiV matrix expression was sufficient. This was to exclude aberrant cell morphology and non-transfected cells. The statistic evaluated was the ratio of the average cytoplasmic region intensity to the average nuclear region intensity for each cell. Since the cytoplasmic/nuclear fluorescent intensity (C:N) ratio for wild-type M is close to 1, C:N ratios greater than 1 implies increased cytoplasmic retention whereas C:N ratios less than 1 indicates increased nuclear retention. Between 10-50 cells were counted for Mwt and all mutants analyzed.

Membrane flotation centrifugation

Membrane flotation centrifugation was performed as described previously [71]. Briefly, transfected HEK293T cells were Dounce-homogenized in cold TNE buffer containing 50 mM Tris-HCl, 150 mM NaCl, 2 mM EDTA, 0.1% 2-mercaptoethanol and protease inhibitors cocktail (Roche). Cell homogenates were clarified at 3,000 rpm for 30 min at 4°C to remove cell debris and nuclei. The cleared cell homogenate was mixed with 85% (w/v) sucrose solution to obtain 73% final concentration and loaded at the bottom of a 5 ml ultracentrifuge tube. The sample was then layered with 3 ml 65% and 0.8 ml 10% sucrose solutions and centrifuged at 100,000×g for 16 hrs at 4°C. Eight fractions (0.6 ml/fraction) were collected from the top and proteins were extracted with methanol/chloroform. Membrane-associated materials were harvested at the interface between 10% and 65% sucrose as "fraction 2".

Supporting Information

Figure S1 Specificity of rabbit anti-M polyclonal antibody. HeLa cells transfected with 3XFLAG-M (upper panel) or empty vector as control (lower panel) were fixed at 24 hpt and stained with rabbit anti-NiV-M antibody followed by Alexa 488-conjugated goat anti-rabbit secondary antibody. DAPI was used for visualization of the nuclei. All the pictures were acquired using the same exposure time.
Found at: doi:10.1371/journal.ppat.1001186.s001 (3.43 MB PDF)

Figure S2 Subcellular localization of NiV-M in transfected HeLa cells. Triple FLAG-tagged NiV-M (3XFLAG-M) was constructed by fusing three copies of the FLAG tag N-terminally to the NiV-M sequence. HeLa cells transfected with 3XFLAG-M were stained with a mouse anti-FLAG monoclonal antibody at **(A)** 12, **(B)** 16 or **(C)** 24 hrs post-transfection and imaged under 60× magnification on a fluorescent microscope. The cells were also stained with DAPI for visualization of the nuclei. At early time points, M staining was prominent in the nucleus (A), whereas at later time points, it was diffused in both the nucleus and the cytoplasm (B and C). At 24 hpt, M also localized to filamentous membrane extensions.
Found at: doi:10.1371/journal.ppat.1001186.s002 (3.96 MB PDF)

Figure S3 Subcellular localization of GFP-fused NiV-M and M mutants. HeLa cells were transfected with the indicated expression constructs and fixed at 24 hpt. Images were acquired under 60× magnification on a fluorescent microscope.
Found at: doi:10.1371/journal.ppat.1001186.s003 (1.64 MB PDF)

Figure S4 VLP budding of 3XFLAG-tagged and untagged NiV-M. HEK293T cells were transfected with the indicated amounts of DNA encoding 3XFLAG-M or untagged M. VLP and cell lysate samples were prepared at 24 hpt and immunoblotted with rabbit anti-M antibody. Arrows point to 3XFLAG-M while arrowheads indicate untagged M.
Found at: doi:10.1371/journal.ppat.1001186.s004 (0.24 MB PDF)

Figure S5 VLP budding of GFP-fused NiV-M. HEK293T cells were transfected with M or GFP-M expression construct. VLP and cell lysate samples were prepared at 24 hpt and immunoblotted with rabbit anti-M antibody.
Found at: doi:10.1371/journal.ppat.1001186.s005 (0.08 MB PDF)

Figure S6 Association between Mwt and various M mutants. HEK293T cells were co-transfected with untagged Mwt and 3XFLAG-tagged Mwt or mutants as indicated. Cells were harvested at 24 hpt, and cell lysates were subjected to immunoprecipitation using anti-FLAG monoclonal antibody M2-conjugated agarose beads (Sigma) per manufacturer's instructions. 3XFLAG peptide was used for elution, and IP samples were immunoblotted with a rabbit anti-M antibody. Arrows indicate 3XFLAG-tagged Mwt or mutants, and the arrowhead points to untagged Mwt. All the mutants tested were able to co-immunoprecipitate with Mwt.
Found at: doi:10.1371/journal.ppat.1001186.s006 (0.10 MB PDF)

Figure S7 Budding rescue of M mutants by wild-type M. HEK293T cells were transfected with 3XFLAG-tagged M mutants alone or together with untagged wild-type M as indicated. VLP and cell lysate samples were prepared 24 hpt. VLPs were immunoblotted with an anti-FLAG antibody to detect only the budding of the mutants, and cell lysates were probed with an anti-M antibody to visualize the expression of both untagged Mwt (arrowheads) and FLAG-tagged mutants (arrows). Mwt was able to rescue the VLP budding of all the mutants tested.
Found at: doi:10.1371/journal.ppat.1001186.s007 (0.10 MB PDF)

Figure S8 Bortezomib inhibits the nuclear export of M. HeLa cells expressing GFP-M were treated with the indicated concentrations of bortezomib for 6 hrs. Cells were then fixed and visualized under 60× magnification on a fluorescent microscope.
Found at: doi:10.1371/journal.ppat.1001186.s008 (1.14 MB PDF)

Figure S9 Budding inhibition of NiV-M by proteasome inhibitors. HEK293T cells expressing 3XFLAG-M were treated with MG132 (10 μM or 50 μM) or bortezomib (1 μM or 10 μM) for 12 hrs. VLP and cell lysate samples were immunoblotted with an anti-FLAG antibody **(A)**, and the budding indices were calculated and normalized to the DMSO control **(B)**.
Found at: doi:10.1371/journal.ppat.1001186.s009 (0.11 MB PDF)

Figure S10 Overexpression of ubiquitin restores budding in the presence of MG132. HeLa cells expressing 3XFLAG-M (left three lanes) or 3XFLAG-M plus HA-Ub (right two lanes) were incubated with DMSO, 10 μM or 50 μM MG132 for 12 hrs, and VLPs produced during this period were harvested as described in *Materials and Methods*. VLPs and cell lysates were immunoblotted with an anti-FLAG antibody, then the cell lysate blot was stripped and re-probed with an anti-β-tubulin antibody as loading control.
Found at: doi:10.1371/journal.ppat.1001186.s010 (0.12 MB PDF)

Figure S11 MG132 and bortezomib are not grossly toxic to the cells under our experimental conditions. HeLa cells were treated with MG132 or bortezomib at the indicated concentrations for 24 hrs. Culture supernatants were collected and the release of adenylate kinase was measured using a ToxiLight BioAssay kit (Lonza) per manufacturer's instructions. Results are shown as percent toxicity with DMSO background subtracted and complete cell lysis by detergent set as 100%. ND = Not Detectable.
Found at: doi:10.1371/journal.ppat.1001186.s011 (0.23 MB PDF)

Figure S12 Ubiquitin promotes the budding of NiV-Mwt, but not the K258A mutant. HEK293T cells were cotransfected with 3XFLAG-M or 3XFLAG-M K258A mutant plus increasing amounts of HA-Ub as indicated. 24hpt, VLPs and cell lysates were prepared as described in *Materials and Methods* and immunoblotted with an anti-FLAG antibody **(A)**. Densitometry was performed to determine the budding index **(B)** as described in *Materials and Methods*.
Found at: doi:10.1371/journal.ppat.1001186.s012 (0.03 MB PDF)

Author Contributions

Conceived and designed the experiments: YEW MRH ANF BL. Performed the experiments: YEW AP MP BT TEY MCW ANF. Analyzed the data: YEW AP ML MCW MRH ANF. Contributed reagents/materials/analysis tools: YEW. Wrote the paper: YEW.

References

1. Eaton BT, Broder CC, Middleton D, Wang LF (2006) Hendra and Nipah viruses: different and dangerous. Nat Rev Microbiol 4: 23–35.
2. Field H, Young P, Yob JM, Mills J, Hall L, et al. (2001) The natural history of Hendra and Nipah viruses. Microbes Infect 3: 307–314.
3. Chua KB, Bellini WJ, Rota PA, Harcourt BH, Tamin A, et al. (2000) Nipah virus: a recently emergent deadly paramyxovirus. Science 288: 1432–1435.
4. Weingartl HM, Berhane Y, Czub M (2009) Animal models of henipavirus infection: a review. Vet J 181: 211–220.
5. Hsu VP, Hossain MJ, Parashar UD, Ali MM, Ksiazek TG, et al. (2004) Nipah virus encephalitis reemergence, Bangladesh. Emerg Infect Dis 10: 2082–2087.
6. (2009) ProMED-mail PRO/AH/EDR> Hendra virus, human, equine - Australia (04): (QL) fatal. 20090903.3098.
7. Lamb RA, Parks GD (2006) *Paramyxoviridae*: The Viruses and Their Replication. In: Knipe DM, Howley PM, eds. Fields Virology. Fifth ed. Philadelphia: Lippincott, Williams and Wilkins. pp 1449–1496.
8. Takimoto T, Portner A (2004) Molecular mechanism of paramyxovirus budding. Virus Res 106: 133–145.
9. Garoff H, Hewson R, Opstelten DJ (1998) Virus maturation by budding. Microbiol Mol Biol Rev 62: 1171–1190.
10. Ciancanelli MJ, Basler CF (2006) Mutation of YMYL in the Nipah virus matrix protein abrogates budding and alters subcellular localization. J Virol 80: 12070–12078.
11. Patch JR, Crameri G, Wang LF, Eaton BT, Broder CC (2007) Quantitative analysis of Nipah virus proteins released as virus-like particles reveals central role for the matrix protein. Virol J 4: 1.
12. Patch JR, Han Z, McCarthy SE, Yan L, Wang LF, et al. (2008) The YPLGVG sequence of the Nipah virus matrix protein is required for budding. Virol J 5: 137.
13. Shaw ML, Cardenas WB, Zamarin D, Palese P, Basler CF (2005) Nuclear localization of the Nipah virus W protein allows for inhibition of both virus- and toll-like receptor 3-triggered signaling pathways. J Virol 79: 6078–6088.
14. Shaw ML, Garcia-Sastre A, Palese P, Basler CF (2004) Nipah virus V and W proteins have a common STAT1-binding domain yet inhibit STAT1 activation from the cytoplasmic and nuclear compartments, respectively. J Virol 78: 5633–5641.
15. Ciancanelli MJ, Volchkova VA, Shaw ML, Volchkov VE, Basler CF (2009) Nipah virus sequesters inactive STAT1 in the nucleus via a P gene-encoded mechanism. J Virol 83: 7828–7841.
16. Watanabe N, Kawano M, Tsurudome M, Kusagawa S, Nishio M, et al. (1996) Identification of the sequences responsible for nuclear targeting of the V protein of human parainfluenza virus type 2. J Gen Virol 77(Pt 2): 327–338.
17. Yoshida T, Nagai Y'Yoshii S, Maeno K, Matsumoto T (1976) Membrane (M) protein of HVJ (Sendai virus): its role in virus assembly. Virology 71: 143–161.
18. Coleman NA, Peeples ME (1993) The matrix protein of Newcastle disease virus localizes to the nucleus via a bipartite nuclear localization signal. Virology 195: 596–607.
19. Peeples ME, Wang C, Gupta KC, Coleman N (1992) Nuclear entry and nucleolar localization of the Newcastle disease virus (NDV) matrix protein occur early in infection and do not require other NDV proteins. J Virol 66: 3263–3269.
20. Peeples ME (1988) Differential detergent treatment allows immunofluorescent localization of the Newcastle disease virus matrix protein within the nucleus of infected cells. Virology 162: 255–259.
21. Ghildyal R, Ho A, Dias M, Soegiyono L, Bardin PG, et al. (2009) The respiratory syncytial virus matrix protein possesses a Crm1-mediated nuclear export mechanism. J Virol 83: 5353–5362.
22. Ghildyal R, Ho A, Wagstaff KM, Dias MM, Barton CL, et al. (2005) Nuclear import of the respiratory syncytial virus matrix protein is mediated by importin beta1 independent of importin alpha. Biochemistry 44: 12887–12895.
23. Ghildyal R, Baulch-Brown C, Mills J, Meanger J (2003) The matrix protein of Human respiratory syncytial virus localises to the nucleus of infected cells and inhibits transcription. Arch Virol 148: 1419–1429.
24. Faaberg KS, Peeples ME (1988) Strain variation and nuclear association of Newcastle disease virus matrix protein. J Virol 62: 586–593.
25. Kanwal C, Li H, Lim CS (2002) Model system to study classical nuclear export signals. AAPS PharmSci 4: E18.
26. Terry LJ, Shows EB, Wente SR (2007) Crossing the nuclear envelope: hierarchical regulation of nucleocytoplasmic transport. Science 318: 1412–1416.
27. Dingwall C, Laskey RA (1991) Nuclear targeting sequences–a consensus? Trends Biochem Sci 16: 478–481.
28. Efthymiadis A, Shao H, Hubner S, Jans DA (1997) Kinetic characterization of the human retinoblastoma protein bipartite nuclear localization sequence (NLS) in vivo and in vitro. A comparison with the SV40 large T-antigen NLS. J Biol Chem 272: 22134–22139.
29. Schlenstedt G (1996) Protein import into the nucleus. FEBS Lett 389: 75–79.
30. Fukuda M, Asano S, Nakamura T, Adachi M, Yoshida M, et al. (1997) CRM1 is responsible for intracellular transport mediated by the nuclear export signal. Nature 390: 308–311.
31. Kau TR, Way JC, Silver PA (2004) Nuclear transport and cancer: from mechanism to intervention. Nat Rev Cancer 4: 106–117.
32. Lohrum MA, Woods DB, Ludwig RL, Balint E, Vousden KH (2001) C-terminal ubiquitination of p53 contributes to nuclear export. Mol Cell Biol 21: 8521–8532.
33. Li M, Brooks CL, Wu-Baer F, Chen D, Baer R, et al. (2003) Mono- versus polyubiquitination: differential control of p53 fate by Mdm2. Science 302: 1972–1975.
34. Trotman LC, Wang X, Alimonti A, Chen Z, Teruya-Feldstein J, et al. (2007) Ubiquitination regulates PTEN nuclear import and tumor suppression. Cell 128: 141–156.
35. Shcherbik N, Haines DS (2004) Ub on the move. J Cell Biochem 93: 11–19.
36. Huang TT, Wuerzberger-Davis SM, Wu ZH, Miyamoto S (2003) Sequential modification of NEMO/IKKgamma by SUMO-1 and ubiquitin mediates NF-kappaB activation by genotoxic stress. Cell 115: 565–576.
37. Randow F, Lehner PJ (2009) Viral avoidance and exploitation of the ubiquitin system. Nat Cell Biol 11: 527–534.
38. Isaacson MK, Ploegh HL (2009) Ubiquitination, ubiquitin-like modifiers, and deubiquitination in viral infection. Cell Host Microbe 5: 559–570.
39. Henderson BR, Eleftheriou A (2000) A comparison of the activity, sequence specificity, and CRM1-dependence of different nuclear export signals. Exp Cell Res 256: 213–224.
40. Pankiv S, Lamark T, Bruun JA, Overvatn A, Bjorkoy G, et al. (2010) Nucleocytoplasmic shuttling of p62/SQSTM1 and its role in recruitment of nuclear polyubiquitinated proteins to promyelocytic leukemia bodies. J Biol Chem 285: 5941–5953.
41. Li SY, Davidson PJ, Lin NY, Patterson RJ, Wang JL, et al. (2006) Transport of galectin-3 between the nucleus and cytoplasm. II. Identification of the signal for nuclear export. Glycobiology 16: 612–622.
42. Rodriguez JJ, Cruz CD, Horvath CM (2004) Identification of the nuclear export signal and STAT-binding domains of the Nipah virus V protein reveals mechanisms underlying interferon evasion. J Virol 78: 5358–5367.
43. Patnaik A, Chau V, Wills JW (2000) Ubiquitin is part of the retrovirus budding machinery. Proc Natl Acad Sci U S A 97: 13069–13074.
44. Schubert U, Ott DE, Chertova EN, Welker R, Tessmer U, et al. (2000) Proteasome inhibition interferes with gag polyprotein processing, release, and maturation of HIV-1 and HIV-2. Proc Natl Acad Sci U S A 97: 13057–13062.
45. Vogt VM (2000) Ubiquitin in retrovirus assembly: actor or bystander? Proc Natl Acad Sci U S A 97: 12945–12947.
46. Morita E, Sundquist WI (2004) Retrovirus budding. Annu Rev Cell Dev Biol 20: 395–425.
47. Hoeller D, Crosetto N, Blagoev B, Raiborg C, Tikkanen R, et al. (2006) Regulation of ubiquitin-binding proteins by monoubiquitination. Nat Cell Biol 8: 163–169.
48. Qian SB, Ott DE, Schubert U, Bennink JR, Yewdell JW (2002) Fusion proteins with COOH-terminal ubiquitin are stable and maintain dual functionality in vivo. J Biol Chem 277: 38818–38826.
49. Carter S, Bischof O, Dejean A, Vousden KH (2007) C-terminal modifications regulate MDM2 dissociation and nuclear export of p53. Nat Cell Biol 9: 428–435.
50. Lee JC, Wang GX, Schickling O, Peter ME (2005) Fusing DEDD with ubiquitin changes its intracellular localization and apoptotic potential. Apoptosis 10: 1483–1495.
51. Spearman P, Wang JJ, Vander Heyden N, Ratner L (1994) Identification of human immunodeficiency virus type 1 Gag protein domains essential to membrane binding and particle assembly. J Virol 68: 3232–3242.
52. Hermida-Matsumoto L, Resh MD (2000) Localization of human immunodeficiency virus type 1 Gag and Env at the plasma membrane by confocal imaging. J Virol 74: 8670–8679.
53. Rodgers W (2002) Making membranes green: construction and characterization of GFP-fusion proteins targeted to discrete plasma membrane domains. Biotechniques 32: 1044–1046, 1048, 1050–1041.
54. Shenoy-Scaria AM, Gauen LK, Kwong J, Shaw AS, Lublin DM (1993) Palmitylation of an amino-terminal cysteine motif of protein tyrosinc kinases p56lck and p59fyn mediates interaction with glycosyl-phosphatidylinositol-anchored proteins. Mol Cell Biol 13: 6385–6392.
55. Elliott PJ, Zollner TM, Boehncke WH (2003) Proteasome inhibition: a new anti-inflammatory strategy. J Mol Med 81: 235–245.
56. Sanchez-Serrano I (2006) Success in translational research: lessons from the development of bortezomib. Nat Rev Drug Discov 5: 107–114.
57. Papandreou CN, Daliani DD, Nix D, Yang H, Madden T, et al. (2004) Phase I trial of the proteasome inhibitor bortezomib in patients with advanced solid

tumors with observations in androgen-independent prostate cancer. J Clin Oncol 22: 2108–2121.
58. Ogawa Y, Tobinai K, Ogura M, Ando K, Tsuchiya T, et al. (2008) Phase I and II pharmacokinetic and pharmacodynamic study of the proteasome inhibitor bortezomib in Japanese patients with relapsed or refractory multiple myeloma. Cancer Sci 99: 140–144.
59. Hicke L (2001) Protein regulation by monoubiquitin. Nat Rev Mol Cell Biol 2: 195–201.
60. Johnson ES (2002) Ubiquitin branches out. Nat Cell Biol 4: E295–298.
61. Tanaka T, Soriano MA, Grusby MJ (2005) SLIM is a nuclear ubiquitin E3 ligase that negatively regulates STAT signaling. Immunity 22: 729–736.
62. Natoli G, Chiocca S (2008) Nuclear ubiquitin ligases, NF-kappaB degradation, and the control of inflammation. Sci Signal 1: pe1.
63. Martin-Serrano J (2007) The role of ubiquitin in retroviral egress. Traffic 8: 1297–1303.
64. Saad JS, Miller J, Tai J, Kim A, Ghanam RH, et al. (2006) Structural basis for targeting HIV-1 Gag proteins to the plasma membrane for virus assembly. Proc Natl Acad Sci U S A 103: 11364–11369.
65. Gonzalo S, Linder ME (1998) SNAP-25 palmitoylation and plasma membrane targeting require a functional secretory pathway. Mol Biol Cell 9: 585–597.
66. Manie SN, de Breyne S, Vincent S, Gerlier D (2000) Measles virus structural components are enriched into lipid raft microdomains: a potential cellular location for virus assembly. J Virol 74: 305–311.
67. Brown G, Rixon HW, Sugrue RJ (2002) Respiratory syncytial virus assembly occurs in GM1-rich regions of the host-cell membrane and alters the cellular distribution of tyrosine phosphorylated caveolin-1. J Gen Virol 83: 1841–1850.
68. Ali A, Nayak DP (2000) Assembly of Sendai virus: M protein interacts with F and HN proteins and with the cytoplasmic tail and transmembrane domain of F protein. Virology 276: 289–303.
69. Reed LJ, Muench H (1938) A simple method of estimating fifty percent endpoints. The American Journal of Hygiene. pp 493–397.
70. Lim KL, Chew KC, Tan JM, Wang C, Chung KK, et al. (2005) Parkin mediates nonclassical, proteasomal-independent ubiquitination of synphilin-1: implications for Lewy body formation. J Neurosci 25: 2002–2009.
71. Guo X, Roldan A, Hu J, Wainberg MA, Liang C (2005) Mutation of the SP1 sequence impairs both multimerization and membrane-binding activities of human immunodeficiency virus type 1 Gag. J Virol 79: 1803–1812.

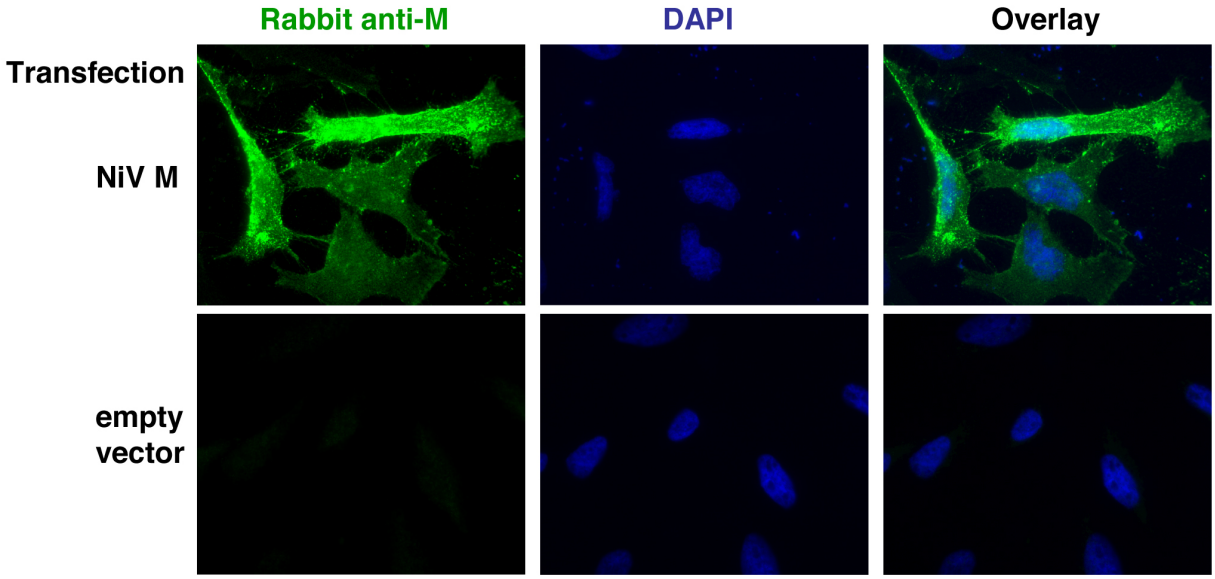

Figure S1. Specificity of rabbit anti-M polyclonal antibody. HeLa cells transfected with 3XFLAG-M (upper panel) or empty vector as control (lower panel) were fixed at 24 hpt and stained with rabbit anti-NiV-M antibody followed by Alexa 488-conjugated goat anti-rabbit secondary antibody. DAPI was used for visualization of the nuclei. All the pictures were acquired using the same exposure time.

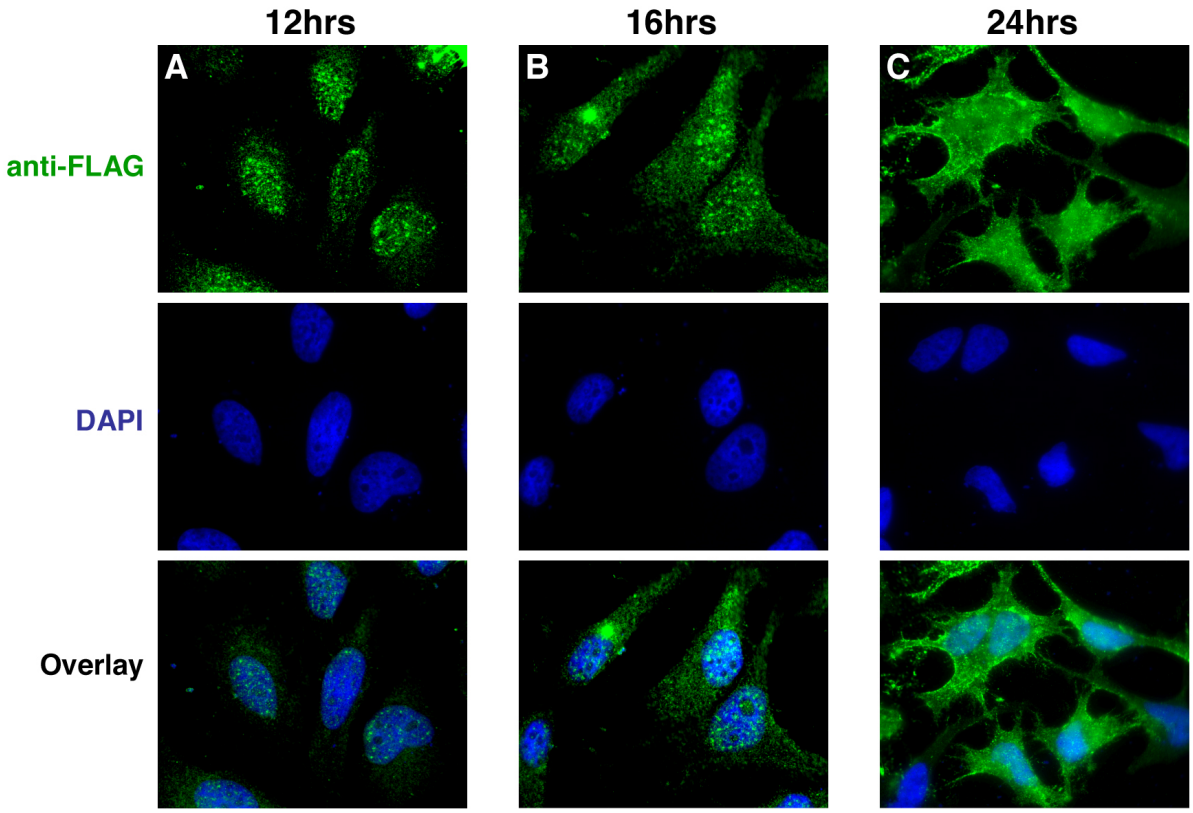

Figure S2. Subcellular localization of NiV-M in transfected HeLa cells. Triple FLAG-tagged NiV-M (3XFLAG-M) was constructed by fusing three copies of the FLAG tag N-terminally to the NiV-M sequence. HeLa cells transfected with 3XFLAG-M were stained with a mouse anti-FLAG monoclonal antibody at **(A)** 12, **(B)** 16 or **(C)** 24 hrs post-transfection and imaged under 60× magnification on a fluorescent microscope. The cells were also stained with DAPI for visualization of the nuclei. At early time points, M staining was prominent in the nucleus (A), whereas at later time points, it was diffused in both the nucleus and the cytoplasm (B and C). At 24 hpt, M also localized to filamentous membrane extensions.

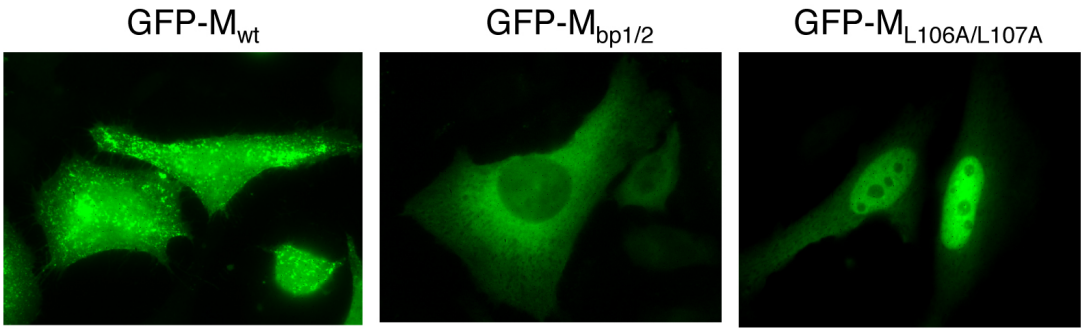

Figure S3. Subcellular localization of GFP-fused NiV-M and M mutants. HeLa cells were transfected with the indicated expression constructs and fixed at 24 hpt. Images were acquired under 60× magnification on a fluorescent microscope.

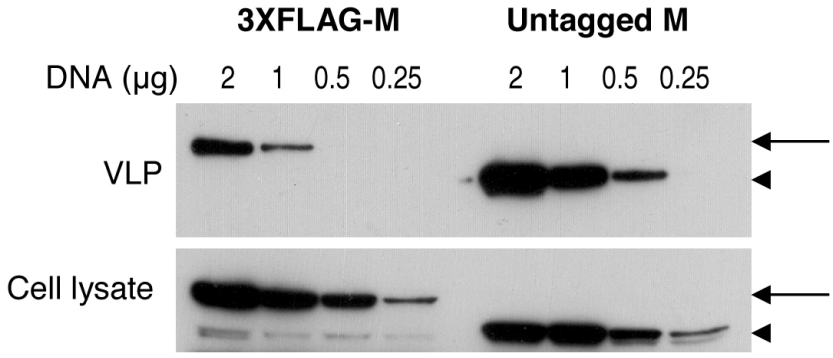

Figure S4. VLP budding of 3XFLAG-tagged and untagged NiV-M. HEK293T cells were transfected with the indicated amounts of DNA encoding 3XFLAG-M or untagged M. VLP and cell lysate samples were prepared at 24 hpt and immunoblotted with rabbit anti-M antibody. Arrows point to 3XFLAG-M while arrowheads indicate untagged M.

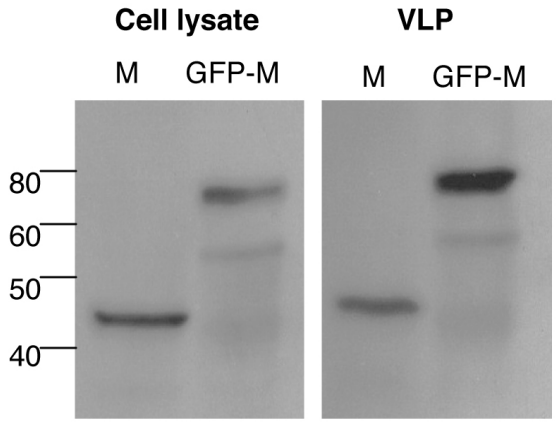

Figure S5. VLP budding of GFP-fused NiV-M. HEK293T cells were transfected with M or GFP-M expression construct. VLP and cell lysate samples were prepared at 24 hpt and immunoblotted with rabbit anti-M antibody.

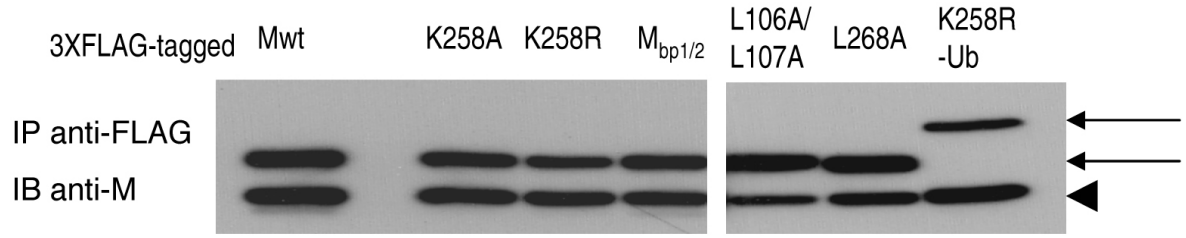

Figure S6. Association between Mwt and various M mutants. HEK293T cells were co-transfected with untagged Mwt and 3XFLAG-tagged Mwt or mutants as indicated. Cells were harvested at 24 hpt, and cell lysates were subjected to immunoprecipitation using anti-FLAG monoclonal antibody M2-conjugated agarose beads (Sigma) per manufacturer's instructions. 3XFLAG peptide was used for elution, and IP samples were immunoblotted with a rabbit anti-M antibody. Arrows indicate 3XFLAG-tagged Mwt or mutants, and the arrowhead points to untagged Mwt. All the mutants tested were able to co-immunoprecipitate with Mwt.

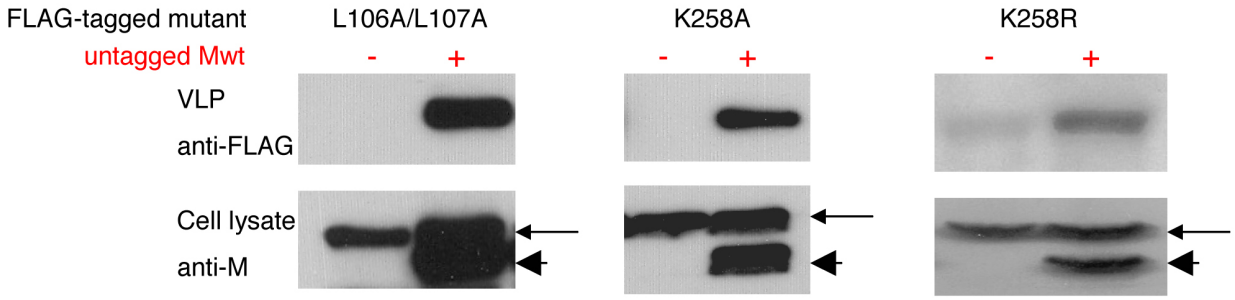

Figure S7. Budding rescue of M mutants by wild-type M. HEK293T cells were transfected with 3XFLAG-tagged M mutants alone or together with untagged wild-type M as indicated. VLP and cell lysate samples were prepared 24 hpt. VLPs were immunoblotted with an anti-FLAG antibody to detect only the budding of the mutants, and cell lysates were probed with an anti-M antibody to visualize the expression of both untagged Mwt (arrowheads) and FLAG-tagged mutants (arrows). Mwt was able to rescue the VLP budding of all the mutants tested.

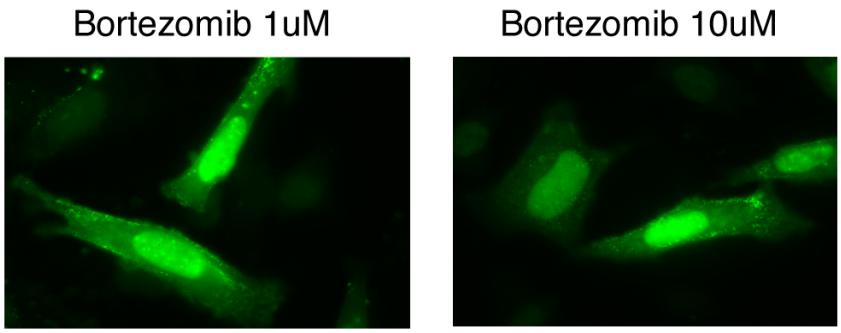

Figure S8. Bortezomib inhibits the nuclear export of M. HeLa cells expressing GFP-M were treated with the indicated concentrations of bortezomib for 6 hrs. Cells were then fixed and visualized under 60× magnification on a fluorescent microscope.

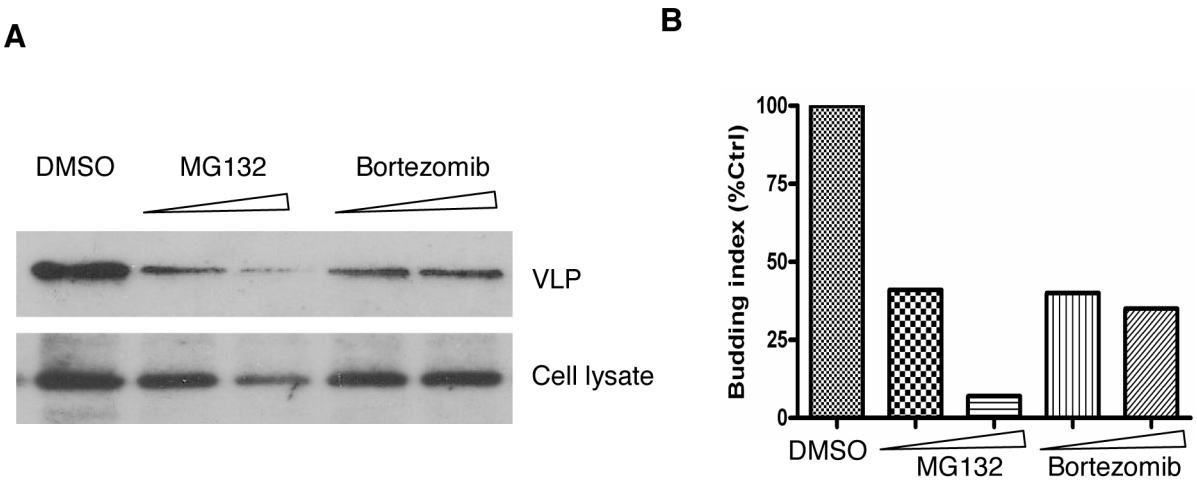

Figure S9. Budding inhibition of NiV-M by proteasome inhibitors. HEK293T cells expressing 3XFLAG-M were treated with MG132 (10 μM or 50 μM) or bortezomib (1 μM or 10 μM) for 12 hrs. VLP and cell lysate samples were immunoblotted with an anti-FLAG antibody **(A)**, and the budding indices were calculated and normalized to the DMSO control **(B)**.

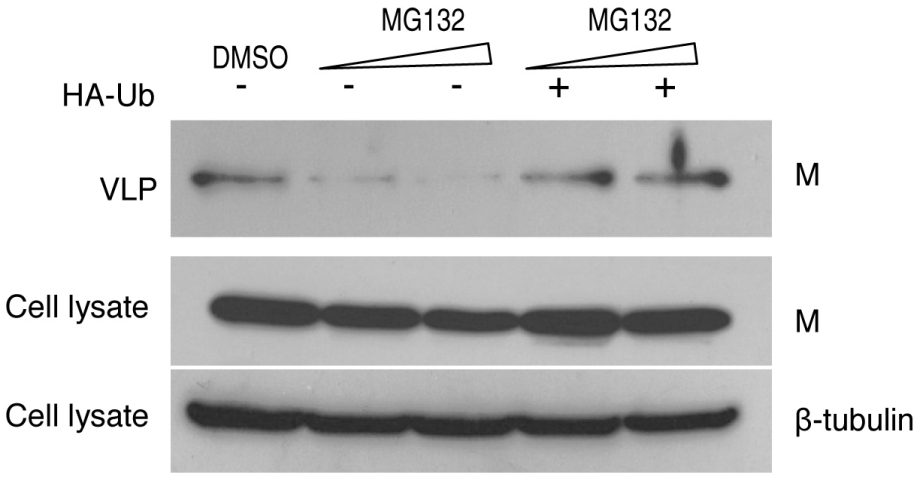

Figure S10. Overexpression of ubiquitin restores budding in the presence of MG132. HeLa cells expressing 3XFLAG-M (left three lanes) or 3XFLAG-M plus HA-Ub (right two lanes) were incubated with DMSO, 10 μM or 50 μM MG132 for 12 hrs, and VLPs produced during this period were harvested as described in Materials and Methods. VLPs and cell lysates were immunoblotted with an anti-FLAG antibody, then the cell lysate blot was stripped and re-probed with an anti-*β*-tubulin antibody as loading control.

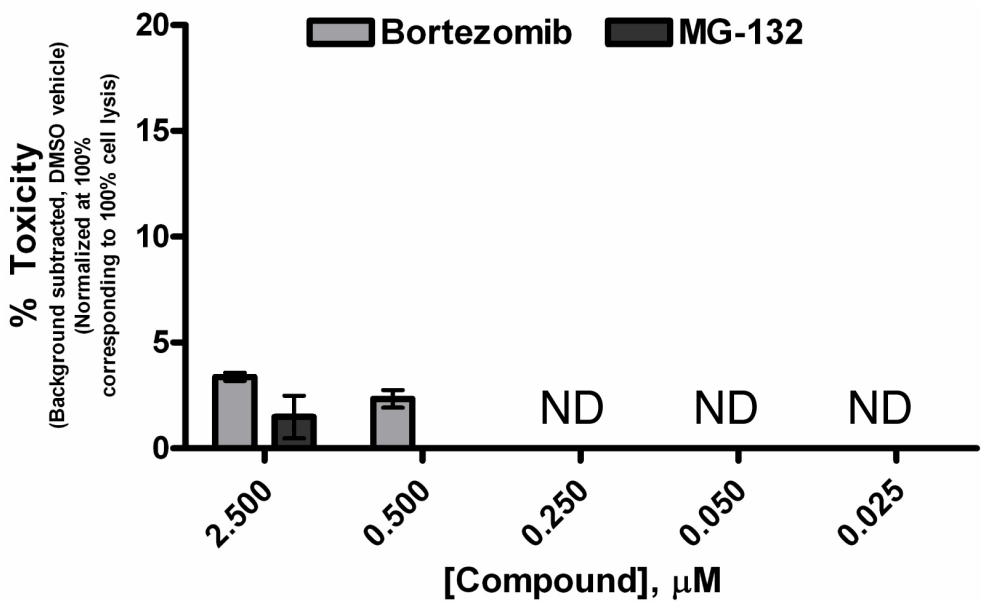

Figure S11. MG132 and bortezomib are not grossly toxic to the cells under our experimental conditions. HeLa cells were treated with MG132 or bortezomib at the indicated concentrations for 24 hrs. Culture supernatants were collected and the release of adenylate kinase was measured using a ToxiLight BioAssay kit (Lonza) per manufacturer's instructions. Results are shown as percent toxicity with DMSO background subtracted and complete cell lysis by detergent set as 100%. ND = Not Detectable.

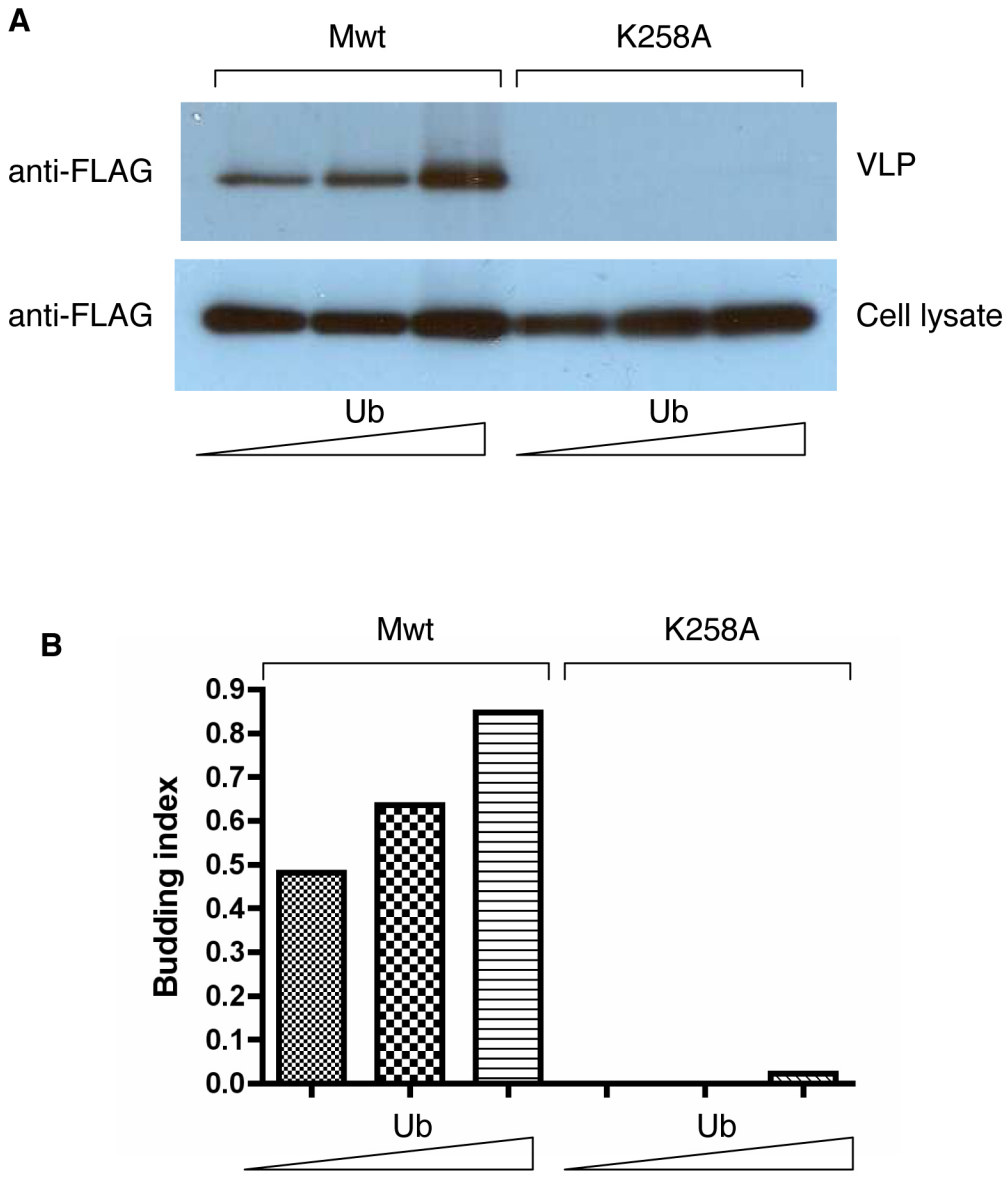

Figure S12. Ubiquitin promotes the budding of NiV-Mwt, but not the K258A mutant. HEK293T cells were cotransfected with 3XFLAG-M or 3XFLAG-M K258A mutant plus increasing amounts of HA-Ub as indicated. 24hpt, VLPs and cell lysates were prepared as described in Materials and Methods and immunoblotted with an anti-FLAG antibody **(A)**. Densitometry was performed to determine the budding index **(B)** as described in Materials and Methods.

REFERENCES

1. Eaton BT, Broder CC, Middleton D, Wang LF (2006) Hendra and Nipah viruses: different and dangerous. Nat Rev Microbiol 4: 23–35.

2. Field H, Young P, Yob JM, Mills J, Hall L, et al. (2001) The natural history of Hendra and Nipah viruses. Microbes Infect 3: 307–314.

3. Chua KB, Bellini WJ, Rota PA, Harcourt BH, Tamin A, et al. (2000) Nipah virus: a recently emergent deadly paramyxovirus. Science 288: 1432–1435.

4. Weingartl HM, Berhane Y, Czub M (2009) Animal models of henipavirus infection: a review. Vet J 181: 211–220.

5. Hsu VP, Hossain MJ, Parashar UD, Ali MM, Ksiazek TG, et al. (2004) Nipah virus encephalitis reemergence, Bangladesh. Emerg Infect Dis 10: 2082–2087.

6. (2009) ProMED-mail PRO/AH/EDR> Hendra virus, human, equine - Australia (04): (QL) fatal. 20090903.3098.

7. Lamb RA, Parks GD (2006) Paramyxoviridae: The Viruses and Their Replication. In: Knipe DM, Howley PM, editors. Fields Virology. Fifth ed. Philadelphia: Lippincott, Williams and Wilkins. pp. 1449–1496.

8. Takimoto T, Portner A (2004) Molecular mechanism of paramyxovirus budding. Virus Res 106: 133–145.

9. Garoff H, Hewson R, Opstelten DJ (1998) Virus maturation by budding. Microbiol Mol Biol Rev 62: 1171–1190.

10. Ciancanelli MJ, Basler CF (2006) Mutation of YMYL in the Nipah virus matrix protein abrogates budding and alters subcellular localization. J Virol 80: 12070–12078.

11. Patch JR, Crameri G, Wang LF, Eaton BT, Broder CC (2007) Quantitative analysis of Nipah virus proteins released as virus-like particles reveals central role for the matrix protein. Virol J 4: 1.

12. Patch JR, Han Z, McCarthy SE, Yan L, Wang LF, et al. (2008) The YPLGVG sequence of the Nipah virus matrix protein is required for budding. Virol J 5: 137.

13. Shaw ML, Cardenas WB, Zamarin D, Palese P, Basler CF (2005) Nuclear localization of the Nipah virus W protein allows for inhibition of both virus- and toll-like receptor 3-triggered signaling pathways. J Virol 79: 6078–6088.

14. Shaw ML, Garcia-Sastre A, Palese P, Basler CF (2004) Nipah virus V and W proteins have a common STAT1-binding domain yet inhibit STAT1 activation from the cytoplasmic and nuclear compartments, respectively. J Virol 78: 5633–5641.

15. Ciancanelli MJ, Volchkova VA, Shaw ML, Volchkov VE, Basler CF (2009) Nipah virus sequesters inactive STAT1 in the nucleus via a P gene-encoded mechanism. J Virol 83: 7828–7841.

16. Watanabe N, Kawano M, Tsurudome M, Kusagawa S, Nishio M, et al. (1996) Identification of the sequences responsible for nuclear targeting of the V protein of human parainfluenza virus type 2. J Gen Virol. 77. (Pt 2): pp. 327–338.

17. Yoshida T, Nagai Y'Yoshii S, Maeno K, Matsumoto T (1976) Membrane (M) protein of HVJ (Sendai virus): its role in virus assembly. Virology 71: 143–161.

18. Coleman NA, Peeples ME (1993) The matrix protein of Newcastle disease virus localizes to the nucleus via a bipartite nuclear localization signal. Virology 195: 596–607.

19. Peeples ME, Wang C, Gupta KC, Coleman N (1992) Nuclear entry and nucleolar localization of the Newcastle disease virus (NDV) matrix protein occur early in infection and do not require other NDV proteins. J Virol 66: 3263–3269.

20. Peeples ME (1988) Differential detergent treatment allows immunofluorescent localization of the Newcastle disease virus matrix protein within the nucleus of infected cells. Virology 162: 255–259.

21. Ghildyal R, Ho A, Dias M, Soegiyono L, Bardin PG, et al. (2009) The respiratory syncytial virus matrix protein possesses a Crm1-mediated nuclear export mechanism. J Virol 83: 5353–5362.

22. Ghildyal R, Ho A, Wagstaff KM, Dias MM, Barton CL, et al. (2005) Nuclear import of the respiratory syncytial virus matrix protein is mediated by importin beta1 independent of importin alpha. Biochemistry 44: 12887–12895.

23. Ghildyal R, Baulch-Brown C, Mills J, Meanger J (2003) The matrix protein of Human respiratory syncytial virus localises to the nucleus of infected cells and inhibits transcription. Arch Virol 148: 1419–1429.

24. Faaberg KS, Peeples ME (1988) Strain variation and nuclear association of Newcastle disease virus matrix protein. J Virol 62: 586–593.

25. Kanwal C, Li H, Lim CS (2002) Model system to study classical nuclear export signals. AAPS PharmSci 4: E18.

26. Terry LJ, Shows EB, Wente SR (2007) Crossing the nuclear envelope: hierarchical regulation of nucleocytoplasmic transport. Science 318: 1412–1416.

27. Dingwall C, Laskey RA (1991) Nuclear targeting sequences–a consensus? Trends Biochem Sci 16: 478–481.

28. Efthymiadis A, Shao H, Hubner S, Jans DA (1997) Kinetic characterization of the human retinoblastoma protein bipartite nuclear localization sequence (NLS) in vivo and in vitro. A comparison with the SV40 large T-antigen NLS. J Biol Chem 272: 22134–22139.

29. Schlenstedt G (1996) Protein import into the nucleus. FEBS Lett 389: 75–79.

30. Fukuda M, Asano S, Nakamura T, Adachi M, Yoshida M, et al. (1997) CRM1 is responsible for intracellular transport mediated by the nuclear export signal. Nature 390: 308–311.

31. Kau TR, Way JC, Silver PA (2004) Nuclear transport and cancer: from mechanism to intervention. Nat Rev Cancer 4: 106–117.

32. Lohrum MA, Woods DB, Ludwig RL, Balint E, Vousden KH (2001) C-terminal ubiquitination of p53 contributes to nuclear export. Mol Cell Biol 21: 8521–8532.

33. Li M, Brooks CL, Wu-Baer F, Chen D, Baer R, et al. (2003) Mono- versus polyubiquitination: differential control of p53 fate by Mdm2. Science 302: 1972–1975.

34. Trotman LC, Wang X, Alimonti A, Chen Z, Teruya-Feldstein J, et al. (2007) Ubiquitination regulates PTEN nuclear import and tumor suppression. Cell 128: 141–156.

35. Shcherbik N, Haines DS (2004) Ub on the move. J Cell Biochem 93: 11–19.

36. Huang TT, Wuerzberger-Davis SM, Wu ZH, Miyamoto S (2003) Sequential modification of NEMO/IKKgamma by SUMO-1 and ubiquitin mediates NF-kappaB activation by genotoxic stress. Cell 115: 565–576.

37. Randow F, Lehner PJ (2009) Viral avoidance and exploitation of the ubiquitin system. Nat Cell Biol 11: 527–534.

38. Isaacson MK, Ploegh HL (2009) Ubiquitination, ubiquitin-like modifiers, and deubiquitination in viral infection. Cell Host Microbe 5: 559–570.

39. Henderson BR, Eleftheriou A (2000) A comparison of the activity, sequence specificity, and CRM1-dependence of different nuclear export signals. Exp Cell Res 256: 213–224.

40. Pankiv S, Lamark T, Bruun JA, Overvatn A, Bjorkoy G, et al. (2010) Nucleocytoplasmic shuttling of p62/SQSTM1 and its role in recruitment of nuclear polyubiquitinated proteins to promyelocytic leukemia bodies. J Biol Chem 285: 5941–5953.

41. Li SY, Davidson PJ, Lin NY, Patterson RJ, Wang JL, et al. (2006) Transport of galectin-3 between the nucleus and cytoplasm. II. Identification of the signal for nuclear export. Glycobiology 16: 612–622.

42. Rodriguez JJ, Cruz CD, Horvath CM (2004) Identification of the nuclear export signal and STAT-binding domains of the Nipah virus V protein reveals mechanisms underlying interferon evasion. J Virol 78: 5358–5367.

43. Patnaik A, Chau V, Wills JW (2000) Ubiquitin is part of the retrovirus budding machinery. Proc Natl Acad Sci U S A 97: 13069–13074.

44. Schubert U, Ott DE, Chertova EN, Welker R, Tessmer U, et al. (2000) Proteasome inhibition interferes with gag polyprotein processing, release, and maturation of HIV-1 and HIV-2. Proc Natl Acad Sci U S A 97: 13057–13062.

45. Vogt VM (2000) Ubiquitin in retrovirus assembly: actor or bystander? Proc Natl Acad Sci U S A 97: 12945–12947.

46. Morita E, Sundquist WI (2004) Retrovirus budding. Annu Rev Cell Dev Biol 20: 395–425.

47. Hoeller D, Crosetto N, Blagoev B, Raiborg C, Tikkanen R, et al. (2006) Regulation of ubiquitin-binding proteins by monoubiquitination. Nat Cell Biol 8: 163–169.

48. Qian SB, Ott DE, Schubert U, Bennink JR, Yewdell JW (2002) Fusion proteins with COOH-terminal ubiquitin are stable and maintain dual functionality in vivo. J Biol Chem 277: 38818–38826.

49. Carter S, Bischof O, Dejean A, Vousden KH (2007) C-terminal modifications regulate MDM2 dissociation and nuclear export of p53. Nat Cell Biol 9: 428–435.

50. Lee JC, Wang GX, Schickling O, Peter ME (2005) Fusing DEDD with ubiquitin changes its intracellular localization and apoptotic potential. Apoptosis 10: 1483–1495.

51. Spearman P, Wang JJ, Vander Heyden N, Ratner L (1994) Identification of human immunodeficiency virus type 1 Gag protein domains essential to membrane binding and particle assembly. J Virol 68: 3232–3242.

52. Hermida-Matsumoto L, Resh MD (2000) Localization of human immunodeficiency virus type 1 Gag and Env at the plasma membrane by confocal imaging. J Virol 74: 8670–8679.

53. Rodgers W (2002) Making membranes green: construction and characterization of GFP-fusion proteins targeted to discrete plasma membrane domains. Biotechniques 32: 1044–1046, 1048, 1050–1041.

54. Shenoy-Scaria AM, Gauen LK, Kwong J, Shaw AS, Lublin DM (1993) Palmitylation of an amino-terminal cysteine motif of protein tyrosine kinases p56lck and p59fyn mediates interaction with glycosyl-phosphatidylinositol-anchored proteins. Mol Cell Biol 13: 6385–6392.

55. Elliott PJ, Zollner TM, Boehncke WH (2003) Proteasome inhibition: a new anti-inflammatory strategy. J Mol Med 81: 235–245.

56. Sanchez-Serrano I (2006) Success in translational research: lessons from the development of bortezomib. Nat Rev Drug Discov 5: 107–114.

57. Papandreou CN, Daliani DD, Nix D, Yang H, Madden T, et al. (2004) Phase I trial of the proteasome inhibitor bortezomib in patients with advanced solid tumors with observations in androgen-independent prostate cancer. J Clin Oncol 22: 2108–2121.

58. Ogawa Y, Tobinai K, Ogura M, Ando K, Tsuchiya T, et al. (2008) Phase I and II pharmacokinetic and pharmacodynamic study of the proteasome inhibitor bortezomib in Japanese patients with relapsed or refractory multiple myeloma. Cancer Sci 99: 140–144.

59. Hicke L (2001) Protein regulation by monoubiquitin. Nat Rev Mol Cell Biol 2: 195–201.

60. Johnson ES (2002) Ubiquitin branches out. Nat Cell Biol 4: E295–298.

61. Tanaka T, Soriano MA, Grusby MJ (2005) SLIM is a nuclear ubiquitin E3 ligase that negatively regulates STAT signaling. Immunity 22: 729–736.

62. Natoli G, Chiocca S (2008) Nuclear ubiquitin ligases, NF-kappaB degradation, and the control of inflammation. Sci Signal 1: pe1.

63. Martin-Serrano J (2007) The role of ubiquitin in retroviral egress. Traffic 8: 1297–1303.

64. Saad JS, Miller J, Tai J, Kim A, Ghanam RH, et al. (2006) Structural basis for targeting HIV-1 Gag proteins to the plasma membrane for virus assembly. Proc Natl Acad Sci U S A 103: 11364–11369.

65. Gonzalo S, Linder ME (1998) SNAP-25 palmitoylation and plasma membrane targeting require a functional secretory pathway. Mol Biol Cell 9: 585–597.

66. Manie SN, de Breyne S, Vincent S, Gerlier D (2000) Measles virus structural components are enriched into lipid raft microdomains: a potential cellular location for virus assembly. J Virol 74: 305–311.

67. Brown G, Rixon HW, Sugrue RJ (2002) Respiratory syncytial virus assembly occurs in GM1-rich regions of the host-cell membrane and alters the cellular distribution of tyrosine phosphorylated caveolin-1. J Gen Virol 83: 1841–1850.

68. Ali A, Nayak DP (2000) Assembly of Sendai virus: M protein interacts with F and HN proteins and with the cytoplasmic tail and transmembrane domain of F protein. Virology 276: 289–303.

69. Reed LJ, Muench H (1938) A simple method of estimating fifty percent endpoints. The American Journal of Hygiene 493–397.

70. Lim KL, Chew KC, Tan JM, Wang C, Chung KK, et al. (2005) Parkin mediates nonclassical, proteasomal-independent ubiquitination of synphilin-1: implications for Lewy body formation. J Neurosci 25: 2002–2009.

71. Guo X, Roldan A, Hu J, Wainberg MA, Liang C (2005) Mutation of the SP1 sequence impairs both multimerization and membrane-binding activities of human immunodeficiency virus type 1 Gag. J Virol 79: 1803–1812.

CHAPTER 3.3

CONSERVATION OF UBIQUITIN-REGULATED NUCLEAR AND SUBNUCLEAR TRAFFICKING AMONG *PARAMYXOVIRINAE* MATRIX PROTEINS

ABSTRACT

The paramyxovirus matrix (M) protein is a molecular scaffold required for viral morphogenesis and budding at the plasma membrane. Transient nuclear residence of some M proteins hints at non-structural roles. However, little is known regarding the mechanisms that regulate the nuclear sojourn. Previously, we found that the nuclear-cytoplasmic trafficking of Nipah virus M (NiV-M) is a prerequisite for budding, and is regulated by a bipartite nuclear localization signal (NLS_{bp}), a leucine-rich nuclear export signal (NES), and monoubiquitination of the K258 residue within the NLS_{bp} itself (NLS_{bp}-lysine). To define whether the sequence determinants of nuclear trafficking identified in NiV-M are common among other *Paramyxovirinae* M proteins, we generated the homologous NES and NLS_{bp}-lysine mutations in M proteins from the five major *Paramyxovirinae* genera. Using quantitative 3D confocal microscopy, we determined that the NES and NLS_{bp}-lysine are functionally conserved for the nuclear export of the M proteins of Nipah virus, Hendra virus, Sendai virus, and Mumps virus. Pharmacological depletion of free ubiquitin or mutation of the conserved NLS_{bp}-lysine to an arginine, which inhibits M ubiquitination, also results in nuclear and nucleolar retention of these M proteins. Recombinant Sendai virus (rSeV-eGFP) bearing the NES or NLS_{bp}-lysine M mutants rescued at similar efficiencies to wild type. However, foci of cells expressing the M mutants displayed marked fusogenicity in contrast to wild type, and infection did not spread. Finally, shotgun proteomics experiments indicated that the interactomes of *Paramyxovirinae* M proteins are significantly enriched for components of the nuclear pore complex, nuclear transport receptors, and nucleolar proteins. We then synthesize our functional and proteomics data to propose a working model for the ubiquitin-regulated nuclear-cytoplasmic trafficking of M proteins. Altogether, our results shed light on the cell biology of paramyxoviral M proteins, and reveal heretofore unappreciated aspects of M function.

AUTHOR SUMMARY

Elucidating virus-cell interactions is fundamental to understanding viral replication and identifying targets for therapeutic control of viral infection. Paramyxoviruses include human and animal pathogens of medical and agricultural significance. Their matrix (M) structural protein organizes virion assembly at the plasma membrane and mediates viral budding. While nuclear localization of M proteins has been described for some paramyxoviruses, the underlying mechanisms of nuclear trafficking and the biological relevance of this observation have remained largely unexamined. Through comparative analyses of M proteins across five *Paramyxovirinae* genera, we identify partially conserved mechanisms of nuclear trafficking. These include a bipartite NLS as well as a NES sequence within M that may mediate the interaction of M with host nuclear transport receptors. Additionally, a conserved lysine within the NLS of some M proteins is required for nuclear export by regulating M ubiquitination. Sendai virus engineered to express a ubiquitination-defective M does not produce infectious virus but instead displays extensive cell-cell fusion while M is retained in the nucleolus. Thus, some *Paramyxovirinae* M proteins undergo regulated and active nuclear and subnuclear transport, a prerequisite for viral morphogenesis, which also suggests yet to be discovered roles for M in the nucleus.

INTRODUCTION

Paramyxoviruses include pathogens of global medical and agricultural concern. These viruses occupy broad ecological niches infecting a wide range of hosts including mammals, reptiles, birds and fish, and they cause diverse outcomes ranging from asymptomatic infection to lethal disease. Measles virus (MeV), mumps virus (MuV), the human parainfluenza viruses (hPIVs), respiratory syncytial virus (RSV), and human metapneumoviruses remain significant causes of human morbidity and mortality.[1] Animal pathogens, such as Newcastle disease virus (NDV) and the recently eradicated Rinderpest virus,[2] have caused significant rates of lethal disease in birds

and cattle, respectively. The newly emergent zoonotic paramyxoviruses Nipah virus (NiV) and Hendra virus (HeV) are among the most deadly known pathogens, showing case-fatality rates in excess of 70% in humans, and are classified as biosafety level 4 pathogens due to the absence of vaccines or therapeutics approved for human use.[3-6]

Paramyxoviruses are released as enveloped viruses from the host cell plasma membrane. Virions tend to measure ~150-300 nm in diameter and are spherical, pleiomorphic or filamentous in shape, depending on the virus and the producer cell-type. The non-segmented, single-strand, negative-sense RNA genomes of paramyxoviruses consist of six principle genes: nucleocapsid (N), phosphoprotein (P), matrix (M), fusion (F) and attachment (HN, H or G) glycoproteins, and polymerase (L).[1,5,7] The attachment and fusion glycoproteins mediate binding to sialic acid moieties or to specific protein receptors on the cell surface and the fusion of the viral envelope with the host cell plasma membrane.[8-10] Within the virion, the ribonucleoprotein (RNP) consists of the RNA-dependent RNA polymerase complex formed by P and L associated with the N-encapsidated RNA genome. L is required for viral RNA synthesis during viral replication.[1,5]

M is the major viral structural protein.[1,5,7] A number of studies have found that M proteins oligomerize, bind lipids, and form a grid-like array on the inner surface of the viral membrane.[7,11-25] M proteins can serve as a molecular scaffold by interacting with the cytoplasmic tails of the transmembrane glycoproteins and the RNP via N.[7,17,25-35] Many paramyxoviral M proteins (NiV-M, MeV-M, NDV-M, SeV-M, and hPIV1-M) can drive viral budding and form virus-like particles (VLPs) in the absence of other viral components,[13,31,36-42] albeit with varying efficiencies. However, the budding of some others (PIV5-M and MuV-M) requires coexpression of N and/or the envelope glycoproteins.[43,44] MeV and SeV engineered with budding-defective or deleted M proteins have been found to have severe defects in viral replication.[45-47]

Although paramyxoviruses are classic cytoplasmic replicating viruses, some paramyxoviral M proteins have been observed to traffic through the nucleus. For example, SeV-

M, NDV-M and RSV-M can be detected in the nucleus at early stages of infection.[48-53] These findings suggest that paramyxoviral M proteins may perform roles beyond viral assembly at the plasma membrane. However, with the exception of RSV, which belongs to the *Pneumovirinae* subfamily, the cell biology of M protein nuclear trafficking has not been examined in a systematic fashion for most *Paramyxovirinae* subfamily members. We previously found that NiV-M translocates to the nucleus at early stages of infection. The high homology between NiV-M and HeV-M (~90% amino acid identity) suggests that HeV-M also localizes to the nucleus, and it was recently found that overexpression of ANP32B, a nuclear protein, results in nuclear accumulation of HeV-M and NiV-M.[54] We have shown that nuclear-cytoplasmic trafficking of NiV-M is mediated by a classical bipartite nuclear localization signal (NLS_{bp}), homologous to NDV-M's NLS_{bp}, and a leucine-rich nuclear export signal (NES).[39,48] We further demonstrated that nuclear trafficking is regulated by ubiquitination, presumably on a conserved lysine residue (K258) located within the NLS_{bp} of NiV-M (^{244}RR-X10-RR**K**^{258}). The K258A mutant is defective in nuclear import, while the K258R mutant retains a functional NLS but is defective in nuclear export; both mutants have decreased levels of ubiquitination and have budding defects.[39]

The canonical NES and NLS_{bp} that we functionally characterized in NiV-M are highly conserved across most, if not all members of the *Paramyxovirinae*. Therefore, it is important to resolve whether ubiquitin-dependent nuclear-cytoplasmic trafficking of M is unique to NiV, or a process shared by other members of the subfamily, as this has direct bearing on the fundamental biology of paramyxoviral replication. Here, we specifically analyze ubiquitin-dependent nuclear-cytoplasmic trafficking of M proteins across representative viruses from all five major genera of *Paramyxovirinae* (*Respirovirus*, *Rubulavirus*, *Morbillivirus*, *Henipavirus*, *and Avulavirus*). We use a panoply of methods including quantitative 3D confocal microscopy analysis of M nuclear localization, bimolecular fluorescence complementation (BiFC) assays of M ubiquitination, and introduction of M mutations into live recombinant virus with the use of reverse genetics. Our findings demonstrate that ubiquitination of M, regulated by the conserved

lysine within the NLS_{bp}, controls the subnuclear and nuclear-cytoplasmic trafficking of M proteins from prototypic viruses of the *Henipavirus*, *Rubulavirus* and *Respirovirus* genera. Proteomic identification of nuclear transport receptors and nuclear pore complex components that co-purify with paramyxoviral M proteins further supports a model for active transport of M in and out of the nucleus, and also hints at possible non-structural functions of M proteins.

MATERIALS AND METHODS

Cell culture and transfection

HeLa, Vero, and HEK 293T cells were maintained at 37°C in a 5% CO_2 atmosphere in Dulbecco's modified Eagle's medium (DMEM) supplemented with 10% fetal bovine serum (FBS) and 1% 100X penicillin/streptomycin solution (Gibco/Life Technologies, Gaithersburg, MD). For confocal microscopy imaging, cells were seeded on 22 mm #1.5 coverglass coated with Collagen Type I (BD Biosciences, San Jose, California). Cells were transfected using Lipofectamine LTX per the manufacturer's instructions (Invitrogen/Life Technologies). 3X-Flag-M Flp-In™ T-REx™-293 cell lines, generated as described below, were maintained at 37°C in a 5% CO_2 atmosphere in DMEM supplemented with 10% dialyzed FBS and 1% 100X penicillin/streptomycin solution. 3X-Flag-M protein expression was induced and immunoprecipitated as described below.

Plasmids, cell lines and virus reverse genetics constructs

Codon optimization and cloning of 3X-Flag-tagged and 3X-Flag-GFP-tagged Nipah virus matrix (NiV-M) and generation of corresponding NiV-M mutants is as described.[39] We similarly codon-optimized and cloned the open reading frames encoding M from Hendra virus (HeV-M, genus *Henipavirus*), Sendai virus (SeV-M, genus *Respirovirus*), Mumps virus (MuV-M, genus *Rubulavirus*), Measles virus (MeV-M, genus *Morbillivirus*), and Newcastle disease virus (NDV-M, genus *Avulavirus*): briefly, eGFP was fused to the N-terminus of M by overlap extension PCR (OE-PCR). WT or GFP-fused HeV-M, SeV-M, RSV-M, MuV-M, and MeV-M were inserted

within the HindIII and XhoI sites of pCMV-3Tag-1, while NDV-M was inserted within HindIII and ApaI sites of pCMV-3Tag-1 (Agilent Technologies, Santa Clara CA) to generate 3X-Flag- and 3X-Flag-GFP-tagged-M constructs. Alignment of M sequences using Clustal Omega identified sequences motifs corresponding to NiV-M's nuclear export sequence (NES) and bipartite nuclear localization sequence (NLS_{bp}).[39,55] Mutations were generated using the QuikChange II site-directed mutagenesis kit using PAGE-purified mutagenesis primers designed using the online QuikChange primer design tool (Agilent Technologies). The construct expressing HA-UbK0 (Addgene; plasmid 17603; all lysines mutated to arginines) is as described.[56]

The FLP-In™ T-REx™ system (Invitrogen) was used to generate doxycycline-inducible 3X-Flag-M cell lines. Codon-optimized 3X-Flag-tagged NiV-M, HeV-M, SeV-M, and NDV-M were inserted within the KpnI and XhoI sites of pcDNA5/FRT/TO. The constructs and pOG44 were co-transfected into Flp-In™ T-REx™-293 cells, and stable cell lines were selected with hygromycin and blasticidin according to the manufacturers instructions.

Constructs for bimolecular fluorescence complementation (BiFC) analyses were generated with split Venus residues 1-172 (VN173) and 155-238, A206K (VC155).[57,58] VN173 and VC155 were PCR-amplified from pBiFC-VN173 (Addgene plasmid 22010) and pBiFC-VC155 (Addgene plasmid 22011), and were fused to the N-termini of Ub and M proteins via a flexible linker encoding GGGGSGGGGGR by OE-PCR. VN173-Ub and VC155-M were inserted within the NotI and XhoI sites of pcDNA3.1(+) (Life Technologies). Mutations within VC155-M constructs were generated using the QuikChange II site-directed mutagenesis kit using PAGE-purified mutagenesis primers designed using the online QuikChange primer design tool (Agilent Technologies).

The recombinant Sendai virus (rSeV) anti-genome RGV0, a Fushimi strain construct with F1-R strain mutations in F and M, and helper plasmids encoding SeV N, P and L were the kind gift of Dr. Nancy McQueen and are as described.[59] The encoded virus has the ability to replicate in mammalian cells without the addition of trypsin. We further modified the rSeV anti-

genome construct by inserting an eGFP reporter flanked at the 3' end by a unique NotI site between the N and P genes. A hammerhead ribozyme sequence was inserted between the optimal T7 promoter and the start of the anti-genome. Mutations were introduced into the SeV-M ORF by OE-PCR using primers containing the desired mutations, followed by insertion into NotI and AfeI sites in the parental rSeV-eGFP construct.

Multidimensional protein identification technology (MudPIT) analysis of matrix interactomes

3X-Flag-M Flp-In™ T-REx™-293 cell lines were grown to ~80% confluency and induced for protein expression with 100 ng/mL doxycycline for 24h. Cells were washed three times in dPBS and lysed in 100 mM Tris-HCL pH 8, 150 mM NaCL, 5 mM EDTA, 5% glycerol, 0.1% NP40, complete protease cocktail (Roche), PhosSTOP (Roche) and 25 mM N-ethylmaleimide. Cell lysate was clarified by centrifugation at >15,000×g for 15 min at 4°C and incubated with lysis buffer-equilibrated anti-Flag M2 affinity gel (Sigma-Aldrich, St. Louis, MO) for 2 hours at 4°C. The affinity gel was extensively washed with lysis buffer and then with elution buffer consisting of 100 mM Tris-HCL pH 8, 150 mM NaCL, 5 mM EDTA, and 5% glycerol. Bound proteins were eluted from the affinity gel with elution buffer containing 3X-Flag peptide (Sigma-Aldrich), were precipitated with trichloroacetic acid, washed with acetone twice, dried, and stored at -20 °C until further processing.

Protein samples were resuspended in 8M urea in 100 mM Tris pH 8.5, reduced, alkylated and digested by the sequential addition of lys-C and trypsin proteases as previously described.[60] The digested peptide solution was fractionated online using strong-cation exchange and reverse phase chromatography and eluted directly into an LTQ-Orbitrap mass spectrometer (Thermofisher).[60,61] MS/MS spectra were collected and subsequently analyzed using the ProLuCID and DTASelect algorithms.[62,63] Database searches were performed against a human database containing the relevant paramyxovirus M protein sequence. Protein and peptide identifications were further filtered with a false positive rate of less than 5% as estimated by a

decoy database strategy.[64] Normalized spectral abundance factor (NSAF) values were calculated as described.[65] Proteins were considered candidate M-interacting proteins if they were identified in the relevant affinity purification but not present in 3 independent control purifications using lysates from the parental Flp-In™ T-REx™-293 cells. Gene-annotation enrichment analysis was performed using DAVID Bioinformatics Resources 6.7.[66,67] Physical and predicted protein interaction networks were visualized using the GeneMANIA plugin for Cytoscape 3.1.[68,69]

Immunoblot analysis of matrix ubiquitination

HEK 293T cells were cotransfected with 3X-Flag-M and HA-UbK0 for 24h. To immunoprecipitate ubiquitinated M, cells were washed once in dPBS and lysed in 100 mM Tris-HCL pH 8, 150 mM NaCL, 5 mM EDTA, 5% glycerol, 0.1% NP40, complete protease cocktail (Roche) and 25 mM N-ethylmaleimide. The cell lysate was clarified by centrifugation at >15,000×g for 15 min at 4°C before incubation overnight at 4°C with lysis buffer-equilibrated anti-Flag M2 affinity gel (Sigma-Aldrich, St. Louis, MO). The affinity gel was extensively washed with lysis buffer and then with elution buffer consisting of 100 mM Tris-HCL pH 8, 150 mM NaCL, 5 mM EDTA, and 5% glycerol. Bound proteins were eluted from the affinity gel with elution buffer containing 3X-Flag peptide (Sigma-Aldrich), were subjected to SDS-PAGE and transferred to Immobilon-FL PVDF membrane (EMD Millipore, Billerica, MA). Membranes were simultaneously probed with mouse anti-Flag M2 primary antibodies (Sigma-Aldrich) and rabbit anti-HA primary antibodies (Novus Biologicals, Littleton, CO) followed by anti-mouse-680 and anti-rabbit-800 secondary antibodies (LI-COR, Lincoln, Nebraska) and imaged on an Odyssey infrared scanner (LI-COR) according to the manufacturer's instructions. To quantify relative ubiquitination, the background subtracted integrated fluorescence intensities of the monoubiquitin bands (Ub) normalized to total M (M_0+M_1) was determined using LI-COR Odyssey software.

Depletion of cellular free ubiquitin

For 3D confocal microscopy analysis, transfected HeLa cells were treated with 50 μM MG132 or 0.5% DMSO at 16 h post-transfection for 8 hours, then fixed and processed for quantitative image analysis as described below. For immunoblot analysis of M ubiquitination during ubiquitin depletion, transfected HEK 293T cells were treated with 10 μM MG132 or 0.1% DMSO at 18 h post-transfection for 6 hours, and 3X-Flag-M was immunoprecipitated as described above.

Quantification of virus-like particle budding

VLP budding assays were performed as described.[39] Briefly, precleared supernatants from 3X-Flag-M-transfected HEK 293T were ultracentrifuged through a 20% (w/v) sucrose at 36,000 rpm for 2 h at 4 °C (AH-650 rotor, Thermo Scientific). VLP pellets and cells were resuspended in lysis buffer and subjected to SDS-PAGE and anti-Flag immunoblotting. Relative integrated intensity of VLP/cell lysate bands were quantified and normalized relative to the budding of 3X-Flag-NiV-M.

Nipah virus infection and recombinant Sendai virus rescue

HeLa cells were infected with Nipah virus under biosafety level 4 (BSL-4) conditions as described.[39] For rescue of WT or mutant rSeV-eGFP, 2X10^6 HEK 293T cells were transfected with recombinant plasmid encoding the anti-genome (4 μg) along with the cognate accessory plasmids encoding SeV NP (1.44 μg), P (0.77 μg), and L (0.07 μg), and a codon-optimized T7 RNA polymerase (4 μg) using Lipofectamine LTX (8.9 μL) and Plus Reagent (5.5 μL), according to manufacturer's instructions. Cells were harvested for FACS analysis at 48 hours post-transfection (the earliest time point when GFP-positive cells can be observed by epifluorescence microscopy, yet when supernatant titer is still not detectable) to quantify rescue efficiency. The number of GFP-positive cells (rescue events) was determined from 500,000 cells analyzed with a FACSCalibur Flow Cytometer (BD Biosciences) and FlowJo software (TreeStar Inc., Ashland, OR). Cells plated on coverslips were fixed at day 6 post-transfection for analysis of rescued virus infection by 3D confocal microscopy. Supernatant was collected from rescue cells at day 6 post-

transfection for quantification of viral titers. Briefly, supernatant stored at -80°C was thawed on ice and serial diluted 2-fold in serum-free DMEM. 100 μL of each dilution was used to infect ~60,000 Vero cells in a 24-well plate for 1 hour. After 1 h, 500 μL of DMEM 10% FBS was added to each well and the cells were incubated at 37°C. Cells were harvested for FACS analysis at 24 h post infection and titers were calculated based on percent infection in the linear range of supernatant dilutions.

Microscopy and antibodies

Nipah virus-infected cells were fixed in 10% formalin solution for a minimum of 24h prior to removal from the BSL-4 laboratory. For all other immunofluorescence microscopy, samples were fixed with 2% paraformaldehyde in 100 mM phosphate buffer (pH 7.4) for 15 min. Fixed cells were permeabilized in blocking buffer containing PBS, 1% saponin, 3% bovine serum albumin, and 0.02% sodium azide. After incubation with antibodies/probes in blocking buffer, samples were extensively washed in blocking buffer and mounted on glass slides with Vectashield mounting medium with DAPI (Vector Laboratories, Burlingame, California, United States). The samples were imaged with a Leica SP5 confocal microscope (Leica Microsystems, Buffalo Grove, IL), acquiring optical Z-stacks of 0.3-0.5 μm steps. Z-stacks were reconstructed and analyzed in three dimensions using Volocity 5.5 software (Perkin Elmer, Waltham, Massachusetts). NiV-M was detected with rabbit anti-NiV-M antibodies (1:1000).[39] SeV-M was detected with mouse anti-SeV-M ascites (1:200), and SeV-F was detected with mouse anti-SeV-F ascites (1:200) kindly provided by Dr. Toru Takimoto.[70] Nucleoli were detected with mouse anti-nucleolin antibodies (1:500) (Invitrogen/Life Technologies) or rabbit anti-fibrillarin antibodies (1:500) (Abcam, Cambridge, MA). Alexa Fluor-conjugated Anti-IgG antibodies of appropriate species reactivity and fluorescence spectra were used for secondary detection (1:300-1:1000) (Invitrogen/Life Technologies). F-actin was visualized by incubating samples with Alexa Fluor-conjugated phalloidins (1:300) (Invitrogen/Life Technologies).

Quantitative analysis of 3D confocal micrographs

Random 40X fields were imaged using acquisition settings ensuring no under-saturated or over-saturated pixel intensities. Volocity 5.5 software was used for quantitative analysis of 3D confocal images. To determine the quantity of nuclear M, the nuclear compartment was defined with the find objects function within the DAPI-fluorescence channel. Holes in objects (DNA-absent regions such as nucleoli) were filled, and fluorescent objects smaller than nuclei were excluded. The entire cell body was defined by drawing a region of interest (ROI) encompassing all F-actin staining. The sum of voxel intensities in the GFP channel was measured within these defined sets. The average voxel fluorescence of untransfected cells was used for background subtraction. To quantify fluorescence from bimolecular fluorescence complementation images, an ROI was drawn around cells fluorescent in the YFP channel. The average voxel fluorescence of untransfected cells was used for background subtraction.

Statistical analysis

For analysis of M nuclear localization, p-values were generated with a Student's t-test when analyzing two sample groups. To analyze three or more sample groups, p-values were generated by ANOVA with Bonferroni correction for multiple comparisons. To analyze BiFC experiments, p-values were generated using a Mann-Whitney test. All graphs and statistical analyses were generated with Prism 6 (GraphPad Software, La Jolla, CA).

RESULTS

Nuclear export of some *Paramyxovirinae* matrix proteins is regulated by the ubiquitin-proteasome system

Since the nuclear-cytoplasmic trafficking of the Nipah virus matrix protein (NiV-M) is regulated by its monoubiquitination,[39] we wondered whether the ubiquitin-proteasome system similarly regulates the nuclear sojourn of other *Paramyxovirinae* M proteins. We cloned 3X-Flag- and GFP-tagged-M from prototypical members of the five *Paramyxovirinae* genera: NiV-M (genus *Henipavirus*), Hendra virus M (HeV-M, genus *Henipavirus*), Sendai virus M (SeV-M, genus

Respirovirus), Mumps virus M (MuV-M, genus *Rubulavirus*), Newcastle disease virus M (NDV-M, genus *Avulavirus*), and Measles virus M (MeV-M, genus *Morbillivirus*). To biochemically detect ubiquitination of M proteins, we co-transfected HEK 293T cells with HA-UbK0 and each of 3X-Flag-tagged NiV-M, HeV-M, SeV-M, MuV-M, NDV-M or MeV-M.[56] HA-UbK0 functions as a ubiquitin (Ub) chain terminator or as monoubiquitin because all lysines have been mutated to arginines. We used this construct to visualize discrete ubiquitin bands and to determine if matrix proteins can be monoubiquitinated since this posttranslational modification can regulate the function of proteins without promoting proteasome-dependent protein degradation.[71] Cell lysates were subjected to anti-Flag immunoprecipitation (IP) and immunoblots were simultaneously probed with anti-HA and anti-Flag antibodies. As shown in Figure 3-19 (panel A), for all the M proteins the majority of M is unmodified (M_0) at steady state. However, a detectable minority of M (M_1) is size-shifted by the molecular weight of at least one ubiquitin monomer (Ub, ~8.5 kDa) (Figure 3-19, panel A, merge). No anti-HA bands were detected when cells were cotransfected with HA-UbK0 and an empty vector (data not shown). These results indicate that all M proteins investigated are ubiquitin substrates.

We have found that proteasome inhibition results in nuclear retention of NiV-M in transfected and in NiV-infected cells (Figure 3-20).[39] Proteasome inhibition stabilizes polyubiquitinated proteins and depletes the cellular levels of free ubiquitin available for conjugation.[72-77] To determine whether ubiquitination is involved in the nuclear export of the other *Paramyxovirinae* M proteins, we treated GFP-M-expressing HeLa cells with the proteasome inhibitor MG132 (Figure 3-19, panels B-G). We used quantitative 3D confocal microscopy to characterize the subcellular localization of M. The cells were counterstained with DAPI to visualize nuclei, and with fluorescent phalloidin to visualize the entire cell, and the proportion of nuclear M was determined computationally as described in Materials and Methods. As with GFP-NiV-M, ubiquitin depletion via proteasome inhibition resulted in significant nuclear retention of GFP-tagged HeV-M, SeV-M and MuV-M (Figure 3-19, panels B-

E),[39] but not NDV-M or MeV-M (Figure 3-19, panels F-G). We further confirmed biochemically that MG132 reduces the direct conjugation of ubiquitin to NiV-M, HeV-M, SeV-M, and MuV-M by co-IP of each 3X-Flag-tagged-M and HA-UbK0, as described above, with quantification of immunoblot band integrated intensities as described in Materials and Methods (Figure 3-21). These results indicate that the nuclear-cytoplasmic trafficking of NiV-M, HeV-M, SeV-M, and MuV-M are controlled by the ubiquitin-proteasome system.

Nuclear export of some *Paramyxovirinae* matrix proteins is regulated by a conserved NES and a conserved lysine within the NLS_{bp}

We have shown that the nuclear-export of NiV-M is regulated by a leucine-rich nuclear export signal (NES) as well as by the K258 lysine residue located within the second basic patch of the bipartite nuclear localization signal (NLS_{bp}; Figure 3-22, panel A, blue residues).[39] A K258A mutation partially disrupts the NLS_{bp} and increases nuclear exclusion of NiV-M, while a K258R mutation is nuclear-retained despite preservation of the positive charge, and both mutants are impaired for ubiquitination.[39] Sequence alignment of M proteins indicates that this NLS_{bp}-lysine is highly conserved across the *Paramyxovirinae* genera. Thus, we hypothesized that this residue might be conserved for regulation of M ubiquitin-dependent nuclear export (Figure 3-22, panel A, bold and underlined blue residues). To interrogate our hypothesis, we mutated the NLS_{bp}-lysine to an arginine in all M proteins studied and analyzed their subcellular localization by quantitative 3D confocal microcopy as described above (Figure 3-22, panels B-G, and quantified in Figure 3-22, panel H). Since NDV-M contains another lysine adjacent to this position, we mutated both (Figure 3-22, panel A, bold and underlined blue residues). A lysine-to-arginine mutation is expected to preserve the nuclear import function of the putative NLS_{bp}, but prevents posttranslational modification at that position. As a comparison for nuclear retention, we also mutated the leucines that correspond to the NES of NiV-M within all M proteins (Figure 3-22, panel A, bold and underlined blue residues).[39]

Mutation of the NES of GFP-NiV-M ($M_{L106A\ L107A}$) resulted in a significant increase in nuclear localization of the protein, which confirms our previous findings (Figure 3-22, panels B and H).[39] Similarly, GFP-tagged HeV-$M_{L106A\ 107A}$, SeV-$M_{L102A\ L103A}$, and MuV-M_{L106A} were also nuclear-retained compared to their respective wild type (WT) proteins (Figure 3-22, panels C-E, H). In contrast, GFP-NDV-$M_{L103A\ L106A}$ had an apparent nuclear exclusion phenotype (Figure 3-22, panels F and H), while the nuclear localization of GFP-MeV-$M_{L90A\ 191A}$ was not significantly different than WT (Figure 3-22, panels G and H).

As quantified in Figure 3-22 (panel H), GFP-tagged NiV-M_{K258R}, HeV-M_{K258R}, SeV-M_{K254R}, MuV-M_{K261R}, and NDV-$M_{K259R\ K260R}$, but not MeV-M_{K240R}, were significantly enhanced in nuclear localization. The spread in the degree of nuclear localization for any given M mutant also emphasizes the need to score a sufficient number of cells by computationally defined volumetric criteria (see Materials and Methods). In contrast to the NLS_{bp}-lysine-to-arginine mutations, disruption of the NLS_{bp} consensus sequence through alanine substitutions resulted in diffuse cytoplasmic localization of GFP-tagged NiV-M, HeV-M, SeVM, and MuV-M (Figure 3-23), as has been previously shown for NDV-M.[48] Combined, these results indicate that NiV-M, HeV-M, SeV-M, and, MuV-M display ubiquitin-dependent nuclear-cytoplasmic trafficking, and that a conserved lysine residue within the conserved NLS_{bp} plays dual roles in regulating this trafficking.

The conserved lysine within the NLS_{bp} regulates ubiquitination of Nipah, Hendra, Sendai and Mumps matrix proteins

Since the proteasome inhibitor MG132 inhibits the nuclear export of NiV-M, HeV-M, SeV-M, and MuV-M (Figure 3-19), we tested whether the conserved NLS_{bp}-lysine that regulates their nuclear export (Figure 3-22) also regulates their ubiquitination. We first assessed the ability of 3X-Flag-tagged NiV-M_{K258R}, HeV-M_{K258R}, SeV-$M_{K254R,}$ and MuV-M_{K261R} to be ubiquitinated biochemically, via co-IP of 3X-Flag-tagged-M with HA-UbK0, as described above (Figure 3-24, panels A-D). 3X-Flag-tagged NiV-M_{K258R} (Figure 3-24, panel A) and HeV-M_{K258R} (Figure 3-24,

panel B) exhibited the greatest reduction in relative monoubiquitination compared to the WT proteins (>70%), while 3X-Flag-tagged SeV-M_{K254R} (Figure 3-24, panel C) and MuV-M_{K261R} (Figure 3-24, panel D) showed only a modest to mild impairment in monoubiquitination (36% and ~15% reduction, respectively).

Ubiquitination is a dynamic process determined in part by the rates of conjugation versus de-conjugation, but our co-IP and immunoblot analysis of HA-UbK0-modified M is a steady-state assay. It is possible that this assay for ubiquitinated M might not efficiently detect subtle differences that arise from such dynamic processes since i) ubiquitinated M proteins are of low stoichiometry relative to unmodified native protein, ii) M proteins might be mono- and/or polyubiquitinated on multiple lysines, iii) ubiquitination is reversible, and iv) HA-UbK0 must compete with endogenous ubiquitin. To overcome these issues, we developed a bimolecular fluorescence conjugation (BiFC) ubiquitination assay in which ubiquitin-conjugation of M produces an irreversible fluorescence signal (Figure 3-25).[78,79] We fused Ub and M to split fragments of the fluorescent protein Venus, VN173 and VC155, respectively. Covalent conjugation of ubiquitin to M brings the spilt Venus fragments into close proximity and allows the two otherwise non-fluorescent Venus fragments to reconstitute a functional fluorophore.[57,80] This complemented Venus will remain associated with M (via VC155-M) even if the VN173-Ub moiety is subsequently cleaved from M by a de-ubiquitinating enzyme (DUB) (Figure 3-25). Analysis of total cellular fluorescence showed that the Ub-M BiFC signal was decreased by almost 80% for the *Henipavirus*-M K258R mutants (Figure 3-24, panels E and F), confirming the significant role of K258 in ubiquitination of NiV-M (Figure 3-24, panels A and E) and HeV-M (Figure 3-24, panels B and F). In addition, we determined that SeV-M_{K254R} (Figure 3-24, panel G) and MuV-M_{K261R} (Figure 3-24, panel H) were also significantly decreased in ubiquitination (~70% reduction in BiFC fluorescence) compared to the WT proteins. Thus, a conserved lysine within the NLS_{bp} regulates both nuclear export and ubiquitination of NiV-M, HeV-M, SeV-M and MuV-M.

Ubiquitination regulates the subnuclear localization of Nipah, Hendra, Sendai and Mumps virus matrix proteins

We observed a punctate localization of GFP-tagged NiV-M, HeV-M, SeV-M, and MuV-M within DNA-void regions of the nucleus when cells were treated with MG132 (Figure 3-19, panels B-E). Native untagged NiV-M also exhibited similar subnuclear localization in NiV infected cells treated with bortezomib, an FDA approved proteasome inhibitor (Figure 3-20). We determined that MG132 redistributes GFP-tagged NiV-M, HeV-M, SeV-M and MuV-M to nucleoli by counterstaining cells with anti-nucleolin antibodies (Figure 3-26, panels A-D, second vertical panels). The nucleolar localization of M proteins during ubiquitin depletion predicts that mutations in M that prevent efficient ubiquitination would also cause nucleolar retention. Indeed, GFP-tagged NiV-M_{K258R}, HeV-M_{K258R}, SeV-M_{K254R} and MuV-M_{K261R} phenocopied the MG132-induced nucleolar localization of the WT proteins (Figure 3-26, panels A-D, compare the second and third vertical panels). In contrast, the nuclear localized NES mutants, GFP-tagged NiV-$M_{L106A\ 107A}$, HeV-$M_{L106A\ 107A}$, SeV-$M_{L102A\ L103A}$, and MuV-M_{L106A}, were primarily enriched within the nucleoplasm and not the nucleolus. Thus, NES mutants are stalled at a different stage of subnuclear trafficking compared to the NLS_{bp}-lysine mutants (Figure 3-26, panels A-D, fourth vertical panels). Moreover, our data supports a model where proper matrix ubiquitination is required for efficient nucleolar exit.

Ubiquitin-dependent nuclear-export of Sendai virus matrix regulates virus replication and cell-cell fusion

We previously determined that NiV-$M_{L106A\ 107A}$ and NiV-M_{K258R} are defective at budding virus like particles (VLPs).[39] We wanted to compare the effects of the corresponding mutations in SeV-M or MuV-M, however these proteins have a poor budding efficiency that is less than 10% of *Henipavirus*-M proteins (Figure 3-27, panel A). Indeed, SeV-M and MuV-M do not efficiently bud VLPs without the support of other viral proteins.[41-43] To overcome this technical difficulty

and to study these mutations in a biologically relevant context, we engineered SeV-$M_{L102A\ L103A}$ and SeV-M_{K254R} into a recombinant T7-driven, GFP-expressing Sendai virus genome (rSeV-eGFP) that can be rescued as live virus via the cotransfection of support plasmids expressing N, P, L (comprising the necessary replication complex) and a codon-optimized T7 polymerase. This highly efficient reverse genetics system allows us to quantify the number of rescue events directly in transfected producer cells at early time-points (see Materials and Methods). At two days post-transfection, GFP-positive cells (rescue events) could be observed by epifluorescence and quantified by FACS analysis. As a control for background GFP expression in the absence of virus production, we found that cotransfection of WT rSeV-eGFP and T7 polymerase without the N, P and L support plasmids resulted in no GFP-positive cells (data not shown). We determined that rSeV-eGFP-$M_{L102A\ L103A}$, and rSeV-eGFP-M_{K254R} rescued at similar if not higher efficiencies than rSeV-eGFP-M_{WT} (Figure 3-27, panel B). However, only rSeV-eGFP-M_{WT} produced infectious viral titers (~10^7 I.U./ml) at day 6 post-rescue, while the mutants did not produce detectible infectious virus (<10 I.U./ml) (Figure 3-27, panel C).

To determine the nature of the defect in viral replication, we counterstained the viral rescue cells with anti-SeV-M or anti-SeV-F antibodies and analyzed them by 3D confocal microscopy. By day 6 post-rescue of rSeV-eGFP-M_{WT}, infection has spread to all cells without evidence of cell-cell fusion (Figure 3-27, panel D). It is known that SeV replication in cell culture does not result in cell-cell fusion,[45,47,81] an unusual phenotype as most paramyxovirus infections result in extensive cell-cell fusion (e.g. see Figure 3-20 and Figure 3-28 for NiV). Interestingly, although the rSeV-eGFP-$M_{L102A\ L103A}$ and rSeV-eGFP-M_{K254R} rescue cells did not produce infectious virus, the GFP-positive rescue cells did initiate the formation of large foci of fused cells (Figure 3-27, panel D, second and third horizontal panels). Virus-cell and cell-cell fusion require the presence of F and HN,[9,10] and we confirmed that SeV-F is expressed on rSeV-eGFP-$M_{L102A\ L103A}$ and rSeV-eGFP-M_{K254R} foci (Figure 3-27, panel E).

To determine the nuclear localization of SeV-M, we counterstained rSeV-eGFP rescue cells with DAPI to visualize nuclei and anti-fibrillarin antibodies to visualize nucleoli. SeV-M_{WT} was primarily extranuclear at the cell periphery (Figure 3-27, panels D and F). SeV-$M_{L102A\ L103A}$ did not have an obvious nuclear localization in the viral context, although intracellular inclusions were apparent, suggesting that this mutant nonetheless had an altered localization (Figure 3-27, panel F). SeV-M_{K254R}, on the other hand, was strongly nuclear and enriched within the nucleoli (Figure 3-27, panels D and F). These results are consistent with the previous transient transfection experiments in which SeV-M_{K254R} was also more strongly localized to the nucleus than SeV-$M_{L102A\ L103A}$ (Figure 3-22, panel H). Thus, these live virus results support our model that ubiquitination regulates the nuclear and subnuclear trafficking of SeV-M.

Proteomics analysis supports a model of regulated nuclear transport of *Paramyxovirinae* matrix proteins that involves a critical nucleolar transit phase

Having characterized determinants of *Paramyxovirinae* M nuclear-cytoplasmic trafficking encoded within the M proteins, we turned to identifying potential cellular regulators of this process. We generated inducible 3X-Flag-M-expressing stable HEK 293 cell lines to efficiently co-purify M-interacting proteins and analyzed their composition using multidimensional protein identification technology (MudPIT) as described in Materials and Methods. We opted to determine the protein interactomes of NiV-M, HeV-M, SeV-M and NDV-M since these are the *Paramyxovirinae* M proteins with confirmed nuclear trafficking during live virus infection (Figure 3-27, also Figure 3-28),[39,48,51-54,82] and because these proteins cover the widest range of sequence homology to NiV-M: ~90% amino acid identity for HeV-M, ~37% amino acid identity for SeV-M, and ~20% amino acid identity for NDV-M.

Comparisons of the NiV-M, HeV-M, SeV-M, and NDV-M interactomes revealed significant overlap; over 60% of the proteins found in any single interactome were also found in the interactomes of one or more of the other three. Furthermore, we identified 178 proteins common to all M interactomes despite using highly conservative specificity criteria (e.g. a

putative M interactor must not be present in 3 independent control purifications using lysates from the parental/isogenic Flp-In™ T-REx™-293 cells). This common set of proteins represents 24-48% of all the proteins in any single viral M interactome (Figure 3-29, panel A). Interestingly, proteins associated with the nuclear pore complex were significantly enriched within individual M interactomes as well as the subset of common interacting proteins (Figure 3-29, panel B, $-\log_{10}$(p-value)>10). These include nuclear pore complex components (RanBP2, Nup37, Nup93, Nup107, Nup155, Nup205, Sec13, Seh1), nuclear transport receptors (NTRs) required for nuclear import of proteins (α/β-importins), nuclear export of proteins (Exp1/Crm1, Exp2), nuclear export of dsRNA/dsRNA-binding proteins (Exp5), nuclear export of tRNA (Exportin-T), nuclear export of mRNA (Rae1), and a regulator of the RanGTP/GDP cycle that modulates the association/dissociation of cargo with NTRs (RanGAP1) (Figure 3-29, panel C). Thus, *Paramyxovirinae* M proteins interact with a highly inter-connected network of proteins necessary for transport of NLS and NES containing cargo proteins across the nuclear pore. Our cell biological and proteomic findings are synthesized into a working model for ubiquitin-regulated nuclear-cytoplasmic trafficking of M proteins shown in Figure 3-29 (panel D). Consistent with the nucleolar transit phase exhibited by the *Paramyxovirinae* M proteins under study, the M interactomes also revealed a significant enrichment of resident or transient nucleolar proteins (Figure 3-29, panels E and F).

DISCUSSION

Whether or not they replicate in the nucleus, many viruses are known to target, modify, and hijack nuclear components and nuclear functions to promote the infectious life cycle. It is generally thought that paramyxoviruses replicate in the cytosol without a nuclear stage. However, it is becoming increasingly clear that nuclear trafficking of M is shared by a number of paramyxoviruses. It was previously observed that SeV-M, NDV-M and RSV-M traffic through the nucleus[49,50,82] and a functional bipartite nuclear localization signal (NLS_{bp}) has been defined

within NDV-M.[48] Here, we show that the NLS_{bp} of NDV-M is functionally conserved for nuclear import along with NiV-M, HeV-M, SeV-M and MuV-M (Figure 3-29, panel D, and also Figure 3-23).[39,48] Since NiV-M and NDV-M have the most divergent sequences within *Paramyxovirinae*, our findings suggest that most M proteins within this subfamily retain a functional NLS_{bp}. NLSs specify translocation through the nuclear pore through high-affinity interactions with importins, which in turn interact with cognate nuclear pore components on the cytoplasmic side.[83] In our proteomic analyses we identified numerous importins, exportins and nuclear pore complex components as common interactors of NiV-M, HeV-M, SeV-M and NDV-M (Figure 3-29). Thus, the size of *Paramyxovirinae* M proteins (>40 kDa), the presence of a functional NLS_{bp} within M proteins, and the interaction with nuclear transport receptors are strong evidence that the nuclear localization of M proteins is an active and regulated transport process. That the M interactomes show such a strong enrichment of proteins involved in nuclear-cytoplasmic transport also suggests that M proteins may antagonize the nuclear-cytoplasmic trafficking of host proteins and RNA to facilitate viral replication.[84]

In addition to the NLS_{bp}, we show that a leucine-rich NES sequence is functionally conserved within NiV-M, HeV-M, SeV-M and MuV-M (Figure 3-22, Figure 3-26, Figure 3-29, panel D). We note that mutation of the corresponding region in NDV-M resulted in decreased nuclear localization. However, this sequence is not as well conserved as in the other M proteins (Figure 3-22, panel A) and a recent study identified other functional NES motifs within different regions of NDV-M.[52] Thus, *Paramyxovirinae* M proteins appear to have both shared and unique determinants of nuclear-cytoplasmic trafficking depending on their evolutionary heritage. We also acknowledge that our experimental system utilizing human cells may not fully recapitulate the regulation of NDV-M trafficking since NDV is an avian virus, while NiV, HeV, SeV, MuV and MeV are mammalian viruses.

Nuclear export of NiV-M, HeV-M, SeV-M and MuV-M is also regulated by a conserved lysine within the NLS_{bp}. Mutating this lysine to an arginine results in decreased ubiquitination

and a nuclear retention phenotype that is phenocopied by pharmacological depletion of free ubiquitin with a proteasome inhibitor (Figure 3-19, panels B-E; Figure 3-22, panels B-E; Figure 3-24). We hypothesize that mutation of this lysine prevents its ubiquitination. Alternately, mutation of this lysine may prevent the ubiquitination of a nearby lysine within the NLS_{bp} by preventing the interaction of M with a ubiquitin ligase.

How could NLS ubiquitination regulate nuclear trafficking? Protein import into the nucleus is regulated by the affinity of importins for cargo NLSs, which can be modulated by intermolecular or intramolecular masking of the NLS itself.[85,86] For example, ubiquitination of the NLS of p53 by MDM2 has been shown to block p53 nuclear import by preventing the binding of importin-α3.[87] It was recently shown that the ubiquitin-conjugating enzyme UBE2O multi-monoubiquitinates tumor suppressor BAP1 on its NLS_{bp} to promote cytoplasmic localization. It was further determined that UBE2O specifically binds and ubiquitinates a number of similar bipartite NLSs within nuclear trafficking proteins known to regulate RNA processing, transcription, DNA replication, and chromatin remodeling.[88] We hypothesize that ubiquitination of M on a lysine within the NLS_{bp} itself prevents importin binding as a means to prevent nuclear re-entry once the protein has completed its nuclear sojourn (Figure 3-29, panel D). Given this model for ubiquitin-dependent nuclear-cytoplasmic trafficking, it is possible that M utilizes a nuclear-resident E3 ubiquitin ligase (Figure 3-29, panel D).[89] Our proteomic analyses identified a number of candidate ubiquitin ligases that interact with M proteins including UBE2O, which was found within the NiV-M and NDV-M interactomes. Further study of these ubiquitin ligases will help resolve the spatiotemporal dynamics of M ubiquitination vis-à-vis nuclear trafficking.

Nuclear-cytoplasmic trafficking is a prerequisite for M budding and viral morphogenesis. We previously showed that NiV-M mutants defective in either nuclear import or nuclear export were also defective at budding VLPs.[39] Here, we engineered M nuclear export mutants into recombinant SeV. rSeV-eGFP-$M_{L102A\ L103A}$ or rSeV-eGFP-M_{K254R} were completely attenuated for

production of infectious virus, but formed large foci of fused cells at sites of viral rescue. Moreover, nuclear localization of SeV-M_{K254R}, the ubiquitination mutant, was observed in both virus rescue and transient transfection experiments (Figure 3-22, panel D; Figure 3-26, panel C; Figure 3-27, panel F). It is known that mutations that abrogate the interaction of M with the glycoproteins, including M deletion, can increase cell-cell fusion in SeV and MeV, while mutations that enhance their interaction can decrease cell-cell fusion.[33,34,45-47,81] Since M and F proteins were expressed in the foci of fused cells, our results indicate that rSeV-eGFP-$M_{L102A\ L103A}$ and rSeV-eGFP-M_{K254R} are defective in proper assembly of viral components at the plasma membrane rather than in expression of viral components necessary for budding *per se*. The link between viral replication and M ubiquitin-dependent nuclear-cytoplasmic trafficking may explain why proteasome inhibitors that deplete free cellular pools of ubiquitin have been found to inhibit SeV and NiV replication.[39,90]

Beyond regulating nuclear import/export itself, we previously found that ubiquitination of NiV-M is necessary for membrane targeting and budding.[39] It is possible that the ubiquitination of M proteins promotes recognition by cellular factors such as ESCRT complexes known to mediate transport and budding of many enveloped viruses,[71,91,92] especially in light of known sequence motifs in PIV5-M, SeV-M and MuV-M that can bind ESCRT complex components.[27,43,93] The status of M ubiquitination may also regulate the interactions of M with cellular factors inside the nucleus and within subnuclear compartments such as the nucleolus. A number of cellular proteins become enriched in the nucleolus upon proteasome inhibition, including p53.[94-103] Similarly, pharmacological or genetic inhibition of NiV-M, HeV-M, SeV-M, and MuV-M ubiquitination sequesters these proteins in the nucleolus (Figure 3-26), and nucleolar localization of SeV-M_{K254R} was also confirmed in the context of rSeV-eGFP rescue (Figure 3-27, panel F). Nucleolar localization of M proteins is a natural feature of the nuclear sojourn of some M proteins, with M enriched at nucleoli during the early stage of live NiV and NDV infections (Figure 3-28).[82,104] Our proteomics experiments identified many nucleolar

proteins whose interaction with M proteins may determine localization to this subnuclear compartment (Figure 3-29, panels E and F), especially since our M proteins do not have evident nucleolar localization sequences distinct from their NLS.[105]

Most, if not all, viral families interact with the nucleolus, often to usurp cellular functions and promote viral replication,[106-108] as the nucleolus is a dynamic structure involved in a vast array of biological functions beyond ribosome biogenesis, including tRNA and mRNA processing and export from the nucleus, cell cycle regulation, and response to cellular stress. Additionally, there is growing recognition that NLS-containing viral proteins target the nuclear pore complex to alter the export of macromolecules and mRNA, thereby counteracting antiviral responses and promoting viral gene expression at the expense of host gene expression.[84] For example, influenza NS1 is a multifunctional protein known to translocate to the nucleolus and to the nuclear pore, where it inhibits host mRNA export factors, thus resulting in impaired immune responses and enhanced viral virulence.[109] Vesicular stomatitis virus M also inhibits mRNA nuclear export through interaction with nuclear pore components.[84,110] Further, RSV-M is shuttled to the host cell nucleus where it inhibits host gene expression and induces cell cycle arrest, indicating that paramyxovirus M proteins also antagonize nuclear functions.[111,112] We hypothesize that ubiquitin-dependent nuclear and subnuclear trafficking of some *Paramyxovirinae* M proteins is part of a viral strategy to promote viral replication. Therefore, the study of M interactions with the nucleolus and the nuclear pore complex represents an opportunity to gain new insights into the cell biology of the nucleus and to identify novel antiviral targets.

FIGURES

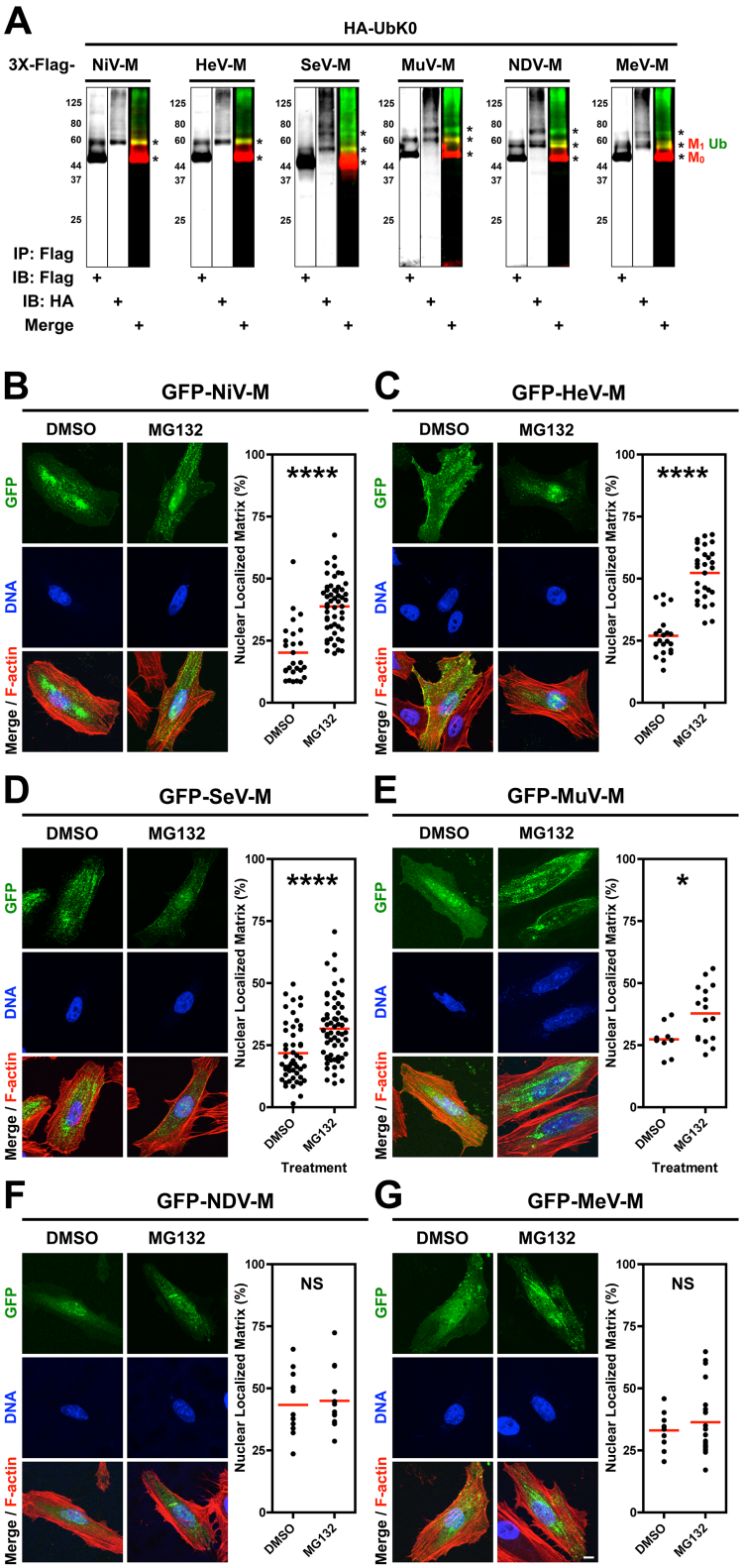
A
HA-UbK0
3X-Flag-
NiV-M
HeV-M
SeV-M
MuV-M
NDV-M
MeV-M
125
80
60
44
37
25
M1 Ub
M0
IP: Flag
IB: Flag
IB: HA
Merge
B
GFP-NiV-M
C
GFP-HeV-M
D
GFP-SeV-M
E
GFP-MuV-M
F
GFP-NDV-M
G
GFP-MeV-M
DMSO
MG132
GFP
DNA
Merge / F-actin
Nuclear Localized Matrix (%)
****
*
NS
Treatment

(*Previous page*)

Figure 3-19. Analysis of the ubiquitin-regulated nuclear export of matrix proteins from five *Paramyxovirinae* genera. (A) Ubiquitination of M proteins. HEK 293T cells were cotransfected with HA-UbK0 and 3X-Flag tagged NiV-M, HeV-M, SeV-M, MuV-M, NDV-M, or MeV-M. After 24h, 3X-Flag-tagged-M was immunoprecipitated, and M and its ubiquitinated species were detected by immunoblotting against Flag and HA, respectively. **(B-G)** 3D confocal analysis of M nuclear localization in cells depleted of free ubiquitin. Extended-focus view of HeLa cells transfected with GFP-tagged **(B)** NiV-M, **(C)** HeV-M, **(D)** SeV-M, **(E)** MuV-M, **(F)** NDV-M, or **(G)** MeV-M. At 16 h post-transfection, cells were treated with 50 μM MG132/0.5% DMSO or 0.5% DMSO for 8h. Cells were counterstained with DAPI to visualize nuclear DNA, blue, and fluorescent phalloidin to visualize the F-actin cytoskeleton, red. Scale bar 10 μm. In the corresponding graphs, the nuclear M fluorescence per cell was quantified from 3D-reconstructed confocal micrographs. *p<0.05; ****p<0.0001; NS, not significant by Student's t-test.

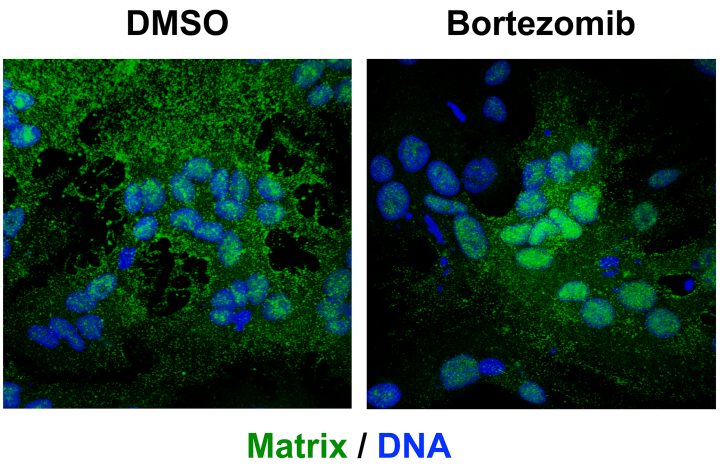

Figure 3-20. Proteasome inhibition sequesters Nipah virus matrix in the nucleus during live virus infection. Extended focus view of HeLa cells infected with Nipah Malaysia strain at MOI 0.1. DMSO or 1 μM bortezomib was added at 8 h post-infection and cells were fixed at 23 h post-infection. Cells were stained with anti-NiV-M antibodies, green, and counterstained with DAPI to visualize nuclear DNA, blue.

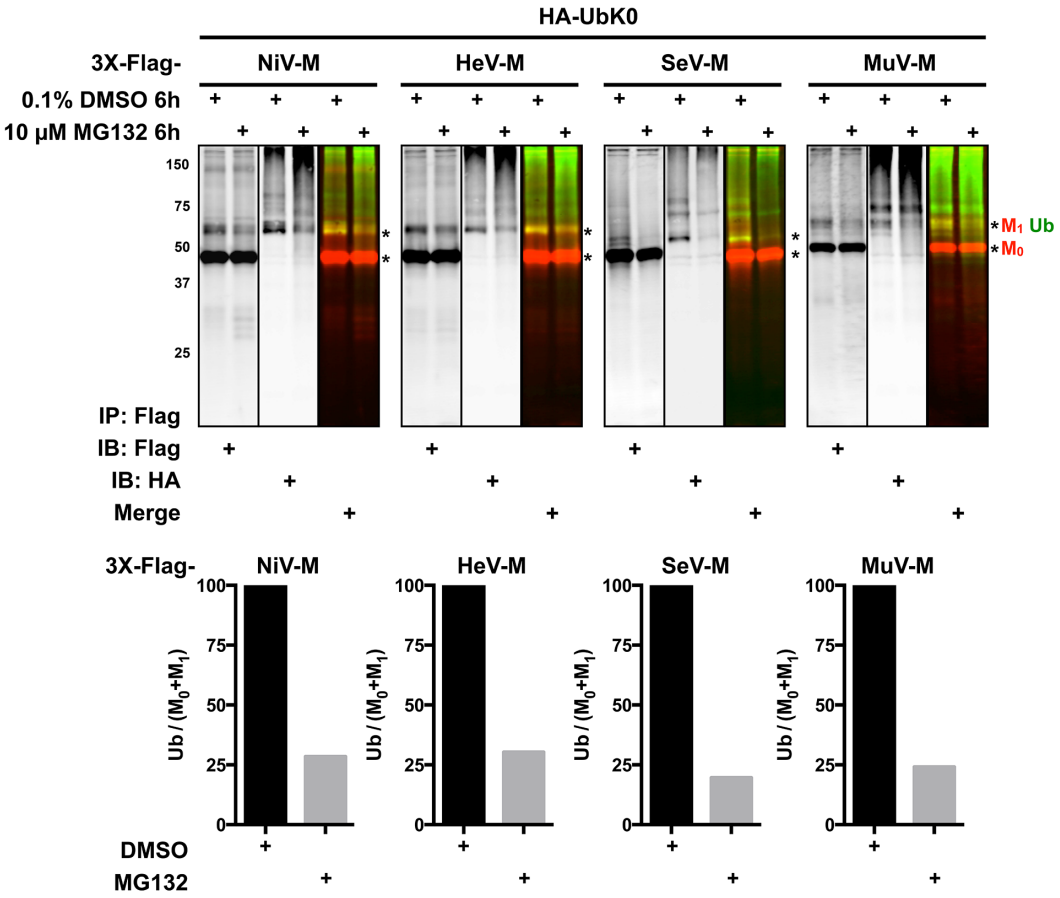

Figure 3-21. Proteasome inhibition reduces monoubiquitination of Nipah, Hendra, Sendai and Mumps virus matrix proteins. HEK 293T cells were cotransfected with HA-UbK0 and 3X-Flag tagged NiV-M, HeV-M, SeV-M, or MuV-M. At 18 h post-transfection, cells were treated with 10 μM MG132/0.1% DMSO or 0.1% DMSO for 6h. 3X-Flag-tagged-M was immunoprecipitated, and M and ubiquitinated species were detected by immunoblotting against Flag and HA, respectively. The background subtracted integrated fluorescence intensities of the monoubiquitin bands (Ub) normalized to total M (M_0+M_1) was determined using LI-COR Odyssey software.

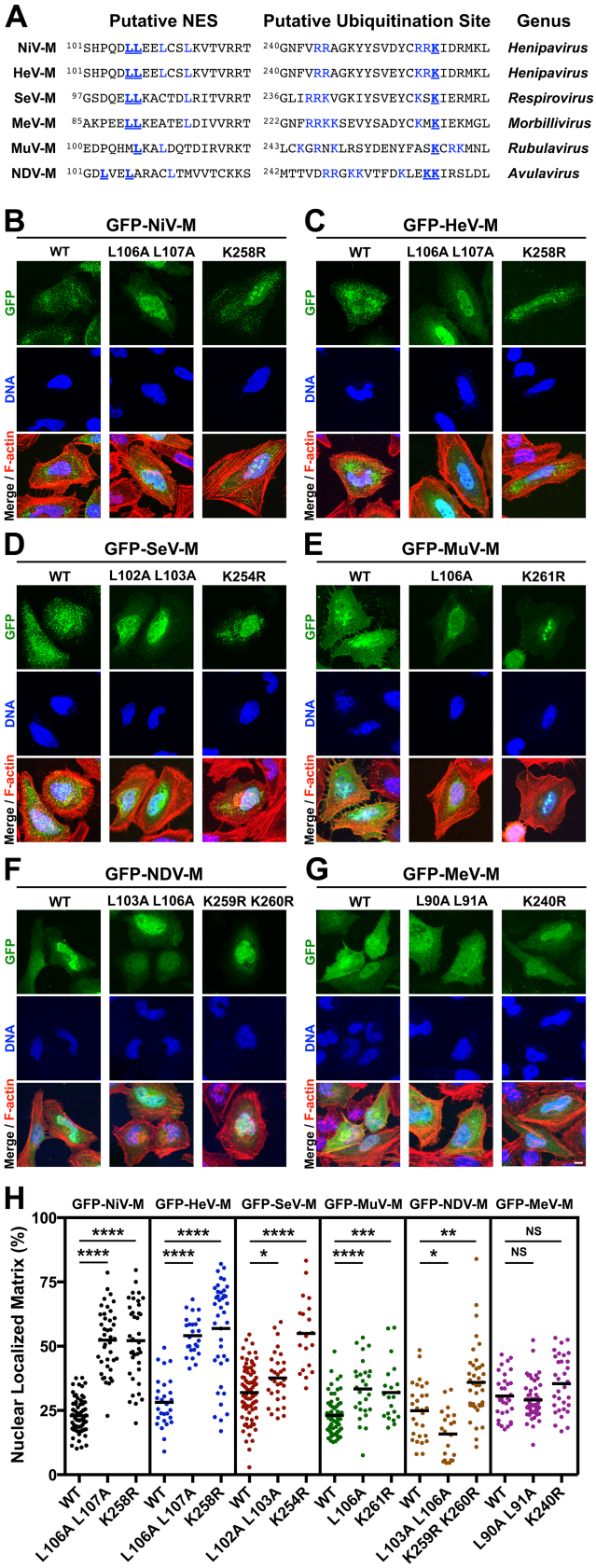
A
Putative NES
Putative Ubiquitination Site
Genus
NiV-M 101SHPQDLLEELCSLKVTVRRT 240GNFVRRAGKYYSVDYCRRKIDRMKL Henipavirus
HeV-M 101SHPQDLLEELCSLKVTVRRT 240GNFVRRAGKYYSVEYCKRKIDRMKL Henipavirus
SeV-M 97GSDQELLKACTDLRITVRRT 236GLIRRKVGKIYSVEYCKSKIERMRL Respirovirus
MeV-M 85AKPEELLKEATELDIVVRRT 222GNFRRKKSEVYSADYCKMKIEKMGL Morbillivirus
MuV-M 100EDPQHMLKALDQTDIRVRKT 243LCKGRNKLRSYDENYFASKCRKMNL Rubulavirus
NDV-M 101GDLVELARACLTMVVTCKKS 242MTTVDRRGKKVTFDKLEKKIRSLDL Avulavirus
B
GFP-NiV-M
WT
L106A L107A
K258R
C
GFP-HeV-M
WT
L106A L107A
K258R
D
GFP-SeV-M
WT
L102A L103A
K254R
E
GFP-MuV-M
WT
L106A
K261R
F
GFP-NDV-M
WT
L103A L106A
K259R K260R
G
GFP-MeV-M
WT
L90A L91A
K240R
GFP
DNA
Merge / F-actin
H
GFP-NiV-M
GFP-HeV-M
GFP-SeV-M
GFP-MuV-M
GFP-NDV-M
GFP-MeV-M
Nuclear Localized Matrix (%)
100
75
50
25
0
****
****
****
****
*
***
****
**
*
NS
NS
WT
L106A L107A
K258R
WT
L106A L107A
K258R
WT
L102A L103A
K254R
WT
L106A
K261R
WT
L103A L106A
K259R K260R
WT
L90A L91A
K240R

(*Previous page*)

Figure 3-22. Mutational analysis of the role of a putative NES and a conserved lysine within the NLS_{bp} in nuclear export of *Paramyxovirinae* matrix proteins. (A) Alignment of *Paramyxovirinae* M sequence motifs that correspond to NiV-M's leucine-rich NES and NLS_{bp}, which contains a putative ubiquitinated lysine. Predicted critical residues are colored blue. Residues mutated in this study are also underlined in bold font. **(B-G)** Extended focus views of HeLa cells transfected with WT, or the indicated mutant GFP-tagged **(B)** NiV-M, **(C)** HeV-M, **(D)** SeV-M, **(E)** MuV-M, **(F)** NDV-M or **(G)** MeV-M. Cells were counterstained with DAPI to visualize nuclear DNA, blue, and fluorescent phalloidin to visualize the F-actin cytoskeleton, red. Scale bar 10 μm. **(H)** The amount of nuclear M fluorescence per cell was quantified from 3D reconstructed confocal micrographs. *p<0.05; ***p<0.001; ****p<0.0001; NS, not significant by one-way ANOVA with Bonferroni adjustment for multiple comparisons.

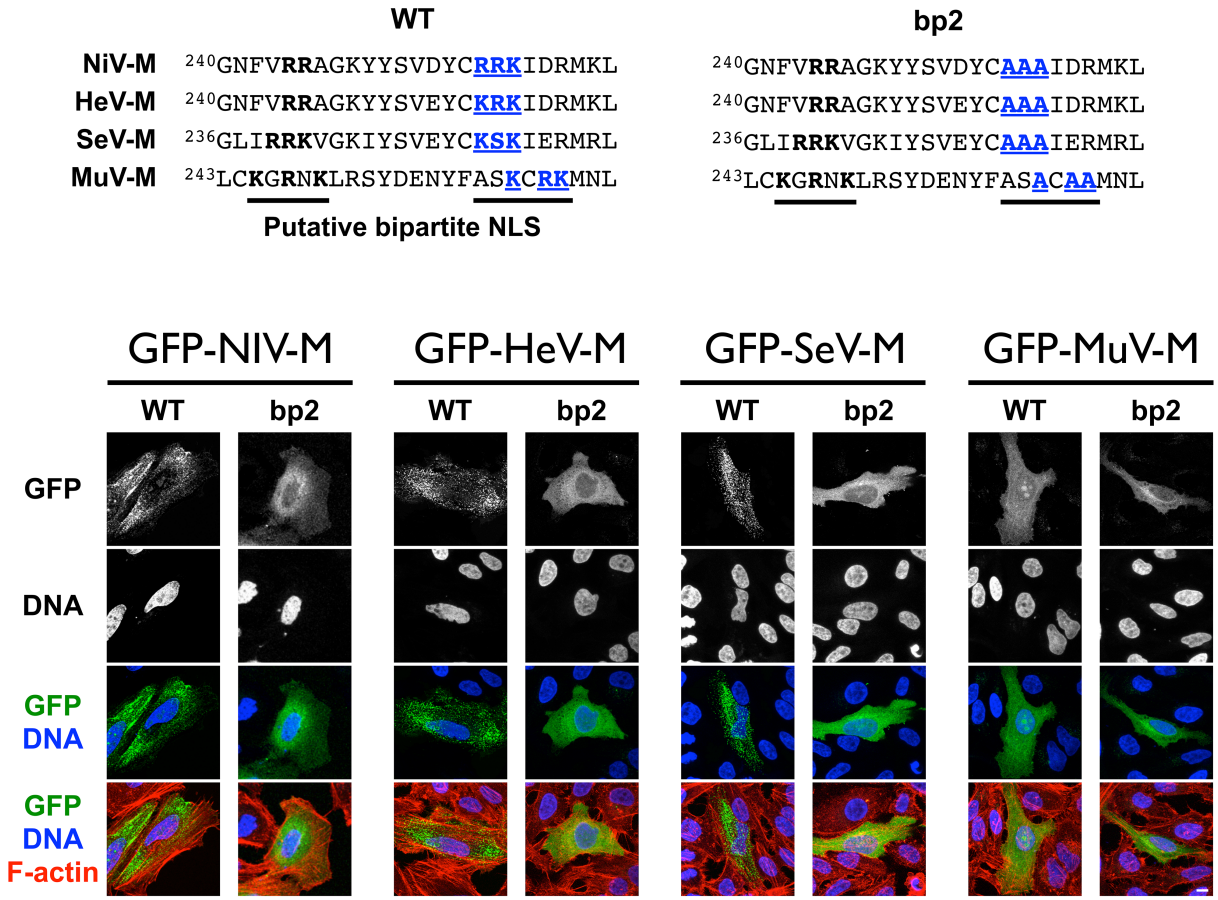

Figure 3-23. Alanine substitution within the second part of the NLS_{bp} disrupts nuclear localization of GFP-tagged Nipah, Hendra, Sendai and Mumps virus matrix proteins. Top, alignments of the NLS_{bp} in WT and bp2-mutants of GFP-tagged NiV-M, HeV-M, SeV-M, and MuV-M. Residues mutated to alanines are underlined in blue. Bottom, extended focus views of HeLa cells transfected with the WT or bp2-mutant GFP-tagged NiV-M, HeV-M, SeV-M and MuV-M. Cells were counterstained with DAPI to visualize nuclear DNA, blue, and fluorescent phalloidin to visualize the F-actin cytoskeleton, red. Scale bar 10 μm.

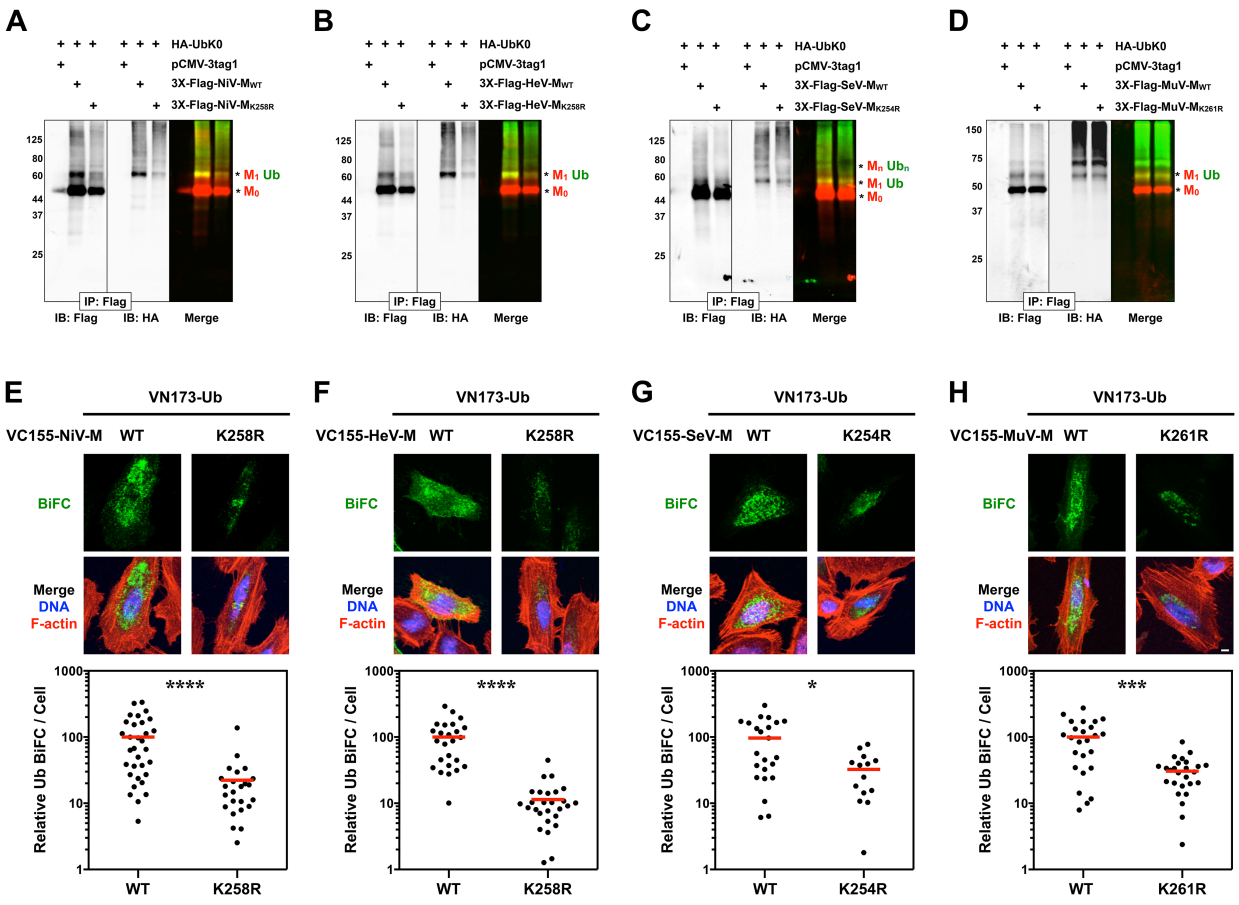

Figure 3-24. Biochemical and quantitative BiFC analysis of Nipah, Hendra, Sendai and Mumps virus matrix ubiquitination regulated by the conserved lysine within the NLS$_{bp}$. (A-D) Immunoblot analysis of ubiquitination of the NLS$_{bp}$-lysine mutants of NiV-M, HeV-M, SeV-M and MuV-M. HEK 293T cells were cotransfected with HA-UbK0 and the WT or the indicated NLS$_{bp}$-lysine mutant 3X-Flag tagged **(A)** NiV-M, **(B)** HeV-M, **(C)** SeV-M and **(D)** MuV-M. After 24h, 3X-Flag-tagged-M was immunoprecipitated, and M and its ubiquitinated species were detected by immunoblotting against Flag and HA, respectively. **(E-H)** Bimolecular fluorescence complementation (BiFC) analysis of ubiquitination of WT or NLS$_{bp}$-lysine mutants of **(E)** NiV-M, **(F)** HeV-M, **(G)** SeV-M and **(H)** MuV-M. Top, extended focus view of HeLa cells cotransfected with VN173-Ub and WT, or the indicated NLS$_{bp}$-lysine mutants of VC155-tagged NiV-M, HeV-M, SeV-M or MuV-M. At 24h post-transfection, cells were counterstained with DAPI to visualize nuclear DNA, blue, and fluorescent phalloidin to visualize the F-actin cytoskeleton, red. BiFC fluorescence is pseudocolored green. Scale bar 10 μm. Bottom, the background subtracted BiFC fluorescence per cell was quantified from 3D-reconstructed confocal micrographs. *p<0.05; ****p<0.0001 by a Mann-Whitney test.

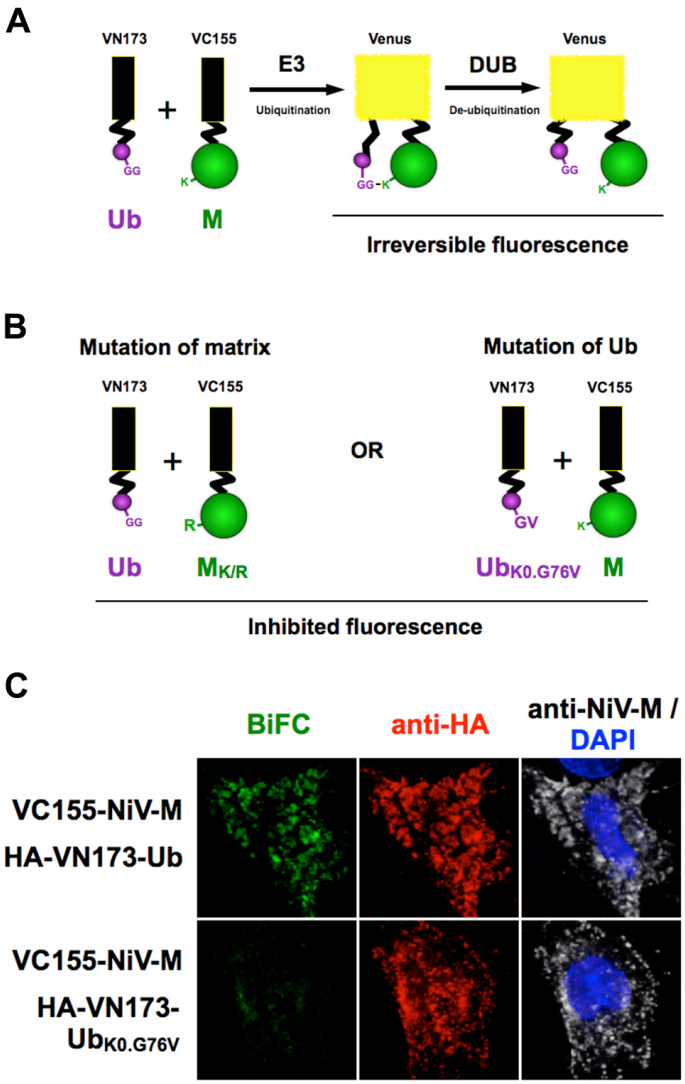

Figure 3-25. Experimental schema of ubiquitin-matrix bimolecular fluorescence complementation (BiFC). (A) The N and C-terminal fragments of Venus (VN173 and VC155, respectively) are fused to the N-terminus of Ubiquitin (Ub) and viral Matrix (M) proteins as described in Materials and Methods. Covalent conjugation of VN173-Ub to VC155-M by a ubiquitin ligase (E3) brings the spilt Venus fragments (VN173 and VC155) into close proximity to reconstitute a functional Venus fluorophore. The reconstituted fluorescent Venus moiety is stable and essentially irreversible. Thus, the fluorescent Venus tag remains associated with M even if M is subsequently de-ubiquitinated by a de-ubiquitinating enzyme (DUB). **(B)** Background controls for ubiquitin-matrix BiFC include mutations in M or ubiquitin that prevent conjugation. **(C)** Extended focus view of HeLa cells cotransfected with VC155-NiV-M and HA-VN173-Ub or a nonconjugable control, HA-VN173-$Ub_{K0.G76V}$. At 24h post-transfection, cells were counterstained with DAPI to visualize nuclear DNA, blue, anti-HA antibodies to visualize the Ub containing Venus fragment, red, and anti-NiV-M antibodies to visualize the NiV-M containing Venus fragment, greyscale. BiFC fluorescence is pseudocolored green. The matrix mutations that result in decreased ubiquitin-matrix BiFC are the data shown in Figure 3-24, panels E-H.

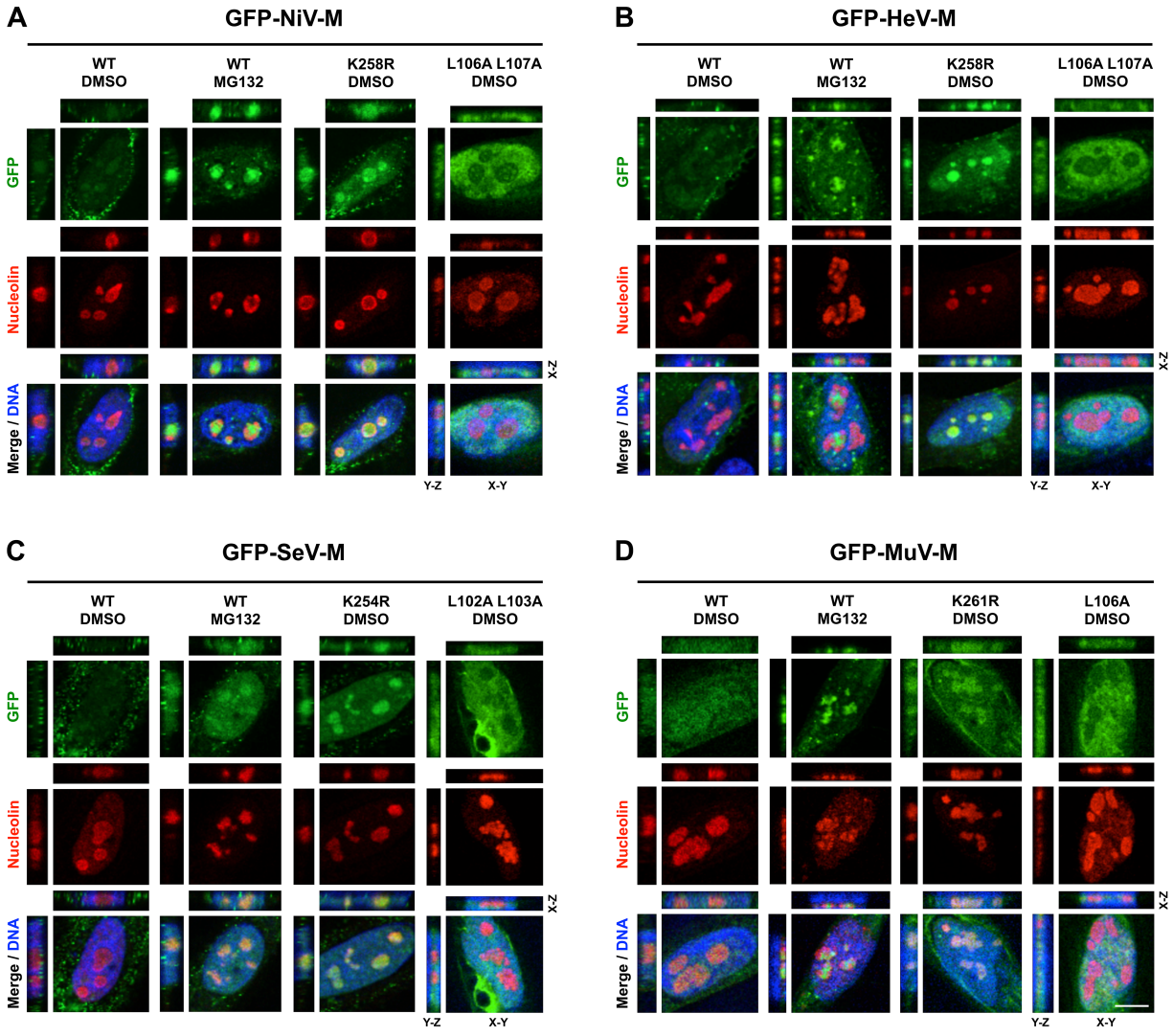

Figure 3-26. Subnuclear localization of Nipah, Hendra, Sendai and Mumps virus matrix during perturbation of ubiquitination. (A-D) Confocal micrographs of HeLa cells transfected with WT or the indicated mutants of GFP-tagged **(A)** NiV-M, **(B)** HeV-M, **(C)** SeV-M or **(D)** MuV-M for 16 h then treated with 50 μM MG132/0.5% DMSO or 0.5% DMSO for 8h. Cells were counterstained with DAPI to visualize nuclear DNA, blue, and anti-nucleolin antibodies to visualize nucleoli, red. Scale bar 10 μm.

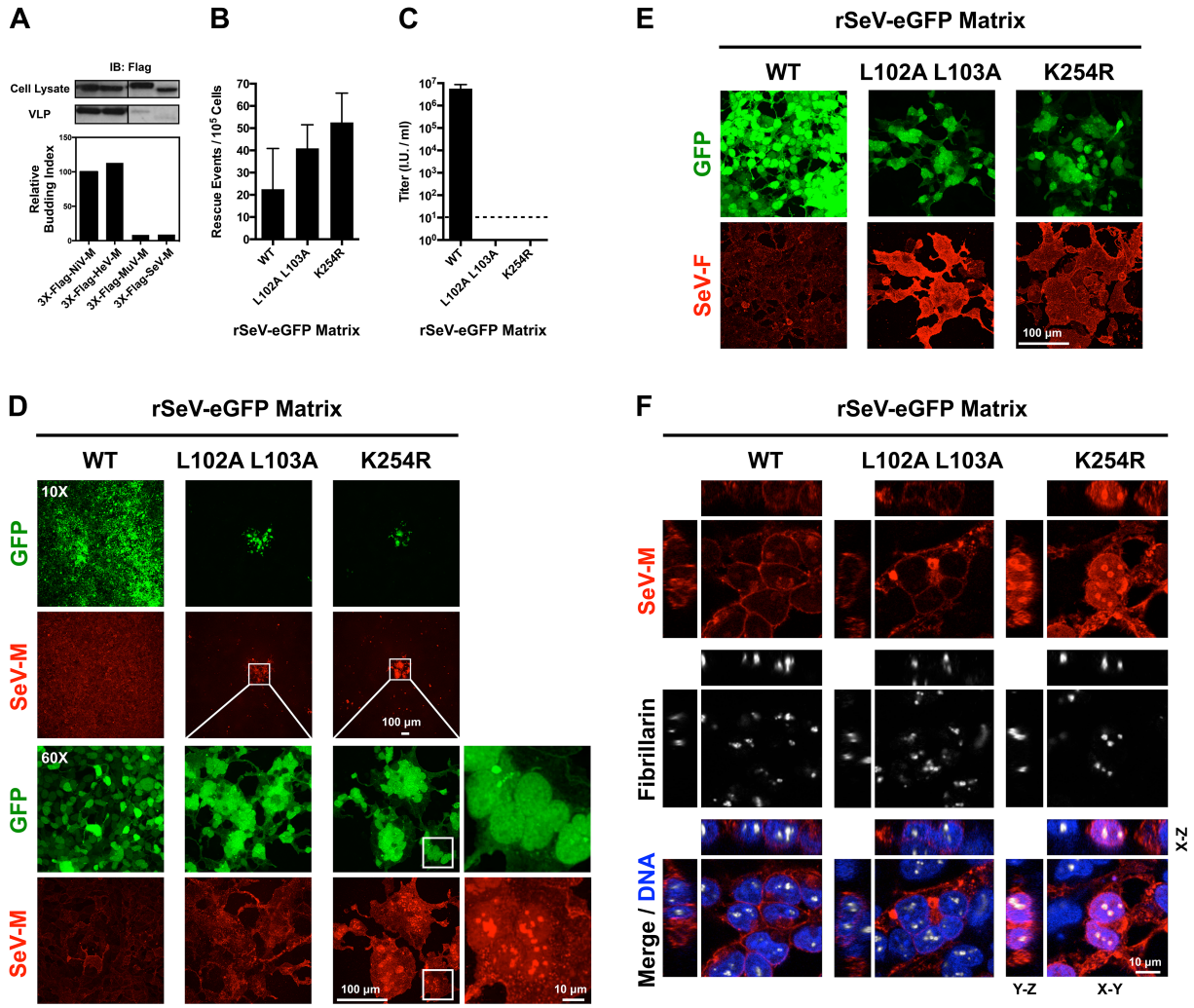

Figure 3-27. Analysis of rescue efficiency, replication, cell-cell fusion and matrix localization of recombinant Sendai virus bearing matrix nuclear export mutants. **(A)** Comparison of virus-like particle (VLP) budding between 3X-Flag-tagged NiV-M, HeV-M, MuV-M, and SeV-M. Anti-Flag immunoblots of cell lysate and purified VLPs from HEK 293T cells 24 h post transfection with the indicated constructs. Normalized budding index was calculated from immunoblot integrated intensities. **(B)** Quantification of rescue events (GFP+ cells) from three independent rescues of rSeV-eGFP containing WT, L102 L103 mutant, or K254R mutant SeV-M at day 2 post rescue in HEK 293T cells. **(C)** Quantification of viral titers from the rescues of rSeV-eGFP containing WT, L102 L103 mutant, or K254R mutant SeV-M at day 6 post rescue in HEK 293T cells. **(D)** Extended focus view of HEK 293T cells at day 6 post rescue of rSeV-eGFP containing WT, L102 L103 mutant, or K254R mutant SeV-M. Cells were counterstained with anti-SeV-M antibodies, red. **(E)** Extended focus view of HEK 293T cells at day 6 post rescue of rSeV-eGFP containing WT, L102 L103 mutant, or K254R mutant SeV-M. Cells were counterstained with anti-SeV-F antibodies, red. **(F)** XY, XZ and YZ planes through 3D confocal micrographs of HEK 293T cells at day 6 post rescue of rSeV-eGFP containing WT, L102 L103 mutant, or K254R mutant SeV-M. Cells were counterstained with DAPI to visualize nuclei, blue, anti-SeV-M antibodies, red, and anti-Fibrillarin antibodies to visualize nucleoli, grayscale.

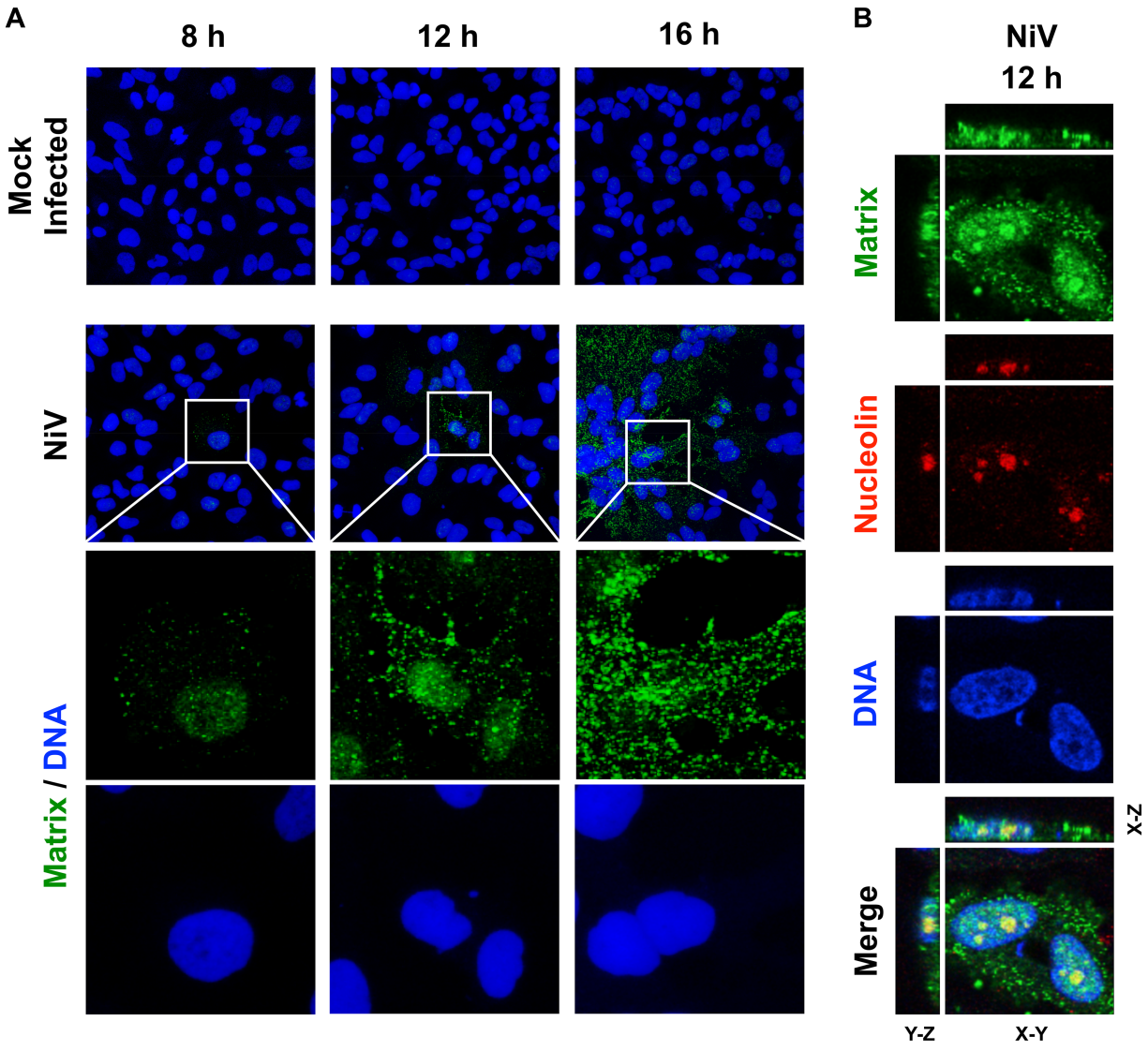

Figure 3-28. Nipah virus matrix localizes to nucleoli during live virus infection. (A) Extended focus view of HeLa cells infected with Nipah Malaysia strain at MOI 10. Cells were fixed with 10% formalin at the indicated time point and stained with anti-NiV-M antibodies, green, and counterstained with DAPI to visualize nuclear DNA, blue. Note prominent nuclear localization at 12 h post-infection. **(B)** XY, XZ and YZ planes through a 3D confocal micrograph of HeLa cells infected with Nipah Malaysia strain at MOI 10 for 12 hours. Cells were stained with anti-NiV-M antibodies, green, and counterstained with anti-nucleolin antibodies to visualize nucleoli, red, and with DAPI to visualize nuclear DNA, blue.

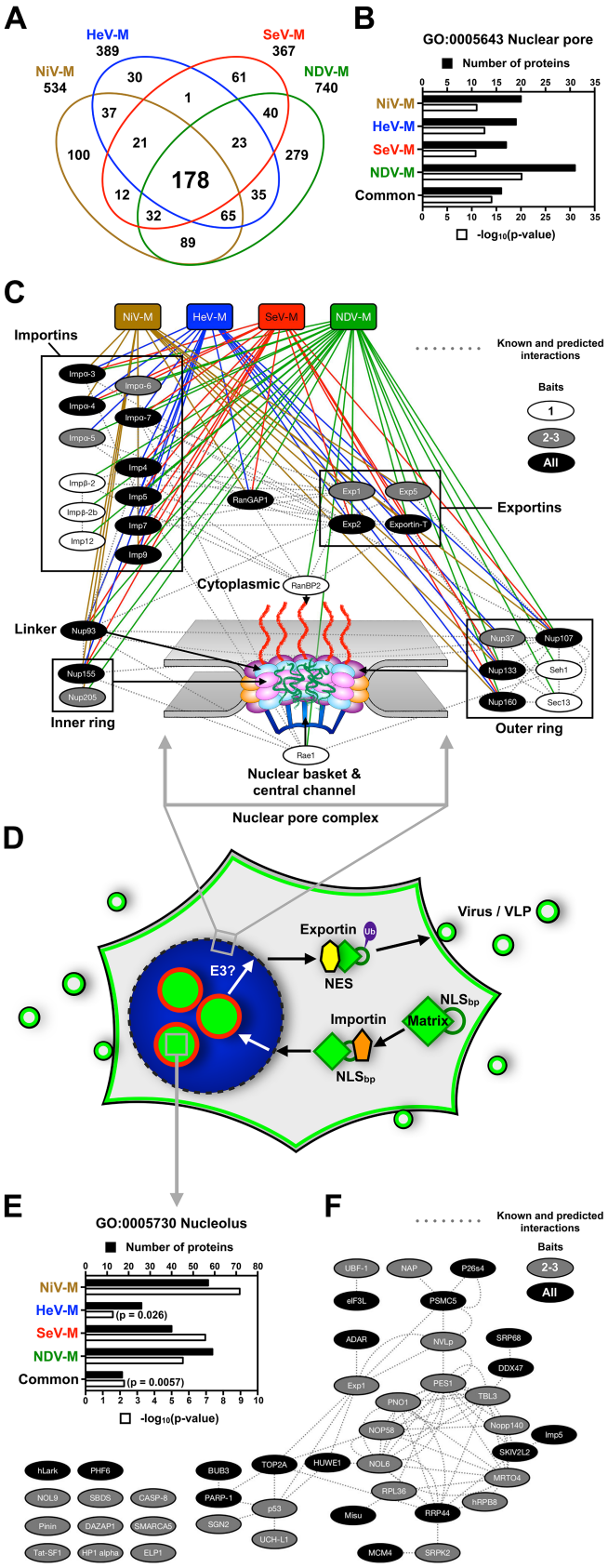
A
HeV-M
389
SeV-M
367
NiV-M
534
NDV-M
740
30
61
1
37
40
21
23
100
279
178
12
35
32
65
89
B
GO:0005643 Nuclear pore
Number of proteins
NiV-M
HeV-M
SeV-M
NDV-M
Common
-log10(p-value)
C
NiV-M
HeV-M
SeV-M
NDV-M
Importins
Impα-3
Impα-6
Impα-4
Impα-7
Impα-5
Imp4
Impβ-2
Imp5
Impβ-2b
Imp7
Imp12
Imp9
RanGAP1
Exp1
Exp5
Exp2
Exportin-T
Exportins
Known and predicted interactions
Baits
1
2-3
All
Cytoplasmic
RanBP2
Linker
Nup93
Nup155
Nup205
Inner ring
Nup37
Nup107
Nup133
Seh1
Nup160
Sec13
Outer ring
Rae1
Nuclear basket & central channel
Nuclear pore complex
D
Virus / VLP
Exportin
Ub
NES
E3?
NLSbp
Importin
Matrix
NLSbp
E
GO:0005730 Nucleolus
Number of proteins
NiV-M
HeV-M
(p = 0.026)
SeV-M
NDV-M
Common
(p = 0.0057)
-log10(p-value)
hLark
PHF6
NOL9
SBDS
CASP-8
Pinin
DAZAP1
SMARCA5
Tat-SF1
HP1 alpha
ELP1
BUB3
PARP-1
SGN2
TOP2A
p53
UCH-L1
HUWE1
F
Known and predicted interactions
Baits
2-3
All
UBF-1
NAP
P26s4
eIF3L
PSMC5
ADAR
NVLp
SRP68
DDX47
Exp1
PES1
TBL3
PNO1
NOP58
Nopp140
Imp5
SKIV2L2
NOL6
MRTO4
RPL36
hRPB8
Misu
RRP44
MCM4
SRPK2

(*Previous page*)
Figure 3-29. Identification of nuclear pore complex proteins, nuclear transport receptors and nucleolar proteins that interact with *Paramyxovirinae* matrix proteins. (A) Overlap of NiV-M, HeV-M, SeV-M and NDV-M protein interactomes identified by MudPIT analysis. **(B)** Functional annotation enrichment of proteins associated with the nuclear pore within the NiV-M, HeV-M, SeV-M, NDV-M and common interactomes using DAVID Bioinformatics Resources. **(C)** Protein-protein interaction network of nuclear pore-complex proteins and nuclear transport receptors within the NiV-M, HeV-M, SeV-M and NDV-M interactomes using Cytoscape with the GeneMANIA plugin. The nuclear pore complex diagram was adapted from [113]. **(D)** A model for matrix nuclear-cytoplasmic trafficking. Import through the nuclear pore complex is mediated by the interaction between an importin and the NLS_{bp} of M proteins. Nuclear export is mediated by the interaction between an exportin and the NES of M proteins. Ubiquitination of some matrix proteins by as yet unknown E3 ubiquitin-ligases regulates nuclear export and/or nuclear re-import by masking the NLS_{bp}. **(E)** Functional annotation enrichment of proteins associated with the nucleolus within the NiV-M, HeV-M, SeV-M, NDV-M and common interactomes using DAVID Bioinformatics Resources. **(F)** Protein-protein interaction network of a subset of proteins associated with the nucleolus within the NiV-M, HeV-M, SeV-M and NDV-M interactomes using Cytoscape with the GeneMANIA plugin. M proteins and the nucleolar proteins bound by only one M-bait were omitted for clarity.

REFERENCES

1. Samal SK. *The Biology of paramyxoviruses*. Norfolk, UK: Caister Academic Press; 2011.

2. Mariner JC, House JA, Mebus CA, et al. Rinderpest eradication: appropriate technology and social innovations. *Science*. 2012;337(6100):1309-1312.

3. Aguilar HC, Lee B. Emerging paramyxoviruses: molecular mechanisms and antiviral strategies. *Expert reviews in molecular medicine*. 2011;13:e6.

4. Eaton BT, Broder CC, Middleton D, Wang LF. Hendra and Nipah viruses: different and dangerous. *Nature reviews Microbiology*. 2006;4(1):23-35.

5. Lamb RA, Parks GD. Paramyxoviridae: The viruses and their replication. In: Fields BN, Knipe DM, Howley PM, eds. *Fields virology*. 6th ed. Philadelphia: Wolters Kluwer Health/Lippincott Williams & Wilkins; 2013:957- 995.

6. Lo MK, Rota PA. The emergence of Nipah virus, a highly pathogenic paramyxovirus. *Journal of clinical virology : the official publication of the Pan American Society for Clinical Virology*. 2008;43(4):396-400.

7. Harrison MS, Sakaguchi T, Schmitt AP. Paramyxovirus assembly and budding: building particles that transmit infections. *The international journal of biochemistry & cell biology*. 2010;42(9):1416-1429.

8. Jardetzky TS, Lamb RA. Activation of paramyxovirus membrane fusion and virus entry. *Current opinion in virology*. 2014;5C:24-33.

9. Lee B, Ataman ZA. Modes of paramyxovirus fusion: a Henipavirus perspective. *Trends in microbiology*. 2011;19(8):389-399.

10. Lamb RA, Paterson RG, Jardetzky TS. Paramyxovirus membrane fusion: lessons from the F and HN atomic structures. *Virology*. 2006;344(1):30-37.

11. Battisti AJ, Meng G, Winkler DC, et al. Structure and assembly of a paramyxovirus matrix protein. *Proc Natl Acad Sci U S A*. 2012;109(35):13996-14000.

12. Terrier O, Rolland JP, Rosa-Calatrava M, Lina B, Thomas D, Moules V. Parainfluenza virus type 5 (PIV-5) morphology revealed by cryo-electron microscopy. *Virus research*. 2009;142(1-2):200-203.

13. Pohl C, Duprex WP, Krohne G, Rima BK, Schneider-Schaulies S. Measles virus M and F proteins associate with detergent-resistant membrane fractions and promote formation of virus-like particles. *The Journal of general virology*. 2007;88(Pt 4):1243-1250.

14. Russell PH, Almeida JD. A regular subunit pattern seen on non-infectious Newcastle disease virus particles. *The Journal of general virology*. 1984;65 (Pt 6):1023-1031.

15. Heggeness MH, Smith PR, Choppin PW. In vitro assembly of the nonglycosylated membrane protein (M) of Sendai virus. *Proc Natl Acad Sci U S A*. 1982;79(20):6232-6236.

16. Hewitt JA, Nermut MV. A morphological study of the M-protein of Sendai virus. *The Journal of general virology*. 1977;34(1):127-136.

17. Buechi M, Bachi T. Microscopy of internal structures of Sendai virus associated with the cytoplasmic surface of host membranes. *Virology*. 1982;120(2):349-359.

18. Bachi T. Intramembrane structural differentiation in Sendai virus maturation. *Virology*. 1980;106(1):41-49.

19. Manie SN, de Breyne S, Vincent S, Gerlier D. Measles virus structural components are enriched into lipid raft microdomains: a potential cellular location for virus assembly. *J Virol*. 2000;74(1):305-311.

20. Vincent S, Gerlier D, Manie SN. Measles virus assembly within membrane rafts. *J Virol*. 2000;74(21):9911-9915.

21. Riedl P, Moll M, Klenk HD, Maisner A. Measles virus matrix protein is not cotransported with the viral glycoproteins but requires virus infection for efficient surface targeting. *Virus research*. 2002;83(1-2):1-12.

22. Subhashri R, Shaila MS. Characterization of membrane association of Rinderpest virus matrix protein. *Biochemical and biophysical research communications*. 2007;355(4):1096-1101.

23. Stricker R, Mottet G, Roux L. The Sendai virus matrix protein appears to be recruited in the cytoplasm by the viral nucleocapsid to function in viral assembly and budding. *The Journal of general virology*. 1994;75 (Pt 5):1031-1042.

24. Caldwell SE, Lyles DS. Dissociation of newly synthesized Sendai viral proteins from the cytoplasmic surface of isolated plasma membranes of infected cells. *J Virol*. 1986;57(2):678-683.

25. Henderson G, Murray J, Yeo RP. Sorting of the respiratory syncytial virus matrix protein into detergent-resistant structures is dependent on cell-surface expression of the glycoproteins. *Virology*. 2002;300(2):244-254.

26. Schmitt AP, He B, Lamb RA. Involvement of the cytoplasmic domain of the hemagglutinin-neuraminidase protein in assembly of the paramyxovirus simian virus 5. *J Virol*. 1999;73(10):8703-8712.

27. Schmitt AP, Leser GP, Morita E, Sundquist WI, Lamb RA. Evidence for a new viral late-domain core sequence, FPIV, necessary for budding of a paramyxovirus. *J Virol*. 2005;79(5):2988-2997.

28. Waning DL, Schmitt AP, Leser GP, Lamb RA. Roles for the cytoplasmic tails of the fusion and hemagglutinin-neuraminidase proteins in budding of the paramyxovirus simian virus 5. *J Virol*. 2002;76(18):9284-9297.

29. Essaidi-Laziosi M, Shevtsova A, Gerlier D, Roux L. Mutation of the TYTLE Motif in the Cytoplasmic Tail of the Sendai Virus Fusion Protein Deeply Affects Viral Assembly and Particle Production. *PloS one*. 2013;8(12):e78074.

30. Ali A, Nayak DP. Assembly of Sendai virus: M protein interacts with F and HN proteins and with the cytoplasmic tail and transmembrane domain of F protein. *Virology*. 2000;276(2):289-303.

31. Coronel EC, Takimoto T, Murti KG, Varich N, Portner A. Nucleocapsid incorporation into parainfluenza virus is regulated by specific interaction with matrix protein. *J Virol*. 2001;75(3):1117-1123.

32. Iwasaki M, Takeda M, Shirogane Y, Nakatsu Y, Nakamura T, Yanagi Y. The matrix protein of measles virus regulates viral RNA synthesis and assembly by interacting with the nucleocapsid protein. *J Virol*. 2009;83(20):10374-10383.

33. Cathomen T, Naim HY, Cattaneo R. Measles viruses with altered envelope protein cytoplasmic tails gain cell fusion competence. *J Virol*. 1998;72(2):1224-1234.

34. Tahara M, Takeda M, Yanagi Y. Altered interaction of the matrix protein with the cytoplasmic tail of hemagglutinin modulates measles virus growth by affecting virus assembly and cell-cell fusion. *J Virol*. 2007;81(13):6827-6836.

35. Ghildyal R, Li D, Peroulis I, et al. Interaction between the respiratory syncytial virus G glycoprotein cytoplasmic domain and the matrix protein. *The Journal of general virology*. 2005;86(Pt 7):1879-1884.

36. Runkler N, Pohl C, Schneider-Schaulies S, Klenk HD, Maisner A. Measles virus nucleocapsid transport to the plasma membrane requires stable expression and surface accumulation of the viral matrix protein. *Cellular microbiology*. 2007;9(5):1203-1214.

37. Ciancanelli MJ, Basler CF. Mutation of YMYL in the Nipah virus matrix protein abrogates budding and alters subcellular localization. *J Virol*. 2006;80(24):12070-12078.

38. Patch JR, Crameri G, Wang LF, Eaton BT, Broder CC. Quantitative analysis of Nipah virus proteins released as virus-like particles reveals central role for the matrix protein. *Virol J*. 2007;4:1.

39. Wang YE, Park A, Lake M, et al. Ubiquitin-regulated nuclear-cytoplasmic trafficking of the Nipah virus matrix protein is important for viral budding. *PLoS Pathog*. 2010;6(11):e1001186.

40. Pantua HD, McGinnes LW, Peeples ME, Morrison TG. Requirements for the assembly and release of Newcastle disease virus-like particles. *J Virol*. 2006;80(22):11062-11073.

41. Takimoto T, Murti KG, Bousse T, Scroggs RA, Portner A. Role of matrix and fusion proteins in budding of Sendai virus. *J Virol*. 2001;75(23):11384-11391.

42. Sugahara F, Uchiyama T, Watanabe H, et al. Paramyxovirus Sendai virus-like particle formation by expression of multiple viral proteins and acceleration of its release by C protein. *Virology*. 2004;325(1):1-10.

43. Li M, Schmitt PT, Li Z, McCrory TS, He B, Schmitt AP. Mumps virus matrix, fusion, and nucleocapsid proteins cooperate for efficient production of virus-like particles. *J Virol.* 2009;83(14):7261-7272.

44. Schmitt AP, Leser GP, Waning DL, Lamb RA. Requirements for budding of paramyxovirus simian virus 5 virus-like particles. *J Virol.* 2002;76(8):3952-3964.

45. Inoue M, Tokusumi Y, Ban H, et al. A new Sendai virus vector deficient in the matrix gene does not form virus particles and shows extensive cell-to-cell spreading. *J Virol.* 2003;77(11):6419-6429.

46. Cathomen T, Mrkic B, Spehner D, et al. A matrix-less measles virus is infectious and elicits extensive cell fusion: consequences for propagation in the brain. *EMBO J.* 1998;17(14):3899-3908.

47. Irie T, Inoue M, Sakaguchi T. Significance of the YLDL motif in the M protein and Alix/AIP1 for Sendai virus budding in the context of virus infection. *Virology*. 2010;405(2):334-341.

48. Coleman NA, Peeples ME. The matrix protein of Newcastle disease virus localizes to the nucleus via a bipartite nuclear localization signal. *Virology*. 1993;195(2):596-607.

49. Ghildyal R, Ho A, Dias M, et al. The respiratory syncytial virus matrix protein possesses a Crm1-mediated nuclear export mechanism. *J Virol.* 2009;83(11):5353-5362.

50. Ghildyal R, Ho A, Wagstaff KM, et al. Nuclear import of the respiratory syncytial virus matrix protein is mediated by importin beta1 independent of importin alpha. *Biochemistry*. 2005;44(38):12887-12895.

51. Duan Z, Li Q, He L, et al. Application of green fluorescent protein-labeled assay for the study of subcellular localization of Newcastle disease virus matrix protein. *Journal of virological methods*. 2013;194(1-2):118-122.

52. Duan Z, Song Q, Wang Y, et al. Characterization of signal sequences determining the nuclear export of Newcastle disease virus matrix protein. *Archives of virology*. 2013;158(12):2589-2595.

53. Yoshida T, Nagai Y'Yoshii S, Maeno K, Matsumoto T. Membrane (M) protein of HVJ (Sendai virus): its role in virus assembly. *Virology*. 1976;71(1):143-161.

54. Bauer A, Neumann S, Karger A, et al. ANP32B Is a Nuclear Target of Henipavirus M Proteins. *PloS one*. 2014;9(5):e97233.

55. Sievers F, Wilm A, Dineen D, et al. Fast, scalable generation of high-quality protein multiple sequence alignments using Clustal Omega. *Molecular systems biology*. 2011;7:539.

56. Lim KL, Chew KC, Tan JM, et al. Parkin mediates nonclassical, proteasomal-independent ubiquitination of synphilin-1: implications for Lewy body formation. *The Journal of neuroscience : the official journal of the Society for Neuroscience*. 2005;25(8):2002-2009.

57. Kerppola TK. Bimolecular fluorescence complementation (BiFC) analysis as a probe of protein interactions in living cells. *Annu Rev Biophys*. 2008;37:465-487.

58. Shyu YJ, Liu H, Deng X, Hu CD. Identification of new fluorescent protein fragments for bimolecular fluorescence complementation analysis under physiological conditions. *Biotechniques*. 2006;40(1):61-66.

59. Hou X, Suquilanda E, Zeledon A, et al. Mutations in Sendai virus variant F1-R that correlate with plaque formation in the absence of trypsin. *Medical microbiology and immunology*. 2005;194(3):129-136.

60. Kaiser P, Wohlschlegel J. Identification of ubiquitination sites and determination of ubiquitin-chain architectures by mass spectrometry. *Methods in enzymology*. 2005;399:266-277.

61. Wohlschlegel JA. Identification of SUMO-conjugated proteins and their SUMO attachment sites using proteomic mass spectrometry. *Methods Mol Biol*. 2009;497:33-49.

62. Tabb DL, McDonald WH, Yates JR, 3rd. DTASelect and Contrast: tools for assembling and comparing protein identifications from shotgun proteomics. *J Proteome Res*. 2002;1(1):21-26.

63. Xu T, Venable J, Park SK, et al. ProLuCID, a fast and sensitive tandem mass spectra-based protein identification program. Paper presented at: Molecular & cellular proteomics2006.

64. Elias JE, Gygi SP. Target-decoy search strategy for increased confidence in large-scale protein identifications by mass spectrometry. *Nature methods*. 2007;4(3):207-214.

65. Florens L, Carozza MJ, Swanson SK, et al. Analyzing chromatin remodeling complexes using shotgun proteomics and normalized spectral abundance factors. *Methods*. 2006;40(4):303-311.

66. Huang da W, Sherman BT, Lempicki RA. Systematic and integrative analysis of large gene lists using DAVID bioinformatics resources. *Nat Protoc*. 2009;4(1):44-57.

67. Huang da W, Sherman BT, Zheng X, et al. Extracting biological meaning from large gene lists with DAVID. *Current protocols in bioinformatics / editorial board, Andreas D Baxevanis [et al]*. 2009;Chapter 13:Unit 13 11.

68. Cline MS, Smoot M, Cerami E, et al. Integration of biological networks and gene expression data using Cytoscape. *Nat Protoc*. 2007;2(10):2366-2382.

69. Montojo J, Zuberi K, Rodriguez H, et al. GeneMANIA Cytoscape plugin: fast gene function predictions on the desktop. *Bioinformatics*. 2010;26(22):2927-2928.

70. Stone R, Takimoto T. Critical role of the fusion protein cytoplasmic tail sequence in parainfluenza virus assembly. *PloS one*. 2013;8(4):e61281.

71. Komander D, Rape M. The ubiquitin code. *Annu Rev Biochem*. 2012;81:203-229.

72. Bailey D, O'Hare P. Comparison of the SUMO1 and ubiquitin conjugation pathways during the inhibition of proteasome activity with evidence of SUMO1 recycling. *Biochem J*. 2005;392(Pt 2):271-281.

73. Hjerpe R, Thomas Y, Chen J, et al. Changes in the ratio of free NEDD8 to ubiquitin triggers NEDDylation by ubiquitin enzymes. *Biochem J*. 2012;441(3):927-936.

74. Mimnaugh EG, Chen HY, Davie JR, Celis JE, Neckers L. Rapid deubiquitination of nucleosomal histones in human tumor cells caused by proteasome inhibitors and stress response inducers: effects on replication, transcription, translation, and the cellular stress response. *Biochemistry*. 1997;36(47):14418-14429.

75. Schubert U, Ott DE, Chertova EN, et al. Proteasome inhibition interferes with gag polyprotein processing, release, and maturation of HIV-1 and HIV-2. *Proc Natl Acad Sci U S A*. 2000;97(24):13057-13062.

76. Patnaik A, Chau V, Wills JW. Ubiquitin is part of the retrovirus budding machinery. *Proc Natl Acad Sci U S A*. 2000;97(24):13069-13074.

77. Xu Q, Farah M, Webster JM, Wojcikiewicz RJ. Bortezomib rapidly suppresses ubiquitin thiolesterification to ubiquitin-conjugating enzymes and inhibits ubiquitination of histones and type I inositol 1,4,5-trisphosphate receptor. *Molecular cancer therapeutics*. 2004;3(10):1263-1269.

78. Fang D, Kerppola TK. Ubiquitin-mediated fluorescence complementation reveals that Jun ubiquitinated by Itch/AIP4 is localized to lysosomes. *Proc Natl Acad Sci U S A*. 2004;101(41):14782-14787.

79. Lee J, Lee Y, Lee MJ, et al. Dual modification of BMAL1 by SUMO2/3 and ubiquitin promotes circadian activation of the CLOCK/BMAL1 complex. *Mol Cell Biol*. 2008;28(19):6056-6065.

80. Kerppola TK. Design and implementation of bimolecular fluorescence complementation (BiFC) assays for the visualization of protein interactions in living cells. *Nat Protoc*. 2006;1(3):1278-1286.

81. Rawling J, Cano O, Garcin D, Kolakofsky D, Melero JA. Recombinant Sendai viruses expressing fusion proteins with two furin cleavage sites mimic the syncytial and receptor-independent infection properties of respiratory syncytial virus. *J Virol*. 2011;85(6):2771-2780.

82. Peeples ME, Wang C, Gupta KC, Coleman N. Nuclear entry and nucleolar localization of the Newcastle disease virus (NDV) matrix protein occur early in infection and do not require other NDV proteins. *J Virol*. 1992;66(5):3263-3269.

83. Kimura M, Imamoto N. Biological Significance of the Importin-beta Family-Dependent Nucleocytoplasmic Transport Pathways. *Traffic*. 2014.

84. Yarbrough ML, Mata MA, Sakthivel R, Fontoura BM. Viral subversion of nucleocytoplasmic trafficking. *Traffic*. 2014;15(2):127-140.

85. McLane LM, Corbett AH. Nuclear localization signals and human disease. *IUBMB life*. 2009;61(7):697-706.

86. Terry LJ, Shows EB, Wente SR. Crossing the nuclear envelope: hierarchical regulation of nucleocytoplasmic transport. *Science*. 2007;318(5855):1412-1416.

87. Marchenko ND, Hanel W, Li D, Becker K, Reich N, Moll UM. Stress-mediated nuclear stabilization of p53 is regulated by ubiquitination and importin-alpha3 binding. *Cell death and differentiation*. 2010;17(2):255-267.

88. Mashtalir N, Daou S, Barbour H, et al. Autodeubiquitination Protects the Tumor Suppressor BAP1 from Cytoplasmic Sequestration Mediated by the Atypical Ubiquitin Ligase UBE2O. *Mol Cell*. 2014;54(3):392-406.

89. von Mikecz A. The nuclear ubiquitin-proteasome system. *J Cell Sci*. 2006;119(Pt 10):1977-1984.

90. Watanabe H, Tanaka Y, Shimazu Y, et al. Cell-specific inhibition of paramyxovirus maturation by proteasome inhibitors. *Microbiology and immunology*. 2005;49(9):835-844.

91. Shields SB, Piper RC. How ubiquitin functions with ESCRTs. *Traffic*. 2011;12(10):1306-1317.

92. Votteler J, Sundquist WI. Virus budding and the ESCRT pathway. *Cell host & microbe*. 2013;14(3):232-241.

93. Irie T, Shimazu Y, Yoshida T, Sakaguchi T. The YLDL sequence within Sendai virus M protein is critical for budding of virus-like particles and interacts with Alix/AIP1 independently of C protein. *J Virol*. 2007;81(5):2263-2273.

94. Moore HM, Bai B, Matilainen O, Colis L, Peltonen K, Laiho M. Proteasome activity influences UV-mediated subnuclear localization changes of NPM. *PloS one*. 2013;8(3):e59096.

95. Vilotti S, Biagioli M, Foti R, et al. The PML nuclear bodies-associated protein TTRAP regulates ribosome biogenesis in nucleolar cavities upon proteasome inhibition. *Cell death and differentiation*. 2012;19(3):488-500.

96. Leljak Levanic D, Horvat T, Martincic J, Bauer N. A novel bipartite nuclear localization signal guides BPM1 protein to nucleolus suggesting its Cullin3 independent function. *PloS one*. 2012;7(12):e51184.

97. Latonen L, Moore HM, Bai B, Jaamaa S, Laiho M. Proteasome inhibitors induce nucleolar aggregation of proteasome target proteins and polyadenylated RNA by altering ubiquitin availability. *Oncogene*. 2011;30(7):790-805.

98. Thoms HC, Loveridge CJ, Simpson J, et al. Nucleolar targeting of RelA(p65) is regulated by COMMD1-dependent ubiquitination. *Cancer research*. 2010;70(1):139-149.

99. Kruger T, Scheer U. p53 localizes to intranucleolar regions distinct from the ribosome production compartments. *J Cell Sci*. 2010;123(Pt 8):1203-1208.

100. Andersen JS, Lam YW, Leung AK, et al. Nucleolar proteome dynamics. *Nature*. 2005;433(7021):77-83.

101. Pokrovskaja K, Mattsson K, Kashuba E, Klein G, Szekely L. Proteasome inhibitor induces nucleolar translocation of Epstein-Barr virus-encoded EBNA-5. *The Journal of general virology*. 2001;82(Pt 2):345-358.

102. Mattsson K, Pokrovskaja K, Kiss C, Klein G, Szekely L. Proteins associated with the promyelocytic leukemia gene product (PML)-containing nuclear body move to the nucleolus upon inhibition of proteasome-dependent protein degradation. *Proc Natl Acad Sci U S A*. 2001;98(3):1012-1017.

103. Matafora V, D'Amato A, Mori S, Blasi F, Bachi A. Proteomics analysis of nucleolar SUMO-1 target proteins upon proteasome inhibition. *Mol Cell Proteomics*. 2009;8(10):2243-2255.

104. Duan Z, Chen J, Xu H, et al. The nucleolar phosphoprotein B23 targets Newcastle disease virus matrix protein to the nucleoli and facilitates viral replication. *Virology*. 2014;452-453:212-222.

105. Scott MS, Troshin PV, Barton GJ. NoD: a Nucleolar localization sequence detector for eukaryotic and viral proteins. *BMC bioinformatics*. 2011;12:317.

106. Greco A. Involvement of the nucleolus in replication of human viruses. *Reviews in medical virology*. 2009;19(4):201-214.

107. Hiscox JA. RNA viruses: hijacking the dynamic nucleolus. *Nature reviews Microbiology*. 2007;5(2):119-127.

108. Salvetti A, Greco A. Viruses and the nucleolus: The fatal attraction. *Biochim Biophys Acta*. 2013.

109. Satterly N, Tsai PL, van Deursen J, et al. Influenza virus targets the mRNA export machinery and the nuclear pore complex. *Proc Natl Acad Sci U S A*. 2007;104(6):1853-1858.

110. von Kobbe C, van Deursen JM, Rodrigues JP, et al. Vesicular stomatitis virus matrix protein inhibits host cell gene expression by targeting the nucleoporin Nup98. *Mol Cell*. 2000;6(5):1243-1252.

111. Ghildyal R, Baulch-Brown C, Mills J, Meanger J. The matrix protein of Human respiratory syncytial virus localises to the nucleus of infected cells and inhibits transcription. *Archives of virology*. 2003;148(7):1419-1429.

112. Bian T, Gibbs JD, Orvell C, Imani F. Respiratory syncytial virus matrix protein induces lung epithelial cell cycle arrest through a p53 dependent pathway. *PloS one*. 2012;7(5):e38052.

113. Strambio-De-Castillia C, Niepel M, Rout MP. The nuclear pore complex: bridging nuclear transport and gene regulation. *Nat Rev Mol Cell Biol*. 2010;11(7):490-501.

CHAPTER 4

NIPAH VIRUS MATRIX AND HOST FACTOR INTERACTIONS

CHAPTER 4.1

HOST FACTORS INVOLVED WITH INTRACELLULAR TRAFFICKING AND CYTOSKELETAL DYNAMICS INTERACT WITH NIPAH VIRUS MATRIX PROTEIN

INTRODUCTION

Despite the nuclear-cytoplasmic trafficking of NiV-M and its potential requirement for interaction with specific host factors for its intracellular trafficking, membrane targeting and budding, only one interacting partner, ANP32B, has been described for NiV-M.[1] While overexpression of ANP32B caused retention of the henipavirus matrix proteins in the nucleus, confirming their direct or indirect interaction, knockdown of ANP32B levels did not affect virus replication. Even from this single study, however, it is abundantly clear from the silver-stained SDS-PAGE of Hendra virus matrix immunoprecipitate that many cellular proteins interact directly or indirectly with the henipavirus matrix protein.[1] To gain deeper insight into the cellular interacting partners of NiV-M and their potential role for virus replication, we immunoprecipitated NiV-M from HEK 293 cell lysates, comprehensively identified NiV-M-interacting host factors by mass spectrometry, and investigated the potential role of three of these factors: the COPII complex responsible for ER-to-Golgi transport, the 14-3-3 proteins that regulate many processes including nuclear-cytoplasmic transport, and the predominantly nucleolar TCOF1/treacle, one of the most abundant factors co-immunoprecipitated with NiV-M.

MATERIALS AND METHODS

For details on virus-like particle budding, immunofluorescence, and immunoprecipitation, refer to Materials and Methods in Chapter 3.1. For details on mass spectrometry and subsequent data analysis, refer to Materials and Methods in Chapter 3.3. For virus growth curves and titrations of virus supernatants, refer to Materials and Methods in Chapter 2.2.

Cell lines, plasmids, and antibodies

NiV-M-inducible cell line. The 3XFLAG-NiV-M-inducible cell line was created by cloning 3XFLAG-NiV-M into pcDNA5/FR/TO (Invitrogen), co-transfecting this plasmid with the pOG44 recombinase (Invitrogen) into Flp-In T-REx-293 cells (Invitrogen), and selecting for recombination of the 3XFLAG-NiV-M into the FRT site with 100 ug/mL hygromycin, along with

5 ug/mL blasticidin to maintain the Tet-off transactivator already present within the cell line. Due to the high efficiency of recombination with this system, it is usually not necessary to single-cell clone, and colonies was therefore pooled before expansion.

Plasmids. GFP-Sec16A was obtained from Addgene (plasmid 15776). Sar1A was obtained from Addgene (plasmid 25531), N-terminally tagged with HA, and inserted into pcDNA3 with or without the H79G dominant negative mutation. CMV-driven VSV-G was as previously described.[2] Arf4-GFP was obtained from Addgene (plasmid 39556). The TCOF1 ORF was obtained from Thermo (Mammalian Gene Collection, Accession BC016144, Clone ID 3921754), N-terminally tagged with HA, and corrected to match isoform e (also known as isoform 7), UniProt Accession Q13428-7. Untagged NiV-M and 3XFLAG-NiV-M were as previously described (see Chapter 3.1).

Antibodies. Mouse monoclonal anti-VSV-G, clone 8G5F11 (EB0010), directed against the ectodomain of VSV-G, Indiana serotype; rabbit polyclonal anti-GFP (598, MBL); rabbit polyclonal anti-14-3-3, pan-reactive against all isoforms (sc-629, Santa Cruz); rabbit polyclonal anti-phospho-(Ser) 14-3-3 binding motif (9601, Cell Signaling); rabbit monoclonal anti-acetyl-α-tubulin (Lys40), clone D20G3 (5335, Cell Signaling), for detection of cilia. Rabbit anti-NiV-M and mouse anti-FLAG were as previously described (see Chapter 3.1).

Flow cytometry

HEK 293T cells in 6-well, transfected with indicated conditions, were resuspended at 16 hours post-transfection in ice-cold PBS with 10 mM EDTA, incubated with mouse anti-VSV-G in ice-cold FACS buffer (PBS with 2% FCS), followed by anti-mouse Alexa Fluor 488 (Invitrogen) in ice-cold FACS buffer, with final fixation in 2% paraformaldehyde.

RESULTS

NiV-M interacts with ribonucleoprotein complexes in RNA-independent interactions

To identify cellular factors that interact with NiV-M, we first created a HEK 293 cell line that inducibly expresses 3XFLAG-tagged NiV-M. Use of a stable cell line that inducibly and uniformly expressed NiV-M avoided the pitfalls of transfection, in which a minority of cells express very high levels of protein, thus skewing results towards chaperones and other factors that respond to overexpression and misfolding, and thus masking potential low stoichiometry interactions of interest during mass spectrometry.[3] Induction of 3XFLAG-NiV-M expression with doxycyline resulted in uniform expression of NiV-M, indeed avoiding the pitfall of very high expression seen with transfection (Figure 4-1).

Immunoprecipitation of NiV-M from HEK 293 cell lysates and subsequent identification of co-immunoprecipitated cellular factors by mass spectrometry identified over 130 NiV-M-interacting factors. Analysis of this data set in the DAVID Bioinformatics Resource (NIAID/NIH) revealed that the most highly enriched gene ontology category was "ribonucleoprotein complex" (p=2.4e-60), comprising half the data set. This finding was not altogether surprising, considering that some paramyxovirus matrix proteins have been shown to bind RNA,[4] perhaps due to positively charged surfaces on matrix that can bind the negatively charged RNA (Figure 3-2 in Chapter 3.1). We therefore questioned how much of the interactome might rely on an indirect RNA-mediated association. We repeated the immunoprecipitation of NiV-M in the presence or absence of RNase, with mass spectrometric analysis of both samples. The overall data revealed that RNase treatment did result in loss of identification of almost half the interacting partners (Figure 4-2); surprisingly, however, RNase treatment resulted in the new identification of over 50 NiV-M-interacting factors, including the Golgi-associated adaptor protein complex AP-3. The detection of new proteins after RNase treatment is likely due to reduced noise, resulting in more sensitive detection of low abundance interacting partners – indeed, the spectral counts of some protein clusters that pulled down regardless of the presence or absence of RNase were significantly increased when RNase was used. Further, all of these subsets were significantly enriched for the ribonucleoprotein complex gene ontology category,

suggesting that the interaction of NiV-M with specific RNA complexes is mediated by protein-protein interactions and of potential significance for structural or non-structural functions of NiV-M. For example, the entire exon junction complex, which associates with spliced mRNA in the nucleus and subsequently regulates mRNA transcription in the cytoplasm,[5,6] pulled down strongly with NiV-M regardless of RNase treatment (Figure 4-2).

We chose to focus our initial efforts on three NiV-M-interacting factors/complexes that pulled down regardless of RNase treatment and had the potential to regulate NiV-M intracellular trafficking: the COPII pathway required for ER-to-Golgi transport, the 14-3-3 proteins that can regulate trafficking via direct binding and resultant steric hindrance of adjacent motifs such as nuclear localization and export sequences, and the predominantly nucleolar TCOF1, which specifically lost interaction with a budding-deficient NiV-M mutant.

The COPII pathway is not required for NiV-M budding

NiV-M co-immunoprecipitated Sec13 and Sec16A, both integral components of the COPII pathway that sorts and transports cargo from the ER to the Golgi. The Ebola virus matrix protein VP40 was previously suggested to rely upon COPII, mediated via VP40 interaction with the COPII inner coat component Sec24, for its transport to the cell surface.[7] We therefore considered whether COPII might play a role in NiV-M budding. Sec13 forms a heterotetramer with Sec31, forming the outer coat of the COPII vesicle, while Sec16A defines and may organize the sites on the ER where COPII coat assembly and vesicle budding take place.[8-11] Although Sec13 is also present within the nuclear pore,[12-14] thus playing a dual role, the sole known role for Sec16A is for COPII function. We therefore confirmed NiV-M co-immunoprecipitation of Sec16A (Figure 4-3). The interaction localized to the C-terminal half of NiV-M, giving greater confidence as to the specificity of the interaction (Figure 4-3). COPII assembly and cycling requires the coordinated activity of the Sar1 GTPase, and constitutively inactive or active Sar1 acts as a dominant negative for COPII function.[11,15] We first confirmed that we could use the Sar1 dominant negative (constitutively active, H79G mutant) to inhibit the well-known COPII-

dependent trafficking of the vesicular stomatitis virus envelope glycoprotein (VSV-G)[16] under our experimental conditions. Co-transfection of dominant negative Sar1 strongly reduced cell surface expression of VSV-G, while co-transfection of wild-type Sar1 did not affect this trafficking (Figure 4-4, panel A, left). Western immunoblotting confirmed that VSV-G was expressed equivalently under these conditions, indicating a specific block to trafficking to the cell surface (Figure 4-4, panel A, right). The downshift in the VSV-G band on SDS-PAGE caused by COPII inhibition is consistent with loss of Golgi-derived post-translational modification. We then assayed the effect of COPII inhibition on NiV-M budding in our semi-quantitative budding assay (see Chapter 3.1 for more details). COPII inhibition had no effect on NiV-M release, indicating that at least for the budding of NiV-M when expressed alone, COPII is not required. However, co-transfection of wild-type Sar1, but not dominant-negative Sar1, causes NiV-M to accumulate in large, saucer-shaped structures that are not seen with NiV-M alone (Figure 4-5). Although these unusual NiV-M structures are seen with variable frequency, they only occurred when Sar1 was overexpressed, suggesting molecular crosstalk between COPII and NiV-M. Therefore, as discussed further below, while the COPII pathway may not play a role in NiV-M budding when matrix is expressed in the absence of other viral components, a role for COPII may become more apparent in a fuller context. It is also possible that NiV-M may interact with COPII for non-structural functions: ER-to-Golgi vesicular trafficking is important for signaling components involved in acute cellular stress and innate immune responses, and pathogens can modulate COPII to effect their own mechanisms of virulence.[17]

14-3-3 may regulate the nuclear-cytoplasmic trafficking of NiV-M

The 14-3-3 proteins are a family of isoforms that homo- or hetero-dimerize and bind specific phosphoserine/phosphothreonine motifs. The dimer forms a rigid clamp, and binding can lead to masking of a motif via steric hindrance, structural changes that lead to altered function, or even linking of different proteins via separate binding of each monomer. The 14-3-3 proteins thus perform an important regulatory function in numerous fundamental cell processes,

including cytoplasmic-nuclear trafficking, ER localization, cell proliferative signaling, apoptosis, etc.[18-20] We noticed that NiV-M harbors a near-consensus 14-3-3-binding site, as well as an additional potential degenerate binding site about 30 a.a. away (Figure 4-6); no other (S/T)XP motifs exist in NiV-M. Although the canonical site is initiated by an arginine, the lysines present in NiV-M are also suitable for 14-3-3 binding.[21,22] Remarkably, these potential binding sites flank the functional nuclear export sequence (NES) we characterized in Chapter 3.2. Binding of 14-3-3 near nuclear localization sequences (NLSs) and NESs can impede nuclear import or export, respectively, by masking these motifs by steric hindrance.[23]

We reasoned that if 14-3-3 binding to NiV-M would mask the NES and thus prevent nuclear export, mutation of the motif should result in apparent nuclear exclusion. Indeed, mutation of S101, the potentially phosphorylated serine in the near-consensus motif, resulted in apparent nuclear exclusion (Figure 4-7). Despite this nuclear exclusion, which for the K258A mutant in Chapter 3.2 correlated to lack of membrane association and budding, the S101A mutant was able to bud with wild-type efficiency (Figure 4-8).

We then attempted to determine if the nuclear exclusion of the S101A mutant was due to loss of 14-3-3 binding to the mutated motif. Mutation of the potentially phosphorylated serines S101 and S132 in both potential 14-3-3-binding motifs did not abolish co-immunoprecipitation of endogenous 14-3-3 with NiV-M (Figure 4-9, panel A). Further, attempts to demonstrate a direct interaction between wild-type NiV-M and 14-3-3 via crosslinking yielded ambiguous results. We therefore considered whether 14-3-3 co-immunoprecipitation with NiV-M might be due to indirect interactions. Use of an antibody highly specific for the phosphorylated (R/K)xpSxP consensus 14-3-3-binding motif detected cellular factors that co-immunoprecipitated with NiV-M, while NiV-M itself was not detected (Figure 4-9, panel B). This result indicated that at least under the conditions tested, S101 was likely not phosphorylated and thus did not mediate direct 14-3-3 binding, while 14-3-3 may partially or wholly co-immunoprecipitate with NiV-M through indirect interactions. It still remains possible

that dynamic phosphorylation of S101 regulates 14-3-3 binding to NiV-M under conditions not yet tested, perhaps especially during earlier time points when NiV-M is more concentrated in the nucleus, as described in Chapter 3.2.

To further establish whether the potential 14-3-3-binding motif might have an effect on virus replication, we introduced the S101A mutation into a NiV reverse genetics construct (the rNiV-EGFP^{NP} design, see Chapter 2.2). Consistent with our previous finding that S101A had wild-type budding efficiency in the M-alone budding assay (Figure 4-8), the mutant virus grew similar to wild-type NiV when Vero cells were infected at a multiplicity of infection of 1 (Figure 4-10). While infection at high dose of this interferon-deficient cell line did not allow for multiple rounds of replication under conditions in which immune responses might reveal differences, these results at least demonstrate that the mutant virus is not overtly defective. Future analysis of growth curve kinetics in innate immune-competent and relevant primary cells such as neurons and microvascular endothelial cells at low multiplicity of infection will be illuminative. This S101A matrix mutant is also the first nuclear trafficking mutant we have observed that also localizes to membrane (Fig. 4-7, see S101A present in filopodial extensions) and is replication-competent when rescued by reverse genetics. This will be a useful construct for ongoing studies in my mentor's lab to study the anti-innate immune function of NiV-M.

TCOF1/Treacle may be required for NiV-M budding

The N-terminus of NiV-M harbors a potential ciliary targeting motif, KVxP (Figure 4-11). In contrast to motile cilia, which are present on specialized cells such as sperm and respiratory epithelial cells, nearly all cells have a single non-motile primary cilium, which plays important roles in sensing and signal transduction.[24-26] The primary cilium is a privileged compartment, and the ciliary trafficking of some cilium components is known to rely on Arf4-mediated recognition of a VxP or RVxPx motif.[27-30] We therefore considered whether NiV-M might traffick to the cilium, or alternatively use this trafficking pathway for its own purposes. Although common cell lines do not typically display the primary cilium in cell culture, the cilium can often

be induced by serum starvation of confluent cultures.[31] We found that incubation of confluent HEK 293T cells in the reduced serum medium Opti-MEM (Invitrogen) resulted in nearly universal display of the primary cilium (Figure 4-12). Expression of NiV-M either before or after induction of cilium formation did not result in observable localization of NiV-M to the cilium, however (Figure 4-13, panel A). Further, although NiV-M co-immunoprecipitates Arf4, alanine mutagenesis of the KVxP motif did not result in loss of Arf4 binding (Figure 4-13, panel B). These results suggested that the KVxP motif in NiV-M does not mediate Arf4-dependent trafficking to the cilium.

We noted, however, that the KVP mutant was completely deficient in virus-like particle budding (Figure 4-14, panel A). Co-expression of wild-type NiV-M was able to "rescue" the budding of the KVP mutant, suggesting that the KVP mutant was not grossly defective in matrix-matrix association and function (Figure 4-14, panel B). To gain further insight into this budding deficiency, we visualized the localization of the KVP mutant by immunofluorescence. Unlike any other NiV-M mutant we have studied, the KVP mutant had an entirely punctate appearance within the cytoplasm (Figure 4-15), as opposed to wild-type NiV-M, which was mostly diffuse as well as punctate, as well as clearly at the membrane and in filopodial extensions (Figures 4-7 and 4-17). The KVP mutant also displayed an often striated appearance (Figure 4-15, panel A), at times reflecting apparent decoration of actin filaments (Figure 4-15, panel B). We therefore considered the possibility that the trafficking of the KVP mutant was blocked due to lost association with a host factor. Consistent with this hypothesis was the N-terminal localization of the KVxP motif, which sits within a flexible region below the homology NiV-M structure, away from the putative membrane-binding surface.

Comparison of cellular factors co-immunoprecipitated with the KVP mutant vs. wild-type NiV-M revealed the striking loss of one high molecular weight band, which was excised and determined by mass spectrometry to be TCOF1/Treacle (Treacher Collins-Franceschetti syndrome 1) (Figure 4-16, panel A). TCOF1 was also identified in our comprehensive NiV-M

interactome, giving more confidence to our finding (Figure 4-2), and we also confirmed the interaction by Western immunoblotting (Figure 4-16, panel B). TCOF1 is known to be both cytoplasmic and nuclear, although it is predominantly within the nucleolus, where it is critical for ribosome biogenesis.[32,33] Co-expression of epitope-tagged TCOF1 with NiV-M revealed co-localization in cytoplasmic punctae, which was not evident with mutant NiV-M (Figure 4-17). We therefore attempted to determine the effect of TCOF1 depletion on NiV-M budding. As a long-lived essential gene, TCOF1 knockdown can take days to achieve with siRNA,[33,34] with the corresponding experimental complications and potential side effects representing major concerns. We therefore used the recently developed and efficient CRISPR/Cas gene-editing method to knock-in a N-terminal destabilization tag at all copies of the TCOF1 allele in HEK 293T cells (see chapter 4.2 for details). Tagged TCOF1 was stabilized in the presence of the compound Shield-1, but removal of Shield-1 resulted in rapid destabilization of TCOF1, by over 3-fold, at the protein level. Destabilization of TCOF1, however, did not affect NiV-M budding (Figure 4-18). The implications of these results are discussed below.

Inclusion of an inhibitor of deubiquitination during NiV-M immunoprecipitation reveals association with many trafficking components

We previously found that inhibition of the ubiquitin-proteasome system inhibited NiV-M trafficking and budding as well as live virus replication (Chapter 3.2 and 3.3). We therefore considered whether inclusion of an inhibitor of deubiquitination during NiV-M immunoprecipitation from cell lysates might modify the identified interactome, especially in light of our initial limited co-immunoprecipitation of factors implicated in intracellular trafficking. Indeed, Coomassie staining of cellular factors co-immunoprecipitated with NiV-M in the absence or presence of N-ethylmaleimide (NEM), which irreversibly blocks the cysteine in the active site of deubiquitinases, showed that inclusion of NEM increased the abundance and perhaps the composition of the interactome (Figure 4-19). As described in Chapter 3.3, we used this updated protocol in our comparative proteomics of matrix proteins from the different

Paramyxovirinae genera. Mass spectrometric analysis of factors co-immunoprecipitated in the presence of NEM revealed a greater abundance of trafficking-related components that were not previously identified, suggesting a role for ubiquitin-dependent interactions in maintaining these associations with NiV-M. A minor possibility is also that blockade of free cysteines with NEM affected cysteine-dependent interactions. Importantly, a comparison of the interactomes of the matrix proteins from NiV, SeV, MeV, and NDV showed that many of these trafficking-related components were pulled down by all of these matrix proteins (Figure 4-20), indicating potential conservation of function. Beyond components related to vesicular trafficking and the Golgi complex, a number of factors involved in actin dynamics were universally co-immunoprecipitated, including a component of the Arp2/3 complex that plays a major role in regulating the actin cytoskeleton (Figure 4-20). These results suggest strongly that host trafficking pathways play an important role in paramyxovirus matrix biology.

DISCUSSION

Only a few cellular interacting partners for any paramyxovirus matrix protein have been described,[4,35-37] and for NiV-M, only one factor of unclear significance.[1] We comprehensively identified NiV-M-interacting cellular factors by mass spectrometry, and we thus identified factors and pathways that may influence NiV-M function, or that may be co-opted or antagonized by NiV-M for its structural and/or potential non-structural functions. In this study, we examined the potential significance of the COPII pathway, 14-3-3 proteins, and TCOF1/Treacle for the budding function of NiV-M.

Inhibition of the COPII pathway, which we verified by inhibiting the COPII-dependent cell surface trafficking of VSV-G, did not affect NiV-M budding. We observed, however, that co-overexpression of wild-type Sar1 with NiV-M led to occasional accumulation of NiV-M in large saucer-shaped structures, suggesting molecular crosstalk between the COPII and M-budding pathways. As we demonstrate in Chapter 5, the influence of a cellular pathway on NiV-M

function may not be apparent in the absence of other virus components or full virus replication. In this sense, although our front-line surrogate NiV-M budding assay is useful as an initial screen, the results should not be regarded as a conclusive statement of importance. For example, it is possible that NiV-M association is not important for budding *per se*, but for some other critical purpose such as initial assembly with the virus envelope proteins, which presumably employ the COPII pathway for their transport; alternatively, the requirement for COPII for budding itself may be imposed by the presence of other viral components. Considering the immunoprecipitation of COPII components by matrix proteins from across the *Paramyxovirinae* (Figure 4-20), we believe the potential role of COPII in virus assembly and budding deserves further investigation.

Likewise, although mutation of the potential 14-3-3-binding site did not affect NiV-M budding, further investigation of the potential role in 14-3-3 in regulating NiV-M nuclear-cytoplasmic trafficking may reveal insight into the importance of NiV-M nuclear trafficking for its structural and/or non-structural functions. Although we did not detect phosphorylation of S101 within the motif, which would be required for 14-3-3 binding, we only tested a single time point (24 hpt), while we previously showed that NiV-M nuclear localization is dynamic and may be more nuclear at earlier time points (Chapter 3.2). As we hypothesize that 14-3-3 binding may be a means to inhibit nuclear export by masking the adjacent NES, phosphorylation of S101 may be a dynamic process that occurs at these earlier time points with the end result of nuclear retention of NiV-M. Further, to determine whether mutation of the motif impacts virus replication, a relevant primary cell line with normal immune responses (e.g., human umbilical vein endothelial cells) should be infected with the S101A mutant NiV at low multiplicity of infection. Multiple rounds of replication under conditions of immune challenge may reveal a non-structural role for the potential 14-3-3-binding motif in NiV-M.

Finally, although knockdown of TCOF1/Treacle did not affect M budding, the degree of knockdown (over 3-fold) might not be sufficient to impact budding, especially in this M-alone

surrogate assay. The effect of TCOF1 destabilization may be more evident in the context of live virus replication. Regardless, the defective trafficking and budding of the KVP mutant deserves further elucidation. Do the mutant punctae co-localize with intracellular markers, and does the association with actin filaments suggest a dependence of NiV-M trafficking and budding on the actin cytoskeleton? The potential direct interaction of the KVxP motif with TCOF1 also deserves further clarification and confirmation. Although bimolecular fluorescence complementation (BiFC), which can suggest molecular proximity, was previously attempted, the KVxP mutation in the BiFC NiV-M construct did not display the known mutant localization phenotype, suggesting that the construct requires further optimization to reflect wild-type function. Further, destabilization of TCOF1 in the knock-in cell line can perhaps be augmented with shRNA against TCOF1 (Chapter 4.2).

It is intriguing to note that the Arf4-dependent ciliary targeting of rhodopsin also involves Rab11 and the Rab11-interacting factor FIP3.[29] The budding of influenza filamentous virions is dependent on Rab11-FIP3 by an unknown mechanism,[38] and respiratory syncytial virus budding relies on Rab11-interacting factor FIP2,[39] also by an unknown mechanism. It is worth exploring whether the KVxP motif may mediate interaction with Rab11 or its cognate interacting factors. We have found that co-expression of a Rab11 dominant negative with NiV-M reduced both cell lysate expression and normalized budding (data not shown), suggesting a possible role of Rab11 in the NiV-M budding pathway. In the same vein, it is also intriguing to note that the cilia represents an apical structure that relies on trafficking of components from the Golgi,[26] altogether reminiscent of NiV-M, which trafficks to the apical side of polarized cells[40] and interacts with components of the secretory pathway. It may therefore be possible that NiV-M recruits components of the ciliary targeting pathway for its own trafficking, without itself localizing to the cilium.

The interactions of NiV-M with numerous but selective trafficking components, many of which are shared among the paramyxovirus matrix proteins, suggest the potential dependence

of NiV-M on cellular pathways for its own trafficking and budding. The co-immunoprecipitation of many factors associated with the Golgi complex as well as actin cytoskeletal dynamics suggests the potential importance of these cellular pathways. As noted previously, however, although M-alone localization and budding represent useful front-line assays for matrix function, it will be important to evaluate the significance of cellular pathways in the context of other viral components and live virus replication. This importance is driven home by our results in Chapter 5, where we find that the dependence of M-driven virus release on the cellular ESCRT pathway is only evident in the presence of the accessory NiV-C protein.

FIGURES

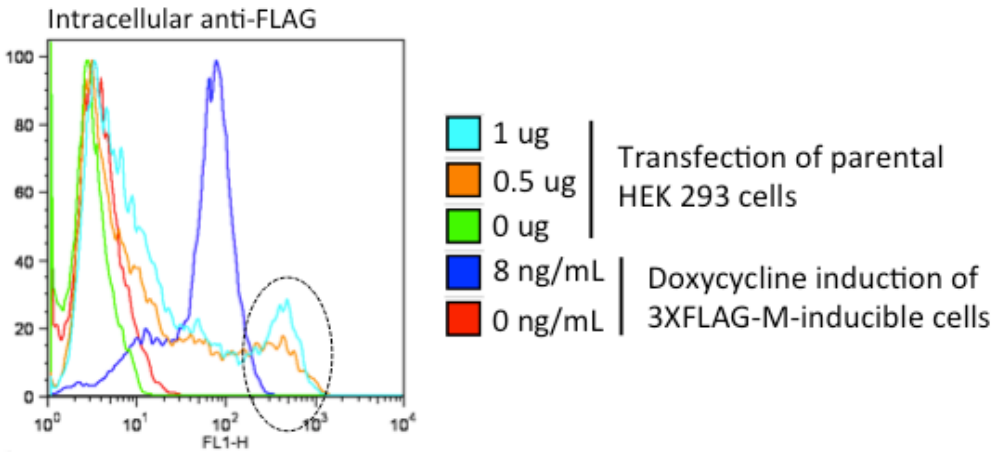

Figure 4-1. Inducible and uniform expression of 3XFLAG-M in HEK 293 cells. 3XFLAG-M-inducible HEK 293 cells were created as described in Materials and Methods. Cells were induced or transfected as indicated, then processed with anti-FLAG intracellular staining for flow cytometry. Inducible expression avoids the pitfalls of extremely high expression in transfected cells (highlighted by the dotted circle).

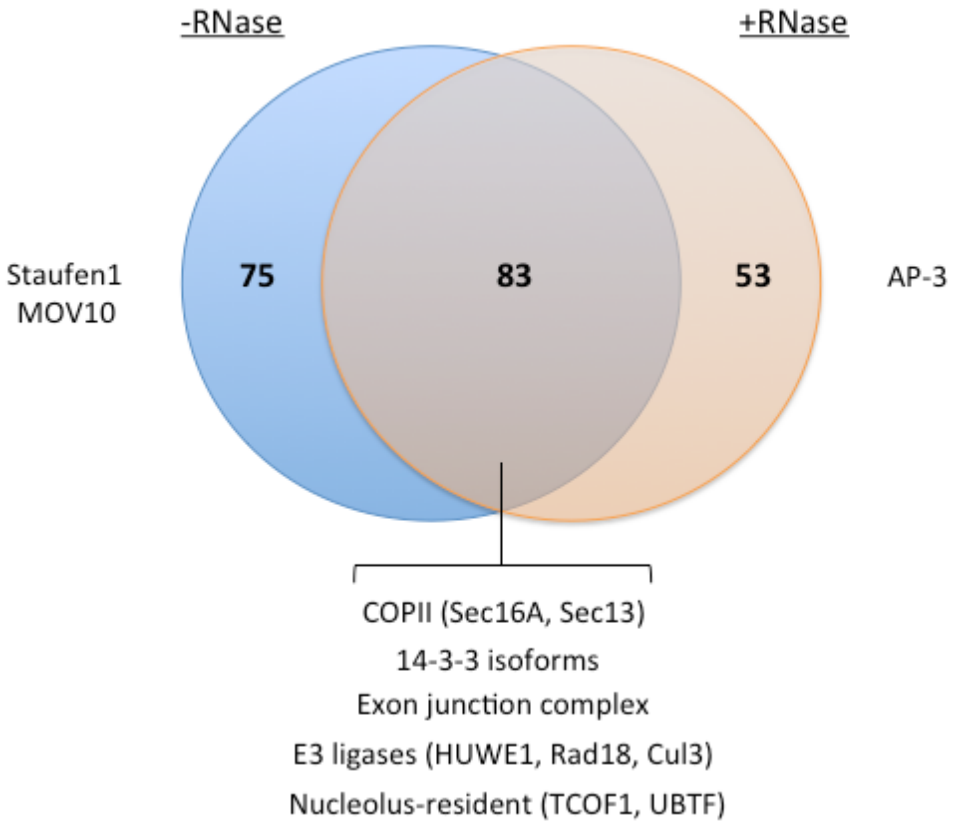

Figure 4-2. NiV-M interacts with many cellular factors via non-RNA-dependent interactions. RNase treatment led to loss of 75 factors, including Staufen1 and MOV10, both RNA-interacting factors that were previously implicated in HIV-1 replication. RNase treatment also led to detection of over 50 new factors, including AP-3, involved in Golgi-to-lysosomal transport. Numerous factors were pulled down regardless of RNase treatment, including those investigated in this chapter.

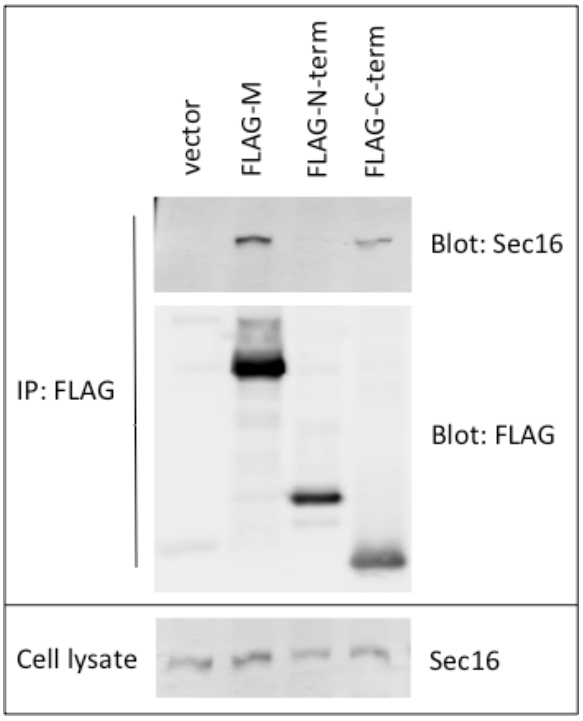

Figure 4-3. The C-terminal half of NiV-M interacts with Sec16A. 3XFLAG-tagged full length NiV-M, or the 3XFLAG-tagged halves, were co-transfected with GFP-Sec16A in HEK 293T cells. Upon FLAG immunoprecipitation (IP), blotting for Sec16A (anti-GFP) revealed co-IP with full-length and C-terminal NiV-M, but not N-terminal NiV-M or the vector control.

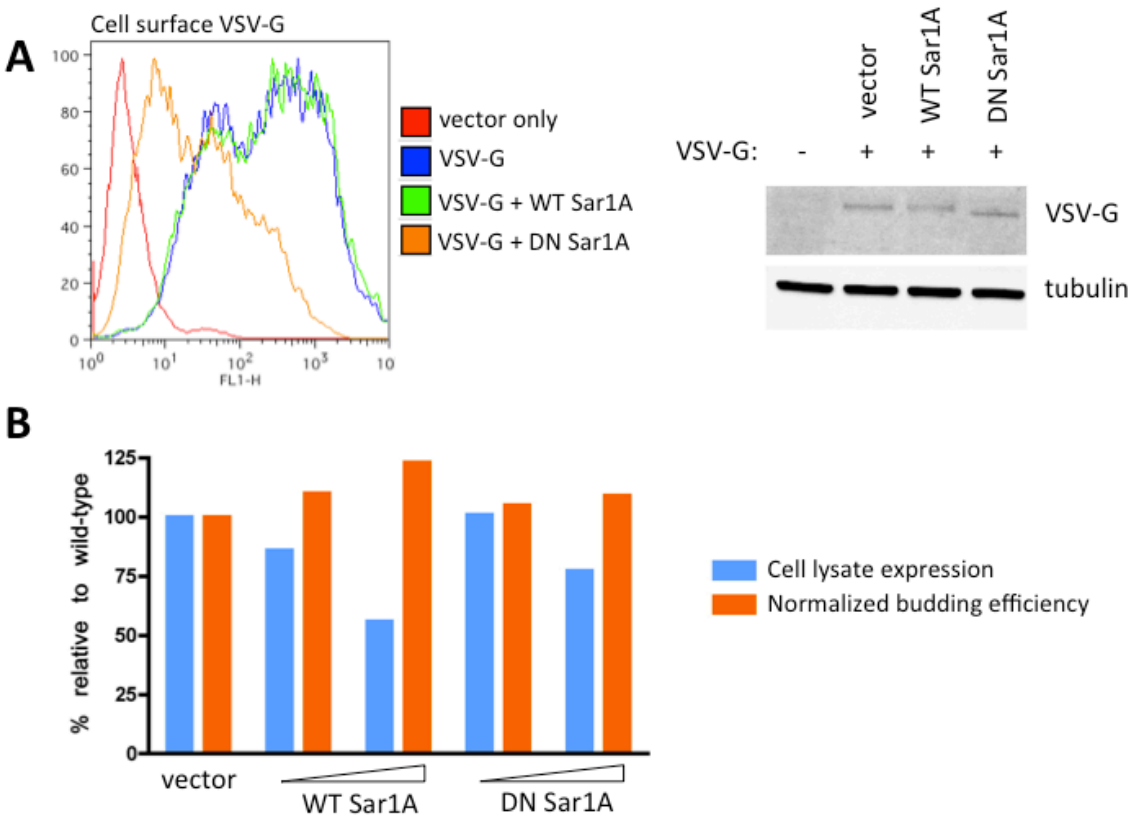

Figure 4-4. Inhibition of COPII does not affect NiV-M budding. (A) Wild-type or dominant-negative (DN) Sar1A (the H79G mutant) was co-transfected with VSV-G in HEK 293T cells. Flow cytometry for the VSV-G ectodomain revealed less VSV-G at the cell surface when the DN was co-expressed. As a control, Western immunoblotting showed equivalent cell lysate expression of VSV-G. **(B)** Co-transfection of DN Sar1A did not affect the efficiency of NiV-M budding.

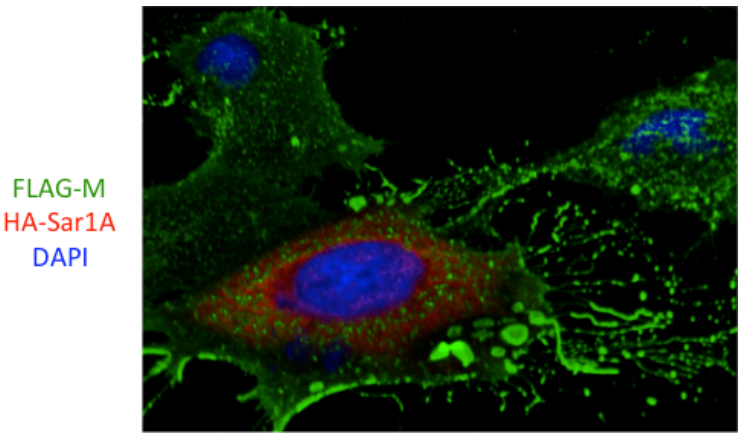

Figure 4-5. Sar1 may modulate NiV-M function. Co-transfection of WT Sar1A occasionally leads NiV-M to accumulate in large saucer-shaped structures. Adjacent cells that are not highly expressing Sar1A, indicated by lack of red color, do not have show such structures.

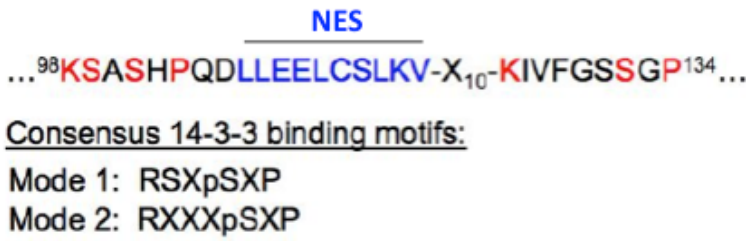

Figure 4-6. NiV-M harbors a consensus 14-3-3 binding motif. 14-3-3 binding requires a phosphorylated serine/threonine within a defined motif, with the consensus shown above. NiV-M has two potential 14-3-3 binding sites, both flanking the characterized nuclear export sequence. The motif starting at K98 matches the mode 1 consensus (with lysine being as effective as arginine at binding 14-3-3).

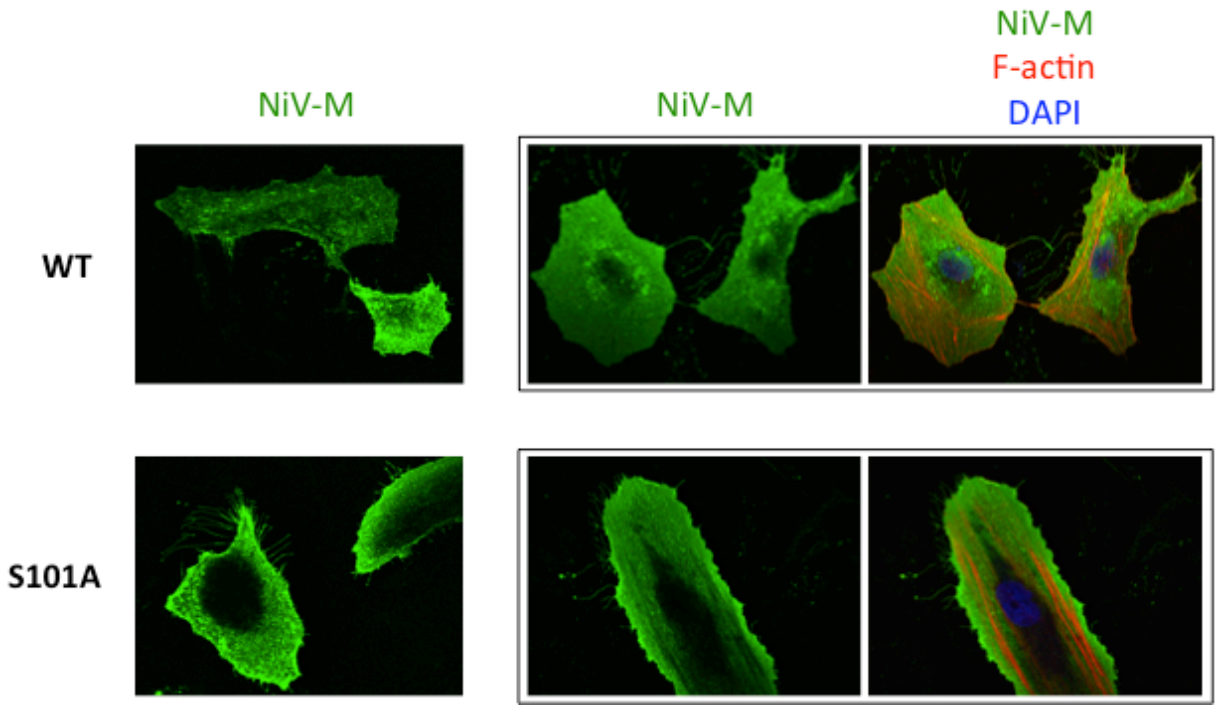

Figure 4-7. The S101A 14-3-3 motif mutant is excluded from the nucleus. In comparison to wild-type NiV-M, which is present throughout the cell including the nucleus, the S101A mutant is not present in the nucleus. Two examples are shown for each, with one of the examples also shown overlaid with DAPI to highlight the nucleus.

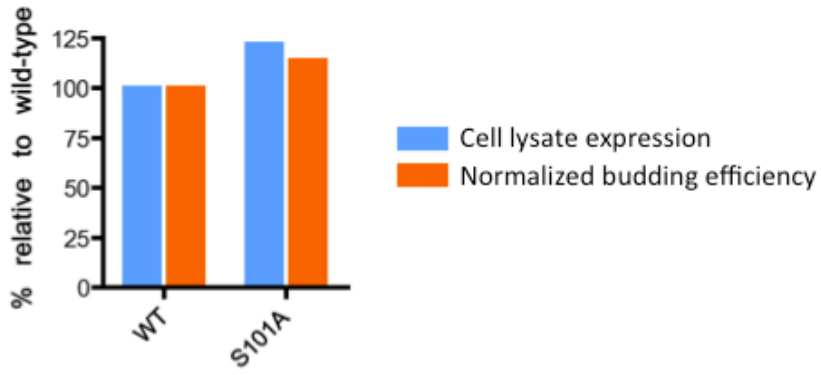

Figure 4-8. The S101A mutant is not budding-deficient. The budding assay was performed as described in Materials and Methods of Chapter 3.1.

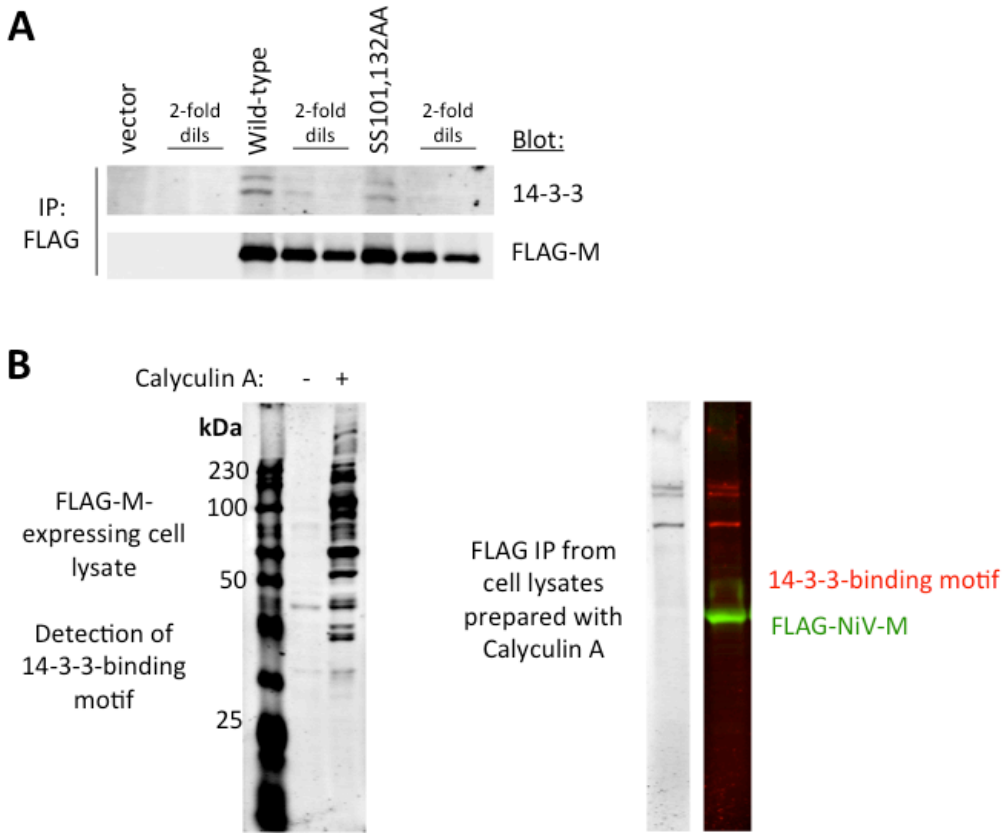

Figure 4-9. NiV-M may bind 14-3-3 via indirect interactions. (A) Wild-type or mutant FLAG-M was immunoprecipitated, and co-immunoprecipitated endogenous 14-3-3 was detected. **(B)** *Left*, The potent phosphatase inhibitor calyculin A prevents dephosphorylation of 14-3-3 binding motifs in cell lysate. *Right*, NiV-M immunoprecipitated in the presence of calyculin A does not show detectable binding of a 14-3-3 binding motif antibody. The upper bands for the 14-3-3 binding motif indicate potential indirect interactions of NiV-M with 14-3-3.

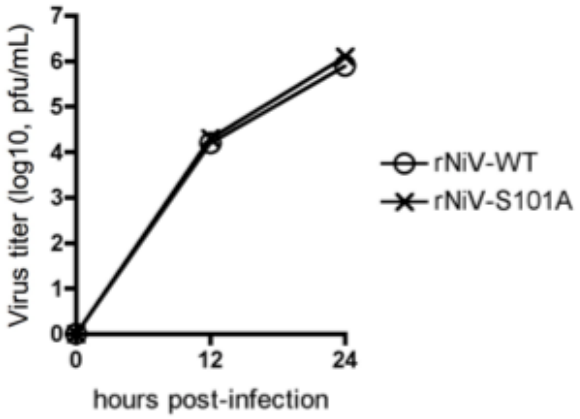

Figure 4-10. S101A mutant live Nipah virus is replication-competent. The S101A mutation was introduced into the rNiV-EGFP^{NP} reverse genetics construct (see Chapter 2.2 for details), rescued, and used to infect Vero cells at multiplicity of infection 1. The mutant virus produced infectious titers similar to wild-type rNiV-EGFP^{NP} over 24 hours.

```
Nipah          MEPDIKSISSE-SMEGVSDFSPSSWEHGGYLDKVEPEIDENGSMIPKYKIYTPGANERKY 59
Measles        -------------MTEIYDFDKSAWDIKGSIAPIQPTTYSDGRLVPQVRVIDPGLGDRKD 47
Sendai         -------------MADIYRFPKFSYEDNGTVEPLPLRTGPDKKAIPHIRIVKVGDPPKHG 47
Mumps          --------MAGSQIKIPLPKPPDSDSQRLNAFPVIMAQEGKGRLLRQIRLRKILSGDPSD 52
Newcastle      -------MDSSRTIGLYFDSAHSSSNLLAFPIVLQDTGDGKKQIAPQYRIQRLDLWTDSK 53
```

Ciliary targeting motifs for:

Rhodopsin: QVAPA
Polycystin-1: KVHPSST
Polycystin-2: RVQPQ

Figure 4-11. The N-terminus of NiV-M harbors a potential (R/K)VxPx ciliary targeting motif. The ciliary targeting motif for the examples shown is characterized by a VxP motif, and in particular (K/R)VxPx for the Polycystin proteins. Potential ciliary targeting motifs near the N-terminus are shown for the different paramyxovirus matrix proteins with blue highlight.

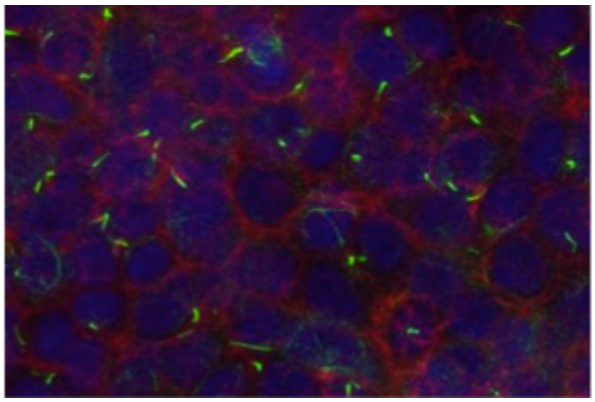

Figure 4-12. The primary cilium is widely induced on HEK 293T cells after serum starvation of confluent cultures. The primary cilium was detected with staining for acetylated tubulin. An extended focus image is shown.

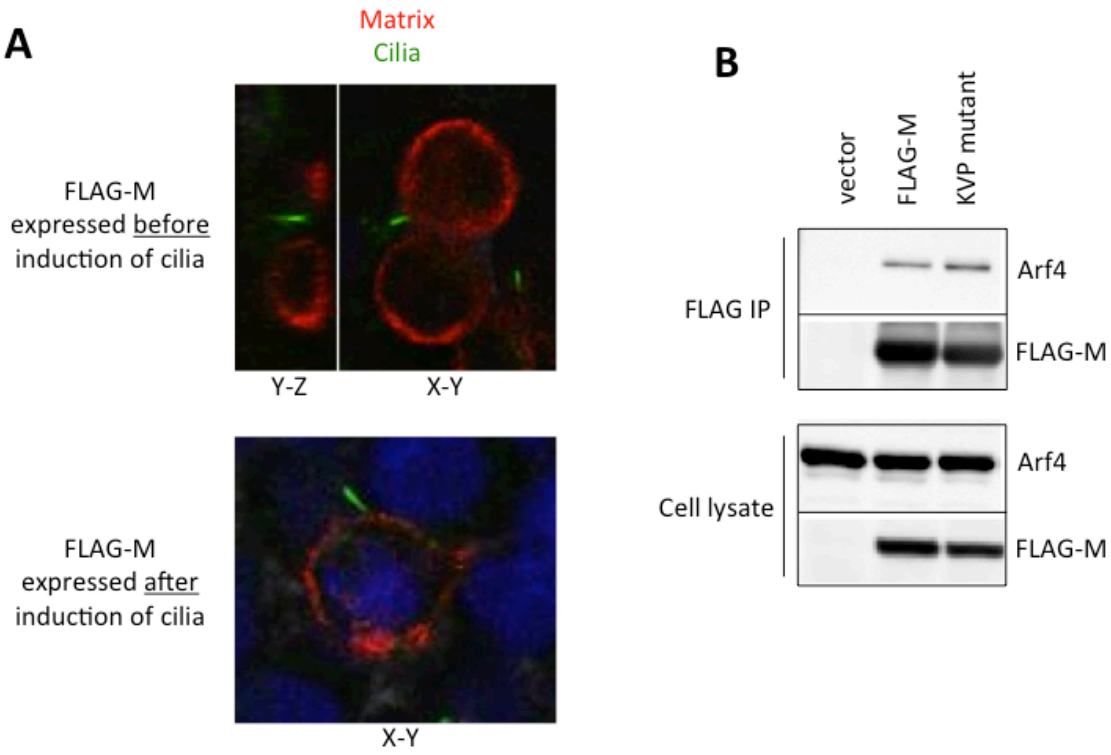

Figure 4-13. NiV-M does not localize to the primary cilium or interact with Arf4 in a KVxPx-dependent manner. (A) To express NiV-M before induction of cilia, 3XFLAG-NiV-M was transfected at about 80% confluency. Upon confluency, cilia were induced with serum starvation. To express NiV-M after induction of cilia, 3XFLAG-NiV-M in pcDNA5/FRT/TO was transfected with the Tet-off transactivator before serum starvation, with M induced with doxycyline at a later time point. **(B)** Arf4-GFP was co-transfected with wild-type or mutant FLAG-M before immunoprecipitation with anti-FLAG. Arf4 (detected with anti-GFP) was co-immunoprecipitated with both wild-type and mutant NiV-M.

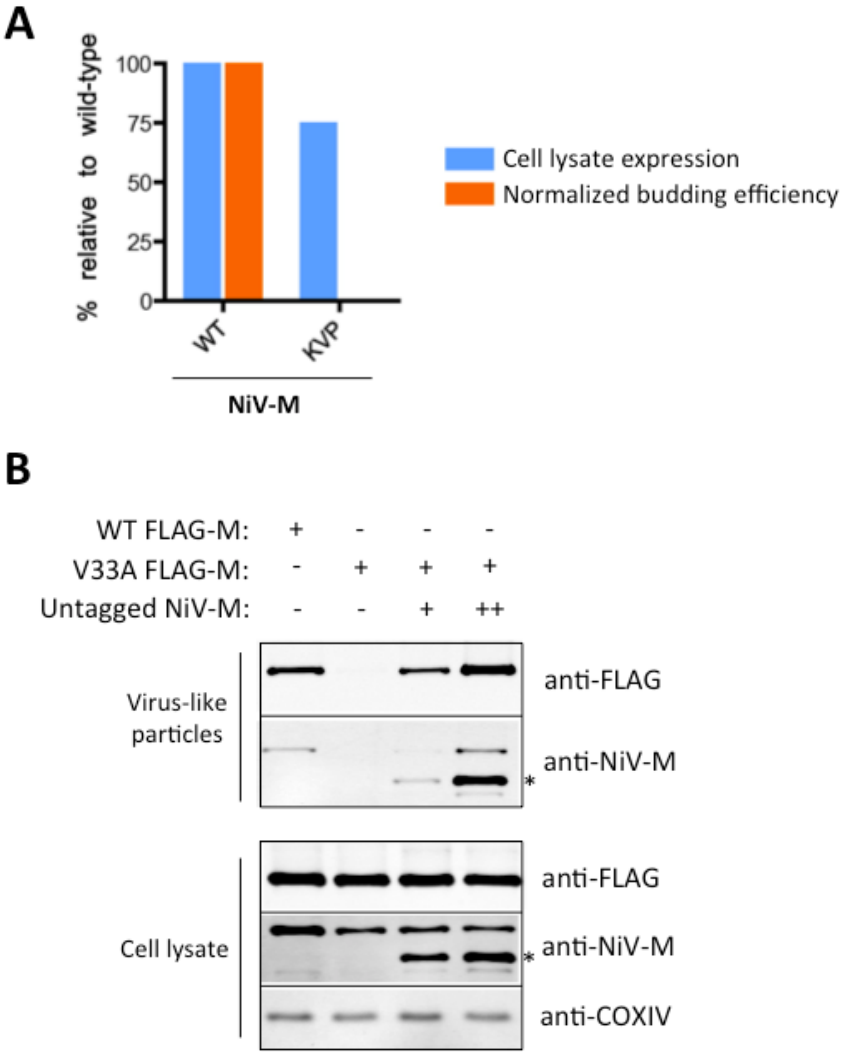

Figure 4-14. The KVP mutant is budding-defective, yet can be rescued by co-expression of wild-type NiV-M. (A) The NiV-M budding assay was performed as described in Chapter 3.1. **(B)** The FLAG-tagged single-alanine V33A mutant (mutated in the "V" of KVP, which phenocopies the KVP mutant in all respects) was transfected on its own or with untagged wild-type NiV-M. Virus-like particle release of FLAG-V33A was only seen with co-expression of wild-type M. The asterisk marks the wild-type untagged M, as the FLAG-V33A mutant is also detected (upper band). Of note, the KVP mutations are within the rabbit anti-NiV-M epitope, hence reducing the binding of anti-NiV-M to the V33A mutant on the Western immunoblot.

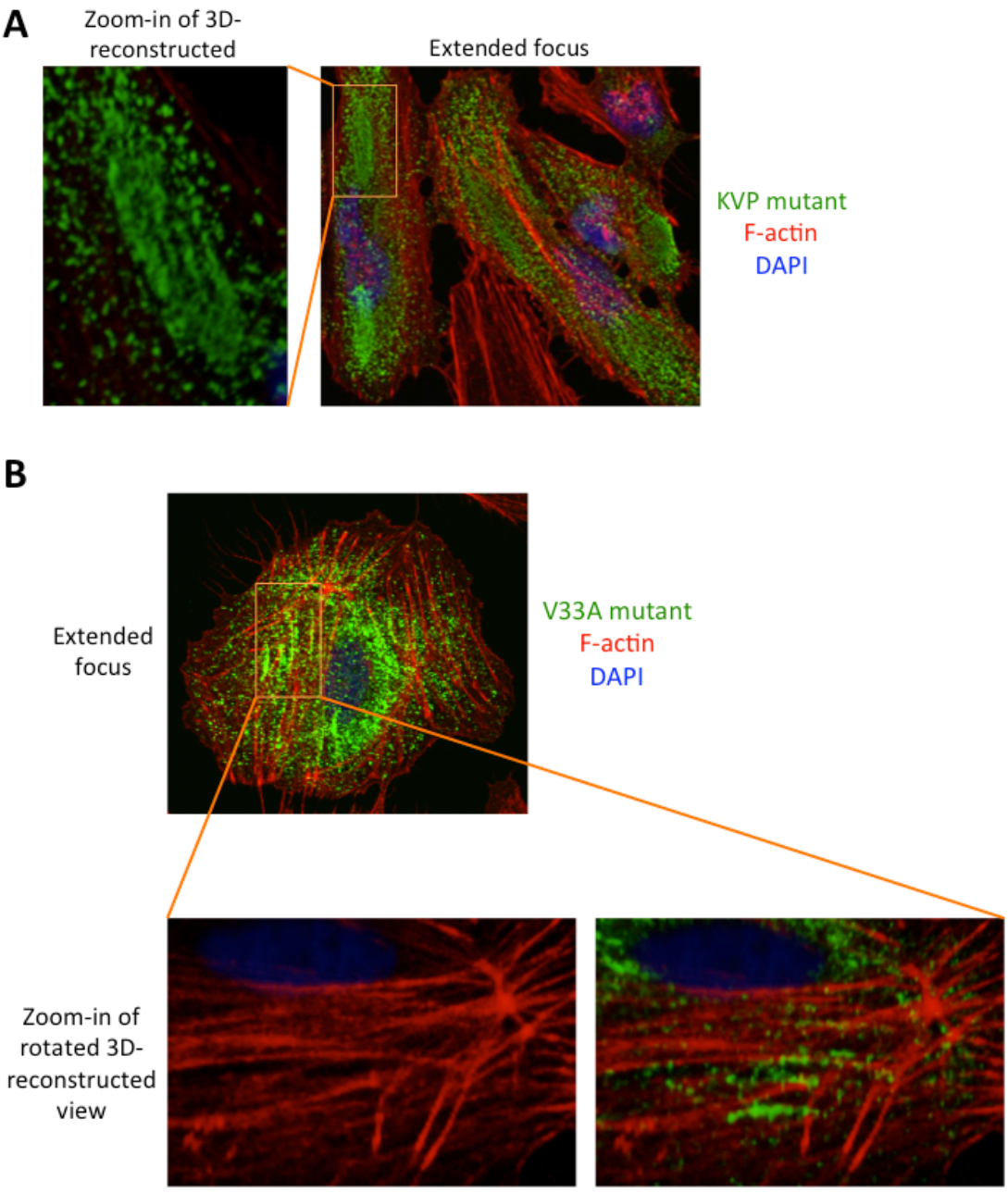

Figure 4-15. The KVP mutant is highly punctate, with punctae often associating with actin filaments. (A) For comparison to wild-type, see Figure 4-7. While wild-type NiV-M is mostly diffuse as well as punctate, the KVP mutant is entirely punctate and not present at the membrane or in filopodial extensions, and often shows a striated appearance. **(B)** The striations are at times visibly associated with actin filaments. The V33A mutant is shown (as mentioned in Figure 4-14, this point mutant phenocopies the KVP mutant).

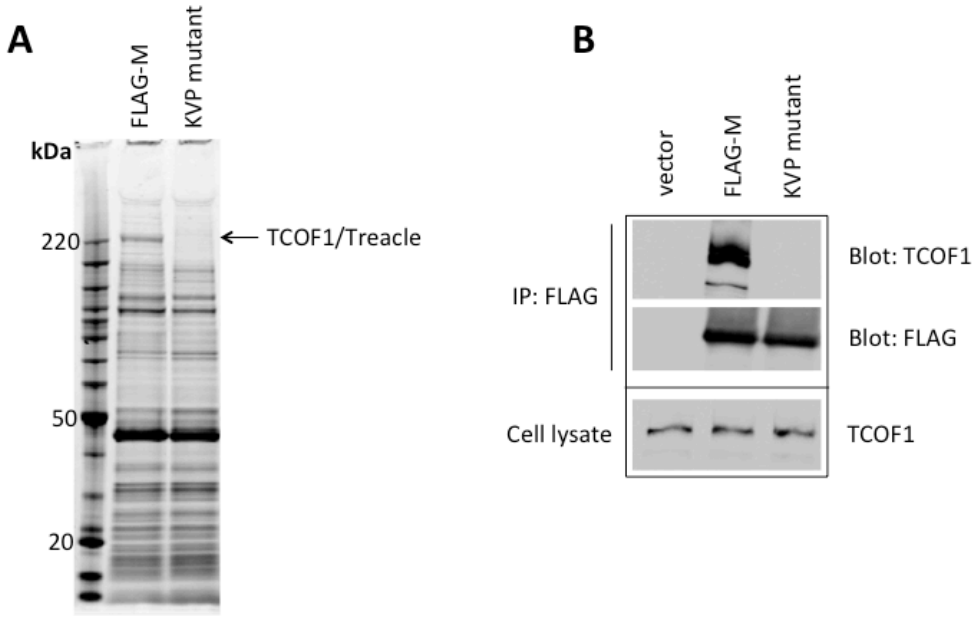

Figure 4-16. The KVP mutant specifically loses interaction with TCOF1/Treacle. (A) The indicated band from the wild-type immunoprecipitation was identified by mass spectrometry to be entirely TCOF1/Treacle. (B) The interaction, and its loss by the KVP mutant, were confirmed by Western immunoblot of co-immunoprecipitated endogenous TCOF1.

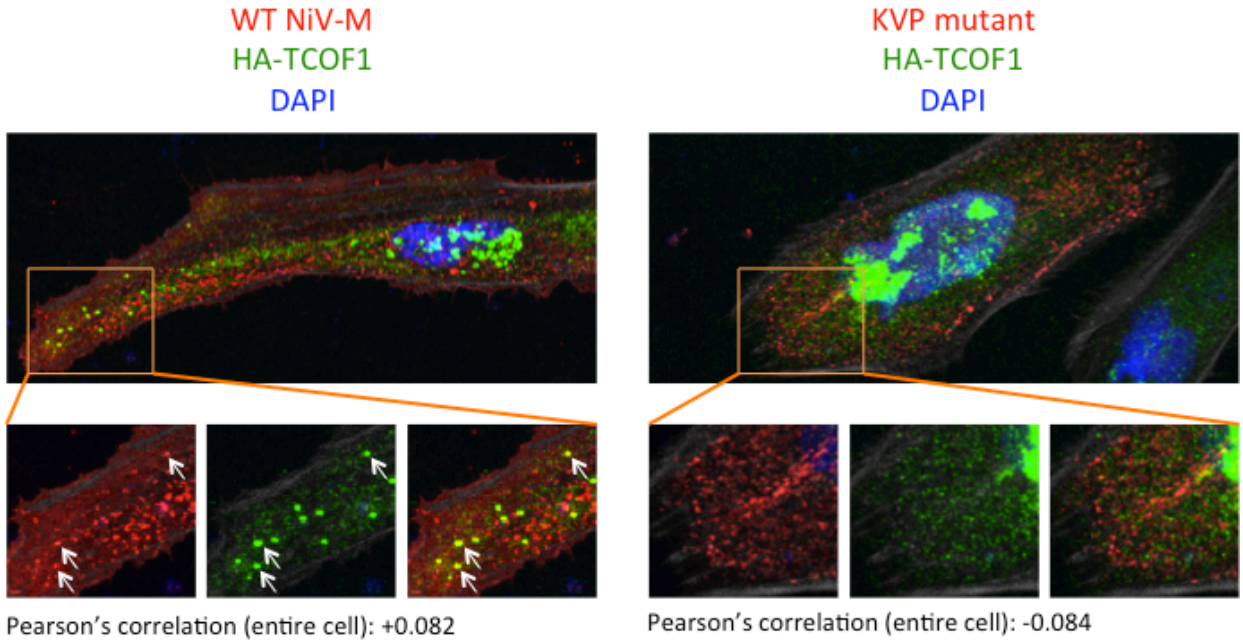

Figure 4-17. HA-TCOF1 co-localizes with wild-type NiV-M but not with the KVP mutant. The Pearson's correlation for colocalization was measured in Volocity image analysis software for the co-transfected cell shown. The analyzed data represented confocal z-stacks spanning the entire cell as determined by actin boundaries (stained by phalloidin, visible as grayscale in the images above).

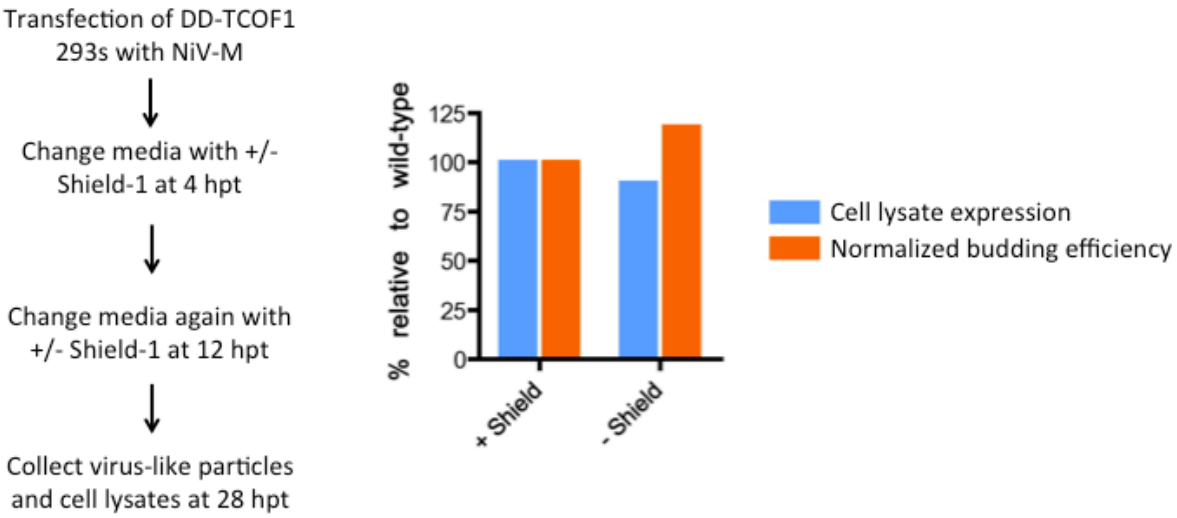

Figure 4-18. Destabilization of TCOF1 does not affect NiV-M budding. A HEK 293 cell line with all endogenous TCOF1 tagged with a destabilization domain was generated (see Chapter 4.2 for details and characterization of the cell line). Shield-1 stabilizes the DD-tagged TCOF1, while removal of Shield-1 destabilizes TCOF1, knocking down protein levels over 3-fold. Destabilization of TCOF1 using this system (indicated by the – Shield condition) did not affect M budding, however.

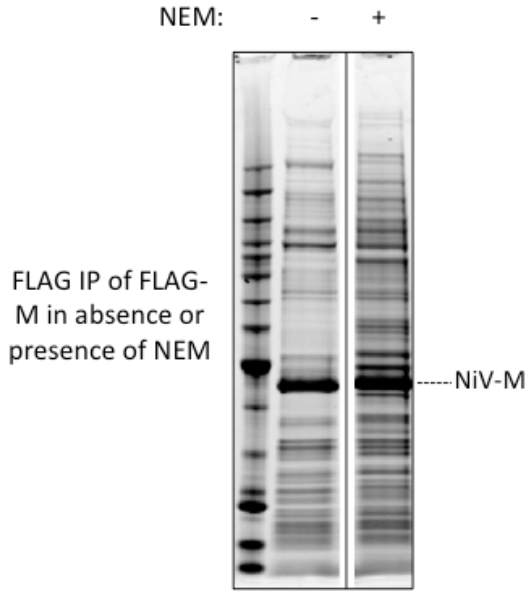

Figure 4-19. Inclusion of an inhibitor of deubiquitination changes the co-immunoprecipitated interactome. N-ethylmaleimide (NEM) inhibits deubiquitinases by irreversibly modifying the conserved active site cysteine. Use of NEM during cell lysis and immunoprecipitation of NiV-M significantly changes the quality (abundance and perhaps composition) of the interactome as seen by Coomassie staining of SDS-PAGE.

COPI

COPB1	Component of COPI coat
COPB2	Component of COPI coat
COPD	Component of COPI coat (also known as ARCN1)
COPE	Component of COPI coat
COPG	Component of COPI coat

COPII

SEC23B	Component of COPII coat
SEC24C	Component of COPII coat

Clathrin-coated vesicle adaptors

AP1M1	Golgi-associated trafficking
AP2A2	Clathrin-dependent endocytosis
AP2B1	Clathrin-dependent endocytosis
AP3D1	Golgi-associated, trafficking to lysosomes

Actin dynamics

ACTA1	Actin
ACTC1	Actin
ACTR2	Component of Arp2/3 complex in actin dynamics
CYFIP1	Formation of membrane ruffles and lamellipodia protrusions, axon outgrowth
DBNL	Actin-binding adaptor
DIAPH1	Nucleates actin filaments
FSCN1	Organizes filamentous actin into bundles
MYO6	Actin-based motor towards minus-end of filaments
PDCD6IP	Also known as ALIX, plays role in both ESCRT and actin dynamics

Other trafficking-related factors

ACBD3	Maintenance of Golgi structure
ARF1	Intra-Golgi transport
ARF3	Protein trafficking, Golgi-associated
ARF5	Protein trafficking, Golgi-associated
CPNE1	Calcium-dependent binding to phospholipids
CPNE3	Calcium-dependent binding to phospholipids
KIAA1279	Required for organization of axonal microtubules
NSF	Required for vesicular transport, involved in vesicle fusion
NSFL1C	Golgi dynamics, may play role in transitional ER
RAB7A	Late endosomal trafficking
SDF4	May regulate calcium-dependent activities in ER lumen
SRP72	Targets secretory proteins to ER
VPS26A	Component of retromer complex (endosome-to-Golgi tranport)

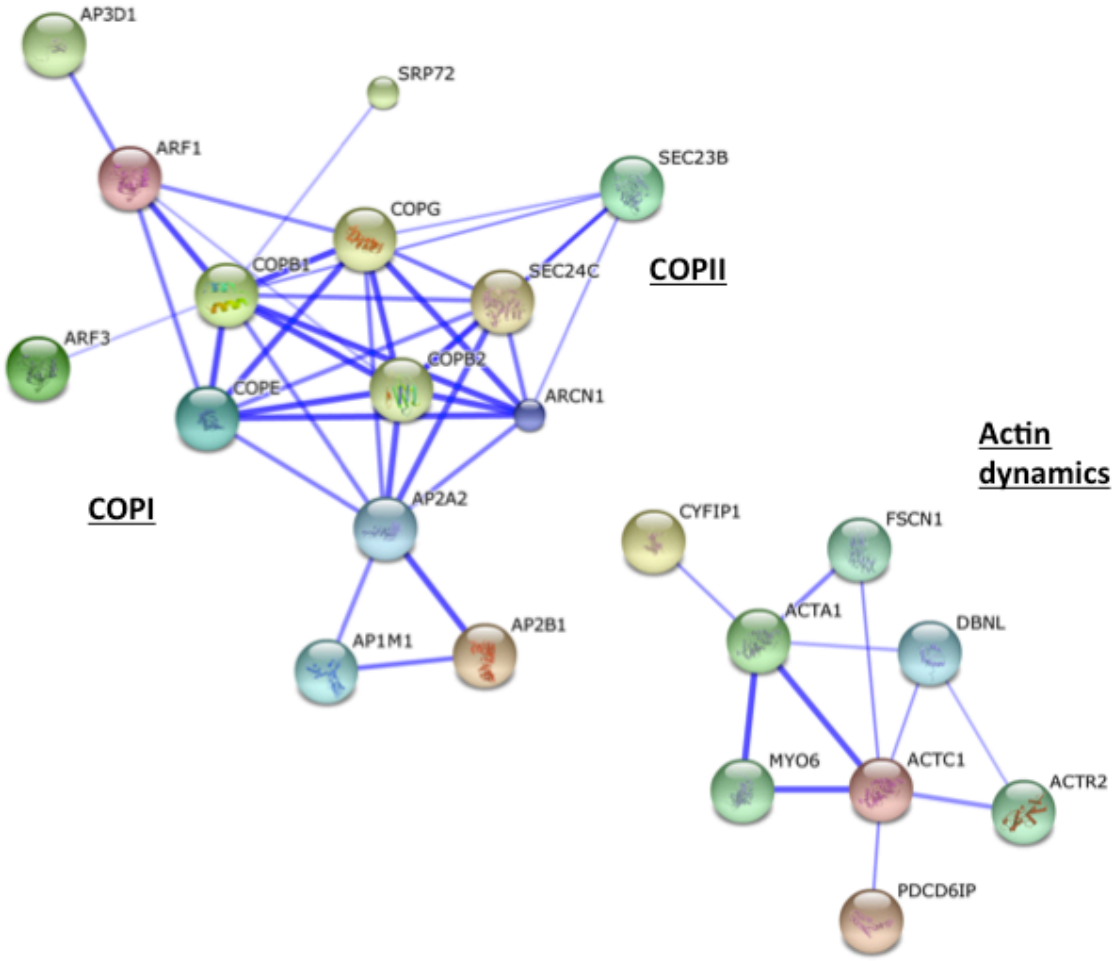

Figure 4-20. Cellular factors involved in trafficking and cytoskeletal dynamics were pulled down with multiple paramyxovirus matrix proteins. With an updated protocol including NEM as well as a broad spectrum phosphatase inhibitor, cellular factors of representative paramyxovirus matrix proteins including NiV-M, Sendai virus (SeV)-M, Newcastle disease virus (NDV)-M, and measles virus (MeV)-M were co-immunoprecipitated and identified by mass spectrometry (see Chapter 2.3 for details). Factors enriched in gene ontology terms related to vesicular/membrane trafficking and cytoskeletal dynamics were identified by analysis in DAVID Bioinformatics Resource (NIAID/NIH). Of these, those factors that were common to NiV, SeV, NDV, and MeV were extracted and listed above. Rendering of this protein list in STRING 9.1 (string-db.org) revealed the known interactions between these factors (only those that were linked by interactions are shown).

REFERENCES

1. Bauer A, Neumann S, Karger A, et al. ANP32B is a nuclear target of henipavirus M proteins. *PloS one*. 2014;9(5):e97233.

2. Negrete OA, Levroney EL, Aguilar HC, et al. EphrinB2 is the entry receptor for Nipah virus, an emergent deadly paramyxovirus. *Nature*. 2005;436(7049):401-405.

3. Gingras AC, Gstaiger M, Raught B, Aebersold R. Analysis of protein complexes using mass spectrometry. *Nature reviews Molecular cell biology*. 2007;8(8):645-654.

4. Harrison MS, Sakaguchi T, Schmitt AP. Paramyxovirus assembly and budding: building particles that transmit infections. *The international journal of biochemistry & cell biology*. 2010;42(9):1416-1429.

5. Le Hir H, Andersen GR. Structural insights into the exon junction complex. *Current opinion in structural biology*. 2008;18(1):112-119.

6. Tange TO, Nott A, Moore MJ. The ever-increasing complexities of the exon junction complex. *Current opinion in cell biology*. 2004;16(3):279-284.

7. Yamayoshi S, Noda T, Ebihara H, et al. Ebola virus matrix protein VP40 uses the COPII transport system for its intracellular transport. *Cell host & microbe*. 2008;3(3):168-177.

8. Gurkan C, Stagg SM, Lapointe P, Balch WE. The COPII cage: unifying principles of vesicle coat assembly. *Nature reviews Molecular cell biology*. 2006;7(10):727-738.

9. Hughes H, Budnik A, Schmidt K, et al. Organisation of human ER-exit sites: requirements for the localisation of Sec16 to transitional ER. *Journal of cell science*. 2009;122(Pt 16):2924-2934.

10. Watson P, Townley AK, Koka P, Palmer KJ, Stephens DJ. Sec16 defines endoplasmic reticulum exit sites and is required for secretory cargo export in mammalian cells. *Traffic*. 2006;7(12):1678-1687.

11. Zanetti G, Pahuja KB, Studer S, Shim S, Schekman R. COPII and the regulation of protein sorting in mammals. *Nature cell biology*. 2012;14(1):20-28.

12. Enninga J, Levay A, Fontoura BM. Sec13 shuttles between the nucleus and the cytoplasm and stably interacts with Nup96 at the nuclear pore complex. *Molecular and cellular biology*. 2003;23(20):7271-7284.

13. Hsia KC, Stavropoulos P, Blobel G, Hoelz A. Architecture of a coat for the nuclear pore membrane. *Cell*. 2007;131(7):1313-1326.

14. Niu X, Hong J, Zheng X, et al. The nuclear pore complex function of Sec13 protein is required for cell survival during retinal development. *The Journal of biological chemistry*. 2014;289(17):11971-11985.

15. Aridor M, Bannykh SI, Rowe T, Balch WE. Sequential coupling between COPII and COPI vesicle coats in endoplasmic reticulum to Golgi transport. *The Journal of cell biology*. 1995;131(4):875-893.

16. Kuge O, Dascher C, Orci L, et al. Sar1 promotes vesicle budding from the endoplasmic reticulum but not Golgi compartments. *The Journal of cell biology*. 1994;125(1):51-65.

17. Ahyi AN, Quinton LJ, Jones MR, et al. Roles of STAT3 in protein secretion pathways during the acute-phase response. *Infection and immunity*. 2013;81(5):1644-1653.

18. Fu H, Subramanian RR, Masters SC. 14-3-3 proteins: structure, function, and regulation. *Annual review of pharmacology and toxicology*. 2000;40:617-647.

19. Morrison DK. The 14-3-3 proteins: integrators of diverse signaling cues that impact cell fate and cancer development. *Trends in cell biology*. 2009;19(1):16-23.

20. Shikano S, Coblitz B, Wu M, Li M. 14-3-3 proteins: regulation of endoplasmic reticulum localization and surface expression of membrane proteins. *Trends in cell biology*. 2006;16(7):370-375.

21. Johnson C, Crowther S, Stafford MJ, Campbell DG, Toth R, MacKintosh C. Bioinformatic and experimental survey of 14-3-3-binding sites. *The Biochemical journal*. 2010;427(1):69-78.

22. Yaffe MB, Rittinger K, Volinia S, et al. The structural basis for 14-3-3:phosphopeptide binding specificity. *Cell*. 1997;91(7):961-971.

23. Muslin AJ, Xing H. 14-3-3 proteins: regulation of subcellular localization by molecular interference. *Cellular signalling*. 2000;12(11-12):703-709.

24. Singla V, Reiter JF. The primary cilium as the cell's antenna: signaling at a sensory organelle. *Science*. 2006;313(5787):629-633.

25. Satir P, Christensen ST. Overview of structure and function of mammalian cilia. *Annual review of physiology*. 2007;69:377-400.

26. Gerdes JM, Davis EE, Katsanis N. The vertebrate primary cilium in development, homeostasis, and disease. *Cell*. 2009;137(1):32-45.

27. Deretic D, Williams AH, Ransom N, Morel V, Hargrave PA, Arendt A. Rhodopsin C terminus, the site of mutations causing retinal disease, regulates trafficking by binding to ADP-ribosylation factor 4 (ARF4). *Proceedings of the National Academy of Sciences of the United States of America*. 2005;102(9):3301-3306.

28. Hoffmeister H, Babinger K, Gurster S, et al. Polycystin-2 takes different routes to the somatic and ciliary plasma membrane. *The Journal of cell biology*. 2011;192(4):631-645.

29. Mazelova J, Astuto-Gribble L, Inoue H, et al. Ciliary targeting motif VxPx directs assembly of a trafficking module through Arf4. *The EMBO journal*. 2009;28(3):183-192.

30. Ward HH, Brown-Glaberman U, Wang J, et al. A conserved signal and GTPase complex are required for the ciliary transport of polycystin-1. *Molecular biology of the cell*. 2011;22(18):3289-3305.

31. Plotnikova OV, Pugacheva EN, Golemis EA. Primary cilia and the cell cycle. *Methods in cell biology*. 2009;94:137-160.

32. Gonzales B, Henning D, So RB, Dixon J, Dixon MJ, Valdez BC. The Treacher Collins syndrome (TCOF1) gene product is involved in pre-rRNA methylation. *Human molecular genetics*. 2005;14(14):2035-2043.

33. Valdez BC, Henning D, So RB, Dixon J, Dixon MJ. The Treacher Collins syndrome (TCOF1) gene product is involved in ribosomal DNA gene transcription by interacting with upstream binding factor. *Proceedings of the National Academy of Sciences of the United States of America*. 2004;101(29):10709-10714.

34. Lin CI, Yeh NH. Treacle recruits RNA polymerase I complex to the nucleolus that is independent of UBF. *Biochemical and biophysical research communications*. 2009;386(2):396-401.

35. Pei Z, Bai Y, Schmitt AP. PIV5 M protein interaction with host protein angiomotin-like 1. *Virology*. 2010;397(1):155-166.

36. Pei Z, Harrison MS, Schmitt AP. Parainfluenza virus 5 m protein interaction with host protein 14-3-3 negatively affects virus particle formation. *Journal of virology*. 2011;85(5):2050-2059.

37. Ravid D, Leser GP, Lamb RA. A role for caveolin 1 in assembly and budding of the paramyxovirus parainfluenza virus 5. *Journal of virology*. 2010;84(19):9749-9759.

38. Bruce EA, Digard P, Stuart AD. The Rab11 pathway is required for influenza A virus budding and filament formation. *Journal of virology*. 2010;84(12):5848-5859.

39. Utley TJ, Ducharme NA, Varthakavi V, et al. Respiratory syncytial virus uses a Vps4-independent budding mechanism controlled by Rab11-FIP2. *Proceedings of the National Academy of Sciences of the United States of America*. 2008;105(29):10209-10214.

40. Lamp B, Dietzel E, Kolesnikova L, et al. Nipah virus entry and egress from polarized epithelial cells. *Journal of virology*. 2013;87(6):3143-3154.

CHAPTER 4.2

CRISPR/CAS9 ALLOWS EFFICIENT AND COMPLETE KNOCK-IN OF A DESTABILIZATION DOMAIN-TAGGED ESSENTIAL PROTEIN IN A HUMAN CELL LINE, ALLOWING RAPID KNOCKDOWN OF PROTEIN FUNCTION

CRISPR/Cas9 Allows Efficient and Complete Knock-In of a Destabilization Domain-Tagged Essential Protein in a Human Cell Line, Allowing Rapid Knockdown of Protein Function

Arnold Park[1], Sohui T. Won[2], Mickey Pentecost[1], Wojciech Bartkowski[1], Benhur Lee[1,2]*

1 Department of Microbiology, Immunology and Molecular Genetics, University of California Los Angeles, Los Angeles, California, United States of America, **2** Department of Microbiology, Icahn School of Medicine at Mount Sinai, New York, New York, United States of America

Abstract

Although modulation of protein levels is an important tool for study of protein function, it is difficult or impossible to knockdown or knockout genes that are critical for cell growth or viability. For such genes, a conditional knockdown approach would be valuable. The FKBP protein-based destabilization domain (DD)-tagging approach, which confers instability to the tagged protein in the absence of the compound Shield-1, has been shown to provide rapid control of protein levels determined by Shield-1 concentration. Although a strategy to knock-in DD-tagged protein at the endogenous loci has been employed in certain parasite studies, partly due to the relative ease of knock-in as a result of their mostly haploid lifecycles, this strategy has not been demonstrated in diploid or hyperploid mammalian cells due to the relative difficulty of achieving complete knock-in in all alleles. The recent advent of CRISPR/Cas9 homing endonuclease-mediated targeted genome cleavage has been shown to allow highly efficient homologous recombination at the targeted locus. We therefore assessed the feasibility of using CRISPR/Cas9 to achieve complete knock-in to DD-tag the essential gene Treacher Collins-Franceschetti syndrome 1 (TCOF1) in human 293T cells. Using a double antibiotic selection strategy to select clones with at least two knock-in alleles, we obtained numerous complete knock-in clones within three weeks of initial transfection. DD-TCOF1 expression in the knock-in cells was Shield-1 concentration-dependent, and removal of Shield-1 resulted in destabilization of DD-TCOF1 over the course of hours. We further confirmed that the tagged TCOF1 retained the nucleolar localization of the wild-type untagged protein, and that destabilization of DD-TCOF1 resulted in impaired cell growth, as expected for a gene implicated in ribosome biogenesis. CRISPR/Cas9-mediated homologous recombination to completely knock-in a DD tag likely represents a generalizable and efficient strategy to achieve rapid modulation of protein levels in mammalian cells.

Citation: Park A, Won ST, Pentecost M, Bartkowski W, Lee B (2014) CRISPR/Cas9 Allows Efficient and Complete Knock-In of a Destabilization Domain-Tagged Essential Protein in a Human Cell Line, Allowing Rapid Knockdown of Protein Function. PLoS ONE 9(4): e95101. doi:10.1371/journal.pone.0095101

Editor: Prasun K. Datta, Temple University, United States of America

Received January 23, 2014; **Accepted** March 21, 2014; **Published** April 17, 2014

Funding: AP was supported by the National Institutes of Health (NIH) Ruth L. Kirschstein National Research Service Award GM007185. MP was supported by NIH T32 AI060567 as well as the NIH Ruth L. Kirschstein National Research Service Award F32 AI100498. The funders had no role in study design, data collection and analysis, decision to publish, or preparation of the manuscript.

Competing Interests: The authors have declared that no competing interests exist.

* E-mail: Benhur.Lee@mssm.edu

Introduction

To determine the functional contribution of a cellular gene to a biological process, a mRNA knockdown or genomic knockout approach is often used. When it comes to genes that are critical for cell viability and growth, however, a knockdown or knockout approach may lead to sickly or nonviable cells that make appropriate comparison to control cells difficult or impossible. Further, RNA knockdown can take days to result in substantial reduction in protein levels, especially if the protein has a long *in vivo* half-life.

To address these concerns and achieve rapid knockdown of an essential gene in mammalian cells, we combined two recent approaches: i) the use of a destabilizing FKBP protein-based 12 kDa tag to confer chemical compound-dependent regulation of protein levels [1], and ii) the CRISPR/Cas9 bacterial homing endonuclease system that allows efficient homologous recombination at endogenous loci [2,3]. The resultant destabilization domain (DD)-tagged protein, when stabilized, allows cell growth and viability, whereas removal of the stabilizing compound results in rapid knockdown at the protein level. Although a knock-in DD-tagging strategy has been employed in parasite models such as *Plasmodium falciparum* and *Toxoplasma gondii* [4,5] (also see [6,7] for recent examples), this has been due to the relative ease of modification of the usually haploid genome; in diploid and hyperploid mammalian cell lines, however, the relative difficulty of complete knock-in in multiple alleles has been a barrier to use of this DD-tagging knock-in strategy. The demonstrated efficiency of CRISPR/Cas9 in stimulating targeted homologous recombination made it reasonable to attempt this knock-in strategy in a standard human cell line.

We chose to test the Cas9-mediated DD-tag knock-in strategy on Treacher Collins-Franceschetti syndrome 1 (TCOF1, also known as treacle), an essential gene encoding a nucleolar protein that is important for ribosome biogenesis, neural crest cell

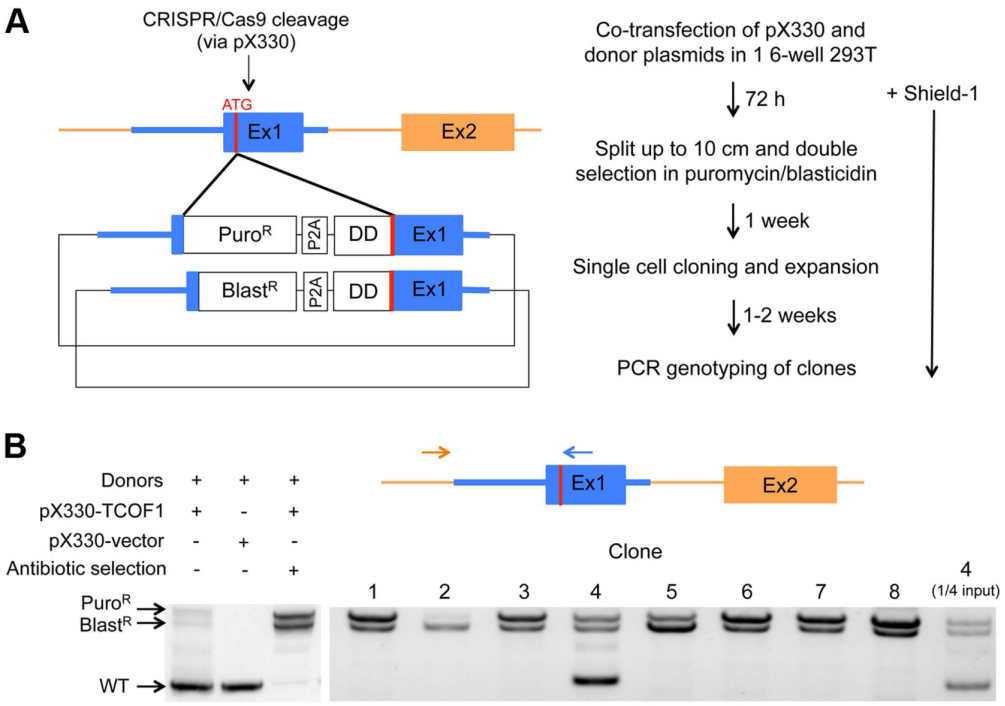

Figure 1. CRISPR/Cas9 allows efficient and complete endogenous knock-in of DD-tagged TCOF1. (**A**) The scheme for CRISPR/Cas9-mediated homologous recombination to insert antibiotic resistance and a DD tag to the N-terminus of TCOF1 is shown. The genomic sequence used in the donor plasmid homology arms is shown in blue. (**B**) PCR genotyping to detect knock-in was performed with the primers indicated on the diagram, and reveals wild-type (960 bp), blasticidin resistance (Blast^R) knock-in (1790 bp), and puromycin resistance (Puro^R) knock-in (1990 bp) bands. ¼ of the clone 4 PCR was also run to illustrate the lack of wild-type allele detection in the other clone PCRs.
doi:10.1371/journal.pone.0095101.g001

development and neurogenesis [8–12]. Haploinsufficiency of TCOF1 in humans is associated with Treacher Collins syndrome, characterized by impaired craniofacial development as well as ear defects leading to deafness [13–16], and the absence of TCOF1-null mice or humans suggests that knockout is embryonic lethal. Haploinsufficiency in mice can result in neonatal death or survival, depending on the genetic background [8,17]. Further, recent genome-wide knockout screens using CRISPR/Cas9 in various human cell lines confirmed that TCOF1 is important for cell viability in all cell types tested [18,19]. Within three weeks of initially transfecting the appropriate TCOF1-specific Cas9 and donor plasmids, we succeeded in expanding numerous single cell clones of human 293T cells with complete knock-in of DD-tagged TCOF1, despite the presence of at least three alleles of TCOF1 in these transformed cells. The compound Shield-1 stabilized DD-TCOF1 in a dose-dependent manner, and the removal of Shield-1 resulted in a several-fold decrease in DD-TCOF1 expression. Consistent with the known role of TCOF1 in ribosome biogenesis, destabilization of TCOF1 resulted in a significant decrease in cell growth.

To the best of our knowledge, this report represents the first demonstration that knock-in of DD-tagged protein in mammalian cells via CRISPR/Cas9 is an efficient strategy for rapid knockdown at the protein level.

Materials and Methods

Cell line and plasmids

293T cells were maintained in DMEM with 10% FCS and supplemented with penicillin/streptomycin. The pX330 CRISPR/Cas9 plasmid, designed by Cong *et al.* [2], was obtained from Addgene (plasmid 42230). For detailed discussion on CRISPR/Cas9 systems and applications, Drs. George Church and Feng Zhang among others maintain helpful resources and FAQs online as well, which can be found through the Addgene website (http://www.addgene.org/CRISPR/). The TCOF1-specific guide RNA sequence (Figure S1) was chosen from the curated database from Mali *et al.* [3] and inserted into the pX330 BbsI cloning site as described [20]. For the donor plasmids (Figure 1A and S2), the left and right homology arms were PCR-amplified using Velocity DNA Polymerase (Bioline) from 293T genomic DNA (isolated using the PureLink Genomic DNA Kit, Invitrogen). The destabilization domain was PCR-amplified from pTRE-Cycle1 (Clontech). The homology arms, antibiotic resistance ORF, and destabilization domain were joined together using standard overlapping PCR, then inserted between the BamHI and EcoRI sites of the PCR2.1 vector (Invitrogen) using In-Fusion (Clontech). 6XHis-tagged FKBP12 with the F36V mutation (on which the destabilization domain was based) in pET-15b (Novagen) was a kind gift of Dr. Thomas Wandless. FKBP-F36V was purified from BL21(DE3) *E. coli* as previously described [21] with minor modifications. Briefly, cells at OD_{600} 0.5 were induced with 2 mM IPTG at 37°C for 3 hours, then collected and lysed in sodium phosphate buffer (pH 8) containing 10 mM imidazole. 6XHis-tagged FKBP was purified on a 5 mL HisTrap HP (GE Healthcare) column via FPLC, with increasing imidazole concentration up to 250 mM. Pure fractions containing FKBP protein were pooled and dialyzed overnight into PBS.

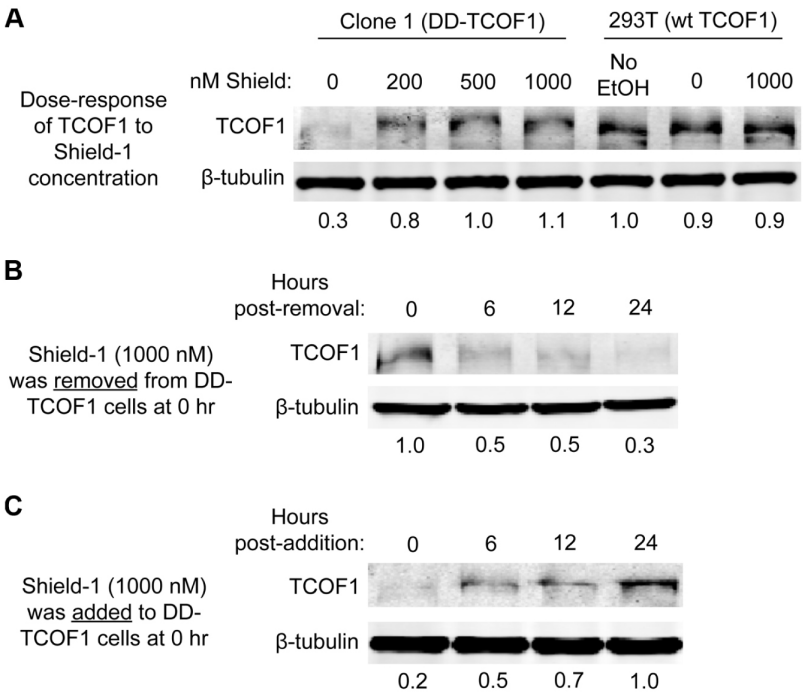

Figure 2. DD-TCOF1 expression is regulated by the concentration of Shield-1. (**A–C**) The Shield-1 concentration- and time-dependent expression of TCOF1 was examined as described in Materials and Methods. Although the EtOH vehicle was kept constant as described, a control without EtOH vehicle was also included for the parental wild-type 293Ts in panel A. As wild-type TCOF1 runs at about 220 kDa, the addition of the 12 kDa DD tag results in small upward shift for knock-in cells. Two-fold dilutions of high TCOF1-expressing sample were included on each gel to allow for standard curves to quantitate relative TCOF1 and β-tubulin. Relative TCOF1 values normalized to β-tubulin are shown below each panel. The data represents one of three experiments with similar results.
doi:10.1371/journal.pone.0095101.g002

Transfection and selection

293T cells at 70% confluence in a 6-well were co-transfected with 1 μg each of pX330 (with TCOF1-specific guide sequence inserted), puromycin resistance donor plasmid, and blasticidin resistance donor plasmid, with 4.5 μL BioT transfection reagent (Bioland). At 24 hours post-transfection, media was changed with 100 nM Shield-1 (Clontech), and cells were subsequently always maintained in Shield-1. At 72 hours post-transfection, the 6-well was trypsinized and seeded into a 10 cm dish with 1 μg/mL puromycin and 3 μg/mL blasticidin. The media with antibiotics was changed every 3 days. Upon complete cell death in the controls (untransfected cells in single puromycin or blasticidin selection) after a week of selection, cells were trypsinized and plated in two 96-wells at a seeding density of 0.3 cells per well. Wells were monitored for single colony formation and expanded upon confluency.

PCR genotyping of knock-in clones

Genomic DNA was isolated using the PureLink Genomic DNA Kit (Invitrogen) and genotyped using Velocity DNA Polymerase (Bioline) and the following primers: TCOF_screen-F: GTTTAGGGTTCCCAGGCAAT and TCOF_screen-R: CAGCAGATGGTGGTAGATC (positions in genomic sequence shown in Figure S1). For the PCR shown in Figure S3, the primers used were TCOF_screen-F and also TCOF_screen-R2: CCACATGAGTAGCCAGGATTAC.

Western analysis of TCOF1 expression

3×10^5 knock-in or parental 293T cells per well were plated in 12-well in no Shield-1 (Figure 2A and C) or 1000 nM Shield-1 (Figure 2B). The following day, for addition of Shield-1, media was simply replaced with the appropriate concentration, with EtOH (the vehicle for Shield-1) remaining constant. For removal of Shield-1, media was replaced with conditioned media supplemented with 5 μM FKBP-F36V for 30 minutes, followed by continued incubation in media without Shield-1. At the indicated time points (24 hours for Figure 2A), cells were collected in cold PBS with 10 mM EDTA, pelleted, lysed in cold lysis buffer (0.1% NP-40, 100 mM Tris-HCl pH 7.5, 150 mM NaCl, 5% glycerol, 1 mM sodium orthovanadate, 1 mM EDTA, 1X protease inhibitor cocktail (Roche)), clarified at 13 k rpm for 5 minutes at 4°C, then stored at -20°C until use. A small portion of cells was reserved for cell counting. Lysates were boiled with Laemmli SDS sample buffer, and the equivalent of 4×10^4 cells were run per sample on 8% Tris-glycine SDS-PAGE. Gels were transferred to PVDF (Immobilon-FL, Millipore) and blocked in Odyssey Blocking Buffer (LI-COR Biosciences) overnight at 4°C. Blots were then incubated in 1:1000 rabbit anti-TCOF1 (11003-1-AP, Proteintech) or 1:100,000 mouse anti-β-tubulin (T7816, Sigma) for 1 hour at room temperature, followed by 1:10,000 of fluorescent secondary antibody (goat anti-rabbit IRDye 800CW or goat anti-mouse IRDye 680LT, LI-COR Biosciences). Fluorescence images were obtained on a LI-COR Odyssey imaging system.

Immunofluorescence staining and data analysis

Wild-type or knock-in cells were plated in EtOH vehicle only or 1000 nM Shield-1 on coverslips that had been coated sequentially with poly-L-lysine and collagen. 24 hours post-plating, cells were fixed in 2% paraformaldehyde, washed 3 times with PBS, incubated in blocking buffer (0.5% saponin, 3% BSA in PBS),

then incubated with 1:200 rabbit anti-TCOF1 (11003-1-AP, Proteintech), 1:500 mouse anti-nucleolin (39-6400, Sigma), and 1:250 Alexa Fluor 647 Phalloidin (Invitrogen) in blocking buffer. After 3 washes in 0.5% saponin in PBS, samples were incubated with 1:1000 secondary antibodies goat anti-rabbit Alexa Fluor 488 and goat anti-mouse Alex Fluor 594 (Invitrogen). After 3 final washes in 0.5% saponin in PBS, samples were incubated with DAPI to stain nuclei before mounting on slides. Confocal imaging was performed on a Leica SP5 confocal microscope, acquiring optical Z-stacks of 0.3 μm steps. Z-stacks were reconstructed and analyzed in three dimensions using Volocity 5.5 software (Perkin Elmer). Individual nuclei were localized and defined in three dimensions by DAPI staining. DNA-absent regions (such as nucleoli) were included in the defined nucleus, touching nuclei were separated, and fluorescence objects smaller than nuclei were excluded from analysis. Fluorescence voxel intensities in all channels were then measured within these computationally defined nuclei.

Growth curves

2×10^4 cells per well for wild-type 293T cells or knock-in cells were plated from master mix cell suspensions into either EtOH- or Shield-1-containing media in 6-well plates. Beginning 1 day post-plating and each day thereafter, cells were trypsinized and counted (in triplicate for each condition). The media was changed on day 3 for cells to be collected on subsequent days.

Results

CRISPR/Cas9 allows efficient and complete knock-in of destabilization domain-tagged TCOF1 at endogenous loci

The double-strand breaks mediated by CRISPR/Cas9 can stimulate homologous recombination in the presence of a DNA donor with appropriate homology arms. We first modified the pX330 Cas9-expressing plasmid [2] to specifically target the human genome near the start codon of TCOF1 (Figure 1A and S1). We then created donor plasmids that would result in knock-in of a DD tag linked to the N-terminus of TCOF1 via a 3XGGGGS flexible linker. To select for cells with knock-in at more than one allele, thus simplifying our screening process for clones with complete knock-in, we designed two donor plasmids with either puromycin or blasticidin resistance, followed by a P2A ribosomal skipping sequence and the DD tag and linker, all flanked by 800 bp homology arms (Figure 1A and S2). The P2A sequence appears to be the most efficient of the 2A skipping sequences in human cell lines [22], and we also included a GSG linker immediately preceding the P2A sequence (Figure S2), which has been shown to ensure essentially complete skipping [23,24]. Upon knock-in, antibiotic resistance is driven off the endogenous promoter, and the DD-tagged protein is translated from the same mRNA transcript via the P2A sequence (Figure 1A). Double antibiotic selection should therefore select for cells with at least two modified alleles.

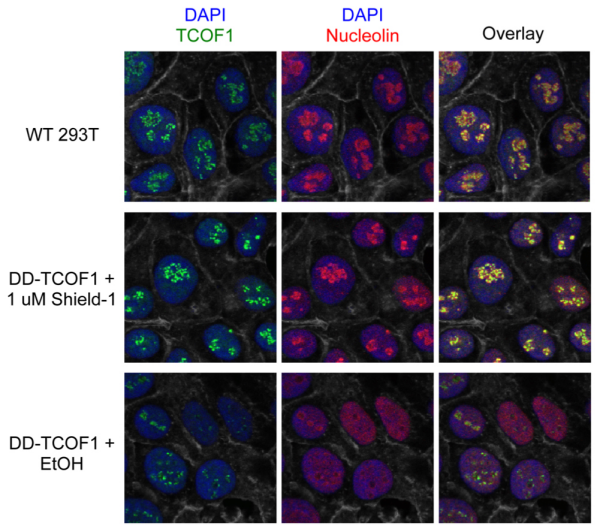

Figure 3. DD-TCOF1 retains the nucleolar localization of wild-type TCOF1. Knock-in cells in Shield-1 or ethanol vehicle alone and parental wild-type 293T cells were stained and imaged as described in Materials and Methods. A single representative z-slice confocal image is shown. The visible grayscale cell boundaries represent F-actin (stained with phalloidin).
doi:10.1371/journal.pone.0095101.g003

A clonal population of 293T cells was co-transfected with the TCOF1-specific pX330 Cas9 plasmid and the two donor plasmids (Figure 1A). At one day post-transfection, the media was changed to include 100 nM Shield-1 to stabilize DD-TCOF1, and Shield-1 was continually present in the media after this point through the entire knock-in process. At three days post-transfection, the cells were expanded and incubated with puromycin and blasticidin at predetermined minimal concentrations. After a week of antibiotic selection (control cells were all dead at this point in either single puromycin or blasticidin selection), cells were collected and single cell-cloned into 96-well dishes with no more subsequent antibiotic selection. Over the next 1-2 weeks, clones were expanded up to two 12-wells, from which one well was frozen for subsequent use and the other well was collected for genomic DNA isolation.

Next, we genotyped the clones by PCR to determine whether knock-in at the endogenous loci had occurred. To ensure specificity for the endogenous locus, while the reverse primer was specific for sequence within the right (3′) homology arm present in the donor plasmids, the forward primer was specific for genomic sequence beyond the left (5′) homology arm, and thus not present in the donor plasmids (Figure 1B). PCR of the wild-type locus results in a 960 bp band, whereas PCR of the knock-in allele results in 1990 and 1790 bp bands for puromycin or blasticidin resistance, respectively. We thus genotyped the eight fastest growing clones, and 7/8 resulted in complete knock-in (Figure 1B). The presence of wild-type and puromycin/blasticidin alleles in clone 4 indicates that there are at least three alleles of TCOF1 in these genetically unstable cells; this is also evident in the apparent predominance of either the puromycin or blasticidin allele in any given clone, indicating more of one or the other allele (note the difference between clones 5 and 6, for example). Although the smaller PCR fragment was useful to better distinguish the size difference between the puromycin/blasticidin alleles, we further confirmed recombination at the right homology arm by using primers specific for genomic sequence beyond both homology arms (Figure S3). For subsequent experiments, we used clone 1 as shown in Figure 1B.

As further evidence for the utility of Cas9 as well as antibiotic selection for this knock-in strategy, 293T cells transfected with the donor plasmids and the original non-TCOF1-specific pX330 did not show visible evidence of knock-in via genotyping PCR, and comparison of cells before and after double selection showed that selection resulted in reduction of the wild-type alleles and predominance of the knock-in alleles in the overall pool (Figure 1B).

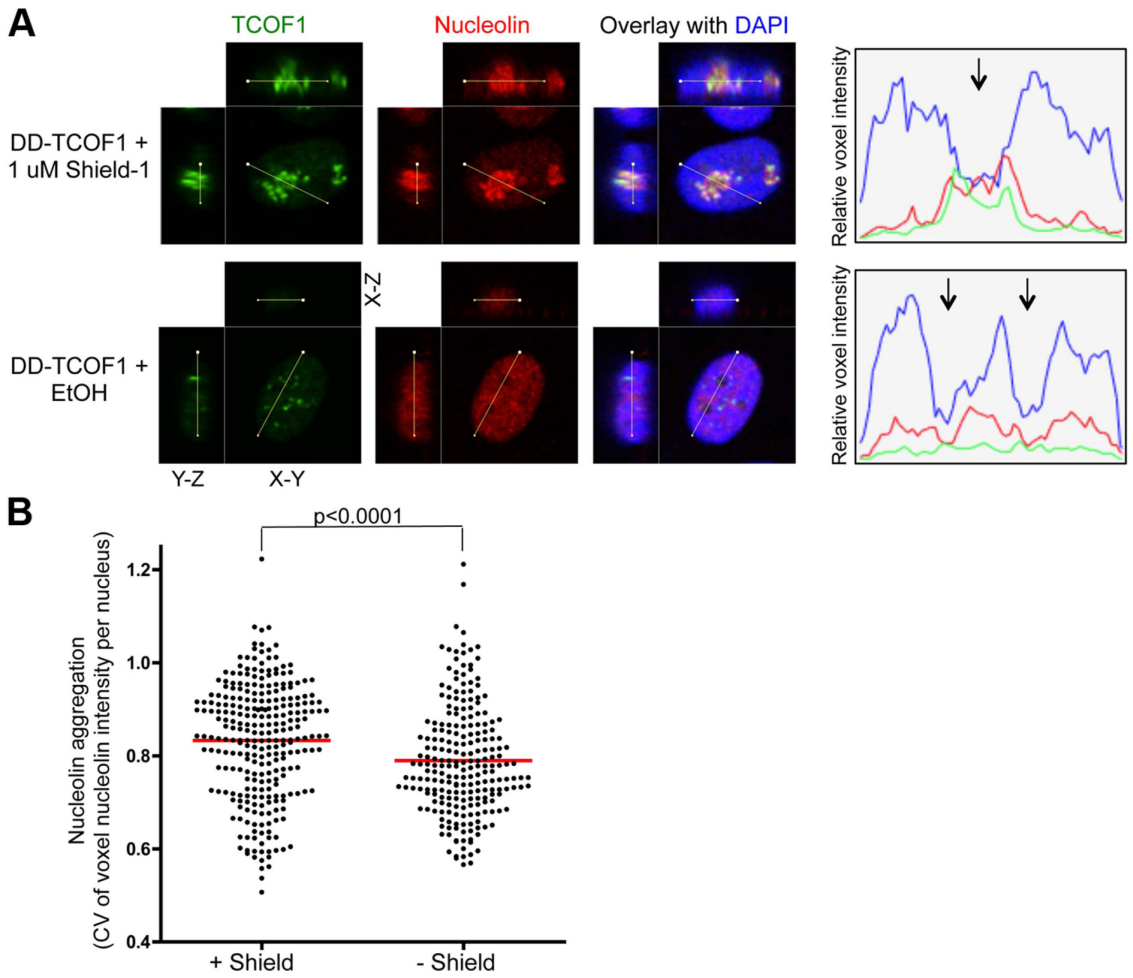

Figure 4. Destabilization of TCOF1 results in dispersal of nucleolin. (**A**) The relative fluorescence intensities across the indicated lines are shown in the graph, and the arrows indicate the position of nucleoli as defined by a hole in the DAPI stain. Representative nuclei from knock-in cells in Shield-1 or ethanol vehicle alone are shown. (**B**) The aggregation of nucleolin was measured by the coefficient of variation (CV, stdev/mean) of nucleolin voxel intensities within DAPI-defined nuclei in 3D reconstructions, as described in Materials and Methods. As examples, this CV metric was 0.95 for the +Shield nucleus and 0.71 for the –Shield nucleus in panel A. The population means are indicated by the red lines. There is significantly less nucleolin aggregation in knock-in cell nuclei in the absence of Shield-1, $p<0.0001$, 2-tailed Student's t-test, $n = 272$ for +Shield and $n = 230$ for –Shield.
doi:10.1371/journal.pone.0095101.g004

DD-TCOF1 expression is regulated by the concentration of Shield-1

To assess whether DD-TCOF1 was expressed in the knock-in cells, we incubated cells with differing concentrations of Shield-1 and collected samples for Western after 24 hours. DD-TCOF1 expression was regulated in a dose-dependent manner, with 1000 nM Shield-1 resulting in over 3-fold more protein than the absence of Shield-1 (Figure 2A). By comparison, TCOF1 expression was not increased by Shield-1 in parental wild-type 293T cells (Figure 2A). We then observed the kinetics of DD-TCOF1 destabilization or stabilization. We either removed Shield-1 from knock-in cells initially in 1000 nM Shield-1, or added 1000 nM Shield-1 to knock-in cells initially without Shield-1. Removal of Shield-1 was facilitated by a brief incubation in conditioned media supplemented with 5 μM FKBP12 (the F36V mutant, from which the DD domain was derived), which acts as a strong thermodynamic sink for residual Shield-1 [21]. Within 24 hours, DD-TCOF1 levels were destabilized or stabilized over 3-fold (Figure 2B and C). The over 3-fold difference we observed was consistent with the 3.7-fold difference in mean fluorescence intensity previously observed for a DD-tagged YFP targeted to the nucleus [25].

DD-TCOF1 retains the nucleolar localization of wild-type TCOF1

We then determined whether the DD-tagged protein retained wild-type characteristics. Although the localization of TCOF1 may be dynamic, it is known to be predominantly nucleolar. The DD-TCOF in knock-in cells was indeed nucleolar, as indicated by strong co-localization with nucleolin in the presence of Shield-1 (Figure 3 and 4A). As a further confirmation of the specificity of our anti-TCOF1 antibody, TCOF1 staining in knock-in cells in the absence of Shield-1 was significantly reduced (Figure 3, also $p<0.0001$ by 2-tailed Student's t-test for +Shield nuclei ($n = 272$) vs. –Shield nuclei ($n = 230$) as described in Materials and Methods, data not shown). Unexpectedly, we noticed that upon DD-TCOF1

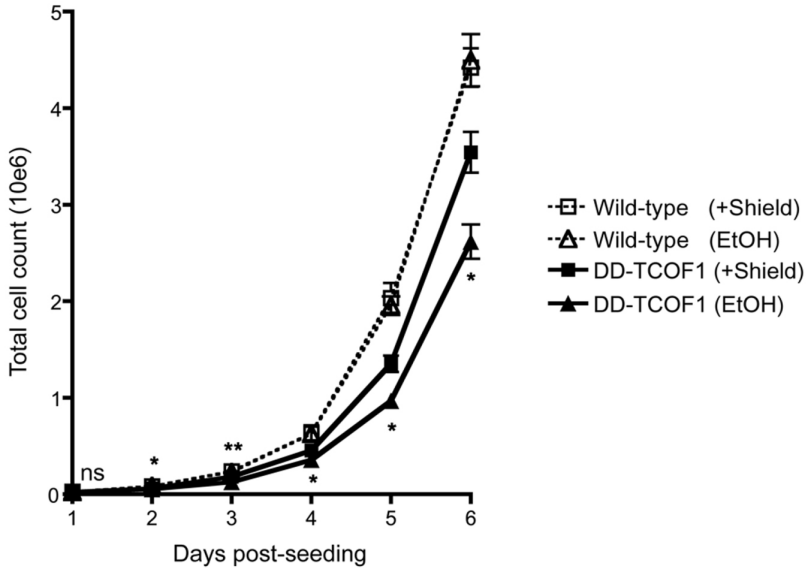

Figure 5. Destabilization of TCOF1 impairs cell growth. The growth of knock-in cells in the presence or absence of Shield-1 was compared as described in Materials and Methods. EtOH represents the vehicle control. Error bars represent SD of 3 replicate samples. The knock-in cell count in the absence of Shield-1 was significantly less than in the presence of Shield-1 except on the first day post-seeding: ns, not significant; *, $p<0.05$; **, $p<0.01$, 2-tailed Student's t-test at each time point. The growth of knock-in cells in the presence or absence of Shield-1 was compared two other times with similar results.
doi:10.1371/journal.pone.0095101.g005

destabilization, nucleolin itself appeared disaggregated and dispersed throughout the nucleoplasm (Figure 3 and 4A). To quantitatively evaluate this observation, we reasoned that within a given nucleus, while aggregation would lead to polarization of the distribution of voxel intensities and thus increased spread of intensity values, dispersion throughout the nucleoplasm should result in a voxel intensity distribution more evenly clustered around the mean and thus reduced spread of intensity values (e.g., see the vertical spreads of nucleolin voxel intensities in Figure 4A). We therefore used the coefficient of variation (the standard deviation normalized to the mean) of nucleolin voxel intensities within 3D reconstructions of DAPI-defined nuclei as a metric for nucleolin aggregation. Indeed, destabilization of DD-TCOF1 appears to result in reduced nucleolin aggregation (Figure 4B), reminiscent of previous findings that TCOF1 knockdown results in dispersion of Pol I and UBF away from nucleoli [11]. Since it is possible that a mutation specific to clone 1 was able to modulate the functional consequence of TCOF1 destabilization, especially in light of possible off-target effects of the CRISPR/Cas9 system [26–31], we confirmed that independent clone 2 also showed destabilization of TCOF1 and significantly reduced nucleolin aggregation ($p<0.0001$) in the absence of Shield-1 (Figure S4).

Destabilization of DD-TCOF1 impairs cell growth

Since TCOF1 is an essential gene important for ribosome biogenesis among other functions, we expected that destabilization of DD-TCOF1 should impair cell growth, although immortalized cell lines might be in general more resistant to the effects of TCOF1 gene disruption. Indeed, we found that while the presence or absence of Shield-1 did not affect the growth of parental wild-type 293Ts, the absence of Shield-1 (which leads to degradation of TCOF1) resulted in significantly reduced growth for the knock-in cells (Figure 5).

Discussion

The CRISPR/Cas9 homing endonuclease system and its utility for efficient genomic engineering has rapidly instigated widespread exploration for various applications. Here we report that the high efficiency of homologous recombination mediated by CRISPR/Cas9 allowed rapid and complete knock-in of destabilization domain-tagged TCOF1 in the hyperploid human 239T cell line. Expression of DD-TCOF1, which retained the subcellular localization and at least the growth-related function of the untagged protein, could be regulated by the stabilizing compound Shield-1. This knock-in strategy likely represents a generalizable and reasonable strategy in other diploid and hyperploid mammalian cells, particularly for essential genes that cannot be knocked out without severely affecting cell viability.

Although siRNA-mediated knockdown of TCOF1 has been attempted in the past, protein reduction is significantly apparent after four days [10,11]; the long time required to achieve significant knockdown may allow secondary effects of reduced viability to accumulate, which might confound the interpretation of results. Our present work demonstrates that efficient complete knock-in of DD-tagged TCOF1 via the CRIPSR/Cas9 system enables relatively rapid knockdown of protein levels upon removal of the stabilizing Shield-1 compound, or conversely, rapid upregulation of TCOF1 levels upon addition of Shield-1. In principle, the use of siRNA (or other means to regulate mRNA expression such as a regulatable Tet system) in knock-in cells in combination with Shield-1 removal might result in an even more dramatic decrease in DD-TCOF1 protein levels, since the basal level of DD-TCOF1 is due to the continual production of more protein from the mRNA. By reducing the mRNA itself, siRNA may enhance the decrease in DD-TCOF1 levels upon Shield-1 removal.

Importantly, although random donor insertion or off-target mutations were possible, biological interrogation of TCOF1

function could occur in an isogenic cellular background except for the modulation of TCOF1 levels via Shield-1. An independent clone confirmed our findings (Figure S4). Although we used the wild-type Cas9 endonuclease that catalyzes both nicks and double-strand breaks (DSBs), the use of a mutant Cas9 that only nicks may be used to avoid DSB-mediated non-homologous end joining mutations in off-target sites [26,30,32].

Although we used the endogenous promoter to drive expression of DD-TCOF1 in this study, a constitutive strong or weak promoter could also be added to the donor and used, depending on the context, in order to modify the dynamic range of DD-tagged protein, from the basal level to the maximally stabilized level of expression at reasonable Shield-1 concentrations. A stronger promoter would likely shift the entire dynamic range higher, while a weaker promoter would shift the dynamic range lower. Such a design would also allow the use of separate promoters for the antibiotic resistance gene and the DD-tagged gene of interest, thus facilitating the removal of the antibiotic gene via Cre/LoxP or FLP/FRT recombination if desired.

One requirement of the FKBP-based destabilization domain for our knock-in strategy for essential genes is that Shield-1 must be maintained on the knock-in cells to maintain cell growth and viability, unless the basal level of DD-tagged protein is sufficient to maintain growth (as in fact appears to be the case for our TCOF1 knock-in clone); this may become cost-prohibitive as Shield-1 is relatively expensive. We also acknowledge the possibility that we may have selected for clones that can tolerate constitutive reduction in TCOF1 protein levels. Fortunately, similar effective DD tag systems may be more cost-effective, such as an *E. coli* dihydrofolate reductase (ecDHFR)-based destabilization domain that is stabilized by the relatively inexpensive trimethoprim [33]. The ecDHFR-based and other recent systems are also orthogonal to the FKBP-based system [33,34], which would allow independent modulation of more than one protein of interest. Systems that allow conditional degradation rather than stabilization in the presence of compound represent another promising approach [35].

Supporting Information

Figure S1 Position of Cas9 guide RNA sequence and genotyping primers in the human genomic sequence.
(PDF)

Figure S2 Annotated sequence of knock-in donor constructs.
(PDF)

Figure S3 Homologous recombination in both 5′ and 3′ homology arms. Genotyping PCR was performed with the same forward primer shown in Figure 1B, but with a reverse primer beyond the 3′ homology arm.
(TIF)

Figure S4 Confirmation of dispersal of nucleolin with an independent clone. Destabilization of DD-TCOF1 in clone 2 was confirmed by Western analysis of cells incubated in either ethanol vehicle control or 1 μM Shield-1. The analysis of nucleolin dispersal was performed as described for Figure 4. CV, coefficient of variation (stdev/mean); $p<0.0001$, 2-tailed Student's t-test, $n = 338$ for +Shield and $n = 243$ for –Shield.
(TIF)

Acknowledgments

The authors would like to thank all members of the Benhur Lee lab for their constructive criticisms and support.

Author Contributions

Conceived and designed the experiments: AP BL. Performed the experiments: AP STW WB. Analyzed the data: AP MP. Wrote the paper: AP STW MP BL WB.

References

1. Banaszynski LA, Chen LC, Maynard-Smith LA, Ooi AG, Wandless TJ (2006) A rapid, reversible, and tunable method to regulate protein function in living cells using synthetic small molecules. Cell 126: 995–1004.
2. Cong L, Ran FA, Cox D, Lin S, Barretto R, et al. (2013) Multiplex genome engineering using CRISPR/Cas systems. Science 339: 819–823.
3. Mali P, Yang L, Esvelt KM, Aach J, Guell M, et al. (2013) RNA-guided human genome engineering via Cas9. Science 339: 823–826.
4. Armstrong CM, Goldberg DE (2007) An FKBP destabilization domain modulates protein levels in Plasmodium falciparum. Nat Methods 4: 1007–1009.
5. Herm-Gotz A, Agop-Nersesian C, Munter S, Grimley JS, Wandless TJ, et al. (2007) Rapid control of protein level in the apicomplexan Toxoplasma gondii. Nat Methods 4: 1003–1005.
6. Child MA, Hall CI, Beck JR, Ofori LO, Albrow VE, et al. (2013) Small-molecule inhibition of a depalmitoylase enhances Toxoplasma host-cell invasion. Nat Chem Biol 9: 651–656.
7. de Azevedo MF, Gilson PR, Gabriel HB, Simoes RF, Angrisano F, et al. (2012) Systematic analysis of FKBP inducible degradation domain tagging strategies for the human malaria parasite Plasmodium falciparum. PLoS One 7: e40981.
8. Dixon J, Jones NC, Sandell LL, Jayasinghe SM, Crane J, et al. (2006) Tcof1/Treacle is required for neural crest cell formation and proliferation deficiencies that cause craniofacial abnormalities. Proc Natl Acad Sci U S A 103: 13403–13408.
9. Sakai D, Dixon J, Dixon MJ, Trainor PA (2012) Mammalian neurogenesis requires Treacle-Plk1 for precise control of spindle orientation, mitotic progression, and maintenance of neural progenitor cells. PLoS Genet 8: e1002566.
10. Valdez BC, Henning D, So RB, Dixon J, Dixon MJ (2004) The Treacher Collins syndrome (TCOF1) gene product is involved in ribosomal DNA gene transcription by interacting with upstream binding factor. Proc Natl Acad Sci U S A 101: 10709–10714.
11. Lin CI, Yeh NH (2009) Treacle recruits RNA polymerase I complex to the nucleolus that is independent of UBF. Biochem Biophys Res Commun 386: 396–401.
12. Gonzales B, Henning D, So RB, Dixon J, Dixon MJ, et al. (2005) The Treacher Collins syndrome (TCOF1) gene product is involved in pre-rRNA methylation. Hum Mol Genet 14: 2035–2043.
13. Bowman M, Oldridge M, Archer C, O'Rourke A, McParland J, et al. (2012) Gross deletions in TCOF1 are a cause of Treacher-Collins-Franceschetti syndrome. Eur J Hum Genet 20: 769–777.
14. Dixon MJ (1996) Treacher Collins syndrome. Hum Mol Genet 5 Spec No: 1391–1396.
15. Sakai D, Trainor PA (2009) Treacher Collins syndrome: unmasking the role of Tcof1/treacle. Int J Biochem Cell Biol 41: 1229–1232.
16. Trainor PA, Dixon J, Dixon MJ (2009) Treacher Collins syndrome: etiology, pathogenesis and prevention. Eur J Hum Genet 17: 275–283.
17. Dixon J, Brakebusch C, Fassler R, Dixon MJ (2000) Increased levels of apoptosis in the prefusion neural folds underlie the craniofacial disorder, Treacher Collins syndrome. Hum Mol Genet 9: 1473–1480.
18. Shalem O, Sanjana NE, Hartenian E, Shi X, Scott DA, et al. (2014) Genome-scale CRISPR-Cas9 knockout screening in human cells. Science 343: 84–87.
19. Wang T, Wei JJ, Sabatini DM, Lander ES (2014) Genetic screens in human cells using the CRISPR-Cas9 system. Science 343: 80–84.
20. Ran FA, Hsu PD, Wright J, Agarwala V, Scott DA, et al. (2013) Genome engineering using the CRISPR-Cas9 system. Nat Protoc 8: 2281–2308.
21. Egeler EL, Urner LM, Rakhit R, Liu CW, Wandless TJ (2011) Ligand-switchable substrates for a ubiquitin-proteasome system. J Biol Chem 286: 31328–31336.
22. Kim JH, Lee SR, Li LH, Park HJ, Park JH, et al. (2011) High cleavage efficiency of a 2A peptide derived from porcine teschovirus-1 in human cell lines, zebrafish and mice. PLoS One 6: e18556.
23. Holst J, Vignali KM, Burton AR, Vignali DA (2006) Rapid analysis of T-cell selection in vivo using T cell-receptor retrogenic mice. Nat Methods 3: 191–197.
24. Szymczak AL, Workman CJ, Wang Y, Vignali KM, Dilioglou S, et al. (2004) Correction of multi-gene deficiency in vivo using a single 'self-cleaving' 2A peptide-based retroviral vector. Nat Biotechnol 22: 589–594.
25. Sellmyer MA, Chen LC, Egeler EL, Rakhit R, Wandless TJ (2012) Intracellular context affects levels of a chemically dependent destabilizing domain. PLoS One 7: e43297.

26. Cho SW, Kim S, Kim Y, Kweon J, Kim HS, et al. (2014) Analysis of off-target effects of CRISPR/Cas-derived RNA-guided endonucleases and nickases. Genome Res 24: 132–141.
27. Cradick TJ, Fine EJ, Antico CJ, Bao G (2013) CRISPR/Cas9 systems targeting beta-globin and CCR5 genes have substantial off-target activity. Nucleic Acids Res 41: 9584–9592.
28. Fu Y, Foden JA, Khayter C, Maeder ML, Reyon D, et al. (2013) High-frequency off-target mutagenesis induced by CRISPR-Cas nucleases in human cells. Nat Biotechnol 31: 822–826.
29. Hsu PD, Scott DA, Weinstein JA, Ran FA, Konermann S, et al. (2013) DNA targeting specificity of RNA-guided Cas9 nucleases. Nat Biotechnol 31: 827–832.
30. Mali P, Aach J, Stranges PB, Esvelt KM, Moosburner M, et al. (2013) CAS9 transcriptional activators for target specificity screening and paired nickases for cooperative genome engineering. Nat Biotechnol 31: 833–838.
31. Pattanayak V, Lin S, Guilinger JP, Ma E, Doudna JA, et al. (2013) High-throughput profiling of off-target DNA cleavage reveals RNA-programmed Cas9 nuclease specificity. Nat Biotechnol 31: 839–843.
32. Ran FA, Hsu PD, Lin CY, Gootenberg JS, Konermann S, et al. (2013) Double nicking by RNA-guided CRISPR Cas9 for enhanced genome editing specificity. Cell 154: 1380–1389.
33. Iwamoto M, Bjorklund T, Lundberg C, Kirik D, Wandless TJ (2010) A general chemical method to regulate protein stability in the mammalian central nervous system. Chem Biol 17: 981–988.
34. Miyazaki Y, Imoto H, Chen LC, Wandless TJ (2012) Destabilizing domains derived from the human estrogen receptor. J Am Chem Soc 134: 3942–3945.
35. Nishimura K, Fukagawa T, Takisawa H, Kakimoto T, Kanemaki M (2009) An auxin-based degron system for the rapid depletion of proteins in nonplant cells. Nat Methods 6: 917–922.

Figure S1. Position of Cas9 guide RNA sequence and genotyping primers in the human genomic sequence.

The human genomic sequence flanking TCOF1 exon 1 is shown.

Exon 1
TCOF1 start codon
Genotyping primers
Guide RNA sequence (inserted into pX330)

…CCCTCATTTGTTCCCTCTTCCCCACCTCACCCCACCCCACCTGGACAGCCCAGCAGCG
CAGACTAGGGGTTCTGGGTTTAGGGTTCCCAGGCAATAGCAGGGTGTTTTCTCATGCCT
AGACTCATGCAGTGCCCTCTGCCAGTCCTCTCCTTTGCACCCAGCAATTTCGGGTGTCT
TTATGCCTCAGCTTAGATATCTCTCTGGGGTTCGGTGCTCCTCCTTGGGGCGCCCATAG
GCTGCATCTGTCCCTGACAAGGCACACAAGATATTGAACTATAGTTGCTTGGTTACGGA
CAGTCGTCTCTGTGAGCTTTGAGGGCAACTGCCATGTATTATGCATCTTTTGAATCCCC
CTAGCCTAGCCGGGTGCTAGCCCAAGTTAGGTGCTTATTACAGATTTGTTCAGTTAGCG
AATGAATCAATGAATAAACTGGCAATTCGTGTCTGGTTCATGGGCACCAAAAACCGTGC
GAAATGGATAAATGAGCAGGTAATGGCAGTACAAAGTTCGGATCTAGAGAAAGATCCAG
ATTAGGGAGTTCAGAGATGAGTAAAACGCAGACCCAGCCATCAGAGAATTAACAAGGAA
GATAAATCTCTTCAAGAAGCCAGCCGGAAGGATTAAAAGAGAGTCGTCCAAGTCCCGGC
CGGCCCCGGGGGCGGGTCCCTGTCTAGCCCCGCATGCTCCGCGCCAATGGGCGGTATTG
TTGATCACGAGTCTCCGCCCCCTTCGCCTTGAGGGGCGGGGCCGGCCACTCCCGGAGAG
GGGACTACGTTTCCCGGCGCGCCGCGCGGCCGGAGC**GAAAGAGGAGCCGGAAGTGGG**
GCGCGCGAGGTCTAAGGGCGCGAGGGAAGTGGCGGGCGGGGACTAAGGCGGG
GCGTGCAGGTAGCCGGCCGGCCGGGGGTCGCGGGTATGGCCGAGGCCAGGAA
GCGGCGGGAGCTACTTCCCCTGATCTACCACCATCTGCTGCGGGCTGGCTAT
GTGCGTGCGGCGCGGGAAGTGAAGGAGCAGAGCGGCCAGGTAAGCGTTCGTGGG
CCGTGTGCGAGGGCCGCGTGCAAGATGTGGAGATCAGCGGCCCGCGGCCCGCGCCCCGT
CCCCAGGCGACCCGGCAGGCGCCCGGAGCCGGGTCCCGCAGTGCTCGACGGCGCGGCCA
GGGGTACCGGAGGAGCCGCAATCTCTGCCTTCCCACTGCGACTTCAGTTCCCCTGGGCC
TCACTTTCCTCATCCGGGCAGTGGGTTGGGCCAGAAAGTGTGCTCGCAGGGGCCGAACT
TTGTAATTCCCGCTTCCCTTACCTCCACGCCCTTCCTGGTAGCGGGTATTTTAAGTTTC
CTAAGTCTCCCGCCACGTGGCTAGGCTCTGCGCGGCCCCCCCTGGGGCAAGGAGGTTGC
TGCGAGTCTCGGGGGTGGATTGCGACCAGCCCCTCGGGGGAGCGCCTGGAAAAGGGACC
CTACAGCCTCTTAGTTGAGCTGGAACTCAGGCCTTTAGCGATTGTCTGTACTGAGACGG
TCAGCTTTGGTACTCGAACTCGTGGTACAGTCATTTCTTACTTGATTAATTCAACTGTT
AATCCGGTACTCAGGGTGCTTCCTGGTGTTCGAATGGTGAGCACCATCTCTCAGCCCTC
CTGGAGCTTACACTCTAGTAAGGTAGACAAATCAAAGAATCACAAAAGTGACTATATGC
TTAGCACCGCAATAAGTGTTAAGAATGAGAGGGATGGGCCGGGCACGGTAGCTCACGCC
TGTAATCCCAGCACTTAGGGAGGCCGAGACTAGCGGATCACCTGAGGTCAGAAGTTCGA
GACCAGCCTGGCCAACATGGTGAAACACCGTTTCTACTAAAAATACAAAAATTAGCTGG
GCATGTTGGCGCACGCCTGTAATCCTGGCTACTCATGTGGCTGAGGCACAAGAATTGCT
TGAACCCGGGAGGCAGAGGTTGCAATGAGTCAAGATCGTGCCACTGCACTCCAGCCTGG
GCGATAAAGCGAGACTCTGCCTCAAAAAAAAAAGAGAGATGGATGGCAGATTGCCCTGG
TCAGGAATAGCTGAGGTGTAAATGCCTTGTGGTGGGAGGGAACTTGTGTACACACTGGC
CTGGAGAAAGTCCACTCTCTTGAGCCCAGGAATTTGAGGATACAGTATGAGCCATGATC
ATGCCACTGCACTCCAGCCTGGGCAACAGAGCAAGACACTGTCTCAAAAAAAAATTTTT
TTTAAGTCCATAGCAGGCCAGGTACGGTAGCTCACGCCTGTAATCCCAGCACTTTGGGA
GGCCGAGGCAGGCGGATCACTTGAGGCCAG…

Figure S2. Annotated sequence of knock-in donor constructs.

The following donor insert was inserted into the PCR2.1 vector (Invitrogen).

BamHI and EcoRI restriction sites
Homology arms (all underlined sequence, regardless of color)
TCOF1 exon 1
Puromycin resistance (alternative Blast^{R} is below)
GSG linker
P2A ribosomal skipping sequence
Destabilization domain
3XGGGGS linker
TCOF1 start codon

GGATCC
CAGCAATTTCGGGTGTCTTTATGCCTCAGCTTAGATATCTCTCTGGGGTTCGGTGCTCC
TCCTTGGGGCGCCCATAGGCTGCATCTGTCCCTGACAAGGCACACAAGATATTGAACTA
TAGTTGCTTGGTTACGGACAGTCGTCTCTGTGAGCTTTGAGGGCAACTGCCATGTATTA
TGCATCTTTTGAATCCCCCTAGCCTAGCCGGGTGCTAGCCCAAGTTAGGTGCTTATTAC
AGATTTGTTCAGTTAGCGAATGAATCAATGAATAAACTGGCAATTCGTGTCTGGTTCAT
GGGCACCAAAAACCGTGCGAAATGGATAAATGAGCAGGTAATGGCAGTACAAAGTTCGG
ATCTAGAGAAAGATCCAGATTAGGGAGTTCAGAGATGAGTAAAACGCAGACCCAGCCAT
CAGAGAATTAACAAGGAAGATAAATCTCTTCAAGAAGCCAGCCGGAAGGATTAAAAGAG
AGTCGTCCAAGTCCCGGCCGGCCCCGGGGGCGGGTCCCTGTCTAGCCCCGCATGCTCCG
CGCCAATGGGCGGTATTGTTGATCACGAGTCTCCGCCCCCTTCGCCTTGAGGGGCGGGG
CCGGCCACTCCCGGAGAGGGGACTACGTTTCCCGGCGCGCCGCGCGGCCGGAGC**GAAAG**
AGGAGCCGGAAGTGGGGCGCGCGAGGTCTAAGGGCGCGAGGGAAGTGGCGGGCGGGGAC
TAAGGCGGGGCGTGCAGGTAGCCGGCCGGCCGGGGGTCGCGGGT
ATGACCGAGTACAAGCCCACGGTGCGCCTCGCCACCCGCGACGACGTCCCCAGGGCCGT
ACGCACCCTCGCCGCCGCGTTCGCCGACTACCCCGCCACGCGCCACACCGTCGATCCGG
ACCGCCACATCGAGCGGGTCACCGAGCTGCAAGAACTCTTCCTCACGCGCGTCGGGCTC
GACATCGGCAAGGTGTGGGTCGCGGACGACGGCGCCGCGGTGGCGGTCTGGACCACGCC
GGAGAGCGTCGAAGCGGGGGCGGTGTTCGCCGAGATCGGCCCGCGCATGGCCGAGTTGA
GCGGTTCCCGGCTGGCCGCGCAGCAACAGATGGAAGGCCTCCTGGCGCCGCACCGGCCC
AAGGAGCCCGCGTGGTTCCTGGCCACCGTCGGCGTCTCGCCCGACCACCAGGGCAAGGG
TCTGGGCAGCGCCGTCGTGCTCCCCGGAGTGGAGGCGGCCGAGCGCGCCGGGGTGCCCG
CCTTCCTGGAGACCTCCGCGCCCCGCAACCTCCCCTTCTACGAGCGGCTCGGCTTCACC
GTCACCGCCGACGTCGAGGTGCCCGAAGGACCGCGCACCTGGTGCATGACCCGCAAGCC
CGGTGCC
GGATCCGGA
GCCACGAACTTCTCTCTGTTAAAGCAAGCAGGAGACGTGGAAGAAAACCCCGGTCCC
ATGGGAGTGCAGGTGGAAACCATCTCCCCAGGAGACGGGCGCACCTTCCCCAAGCGCGG
CCAGACCTGTGTGGTGCACTACACCGGGATGCTTGAAGATGGAAAGAAAGTCGATTCCT
CCCGGGACAGAAACAAGCCCTTTAAGTTTATGCTAGGCAAGCAGGAGGTGATCCGAGGC
TGGGAAGAAGGGGTTGCCCAGATGAGTGTGGGTCAGAGAGCCAAACTGACTATATCTCC
AGATTATGCCTATGGTGCCACTGGGCACCCAGGCATCATCCCACCACATGCCACTCTCG
TCTTCGATGTGGAGCTTCTAAAACCGGAA

GGT GGA GGT GGA TCT GGT GGA GGT GGA TCT GGT GGC GGC GGT TCA
ATGGCCGAGGCCAGGAAGCGGCGGGAGCTACTTCCCCTGATCTACCACCATCTGCTGCG
GGCTGGCTATGTGCGTGCGGCGCGGGAAGTGAAGGAGCAGAGCGGCCAGGTAAGCGTTC
GTGGGCCGTGTGCGAGGGCCGCGTGCAAGATGTGGAGATCAGCGGCCCGCGGCCCGCGC
CCCGTCCCCAGGCGACCCGGCAGGCGCCCGGAGCCGGGTCCCGCAGTGCTCGACGGCGC
GGCCAGGGGTACCGGAGGAGCCGCAATCTCTGCCTTCCCACTGCGACTTCAGTTCCCCT
GGGCCTCACTTTCCTCATCCGGGCAGTGGGTTGGGCCAGAAAGTGTGCTCGCAGGGGCC
GAACTTTGTAATTCCCGCTTCCCTTACCTCCACGCCCTTCCTGGTAGCGGGTATTTTAA
GTTTCCTAAGTCTCCCGCCACGTGGCTAGGCTCTGCGCGGCCCCCCCTGGGGCAAGGAG
GTTGCTGCGAGTCTCGGGGGTGGATTGCGACCAGCCCCTCGGGGGAGCGCCTGGAAAAG
GGACCCTACAGCCTCTTAGTTGAGCTGGAACTCAGGCCTTTAGCGATTGTCTGTACTGA
GACGGTCAGCTTTGGTACTCGAACTCGTGGTACAGTCATTTCTTACTTGATTAATTCAA
CTGTTAATCCGGTACTCAGGGTGCTTCCTGGTGTTCGAATGGTGAGCACCATCTCTCAG
CCCTCCTGGAGCTTACACTCTAGTAAGGTAGACAAATCAAAGAATCACAAAAGTGACTA
TATGCTTAGCACCGCAATAAGGGCCGGCCAAAAGGGC
GAATTC

Blasticidin resistance:
ATGGCCAAGCCTTTGTCTCAAGAAGAATCCACCCTCATTGAAAGAGCAACGGCTACAAT
CAACAGCATCCCCATCTCTGAAGACTACAGCGTCGCCAGCGCAGCTCTCTCTAGCGACG
GCCGCATCTTCACTGGTGTCAATGTATATCATTTTACTGGGGGACCTTGTGCAGAACTC
GTGGTGCTGGGCACTGCTGCTGCTGCGGCAGCTGGCAACCTGACTTGTATCGTCGCGAT
CGGAAATGAGAACAGGGGCATCTTGAGCCCCTGCGGACGGTGCCGACAGGTGCTTCTCG
ATCTGCATCCTGGGATCAAAGCCATAGTGAAGGACAGTGATGGACAGCCGACGGCAGTT
GGGATTCGTGAATTGCTGCCCTCTGGTTATGTGTGGGAGGGC

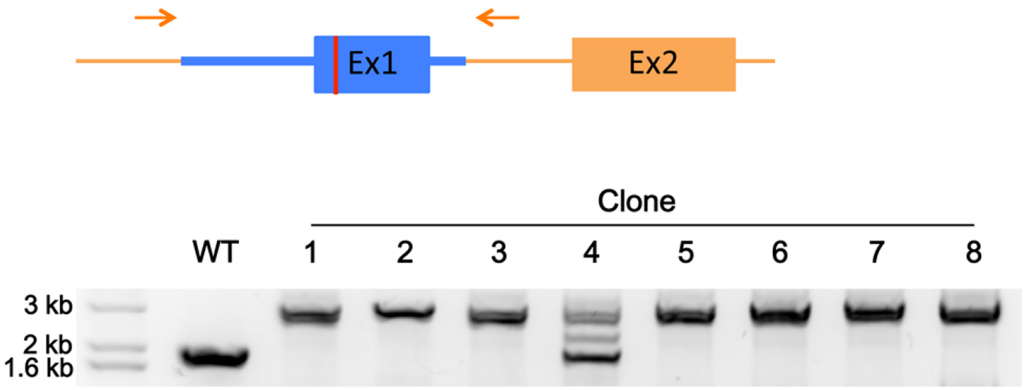

Figure S3. Homologous recombination in both 5' and 3' homology arms. Genotyping PCR was performed with the same forward primer shown in Figure 1B, but with a reverse primer beyond the 3' homology arm.

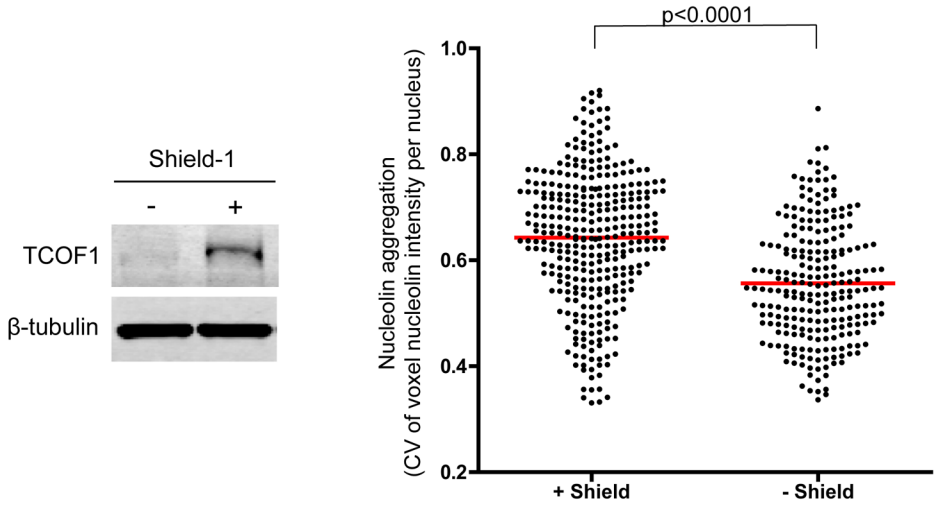

Figure S4. Confirmation of dispersal of nucleolin with an independent clone. Destabilization of DD-TCOF1 in clone 2 was confirmed by Western analysis of cells incubated in either ethanol vehicle control or 1 μM Shield-1. The analysis of nucleolin dispersal was performed as described for Figure 4. CV, coefficient of variation (stdev/mean); $p<0.0001$, 2-tailed Student's t-test, n = 338 for +Shield and n = 243 for –Shield.

REFERENCES

1. Banaszynski LA, Chen LC, Maynard-Smith LA, Ooi AG, Wandless TJ (2006) A rapid, reversible, and tunable method to regulate protein function in living cells using synthetic small molecules. Cell 126: 995–1004.
2. Cong L, Ran FA, Cox D, Lin S, Barretto R, et al. (2013) Multiplex genome engineering using CRISPR/Cas systems. Science 339: 819–823.
3. Mali P, Yang L, Esvelt KM, Aach J, Guell M, et al. (2013) RNA-guided human genome engineering via Cas9. Science 339: 823–826.
4. Armstrong CM, Goldberg DE (2007) An FKBP destabilization domain modulates protein levels in Plasmodium falciparum. Nat Methods 4: 1007–1009.
5. Herm-Gotz A, Agop-Nersesian C, Munter S, Grimley JS, Wandless TJ, et al. (2007) Rapid control of protein level in the apicomplexan Toxoplasma gondii. Nat Methods 4: 1003–1005.
6. Child MA, Hall CI, Beck JR, Ofori LO, Albrow VE, et al. (2013) Small-molecule inhibition of a depalmitoylase enhances Toxoplasma host-cell invasion. Nat Chem Biol 9: 651–656.
7. de Azevedo MF, Gilson PR, Gabriel HB, Simoes RF, Angrisano F, et al. (2012) Systematic analysis of FKBP inducible degradation domain tagging strategies for the human malaria parasite Plasmodium falciparum. PLoS One 7: e40981.
8. Dixon J, Jones NC, Sandell LL, Jayasinghe SM, Crane J, et al. (2006) Tcof1/Treacle is required for neural crest cell formation and proliferation deficiencies that cause craniofacial abnormalities. Proc Natl Acad Sci U S A 103: 13403–13408.
9. Sakai D, Dixon J, Dixon MJ, Trainor PA (2012) Mammalian neurogenesis requires Treacle-Plk1 for precise control of spindle orientation, mitotic progression, and maintenance of neural progenitor cells. PLoS Genet 8: e1002566.
10. Valdez BC, Henning D, So RB, Dixon J, Dixon MJ (2004) The Treacher Collins syndrome (TCOF1) gene product is involved in ribosomal DNA gene transcription by interacting with upstream binding factor. Proc Natl Acad Sci U S A 101: 10709–10714.
11. Lin CI, Yeh NH (2009) Treacle recruits RNA polymerase I complex to the nucleolus that is independent of UBF. Biochem Biophys Res Commun 386: 396–401.
12. Gonzales B, Henning D, So RB, Dixon J, Dixon MJ, et al. (2005) The Treacher Collins syndrome (TCOF1) gene product is involved in pre-rRNA methylation. Hum Mol Genet 14: 2035–2043.
13. Bowman M, Oldridge M, Archer C, O'Rourke A, McParland J, et al. (2012) Gross deletions in TCOF1 are a cause of Treacher-Collins-Franceschetti syndrome. Eur J Hum Genet 20: 769–777.
14. Dixon MJ (1996) Treacher Collins syndrome. Hum Mol Genet 5 Spec No: 1391–1396.

15. Sakai D, Trainor PA (2009) Treacher Collins syndrome: unmasking the role of Tcof1/treacle. Int J Biochem Cell Biol 41: 1229–1232.

16. Trainor PA, Dixon J, Dixon MJ (2009) Treacher Collins syndrome: etiology, pathogenesis and prevention. Eur J Hum Genet 17: 275–283.

17. Dixon J, Brakebusch C, Fassler R, Dixon MJ (2000) Increased levels of apoptosis in the prefusion neural folds underlie the craniofacial disorder, Treacher Collins syndrome. Hum Mol Genet 9: 1473–1480.

18. Shalem O, Sanjana NE, Hartenian E, Shi X, Scott DA, et al. (2014) Genome-scale CRISPR-Cas9 knockout screening in human cells. Science 343: 84–87.

19. Wang T, Wei JJ, Sabatini DM, Lander ES (2014) Genetic screens in human cells using the CRISPR-Cas9 system. Science 343: 80–84.

20. Ran FA, Hsu PD, Wright J, Agarwala V, Scott DA, et al. (2013) Genome engineering using the CRISPR-Cas9 system. Nat Protoc 8: 2281–2308.

21. Egeler EL, Urner LM, Rakhit R, Liu CW, Wandless TJ (2011) Ligand-switchable substrates for a ubiquitin-proteasome system. J Biol Chem 286: 31328–31336.

22. Kim JH, Lee SR, Li LH, Park HJ, Park JH, et al. (2011) High cleavage efficiency of a 2A peptide derived from porcine teschovirus-1 in human cell lines, zebrafish and mice. PLoS One 6: e18556.

23. Holst J, Vignali KM, Burton AR, Vignali DA (2006) Rapid analysis of T-cell selection in vivo using T cell-receptor retrogenic mice. Nat Methods 3: 191–197.

24. Szymczak AL, Workman CJ, Wang Y, Vignali KM, Dilioglou S, et al. (2004) Correction of multi-gene deficiency in vivo using a single 'self-cleaving' 2A peptide-based retroviral vector. Nat Biotechnol 22: 589–594.

25. Sellmyer MA, Chen LC, Egeler EL, Rakhit R, Wandless TJ (2012) Intracellular context affects levels of a chemically dependent destabilizing domain. PLoS One 7: e43297.

26. Cho SW, Kim S, Kim Y, Kweon J, Kim HS, et al. (2014) Analysis of off-target effects of CRISPR/Cas-derived RNA-guided endonucleases and nickases. Genome Res 24: 132–141. d

27. Cradick TJ, Fine EJ, Antico CJ, Bao G (2013) CRISPR/Cas9 systems targeting beta-globin and CCR5 genes have substantial off-target activity. Nucleic Acids Res 41: 9584–9592.

28. Fu Y, Foden JA, Khayter C, Maeder ML, Reyon D, et al. (2013) High-frequency off-target mutagenesis induced by CRISPR-Cas nucleases in human cells. Nat Biotechnol 31: 822–826.

29. Hsu PD, Scott DA, Weinstein JA, Ran FA, Konermann S, et al. (2013) DNA targeting specificity of RNA-guided Cas9 nucleases. Nat Biotechnol 31: 827–832.

30. Mali P, Aach J, Stranges PB, Esvelt KM, Moosburner M, et al. (2013) CAS9 transcriptional activators for target specificity screening and paired nickases for cooperative genome engineering. Nat Biotechnol 31: 833–838.

31. Pattanayak V, Lin S, Guilinger JP, Ma E, Doudna JA, et al. (2013) High-throughput profiling of off-target DNA cleavage reveals RNA-programmed Cas9 nuclease specificity. Nat Biotechnol 31: 839–843.

32. Ran FA, Hsu PD, Lin CY, Gootenberg JS, Konermann S, et al. (2013) Double nicking by RNA-guided CRISPR Cas9 for enhanced genome editing specificity. Cell 154: 1380–1389.

33. Iwamoto M, Bjorklund T, Lundberg C, Kirik D, Wandless TJ (2010) A general chemical method to regulate protein stability in the mammalian central nervous system. Chem Biol 17: 981–988.

34. Miyazaki Y, Imoto H, Chen LC, Wandless TJ (2012) Destabilizing domains derived from the human estrogen receptor. J Am Chem Soc 134: 3942–3945.

35. Nishimura K, Fukagawa T, Takisawa H, Kakimoto T, Kanemaki M (2009) An auxin-based degron system for the rapid depletion of proteins in nonplant cells. Nat Methods 6: 917–922.

CHAPTER 5

CONTRIBUTION OF OTHER VIRAL PROTEINS TO MATRIX-DRIVEN VIRAL RELEASE

CHAPTER 5.1

THE NIPAH VIRUS C PROTEIN RECRUITS TSG101 TO ENHANCE VIRAL RELEASE IN AN ESCRT-DEPENDENT MANNER

INTRODUCTION

As discussed in Chapters 1.2 and 3.3, while some paramyxovirus matrix proteins require the co-expression of other viral components for efficient budding, the efficiency of NiV-M budding is not enhanced by co-expression of the nucleocapsid, fusion or attachment proteins.[1] The potential for other viral components to contribute to the efficiency of NiV-M budding has not been examined, however. For Sendai virus (SeV), the accessory C protein was suggested to enhance SeV-M-driven virus-like-particle (VLP) budding through recruitment of the cellular ESCRT pathway (introduced in Chapter 1.2) component Alix[2,3]; in contrast, another study determined that knockdown of C protein expression or inhibition of ESCRT did not affect live SeV budding,[4] thus leaving the significance of the SeV-C for the budding process unclear.

To determine if other virus proteins affected the efficiency of M-driven release, we co-expressed all other virus proteins individually with NiV-M. Reminiscent of the previous findings for SeV, we found that NiV-C enhanced NiV-M budding. Upon further investigation, we discovered that NiV-C interacted with the ESCRT component Tsg101, and that inhibition of ESCRT abrogated NiV-C enhancement in the VLP budding assay. Using a recombinant Nipah virus expressing secreted *Gaussia* luciferase to control for virus protein production, we found that inhibition of ESCRT strongly inhibited live NiV budding without affecting protein production. As NiV-M-alone budding is ESCRT-insensitive, these findings underscore the importance of evaluating the role of cellular pathways in the context of multiple virus components or the full virus.

MATERIALS AND METHODS

For the virus-like particle budding assay, multiple sequence alignment, protein homology searching and structure modelling, immunoprecipitations, and Western immunoblotting, refer to Chapter 3.1. For creation of doxycyline-inducible HEK 293 cell lines, refer to Chapter 4.1. For rescue of live NiV via reverse genetics, refer to Chapter 2.2.

Plasmids and antibodies

Plasmids. The Vps4A and Vps4B ORFs were a kind gift of Jiro Yasuda. Wild-type and dominant-negative Vps4 were N-terminally HA-tagged and inserted into pcDNA3 (Invitrogen). DsRed-CHMP6 was the kind gift of Wesley Sundquist. The human Vps28 C-terminal domain was synthesized by GeneArt (Invitrogen).

Antibodies. Endogenous Tsg101 was detected with mouse monoclonal clone 4A10 (GTX70255, GeneTex). DsRed-CHMP6 was detected with rabbit polyclonal anti-DsRed (632496, Clontech).

Live virus infection of Vps4-inducible cells

8 x 10e5 wild-type or dominant-negative Vps4A-inducible 293 cells were plated in poly-L-lysine-coated 12-well dishes. The following day, cells were infected with rNiV-Gluc (see Chapters 2.4 and 2.5) or rSeV-Gluc at a multiplicity of infection of 2. After 1 hr at 37C, cells were washed 4 times in media, with the last wash saved for determination of residual background from the infecting inoculum. Supernatants were collected and replenished at 12 hours post-infection, and finally at 24 hours post-infection. Gluc-catalyzed luminescence and viral titer was determined as previously described (Chapters 2.4 and 2.5).

RESULTS

NiV-C enhances NiV-M virus-like particle budding

We transfected HEK 293T cells with either NiV-M alone or NiV-M with each of the other NiV proteins. Only NiV-C clearly enhanced NiV-M virus-like particle budding (Figure 5-1, panel B). Although NiV-C cell lysate expression was not visible on the Western blot due to a low level of expression, a re-run of the cell lysates with more sample confirmed NiV-C expression (Figure 5-1, panel C).

NiV-C enhancement of NiV-M budding is ESCRT-dependent

To gain insight into the potential mechanism of the budding enhancement, we evaluated the sequence of NiV-C in the homology search and modelling program Phyre2. We were surprised

to find that the middle half of the NiV-C protein aligns with the C-terminal domain of *X. laevis* Vps28 (Figure 5-2), an essential component of the ESCRT pathway, which is critical for catalyzing the membrane fission event during virion formation for many enveloped viruses, including HIV-1.[5,6] We therefore considered whether NiV-C might mimic an ESCRT-related function of Vps28 to enhance M budding in a ESCRT-dependent manner. Although the budding of Nipah virus was previously considered to be independent of the ESCRT pathway, this result was based on inhibition of ESCRT in a NiV-M-alone budding assay that lacked co-expression of other viral components.[7] The Vps4 ATPase is the molecular engine of the ESCRT pathway, catalyzing the constriction of the membrane bud neck,[8,9] and a Vps4 dominant negative that cannot bind or hydrolyze ATP strongly inhibits this process. We found that co-transfection of dominant-negative Vps4 inhibited the C enhancement of M budding, while wild-type Vps4 did not affect the enhancement (Figure 5-3), suggesting that the enhancement is dependent on ESCRT function.

NiV-C interacts with Tsg101 and NiV-M

ESCRT is composed of multiple subcomplexes (ESCRT-0, -I, -II, and -III), which recruit each other sequentially, leading to catalysis of membrane fission by ESCRT-III in conjunction with Vps4 ATPase activity.[8,9] ESCRT-0 and ESCRT-I both bind to membrane targets, particularly ubiquitinated membrane proteins that are then targeted for downregulation via internalization into multivesicular bodies and subsequent sequestration or lysosomal degradation.[10] Vps28 is a core component of ESCRT-I with Tsg101, Vps37, and Mvb12. The N-terminal domain (NTD) of Vps28 binds the C-terminal domain (CTD) of Tsg101, forming part of the core ESCRT-I complex, while the CTD of Vps28 appears to represent a conserved adaptor domain that can interact with downstream ESCRT-II or -III components (see the schematic in Figure 5-8, which illustrates these interactions).[11-14] In yeast, the Vps28 CTD interacts with both the downstream ESCRT-II component Vps36[15] and the ESCRT-III component Vps20.[16] In humans, the Vps28 (hVps28) CTD also binds EAP45[17] and likely also CHMP6,[16] the human ESCRT-II and -III

components homologous to yeast Vps36 and Vps20, respectively. However, the specific binding interface between the yeast and human homologs of Vps28 and their respective ESCRT-II and -III partners may differ slightly. Interestingly, a linear patch of 7 amino acids in the CTD of Vps28 that includes residues implicated in Vps28-Vps36 interactions is almost identical between yeast, *Xenopus* and human Vps28 and NiV-C, suggesting that NiV-C, as a potential viral Vps28 homolog, might also bind to EAP45, the human ESCRT-II homolog of yeast Vps36 (Fig. 5-2, green highlighted region in aligned sequence and threaded structure). This potential interaction between NiV-C and EAP45 remains to be tested. On the other hand, conserved residues in Vps28 CTD required for Vps20/CHMP6 (ESCRT-III component)-binding are not present in NiV-C (Figure 5-2, red highlight on the aligned sequence). Consistent with this insight from the sequence alignment, we did not detect CHMP6 co-immunoprecipitation with NiV-C (Figure 5-4).

Thus, if NiV-C were mimicking the function of Vps28, we wondered if NiV-C would similarly interact with Tsg101, which is often the target of virus recruitment and hijacking of the ESCRT machinery.[6] We found that NiV-C immunoprecipitates endogenous Tsg101 (Figure 5-5, panel A). NiV-C also co-immunoprecipitated with NiV-M (Figure 5-5, panel B), suggesting that NiV-C recruitment of Tsg101 to sites of NiV-M budding might thereby recruit the ESCRT pathway to aid the virus budding process.

To further define the interaction between Tsg101 and NiV-C, we made truncation mutants of both proteins. We hypothesized that NiV-C, like Vps28, would interact with the Tsg101 CTD (Figure 5-6, panel A). Indeed, truncation of the Tsg101 CTD led to loss of pulldown with NiV-C, indicating that the Tsg101 CTD was necessary for interaction with NiV-C (Figure 5-6, panel B). We then evaluated whether the Tsg101 CTD was not only necessary, but also sufficient, for this interaction. Due to its small size, we appended the Tsg101 CTD to the C-terminus of EGFP. This fusion protein pulled down with NiV-C, while EGFP alone did not, indicating that the Tsg101 CTD was both necessary and sufficient for the interaction with NiV-C.

Next, we sought to localize the Tsg101 interaction domain within NiV-C. We made a series of truncation mutants, each with one domain removed (NTD, middle domain "Mid", or CTD) to examine whether loss of a specific domain would result in loss of interaction with Tsg101 (Figure 5-7, panel A). While removal of the NiV-C CTD led to loss of Tsg101 interaction, removal of the NTD had no effect (Figure 5-7, panel B). The third mutant, representing removal of the middle domain, was poorly expressed, perhaps reflecting the minimal size of the expected protein product (< 90 a.a.). The results nevertheless implicated the potential role of the NiV-C CTD in mediating interaction with Tsg101. We therefore further examined whether the NiV-C CTD was sufficient for interacting with Tsg101. Due to the minimal size, we appended the NiV-C CTD to the C-terminus of EGFP via a GSG linker. This fusion protein co-immunoprecipitated Tsg101, suggesting that the NiV-C CTD was both necessary and sufficient for interaction with Tsg101 (Figure 5-7, panel C). In summary, NiV-C interacted with Tsg101 in a manner analogous to Vps28, which is summarized in the schematic shown in Figure 5-8. We propose that NiV-C may act as a viral Vps28 mimic that serves to recruit critical ESCRT components to areas of NiV-M assembly.

A chimeric NiV-C substituted with the Vps28 C-terminal domain enhances NiV-M release

The middle domain of NiV-C aligns with the Vps28 CTD, which serves as an adaptor that links ESCRT-I components such as Tsg101 to downstream ESCRT-II and ESCRT-III components (Figure 5-8). Our model predicts that if NiV-C were a viral Vps28 mimic, then the Vps28 CTD may substitute for the function of the NiV-C middle domain in the enhancement of NiV-M budding. Indeed, when we substituted the middle domain of NiV-C with the well-defined hVps28 CTD in its entirety, we found that this C-Vps28CTD-Full chimera clearly enhanced NiV-M budding, albeit not as well as wild-type NiV-C (Figure 5-9). When a truncated hVps28 CTD (lacking the C-terminal 14 a.a. and ending in "MLFD" in hVps28, see alignment in Figure 5-2) was used, no enhancement of NiV-M budding was seen. Although the full Vps28 CTD extended

14 a.a. beyond the precisely aligned sequence with the NiV-C middle domain, it appears that the full Vps28 CTD must be used in order to supply its complementary function in a heterologous context. We acknowledge it is also possible that for a structural or other reason, the full domain does not interfere with the budding enhancement function provided by the N- and C-terminal portions of the NiV-C protein, whereas the truncated aligned portion does interfere; this concern will only be resolved with a deeper understanding of the specific function or critical interaction of the NiV-C middle domain that is substituted by the Vps28 CTD, which awaits further characterization. Nevertheless, our findings support our model of NiV-C serving as a Vps28 mimic to recruit the ESCRT pathway for efficient budding of NiV-M.

The budding of Nipah virus is ESCRT-dependent

With these promising results in the NiV-M surrogate budding assay, we sought to determine whether the budding of *replication-competent* NiV was ESCRT-dependent. In lieu of transfecting cells with wild-type or dominant-negative Vps4 constructs before infection with live NiV, which would lead to uneven and incomplete Vps4 expression as well as potentially affecting the efficiency of NiV infection itself, we developed HEK 293 cells with doxycyline-inducible expression of wild-type or dominant-negative Vps4 (Figure 5-10). We first confirmed that the cell lines recapitulated our previous results with transfected NiV-M and NiV-C. Induction of dominant-negative Vps4 abrogated the enhancement, while induction of wild-type Vps4 had no effect (Figure 5-11). In addition, to ensure that any differences in released virus titer were not due to changes in virus protein production, we used a recombinant NiV that expresses secreted *Gaussia* luciferase (rNiV-Gluc, used previously in Chapters 2.3 and 2.4), which can be measured as an indicator of protein production. Wild-type or dominant-negative Vps4-inducible cells were infected with rNiV-Gluc at BSL4 using a high multiplicity of infection to ensure infection of all cells, then incubated with or without doxycyline. While induction of wild-type Vps4 did not affect infectious virus production, induction of the dominant negative strongly inhibited release of infectious virus by several logs (Figure 5-12, panel A). There was no significant difference in

Gluc production, indicating that the defect in viral release did not lie in lower protein production in the presence of the Vps4 dominant negative (Figure 5-12, panel B).

C-deficient NiV may reveal a replication defect specifically at the budding step

Several research groups have generated C-deficient Nipah viruses, all finding that C-deficient NiV is viable but significantly attenuated both *in vitro* and *in vivo*.[18-21] Although anti-innate immune function has been ascribed to NiV-C, such function would not explain why C-deficient virus is attenuated even in growth on Vero cells,[18,19,21] which lack interferon production and therefore cannot amplify an immune response.[22] To establish a defect specifically at the budding step, we have generated C-deficient NiV in the rNiV-Gluc backbone (Figure 5-13). Preliminary observations upon mutant virus expansion in cell culture indicate a significantly slower rate of virus spread, consistent with the previous reports of attenuated growth. In future experiments, infection of Vero cells with C-deficient virus should result in significantly less virus production than wild-type NiV, both determined by titer as well as Western analysis, and controls for protein production as well as immunofluorescence of matrix at the cell surface would confirm a budding-specific defect. Further, C-deficient virus should be relatively insensitive to dominant-negative Vps4 inhibition, in contrast to our findings with wild-type NiV.

Sendai virus may be moderately ESCRT-dependent

As mentioned in the Introduction, conflicting reports left the possible ESCRT-dependence of SeV budding unclear. The potentially analogous situation of the C protein enhancing virus budding in an ESCRT-dependent manner led us to examine the ESCRT-dependence of SeV budding under our experimental conditions. We infected the Vps4-inducible cell lines with Gluc-expressing recombinant SeV in a similar manner as with NiV. We found a potential moderate ESCRT-dependence of SeV budding (Figure 5-14), although repetition will be required to determine if the 2-to-3-fold decrease in titers upon dominant-negative Vps4 induction is consistent.

DISCUSSION

Of the paramyxoviruses, it was previously known that measles virus is ESCRT-independent,[23] while Sendai virus, as mentioned, had conflicting reports. Nipah virus was suggested to be ESCRT-independent,[7] and mumps virus ESCRT-dependent,[24] although these findings were based on transfection of individual viral proteins only, and not on live virus replication. Here, we demonstrate that the budding of NiV is ESCRT-dependent, likely through the recruitment of the ESCRT component Tsg101 to sites of budding by the NiV-C protein. In addition to the results presented here, we intend to i) confirm that the reduced titer of rNiV-Gluc upon induction of dominant-negative Vps4 is due to reduced budding, not production of non-infectious particles, by Western blotting for matrix in virus pellets vs. cell lysates; ii) visualize cell surface NiV-M by immunofluorescence to confirm that the defect is not due to impaired trafficking to the membrane; iii) characterize the C-deficient NiV to localize the attenuating defect specifically to the budding step; and iv) further define the role of the middle domain of NiV-C that aligns with the Vps28 CTD.

The Vps28 CTD plays an adaptor function, linking ESCRT-I to downstream ESCRT complexes, although the details of these interactions may vary from yeast to mammals. Although we did not detect co-immunoprecipitation of ESCRT-III component CHMP6 with NiV-C, a potential interaction with ESCRT-II component EAP45 should be investigated. Barring this possibility, an unbiased approach such as immunoprecipitation and proteomic identification may be warranted, considering that is has been suggested that the structure of the Vps28 CTD lends itself to multiple interactions.[16]

The ability of the NiV-C-Vps28 chimera to enhance NiV-M budding suggests that the CTD of human Vps28 can transfer a necessary function to NiV-C, although this function may even be structural in nature. It would be informative to examine whether a human Vps28 CTD mutated in conserved residues, or the homologous domain from yeast, could also substitute for the NiV-C middle domain. Mutagenesis of NiV-C itself could reveal the role of residues

conserved between NiV-C and the Vps28 CTD domains. We note the presence of a 7-a.a. stretch in the NiV-C aligned domain that is uniquely nearly identical to the corresponding sequence in hVps28, except for a highly similar serine vs. threonine difference at one residue. Remarkably, this segment, highlighted in green in both the sequence alignment as well as on the threaded structure in Figure 5-2, contains residues that are critical for the Vps28-Vps36 interaction in yeast.[15] This characterized interface is disrupted in metazoans, however, by the presence of charged side chains elsewhere in the overall interface (Figure 5-2, blue asterisks and blue highlight – one of the two is charged in NiV-C). Mutagenesis of the conserved segment in NiV-C may therefore reveal the basis for the continued interaction between metazoan Vps28 and the corresponding Vps36 homolog.

Finally, the ESCRT recruitment of NiV-C may explain the generally weak innate immune antagonism previously ascribed to the NiV-C protein. As the cellular pathway required for all intracellular membrane fission events in which cytoplasmic factors have access to the inside of the constricting bud neck, ESCRT is necessary for cytokinesis as well as multivesicular body formation, which is important for downregulation of transmembrane proteins via internalization into endosomes and subsequent degradation. Inhibition of ESCRT therefore inhibits these essential cell processes, leading to pleiotropic effects, including induction of autophagy and dysregulation of signaling pathways.[25-27] Even RNAi activity is affected by ESCRT inhibition, as RISC complexes (RNA-induced silencing complexes) are assembled on multivesicular bodies.[28] Since recruitment of Tsg101 and/or other ESCRT components would sequester them from their usual functions in ESCRT, NiV-C expression may thereby indirectly affect a number of cellular processes, including innate immune responses.

FIGURES

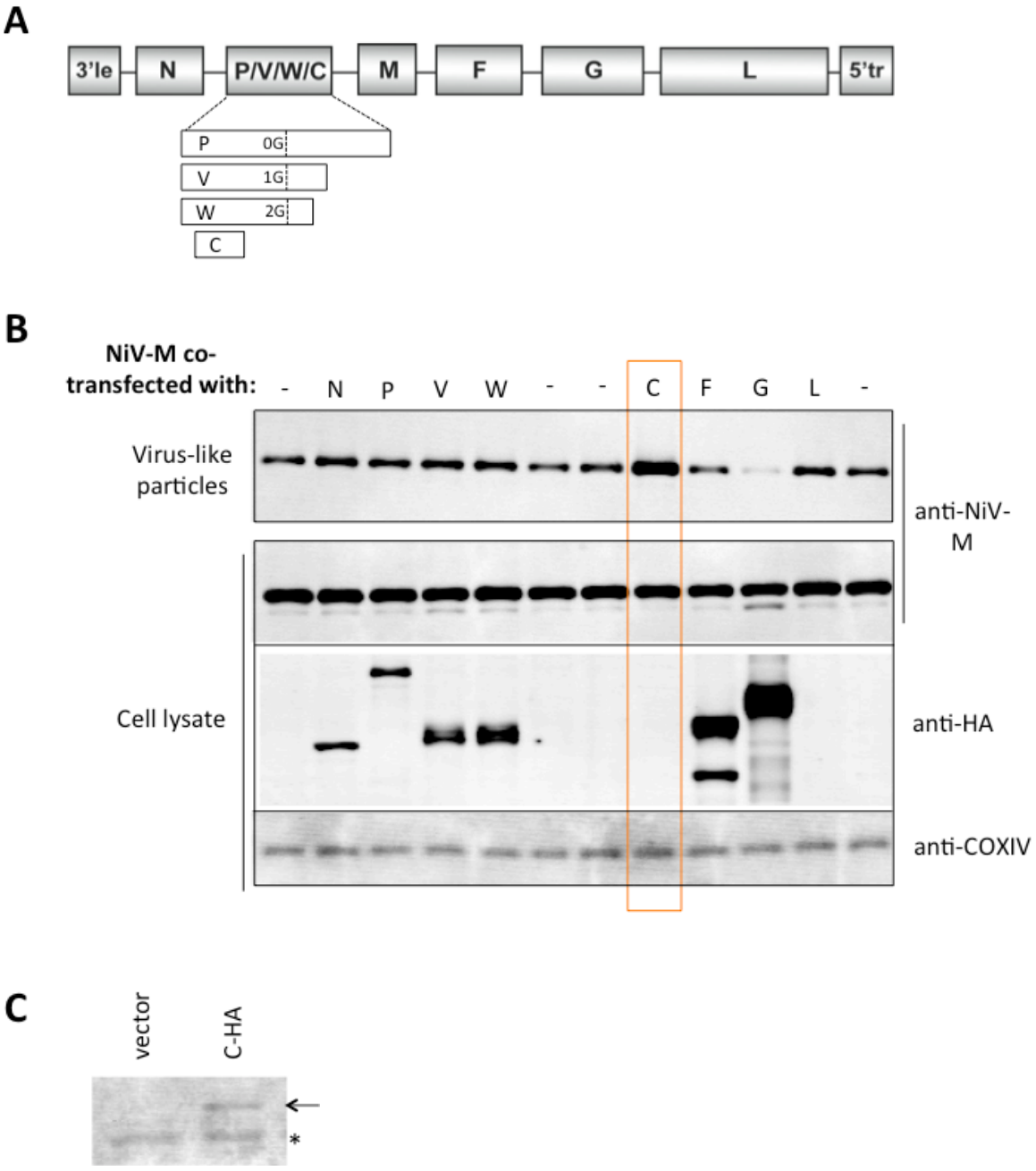

Figure 5-1. NiV-C co-expression enhances NiV-M budding. (A) All the NiV proteins are shown, including the alternate P gene products: V and W result from insertion of 1 or 2 Gs at a RNA-editing site, and C is translated from an alternate start codon in a frame-shifted ORF. **(B)** HA-tagged NiV proteins or vector control were co-transfected with NiV-M in HEK 293T cells. Only NiV-C clearly enhanced M virus-like particle release. Both NiV-C and NiV-L were not detected in the cell lysate by Western due to low abundance. COX IV represent the loading control. **(C)** NiV-C (indicated by arrow) expression was confirmed by re-running more protein sample. The background band (indicated by asterisk) serves as a convenient loading control.

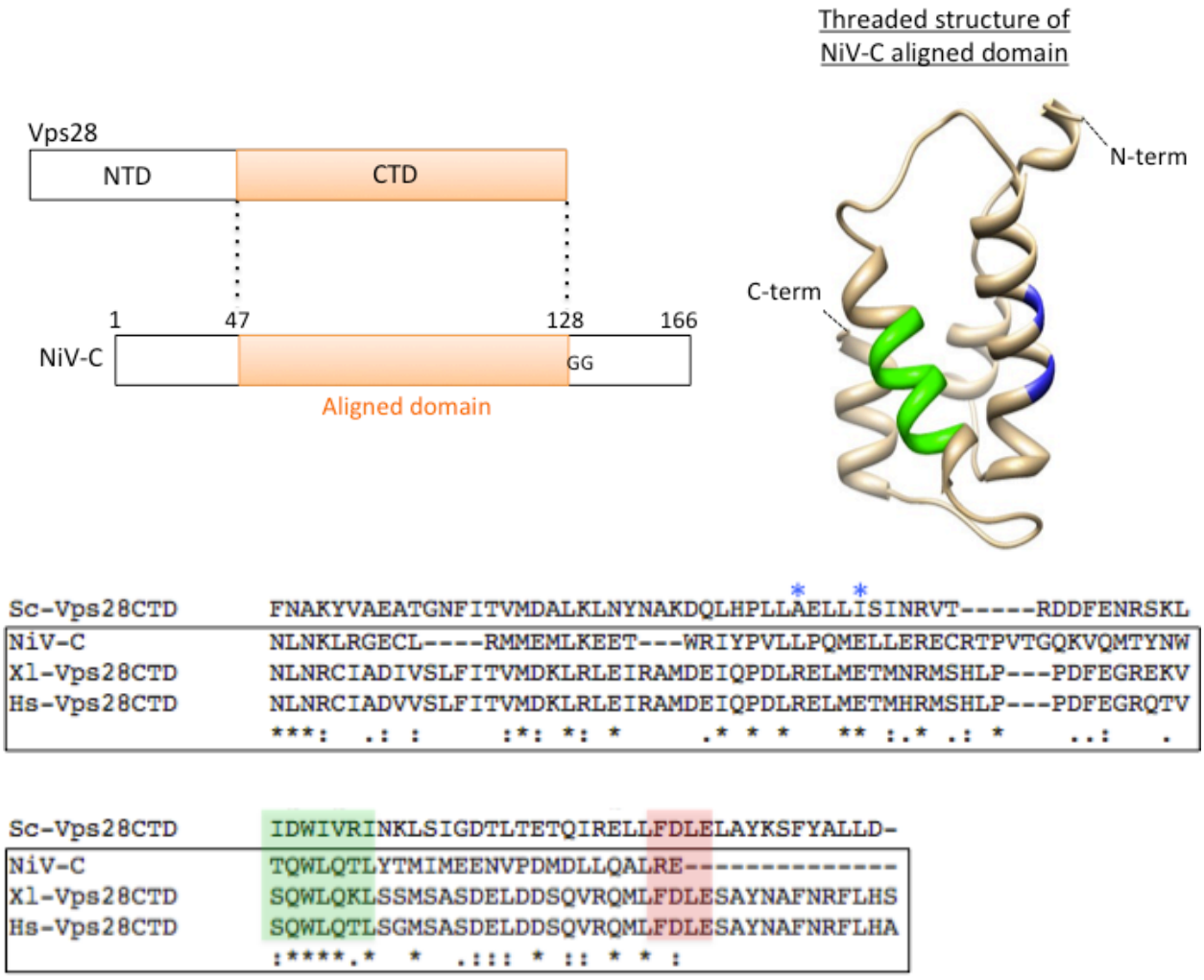

Figure 5-2. The middle half of NiV-C aligns with the *X. laevis* Vps28 C-terminal domain (CTD). Evaluation of the NiV-C sequence in the homology search and modelling program Phyre2 revealed an alignment of the middle half of NiV-C with the *X. laevis* Vps28 CTD. The threaded model of the NiV-C aligned domain is shown, forming the 4-helix bundle characteristic of the Vps28 CTD. Clustal omega multiple sequence alignment demonstrated an equally strong alignment between NiV-C and the *H. sapiens* Vps28 CTD. The *S. cerevisiae* Vps28 CTD is shown as well for comparison. *, identical residues; colon, strongly similar residues; period, weakly similar residues. The red highlight indicates the residues for Vps28 implicated in binding CHMP6 (yeast Vps20). The blue asterisks indicate the residues critical for the interface between Vps28 and Vps36 in yeast; in metazoans, however, these residues are charged, leading to disruption of the interface (in NiV-C, one of the two is charged). The green highlight indicates a 7 a.a. region of nearly identical sequence between NiV-C and *H. sapiens* Vps28. This region includes residues also implicated in the yeast Vps28-Vps36 interaction. The green and blue colors on the alignment sequence correspond to the colored highlights on the NiV-C threaded structure. Further, the presence of a "GG" sequence immediately following the aligned domain in NiV-C (see schematic above) suggests that it may act as a linker between protein domains.

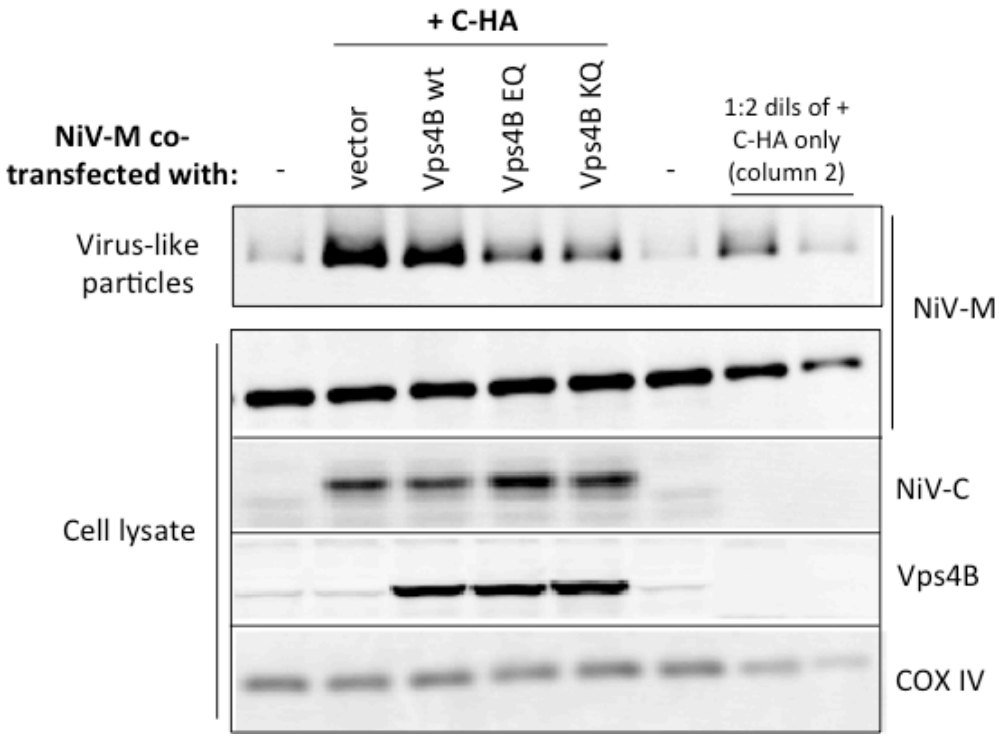

Figure 5-3. Inhibition of ESCRT inhibits C enhancement of M release. NiV-M was co-transfected with vector alone, C-HA with vector, or C-HA with HA-Vps4B, with total DNA remaining constant per condition. Vps4B EQ and KQ are the dominant-negative ATP-hydrolyzing and ATP-binding mutants, respectively. Both NiV-C and Vps4B were detected with anti-HA. COX IV represents the loading control.

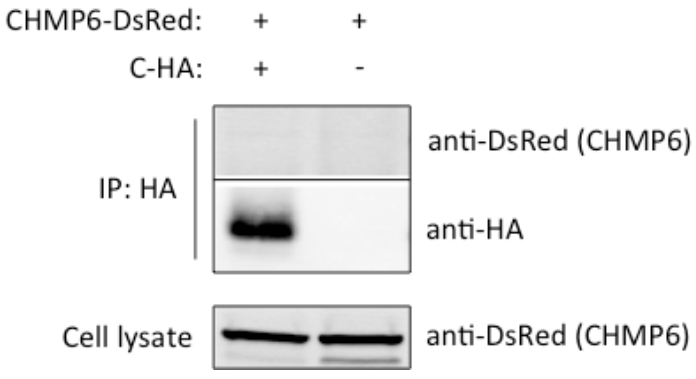

Figure 5-4. NiV-C does not co-immunoprecipitate CHMP6. Co-expressed CHMP6 did not detectably co-immunoprecipitate with NiV-C, confirming the implications of the sequence alignment in Figure 5-2, which showed the absence of residues important for CHMP6 binding in NiV-C (Figure 5-2, red highlight of alignment).

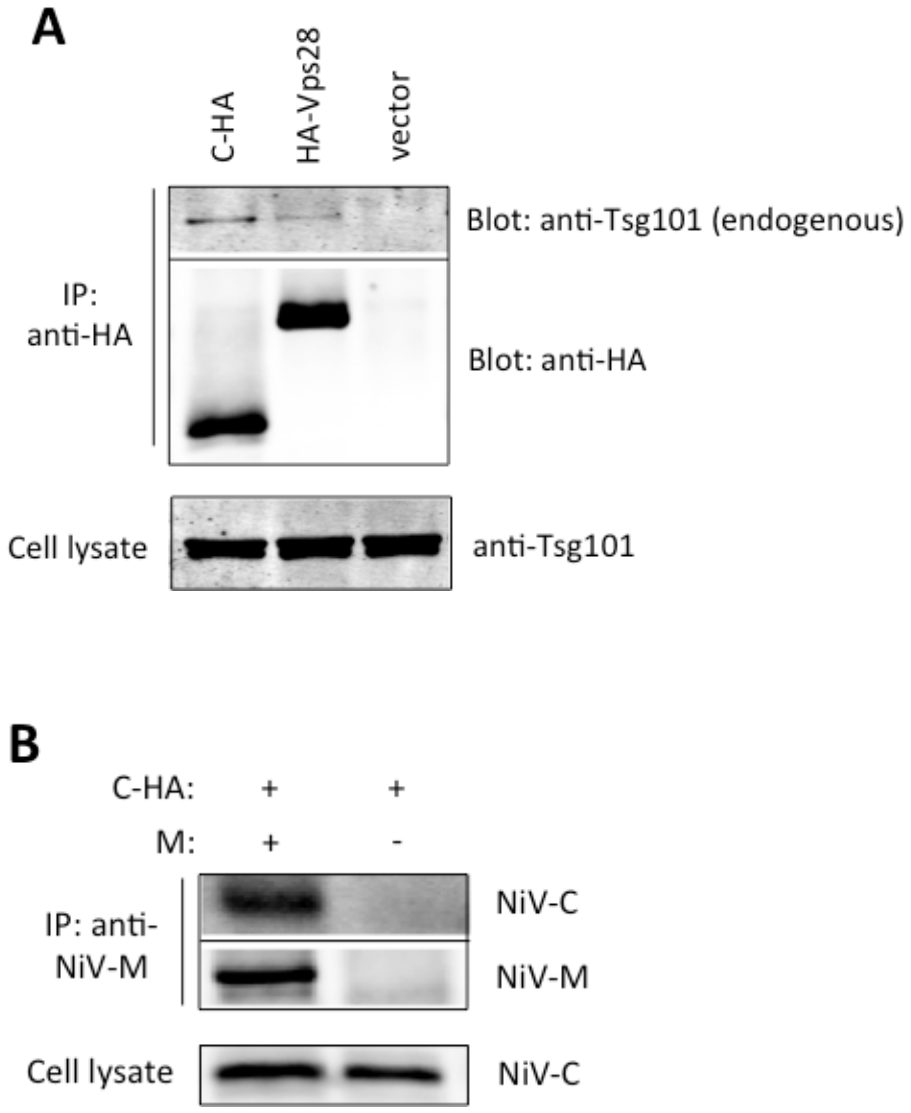

Figure 5-5. NiV-C interacts with both endogenous Tsg101 and NiV-M. (A) NiV-C-HA co-immunoprecipitated endogenous Tsg101 from HEK 293 cells. As a positive control, HA-Vps28 also pulled down Tsg101, as expected. **(B)** NiV-C co-immunoprecipitated with NiV-M, indicating a potential mechanism of recruitment of ESCRT to sites of M budding, mediated by C protein.

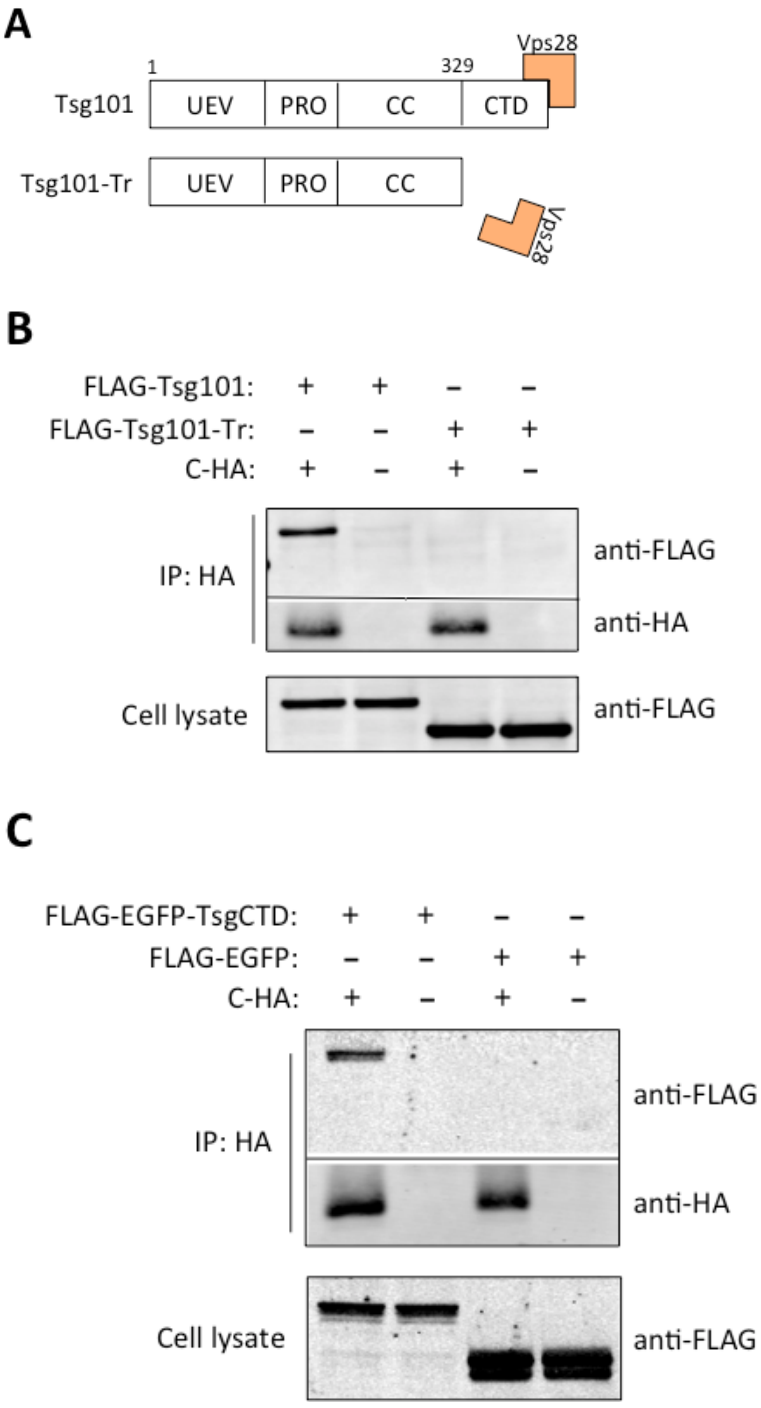

Figure 5-6. The C-terminal domain of Tsg101 is necessary and sufficient to interact with NiV-C. (A) The CTD of Tsg101 is known to bind Vps28. As we have verified ourselves (data not shown), the truncation mutant of Tsg101 does not bind Vps28. UEV, Ubiquitin E2 variant, binds ubiquitin and other factors; PRO, proline-rich; CC, coiled-coil. **(B)** Full-length but not truncated Tsg101 co-immunoprecipitates with NiV-C, indicating the Tsg101 CTD is necessary. **(C)** The Tsg101 CTD alone is sufficient to interact with NiV-C. As a negative control, the EGFP-alone control did not show detectable pulldown with NiV-C

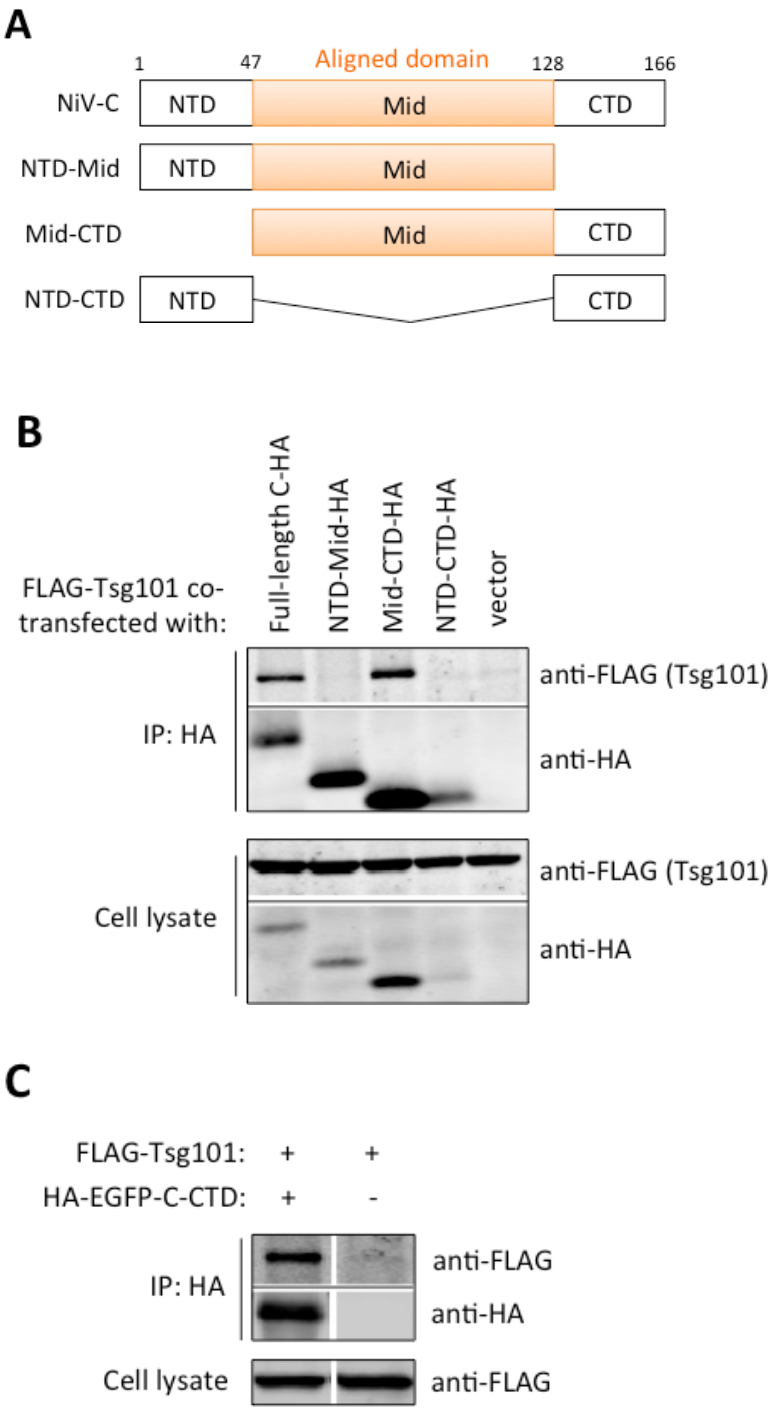

Figure 5-7. The C-terminal domain of NiV-C is necessary and sufficient to interact with Tsg101. (A) Single domain deletion mutants of NiV-C are shown. **(B)** Loss of the NiV-C-CTD resulted in loss of interaction (column 2). Although the CTD was also present in the NTD-CTD construct, which did not show Tsg101 pulldown (column 4), the mutant was poorly expressed. **(C)** The C-CTD alone, appended to EGFP, is sufficient to interact with Tsg101. One caveat here is the lack of a EGFP-alone negative control, which will be included in subsequent repeats.

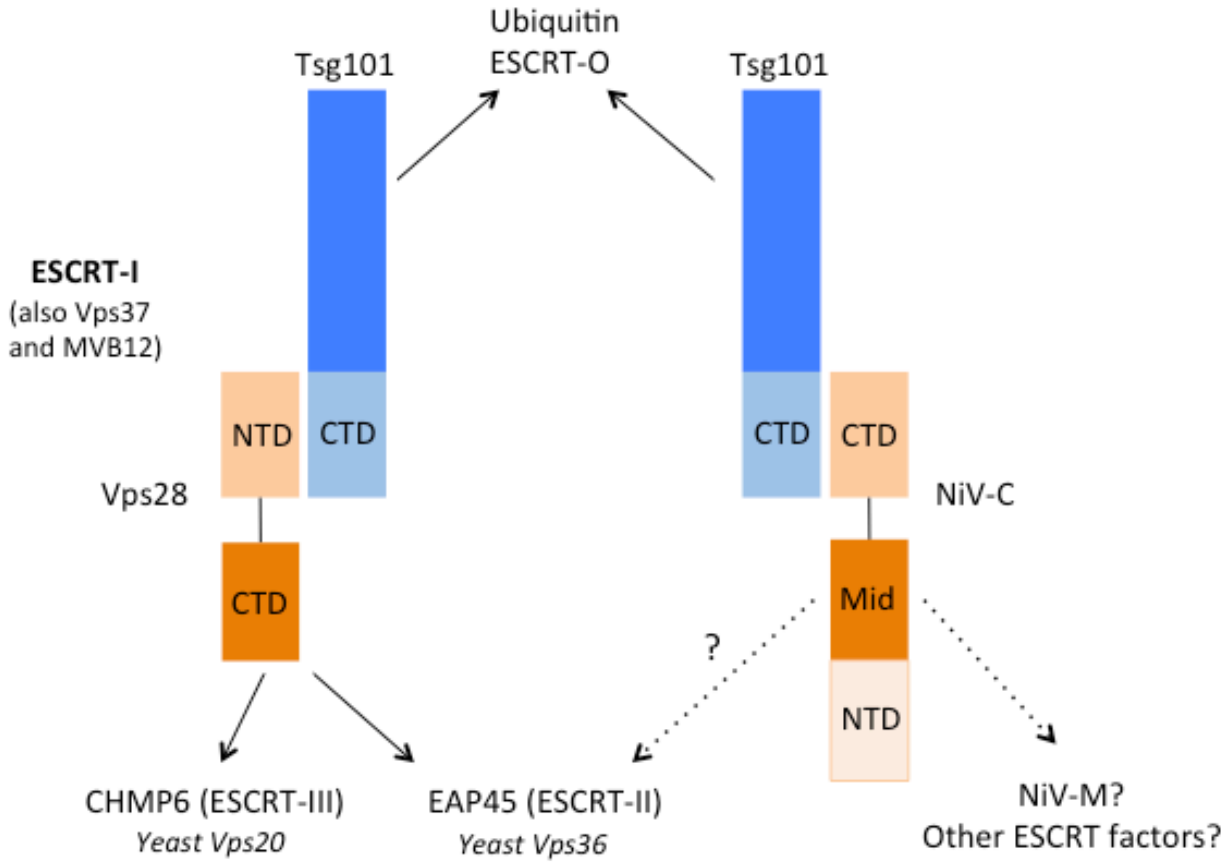

Figure 5-8. Schematic of interactions between Tsg101 and Vps28/NiV-C. On the left side, the known interaction between the Tsg101 CTD and Vps28 NTD is shown. The Vps28 CTD then acts as an adaptor for downstream components. On the right side, the analogous interaction of Tsg101 with the NiV-C CTD is shown. The middle domain that aligns with the Vps28 CTD may also act as an adaptor to other ESCRT components, potentially EAP45.

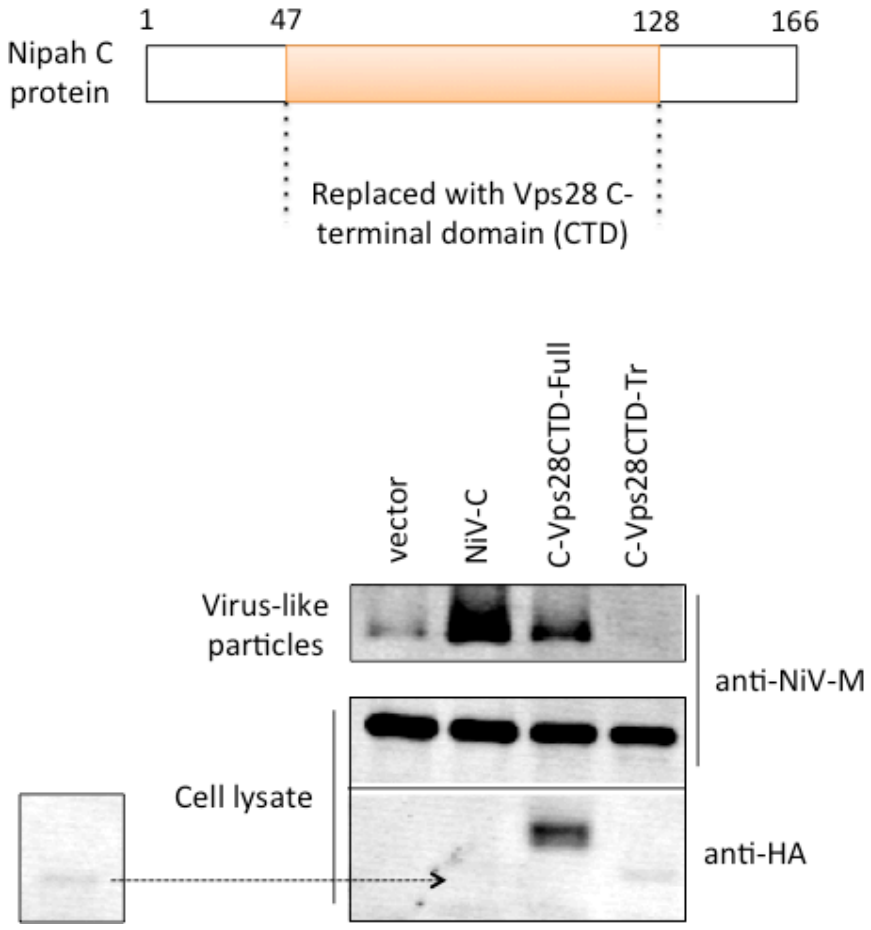

Figure 5-9. A NiV-C chimera with the middle domain substituted by the Vps28 CTD enhances M release. The middle aligned domain of NiV-C was replaced either by the precise aligned domain of Vps28 (ending 14 a.a. before the Vps28 CTD C-terminus), or the full Vps28 CTD (see alignment in Figure 5-2). Co-expression of the NiV-C chimera incorporating the full Vps28 CTD (C-Vps28CTD-Full), but not the truncated CTD representing the exact aligned portion (C-Vps28CTD-Tr), enhanced M budding. Due to low expression, wild-type NiV-C was not visible on the cell lysate immunoblot. Another replicate was present elsewhere on the same blot and showed a detectable NiV-C band, which is shown for illustration. The C-Vps28CTD-Full band runs above the NiV-C and C-Vps28CTD-Tr bands due to the additional 14 residues.

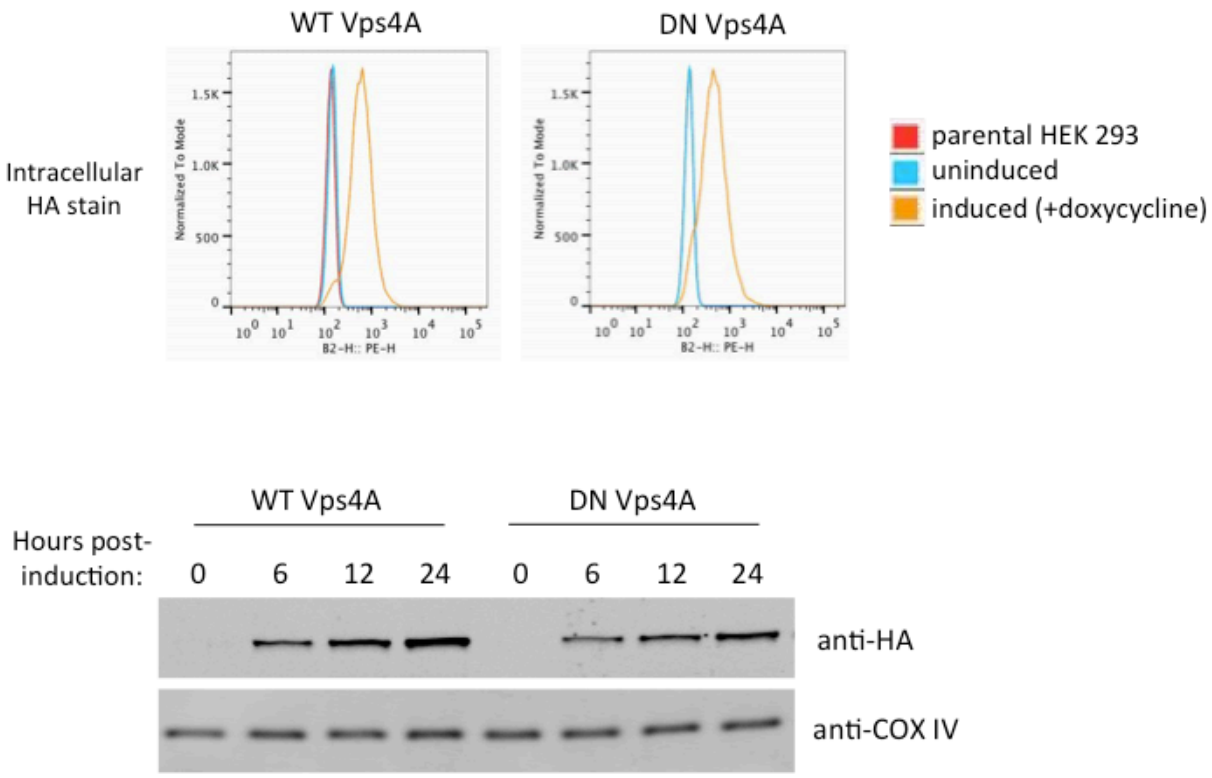

Figure 5-10. HA-Vps4-inducible HEK 293 cells uniformly express Vps4 within 6 hours after induction. HA-tagged wild-type or dominant-negative (the KQ mutant that does not bind ATP) Vps4A were introduced into FLP-In HEK 293 doxycyline-inducible cell lines as described previously for the paramyxovirus matrix proteins (Chapters 2.3 and 4.1). *Top panel*, Addition of doxycyline results in uniform expression of the HA-Vps4A proteins at 24 hours post-transfect. *Bottom panel*, the HA-Vps4A proteins are expressed within 6 hours of doxycyline induction. As cell lysates were collected at different time points and thus different cell densities, a preliminary blot was run to evaluate COX IV expression to normalize loading for the subsequent detection of HA-Vps4A.

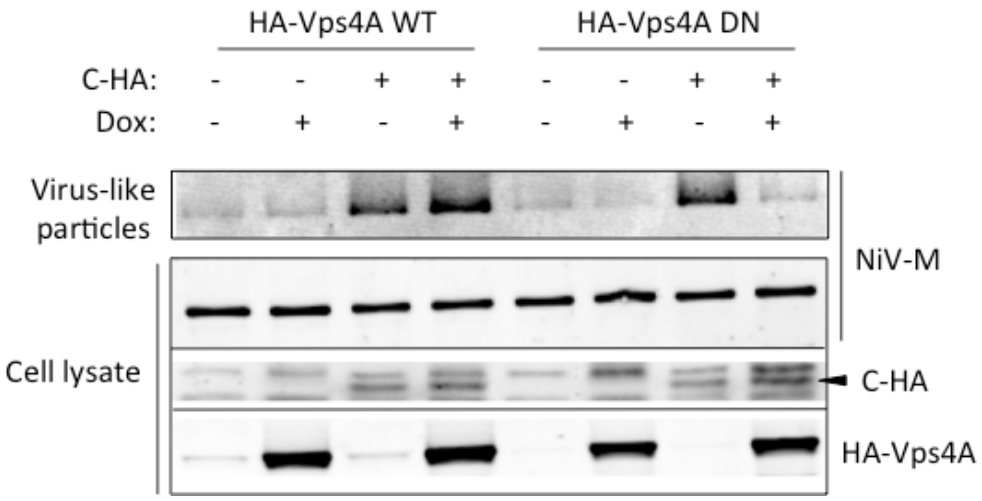

Figure 5-11. Induction of dominant-negative Vps4, but not wild-type Vps4, inhibits C enhancement of M budding. The HA-Vps4-inducible cell lines confirm the ESCRT-dependence of C enhancement. While induction of wild-type Vps4A with doxycyline did not inhibit virus-like particle release, induction of dominant-negative Vps4A reduced budding to non-enhanced levels.

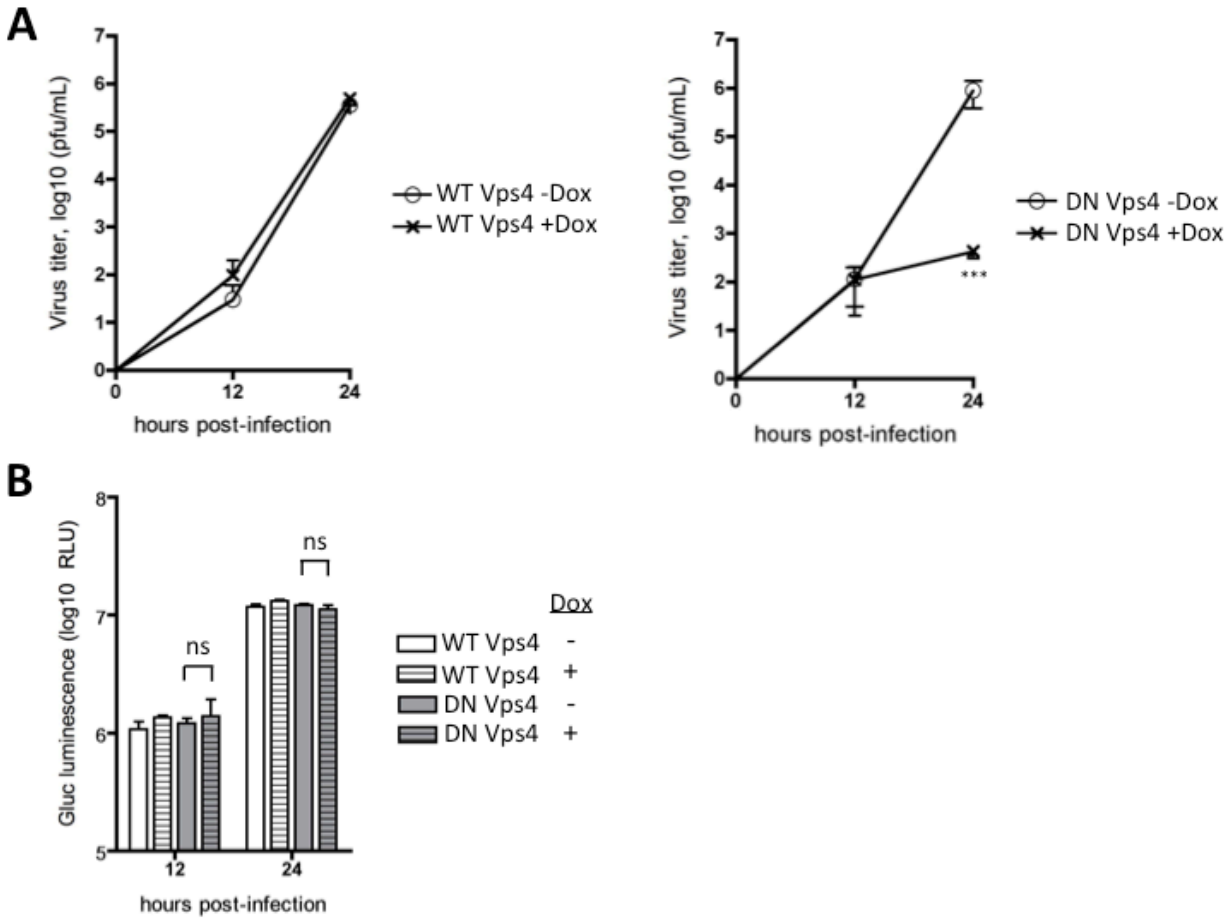

Figure 5-12. Induction of dominant-negative Vps4, but not wild-type Vps4, inhibits live NiV infectious particle production at an early time point post-infection. (A) Vps4-inducible cells were infected with wild-type rNiV-Gluc at a multiplicity of infection of 2. The cells were washed several times, with the last wash being saved for determination of residual background virus from the infection process. After washing, cells were incubated with or without doxycycline. Induction of wild-type Vps4A had no effect on subsequent production of infectious virus, whereas induction of dominant-negative Vps4A led to a significant decrease in infectious titers. ***, $p<0.001$. **(B)** Supernatants from the infection assay were evaluated for secreted Gluc-catalyzed luminescence at the indicated time points. The lack of difference between induced and non-induced conditions for the DN Vps4 cells indicates that lower protein production does not account for the defect in infectious virus production.

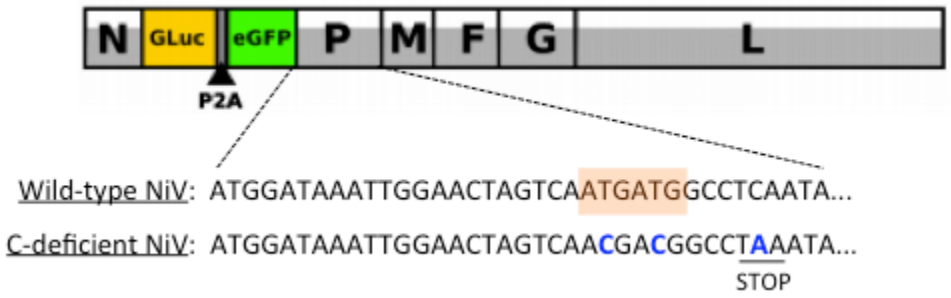

Figure 5-13. Rescue of C-deficient NiV via reverse genetics. C-deficient NiV was generated by mutating the indicated residues (blue highlight), thus removing the double alternative start codons as well as introducing a stop codon in the C ORF frame, all without affecting the coding sequence of the frame-shifted P gene. See Chapter 2 for details on this particular construct as well as henipavirus and paramyxovirus reverse genetics in general.

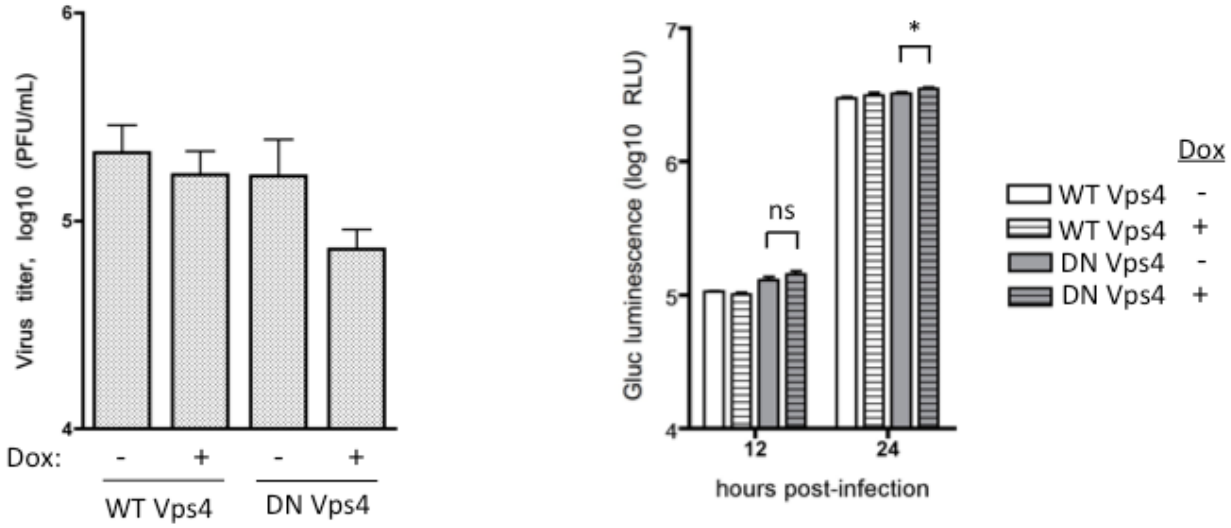

Figure 5-14. Sendai virus may display moderate ESCRT-dependence. In a similar experiment as shown in Figure 5-12, recombinant Sendai virus also expressing Gluc was tested for ESCRT-dependence of infectious virus production. Induction of DN Vps4 resulted in a modest decrease in titer (2-3-fold – note the log scale), although variability in the assay requires further confirmation. Similar to the experiment with NiV, induction of DN Vps4 did not lead to a defect in protein production, in fact leading to a minor increase in detected Gluc (*, $p < 0.05$).

REFERENCES

1. Patch JR, Crameri G, Wang LF, Eaton BT, Broder CC. Quantitative analysis of Nipah virus proteins released as virus-like particles reveals central role for the matrix protein. *Virology journal*. 2007;4:1.

2. Irie T, Nagata N, Yoshida T, Sakaguchi T. Recruitment of Alix/AIP1 to the plasma membrane by Sendai virus C protein facilitates budding of virus-like particles. *Virology*. 2008;371(1):108-120.

3. Sakaguchi T, Kato A, Sugahara F, et al. AIP1/Alix is a binding partner of Sendai virus C protein and facilitates virus budding. *Journal of virology*. 2005;79(14):8933-8941.

4. Gosselin-Grenet AS, Marq JB, Abrami L, Garcin D, Roux L. Sendai virus budding in the course of an infection does not require Alix and VPS4A host factors. *Virology*. 2007;365(1):101-112.

5. McDonald B, Martin-Serrano J. No strings attached: the ESCRT machinery in viral budding and cytokinesis. *Journal of cell science*. 2009;122(Pt 13):2167-2177.

6. Votteler J, Sundquist WI. Virus budding and the ESCRT pathway. *Cell host & microbe*. 2013;14(3):232-241.

7. Patch JR, Han Z, McCarthy SE, et al. The YPLGVG sequence of the Nipah virus matrix protein is required for budding. *Virology journal*. 2008;5:137.

8. Hanson PI, Shim S, Merrill SA. Cell biology of the ESCRT machinery. *Current opinion in cell biology*. 2009;21(4):568-574.

9. Williams RL, Urbe S. The emerging shape of the ESCRT machinery. *Nature reviews Molecular cell biology*. 2007;8(5):355-368.

10. Raiborg C, Stenmark H. The ESCRT machinery in endosomal sorting of ubiquitylated membrane proteins. *Nature*. 2009;458(7237):445-452.

11. Bishop N, Woodman P. TSG101/mammalian VPS23 and mammalian VPS28 interact directly and are recruited to VPS4-induced endosomes. *The Journal of biological chemistry*. 2001;276(15):11735-11742.

12. Kostelansky MS, Sun J, Lee S, et al. Structural and functional organization of the ESCRT-I trafficking complex. *Cell*. 2006;125(1):113-126.

13. Martin-Serrano J, Zang T, Bieniasz PD. Role of ESCRT-I in retroviral budding. *Journal of virology*. 2003;77(8):4794-4804.

14. Teo H, Gill DJ, Sun J, et al. ESCRT-I core and ESCRT-II GLUE domain structures reveal role for GLUE in linking to ESCRT-I and membranes. *Cell*. 2006;125(1):99-111.

15. Gill DJ, Teo H, Sun J, et al. Structural insight into the ESCRT-I/-II link and its role in MVB trafficking. *The EMBO journal*. 2007;26(2):600-612.

16. Pineda-Molina E, Belrhali H, Piefer AJ, Akula I, Bates P, Weissenhorn W. The crystal structure of the C-terminal domain of Vps28 reveals a conserved surface required for Vps20 recruitment. *Traffic*. 2006;7(8):1007-1016.

17. Im YJ, Hurley JH. Integrated structural model and membrane targeting mechanism of the human ESCRT-II complex. *Developmental cell*. 2008;14(6):902-913.

18. Ciancanelli MJ, Volchkova VA, Shaw ML, Volchkov VE, Basler CF. Nipah virus sequesters inactive STAT1 in the nucleus via a P gene-encoded mechanism. *Journal of virology*. 2009;83(16):7828-7841.

19. Lo MK, Peeples ME, Bellini WJ, Nichol ST, Rota PA, Spiropoulou CF. Distinct and overlapping roles of Nipah virus P gene products in modulating the human endothelial cell antiviral response. *PloS one*. 2012;7(10):e47790.

20. Mathieu C, Guillaume V, Volchkova VA, et al. Nonstructural Nipah virus C protein regulates both the early host proinflammatory response and viral virulence. *Journal of virology*. 2012;86(19):10766-10775.

21. Yoneda M, Guillaume V, Sato H, et al. The nonstructural proteins of Nipah virus play a key role in pathogenicity in experimentally infected animals. *PloS one*. 2010;5(9):e12709.

22. Emeny JM, Morgan MJ. Regulation of the interferon system: evidence that Vero cells have a genetic defect in interferon production. *The Journal of general virology*. 1979;43(1):247-252.

23. Salditt A, Koethe S, Pohl C, et al. Measles virus M protein-driven particle production does not involve the endosomal sorting complex required for transport (ESCRT) system. *The Journal of general virology*. 2010;91(Pt 6):1464-1472.

24. Li M, Schmitt PT, Li Z, McCrory TS, He B, Schmitt AP. Mumps virus matrix, fusion, and nucleocapsid proteins cooperate for efficient production of virus-like particles. *Journal of virology*. 2009;83(14):7261-7272.

25. Babst M, Odorizzi G. The balance of protein expression and degradation: an ESCRTs point of view. *Current opinion in cell biology*. 2013;25(4):489-494.

26. Rusten TE, Vaccari T, Stenmark H. Shaping development with ESCRTs. *Nature cell biology*. 2012;14(1):38-45.

27. Wegner CS, Rodahl LM, Stenmark H. ESCRT proteins and cell signalling. *Traffic*. 2011;12(10):1291-1297.

28. Siomi H, Siomi MC. RISC hitches onto endosome trafficking. *Nature cell biology*. 2009;11(9):1049-1051.

CHAPTER 6

SUMMARY

In this work, we have established methods that facilitate investigations into henipavirus (and, more broadly, paramyxovirus) biology and virus-host interactions. We used these methods in subsequent studies of the biology and function of the Nipah virus matrix protein, which plays the central role in virus assembly and budding. Mutagenesis of conserved residues and motifs in the Nipah virus matrix protein revealed insights into matrix function, including post-translational modifications and intracellular trafficking events important for matrix function. Comprehensive identification of cellular factors that interact with Nipah virus matrix, as well as with the matrix proteins from other paramyxoviruses that represent the major genera of *Paramyxovirinae*, confirmed the importance of host intracellular trafficking pathways for paramyxovirus matrix function. We then characterized the recruitment and role of a specific host pathway, the ESCRT pathway that catalyzes membrane fission events, in the Nipah C protein-mediated, matrix protein-driven budding of Nipah virus.

Reverse genetics as a critical tool for molecular investigations

Similar to the importance of gene knockout and modification technology for cell lines and animals models for cell biological and developmental studies, reverse genetics is a critical tool for the detailed study of virus biology. In this study, we established reverse genetics systems for Nipah and Hendra viruses, and we improved the efficiency of virus rescue for the henipaviruses as well as other paramyxoviruses as compared to existing systems. In subsequent studies, we used these systems to make recombinant viruses expressing useful fluorescent and bioluminescent reporters, as well as viruses modified with specific mutations under investigation. To a degree we did not anticipate when we began working with this technology, reverse genetics, and the recombinant viruses we have rescued, have become integral to our studies of virus biology and virus-host interactions.

The use of CRISPR/Cas gene-editing technology to inducibly knockdown host factors

In Chapter 4.2, we report an application of the recent CRISPR/Cas gene-editing technology, which makes it relatively straightforward to specifically modify the genomes of diploid and hyperploid cells, to inducibly knockdown an essential host factor of interest. A destabilization domain (DD) was N-terminally tagged on the essential host protein TCOF1/Treacle at all alleles, resulting in a tagged protein that maintained wild-type function in the presence of the stabilizing Shield-1 compound, but was rapidly destabilized and degraded in the absence of the compound. This method therefore represents a way to rapidly knockdown host factors at the protein level, especially useful in cases where the protein is essential for host viability. We anticipate that not only this specific method, but our increased facility with the CRISPR/Cas gene-editing technology as a consequence of developing this method, will facilitate our future work investigating the interface between virus and host. As an example of the new horizons that the technology opens, our work in Chapter 5 suggests that the middle domain of NiV-C may mimic some of the function of the Vps28 C-terminal domain. Since it is known that the Vps28 C-terminal domain is required for ESCRT function,[1] would completely knocking-in the middle domain of NiV-C in place of the Vps28 C-terminal domain, instead of removing the Vps28 C-terminal domain altogether, allow cell viability? Before the advent of efficient gene-editing technologies, such experiments would have been inordinately arduous and likely not considered; with the most recent technology, however, such experiments are now not only possible but also relatively simple to plan and perform.

Post-translational modification and intracellular trafficking pathways in matrix function

In this work, we describe palmitoylation and ubiquitination as post-translational modifications that are critical for matrix function. Although work remains to be done to conclusively confirm NiV-M palmitoylation and the conservation of this modification with other paramyxovirus matrix proteins, this finding would be both novel, as palmitoylation of paramyxovirus matrix proteins has not been described, as well as illuminative for understanding the trafficking

pathway of paramyxovirus matrix proteins. In Chapter 3.2, we described the lack of membrane association of a single point mutant, K258A, despite preservation of much of the putative charged membrane-binding surface illustrated in Chapter 3.1. It therefore seems there may be determinants of membrane-binding and trafficking that are not solely determined from the charged residues of the matrix protein alone. It is intriguing to note that in Chapter 4.1, we describe the interaction of paramyxovirus matrix proteins with many components associated with the Golgi complex and Golgi trafficking. The Golgi has in fact been described as a "super-reaction center" for palmitoylation,[2] as the dynamics of palmitoylation occurs in specific cellular locations, and often at the Golgi complex.[3,4] The trafficking of matrix proteins and their requirements for specific post-translational modifications may therefore be linked.

We found such an association between trafficking and the post-translational modification of ubiquitination, as we found that ubiquitination of a conserved lysine within the bipartite nuclear localization sequence of Nipah virus matrix regulated the nuclear-cytoplasmic trafficking of NiV-M (Chapter 3.2). This nuclear-cytoplasmic trafficking was a central feature of matrix biology, as mutations of this lysine that prevented nuclear import or resulted in nuclear retention prevented matrix budding. These findings were extended to representative paramyxoviruses from the major genera of the *Paramyxovirinae*, where we found that, as for NiV-M, the matrix proteins of Sendai virus and mumps virus likewise displayed a reliance on ubiquitination of the conserved lysine for their function (Chapter 3.3). In sum, these findings underscore the role of nuclear-cytoplasmic trafficking of the matrix protein in the paramyxovirus life cycle; however, the ultimate significance of this trafficking for matrix function and virus replication remains unclear. It remains to be seen whether the matrix proteins of some paramyxoviruses require nuclear trafficking to gain an important modification or interaction for virus replication, whether they conversely interfere with host processes to benefit virus replication, or perhaps both.

Finally, our findings that overexpression of, or lost interaction with, cellular host factors modulate the localization and function of NiV-M (Chapter 4.1), in combination with our identification of numerous components involved in vesicular trafficking and cytoskeletal dynamics as paramyxovirus matrix-interacting factors, strongly suggest the importance of cellular trafficking pathways for matrix function. To gain the full measure of the role of these interactions, however, it will be critical to evaluate these interactions in the context of other viral components. Although possible for certain functions, it would be surprising if the matrix protein did not evolve to act in concert with other viral factors; after all, the matrix protein has never been required to act on its own, in isolation from the full virus context. We found this necessity to examine matrix function in a fuller context to be essential even in that step of virus replication considered to be the primary domain of matrix, the final budding step during virion formation.

The efficient budding of Nipah virus requires C-mediated recruitment of the host ESCRT pathway

In our concluding work, we demonstrated that the budding of Nipah virus is dependent on the host ESCRT pathway, which catalyzes intracellular membrane fission events where the cytoplasm has access to the inside of the constricting neck (as during virion formation). The C protein, by interacting with both NiV-M and the host ESCRT factor Tsg101, mediated this dependence. Although we first noticed the C enhancement of NiV-M budding without consideration of ESCRT, we came to examine the role of ESCRT upon determining that the middle half of the C protein aligns with a core component of ESCRT, Vps28. Although many viruses have been described to use small peptide motifs to recruit the ESCRT pathway (i.e., “PTAP” on HIV-1 Gag), our findings on NiV-C represent the first time that mimicking of an entire host domain to recruit the ESCRT pathway has been described. Such an extensive alignment with a host factor is all the more remarkable considering the constraints placed on the C protein sequence, which, as an alternative ORF within the viral phosphoprotein gene (a

subunit of the viral polymerase), must evolve its sequence in ways that do not affect the function of the main ORF. As indicated in Chapter 5, the conservation of specific residues between NiV-C and human Vps28, in particular a conserved patch of 7 a.a., is an opportunity to further define the interactions of human Vps28 itself, which remain unclear. Although future experiments will illuminate the specific role of this aligned domain within the C protein for its function in the budding process, our findings have already clarified the literature regarding the function of the Nipah C protein, revised the role of ESCRT for Nipah virus replication, and further emphasized the importance of examining matrix function in a broader viral context.

REFERENCES

1. Kostelansky MS, Sun J, Lee S, et al. Structural and functional organization of the ESCRT-I trafficking complex. *Cell*. 2006;125(1):113-126.

2. Salaun C, Greaves J, Chamberlain LH. The intracellular dynamic of protein palmitoylation. *The Journal of cell biology*. 2010;191(7):1229-1238.

3. Rocks O, Gerauer M, Vartak N, et al. The palmitoylation machinery is a spatially organizing system for peripheral membrane proteins. *Cell*. 2010;141(3):458-471.

4. Linder ME, Deschenes RJ. Palmitoylation: policing protein stability and traffic. *Nature reviews Molecular cell biology*. 2007;8(1):74-84.